Mechanical, Industrial and Manufacturing Technologies

Edited by
Li Kai

TRANS TECH PUBLICATIONS

Mechanical, Industrial and Manufacturing Technologies

Edited by
Li Kai

Mechanical, Industrial and Manufacturing Technologies

Selected, peer reviewed papers from the
2012 3rd International Conference on
Mechanical, Industrial and Manufacturing Technologies
(MIMT 2012),
March 24 - 25, 2012, Shenzhen, China

Edited by

Li Kai

Copyright © 2012 Trans Tech Publications Ltd, Switzerland

All rights reserved. No part of the contents of this publication may be reproduced or transmitted in any form or by any means without the written permission of the publisher.

Trans Tech Publications Ltd
Kreuzstrasse 10
CH-8635 Durnten-Zurich
Switzerland
http://www.ttp.net

Volume 187 of
Applied Mechanics and Materials
ISSN 1662-7490

Full text available online at *http://www.scientific.net*

***Distributed** worldwide by*

Trans Tech Publications Ltd
Kreuzstrasse 10
CH-8635 Durnten-Zurich
Switzerland

Fax: +41 (44) 922 10 33
e-mail: sales@ttp.net

and in the Americas by

Trans Tech Publications Inc.
PO Box 699, May Street
Enfield, NH 03748
USA

Phone: +1 (603) 632-7377
Fax: +1 (603) 632-5611
e-mail: sales-usa@ttp.net

PREFACE

Dear Distinguished Delegates and Guests,

The Organizing Committee warmly welcomes our distinguished delegates and guests to 2012 3rd International Conference on Mechanical, Industrial, and Manufacturing Technologies (MIMT 2012) held during March 24-25, 2012 in Shenzhen, China.

MIMT 2012 is sponsored by International Association of Computer Science and Information Technology (IACSIT) and Guizhou University. The conferences together report the results of research efforts in a broad range of Mechanical, Industrial, and Manufacturing Technologies. These conferences are aimed at discussing with all of you the wide range of problems encountered in present and future high technologies. The MIMT 2012 is organized to gather members of our international community scientists so that researchers around the world can present their leading-edge work, expanding our community's knowledge and insight into the significant challenges currently being addressed in that research. The conference Program Committee is itself quite diverse and truly international, with membership from the Americas, Europe, Asia, Africa and Oceania.

This proceeding records the fully refereed papers presented at the conference. The main conference themes and tracks are Mechanical, Industrial, and Manufacturing Technologies. The main goal of these events is to provide international scientific forums for exchange of new ideas in a number of fields that interact in-depth through discussions with their peers from around the world. Both inward research; core areas of Mechanical, Industrial, and Manufacturing Technologies and outward research; multi-disciplinary, inter-disciplinary, and applications will be covered during these events.

The conference has solicited and gathered technical research submissions related to all aspects of major conference themes and tracks. All the submitted papers in the proceeding have been peer reviewed by the reviewers drawn from the scientific committee, external reviewers and editorial board depending on the subject matter of the paper. Reviewing and initial selection were undertaken electronically. After the rigorous peer-review process, the submitted papers were selected on the basis of originality, significance, and clarity for the purpose of the conference. The selected papers and additional late-breaking contributions to be presented as lectures will make an exciting technical program. The conference program is extremely rich, featuring high-impact presentations.

The high quality of the program – guaranteed by the presence of an unparalleled number of internationally recognized top experts – can be assessed when reading the contents of the program. The conference will therefore be a unique event, where attendees will be able to appreciate the latest results in their field of expertise, and to acquire additional knowledge in other fields. The program has been structured to favor interactions among attendees coming from many diverse horizons, scientifically, geographically, from academia and from industry. Included in this will to favor interactions are social events at prestigious sites.

We would like to thank the program chairs, organization staff, and the members of the program committee for their work. Thanks also go to Editors from TTP Press, for their wonderful editorial service to this proceeding. We are grateful to all those who have contributed to the success of MIMT 2012. We hope that all participants and other interested readers benefit scientifically from the proceedings and also find it stimulating in the process. Finally, we would like to wish you success in your technical presentations and social networking.

We hope you have a unique, rewarding and enjoyable week at MIMT 2012 in Shenzhen of China.
With our warmest regards,

MIMT 2012 Organizing Committees
March 24-25, 2012

Shenzhen, China

Committees

Honorary Chair

IEEE Fellow, Prof. Wang Jun, The Chinese University of Hong Kong, Hong Kong (2011 Keynote)
IEEE Fellow, Prof. Ning Xi, City University of Hong Kong, Hong Kong (2011 Keynote)
ASME Fellow, Prof. Wei-Hsin Liao, Chinese University of Hong Kong, Hong Kong (2011 Keynote)
IEEE Fellow, Prof. Chin-Chen Chang, Feng Chia University, Taiwan

Conference Chairs

Senior Member, Prof. Steve Thatcher, University of South Australia, Australia
Senior Member, Prof. Promod K. Jain, Indian Institute of Technology, India

Program Committee Chairs

Senior Member, Prof. Reza Malekian, Azad University, Iran
Senior Member, Prof. Dehai Zhang, Yunnan University, China
Senior Member, Prof. Amit Kumar Saxena, G G University, India
Senior Member, Prof. Adel A. Sharif, California State University Los Angeles, USA
Senior Member, Prof. Debojyoti Mitra, Sir Padampat Singhania University, India

Conference Steering Chairs

Senior Member, Prof. Othman Inayatullah, Malaysia Perlis University, Malaysia
Senior Member, Prof. Jun Guo, East China Normal University, China
Senior Member, Prof. M. Sreekumar, Indian Institute of Information Technology, India

Table of Contents

Preface and Committees

Chapter 1: Research in Numerical Simulation and Optimisation

Numerical Simulation on Shock Initiation of Double-Shell Charges by High Velocity Impact
X. Liu and Q.M. Zhang 3

Research on Simulation System of Aero-Generator
X.J. Zang and J. Song 8

Real-Time Attitude Simulation of Aerocraft Using dSPACE Emulator and Three-Axis Turn Table
D.C. Xie, Z.W. Wang and Q.H. Zeng 15

Electric Vehicle Transmission Gear Ratio Optimization Based on Particle Swarm Optimization
Q. Gu and X.S. Cheng 20

Numerical Simulation Research on the Hydrodynamic Forces Acting on a Tanker in Oblique Motion
C.S. Zhan 27

Study on the Efficiency Optimization of U-Shaped Curve Rail Type AS/RS
H. Liu, Y.B. Huang and Y. Xing 33

Chapter 2: Characteristic Studies of Mechanical and Material Systems

Study on Sheet Bonding and Break Strength Characteristics
J.S. Tao and P.S. Yang 41

Static and Dynamic Stiffness Characteristics Analysis of Hydro-Pneumatic Suspension
J.H. Wei, H. Du and H. Lin 46

Evaluation of Tensile Properties of Pressure Vessel Materials by Shear Punch Test Method
T. Ramesh, R.V. Prakash, S. Suresh and N. Raju 53

Analysis of the Dynamic Response of a Cracked Beam Structure
D.N. Thatoi, J. Nanda, H.C. Das and D.R. Parhi 58

Visualization of Supersonic Non-Newtonian Liquid Jets
A. Matthujak, C. Kasamnimitporn, W. Sittiwong and K. Pianthong 63

Deformation and Stresses Analysis in FG Rotating Hollow Disk and Cylinder Subjected to Thermal and Mechanical Load
A.R. Khorshidvand and M. Javadi 68

Test and Numerical Analysis of Underwater Explosion on Circular Plates
A.A.S. Koohsar, S.M.S. Nasereddini and E. Bazrafshan 74

Comparing of the Welding Atmosphere Moisture Effect on Hydrogen Distribution in TI-6AL-4V, Pure Commercial Titanium and TI-15V-3CR-3SN-3AL Weld Joints
S.M.S. Nasereddini, A.A.S. Koohsar and E. Bazrafshan 80

Chapter 3: Chaotic States and Analysis of Systems

Design and Research of Electric Vehicle Driving System Based on SOPC
Y. Zhao and H. Qi 87

Study on the Temperature Filed of Wet Dual Clutch Transmission during Starting Process
X. Liu, X.S. Cheng, Y. Li, Q. Gu and Y.S. Wang 95

Research on Taylor Vortices in the Wedge-Shaped Air Gap of Evaporation Cooling Turbo Generator
J.S. Gao and G.B. Gu 103

Omni-Vision System of Intelligent Car Based on DSP & FPGA
Y.B. Zhou and Y.N. Yang 109

Finite-Time Chaos Control and Synchronization of the New Chaotic System with Unknown Parameters
K.E. Li and Y.H. Xu 115

Chaotic Analysis of the Velocity Signal in Impinging Stream Mixer
J.W. Zhang and Y.F. Song 122

Modeling and Experiment on Active Vibration Control of Hydraulic Excitation System
H.X. Zhang and L.X. Miao 130

The Study of Ball and Plate System Based on Non-Linear PID
S.Q. Sun and L. Li 134

Finite Element Analysis of the Static/Dynamic Behavior of Wind Turbine Gearbox
W. Jing, X.J. Sun, W. Sun and A.G. Guo 138

Design of Auto Route Identified Vehicle Model Based on MC9S12XS128
F. Zheng 146

Finite Element Analysis of Flextensional Transducer with Slotted Shell
S. Chen and Y. Lan 151

Chapter 4: Vibrational Analysis and Mechanics of Structures etc.

Experimental Study on Bending Capacity of Plain Wall System
H.M. Yee, C.K. Keong and R. Rohim 157

Gear Vibration Monitoring System Based on Virtual Instruments
C.H. Wu, Y. Guo and Y.J. Fan 161

Design and Dynamic Walking Control of Humanoid Robot SCUT-*I*
S. Bi, Z.J. Zhuang, H.Q. Min and H.X. Mo 165

Maximum Bending Moment and Maximum Additional Bending Moment for High Vertical Vessels under Wind Pressure
J. Tian and Z.N. Zhang 173

Experimental Research on Trajectory Control of Walking Rehabilitation Training Robot
Z. Wen, J.W. Qian, L.Y. Shen and Y.N. Zhang 177

Kinematics Simulation and Control System Design of Serial Robot Based on ADAMS and Pro/E
H.M. Fan 186

Design of an Adaptive Terminal Dynamic Sliding Mode Controller for Anti-Ship Missiles
P.C. He, L.S. Jia, Y.L. Wang and W.G. Zhang 190

Seismic Analysis for the Suspended Converter Valve Tower of the UHV
Q.G. Sun, X.F. Wu, J.J. Di and Y.C. Zhou 196

Chapter 5: Materials Science and Technologies

Electronic Structures of X Level due to Indium-Carbon Dimers in Silicon
H. Kawanishi and Y. Hayafuji 205

Improvement of Corrosion Resistance of Rare Earth Element (REE)-Based Anodic Oxidation Coating on AZ91D Magnesium Alloy
M.Z.M. Zain, S. Illias, M.M. Salleh, K.A. Ismail and Z. Nooraizedfiza 210

Enhancement of Mica Paper Insulation Strength with Surface Modification
X.W. Zhang, S.P. Liu, Y.P. Qian and Y.B. Zhu 215

Index Loss Analysis of YBCO Coated-Conductor Coils by Means of Simulation
X. Li, Y.S. Wang and Y.R. Zhang 220

The Synthesize and Properties of Aquosity Polyester Acrylate Nanoemulsion
C. Yan, C.Z. Ma, G.C. Zhang and F.J. Qi 227

A Novel Anti-Fuse Based on (Ba, Sr)TiO_3(BST) and Pb(Zr, Ti)O_3 (PZT) Thin Films
Q.Y. Tang, L. Yuan, Y.F. He, P. Li, X.D. Xie and G. Wang 231

Fiber-Optic Electric Field Sensor Based on Electrostriction Effect
J. Zhao, H.Y. Zhang, Y.S. Wang and H.W. Liu 235

Life Prediction for Silicon Pressure Sensor Based on SVR
Z.H. Zhai and P.L. Wu 241

Research on Ytterbium Doped Phosphate Glasses
L.D. Fan and L.H. Wu 245

Synthesis of an Oxidation Resistant Coating for Ni-Based High Temperature Structural Materials by Dip Coating
W.T. Chen, R.T. Wu, K. Chien, L.T. Wu, H. Gao and H. Harada 251

The Study of TiCN Coating Based on Vacuum Arc Ion Plating and its Performance
L.J. Zou 255

A New Design of Underwater Robot Fish System Using Shape Memory Alloy
P.H. Huang and J. Wang 260

Au Plating Failure Prevention on the Electronic Industry
X.G. Liu, P. Liu, X.L. Gu and X.B. Zhao 267

Thermodynamic Evaluation and Assessment of the Ti-U Binary System
Z.M. Cao, K.P. Wang, G.W. Du and Z.Y. Qiao 272

Chapter 6: Mechanical/ Automotive Systems and Allied Topics

Design and Implementation of SCM-Based Smart Cars
M. Lin, Y.M. Zhang and L.G. Cui 281

Traction Control for a Fuel Cell Hybrid Vehicle (FCHV)
W.J. Yang and Y.B. Kim 286

Kinematic Analysis of an Anthropomorphic Robot Hand
P.K. Parida, B.B. Biswal and D.N. Thatoi 293

The Fuzzy Comprehensive Evaluation of Laser Weapon System Combat Effectiveness
H. Li and L.H. Guo 298

Research on a Nonlinear Fuzzy Comprehensive Assessment Method for Oil & Gas Pipeline Failure Based on Fault Tree Analysis
X. Wu, C.Y. Xiao and X.Y. Xu 304

Damping Force Analysis of Magnetorheological (MR) Dampers
H.J. Xing 311

Numerical Investigation of a Blade Riblet Surface for Drag Reduction Applications with Large Eddy Simulation Method
N.H. Wu, Y.H. Tang, C.B. Zhao, W. Lin, X.M. Chen and R.H. Li 315

The Design and Manufacture of the Intelligent Electric Cars for Firefighting Based on SCM
M.L. Tang, L. He, H.Y. Wu, W. Wang and L.S. Cai 320

Investigation of the Temperature Distribution in the Lithium-Ion Battery for Pure Electric Vehicles
L. Zheng, B. Wu and G.Q. Xu 324

CHAPTER 1:

Research in Numerical Simulation and Optimisation

© (2012) Trans Tech Publications, Switzerland
doi:10.4028/www.scientific.net/AMM.187.3

Numerical Simulation on Shock Initiation of Double-shell Charges by High Velocity Impact

Xue Liu [1, 2, a], Qingming Zhang [2,b]

[1] Key Laboratory of Urban Security and Disaster Engineering of China Ministry of Education, Beijing University of Technology, Beijing, China

[2] State Key Laboratory of Explosion Science and Technology, Beijing Institute of Technology, Beijing, China

[a]liuxue429@sohu.com, [b]qmzhang@bit.edu.cn

Keywords: high velocity impact, double-shell charges, shock initiation

Abstract. A two dimensional axisymmetric finite element analysis is preformed using AUTODYN-2D hydrocode, to simulate the dynamic response of explosive, named PBX9404 which is located behind double-shell, by the impact to shell surface resulted from high velocity spherical projectile. Simulation results shows that shock to detonation transition occurs when impact velocity is between 3.6~3.9km/s; but when the velocity increases to 4~4.3km/s, projectile will break up into pieces and the surface momentum density of debris cloud to second shell will decrease dramatically so no shock to detonation could occur. When the velocity further elevates to 4.4 km/s and above, projectile kinetic energy will cover the energy of projectile break-up, and also provide sufficient energy to further increase the surface momentum density of debris cloud, with a result that shock to detonation can be observed again. In conclusion, there is a velocity blind zone in shock to detonation of high velocity projectile to double-shell charges.

Introduction

A great number of studies on shock initiation of single-shell charges impacted by projectile have been reported. Most of them investigated the effect of projectile mass, nose shape, shell thickness and etc. on threshold impact velocity, and mainly focused on low velocity projectile [1-3]. Only a few literatures on shock-induced initiation caused by high velocity projectiles are available.

Shock initiation of covered explosive caused by projectile with velocity 3～6km/s is in field of high velocity impact. And high temperate, high pressure, break-up of projectile, complicated physics processes are all involved in the high velocity impact.

In this paper, we investigated shock-induced initiation of double-shell charges by an impact of high velocity projectile using numerical simulation analysis. Due to the limitation of experimental equipments capability, only two-stage light gas gun can launch projectile with mass about 1g to the velocity 3～6km/s [4]. However, light gas gun target chamber cannot stand the overpressure damage caused by detonation, so using computer simulation to study the shock-detonation process is feasible.

Computational modeling

AUTODYN-2D was used to simulate the shock-induced initiation of PBX9404 explosive with double-shell. Due to the symmetry of the structural geometry and the impact loading, two-dimensional axisymmetric model was applied to perform the analysis. The schematic sketch for the numerical modeling is depicted in Figure 1 (a). The projectile is steel sphere of 5mm in diameter; the double-shell is consisted of double aluminum alloy shell of 5mm in thickness and net distance is 50mm between shells; PBX9404 explosive, which is covered by second layer shell, is 10mm in thickness and 20mm in diameter. To record the time history profile of the pressure and reaction fraction, 10 gauges with interval 1mm were assigned in the explosive along positive x-axis direction, as shown in Figure 1 (b).

For high velocity impact, most severe deformation will occur in the interface between projectile and shells and also the free surface because of the high impact velocity. Thereby the Lagrange arithmetic is not applicable. In this paper, SPH (smoothed particle hydrodynamics) arithmetic was adopted to set up modeling of projectile and shells, to avoid the grid distortion and negative volume in finite elements method [5]. Hydrodynamic tensile failure model was used to describe the spalling and cavitation of projectile and shell material. Table 1 shows the different calculation, equation of state, strength model and failure model of projectile, shell and explosive.

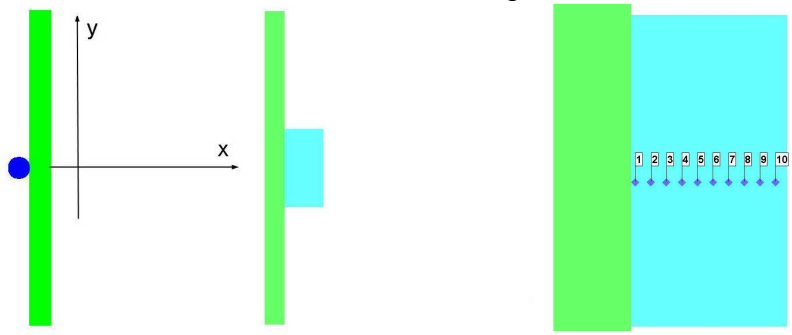

(a) (b)

Fig. 1 Schematic sketch of two-dimensional numerical model (a) finite element model (b) 1#~10# gauges

Table 1 Materials and computed model

Materials	Arithmetic	EOS	Strength Model	Failure Model
Projectile/Steel 1006	SPH	Shock	Johnson Cook	Hydro Tensile
Shell/7075T6AL	SPH	Tillotson	Steingerg Guinan	Hydro Tensile
Explosive/PBX 9404	Lagrange	Lee-Tarver	Von Mises	None

Material models

To describe the initiation of PBX9404 explosive, the Lee-Tarver ignition and growth model [6] is employed. The reaction rate for the conversion of unreacted explosive to product is given by

$$\frac{\partial F}{\partial t} = I(1-F)^x (V_0/V_1 - 1)^y + G(1-F)^x F^y p^z \quad (1)$$

Where F is the reaction fraction, p is the pressure, V_0 is initial specific volume, V_1 is current specific volume, and I, b, x, G, c, d, and y are constant.

Jones-Wilkins-Lee (JWL) equation of state (EOS) [7] is used to describe the unreacted explosive and the gaseous product. The EOS is given by

$$p = A(1-\frac{\omega}{R_1 V})e^{-R_1 V} + B(1-\frac{\omega}{R_2 V})e^{-R_2 V} + \frac{\omega E}{V} \quad (2)$$

Where $V = \rho / \rho_0$ the relative volume, e is the internal energy, and A, B, R_1, R_2 , and ω are constants.

In hypervelocity impact conditions, materials usually melt or even gasify. To meet phase transition under high pressure, Tilloston EOS [8] is selected, which can describe solid phase, liquid phase and even gas phase. Parameters of JWL model, Lee-Tarver model and Tilloston EOS are shown in Table 2, 3, 4 respectively.

Table 2 Parameter of JWL model

Explosive	Model Parameter				
	ω	$A[Mbar]$	$B[Mbar]$	R_1	R_2
Unreacted	0.8867	952.2	-0.05944	14.1	14.1
Reaction	0.38	8.524	0.1802	4.6	1.3

Table 3 Parameter of Lee-Tarver model

Explosive	$\rho_0[g\cdot cm^{-3}]$	$I[\mu s^{-1}]$	x	γ	$G[\mu s^{-1}\cdot Mbar^{-z}]$	y	z
PBX 9404	1.84	44	0.222	4	200	0.667	1.6

Table 4 Parameter of Tilloston EOS

Materials	Model Parameter								
	a	b	$A[Mbar]$	$B[Mbar]$	$E_0[kJ\cdot g^{-1}]$	α	β	$E_s[kJ\cdot g^{-1}]$	$E_s^{'}[kJ\cdot g^{-1}]$
AL	0.5	1.63	0.752	0.65	5.0	5	5	3.0	15
Steel 1006	0.5	1.5	1.279	1.05	9.5	5	5	2.44	10.2

Results and discussion

Fig. 2 shows the time history curve of reaction fraction and pressure at gauges 1# to 10# caused by the 5g spherical projectile with velocity of 3.8 km/s, 4.1 km/s, 4.2 km/s and 4.4km/s respectively. The reaction fraction F is an indicator for explosive detonation, with which an explosive is said to be fully reacted when F=1, and partially reacted when 0<F<1 [9].As indicated in Fig. 2, the reaction fraction quickly increased to the maximum value 1 at the velocity of 3.8 km/s, that is to say, the explosive is decomposed thoroughly. However, the reaction fraction was only 0.35 when the velocity was 4.1 km/s and 4.2 km/s, meaning the explosive didn't decompose completely. When the velocity increased to 4.4km/s, the reaction fraction reached maximum value 1 once again. As shown in Fig. 2(b) and (d) with projectile velocity 3.8km/s and 4.4km/s, once the shock wave entered explosive, the pressure increased quickly and reached the stable denotation pressure (Chapman-Jouguet pressure), i.e., shock detonation transition occurred. In Fig. 2(c) with projectile velocity 4.1km/s, the shock wave strength dramatically dropped in the explosive, the pressure increased a little due to local decomposition, but this pressure can not offset the attenuation of rarefaction wave, so that no denotation could take place. Therefore, we think there is a velocity interval with no shock initiation observed when a high velocity projectile impact double-shell charges.

Below is shock-induced initiation mechanism of double-shell charges impacted by projectile, projectile impacts the first shell and generates debris clouds, which after flying a distance will freely expand and then impact the second shell, and deliver shock wave to the explosive.

Shock wave transmit in the explosive, when the shock wave reaches the critical value, the hole collapse and crystal granule within the explosive will result in local thermal spot. When thermal spot temperature is higher than the explosive thermal decomposition temperature, the explosive will decompose and impose high temperature and high pressure on the surrounding medium. Further accelerate explosive decomposition and more local thermal spots will be generated. With more and more spots generating, explosive will decompose completely and transmit to the denotation phase.

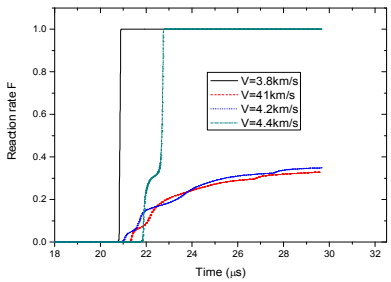

(a)

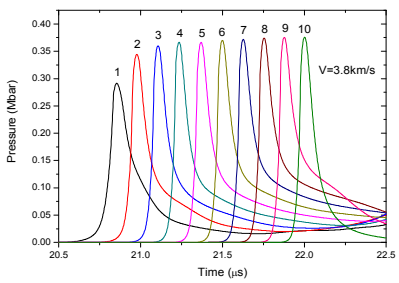

(b)

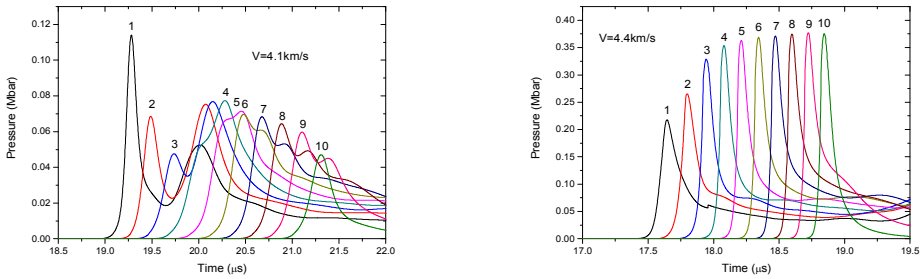

(c) (d)

Fig. 2 (a) Time history of reaction fraction at gauges #1~#10 at impact velocity 3.8km/s, 4.1 km/s, 4.4km/s; (b) (c) (d) Time history of pressure at gauges #1~#10 at velocity 3.8km/s, 4.1 km/s, 4.4km/s respectively.

The reason of velocity blind zone exists, is that when the velocity is ranging from 4～4.3km/s, projectile impact the first layer of shell and then severely break up, portion of the shock energy are converted to break-up energy, and the generated debris cloud will only impose a lower the surface momentum density to the second layer of shell. And below are the criteria to evaluate whether shock-induced denotation of PBX9404 explosive will occur:

$$p^n \tau = const \tag{3}$$

Where p is entering pressure, τ is pressure duration time, and n is explosive constant. For PBX 9404 explosive, n=2.3 [10].

Fig.3 shows the fitting curve of numerical simulation data of energy entering explosive at different impact velocity. The energy equals to square of the pressure entering explosive on the time integral. It is obvious that explosive energy decreased dramatically at velocity 3.9km/s, and reached a stable low value at velocity 4~4.3km/s, explosive input energy instantly elevated at velocity 4.4km/s.

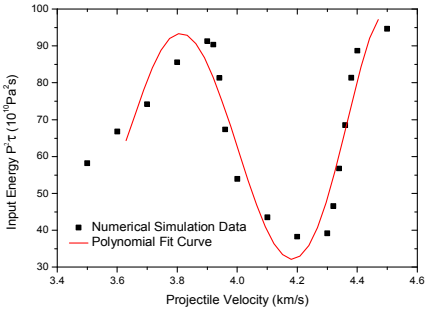

Fig. 3 Fitting curve of numerical simulation data of energy entering explosive at different impact velocity

Conclusions

Numerical simulation shows that the break-up of projectile can significantly affect the response of explosive with double-shell. Whether shock initiation of explosive occurs, mainly depends on the input energy of shock wave in the explosive. Also, the projectile break-up completely during specific high velocity impact and portion of the limited projectile kinetic energy are converted to break-up energy, is the root cause why low velocity will induce shock initiation but comparatively high velocity will not. This conclusion is very helpful to guide the safety study on shell charges structure.

The characteristics of initiation for double-shell charges is a function of many parameters including projectile diameter, impact velocity, impact angle, material density and volume density, and more. Further investigations on coupling of many parameters are suggested.

Acknowledgment

The authors are grateful to Dr. Xianghua Guo, Dr. Dangyong Shi, Dr. Qingtao Wang of Beijing Institute of Technology for their valuable discussion.

References

[1] Shin Hyunho, Lee Woong. "A numerical study on the detonation behavior of double reactive cassettes by impacts of projectiles with different nose shapes," International Journal of Impact Engineering, vol. 28, pp. 349-362, 2003.

[2] D. Touati, G. Tivon, S. Peles, A. Alfo, L. Bank, A. Shvarts, et al. "Numerical prediction of the initiation of confined heterogeneous explosives by fragment penetration," 23rd International Symposium on Ballistics. Tarragona, Spain, 2007, pp.145-152.

[3] Wei Yuzhang, Fang Qing, Tan Hua, Zhang Shouqi. "On the projectile oblique impact initiation conditions for explosives covered with a plate," 16th International Symposium on Ballistics. San Francisco, California, 1996, pp.87-91.

[4] C. Doolan, "Two-stage light gas gun for the study of high speed impact in propellants," p. 30p, 2001.

[5] Larry D. Libersky, Albert G. Petschek, Theodore C. Carney, Jim R. Hipp, Firooz A. Allahdadi. "High strain lagrangian hydrodynamics: a three-dimensional SPH code for dynamic material response," Journal of Computational Physics, vol. 109, pp.67-75, 1993.

[6] E. L. Lee, C. M. Tarver. "Phenomenological model of shock initiation in heterogeneous explosives," Physics of Fluids, vol. 23, pp. 2362-2372, 1980.

[7] E. L. Lee, H. C. Hornig, J. W. Kury. "Adiabatic expansion of high explosive detonation products," United States: California Univ., Livermore. Lawrence Radiation Lab., UCRL-50422, 1968.

[8] J. H. Tillotson. "Metallic equations of state for hypervelocity impact," United States: General Dynamics Corp San Diego Calif General Atomic Div, AD4867115, 1962.

[9] W. Fickett and W. C. Davis, Detonation. Berkeley: University of California Press, 1979.

[10] R. B. Frey, G. Melani, M. Chawla, J. Trimble. "Initiation of violent reaction by projectile impact," Proceedings 6th Symposium (International) on Detonation. Coronado, California. 1976.

© (2012) Trans Tech Publications, Switzerland
doi:10.4028/www.scientific.net/AMM.187.8

Research on Simulation System of Aero-generator

Zang Xiao-Jie[a], Song Jian

Civil Aviation University of China, Tianjin, China

[a]xjzang@cauc.edu.cn.

Keywords: Simulation; Aero-generator;Inverter; SIMULINK

Abstract. This paper presents a kind of simulation program of aero-generator, that inverter adopts a computer-controlled manner to simulate actual working features of aero-generator, based on test platform status of aero-generator. And design of the structure of simulation system , analyze the working principle of aero-generator, and then set up simulation model of three-stage brushless aero-generator under SIMULINK. Finally ,simulation results show the accuracy of this program.

Introduction

Aero-generator is a core part of the aircraft power system, while the normal operation of power systems plays a vital role on aircraft safety. As the aero-generator runs in the special high-altitude environment, and not allow to simulate its fault, That greatly limits the fault prediction of aero-generator, Increasing aviation security risks. Existing ground testing platform of aero-generator is tested by high-power motor to drive the generator. The method effectively solves the test of generator, but lack fault simulation of the special high-altitude environment , and high cost.

Simulation of Power System develops rapidly, and towards to real-time simulation, which almost uses MATLAB /RTW as development platform, or uses the third-party application development platform based on MATLAB /RTW interface[1-3]. This paper presents a kind of simulation program of aero-generator ,based on the most commonly used three-stage brushless alternators in constant speed constant frequency AC power system[4], Frequency 400Hz, voltage 115/200V,which are used on the current large-scale jet. And uses MATLAB as the simulation software. In the end, shows the accuracy of this program with the simulation results.

System Structure

Design of System Structure. Simulation System of aero-generator simulates the aero-generator 's real properties by the way that inverter is controlled by computer. Primarily, according to the principle of aero-generator , to build up the simulation model of aero-generator ， and to run simulation model of aero-generator on computer. Aero-generator models complete the real computation. Then, with D / A, the calculated current controls the inverter to produce corresponding current to drive the load, in the middle through the LC filter. Then put the measured voltage at the load end to the generator control model of computer through the A / D. In order to achieve closed-loop control, the measured current as a bias correction with the generator model output current for hysteresis tracking control. That aero-generator simulates the real operating characteristics. Figure 1 shows structure drawing of simulation system of aero-generator.

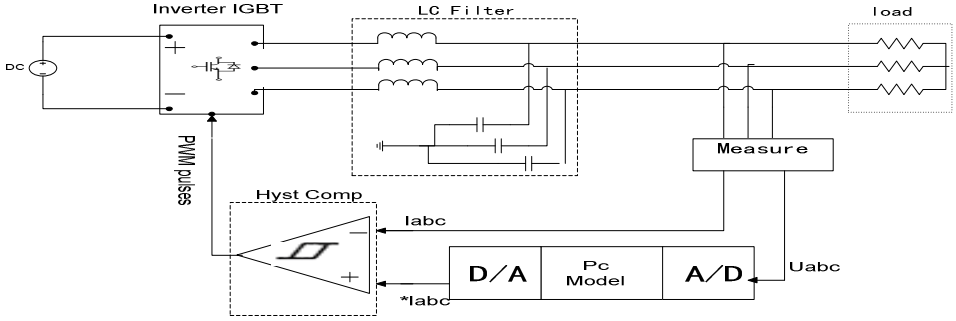

Fig. 1. Structure drawing of simulation system of aero-generator

System Require. Because of the frequency of generator up to 400HZ, in order to ensure current tracking response speed. Inverter adoptes PWM control method, high-speed switch devices(IGBT). Using LC filters to eliminate higher order harmonics.

In order to ensure real-time, the sampling time of generator model is less than 100us. System uses high-speed AD / DA control board. Using MATLAB / RTW as a development platform.

To ensure the reliability of the system , require the distortion rate of the three-phase 400Hz current waveform of the actual output less than 5%.

Choice of Controller. System selects hysteresis control circuit. Because the hysteresis control has the following advantages:

- Simple hardware circuit.
- Current responses rapidly, can improve the real-time.
- No need carrier output waveform, without a specific harmonic frequency.
- Operate Simplely, only need adjustment ring width. More suitable for the changes of controlled object. So easy to operate.
- Closed loop, which is a common of variety of track-type PWM converter circuit.

Disadvantage of hysteresis control :

the output current contains many harmonics.So LC filter is needed to eliminate harmonics.

Generator model

Work Principle of Three-stage Brushless Generator. Three-stage brushless generator is composed of the vice exciter, main exciter, voltage regulator, rotating rectifiers, main generator. Figure 2 shows the Structure of three-stage brushless generator. When the rotating rotor is drove by aircraft engine, the permanent magnet rotor of vice exciter generates flux. Armature windings of vice exciter issue three-phase AC to supply voltage regulator and excitation windings of the main excitation machine by rectifying. Armature windings of main excitation machine generate three-phase AC,rectified to the required DC by three-phase rotating rectifier,and to supply the main generator's field windings. Finally,The armature windings of main generator supply electrical equipment for three-phase power. To ensure the main generator voltage constant.Voltage regulator adjusts field current of the main exciter according to the changes of voltage.Three-stage brushless alternator excites reliably, has a hard external characteristic, has a strong shock ability, etc, which is the commonly used form in advanced large and medium-sized aircraft.

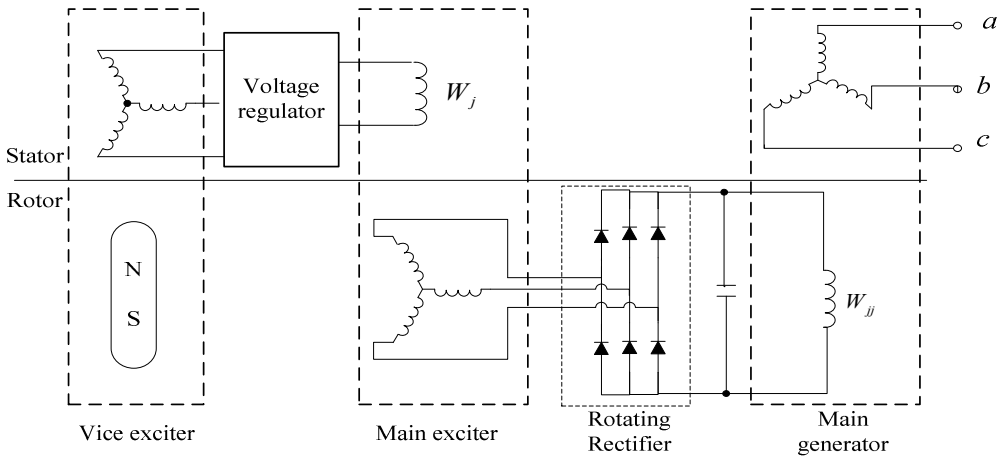

Fig. 2. Three-stage brushless aero-generator

Mathematical Model. Ignore the saturation, hysteresis and other factors of aero-generator, establish mathematical model of the main generator under the Park equation[5]. Including flux equation and the voltage equation and torque equation.

Flux equation:

$$\begin{bmatrix} \Psi_d \\ \Psi_q \\ \Psi_o \\ \Psi_f \end{bmatrix} = \begin{bmatrix} -L_q & 0 & 0 & -M_{af} \\ 0 & -L_q & 0 & 0 \\ 0 & 0 & -L_o & 0 \\ M_{af} & 0 & 0 & L_f \end{bmatrix} \begin{bmatrix} i_d \\ i_q \\ i_o \\ i_f \end{bmatrix} \tag{1}$$

Voltage equation:

$$\begin{bmatrix} u_d \\ u_q \\ u_o \\ u_f \end{bmatrix} = \begin{bmatrix} -r & 0 & 0 & 0 \\ 0 & -r & 0 & 0 \\ 0 & 0 & -r & 0 \\ 0 & 0 & 0 & r_f \end{bmatrix} \begin{bmatrix} i_d \\ i_q \\ i_o \\ i_f \end{bmatrix} + \begin{bmatrix} \dot{\Psi}_d \\ \dot{\Psi}_q \\ \dot{\Psi}_o \\ \dot{\Psi}_f \end{bmatrix} + \begin{bmatrix} -\omega\Psi_q \\ \omega\Psi_d \\ 0 \\ 0 \end{bmatrix} \tag{2}$$

Torque equation:

$$Te = 1.5\ p\ (\Psi d\ iq - \Psi q\ i\ d\ ) \tag{3}$$

The Main Generator Model. Establish the core model of the main generator according to mathematical model.Figure 3 shows the Simulink model of the main generator model. Ud, Uq, Uo, Uf of the moter as the inputs of model. Id, Iq, If, Io of the moter as the outputs of model. Block abc2qd in figure 3 achieves dq transformation. Block qd2abc in figure 3 not only achieves dq inverse transformation,but also converts the signal of model to PSB signal through the controlled current source.

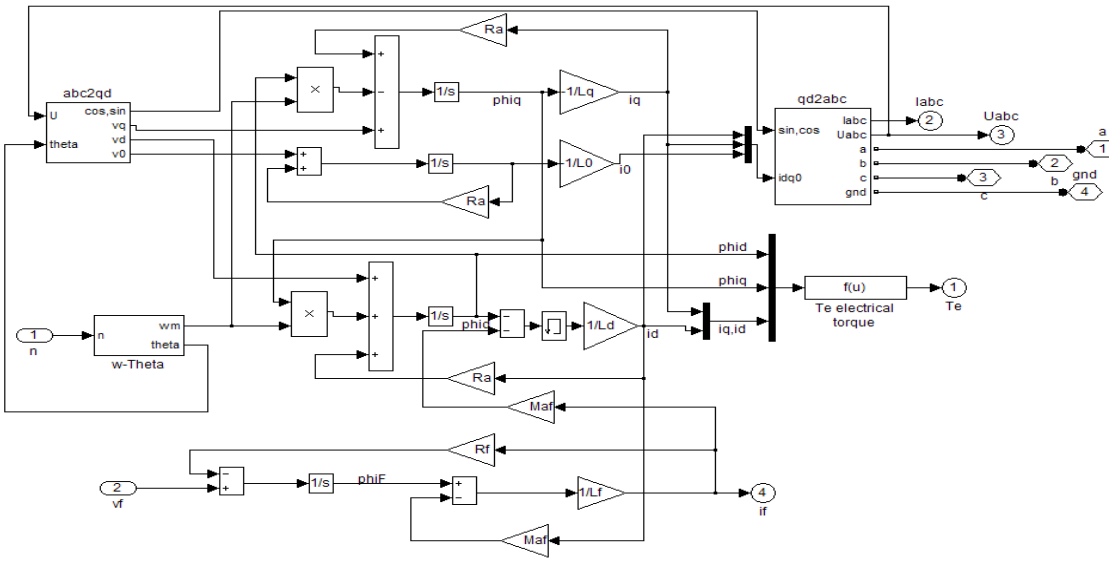

Fig. 3. The main genetator core model

After module package ,adding excitation drive module on the basis of the main generator core model in figure 3,which is drove by the controlled current source. Then add a single-phase voltage RMS module. This module is used for the voltage regulator. Finally,get the Simulink model of the main generator .Figure 4 shows the main generator Simulink model.Block main in figure 4 is the main generator core model. At the same time, Mask function can also be used on the package of the main generator Simulink model, to treat it as a whole, and can set the parameters in the package interface.

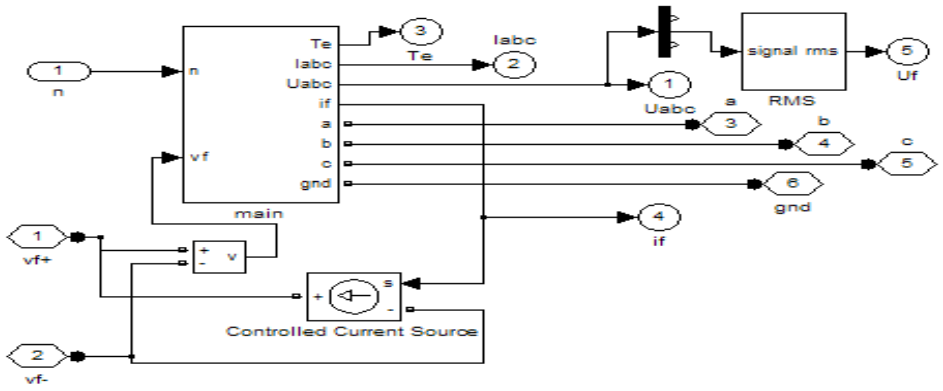

Fig. 4. The main genetator Simulink model

The Three-stage Brushless Generator Model. The model of three-stage brushless generator consist of vice exciter, main exciter,main generator, three-phase bridge. Three-phase bridge links modules . The difference between two exciters and the main generator are without damper winding.However,the modeling is the same.Figure 5 shows the three-stage brushless aero-generator model.

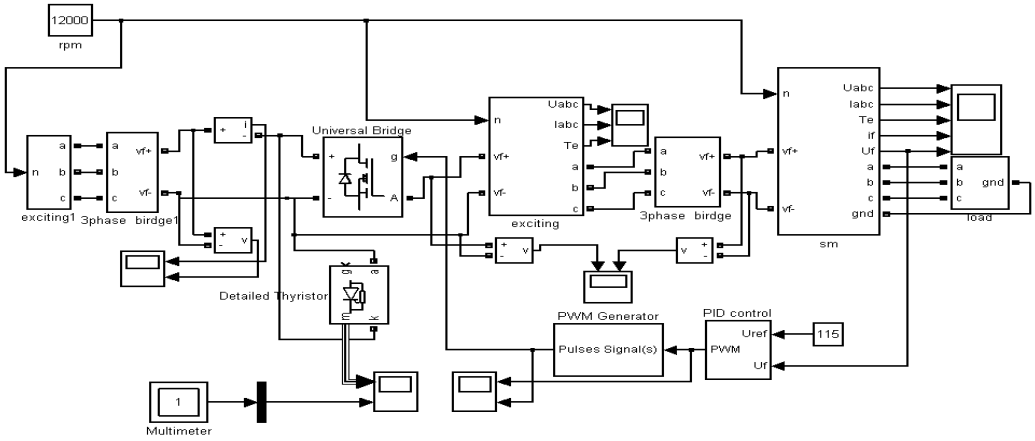

Fig. 5. Three-stage brushless aero-generator model

Voltage Regulator Model. In figure 5 , regulator model is introduced into the three-stage brushless aero-generator model,which consist of voltage control model and exciter circuit model. Voltage control model consists of the PID control module and the PWM generator module in figure 5, Figure 6 shows PID control model . Exciter circuit model constitute by the Universal Bridge by IGBT way. Model output single-phase voltage RMS (Uf) inputs PWM generator module through PID regulator. And generates PWM signal which is needed by excitation circuit. So achieves regulating voltage.

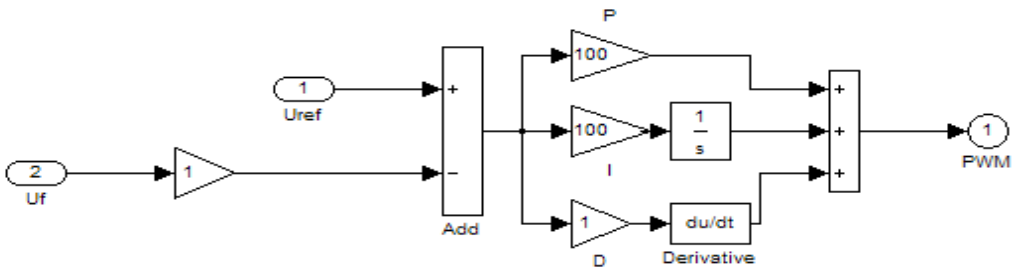

Fig. 6. PID control model

Generator Model Simulation Analysis. After generator model is established, to simulate a 50KVA three-stage brushless Generator of aviation. Parameters as follow: rated voltage 115/200V, rated frequency 400HZ, rated speed 12000rpm.

Figure 7-9 show three-phase current waveform of main generator, three-phase voltage waveform of main generator and single-phase voltage RMS waveform. The following chart,in 0.6s increases suddenly in 5 times load, at 1.0s, removals suddenly of the sudden load and restores the original setting.

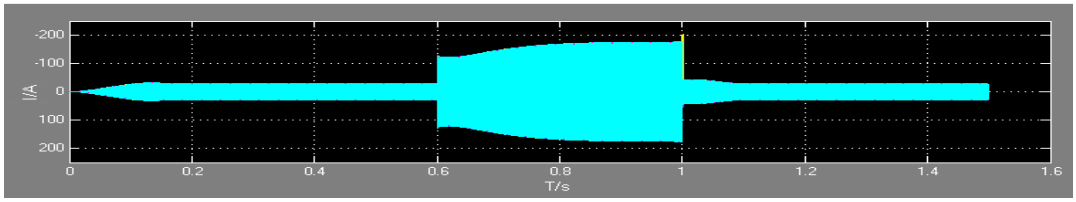

Fig. 7. Three-phase current waveform of main generator

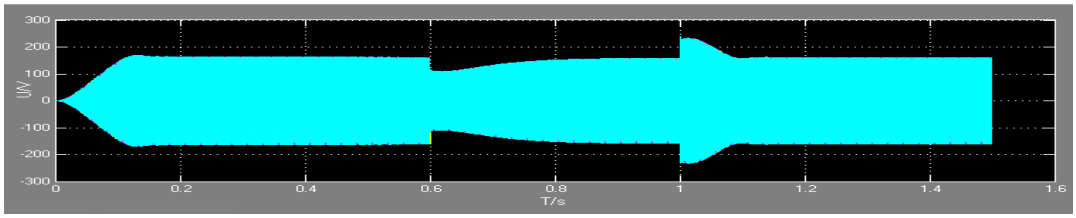

Fig. 8. Three-phase voltage waveform of main generator

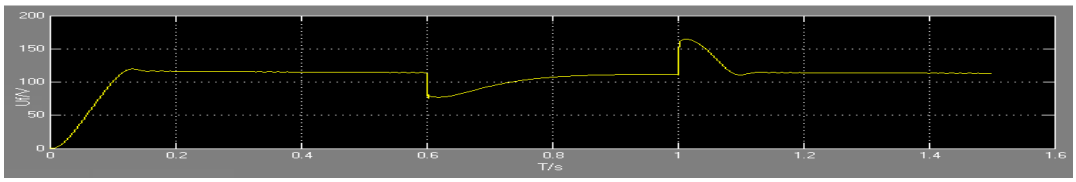

Fig. 9. Single-phase voltage RMS waveform

The figures show: because of the reasons of the motor ,when increase suddenly load. The voltage of the main generator will suddenly decrease, but the role of regulator, voltage will to balance. Similarly, unload the load as same.

Verification of system simulation

Establishing of System Model. In order to quickly set up the system simulation model. Effectively and easily verify the accuracy and feasibility of the system. In this paper, to establish the verification simulation model of system based on the main generator shown in figure 10. the inputs in figure 10 come from output of the main generator model, but the block qd2abc in main generator core model does not introduce controlled current source, and put directly the SIMULINK signal into the needed current value of figure 10 , and put three-phase voltage (Uabc) in figure 10 back into voltage of blcok abc2qd(U) of the main generator core model,and the main generator SIMULINK model has no single-phase voltage RMS modules.

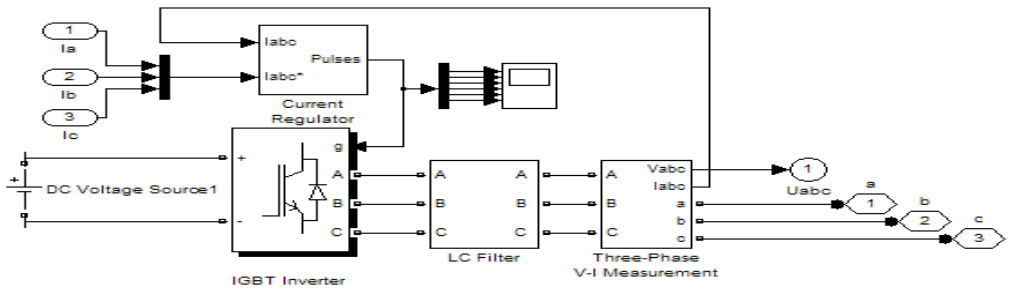

Fig. 10. Verification simulation model of system

Verification simulation model of system includes LC filter module, hysteresis loop control module, inverter module. First of all, according to the main generator output, inverter track the three-phase current waveform through hysteresis control. In order to eliminate higher order harmonics, use LC filter control. Figure 11 shows LC filter model , this model is the LC filter module in figure 10 .

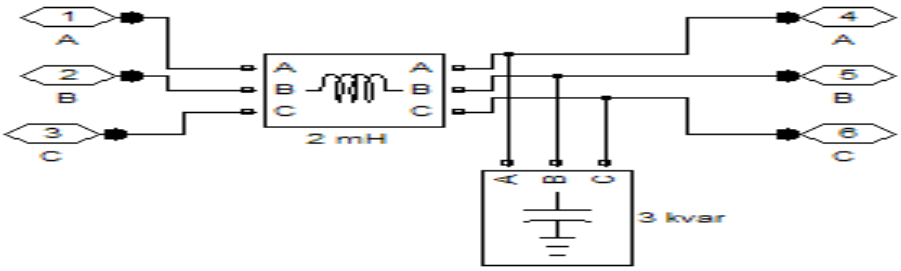

Fig. 11. LC Filter model

Figure 12 shows hysteresis loop control model , this model is Current Regulator module in figure 10. Hysteresis width set 2.

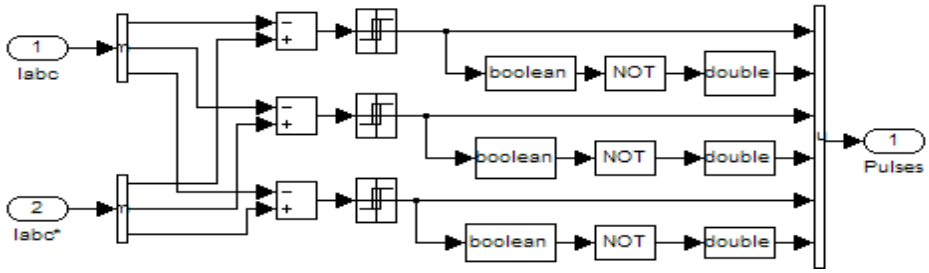

Fig. 12. Hysteresis loop control model

Test Results and Analysis. After the establishment of validation simulation model of system,start to simulate for system. In Simulation process, connect the main generator model,validate simulation model and load model. Adopt Hysteresis tracking way to make inverter output the actual current value track the three-phase current waveform that the main generator model output.

When simulate, in the 0.4s, the suddenly removal of the 20% load, in the 0.6s add suddenly load, to restore the original load. Figure 13 shows hysteresis tracking three-phase current waveform of main generator(I*abc). Figure 14 shows the actual output three-phase current waveform (Iabc).

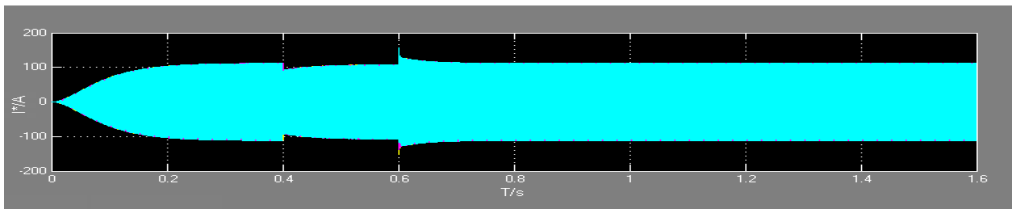

Fig. 13. Hysteresis tracking three-phase current waveform of main generator

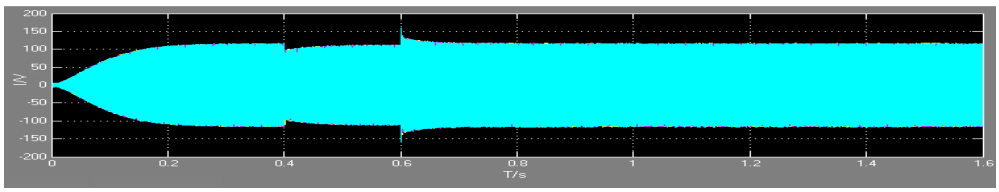

Fig. 14. The Actual output three-phase current waveform

The system test results charts show waveform distortion rate between the actual output three-phase current waveform (Iabc) and hysteresis tracking three-phase current waveform of the main generator (I*abc) is less than 5%. Meanwhile, while the system load is changed, waveform distortion does not increase. Therefore, this program meet the system requirements .

Conclusion

This paper presents a simulation program of aero-generator, and designs the structure of program, and establishs a three-stage brushless aero-generator model. Finally , built verification simulation model of system. Validation results show that the scheme is reasonable, meet the system requirements. The programs is important to test of aero-generator.

Acknowledgements

This paper presents a simulation program of aero-generator, and designs the structure of program, and establishs a three-stage brushless aero-generator model. Finally , built verification simulation model of system. Validation results show that the scheme is reasonable, meet the system requirements. The programs is important to test of aero-generator.

References

[1] Yuji Yasuda, Akihiko Yotoyama, yasuyuki Tada, hiroshi Okamoto.Study on Low-Cost&Easy-Use Real-Time Digital Power System Simulator in MATLAB/SIMULINK Environment[C]. *2000 International Conference on Power System Technology* P*roceedings* ,Perth,2000:921-926.

[2] Yue Chengyan,Song Ruihua,Li ruomei, Zhou Xiaoxin. Study on the development of real-time digital simulation based on Matlab[C]. 2002 *International Conference on Power System Technology Proceedings* ,KunMing,2002 :2004-2008 .

[3] Christian Dufour,Jean Belan,Simon Abourida,Vincent Lapointe.FPGA-Based Real-Time Simulation of Finite-Element Analysis Permanent Magnet Synchronous Machine Drives.*IEEE* 3*8th Annual Power Electronics Specialists Conference*, 2007:909-915

[4] Jian-ying Liu, Jian-Zhong Yang. Aircraft Electrical Power System [M]. Beijing: Ordnance Industry Press, 2004.

[5] Gu Yikang. Research on the New Start Scheme for Brushless Eleetro-Magnetic Synchronous AC motor[D]. Nanjing: Nanjing University of Aeronautics and Astronautics, 2002.

[6] Liaoying Xi, Xin-Hua Mu, Juan Ge. Modeling and Simulation Analysis of Three-Stage Brushless AC Generator Automatic Voltage Regulator[J]. The world of power Supply, 2006,5, P47-49.

[7] Ahmed N, Abd Alla.Simulation Model of Brushless Excitation System[J]. A*merican journal of applied sciences,*2007, 4(12),P1079-1083

© (2012) Trans Tech Publications, Switzerland
doi:10.4028/www.scientific.net/AMM.187.15

Real-time Attitude Simulation of Aerocraft using dSPACE Emulator and Three-axis Turn Table

Xie Daocheng[1,a], Wang Zhongwei[1], Zeng Qinghua[1]

[1]College of Aerospace and Material Engineering, National University of Defense Technology, Changsha 410073, China

[a]xdc_1984@163.com

Keywords: Dspace real-time emulator; Three-axis turn table; Dynamic model downloading; Serial-port communication; Simulation of aerocraft attitude; Operating status monitoring

Abstract. To solve the problem of ground simulation of aerocraft attitude in hardware-in-the-loop simulation (HILS), recurrence of aerocraft attitude is realized using dSPACE emulator and three-axis turn table. The hardware configuration and key technologies of control system are introduced. Construction and downloading of the dynamic model is done in dSPACE monitor computer, the model is calculated in dSPACE emulator. The communication between dSPACE and turn table is settled with serial-port of DS4201s card. The rotate motion of the inner middle and outer axis correspond to the three-channel motion of the aerocraft body. Simulation results indicate that dSPACE finish calculating complicated dynamic model, sending and receiving velocity data through serial-port is proper, bandwidth of turn table satisfies the need of simulation. Real rotating velocity of turn table is displayed using Controldesk tools, and fits well with the digital simulation data in pitching yawing and rolling directions, and the need for real-time attitude simulation in HILS is satisfied.

Introduction

Real-time attitude simulation of aerocraft in laboratory is significant in hardware-in-the-loop simulation (HILS) [1]. Three-axis turn table receives the attitude command which resolved by dSPACE emulator, the gyro measures real position and velocity of turn table. The performance of the controller and the correctness of the navigation algorithm are verified through ground testing [2]. Analyzing the data gathered from HILS is indispensable in control system design of aerocraft, it's important for pre-flight testing.

Developing HILS system rapidly is the main challenge after scheme design and numerical simulation [3,4]. The key technologies of HILS are signal transferring such as A/D and ground simulation of aerocraft attitude.

This paper realizes the simulation of aerocraft attitude using dSPACE real-time environment and multifunctional three-axis turn table. Six-DOF dynamic model of aerocraft is a key segment in HILS; it sends the real-time attitude to other measure units and also receives the feedback signals of actuators. dSPACE emulator has rich I/O card resources and turn table has high degree of accuracy in response to outer order, it enlightens us to construct a control model to realize attitude simulation using these two equipment.

Configuration of Attitude Simulation system of Aerocraft

Six-DOF dynamic model is built using Matlab/Simulink tools, the model is downloaded to the emulator after compiling successfully, and the execution file of the model is nominated as xx.sdf. All variables can be supervised with Controldesk tools which are assembled in the monitor. dSPACE is rich in card resources. DS2103 is used for A/D signals acquisition, DS2002 is used for D/A transfer, DS4201s communicates with other devices using 232/422 serial-port [5, 8].

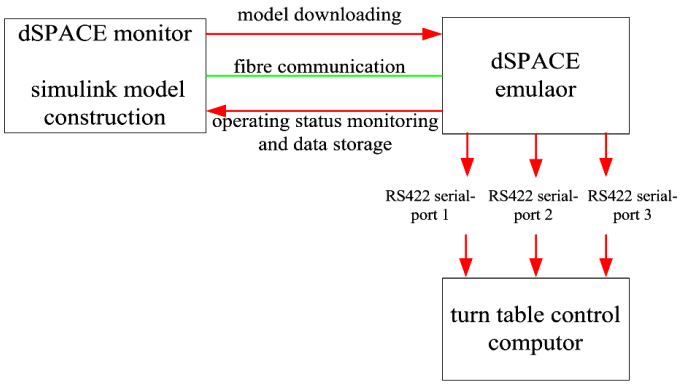

Fig. 1. Scheme of the attitude simulation system with dSPACE and turn table

Control computer of the turn table receive position and velocity command of pitch/yaw/roll channels. Command is sent by the emulator through analog interface and digital interface. Building analog communication model is easier than digital communication model comparatively. But analog model is unilateral, it can't receive signal from turn table. We choose serial-port communication to send orders and receive signal here. Figure 1 shows the scheme of the control system with dSPACE and turn table.

Key Technologies and Simulation Results of Aerocraft of Attitude Simulation System Using dSPACE and Turn Table

Serial-Port Communication Model between dSPACE and Turn Table

Three serial-ports on DS4201s card send the angle velocity of three axes which represents three channels of aerocraft. Data transport between two control computers adopt the standard agreement named "record". Each record contains eight bytes, which is the value of angle position or velocity. dSPACE receives the data turn table sends, each record contains five bytes, as shown in Figure 2.

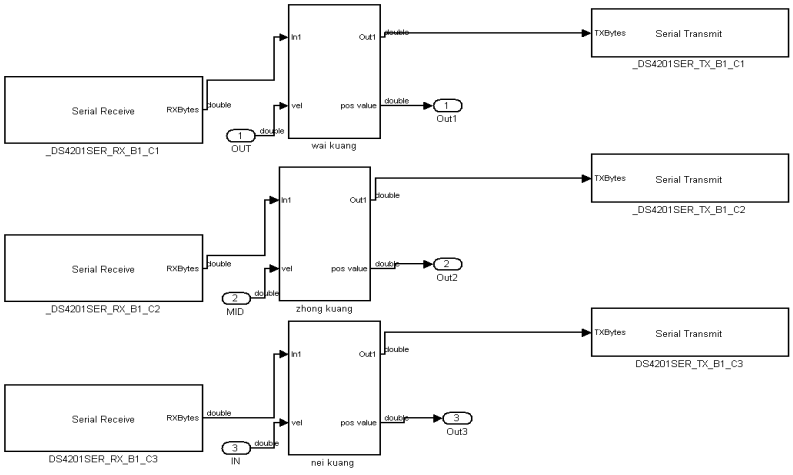

Fig. 2. Simulink model of serial-port communication between 4201S card of dSPACE emulator and cotrol computor of turn table

Declaration of the DS4201s card should be done before using it [7]. In the communication model, initialization of this card is added to the whole simulink model. The format of the serial-port communication: eight data bit; one cease bit; none odd-even check; MODEM-vacancy easy link mode; 9600 Baud rate. Data transferred between two devices is listed in Table 1.

Table 1. An example of a table

data	source	destination	unit	range
position command of outer frame	CSC3	CSC1	0.01°/LSB	±360
velocity command of outer frame	CSC3	CSC1	0.01/S°/LSB	±200
position command of middle frame	CSC3	CSC1	0.01°/LSB	±90
velocity command of middle frame	CSC3	CSC1	0.01/S°/LSB	±200
position command of inner frame	CSC3	CSC1	0.01°/LSB	±120
velocity command of inner frame	CSC3	CSC1	0.01/S°/LSB	±200
real position of outer frame	CSC1	CSC3	0.01°/LSB	±360
real position of middle frame	CSC1	CSC3	0.01°/LSB	±120
real position of inner frame	CSC1	CSC3	0.01°/LSB	±90

Construction of Six-DOF Dynamic Model of Aerocraft

Six-DOF dynamic model of aerocraft includes kinetics module and GNC (guidance, control and navigation) interface. The dynamic model is built with dSPACE monitor computer, and then downloaded to the emulator if compiled successfully. The simulink model is changed into C codes with RTW tools, the C codes run in the DS1005 processor. Designer may monitor of the variable he has interest in, the varying curve shows in the monitor computer.

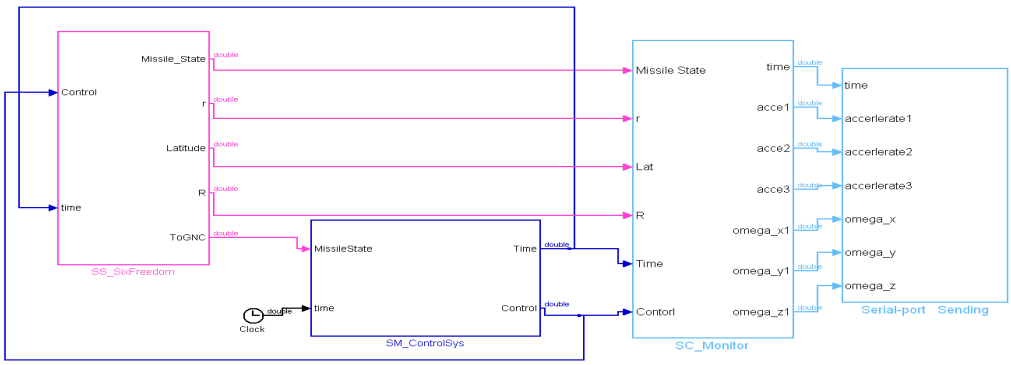

Fig. 3. Simulink model of 6-DOF aerocraft dynamic with GNC

We can only use the common module Simulink offers when building complicated model, the schedule of system developing may be delayed. Here we use S-function to construct simulink models, S-function module can be downloaded to the emulator [6].

dSPACE supports the C code compiled S-funtion.Fig.3 shows the whole simulink model of aerocraft dynamic with GNC system [8].

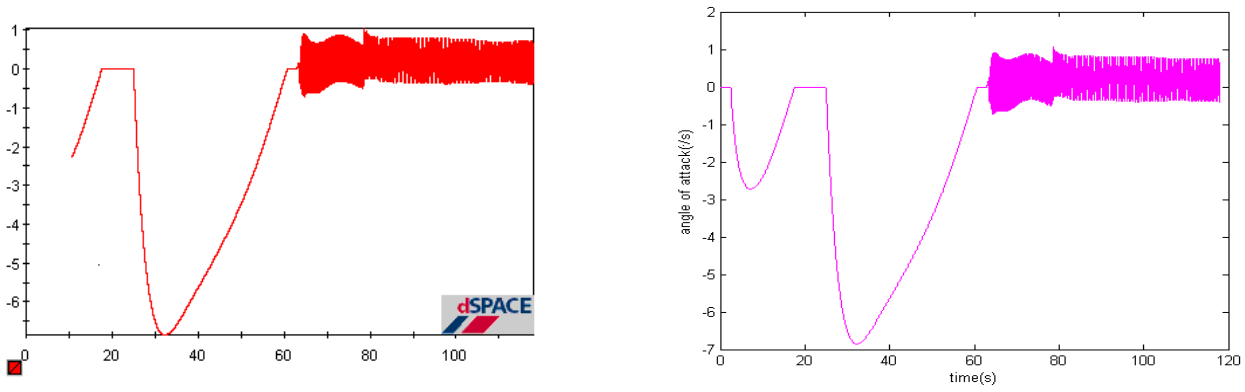

Fig. 4. Curve of angle of attack varying with time running in Simulink comparision with that run in dSPACE emulator

Figure 4 shows angle of attack (AOA) rate of the aerocraft run in PC comparison with that run in dSPACE environment. These two curves fit well, which indicates that the simulation results derived from simulink and dSPACE both are correct, and dSPACE has the capability of calculating very complicated dynamic simulink model nearly with no delay.

Simulation Equipment

Control computer of turn table receive angle position and velocity of three channels from the emulator, turn table response to the order. Control precision of angle position is $\pm 20''$, pass band of simulation in outer frame, middle frame and inner frame is 10Hz, 12Hz, 15Hz, which is above the nature frequency of the aerocraft body. The equipment satisfies the attitude simulation.

DS1005 card in dSPACE emulator uses PowerPC 750 as real-time processor, which mainly answer for model calculating and accessing to I/O card through PHS bus, as is shown in Figure 5.

Fig. 5. Picture of the three-axis turn table and dSPACE emulator

Real Rotation Angle Velocity of Turn Table Monitored by Controldesk Tools

Controldesk monitor the operating status in dSPACE emulator; modify the variable real-time value for getting better simulation results customers wants; save and display the simulation Data. Turn table rotates in two modes: angle velocity and angle position. DS4201s card receives real operating state while sending command. We build an instrument panel to show the varying curve of those important parameters.

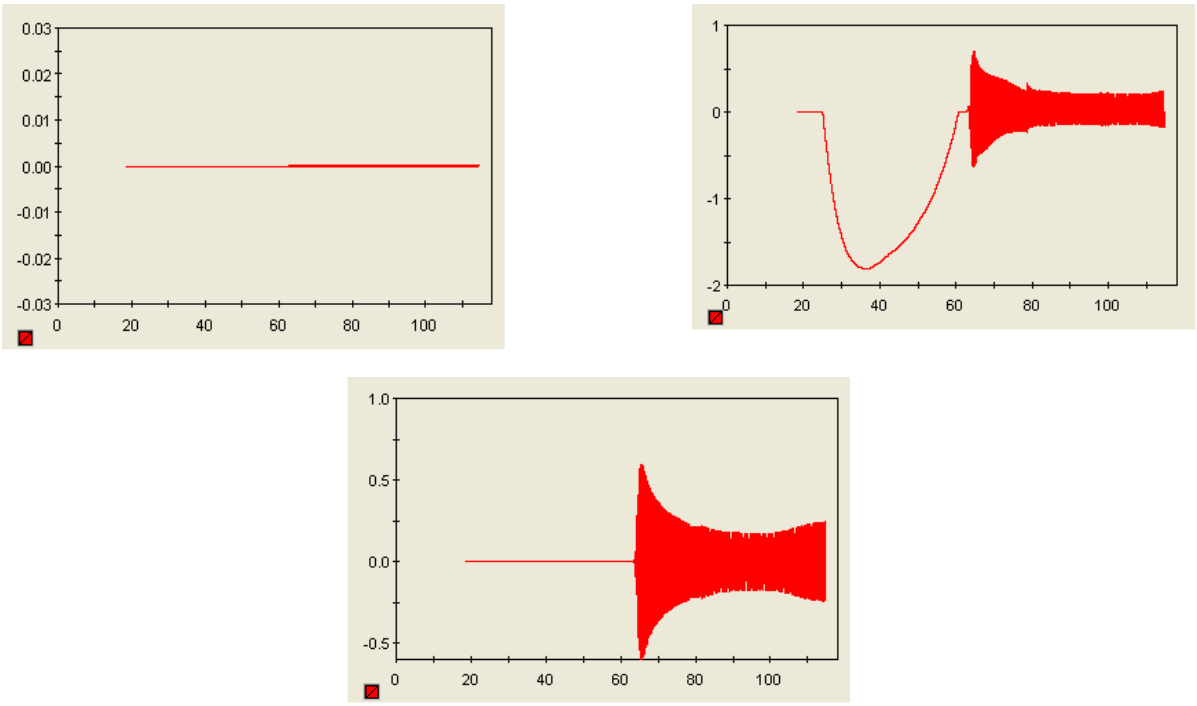

Fig. 6. Angle velocity of roll/pitch/yaw motion of turn table monitored with Controldesk tools

Figure 6 shows the angle velocity of three-axis, it recur the attitude of aerocraft preferably. The rotating rates of three axes correspond to the angle rates of pitching/yawing/rolling channels of aerocraft body.

Conclusion

Real-time Simulation of aerocraft attitude is realized using the perfect acquisition and handling capability of dSPACE emulator. High-precision turn table response rapidly to the command sent by the emulator. We realize to gather the attitude information of aerocraft in ground simulation. Conclusions are as follows:

1) Data Sending and receiving in real-time simulation is resolved using rich card resources of dSPACE. The emulator has abundant channel and high precision, which facilitates design and testing of controller.

For constructing an integrate HILS system, we can also choose dSPACE as the main processor, it also has good performance in analog signal acquisition, its digital transfer precision reach 0.0001.

2)The dynamic model is built rapidly with RTW tools which offerd by Matlab/Simulink. The powerful processing capability of dSPACE gurantee the model calculating, which is significnant in high-precision and short-sequence simulation.

3)422 serial-port communication between the emulator and turn table is proper, high-precision turn table response to the digital command of the dynamic model rapidly. Simulation results indicates that the rotate rates of three axes is nearly the same with the real body rotation angle rate in pitching/yawing/rolling directions. Real-time attitude simulation of aerocraft is realized with dSPACE and turn table. The velocity and position precision of three-axis motion satisfy the need of HILS.

References

[1] Marko Bacic, Monte MacDiarmid. Hardware in-the-loop simulation of aerodynamic objects[C]. AIAA2007-6465, AIAA modeling and simulation technologies conference and exhibt, South Carolina, USA, August 20-23,2007.

[2] Modeling and Simulation Technologies:Reconfigurable Flight Simulators in Modeling and Simulation[C]. AIAA2004-5459, AIAA modeling and simulation technologies conference and exhibt, Rhode Island, USA, August 16-19,2004.

[3] Zhai Kun, Yang Di, Zhu Chen-yuan. Real Tilne Simulation System for Attitude and Orbit ControlSystem of Flexible Satellite Based on dSPACE Multiprocessor Systems[J]. Aerospace Control, 2004, 22(1): 17-25.

[4] Wang Ji-he, Wang Feng, Shi Li. dSPACE-based micro core simulation system [J]. System Engineering and Electronics, 2007, 29(12): 2149-2153.

[5] Zhu Chen-yuan, Yang Di, Yang Xu. dSPACE-based micro core simulation system [J]. System Engineering and Electronics, 2007, 29(12): 2149-2153.

[6] Farhan A. Faruqi, Thanh Lan Vu. Mathematical Models for a Missile Autopilot Design[R]. Weapons Systems Division Systems Sciences Laboratory, Australia, August 2002.

[7] dSPACE RealTime Interface(RTI and RTI- MP)Implementation Guide[M]. dSPACE GmbH. 2001

[8] Hardware Installation and Configuration Reference, Germany[M]. dSPACE GmbH. 2004.

© (2012) Trans Tech Publications, Switzerland
doi:10.4028/www.scientific.net/AMM.187.20

Electric Vehicle Transmission Gear Ratio Optimization Based on Particle Swarm Optimization

Qiang Gu[a] and Xiu-sheng Cheng

College of Automotive Engineering of Jilin University,No.5988 Renmin Street,Changchun 130022,P.R.C.

[a] jason_2010gu@yahoo.com.cn

Keywords: Particle swarm optimization; Electric vehicle; Gear ratio optimization

Abstract. The driving range of electric vehicles is less than traditional vehicles due to the restriction of energy storage. It is raising the efficiency of each power component that is one of increasing electric vehicle driving range methods. A particle swarm optimization is used to optimize transmission gear ratio on established electric vehicle power component models. A simulation that simulates the energy consumption of vehicle after gear ratio optimization is given to compare with the actual energy consumption data of the vehicle before gear ratio optimization. The results show that the energy consumption and driving range of the latter are better than the former therefore this optimization is valid.

Introduction

With the problems of petroleum resources shortage and environmental pollution becoming more and more serious, it is not surprising to see the rapid development of electric vehicles which are characterized by energy recycling and zero emission. Electric vehicles are different from hybrid vehicles in that the power for the driving system is wholly derived from power storage system (e.g. battery) [1] [2]. Most published studies are mainly focused on electric vehicle power storage systems and driving systems. As the energy density of present batteries is much less than that of fossil fuel, driving range of electric vehicles is much less than that of traditional vehicles. Nowadays the power storage system is a bottleneck for the electric vehicle development. Optimizing the transmission system of the electric vehicle can improve vehicle performance including power output and economical efficiency before breakthrough developments occur in battery power levels.

At present, traditional optimization methods typically include gradient algorithm, simplex method and so on. The objective function of electric vehicle transmission optimization models is generally non-differentiable, discontinuous and nonlinear. Traditional optimization methods (e.g. gradient algorithm) require that the function is continuous, differentiable and satisfies the Lipschitz conditions, while the electric vehicle transmission optimization objective function does not easily meet these restrictions. Furthermore, the traditional optimization calculation usually gets a locally-best solution, rather than the global optimal solution [3] [6].

Particle swarm optimization is a new kind of algorithm developed in recent years, which is characterized by fast convergence and parallel computation, and has powerful search abilities and robustness for non-linear problems. Therefore, it is very suitable for electric vehicle transmission optimization.

In this study, numerical models are established for each power component of the electric vehicle named as EV-JD and then the particle swarm optimization is applied to optimize the transmission gear ratio based on these models. Finally, the optimized solution is compared to the test data to prove the optimization method is effective for electric vehicle transmission gear ratio optimization.

Nomenclature

δ	Rotating Mass Conversion Factor	α	Angle of Slope
A	Area of Front Face	η_T	Transmission Efficiency
f	Coefficient of Rolling Resistance	i_1	1st Gear Ratio
v	Vehicle Speed	ω_{mmax}	Motor Maximum Rotating Speed
g	Acceleration of Gravity	v_{max}	Vehicle Maximum Speed
ρ	Air Density	i_2	2nd Gear Ratio
m	Vehicle Mass	n_b	Motor Nbase
M_{mmax}	Maximum Output Torque of Electric Motor	k_1	Proportional Coefficient
r	Rolling Radius of Wheel	k_2	Proportional Coefficient
V_c	Vehicle Climbing Speed	P_e	Rated Power
$M_{\omega max}$	Motor Maximum Torque at Maximum Rotating Speed		
n_e	Rated Rotate Speed of Motor		
L_2	Conversion Inductance of Rotor		
Δn	Given Slipping Speed		

Configuration of Electric Vehicle and Control Strategy

Configuration of electric vehicle. The configuration of EV-JD is shown in Fig. 1. The NIMH power battery drives the electric motor through the controller, while the motor can recycle some of the braking energy by sending it to the battery. Research has shown that electric vehicle transmission systems with only two gears can satisfy the driving requirements.

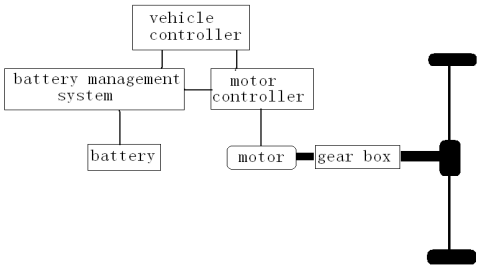

Fig. 1. Configuration of EV-JD

Therefore, a two-gear transmission box is installed in EV-JD. Other parameters of EV-JD are shown in table 1.

Table 1. Parameters of EV-JD

Item	Value	Item	Value
Coefficient of rolling resistance	0.315	Battery mass(kg)	200
Radius of wheels(m)	0.3	Area of front face (m^2)	2.041
Mass of vehicle(kg)	1100	Motor mass(kg)	85

Control Strategy. The control strategy of the electric vehicle under normal conditions can be classified into four stages including stop, drive, brake, and slide. The speed of the vehicle is at zero, the brake pedal is pressed, the accelerator pedal is released and the electric motor is off with no torque output in stop status. In drive status, the brake pedal is released and the motor outputs torque

according to the position of accelerator pedal; when the electric motor is on overload for a long period of time, it will automatically switch off to protect itself. In brake status, the brake pedal is pushed while the accelerator pedal is released, the braking energy is recycled with the amount of recycled brake energy depending on the speed. In slide status, the brake pedal and accelerator pedal are both released and the motor is off with no torque output and no energy recycled.

Electric Vehicle Transmission Optimization Model

Optimization Goal. Because of the present restrictions of gravimetric specific energy and gravimetric specific power, the maximum driving range and the highest speed are both limited. In addition, the features of no idle power consumption and low noise make the electric vehicles more suitable for city conditions. For this reason, more emphasis is put on economical efficiency than on power performance when optimizing the transmission gear ratio in this study. Thus, the object of electric vehicle optimization can be summarized as that, suitable transmission ratios are chosen in order to minimize the energy consumption in each driving mileage. The objective function can be expressed as below:

$$\begin{cases} \min\limits_{X\in\Omega} F(X) \\ s.t.: S_i(X) > 0 \\ i = 1,2,3,... \end{cases} \tag{1}$$

In expression (1), $X = [x_1, x_2]^T$ is transmission ratio variable, and Ω denotes the vector space of solution, $S_i(\cdot)$ denote constraint conditions [6].

Fitness Function of Particle Swarm Optimization. In the study, a particle flies in the search space at a certain speed at which it adjust dynamically according to the flight motion of itself and other particles. Each particle has a fitness that is determined by the objective function. It is very important to select a suitable fitness function, which has a strong influence on convergence speed and realization of optimal solution. According to the optimization objective function, the fitness function is defined as equation (2).

$$g(X) = \frac{\int p_{in}(t)d(t)}{\int v(t)d(t)} \tag{2}$$

where,

$P_{in}(t)$ denotes input power, and v is the vehicle speed. The smaller the value of g(X) is, the better the fitness of particle is.

Power consumption function p(t) is established and calculated according to the vehicle dynamics model. It is assumed that the vehicle runs on straight roads. Then resistance factors suffered by the vehicle include air resistance F_w, rolling resistance F_f, and acceleration resistance F_a. These resistances can be expressed as follows.

$$F_w = \frac{\rho C_d A v^2}{2} \tag{3}$$

$$F_f = mgf \tag{4}$$

$$F_a = \delta m \frac{dv}{dt} \tag{5}$$

$$F = F_w + F_f + F_a \tag{6}$$

Pin can be expressed by variable P and variable X. Optimizing variable X will change the value of Pin and fitness function G(X) to realize the optimizing object.

Search Space of Particle Swarm

When the particle swarm algorithm searches solution in a large area of space, the search space must satisfy the solution vector space constraint conditions, expressed in (1). Otherwise, even if the optimal solution can be obtained, it cannot meet actual driving requirements of vehicles. The following analysis of the constraint conditions according to vehicle driving requirements is carried out to derive the solution vector space that satisfies vehicle driving requirements.

The power source of electric vehicle is the electric motor. The motor must assure the vehicle is able to run up to a slope at a certain speed under the maximum motor output torque. That is to say, when the gear box is set at 1st gear, transmission gear ratio should satisfy the following restriction.

$$\frac{M_{m\max} i_1 \eta_T}{r} \geq mgf\cos\alpha + \frac{\rho C_d A}{2} v_e^2 \tag{7}$$

The speed that is transmitted at 2nd gear from the electric motor under maximum rotating speed of the wheels should be larger than the vehicle maximum speed [5]. Vehicle traction force that is transferred at 2nd gear from the maximum torque of the electric motor under maximum rotating speed should also be larger than the drive resistance under vehicle maximum speed. Both of them are shown in expression (8) and (9).

$$2\pi r \omega_{m\max} \geq v_{\max} i_2 \tag{8}$$

$$M_{\omega\max} i_2 \geq mfg + \frac{\rho C_d A}{2} v_{\max}^2 \tag{9}$$

The particle swarm search space Ω can be derived from (7), (8), (9).

Electric Motor Model. A 75kw AC induction motor is adopted in the study. The equivalent circuit of the motor is as shown as fig.2.

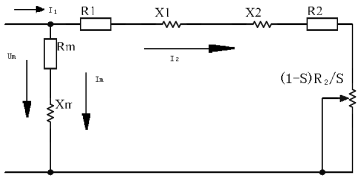

Fig. 2 Equivalent circuit of Motor

In fig.2, R_1 denotes stator resistance of each phase, X_m denotes excitation winding inductance, X_1 denotes stator inductance, I_1 denotes stator current, R_2 denotes rotor conversion resistance, X_2 denotes rotor converted inductance, I_m denotes excitation current, R_m denotes excitation winding resistance, S denotes slip ratio.

According to the equivalent circuit, the electric motor output torque M can be expressed as follows.

$$M = \begin{cases} \dfrac{90R_2k_1^2\Delta n}{\pi[R_2^2 + (\pi L_2 m\Delta n/30)^2]} & (0 \leq n \leq n_b,\ k_1 = \dfrac{U_e}{\sqrt{n_b + \Delta n}\sqrt{n_e + \Delta n S}}) \\ \dfrac{90R_2k_1^2\Delta n}{\pi[R_2^2 + (\pi L_2 m\Delta n/30)^2](n+\Delta n)^2} & (n_b \leq n \leq n_e, k_2 = \dfrac{U_e}{\sqrt{n_e + \Delta n S}}) \\ \dfrac{90R_2U_e^2\Delta n}{\pi[R_2^2 + (\pi L_2 m\Delta n/30)^2](n+\Delta n)^2} & (n_e \leq n \leq n_{\max}) \end{cases} \tag{10}$$

The rotor phase current I_2 can be calculated from the following equations.

$$I_2 = \begin{cases} \dfrac{k_1\Delta n}{\sqrt{R_2^2 + (\pi L_2 m\Delta n/30)^2}} & (0 \leq n \leq n_b) \\ \dfrac{k_2\Delta n}{\sqrt{[R_2^2 + (\pi L_2 m\Delta n/30)^2](n+\Delta n)}} & (n_b \leq n \leq n_e) \\ \dfrac{\Delta n U_e}{\sqrt{[R_2^2 + (\pi L_2 m\Delta n/30)^2](n+\Delta n)}} & (n_e \leq n \leq n_{\max}) \end{cases} \tag{11}$$

Power loss of the motor includes copper loss of stator (ΔP_{cu1}), iron loss of stator (ΔP_{fe1}), copper loss of rotor (ΔP_{cu2}), machinery loss and other miscellaneous losses (ΔP). The electric motor efficiency can be expressed as follows.

$$\eta = 1 - \frac{\Delta P_{cu1} + \Delta P_{cu2} + \Delta P_{fe} + \Delta P_{\Delta}}{P_1} \tag{12}$$

where,

$$\Delta P_{cu1} = 2I_1^2 R_1$$

$$\Delta P_{cu2} = 3I_2^2 R_2$$

$$\Delta P_{fe} = 3I_m^2 R_m$$

$$\Delta P_{\Delta} = 0.01 P_e$$

According to motor load and rotating speed, using (11) and (12) the motor efficiency shown in fig.3 and the efficiency map shown in fig.4 can be obtained.

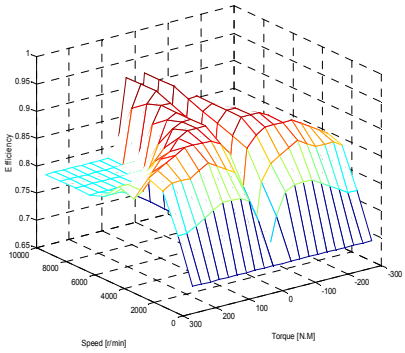

Fig. 3 Electric Motor Efficiency

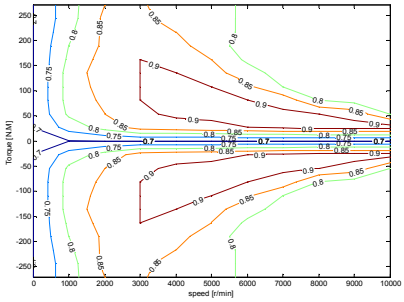

Fig. 4 Map of Motor Efficiency

Electric Motor Model. There are generally several kinds of power battery models, such as equivalent Thevenin model, Randels-Ershler model, internal resistance model, RC model and so on. Each model has advantages and disadvantages in the accuracy of model description and computation. Typical internal resistance model shown in fig.5 is applied in this study.

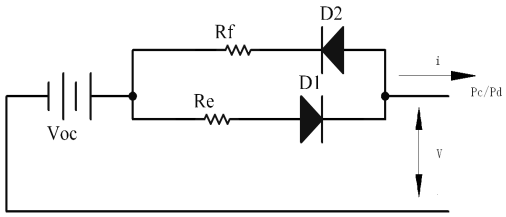

Fig. 5 Battery Internal Resistance Model

In the fig. 5, P_c is charging power and P_d is discharged power. The open circuit voltage of battery (Voc) which is related to the state of charge(SOC) of the battery can be obtained from test data. R_f is charging resistance and R_e is discharged resistance. R_f and R_e, which can be expressed by a function of SOC can be measured through experimentation. I is the charging or discharging current, and V is the terminal voltage of battery [2].

Assuming that the required discharge power is P, an expression can be established according to the battery equation model.

$$-R_e i^2 + V_{oc} i - P = 0 \tag{13}$$

The discharge efficiency can be expressed as follows.

$$\eta_d = \frac{p}{V_{oc} i} \tag{14}$$

When charging power is P_c, the charging model can be expressed as follows in a similar way.

$$-R_f i^2 + V_{oc} i - P_c = 0 \tag{15}$$

The following charging efficiency expression can be derived from (15).

$$\eta_c = 1 - \frac{R_f i}{P_c} \tag{16}$$

The discharging efficiency curve of the battery, shown in fig.6, can be drawn according to (14), and charging efficiency curve, shown in fig.7, can be drawn according to (16).

Optimization Simulation and Analysis

By taking gear ratio X as the optimization variable, and combining (7), (8) and (9) to form a search space, a particle swarm optimization algorithm is used to optimize gear ratio. In this study, the drive circle of GB12545.1-2001 is selected as the driving curve. Fig.8 shows a diagram of one driving circle curve.

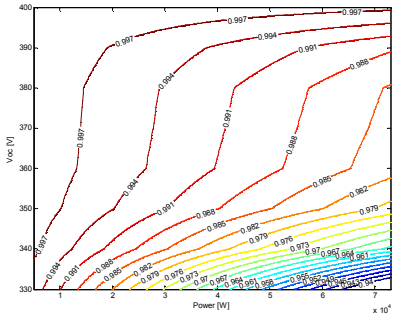

Fig. 6 Discharging Efficiency Curve of Battery

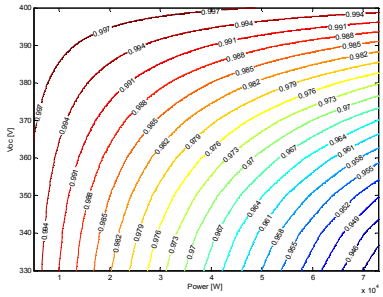

Fig. 7 Charging Efficiency Curve of Battery

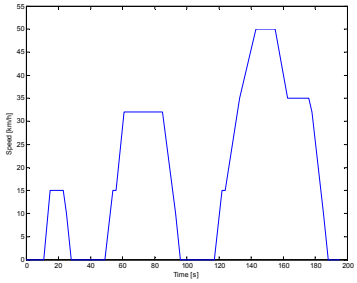

Fig. 8 Driving Circle Curve

According to the models of the motor and battery, and by using the relationship of drive dynamics, the energy consumption of a vehicle under one circle can be computed. The optimization solution of the gear ratio can be achieved under the criterion of fitness function by using iterative computation of particle swarm optimization.

The optimization solution of gear ratio is i_1=29.36, i_2=8.85.The vehicle speed, motor efficiency, motor power and energy consumption under one drive circle are shown separately in fig.9.

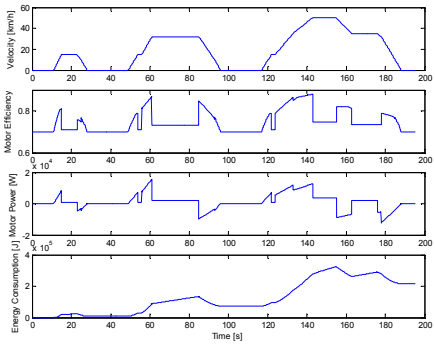

Fig. 9 Vehicle Speed, Motor Efficiency, Motor Power and Energy Consumption under Optimization

In studying fig.9, the energy consumption of vehicle with optimized gear ratio is 217KJ which is relatively low because the motor works at high efficiency areas under one drive circle. The speed and energy consumption of the vehicle with the original gear ratio before optimization are shown in fig.

10.The energy consumption between the optimized gear ratio and the original one, the latter is 3.5 per cent greater. In addition, comparing the driving range between them, the former is 3.37% greater. Therefore, using particle swarm optimization to optimize gear ratio is valid.

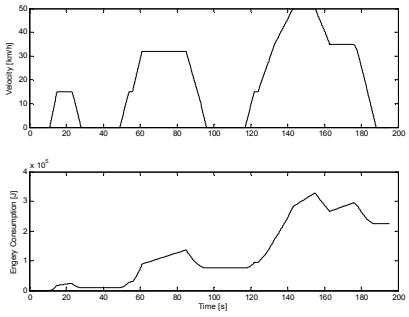

Fig. 10 Energy Consumption before Optimization

Conclusion

In this study, a minimum vehicle energy consumption model which fulfills the drive circle and vehicle drive requirement is given, using the particle swarm optimization. A simulation of an established model is carried out. Both of the motor efficiency and drive range of a vehicle with optimized gear ratio are greater than the original, without optimization. Therefore, a method of designing electric vehicle gear ratio is given.

References

[1] Markel T,Brooker A， Hendricks T, “Advisor: a system analysis tool for advanced vehicle modeling,” Journal of Power Sources ,2002, 110,pp.255-266.

[2] S.Rodrigues, N.Munichandraiah,and A.Shukla, “A review of state-of-charge indication of batteries by means of A.C. impedance measurements,”Journal of Power Sources, 2000, Vol.87, No.1-2, pp.12-20.

[3] Gao Wenzhong ,Porandla S K, “Design Optimization of a Parallel Hybrid Electric Powertrain,” IEEE Conference on Vehicle Power and Propulsion 2005, pp530-535.

[4] Wang Zhangcheng, Li Weinmin, “Optimization of Series Hybrid Electric Vehicle Operational Parameters By Simulated Annealing Algorithm,” 2007 IEEE International Conference on Control and Automation,Guangzhou,China.

[5] Chu L, Li Y, Wang Q N, “Study on the parametric optimization for parallel hybrid electric vehicle power train,” SAE 2000-01-3109.

[6] GakdiV, Ippolite L, Piccolo A, “Evaluation of Emission Influence on Hybrid Electric Vehicles Sizing,” Process of International Conference on Power Electronics Electrical Drives Advanced Machines and Power Quality,2000, Ischia, Italy,pp:1-7.

© (2012) Trans Tech Publications, Switzerland
doi:10.4028/www.scientific.net/AMM.187.27

Numerical Simulation Research on the Hydrodynamic Forces Acting on a Tanker in Oblique Motion

Zhan Chengsheng

School of Transportation, Wuhan University of Technology, Wuhan, 430063, China

zhancs@163.com

Keywords: Numerical Simulation; Hydrodynamic Force; Oblique Motion; Viscous Flow.

Abstract. It is easy to generate the separation of the flow in the stern when the ship is in oblique motion, and the flow around the hull is complex. In this article, the viscous flow around a tank in oblique motion is simulated using viscous method, and the maneuvering hydrodynamic forces are calculated and compared with experimental results. It is shown that the present method of the numerical simulation is feasible.

Instruction

In recent years, with the rapidly development of computional fluid dynamics (CFD) technology, the application of CFD technology to simulate the complex flow around the ship is more and more extensive. 3D viscous flow methods for calculating the ship hydrodynamic performances are important development direction for the ship CFD[1,2]. For large tanker, due to the full ship hull, the flow around the hull is more complex, especially the flow is easy to generate the separation when the ship is in oblique motion. Using CFD technology, simulate the pressure distribution on the hull surface and the flow field details accurately, predict the maneuvering hydrodynamic performance, these research works are great significant to the ship design.

At the same time, using CFD methods to replace or partially replace the ship performance experiments is the researchers' ultima aim, but the reliability and feasibility of CFD methods has always been the focus of researchers'attention in recent years[3,4]. A number of viscous flow CFD simulations have been instituted on standard ships such as: KCS, DDG- 51, KVLCC etc.[5~7]. Its' objective were to test the feasibility and effectiveness of CFD methods on the calculation of ship performance. According to published literatures, the accuracy of CFD simulation lies on the computational model, of which the ship viscous flow simulation's accuracy lies on computational grid, turbulence model and boundary conditions. In this article, using FLUENT software, suitable calculation model is constructed to simulate the viscous flow around the tank KVLCC2 ship model in oblique motion, such as: the high quality three-dimensional grid is generated, appropriate turbulence model and boundary conditions are selected. A set of effective CFD calculation method of the maneuvering hydrodynamic forces acting on a tanker in oblique motion is obtained.

Solution model

For the simulation of the viscous flow around a hull in oblique motion, the viscous solver of FLUENT software is adopt. Firstly, the IGES file of the hull surface is inport to the GAMBIT module, then the solution domain around the hull is established. Secendly, the 3D grids are generated in solution domain. Thirdly, the grid file is inport to FLUENT software, then the Boundary conditions are set on the boundarys of the solution domain, and then the control equations are discretizated. Finally, the flow around the hull in oblique motion with different heading angles are simulated and the hydrodynamic forces on the hull are calculated.

Solution domain. For large tanker, the wave-making is weak because it is generally in the low speed. In this article, the wave-making's influence is ignored in the calculation of ship hydrodynamic forces in oblique motion. The double model was established to simulate the viscous flow around the ship hull by Solving the RANS equations with the semi-cylindrical solution domain. The solution domain is shown in Fig. 1.

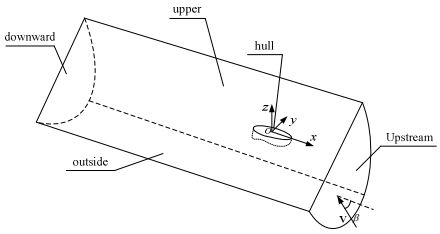

Fig. 1 Solution domain model

Cartesian coordinate system fixed on the ship hull was adopt. The ship hull is considered that is not moving, the flow is considered that flow into the control volum with ship speed. x-axis and y-axis in the still water plane, x-axis pointing forward from the stern to bow and the x-axis origin on the midship. y-axis pointing forward from the starboard to larboard. z-axis vertically upward. The angle between the negative direction of the flow and the positive x-axis angle was the heading angle β . The solution's control equations are the incompressible fluid continuity equation and the RANS equations in solution domain.

Boundary conditions. The velocity inlet boundary condition is adopted on the upstream inlet boundary, where uniform flow is prescribed. On the outside boundarys, the moving wall boundary condition is set. The outflow boundary condition is set on the downward outlet boundary. Non-slip condition is used on the hull surface. Symmetry condition is adopted on the upper boundary.

Computational grids and equations discretization. Flow around Large tanker in oblique motion is complex, high-quality grid is required when the simulation is carried out. In this article, The four sides mesh is adopt on the hull surface. The solution domain is divided into several blocks, of which the grids of the blocks around the hull are refined where the y plus of hull surface approximate 200. In the block around the stern, the unstructured hexahedral grids are adopted, structured hexahedral grids are adopt in the rest blocks.

Second order upwind difference schemes are applied to momentum equation and $k-\varepsilon$ or $k-\omega$ equations. SIMPLEC method is used for dealing with the pressure-velocity coupling.

Simulation and results

Calculation object. The tanker KVLCC2, one of the standard ship forms used in the CFD simulation comparative research is taken as the object. It's experimental datas are abundance and integrate. The corresponding parameters for the ship model: length between perpendiculars $L_{pp}=4.97m$,breadth moulded $B=0.901m$,draft $d=0.323m$, towing speed $V=0.994m/s$, corresponding $f_r=0.142$ and $\mathrm{Re}=3.945\times10^6$. The semi-cylinder domain is Selected as the calculation domain, the radiu of the cylinder is 2 times of L_{PP} , 2 times of L_{PP} is extended to the upstreams, and 2 times of L_{PP} is extended to the downstream. The hexahedral grids in the calculation domain are shown in Figure 2. And the number of the grid nodes is about 2.5 million.

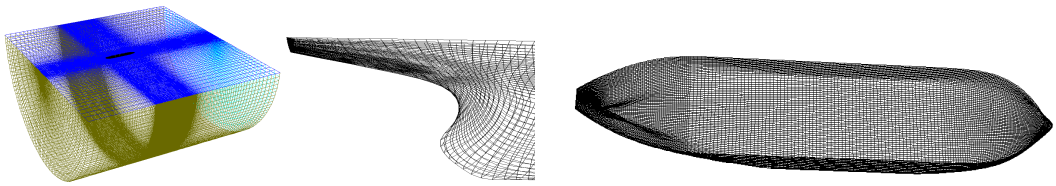

Fig. 2 Solution domain grid and hull surface mesh

Simulation results. A. Results of the simulation with different Turbulence models

Three kinds of turbulence (RNG $k-\varepsilon$ turbulence model, Realizable $k-\varepsilon$ turbulence model and the $k-\omega$ SST turbulence model) were used to simulated the flow around the hull in oblique motion respectively. Near-wall turbulence model is dealed with the Non-Equilibrium Wall Functions. The flow around the hull which the ship in oblique motion with 12^0 heading angle is simulated, and the hydrodynamic coefficients is calculated, the results are shown in Fig.3 and Table 1.

From Fig.3 and Table 1, it can be seen that the accuracy of the simulation is affected by the turbulence models. However, compared the hydrodynamic coefficients of calculation with the experimental results, the difference of the calculation accuracy which different turbulence models are adopt is not obvious. By comparison, the calculation results with $k-\omega$ SST turbulence model are closer to experimental results. At the slice of disc, the axial velocity distribution of calculation are compared with the experimental results. In the same way, the calculation result with $k-\omega$ SST turbulence model is closer to experimental result. So the $k-\omega$ SST turbulence model are used in the following simulation.

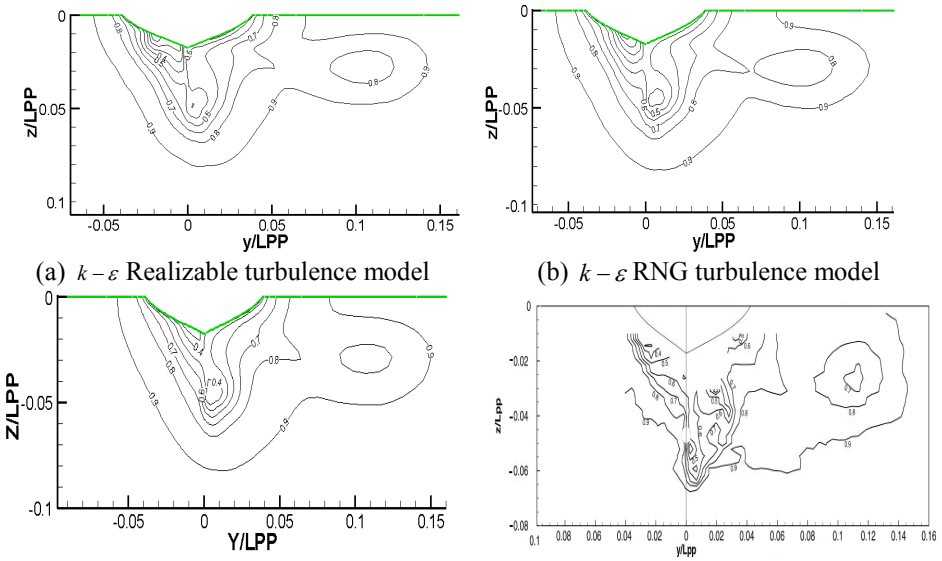

(a) $k-\varepsilon$ Realizable turbulence model (b) $k-\varepsilon$ RNG turbulence model

(c) $k-\omega$ SST turbulence model (d) experimental

Fig. 3 Contours of axial velocity at slice of disc($\beta=12^0$)

Table 1 Ship hydrodynamic coefficients in oblique motion

	SST $k-\omega$	Realizable $k-\varepsilon$	RNG $k-\varepsilon$	Experiment
C_x	0.01772	0.01922	0.01823	0.01750
C_y	0.06770	0.06793	0.06826	0.07082
C_N	0.02704	0.02808	0.02707	0.02539

While the dimensionless Risitance coefficient $C_x=\dfrac{-F_x}{\frac{1}{2}\rho V^2 L_{PP}d}$, Lateral force coefficient $C_y=\dfrac{-F_y}{\frac{1}{2}\rho V^2 L_{PP}d}$,Yaw moment coefficient $C_N=\dfrac{N}{\frac{1}{2}\rho V^2 L_{pp}^2 d}$.

B. Simulation results of different heading angle

The towing tests which the ship model are towed with different heading angles are simulated. The heading angels are respectively 0^o, 3^o, 6^o, 9^o and 12^o, Hydrodynamic coefficients are shown in Table 2.

Table. 2 Hydrodynamic coefficient of different heading angles

β		C_x	Error	C_y	Error	C_N	Error
0^o	CFD	0.01865	6.21%	—	—	—	—
	Exp.	0.01756		0.00004	—	0.00006	—
3^o	CFD	0.01857	4.57%	0.01326	4.98%	0.00708	15.7%
	Exp.	0.01776		0.01263		0.00612	
6^o	CFD	0.01847	4.30%	0.02566	0.25%	0.01445	3.80%
	Exp.	0.01771		0.02560		0.01392	
9^o	CFD	0.01792	3.66%	0.04459	-2.06%	0.02034	4.86%
	Exp.	0.01729		0.04553		0.01940	
12^o	CFD	0.01772	1.26%	0.06770	-4.40%	0.02704	6.50%
	Exp.	0.01750		0.07082		0.02539	

It can be seen from Table 2, the present hydrodynamic coefficients are consistent with experimental results, the error of the present drag coefficient and lateral force coefficient approximately to be less than 6.5%. Except for the state of the heading angle $\beta = 3^0$, the errors of the yaw moment coefficients are also less than 6.5%. Therefore, the caculation of the maneuvering hydrodynamic forces is accurate.

The present pressure distribution on hull and the experimental results are shown in Fig. 4 and Fig. 5.

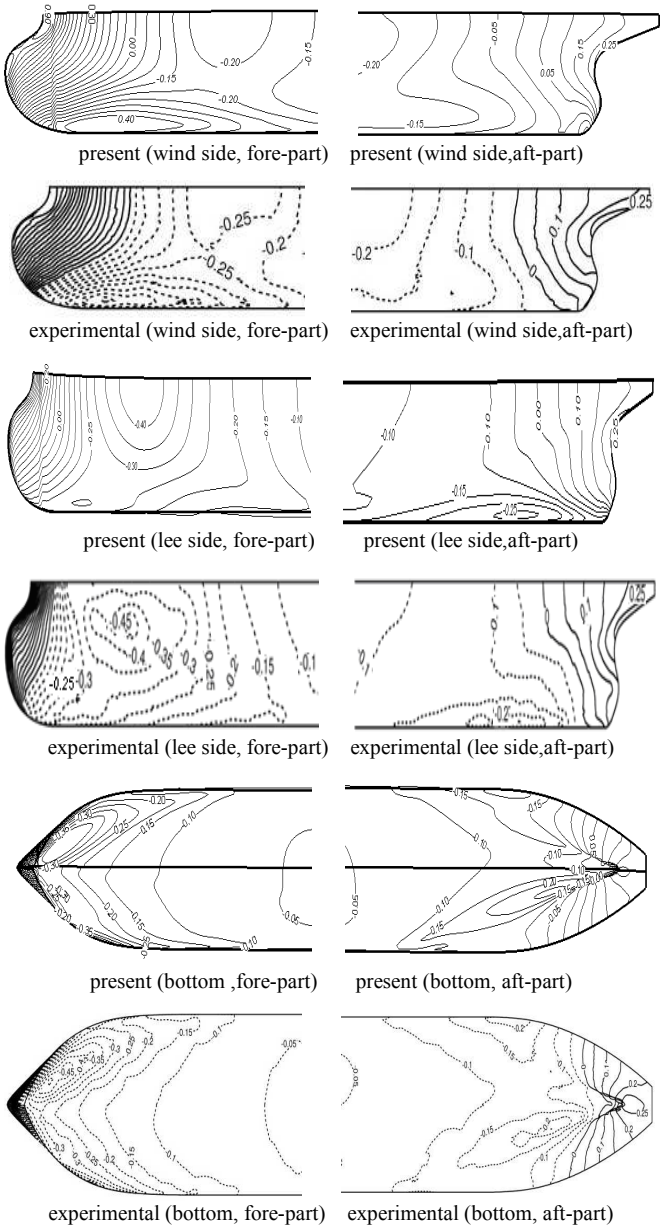

Fig. 4 Pressure coefficient distribution on the hull surface at $\beta = 6^0$

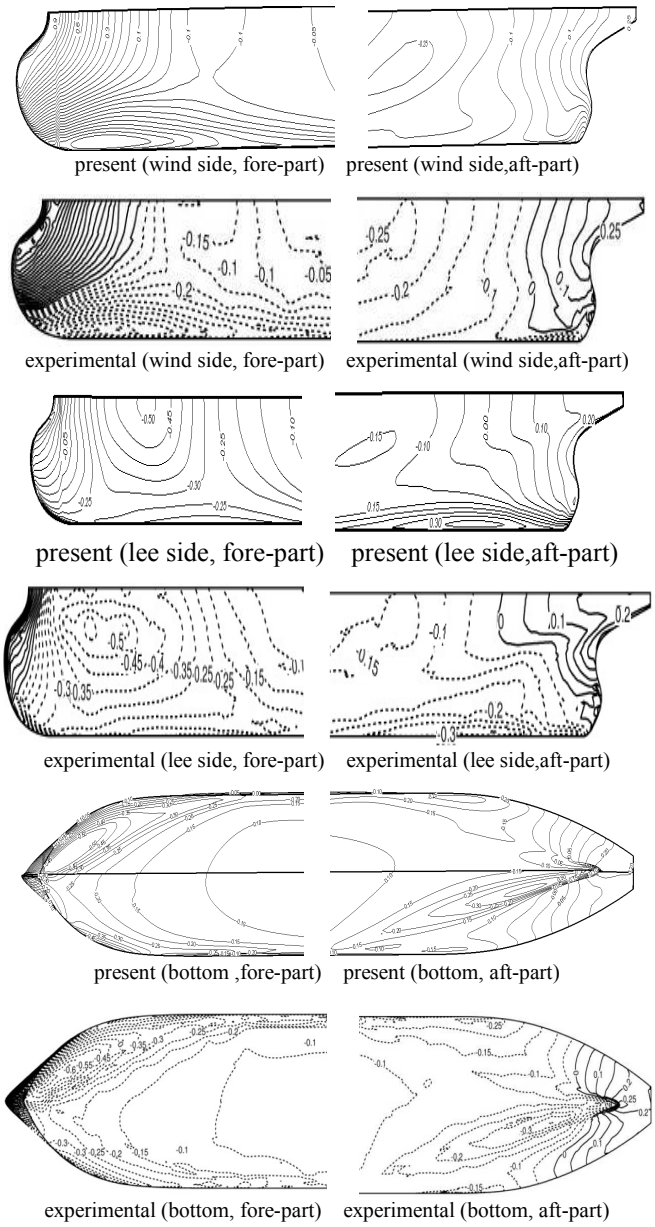

Fig. 5 Pressure coefficient distribution on the hull surface at $\beta = 12^0$

It can be seen from Fig.4 and Fig.5: at the lee side of the fore-part when the heading angle are $\beta = 6^0$ and $\beta = 12^0$, the present results of pressure distribution are different from the experimental results, the present pressure coefficient contours are semi-circular, while the experimental contours are closed circles, and the experimental center of low pressure is closer to the bow than present result. Except these, the present pressure distribution is consistent with the experimental results, the present pressure distribution on hull surface shows the details of the viscou flow around the hull in oblique motion.

Conclusion

(1) In this article, the simulation model can simulate the viscous flow of the tanker in oblique motion effectively. The maneuvering hydrodynamic forces can be calculated accurately.

(2) It was found that when the complex viscous flow of the tanker in oblique motion was simulated, the caculation precision is relation to the quality of the grid, and the high-quality structured grid is beneficial to the precision. As the complexity of the 3D hull surface, the unstructured grid is generated in the block of the stern in this article. so as when high-quality structured grids is generated in the whole solution domain, the precision still can be improved.

(3) Turbulence model also affects the accuracy of the simulation, but the effect is not obvious.

Acknowledgements

The reasearch is surpported by National Natural Science Foundation of China (ID: 10772139) and (ID: 50909079), key project of Ministry of Education of China (ID: 109109). And the reasearch is surpported by key laboratory of high speed ship engineering (Wuhan university of Technology), ministryof education, china.

References

[1] Liu Y.Z. , Zhang H.X. , Li Y.L. , Miao G.P., Calculations of the Ship Performances and Solving of RANS Equations in the 21st Century, *Journal of Ship Mechanics*, 2001, Vol.5, No. 5 , p.66–84

[2] Cai R.Q. Current situation of ship CFD and our knowledge, *SHIP &BOAT*, 2002, No. 1, p.29–37

[3] Kume K.,Hasegawa J.,Tsukada Y., Measurements of hydrodynamic forces,surface pressure, and wake for obliquely towed tanker model and uncertainty analysis for CFD validation, *Journal of Marine Science and Technolog*, 2006, Vol.11, No.2 , p.604–611

[4] The Manoeuvring Committee of ITTC. Final Report and recommendations to the 24th ITTC[C]. Edinburgh UK: *Proc. of 24th ITTC*, 2005, Vol. 1

[5] Kouh J.S., Yang M.W.,Computation of Turbulent Flow around Submarine Under Oblique Towing Condition, *NTU-ESOE.-Tech*. Report 838,2005

[6] Gorski, J.J., Coleman, R.M.,Computations of the KVLCC2M Tanker Under Yawed Conditions. *Proc. CFD WORKSHOP TOKYO 2005*, Tokyo, Japan, 2005

[7] Tian X.M. A Numerical and Experimental Research on the Viscous Hydrodynamic Forces Action on a Ship in Manoervring Motion, *[H] Shanghai Jiao Tong University*,2008

© (2012) Trans Tech Publications, Switzerland
doi:10.4028/www.scientific.net/AMM.187.33

Study on the Efficiency Optimization of U-shaped curve rail type AS/RS

Hui Liu[a]*, Yangbo Huang[b], Ying Xing[a]

[a]School of Electronics and Information Engineering, Liaoning Technical University,Huludao, 125105,China
[b] Information Network Center,Tieling Normal College,Tieling,112000,China

* Hui Liu. Tel.: 13591990868, E-mail address: liuhui0990@163.com.

Keywords: Automated Storage and Retrieval System (AS/RS); particle swarm optimization (PSO); U-shaped rail; optimization

Abstract

We analyze the overall operation process and storage model of U-shaped curve rail type AS/RS, put forward an optimization designing method based on minimal operating time, set up a mathematical model, and make verifications using genetic algorithm which show that this optimization method greatly increases the operating efficiency of U-shaped curve rail type AS/RS, and provides a powerful reference for its application.

1. Introduction

As the core of logistics system, Automated Storage and Retrieval System (AS/RS) is of great importance in modern logistics. AS/RS brings huge benefit to enterprises, but it seems to be untouchable to most small-and-medium-sized enterprises in our country for its high cost in the original investment and long cycle of cost-recovering. In order to increase the utilization of AS/RS and integrate warehouse management with modern logistics, the warehousing planning scheme must be studied carefully to realize the rapid and accurate movement of goods, meanwhile lowering the cost of construction and usage [1], so that more enterprises will be able to use AS/RS. Given location allocations with the same set, those warehouses with U-shaped rail will reduce the number of stacking machine, save user investment and the cost of equipment maintenance to a certain extent. Further more the operation expenditure [2] mainly involves energy, to be more precise, the operating efficiency of the stacking machine, that is to say, the more efficiently the stacking machine operates, the less energy it consumes. So the key issue is the design of the efficiency optimization algorithm of U-shaped rail AS/RS.

The problem is a traveling salesman problem (TSP [3]), which is one of NP-complete combinatorial optimization problems [4]. Particle swarm optimization (PSO), as a swarm intelligence optimization algorithm through simulating bird foraging behaviors [5], is proposed in recent years. PSO has many advantages including the simple programming, few parameters, easy implementation, etc. Therefore an effective PSO algorithm for solving U-retrieval machine scheduling problem is designed in the paper.

2. Basic structure of U-shaped curve rail type AS/RS

The planar structure of U-shaped curve rail type AS/RS is shown in Figure1.The U-shaped curve rail connecting two rails enables the stacking machine to enter one rail directly from the other one, realizing the storage and retrieval of goods in two rails and four row locations by only one stacking machine.

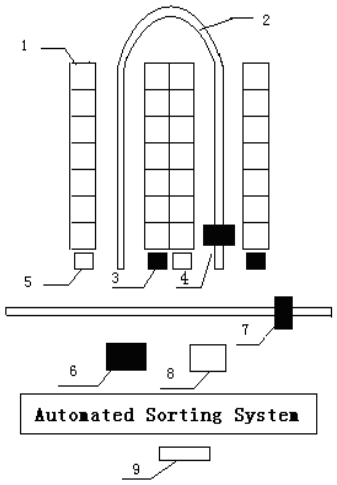

1. Shelf 2. Track of Stacking Machine
3. Shelf Storage Platform 4.Stacking Machine
5. Shelf Retrieval Platform 6. Storage Platform
7. Automatic Guided Vehicle (AGV)
8. Retrieval Platform 9. Picking Location

Fig. 1. Schematic diagram of the planar structure of U-shaped curve rail type AS/RS

3. Factors influencing the efficiency of U-shaped curve rail type AS/RS

In practice, many factors are influencing the operating efficiency of U-shaped curve rail type AS/RS, which should mainly include as follows:

3.1. Location Allocation Codes

If location allocation is provided with optimized code that meets the principles of uniform load, lowering the center of gravity, storage by rails, and proximity of storage/retrieval operation, at the beginning of warehouse construction, the operating time and energy consumption of the stacking machine will be reduced and the efficiency of the system will be increased.

3.2. Timeliness of Materials

That is the principle of first in first out of goods. Goods at maturity have the priority to be first chosen so as to speed the turnover of materials and avoid the damage of rustiness, distortion and metamorphose caused by long-term overstock of goods.

3.3. Priority of Operations

Namely assign priority to system operations. Operations are managed according to their priorities. The operation with the highest priority is managed first. In general, retrieval operations have priority over storage operations to ensure immediate retrieval and avoid the delay of the usage of components out.

3.4. Choice of Operation Paths

The same operation queue may adopt different operation sequences. If the stacking machine takes different paths, then the operating time, energy consumption, cost and efficiency are all different.

As the operation path is an important factor of influencing the working efficiency, therefore this paper mainly aims at the operation path to optimize.

4. Analysis of the operation of U-shaped curve rail type AS/RS

4.1. Problem Definition

As shown in Figure 1 we can see the practical operations of U-shaped curve rail type AS/RS are divided in the straight rails and the curve rails. To U-shaped rail, the stacking machine platforms corresponding to the straight rails at two sides are common for operations. The operations at the straight rails at two sides are consistent with those at the straight line of single-rail stacking machine. We divide operations of random distribution into two rails 1 and 2, get M—the number of freight sections of rail 1 and N—that of rail2. The stacking machine operation begins from the rail where the stacking machine is awaiting, and after the completion here it turns to the other rail. Then the operation paths of U-shaped curve rail type AS/RS are the addition of the path in the two straight lines and that in the curve.

4.2. Basic Assumptions

- The stacking machine operations can be carried out at both the platforms at two sides and two rails. The stacking machine has two awaiting locations. Operations may stop at each platform after completion.
- The two straight rails are 1 and 2. The horizontal moving direction of the stacking machine is x, and vertical direction y. The warehouse locations are *i* and *j*. Then the locations in rails 1 and 2 are *1i*, *1j* and *2i*, *2j*.
- The stacking machine may move horizontally and vertically simultaneously at operation speeds V_x and V_y respectively.
- Constants are set to the braking and starting of the stacking machine and the stacking machine time, which may be omitted in calculation.
- In Storage and Retrieval operations, the pallets of the warehouse are corresponding to the locations respectively.
- Without loss of generality, each freight section is set the same height, length and weight of container.

Following above assumptions, we can get the total operating time when we select *M* order picking locations from rail 1 and N order picking locations from rail 2:

$$T = \sum_{i=1}^{m}(T_{10,1i} + T_{1i,10}) + \sum_{i=0,j=i+1}^{m-1} T_{1i,1j} + T_{1m,0} + T_s + \sum_{i=1}^{n}(T_{20,2i} + T_{2i,20}) + \sum_{i=0,j=i+1}^{n-1} T_{2i,2j} + T_{2n,0} \tag{1}$$

In formula (1), $\sum_{i=1}^{m}(T_{10,1i} + T_{1i,10}) + T_{1m,0}$ and $\sum_{i=1}^{n}(T_{20,2i} + T_{2i,20}) + T_{2n,0}$ are fixed when the sequence of the location allocations [6] [7] is selected, T_s is operating time in the curve rail which is fixed. So we simplify the factors that influence the total S/R time T as

$$\begin{aligned} T &= \sum_{i=0,j=i+1}^{m-1} T_{1i,1j} + \sum_{i=0,j=i+1}^{n-1} T_{2i,2j} \\ &= \sum_{i=0,j=i+1}^{m-1} \max(T_{1x_{ij}}, T_{1y_{ij}}) + \sum_{i=0,j=i+1}^{n-1} \max(T_{2x_{ij}}, T_{2y_{ij}}) \\ &= \sum_{i=0,j=i+1}^{m-1} \max\left(\frac{D_{1x_{ij}}}{V_x} + \frac{D_{1y_{ij}}}{V_y}\right) + \sum_{i=0,j=i+1}^{n-1} \max\left(\frac{D_{2x_{ij}}}{V_x} + \frac{D_{2y_{ij}}}{V_y}\right) \end{aligned} \tag{2}$$

We code the m order-picking positions in rail 1 as {1,2,3……m}，and m order-picking positions in rail 2 as {1,2,3……n}, and based on these codes we set up the following mathematical models:

$$T_{\min} = \min T \tag{3}$$

$D_{1x_{ij}}$ is the horizontal distance between the two operation points i, j in rail 1; $D_{1y_{ij}}$ is the vertical distance between the two operation points i,j in rail 1; $D_{2x_{ij}}$ is the horizontal distance between the two operation points i,j in rail 2; $D_{2y_{ij}}$ is the vertical distance between the two operation points i, j in rail 2.

5. Algorithm Design

5.1. PSO Introduction

PSO can simulate bird foraging behaviors to make birds through a collective collaboration among the groups to achieve optimal objective [8], which is based on swarm intelligence optimization methods. This algorithm is similar with the genetic algorithm is also an iterative algorithm based on group, but no crossover and mutation of genetic algorithm, through the particles searching in the solution space of the particles to follow the optimal.

5.2. PSO Principle

According to the above data model, if we want to calculate the shortest operating time, we need to know the location of each order picking. To facilitate solving of PSO, the form of natural coding is used for each order picking location. Different natural sequence is defined as an order picking path. Each path is a feasible solution, called particles. The collection of many particles is called population.

PSO randomly initializes a set of solutions for the problem, set the search space for the D-dimensional, the total number of particles is n. I-particles in d-dimensional position of the solution space is represented as $X_i = (x_{i1}, x_{i2}, ..., x_{iD})$, the i-particles rate of position change (speed) is represented as $V_i = (v_{i1}, v_{i2}, ..., v_{iD})$. In the process of searching, the particles dynamically adjust their position through the population and individual experience. In the PSO, the particles by tracking two extremes to update their own, one is the best solution $P_i = (p_{i1}, p_{i2}, ..., p_{iD})$ of a own particle, the other is the best solution Pg of all the population. The computation of the speed and the location (as the fitness evaluation) of particles in each generation completed by iterative formula as follows.

$$v_{id}(t+1) = w \times v_{id}(t) + c_1 \times rand() \times [p_{id}(t) - x_{id}(t)] + c_2 \times rand() \times [p_{gd}(t) - x_{gd}(t)] \quad (4)$$

$$x_{id}(t+1) = x_{id}(t) + v_{id}(t+1) \ (1 \le i \le n, 1 \le d \le D) \quad (5)$$

Among (4) and (5), c_1 and c_2 is positive constants, called the acceleration factor; $rand()$ is a random between 0 and 1; w is an inertia factor.

Location of the particle represents a feasible solution, and the particle fitness function can be represented as

$$f(x) = T \quad (6)$$

Particle swarm optimization can be expressed as computing the minimum of $f(x)$.

The rate of the particle swarm algorithm is designed as the exchange set of order picking locations, and different swap sequences can produce different solutions, so as to achieve the purpose of generating new solutions.

5.3. Algorithm Steps

1) Initialize the population according to the problem and set the parameters c_1, c_2 and w.

2) Determine whether to meet the maximum number of iterations or the termination conditions, if yes, go to 7); otherwise continue;

3) Calculate the fitness of each particle;

4) For each particle, if the particle's fitness is better than its history best fitness, then the current value as the new optimal solution p_{id} of the particles;

5) In the population, finding a better global optimal solution as the best optimal solution p_{gd} of all particles;

6) According to the particle current location, in accordance with the iterative formula (1) and (2), calculate to the next position of the particle;

7) Get the best result and output it.

6. Experiment Verification

Adopting PSO to solve optimization problem of U-shaped curve rail operation path, we can get the experiment results as follows.

There are 6 layers and 15 columns in each freight section, the size of a freight section is 2*1 unit, the speed V_x =80m/min, V_y =30m/min, curve speed is 30m/min. The parameters of PSO: the number of particles n = 30, w = 0.8; $c_1 = c_2 = 1.7$; iterations is 1000.

From the aspect of operating times [9], we get the operating efficiency comparison before and after optimization if we choose different numbers of operations for many times as shown in Figure 5:

	Parameters	OTBO	OTAO	PTS
	ONR1=25 ONR2=20	465.46	242.63	47.87%
	ONR1=20 ONR2=30	528.16	293.30	44.47%
	ONR1=18 ONR2=12	310.26	205.38	33.80%
	ONR1=22 ONR2=16	390.44	246.52	36.86%
	ONR1=16 ONR2=28	448.26	261.27	41.71%
	ONR1=14 ONR2=22	375.02	242.23	35.41%

Operation Numbers in Rail 1 (ONR1)
Operation Numbers in Rail 2 (ONR2)
Operating Time before Optimization (OTBO)
Operating Time after Optimization (OTAO)
Percentage of Time Saved (PTS)

Fig. 2. Schematic diagram of the operating efficiency comparison before and after optimization

We can see that after the adoption of the algorithm, the operating efficiency of the stacking machine is increased significantly, and the operations are chosen at random, so it is of generality. The warehousing layout of U-shaped curve rail type AS/RS causes limited optimization and optimizing efficiency is lower than ordinary straight rail AS/RS, but U-shaped curve rail type AS/RS is a better choice if the Storage and Retrieval operations are not very frequently performed.

7. Conclusion

In this paper we analyze the overall order picking operation of U-shaped curve rail type AS/RS, put forward an optimization designing method based on the minimal operating time [8], set up a mathematical model, and make verifications using PSO which show that this method significantly reduces the operating time and energy consumption of the storage/retrieval machine, saves operation costs, greatly increases the operating efficiency, and provides a powerful reference for its application. And we also make clearer that our next step is to study those factors that influence the overall storage and retrieval capability of U-shaped curve rail type AS/RS such as uniform allocation of goods and sorting probability of the operation in the two straight rails.

References

[1] Francesco Amato, Francesco Basile etal. "Crane and Shuttle Optimiaztion in Warehousing Systems," Proceedings of the 2002 IEEE International Conference on Robotics & Automation. Washington, DC, May, 2002.

[2] G. L. Tu, Y. C. Wan, M. Zhang, S. C. Quan, J. M. Yang, " A comparative research on the operation efficiency of the straight and curve rail type stacking machine under equiprobable condition," Logistics Technology, 28(3), pp. 142-143,151,2009.

[3] Thomas Fischer, Thomas Stiitzle, "Holger Hoos et al. An analysis of the hardness of TSP instances for two high-performance algorithms, "The 6th Metaheuristics International Conference. Vienna, Austria, 8:361-367, 2005.

[4] Tali Eilam Tzoreff, Daniel Granot. "The Vehicle Route Problem with Pickup and Delivery on Some Special Graphs, "Discrete Applied Mathematics, 116, pp. 193–229, 2002.

[5] C. Y. Peng, L. Gao, X. Y. Shao, C. Zhou. "General particle swarm optimization algorithm for job-shop scheduling problem," Computer Integrated Manufacturing Systems , 12(6), pp. 1027-1037, 2006.

[6] G. H. Tian, P. Zhang , X. L. Li, J. Q. Yin, F. Lu, " Research on One Class of Optimization Problem of the Automated Warehouse Using a New Kind of Hybrid Genetic Algorithm, " System Simulation,16 (6), pp. 1198-1201,2004.

[7] G. Q. Yin, F. Y. He, D. F. Sheng, "Research on the storage alignment optimization model fro automated warehouse," Journal of fujian university of technology, 4(3), pp.347-350, June, 2006.

[8] J. M. Xiao, J. J. Li, X. H. Wang. “A Modified Particle Swarm Optimization for Traveling Salesman Problems”, Computer Engineering and Applications, 35, pp. 50-52, 2005.

[9] SUK-HWA CHANG and PIUS J. EGBELU. "Relative pre-positioning of storage/retrieval machines in automated storage/retrieval systems to minimize maximum system response time," IIE Transactions, 29, pp. 303–312, 1997.

CHAPTER 2:

Characteristic Studies of Mechanical and Material Systems

© (2012) Trans Tech Publications, Switzerland
doi:10.4028/www.scientific.net/AMM.187.41

Study on Sheet Bonding and Break Strength Characteristics

Jinsong Tao* and Pisen Yang
State Key Laboratory of Pulp & Paper Engineering
South China University of Technology
Guangzhou,510640, P.R. China
* Corresponding author. E-mail address: jstao@scut.edu.cn

Keywords: PAPER BONDING AND BREAK, ELASTIC MODULUS, YIELD STRENGTH, BREAK STRENGTH

Abstract
For researching the paper sheet bonding and break characteristics, hardwood pulp, bamboo pulp and softwood pulp were used to form sheet, and beating degree, basis weight and PAM were changed to research the influence on elastic modulus and the specific value of yield strength to break strength. The result shown that beating degree, basis weight and PAM have influence on elastic modulus and have minor influence on the specific value.

1. Introduction

The sheet tensile strength is an important characteristic because the small tensile strength will lead to sheet break and affect the paper machine's runnability and stability, so the tensile strength is also called break strength. From the technological point of view, these factors are affected by different equipment solutions and selection of materials.

The use of gap formers has increased the tensile strength of paper, and therefore runnability is better than before. A good moisture profile and high dry matter content such as PAM are also essential factors affecting runnability in the press section. To ensure an adequate dry matter content, a fourth press is commonly used. A high pressing temperature with a heated centre roll and steam box is another way to increase the dry matter content [1].

Material selection also has its own effect on the web's adhesion to the rolls, which may occasionally limit the runnability of the paper machine. Problems with detachment may also be caused by the increase in machine speed, closing of water circulation, and chemicals and other elements that affect the wet end chemistry of the paper machine [2]. The short circulation together with the head box is usually considered the most sensitive part of the paper machine. Even small variations in consistencies, process flows or other operating parameters affect paper quality such as basis weight or cause web breaks.

The paper break has close relations with the paper tensile strength, the paper will breaks when the strain on it is greater than the strength of the paper. And the strain and tress is an important character when paper sheet break. This paper will carry on experiments to research the strain and stress as well as the sheet yield strength and break strength.

2. Experiments

2.1. Raw material and instruments

2.1.1. Raw materials

Un-bleached Kraft hardwood pulp, Kraft softwood pulp and Kraft bleached bamboo pulp were the raw material and PAM was used in the experiments.

2.1.2. Instruments

Mark_V1 PFI beater, Hamjern Maskin 621 beater, paper sheet former, digital INSTRON 5566 stress-strain measuring equipment, J-DHY03A thickness measurer and beating degree measurer.

2.2. Experiments procedure

The three kinds of pulp board were dipped into water and beat with PFI beater and Hamjern Maskin 621 beater, the PAM was added into the pulp, then the beating degree was measured, then the pulp was formed to sheet and the wet sheet was pressed at 9 bar pressure. Then the beating degree, basis weight and the quantity of PAM ware changed at experimental range, the paper sheets were break on the stress-strain measuring equipment to get the paper sheet elastic modulus and the break strength, the yield strength was calculated with the measured data.

3. Results and Discussion

3.1. The influence on elastic modulus of beating degree, basis weight and PAM

3.1.1. Beating degree

The softwood, hardwood and bamboo pulp were beat at 22, 33, 44, 53, 63 ^{O}SR, the basis weight was 75 g/m^2, and the PAM wasn't added into the pulp. The elastic modulus of the each sheet was shown in Fig.1.

From Fig.1, we can find the influence trend of beating degree on elastic modulus is that it improve fist with the beating degree improve, and decline when arriving the peak value. It's because the first step of beating is to let fiber to fibrillation which will offer more bonding area, and the bonding strength will improve that result in the elastic modulus improve, and the second step of beating is cut the fiber which will let the fiber loss many bonding pot. The bamboo pulp and hardwood pulp sheet is easy to arrive peak value at 30^{o}SR and 33 ^{o}SR, and the softwood pulp sheet is at 42 ^{o}SR, it maybe the softwood fiber is difficult to fibrillation.

The sheet elastic modulus will change along with the beating degree change, the variations range softwood pulp sheet is the biggest which is 19.9%, and the second is hardwood pulp sheet which is 13.8% and the final is bamboo pulp sheet which is 9.6%. When the fiber was beating at the same beating degree, the hardwood sheet will get the biggest elastic modulus, then is the bamboo pulp sheet and the softwood pulp sheet, because the hardwood pulp fiber is longer than bamboo pulp fiber and bamboo pulp fiber is longer than softwood pulp fiber. To get the same elastic modulus, the beating degree is that softwood is smaller than bamboo pulp; and bamboo pulp smaller than hardwood. From the data in the Fig.1, we can find when the beating degree is the same, softwood pulp sheet is easy to strain, then is bamboo pulp sheet and hardwood pulp sheet, that's to say, if we want to make good stiffness paper sheet, the hardwood pulp is the best than the other two pulp.

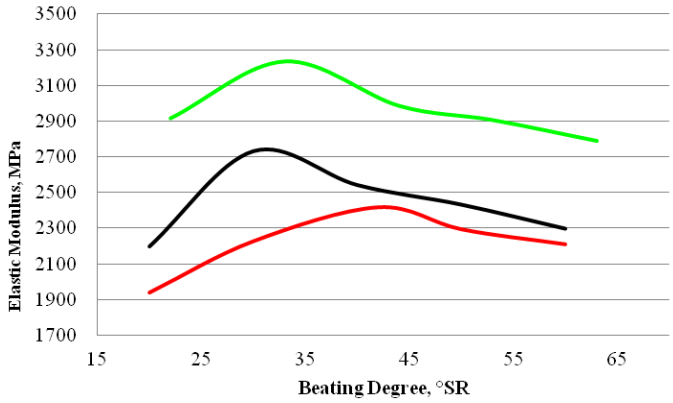

Fig. 1. The influence on elastic module of hardwood, softwood and bamboo pulp with beating degree (----Green line: hardwood pulp sheet; -----black line: bamboo pulp sheet; -----red line: softwood pulp sheet)

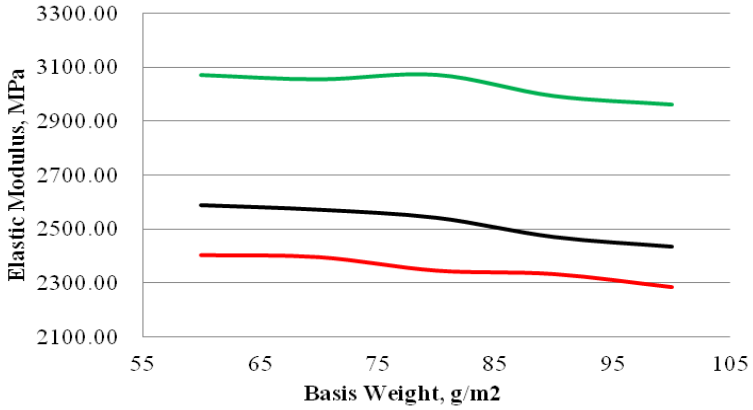

Fig.2. The influence on elastic module of hardwood, softwood and bamboo pulp with basis weight (----Green line: hardwood pulp sheet; -----black line: bamboo pulp sheet; -----red line: softwood pulp sheet)

3.1.2. Basis weight

The three kind of pulp was beat at 35 °SR and were formed at 60,70,80,90,100 g/m^2, the influence of basis weight on elastic modulus is as Fig.2.

From the Fig.2, we can find the elastic modulus decline with the enhance of basis weight. That's to say, more bigly of basis weight, the sheet is harder to strain and the stiffness is good. So we can improve the basis weight to improve the stiffness sometimes if we don't care about the material cost. When the basis weight is same, the hardwood pulp sheet's elastic modulus is the biggest.

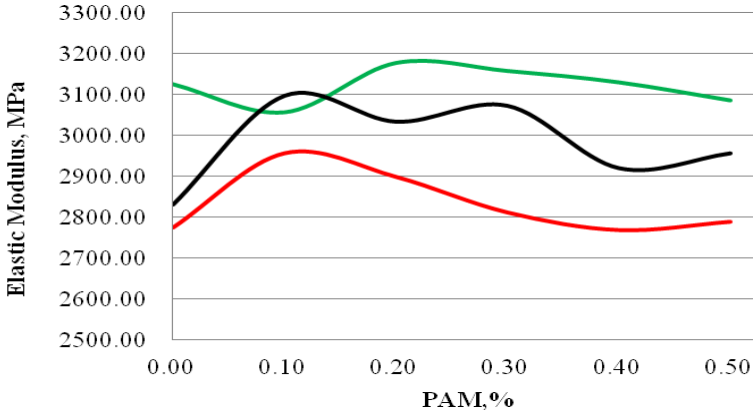

Fig.3. The influence on elastic module of hardwood, softwood and bamboo pulp with different PAM (----Green line: hardwood pulp sheet; -----black line: bamboo pulp sheet; -----red line: softwood pulp sheet)

3.1.3. PAM

The three kind of pulp was beat at 35 °SR, and were formed at 75 g/m^2, and add PAM at 0, 0.1%, 0.2%, 0.3%, 0.4%, 0.5%, the influence of PAM on elastic modulus is as Fig.3.

From the Fig.3, for bamboo pulp sheet and softwood pulp sheet, the elastic modulus will improve with the content of PAM enhance firstly, and when arrive the peak value, the elastic modulus will decline. It because appropriate amount PAM will improve the fiber bonding strength especially for shear bonding strength, when adding too much, the PAM will flocculate.

3.2. The influence on specific value of yield strength to break strength of beating degree, basis weight and PAM

3.2.1. Beating degree

The yield strength is defined as the stress at which a predetermined amount of permanent deformation occurs. When the sheet is drawn to break, during the elastic deformation, it conforms to Hook's law. The yield strength is the biggest strain when the sheet is at the elastic deforms stage.

In order to research the relation between yield strength and break strength, three kind of pulp sheet was carried out experiments; the result is as shown in Fig.4.

From Fig.4, for different kind of pulp sheet, we can find the specific value of yield strength to break strength with different beating degree isn't change too much, the value of hardwood pulp sheet is 0.25~0.32; and bamboo pulp sheet is 0.38~0.42, and softwood pulp sheet is 0.41~0.45. That's to say, when the beating degree is changing, softwood pulp sheet elastic-plastic and plastic deformation isn't too much, it because the softwood fiber is short.

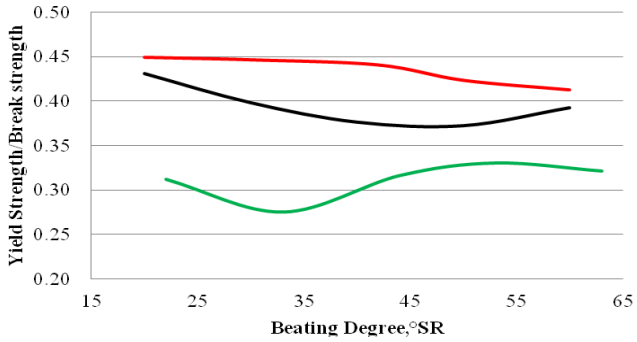

Fig. 4. The influence on the specific value of yield strength to break strength of hardwood, softwood and bamboo pulp with beating degree (----Green line: hardwood pulp sheet; -----black line: bamboo pulp sheet; -----red line: softwood pulp sheet)

3.2.2. Basis weight

The three kind of pulp was beat at 35 °SR and were formed at 60,70,80,90,100 g/m^2, the influence of basis weight on the specific value of yield strength to break strength is as Fig.5.

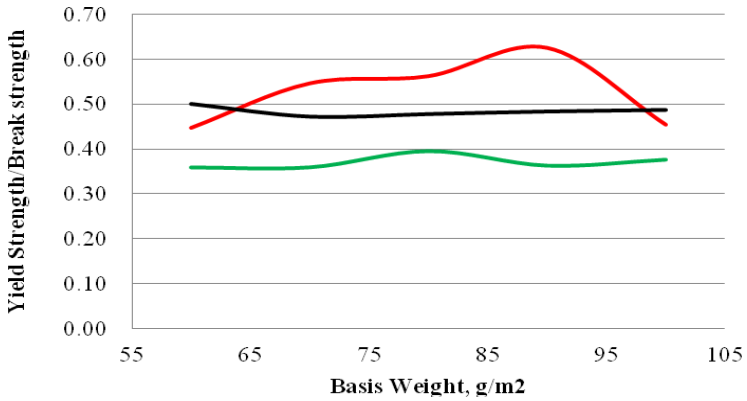

Fig.5. The influence on the specific value of yield strength to break strength of hardwood, softwood and bamboo pulp with basis weight (----Green line: hardwood pulp sheet; -----black line: bamboo pulp sheet; -----red line: softwood pulp sheet)

From the Fig.5, we can find the specific value of hardwood pulp sheet and bamboo pulp sheet are almost constant and softwood sample is about 0.38 and bamboo sample is about 0.49, and the softwood sample is about 0.45~0.61.When the basis weight is the same, the value of softwood is the biggest, then is bamboo sample and hardwood sample. That's to say, the hardwood sheet has a longer elastic-plastic and plastic deformation.

3.2.3. PAM

The three kind of pulp was beat at 35 °SR, and were formed at 75 g/m^2, and add PAM at 0, 0.1%, 0.2%, 0.3%, 0.4%, 0.5%, the influence of PAM on the specific value of yield strength to break strength is as Fig.6.

From Fig.6, the influence range of hardwood sample is 0.28~0.32; bamboo sample is 0.40~0.47; and softwood sample is 0.46~0.50. For hardwood pulp, PAM can improve break strength much comparing with yield strength. But for bamboo pulp, PAM can improve yield strength.

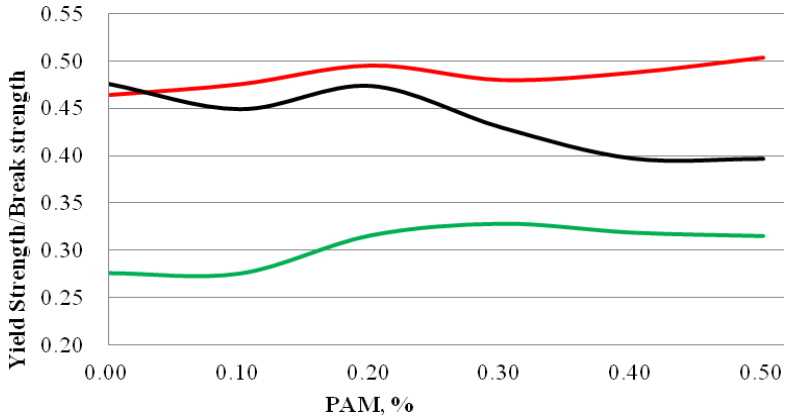

Fig.6. The influence on the specific value of yield strength to break strength of hardwood, softwood and bamboo pulp with different PAM (----Green line: hardwood pulp sheet; -----black line: bamboo pulp sheet; -----red line: softwood pulp sheet)

Conclusion

Beating has some influence on elastic modulus for hardwood pulp sheet, bamboo pulp sheet and softwood pulp sheet, it improves the elastic modulus first and then decline according beating degree enhance. And beating almost has no influence on the specific value of yield strength to break strength.

Basis weight reduces elastic modulus for three kind samples and almost has no influence on hardwood pulp sheet and bamboo pulp sheet.

PAM improve the elastic modulus first for bamboo pulp sheet and softwood pulp sheet and almost have no influence on hardwood pulp sheet.

Acknowledgements

The authors would like to acknowledge the financial support from the Natural Science Foundation of China (Grant No. 20906030), Guangdong Natural Science Foundation (Grant No.10151064101000055), the Fundamental Research Funds for the Central Universities (Grant No.2011ZM0100) and the Youth Innovation Program Foundation of State Key Laboratory of Pulp and Paper Engineering of South China University of technology.

References

[1] Neimo L . Papermaking Chemistry. *Papermaking Science and Technology*, Book 4, Finnish Paper Engineers' Association and TAPPI. Fapet Oy, Jyväskylä, Finland.1999

[2] Juuso E K, Ahola T, Kumpula H . Case Based Intelligent Indicator for Paper Web Breaks.*In Proceedings of IPMU2002- 9th International Conference on Information processing andManagement of Uncertainty in Knowledge Based Systems*.2001, July 1-5. Annecy, France.

© (2012) Trans Tech Publications, Switzerland
doi:10.4028/www.scientific.net/AMM.187.46

Static and Dynamic Stiffness Characteristics Analysis of Hydro-pneumatic Suspension

Wei Jianhua[1,a], Du Heng[1], Lin Hai[1]

[1]The State Key Laboratory of Fluid Power Transmission and Control, Zhejiang University, Hangzhou 310027, China

[a]jhwei@zjuem.zju.edu.cn.

Keywords: Suspension; Stiffness; Linearization; Simulation

Abstract. A simplified nonlinear model in time domain and a linear model of hydro-pneumatic suspension in frequency domain were established and the expression of static stiffness and dynamic stiffness of hydro-pneumatic suspension were derived out. The expression of dynamic stiffness contains the static stiffness. Equivalent static stiffness rises with tire stiffness increasing, with the pressure of non-rod cavity of suspension cylinder increasing and with the initial position of suspension cylinder decreasing. Dynamic stiffness related to frequency increases dramatically as the frequency increases. The concept of the dynamic stiffness was proposed. The vibration characteristics of hydro-pneumatic suspension in the view of frequency domain can be analyzed and it is the reference to analyze the stiffness characteristics for suspension.

Introduction

Hydro-pneumatic suspension involves flexible components and damping components, which stiffness and damping coefficients are changing with dynamic route. The advantages of nonlinear stiffness make natural frequency of the vehicle with hydro-pneumatic suspension vary little under a large range of dynamic route, so the comfort of the vehicle is good and changing little. It can absorb more energy to avoid too much impact on account of the damping orifice in hydro-pneumatic suspension, maintaining comfortable when driving. Also it can reduce the probability of collision between the suspension and the limiter to improve the driving stability. Based on these well characteristics, hydro-pneumatic suspension is applied widely on the large construction vehicles. In order to design a pretty hydro-pneumatic suspension system, the static and dynamic stiffness characteristics of the system are required to be analyzed to provide an effective theoretical reference when designing hydro-pneumatic suspension system [1,2].

In this paper, the model of the system in time domain is established and linearly analyzed according to a simplified hydro-pneumatic suspension system to derive out the expression of static and dynamic stiffness characteristics. In Matlab/Simulink simulation environment, the model in time domain is simulated, the validity of the frequency linear model is verified. Then the static and dynamic stiffness characteristic is explained theoretically.

Hydro-Pneumatic Suspension Simplify Model

To clarify stiffness and damping characteristics of hydro-pneumatic suspension, the suspension system is simplified and shown in Figure 1 to highlight the suspension stiffness characteristic. The wheel is equivalent to a spring damping system. The nonlinear stiffness of the wheels is neglected due to the little influence on the vehicle body vibration comparing to the suspension. Set tire stiffness coefficient as K and damping coefficient as B and they are constant. Suspension cylinder is regarded as hydro-pneumatic suspension system supporting component and force component, which area in non-rod cavity is A_0. Accumulator can absorb road shock and reduce vibration as the rigid component of hydro-pneumatic suspension. The damper is installed between the cylinder non-rod chamber and the accumulator as resistive component of hydro-pneumatic suspension, which can reduce the vibration of system and convert the kinetic energy into heat energy to be consumed. The impact of connecting pipe is ignored.

When confronted with a raised random road input, the tire is compressed through spring damping system. Suspension cylinder compressed non-rod chamber after forced. The high pressure oil in suspension cylinder enters into accumulator through the damper. Nitrogen in the accumulator is compressed by the high-pressure oil and then absorbs the impact of the road caused by surface roughness. Orifice will absorb energy and attenuate vibration when oil passes through. When confronted with a depressed random road input, the suspension cylinder pushes the spring damping system of the tire close to the ground which makes the pressure in non-rod cavity decreases after moving a certain distance while the pressure in the accumulator is high. The vibration will be attenuated when the oil in the accumulator pass through dampers into suspension cylinder. So using hydro-pneumatic suspension system can attenuate road vibrations, keeping the vehicle body stable.

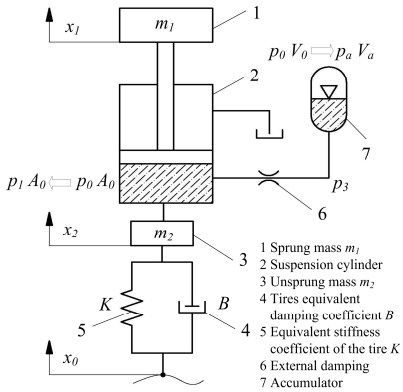

Fig. 1. A simplify hydro-pneumatic suspension model

Mathematic Model

Kinetic Equation of Vehicle Body and Wheel

Kinetic equation of vehicle body and wheel are established as follow:

$$m_1\ddot{x}_1 = p_1A_1 - m_1g \tag{1}$$

$$m_2\ddot{x}_2 = K\left(x_{k0} + x_0 - x_2\right) + B\left(\dot{x}_0 - \dot{x}_2\right) - p_1A_1 - m_2g \tag{2}$$

$$Kx_{ko} = m_1g + m_2g \tag{3}$$

According to (1)(2)(3), we can get:

$$m_1\ddot{x}_1 + m_2\ddot{x}_2 = K\left(x_0 - x_2\right) + B\left(\dot{x}_0 - \dot{x}_2\right) \tag{4}$$

Where: m_1, m_2 are body and wheel mass; p_1, A_1 are pressure and active area of non-rod chamber; x_0, x_1, x_2 are road surface displacement, wheel displacement and body displacement; K, B are equivalent spring stiffness coefficient and the equivalent damping coefficient of the tire; x_{k0} is the initial state compression amount of equivalent springs of the tires.

Laplace transform of equation (1) (4):

$$m_1s^2X_1(s) = P_1(s)A_1 \tag{5}$$

$$m_1s^2X_1(s) + m_2s^2X_2(s) = (K + Bs)[X_0(s) - X_2(s)] \tag{6}$$

Flow Equation

Assume that the oil is incompressible before the establishment of flow equation of suspension cylinder. In other word, the effect on the dynamic characteristics caused by oil pressure is ignored. That's reasonable, because the vibration characteristics of the hydro-pneumatic suspension stands in the low frequency while the dynamic characteristics caused by elastic modulus of oil stands in high frequency; Secondly leakage of suspension cylinder was ignored. Actually suspension cylinder in hydro- pneumatic suspension can also be made no leakage. In the sum, flow equation of cylinder and damper is as follow:

$$q = A_1(\dot{x}_2 - \dot{x}_1) \tag{7}$$

$$q = C_dA_0\sqrt{2(p_1 - p_3)/\rho} \tag{8}$$

Where: q is the flow from cylinder through the damper; C_d is the flow coefficient; A_0 is the flow area of the damper; p_3 is the pressure at the entrance of the accumulator; ρ is the density of oil.

Laplace transform of equation (7):

$$Q(s) = A_1 s[X_2(s) - X_1(s)] \tag{9}$$

Laplace transform of the linearized equation (8) becomes:

$$Q(s) = G_0[P_1(s) - P_3(s)] \tag{10}$$

Where： G_0 is the linearization point liquid derivative and equation of G_0 becomes:

$$G_0 = C_d A_0 / 2\sqrt{2(p_{10} - p_{30})} \tag{11}$$

Where： p_{10}, p_{30} are the value of the linearization point p_1 and p_3.

Accumulator Dynamic Model

Since the accumulator is an important rigid component in hydro-pneumatic suspension system, the dynamic and static characteristics of the system are affected significantly by its characteristics. In order to analyze the static and dynamic stiffness characteristics in the suspension system, the accumulator model refer to [3~5] are as follows:

$$\frac{P_2(s)}{P_3(s)} = \frac{1}{\frac{s^2}{\omega_n^2} + \frac{2\xi_n}{\omega_n} s + 1} \tag{12}$$

$$\frac{P_3}{Q} = \frac{K_e}{s}\left(\frac{s^2}{\omega_n^2} + \frac{2\xi_n}{\omega_n} s + 1\right) \tag{13}$$

$$K_e = NP_{20} / V_{20} \tag{14}$$

$$\omega_n = \sqrt{K_e / M_e} \tag{15}$$

$$\xi_n = R_e / 2\sqrt{K_e M_e} \tag{16}$$

Where: N is the polytropic exponent of the gas; p_{20}, V_{20} are the pressure and volume inside the accumulator at the linearization point, respectively; K_e, M_e, R_e are elasticity coefficient of the gas spring in the accumulator, accumulator equivalent quality and equivalent damping coefficient, respectively; ω_n, ξ_n are natural frequency and damping ratio of the accumulator respectively.

Analysis can be drawn from the above equations (5),(6), (9),(10),(12)~(16), which were the frequency domain model of hydro-pneumatic suspension system.

Characteristics Analysis of Static and Dynamics Stiffness

Characteristics Analysis of Static Stiffness

During the stiffness analysis, we can assume that the vehicle body is fixed, but there is displacement input on the road. The relationship between vehicle body force and the road displacement input is the stiffness characteristics of hydro-pneumatic suspension. When the input displacement signal of the road is Δx_0, movement displacement upward of the cylinder is Δx_2, the following equation emerges when achieving the stable state:

$$(p_1 - p_0)A_1 - K(\Delta x_0 - \Delta x_2) = 0 \tag{17}$$

Where: p_0 is the pressure in non-rod chamber of cylinder in the steady state before loading; p_1 is the pressure in non-rod chamber of cylinder in the steady state after loading.

If we consider the compressibility of the oil, flow equation can be obtained from the analysis on the cavity volume in the non-rod chamber of the cylinder as follow:

$$A_1 \Delta x_2 - V_q = V_1(p_1 - p_0) / E \tag{18}$$

Where: V_q is the outflow liquid volume from the non-rod chamber of cylinder; V_1 is the volume in non-rod chamber of cylinder in the steady state before loading; E is the elastic modulus of the oil.

Assuming loading slowly, nitrogen in the accumulator is isothermal changing. Gas state equation and flow equation of the accumulator are as follows:

$$p_0 V_0 = p_a V_a \tag{19}$$

$$V_0 - V_a = V_q \tag{20}$$

$$p_1 = p_a \tag{21}$$

Where: V_0 is the volume of the nitrogen in the accumulator before loading; V_a is the volume of the nitrogen in the accumulator after loading.

According to equation (18) ~ (21), we can get:

$$\begin{cases} \dfrac{V_1}{E}\Delta p + \dfrac{\Delta p}{p_0 + \Delta p} V_0 = A_0 \Delta x_2 \\ \Delta p = p_1 - p_0 \end{cases} \tag{22}$$

Due to $\Delta p \ll p_0$, there are:

$$(\frac{V_1}{E} + \frac{V_0}{p_0})\Delta p = A_1 \Delta x_2 \tag{23}$$

According to (17) and (23), we can get the static stiffness of hydro-pneumatic suspension as follow:

$$K_t = \frac{\Delta F}{\Delta x_0} = \frac{A_1^2}{\dfrac{A_1^2}{K} + \dfrac{V_1}{E} + \dfrac{V_0}{p_0}} \tag{24}$$

The above equation considers the compressibility of oil. Without considering the compressibility of the oil, the above equation simplifies to:

$$K_t = \frac{\Delta F}{\Delta x_0} = \frac{A_1^2}{\dfrac{A_1^2}{K} + \dfrac{V_0}{p_0}} \tag{25}$$

If we set that cylinder piston displacement before loading and it is x_p, then the above equation simplifies to:

$$K_t = \frac{A_1}{\dfrac{A_1}{K} + \dfrac{x_p}{p_0}} \tag{26}$$

It can be seen from the above equation that, the static stiffness of hydro-pneumatic suspension is concerned with non-rod chamber area of suspension cylinder, tire stiffness, suspension cylinder displacement and non-rod chamber pressure of suspension cylinder chamber. Under normal circumstances, A_1 and K are constant while the suspension cylinder displacement x_p is changing. So when the road input displacement gradually increases, the static stiffness of pneumatic suspension will gradually increase, making the body reduce vibration displacement to improve comfort. Then it can not be increased too much, otherwise it will increase the vibration acceleration of the body and reduce the comfort. As before, p_0 and the static stiffness of pneumatic suspension will gradually increase with the vehicle load increasing, even if the load changes, but little change happen on natural frequency of the vehicle. It can be seen that nonlinear static stiffness characteristics of hydro-pneumatic suspension will effectively improve vehicle comfort.

Characteristics Analysis of Dynamic Stiffness

As it is assumed that the vehicle body is fixed and the road generates the displacement, the force signal supplied by the road is as follow:

$$F = p_1 A_1 + m_2 \ddot{x}_2 + m_2 g \tag{27}$$

Laplace transform of the above equation becomes:

$$F(s) = p_1(s) A_1 + m_2 s^2 X_2(s) \tag{28}$$

According to (28) and frequency domain model of hydro-pneumatic suspension, the expression of dynamic stiffness can be gained as follow [6]: $K_s = F(s) / X_0(s) =$

$$\frac{(K + Bs)[(\frac{m_2}{A_1^2 K_e} + \frac{1}{\omega_n})s^2 + (\frac{2\xi}{\omega_n} + \frac{1}{A_1^2 K_e G_0})s + 1]}{(\frac{m_2}{A_1^2 K_e} + \frac{1}{\omega_n})s^2 + (\frac{B}{A_1^2 K_e} + \frac{2\xi}{\omega_n} + \frac{1}{A_1^2 K_e G_0})s + 1 + \frac{K}{A_1^2 K_e}} \tag{29}$$

Based on the concept of dynamic stiffness and above equation, it can be seen that stiffness is related to vibration frequency of the signal.

According to the equation (29), when $s = 0$, it can be simplified as follow:

$$K_s = \frac{K}{1 + \frac{K}{A_1^2 K_e}} = \frac{A_1}{\frac{A_1}{K} + \frac{x_p}{p_0}} \tag{30}$$

Comparing analytically to static stiffness equation(26) , it shows that the expression of dynamic stiffness (29) also includes the static stiffness.

Simulation Analysis

In order to get an intuitive understanding on dynamic and static stiffness of hydro-pneumatic suspension system, the actual hydro-pneumatic suspension parameters on a large construction vehicle to simulate was selected.

System Dynamics Characteristics Analysis

Based on the frequency domain model of hydro-pneumatic suspension system, we can draw that transfer function between the vehicle body suspension output displacement and road surface input displacement are such as follows:

$$\begin{cases} \dfrac{X_1(s)}{X_0(s)} = \dfrac{A_1^2 K_e (K + Bs) H_1}{A_1^2 K_e H_1 H_2 + H_3} \\ H_1 = \dfrac{s^2}{\omega_n^2} + \dfrac{2\xi_n}{\omega_n} s + 1 \\ H_2 = (m_1 + m_2)s^2 + Bs + K \\ H_3 = m_1 s^2 (m_2 s^2 + Bs + K) \end{cases} \tag{31}$$

Hydro-pneumatic suspension parameters are such as follows [7]:

Table 1. Hydro-pneumatic suspension parameters

Symbol	Value	Unit
m_1	6500	Kg
m_2	1500	Kg
K	100000	N/m
B	1000	N/(m/s)
A_1	0.0095	m^2
G_0	4.72e-8	N/(m/s)
K_e	2.08e9	N/m^5
ω_n	1.126	Hz
ξ	2.153	Dimensionless

The system Bode plot can be got in application with Matlab software based on the above parameters as follows:

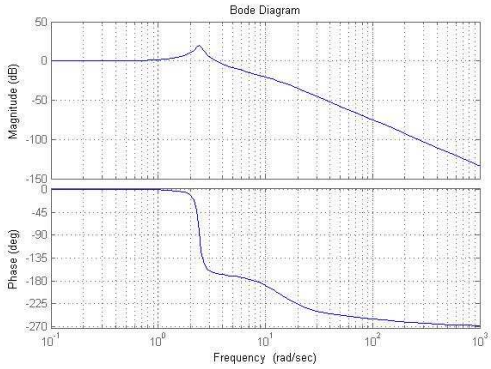

Fig. 2. Bode diagram of $X_1(s)/X_0(s)$

From the bode diagram, it can be seen that the hydro-pneumatic suspension system is equivalent to a low-frequency filter link. It attenuates the high-frequency signal from road sharply, only allowing low-frequency signals affects on the vehicle body. The natural frequency of the system approximately 1.4Hz and the amplitude of the system is the greatest at this frequency.

Simulation Analysis of Dynamic Stiffness

In order to analyze the influence of input signal frequency on the dynamic stiffness of the hydro-pneumatic suspension system, the data in Table 1 can be applied to the dynamic stiffness expression (29). Make bode plot with the application of Matlab software as follows:

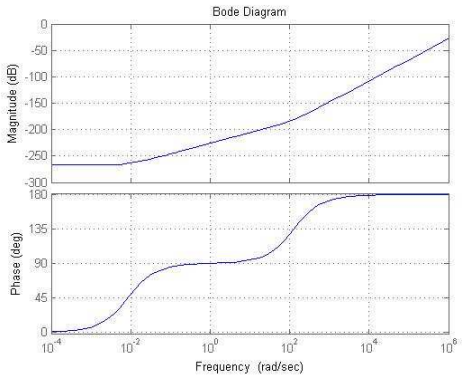

Fig. 3. Bode diagram of dynamic stiffness

From the above diagram we can see that the dynamic stiffness of hydro-pneumatic suspension will be increased significantly as the signal frequency increases much larger than the static stiffness. High frequency vibration on vehicle body does not happen when there is high frequency oscillation on the road surface, because the stiffness of hydro-pneumatic suspension at this time is very large. It does not lead to the displacement of vehicle body. Similarly the transfer function of the hydro-pneumatic suspension can also explain this phenomenon. As hydro-pneumatic suspension system is actually a part of low-pass filter, the high frequency signal is attenuated out and will not produce high-frequency vibration.

Conclusion

This article establishes frequency domain model of hydro-pneumatic suspension and derives out the expression of static stiffness of the hydro-pneumatic suspension system, from which it can be clearly seen that the variable stiffness characteristics is apparent. Equivalent stiffness rises with tire stiffness increasing, with the pressure of non-rod cavity of suspension cylinder increasing and with the initial position of suspension cylinder decreasing. Transfer function expression between vehicle body displacement and road surface input is derived from the frequency domain model of hydro-

pneumatic suspension. And we get to know that transfer function is a low-pass filter link from simulation. The concept of the dynamic stiffness of hydro-pneumatic suspension is proposed and its expression is derived out, from which we know that there is a relationship between the frequency of the signal and suspension stiffness. As the simulation obtained, the stiffness of hydro-pneumatic suspension increases dramatically when the frequency increase.

References

[1] Moulton A E, Best A. *Hydragas suspension*. SAE Paper 790374,1979.

[2] Guo Jianhua. *Stduy on the model and dynamics simulation of the HPS system of all terrain crane*. Master Thesis, Jilin University, 2005.

[3] Cao Donghui. *Design theory and basic technologies research of the high frequency hydraulic accumulator and damping equipment.* PhD Thesis, Zhejiang University,1987.

[4] Quan Lingxiao, Kong Xiangdong. *Theory and experiment of accumulator absorbing pressure pulsation without regard to its entrance characteristics*. Chinese journal of mechanical engineering, 2007, (43) 9:28-32.

[5] Zhou Yinghua. *Dynamic characteristic analysis on accumulators absorbing pressure fluctuation*. Agricultural equipment & Vehicle engineering, 2007, (5):33-38.

[6] H. E. MerritI. *Hydraulic control systems*. New York: Wiley & Sons Inc, 1967.

[7] Du Heng, Wei Jianhua, Kong Xiaowu. *Lifting synchronization control for interconnected hydro-pneumatic suspension*. Transactions of the Chinese Society for Agricultural Machinery, 2010, 41(3):29-32.

© (2012) Trans Tech Publications, Switzerland
doi:10.4028/www.scientific.net/AMM.187.53

Evaluation of tensile properties of pressure vessel materials by shear punch test method.

T. Ramesh[1], Raghu V. Prakash[1, a], S. Suresh[2], and N. Raju[2]

[1]Department of Mechanical Engineering, Indian Institute of Technology Madras, Chennai 600 036, India

[2]Welding Research Institute, Bharat Heavy Electricals Limited, Tiruchirappalli 620 014, India

[a]raghuprakash@iitm.ac.in

Keywords: Small specimen testing, shear punch test; boiler materials; shear stress; normalized displacement; ultimate tensile stress.

Abstract: A **s**hear punch test is a very useful small specimen test method for evaluating the mechanical properties of in-service components, in view of the requirements of small size sample material. This paper presents the results of shear punch tests on five grades of steels used in boiler construction, along with the correlation with yield stress and ultimate tensile stress obtained ASTM standard specimens. The design of the shear punch fixture and procedure to carry out the shear punch test is also highlighted.

Introduction

A shear punch test is a very useful test technique for evaluating mechanical properties from small volumes of material [1-4]. This feature of shear punch test has made it promising in areas like structural health monitoring, weld quality assessment and in-situ testing for aged components. Mechanical properties like yield strength, ultimate strength can be evaluated from shear punch test data.

In principle, shear punch test involves blanking of specimen, by clamping it in between a pair of dies. The specimen region, which lies in the clearance zone, will experience shear stress due to punch motion. As there is flow and fracture of material around the clearance zone, data obtained from a shear punch test provides an indication of material strength and ductility. The load-displacement response due to punching is similar to conventional tensile test with distinct linear elastic region, yield zone, strain hardening, ultimate load point and fracture as shown in Fig. 1.

Evaluation of mechanical properties of an in-service material has the problem of limited material availability for testing. This drawback can be overcome by using shear punch test, as the specimen used for shear punch test is a disk of 6 mm diameter and 0.4-0.8 mm in thickness.

Experimental details

Shear punch test fixture- The shear punch test (SPT) fixture used in the current work is designed and developed in the first author's laboratory [5]. The dies were made of high strength En 24 (AISI 4340) steel and punch was made of En31 (OHNS) steel. The dies were subjected to quench and temper heat treatment to 48 HRC and the punch was quenched and tempered to 63 HRC to improve the strength. The punch used is of cylindrical flat end type with a diameter of 3 mm. Lower die hole diameter is set to 3.04 mm, which when assembled gives a radial clearance of 0.02 mm between the punch and the die, which is also called as the shear process zone. Figure 2 presents the details of test fixture. The punch is attached to a load cell for load measurement and clip-on-displacement (COD) gage is used to measure the displacement data close to the shear zone. All the shear punch tests were carried out with a constant cross head speed of 0.005 mm/sec.

Tensile tests –Tensile tests were done on all the materials for comparison with the SPT results. Room temperature tensile tests were made on an MTS machine with a nominal cross head velocity of 0.5 mm/min.

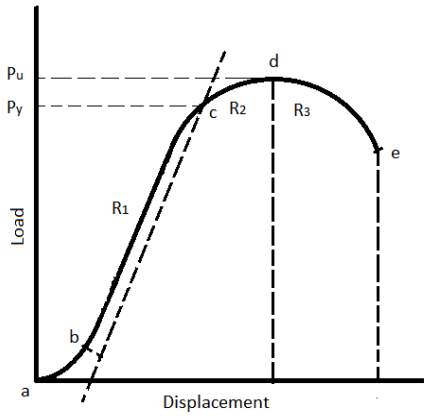

R_1=linear portion, R_2= Strain hardening, R_3= failure, c= yield point, d=ultimate point, e =fracture

Fig. 1. Load-displacement curve for shear punch test

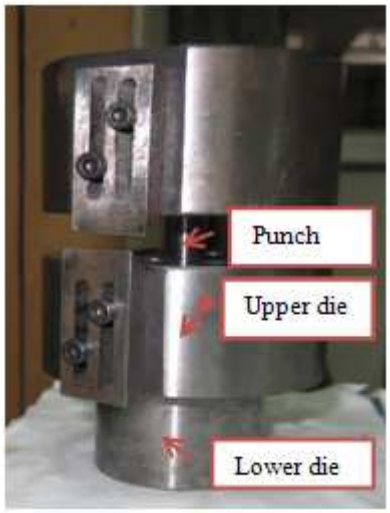

Fig.2. Fixture developed for shear punch test

Materials used for testing- Pressure vessel steels conforming to grades P12, P22, IS: 2062, SA 106 GrC, and SA299 were used for shear punch testing. In addition to this, an in-service material P22 (SM), taken from a final superheater after 100,000 hours of service was taken in strip form (10 mm×8 mm with various thicknesses). These materials were cut into circular discs of 6 mm in diameter with various thicknesses ranging from 0.4 mm to 1 mm. The specimens were polished using abrasive sheet having grit sizes of 600, 800 and 1200 to have a smooth surface finish. Brass samples were also tested to validate the test for low strength metals.

Procedure- The polished specimen is placed in between the dies and the total assembly is mounted on a 100-kN MTS servo-hydraulic materials testing system. The punch is displaced from the top and the load-displacement response is recorded. The frictional component, represented by segment a-b in Fig. 1 is truncated and the point b is shifted to origin and the shear stresses are calculated [1, 5, 6]. The load-displacement data is further converted to shear stress-normalized displacement response by using Eq. 1 and Eq. 2, given below:

$$\text{Shear stress } \tau = P/(\pi \times D \times t), \quad (1)$$

$$\text{Normalized displacement } \delta = z/t, \quad (2)$$

Where P = punch load, D = mean diameter of punch and hole, t = thickness of specimen, and z = punch displacement.

Results and discussion

Results of shear punch test carried out on all the materials and the load- displacement responses obtained are shown in Fig. 3, with corresponding thickness.

Punch and fixture compliance- The test setup compliance plays a very important role in interpreting the shear punch test results. Various approaches are followed to eliminate the fixture and punch compliance. One method is to subtract the elastic deformation of the punch from the total deformation, as proposed by Guduru et al [6]. Other approach followed by Karthik et al [5] is a two-fold process: first step is to modify the test setup by attaching the LVDT at the bottom of the specimen, and the second step is to perform an elastic loading test on the punch.

In the present work, a balanced approach with simplicity is followed to eliminate the fixture compliance. The displacement is measured on the punch top and the compliance of the fixture is evaluated from an elastic loading test. The compliance corrected punch displacements are calculated from Eq. 3. Load-displacement responses for compliance corrected and uncorrected cases are shown in Fig. 4. All the shear stress- normalized displacement responses given in this paper have been corrected for compliance unless otherwise stated.

$$d_c = z - (C \times P) \quad (3)$$

Where C= inverse of the slope of elastic loading test of the punch. Here C= 6.3×10^{-5} mm/N.

The shear stress-normalized displacement response for SA299 steel, with all required data processing is given in Fig. 5. All the shear stress-normalized displacement results presented in this paper are further normalized for specimen thickness, because normalizing the data for various thicknesses, produces a master curve for a particular material which makes the shear stress independent of material dimensions [6], and shear stress value thus obtained can be treated as a material property. The effect of normalization of data on shear stress plots is shown in Fig. 6.

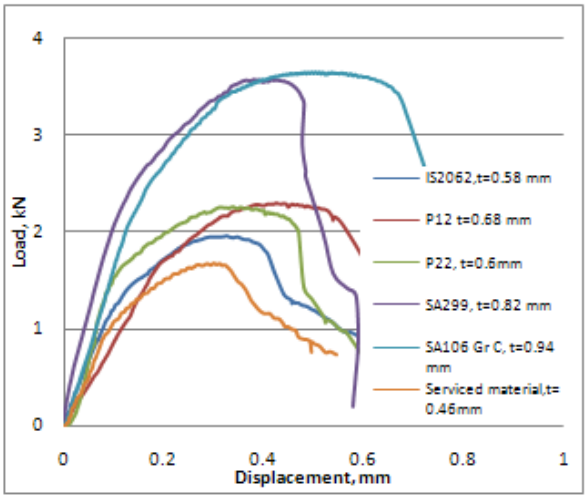

Fig. 3. Load –displacement traces from shear punch test

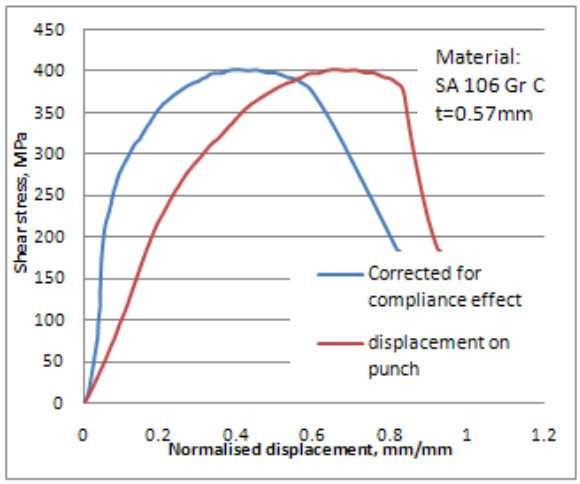

Fig. 4. Effect of compliance correction on shear stress- normalised displacement traces.

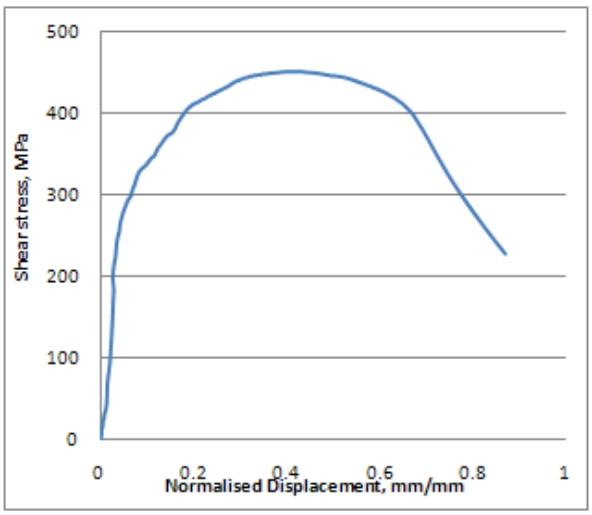

Fig.5. Shear stress-normalized displacement plot for SA299, t=0.57 mm

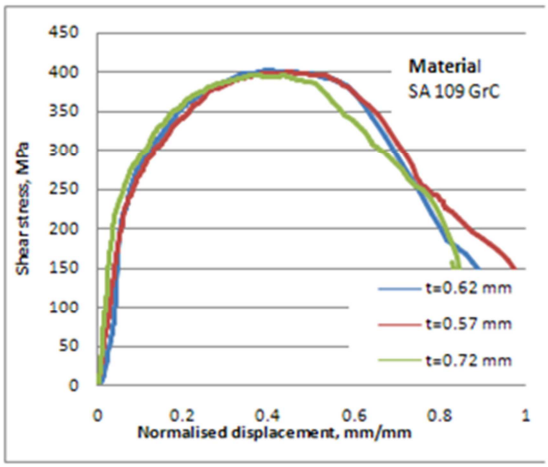

Fig. 6. Master curve obtained by normalization of displacements with corresponding thicknesses

Identification of yield and ultimate points- Yield point in shear punch test is identified by taking 1% offset line on shear stress- normalized displacement traces as discussed in Ref. 6. The peak stress point is taken as ultimate point. These obtained values from shear punch test are correlated with corresponding tensile yield stress (0.2% offset) and ultimate strength.

The correlations obtained by comparison of shear and tensile properties of all the materials tested are shown in Table 1. The graphs showing the correlations of yield and ultimate points of shear punch and tensile tests are shown in Fig. 7 and Fig. 8.

Table 1. Shear punch test data and tensile test data of materials tested with corresponding thicknesses. Average value of the three tests is taken for calculating mechanical properties using shear punch test .

S. No	Material	Thickness , mm	Tensile Yield Stress , MPa	Shear yield stress, MPa	Ultimate tensile Strength, MPa	Ultimate shear strength, MPa
1	IS2062	0.67,0.7,0.58	340.58	211.23	494.43	354.56
2	P12	0.29,0.3,0.68	400.39	232.52	531.67	395.52
3	P22	0.47,0.47,0.6	405.73	246.69	571.37	387.85
4	SA 299	0.56,0.58,0.83	378.62	215.8	615.75	459.14
5	SA109 Gr C	0.71,0.56,0.94	398.54	238.56	570.12	408.365
6	P22, SM	0.47,0..46,0.46	342.64	196.68	533.8	375.43
7	Brass	0.5	224.67	126.46	356.7	264.8

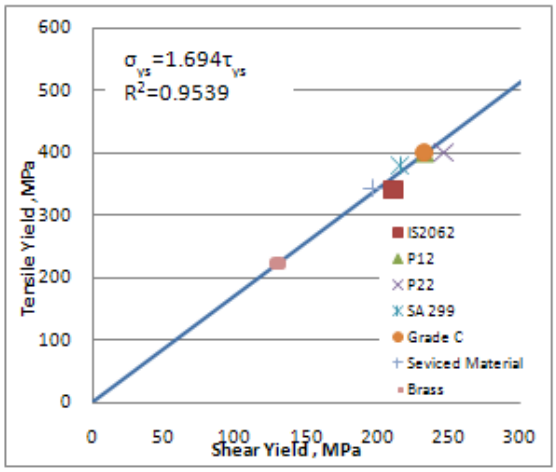

Fig. 7. Yield point correlation between shear punch test and tensile test data

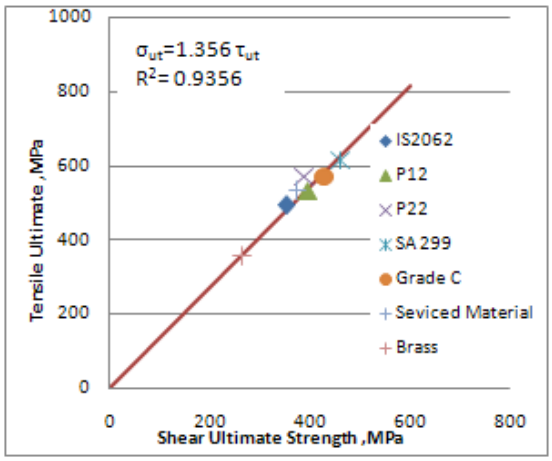

Fig. 8. Ultimate strength correlation between shear punch test and tensile test data

The shear and tensile strength values are correlated using a linear relation of the form σ (yield, ultimate) = m ×τ (yield, ultimate). Regression analysis was carried out to find the constant 'm' and R-squared value. The value of 'm' obtained by the above curve fitting process are given as m=1.694, R^2=0.954 for yield point correlation and m=1.356, R^2=0.936 for ultimate point correlation. This provides a valuable input for subsequent material property evaluations by shear punch test.

Conclusion

The development of a test fixture for shear punch test was discussed with focus on compliance correction methods. The yield point identified by 1% offset on normalized displacement traces are correlated to the tensile test data. The effects of the punch compliance and displacement normalization on test data were also discussed in this work.

References

[1] G.E. Lucas, G.R. Odette, J.W. Sheckherd, in. W.R. Corwin, G.E. Lucas (Eds.), *The use of small-scale specimens for Testing Irradiated Materials,* ASTM STP 888,1988, p. 112.

[2] G. E. Lucas, *Review of small specimen testing techniques for irradiation testing*, Metallurgical transactions A, Volume 21A, May 1990, p1105.

[3] J.M. Baik, J. Kameda and O. Buck. ASTM STP 888, ASTM, Philadelphia, PA, 1986, p.92-110

[4] M.P. Manahan, A.S. Argon, and O.K. Harling, J. Nucl.Mater., 1981, vol. 103-104, pp. 1545-50

[5] V. Karthik, K. Laha, K.V. Kasiviswanathan, Baldev Raj, *Tensile-shear correlations obtained from a shear punch test using new experimental approach,* Journal of nuclear materials 2009;425-432.

[6] R.K. Guduru, K.A. Darling, R. Kishore, R.O. Scattergood, K.L. Murty, *Evaluation of mechanical properties from shear punch test.* Mater. Sci. Eng.A 395 (2005) 307.

© (2012) Trans Tech Publications, Switzerland
doi:10.4028/www.scientific.net/AMM.187.58

Analysis of the dynamic response of a cracked beam structure

D. N. Thatoi[1, a], J. Nanda[1, b], H. C. Das[1, c], D. R. Parhi[2, d]

[1]ITER,S 'O' A University, Odisha, India

[2]N.I.T. Rourkela, Odisha, India

[a]dnthatoi@gmail.com,[b]nandajajneswar@yahoo.in,[c]harishdas1965@gmail.com,
[d]dayalparhi@yahoo.com

Key words: Vibration; crack; mode shape; natural frequency; FEA.

Abstract. In this research, dynamic behaviour of a cracked cantilever beam has been analysed using finite element and experimental analysis. Deviations in mode shapes and natural frequencies have been noticed due to the presence of crack in the beam. The variation in the dynamic response is due to change in local flexibility because of the presence of crack in the beam. Finite element and experimental analyses have been carried out to find out the vibration indices of the cracked cantilever beam for validating the robustness of the theoretical model used for crack detection. The numerical results obtained through FEA are in good agreement with experimental results.

Introduction

Vibration measurement and analysis being an effective and convenient way to detect cracks in structures is mostly being used by researchers. Zheng et al. [1] proposed an 'overall additional flexibility matrix' instead of earlier developed 'local flexibility matrix' of a cracked beam using finite element method (FEM). The new stiffness matrix has been computed. A new shape function developed through a 128-point (ID) Gauss quadrature and best fitment through least square methods satisfies the local flexibility conditions which can predict accurate vibration modes. FEM techniques in combination with discreet element techniques (DET) have gained ground over time due to the easiness in analysis using programming tools. Ariaei et al. [2] have analyzed the dynamic response of a cracked beam subjected to moving masses using DET and FEM techniques. Differential quadrature method (DQM) for analysis of motion of cracked beams is significantly being used for its simplicity of problem formulation. The change in first frequency with crack depth analysed by Hsu [3] on cracked beam with axial loading and excitation force using DQM proves the correlation of crack position and depth with the change in first frequency. Xiang et al. [4] have used finite element method of a B-spline wavelet on the interval (FEM BSWI). The first three frequencies influencing function of normalized crack location and size have been approximated using surface fitting techniques. A smoothed finite element method (SFEM) using cell-based smoothening domain is an integrating FEM and strain smoothening technique and is used for better solution of vibration problems. This method uses cell-based smoothening domains by further division of elements in the FEM techniques. Liu et al. [5] later presented a novel numerical method using an edge based smooth finite element method (ES-FEM). Using this method they simulated the singular stress field for mode-1 fracture problem. The shape function has been devised using the displacement values on the boundary of the smoothening domains and have demonstrated better results of strain energy, displacement and J-Integral compared with simple FEM analysis. The non-linear dynamics of a cracked beam has been studied by Andreaus et al. [6] through some modification with respect to linear one. In their work they have taken the case of a cantilever beam with an asymmetric edge crack subjected to a harmonic forcing at the tip and solved the problem using two-dimensional finite element by simulating the crack as a frictionless contact type between the interacting surfaces. Considerable effect of vibrations of cracked beam on both strain energy and stress fields have been established by Mazanoglu et al. [7]. Rayleigh-Ritz approximation method has been used to study the stress field caused by the angular displacement of the beam due to bending. Rubio et al. [8] have developed the flexibility matrix based on the polynomial fitting of the stress intensity factors integrating along the elliptical front characterized by its shape and length. They have also calculated the static displacement in bending of the shaft under different support condition and compared with results obtained through FEM to validate the polynomial function.

In the current work, finite Elements Analysis and experimental technique have been performed to validate the proposed procedure. For different relative crack depths and locations, natural frequencies and the mode shapes of the cracked cantilever beam specimen have been found out using finite element method. At the crack location, significant changes in mode shape are observed. It can be proposed that, the variation in dynamic characteristics of the cracked cantilever beam can be utilized for early assessment of cracks.

Analysis of cracked beam using finite element method (FEM)

Finite Element Formulation

A beam with cracks has smaller stiffness than a normal beam. This decreased local stiffness can be formulated as a matrix. The free bending vibration of an Euler-Bernoulli beam of a constant rectangular cross section is given by the following differential equation as: $EI\frac{d^4V}{dx^4}-m\omega_i^2V=0$

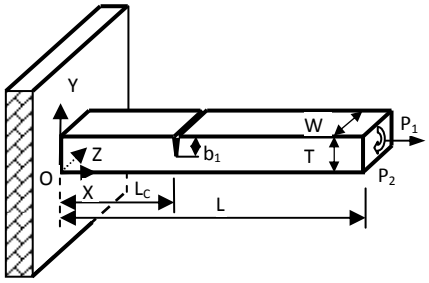

Fig.1 Beam model

Where 'm' is the mass of the beam per unit length 'ω_i' is the natural frequency of the i^{th} mode, E is the modulus of elasticity (N/m^2) and I is the area moment of inertia. By defining $\lambda^4=\frac{m\omega_i^2}{EI}$ equation is rearranged as follows: $\frac{d^4y}{dx^4}-\lambda^4y=0$

The general solution to the above equation is, $y=A\cos\lambda_i x+B\sin\lambda_i x+C\cosh\lambda_i x+D\sinh\lambda_i x$ (15)

where A,B,C,D are constants and 'λ_i' is a frequency parameter. Adopting Hermitian shape functions, the stiffness matrix of the two-noded beam element without a crack is obtained using the standard integration based on the variation in flexural rigidity. The element stiffness matrix of the un-cracked beam is given as

$\left[K^e\right]=\int\left[B(x)\right]^T EI\left[B(x)\right]dx$,

where $\left[B(x)\right]=\left\{H_1''(x)H_2''(x)H_3''(x)H_4''(x)\right\}$

and $H_1(x)$, $H_2(x)$, $H_3(x)$, $H_4(x)$ are the Hermitian shape functions. The beam rigidity EI is constant and is given by EI_0 within the element. We know that, due to the presence of the crack there is a reduction in the stiffness.

$\left[K_c^e\right]=\left[K^e\right]-\left[K_c\right]$

$\left[K_c^e\right]$ = stiffness matrix of the cracked element, $\left[K^e\right]$ = stiffnes matrix of the continuous beam and $\left[K_c\right]$= reduction in stiffness matrix due to the crack.

The beam rigidity EI is constant and is given by EI_0 within the element.

$$\left[K^e\right]=\frac{EI_0}{l^3}\begin{bmatrix}12 & 6l & -12 & 6l\\ 6l & 4l^2 & -6l & 2l^2\\ -12 & -6l & 12 & -6l\\ 6l & 2l^2 & -6l & 4l^2\end{bmatrix}, \qquad \left[K_c\right]=\begin{bmatrix}K_{11} & K_{12} & -K_{11} & K_{14}\\ K_{12} & K_{22} & -K_{12} & K_{24}\\ -K_{11} & -K_{12} & K_{11} & -K_{14}\\ K_{14} & K_{24} & -K_{14} & K_{44}\end{bmatrix}$$

It is supposed that the crack does not affect the mass distribution of the beam. Therefore, the consistent mass matrix of the beam element can be formulated directly as

$$\left[M^e\right]=\int_0^1 \rho A\left[H(x)\right]^T\left[H(x)\right]dx=\left[M^e\right]=\frac{\rho Al}{420}\begin{bmatrix}156 & 22l & 54 & -13l\\ 22l & 4l^2 & 13l & -3l^2\\ 54 & 13l & 156 & -22l\\ -13l & -3l^2 & 22l & 4l^2\end{bmatrix}$$

The natural frequency then can be calculated from the relation.

$$\left[-\omega^2\left[M\right]+\left[K\right]\right]\{q\}=0,$$

where q = displacement vector of the beam. The results of the finite element analysis for the first three mode shapes of the cracked beam are compared with that of the numerical analysis of the cracked beam and are presented in Tables 1.

Beam specification

In the current investigation using numerical analysis of a cracked cantilever beam, the following dimensions are being considered.

1) Length of the Beam, 'L' = 800 mm.
2) Width of the Beam, 'W' = 38 mm.
3) Height of the Beam, 'T' = 6 mm.
4) The relative crack depth ($\delta_1 = b_1/T$) = varies from 0.05 to 0.8
5) The relative crack location ($\alpha = L_c/L$) = varies from 0.0125 to 0.95

Experimental Setup

An experimental set-up is used for carrying out the experiment as shown in the schematic diagram (Fig. 2). A number of tests are conducted on aluminium beam specimen (800 x 30 x 6 mm) with a transverse crack as shown in Fig. 1 for determining the amplitude of vibration, natural frequencies and mode shapes. The beam is allowed to vibrate under 1st, 2nd and 3rd modes of vibration.

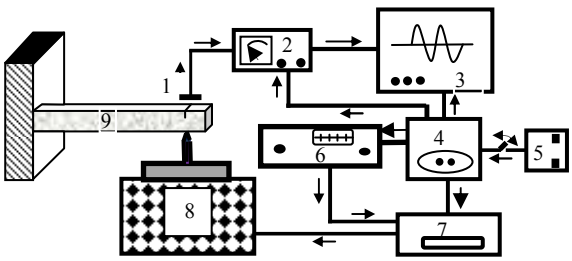

1. Vibration Pick-up (Accelerometer)
2. Vibration analyser (PULSE Lite Type
3. Vibration indicator with software (Pulse Labshop software)
4. Distribution box
5. Power supply
6. Function generator
7. Power amplifier
8. Vibration exciter
9. Cantilever beam specimen

Fig. 2 Schematic block diagram of experimental set-up

Results and Discussions

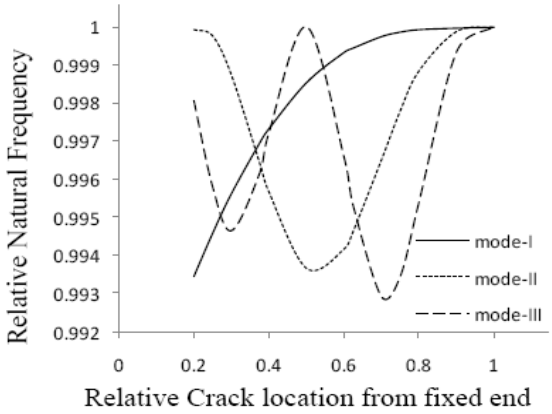

Fig. 3. Relative Natural Frequency vs. Relative Crack Location from the fixed end b1/T = 0.3

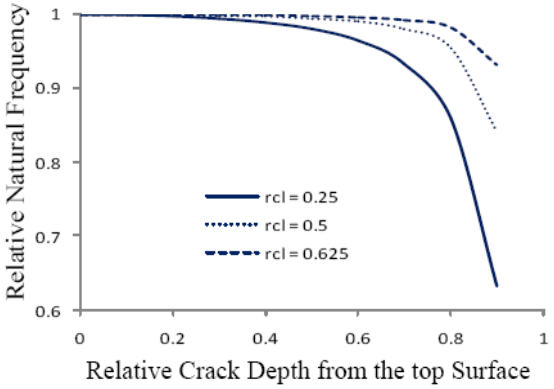

Fig. 4. Relative Natural Frequency vs. Relative Crack Depth from the Top surface (1st Mode of vibration)

Based on the results obtained from the finite element and experimental analyses, the following discussions can be made. From Fig.3, it is seen that the relative frequency for mode-I is on increasing trend while for other two modes attains minimality and maximality at different crack location. Moreover, the first mode frequency takes sharp decline at a particular crack depth (Fig.4). It is observed that there are reasonable changes in mode shapes due to the presence of crack with higher intensity in the beam (Fig. 5, Fig. 6 and Fig. 7). Table 1 shows the comparison of relative natural frequencies and relative mode shape differences obtained from finite element method and experimental method. The values (from numerical analysis (FEA) and experimental) given in the tables are in agreement.

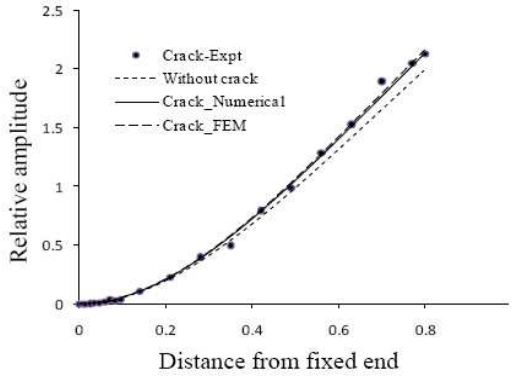

Fig. 5 Relative amplitude vs. distance from the fixed end (1st Mode of vibration) $L_c = 0.1$ m, $b_1/T = 0.4$

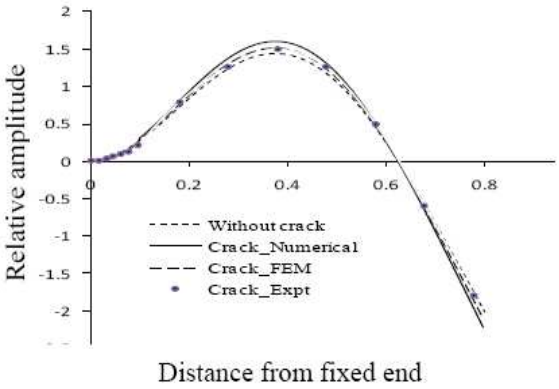

Fig.6 Relative amplitude vs. distance from the fixed end (2nd Mode of vibration) $L_c = 0.1$ m, $b_1/T = 0.4$

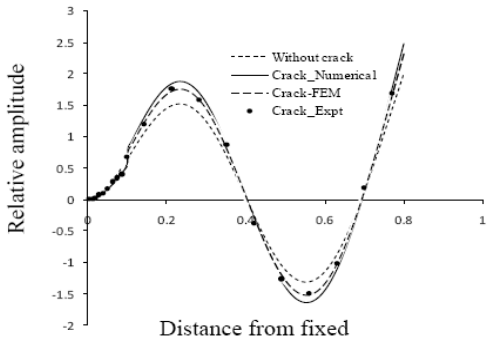

Fig.7 Relative amplitude vs. distance from the fixed end (3rd Mode of vibration) $L_c = 0.1$ m, $b_1/T = 0.4$

Table 1 Comparison of results between FEM and Experimental setup.

Relative first natural frequency "fnf"	Relative second natural frequency "snf"	Relative third natural frequency "tnf"	Relative first mode shape difference "fmd"	Relative second mode shape difference "smd"	Relative third mode shape difference "tmd"	Finite Element (relative crack depth "rcd" and location"rcl")		Experimental (relative crack depth "rcd" and location"rcl")	
						rcd	rcl	rcd	rcl
0.9848	0.9958	0.9975	0.2709	0.2372	0.3158	0.204	0.0734	0.205	0.0738
0.9673	0.9874	0.9943	0.3969	0.3247	0.3923	0.437	0.0850	0.43	0.0853
0.9623	0.9948	0.9983	0.1814	0.0279	0.0774	0.562	0.1621	0.568	0.1628
0.9756	0.9976	0.9972	0.1383	-0.0823	0.1898	0.386	0.1931	0.391	0.1923
0.9852	0.9984	0.9967	0.01	-0.8678	0.2572	0.224	0.2445	0.23	0.2435
0.9723	0.9961	0.9818	0.1947	0.0672	0.4105	0.549	0.2932	0.545	0.2923
0.9823	0.9872	0.9919	0.0726	0.2567	0.3994	0.441	0.4151	0.447	0.4153
0.981	0.9809	0.9931	0.0898	0.3154	0.392	0.492	0.4351	0.495	0.4346
0.986	0.9842	0.9988	-0.032	0.322	0.3965	0.423	0.5147	0.425	0.5153
0.9834	0.9685	0.9974	0.038	0.4558	0.3507	0.531	0.5466	0.535	0.5474

Conclusions

The conclusions drawn from the above discussion shows that the mode shapes and natural frequencies of the cracked elastic structures are strongly influenced by the crack location and its intensity. The significant changes in mode shapes are observed at the vicinity of crack location. These changes in mode shapes and natural frequencies will be helpful in prediction of crack location and its intensity. The natural frequencies and mode shapes for the cracked beam obtained numerically through FEM are compared with the corresponding experiments and are found to be in close agreement.

References

[1] D. Y. Zheng and N. J. Kessissoglou, Free vibration analysis of a cracked beam by finite element method, *Journal of Sound and Vibration,* 273 (2004) 457–475.

[2] Ariaei, S. Ziaei-Rad and M. Ghayour, Vibration analysis of beams with open and breathing cracks subjected to moving masses, *Journal of Sound and Vibration,* 326 (2009) 709–724.

[3] Ming-Hung Hsu, Vibration analysis of edge-cracked beam on elastic foundation with axial loading using the differential quadrature method, *Computer Methods in Applied Mechanics and Engineering,* 194 (2005) 1–17.

[4] J. W. Xiang, X. F. Chen, B. Li, Y. M. He, and Z. J. He, Identification of a crack in a beam based on the finite element method of a B-spline wavelet on the interval, *Journal of Sound and Vibration,* 296 (2006) 1046–1052.

[5] G. R. Liu, N. Nourbakhshnia and Y. W. Zhang, A novel singular ES-FEM method for simulating singular stress fields near the crack tips for linear fracture problems, *Engineering Fracture Mechanics,* 78 (2011) 863–876.

[6] U. Andreaus, P. Casini and F. Vestroni, Non-linear dynamics of a cracked cantilever beam under harmonic excitation, *International Journal of Non-Linear Mechanics* ,42 (2007) 566 – 575.

[7] K. Mazanoglu, I. Yesilyurt and M. Sabuncu, Vibration analysis of multiple-cracked non-uniform beams, *Journal of Sound and Vibration,* 320 (2009) 977–989.

[8] L. Rubio, B. Munoz-Abella and G. Loaiza, Static behaviour of a shaft with an elliptical crack, Mechanical Systems and Signal Processing 25 (2011) 1674–1686.

© (2012) Trans Tech Publications, Switzerland
doi:10.4028/www.scientific.net/AMM.187.63

Visualization of supersonic non-Newtonian liquid jets

Anirut Matthujak[a] , Chaidet Kasamnimitporn[b], Wuttichai Sittiwong[c] and Kulachate Pianthong[d]

Combustion and Jet Application Research Laboratory (CJARL), Department of Mechanical Engineering, Faculty of Engineering, Ubon Ratchathani University, Ubon Ratchathani, Thailand

email: [a]Anirut.Mat@gmail.com, [b]chaidet_peat@hotmail.com, [c]sittiwong@hotmail.com and [d]K.Pianthong@ubu.ac.th

Keywords: supersonic jet, non-Newtonian liquid, impact driven method, shadowgraph.

Abstract. This paper describes the characteristics of supersonic non-Newtonian liquid jets injected in ambient air. The main focus is to visualize three types of time-independent non-Newtonian liquid jet and to describe their behaviors. Moreover, comparisons between their dynamic behaviors with Newtonian liquid jet are reported. The supersonic liquid jets are generated by impact driven method in a horizontal single-stage power gun. Jets have been visualized by the high speed digital video camera and shadowgraph method. Effects of different liquid types on the jet penetration distance, average jet velocity and other characteristics have been examined. From shadowgraph images, the unique dynamic behaviors of each non-Newtonian liquid jets are observed and found obviously different from that of the Newtonian liquid jet. The maximum average jet velocity of 1,802.18 m/s (Mach no. 5.30) has been obtained. The jet penetration distance and average velocity are significantly varied when the liquid types are different.

Introduction

Recently, high speed liquid jets are well known in extensive engineering applications such as the cleaning and cutting technologies, mining, and tunneling, SCRAM (Supersonic Combustion RAM) jets, direct injection (DI) diesel, drug injection, tissue cutting, and removing of a cerebral thrombus [1-4]. Hence, their characteristics or dynamic behaviors have been intensively gained attention and continuously studied by many researcheres [5-9].

However, most of the previous studies have been interested at only high speed Newtonian liquid jets such as water, diesel fuel, gasoline, kerosene, and alcohol jets while there have been few studies about high speed non-Newtonian liquid jet [7]. Therefore, the understanding on the dynamic behaviors of high speed non-Newtonian liquid jet at the speed of supersonic range is still needed. In this study, supersonic non-Newtonian fluid jets were generated by impact driven method and visualized by shadowgraph technique. Three types of time-independent non-Newtonian fluid jets, which are milk, salad dressing, and toothpaste jets being classified as pseudo plastic, dilatant, and bingham plastic fluids, respectilvely, are clarified. Effect of verious jet types on jet penetration distance and average jet velocity are also analyzed. Moveover, the distinction of charateristics between newtonian and non-Newtonian fluid jets are described.

Experimental apparatus

In this study, supersonic liquid jets are generated by impact driven method [5]. Using this technique, the liquid retained in the nozzle cavity is impacted by a high velocity projectile. The liquid obtains the momentum transfer from the projectile and is injected from the nozzle. The high velocity projectile in this technique has been generated by the horizontal single stage powder gun (HSSPG) as shown in Fig. 1a. The HSSPG consists of the launcher, launch tube, pressure relief section, and test chamber. The launch tube has a diameter of 8 mm and length of 1.5 m. The pressure relief section has a length of 40 cm, which is designed to diminish the blast wave in front of the projectile. The pressure relief section has 3 slots, which each slot has an open grap of 4 mm in width and 36 cm in length. The test chamber is a square tank of 350×350 mm in width and 590 mm in length with polymethyl

methacrylate (PMMA) windows on two sides for visualization. The projectile is made of polymethyl methacrylate (PMMA), is cylindrical shape with diameter of 15 mm and length of 8 mm (weight of 0.92 g) as shown in Fig. 1b. This HSSPG has been employed to generate the high speed liquid jet velocity ranged from 550 to 2,290 m/s injected into air. The nozzle being connected to pressure relief section made of mild-steel, whose dimension is shown in Fig. 1c. In this study, the gunpowder of 5 g is used, which can launch the projectile speed of about 952 ± 32 m/s.

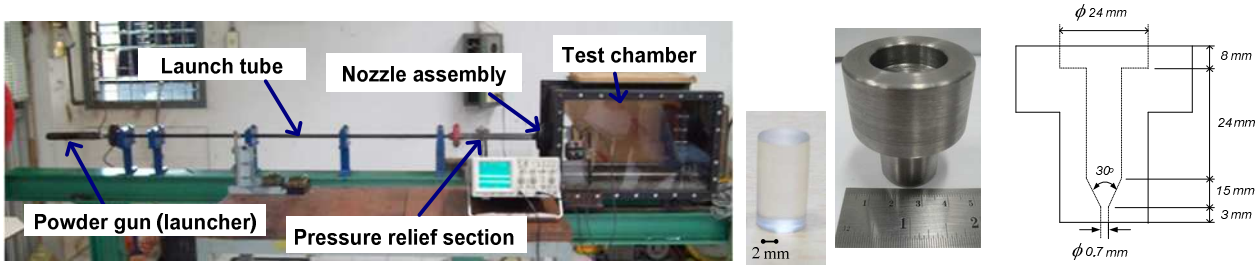

(a) (b) (c)

Figure 1 (a) Horizontal Single-Stage Powder Gun**,** (b) projectile, and (c) Nozzle geometry

Visualization method

In this study, a high speed digital video camera and shadowgraph optical was used for visualization as shown in Figure 2. The dynamic formation of supersonic jets is quanlitatively measured by sequential observations. A Xenon lamp is used as a light source. Thereafter, the source light is passed through a concave lens and a circular slit. The laboratory space is limited so that two plane mirrors of diameter 190 mm are combined in this arrangement. Two paraboloidal schlieren mirrors of diameter 300 mm were used for collimating source light beam passing the test section area. A Nikon 60 mm Macro lens was used to focus the object image on the camera screen. The high speed digital video camera is a Photron SA5 at frame rate of 30,000 f/s, minimum shutter speed of 1 μs, and 5.46 seconds record time at full resolution.

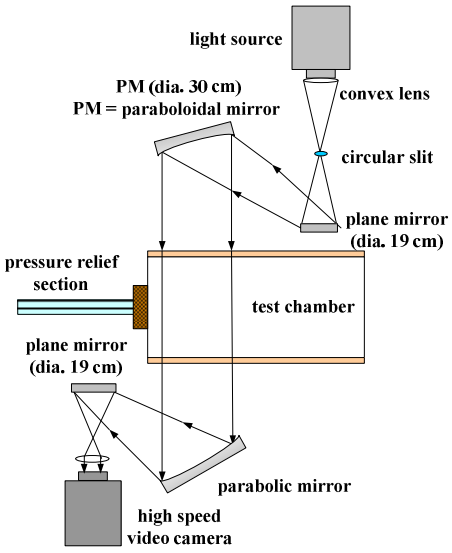

Figure 2 Arrangement of shadowgraph optical system and high speed digital video camera

Results and discussion

Using a high speed digital video camera, Photron SA5 could record shadowgraph images at frame rate of 30,000 f/s and shutter speed of 1 μs. This sequential recording is very useful to observe the jet formation. Four liquids, which are water, milk, salad dressing, and toothpaste being classified as newtonian, pseudo plastic, dilatant, and bingham plastic fluids, respectively, are investigated in this study. Since not all frames from the camera can be displayed in the paper, only twelve sequential images are selected to represent the stages in jet development, as shown in Fig. 3.

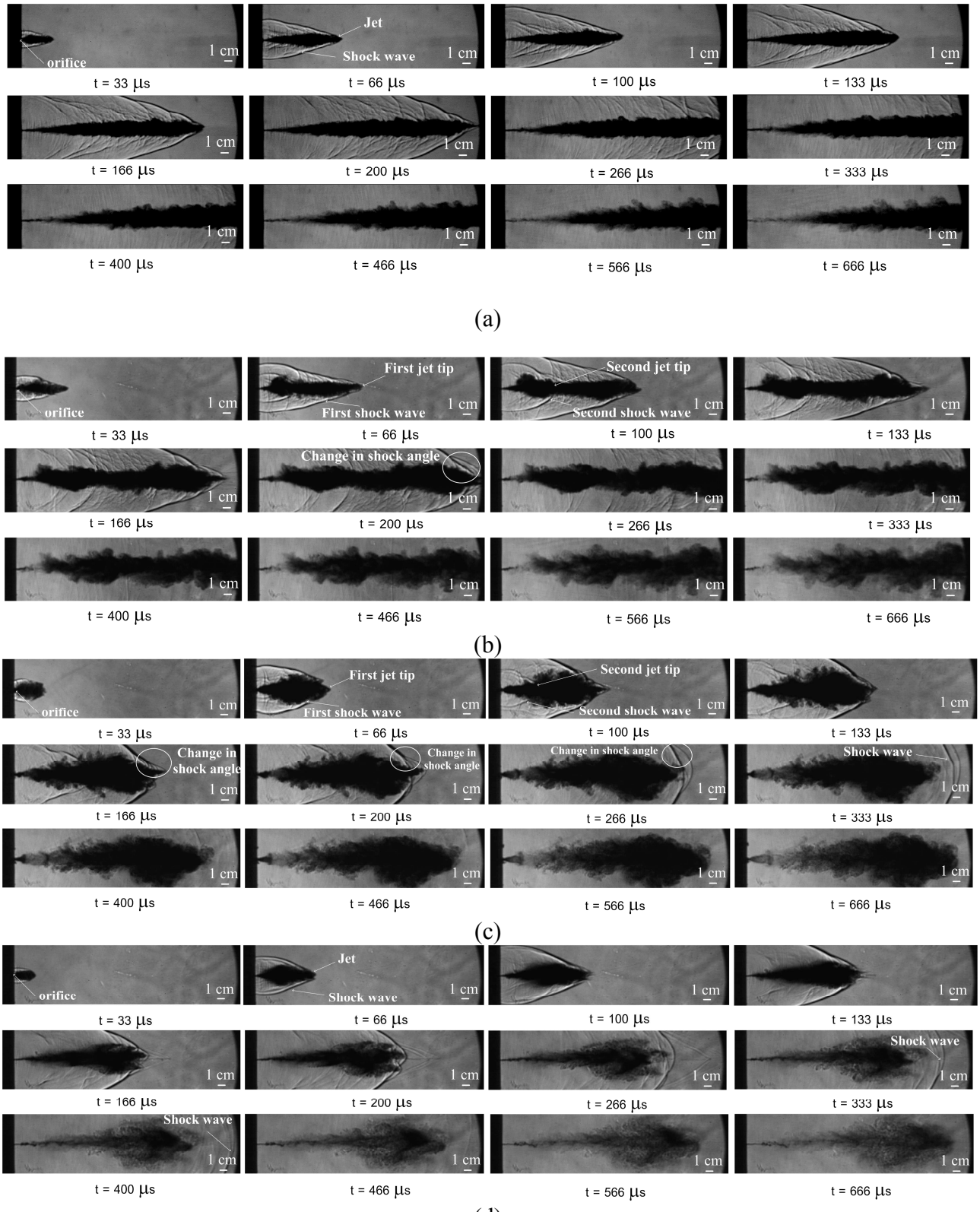

Figure 3 Jet formation (a) water jet (b) milk jet (c) salad dressing jet (d) toothpatse jet

In order to compare with non-Newtonian liquid jet, a water jet formation being classified as newtonian liquid jet is shown in Fig 3a. Its dynamic behaviors have been clearly described in Matthujak's study [10]. The water jet shows the slim width and looks more elongated to be over 213 mm at 166 μs. Its averaged speed at 166 μs is 1,282 m/s being Ms = 3.77 in room temperature air. The jet motion is supersonic so that oblique shock waves are created over its tip and also the jet's nodes as shown in the figure.

Figure 3b shows a milk jet formation, which is classified as pseudo plastic fluid. The milk jet is similar to the water jet at the earlier stage, being the elasped time (t) of 33 to 133 μs. The second shock wave and the change in shock angle was obviously observed at t = 66–133 μs and t = 200 μs, respectively. Such both behaviors were implied that the second jet took place from a single impact of the projectile (this behavior has been described in Pianthong's and Matthujak's study [8, 9]). Base upon the rheology of pseudo plastic fluid, which its dynamic viscosity decreases as the rate of shear increases, therefore, the nodes created over the milk jet look more bulkier than those in water jet at t = 166–333 μs and the atomization of milk jet look more stronger than that of water jet at t = 400–666 μs.

Figure 3c shows a salad dressing jet formation, which is classified as dilatant fluid. The general trend is much different from water and milk jets. The jet was quickly and strongly atomized once it was injected from the orific while the strong atomization of the water and the milk jets took place at the later stage. It may be because of the rheology of dilatants fluid, which its dynamic viscosity increases as the rate of shear increases. From the images, the second shock wave and the change in shock angle was obviously observed at t = 100–200 μs and t = 166-266 μs, respectively. Both behaviors implied that the second jet took place similar to the milk jet. After 333 μs, the jet boundary on images looks blurred. A shock wave is attached at the jet's leading edge but after 333 μs it becomes a detached shock wave because the jet penetration is much slower than the shock motion. The atomization mechanism of the salad dressing jet was seemingly quicker than that of water and milk jets since that of the salad dressing jet was nearly finished at t = 400–666 μs while that of water and milk jets was not at those times.

Figure 3d shows toothpaste jet formation, which is classified as bingham plastic fluid. Its general trend is not much different from water and milk jets at the earlier stage, being the elasped time of 33–133 μs. After t = 166 μs, a shear layer occurring around the toothpaste jet is the strongest, which is implied that its atomization is the strongest. It may be due to the rheology of bingham plastic fluid, which the shear stress must reach a certain minimum value before flow commences. Thereafter, dynamic viscosity decreases as the rate of shear increases, being similar to pseudo plastic fluid. After t = 266 μs, a shock wave was detached at the jet's leading edge due to the slow jet penetration and such shock was still undulated far from the jet tip even though the jet did not penetrate. A strong atomization of the jet was clearly seen at t = 333–666 μs.

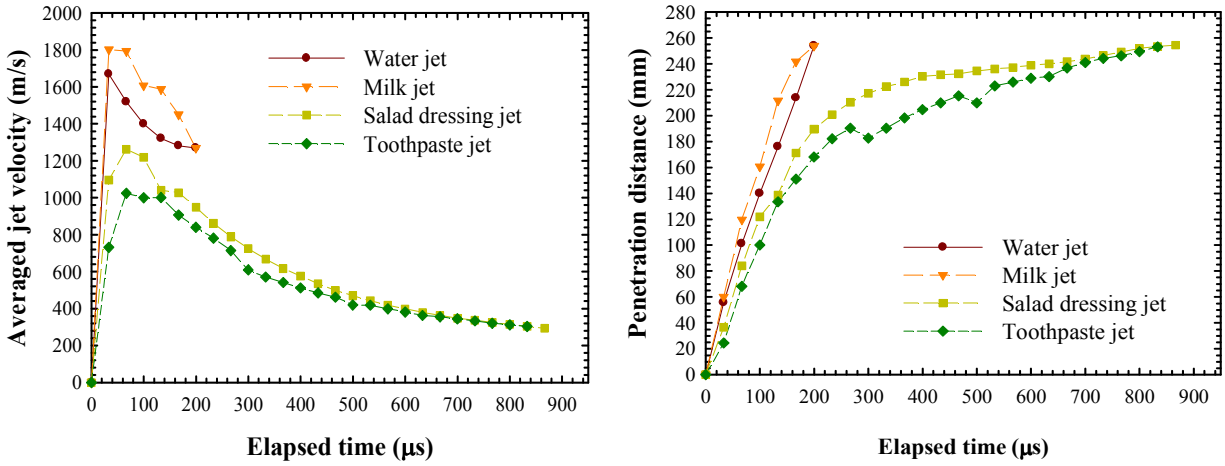

(a) (b)

Figure 4 Effect of difference liquids on (a) average jet velocity (b) jet penetration distance

Fig. 4a shows the effect of different liquid jets on the average jet velocity. During the maximum velocity point at the emerging time of around 33 μs, the velocity of all liquid jets drops gradually as obviously seen in the figure. The maximum averag velocity of milk jet is the highest, being 1,802.18 m/s approximately. The next one is water, salad dressing, and toothpatse jets, respectively, which are estimated to be 1,669.03 m/s, 1,262.38 m/s, and 1,024.35 m/s, respectively. The jet velocity certainly

affects on the penetration distance as plotted in Fig. 4b. It is found that the faster the average jet velocity is, the longer the jet penetrates. Hence, the penetration distance of the milk jet is the longest at the same elapsed time as shown in the figure. The second one is water and salad dressing jets, respectively. The shortest penetration distance is toothpatse jet. It can be noticed that at the later stage the average velocity of the salad dressing jet and the toothpaste jet is quite similar at the same elasped time.

Concluding remarks

This study reports the formation of supersonic water, milk, salad dressing and toothpaste jets injected in air. These are defined as newtonian, pseudo plastic, dilatant, and bingham plastic fluids, respectively. Using a high speed digital video camera with shadowgraph optical arrangement, the dynamic behaviors of all jets have been clearly revealed. From the visualization results, the shock wave around the jet is clean and smooth. The milk jet is similar to the water jet at the earlier stage, being narrow and long. The salad dressing jet was quickly and strongly atomized once it was injected from the orific. However, a shear layer of the toothpaste jet occurring around the jet or the atomization was seemingly strongest. The jet penetration distance and average jet velocity are significantly varied when the liquid types are different. The maximum average jet velocity of 1,802.18 m/s (Mach no. 5.30) has been obtained from the milk jet. That provides the milk jet to have the longest penetration distance at the same elasped time.

Acknowledgement

We would like to acknowledge the National Research Council of Thailand (NRCT) through Ubon Ratchathani University Research grant 2011, Thailand Research Fund (RTF) contract MRG5180046, Thailand Toray Science Foundation 2011, and Department of Mechanical Engineering, Faculty of Engineering, Ubon Ratchathani University for the financial support

References

[1] M.C. Rochester and J.H. Brunton: *High speed impact of liquid jets on soli*d, 1st International Symposium on Jet Cutting Technology, paper A1, Coventry, UK (1972)

[2] F.S. Billig : *Research on supersonic combustion*, Journal of Propulsion and Power, 9(4) (1993), pp 499–514.

[3] B.E. Milton, and K. Pianthong: *Pulsed, supersonic fuel jets - A review of their characteristics and potential for fuel injection*. Int J Heat and Fluid Flow, 26(4) (2005), pp. 656-671.

[4] T. Ohki, A. Nakagawa, T. Tominaga and K. Takayama : *Experimental application of Pulsed Ho: YAG laser-induced liquid jet as a novel device for rigid neuroendoscope*, Laser Surg Med, 34 (2004), pp 227.

[5] F.P. Bowden and J.H. Brunton, *Damage to solids by liquid impact at supersonics speeds*, Nature, vol.181(1958), pp 873-875.

[6] J.D. O'Keefe, W.W. Wrinkle and C.N. Scully : *Supersonic liquid jets*, Nature, vol.213(1967), pp. 23-25.

[7] H.H. Shi: *Study of Hypersonic Liquid Jets*. Ph.D. thesis, Tohoku University, Sendai, Japan (1994).

[8] K. Pianthong: *Supersonic liquid diesel fuel jets; generation, shock wave; Characteristics, Auto-ignition Feasibilities*. Ph.D. Thesis, Univ New South Wales, Sydney, Australia (2002).

[9] A. Matthujak : *Experimental study of impact-generated high-speed liquid jet*. Ph.D. thesis, Tohoku University, Sendai, Japan (2007).

[10] A. Matthujak, C. Kasamnimitporn, W. Sittiwong and K. Pianthong: *Effects of different liquid properties on the characteristics of impact-generated high-speed liquid jets*, Applied Mechanics and materials, 110-116 (2011), pp 370–376.

© (2012) Trans Tech Publications, Switzerland
doi:10.4028/www.scientific.net/AMM.187.68

Deformation and Stresses Analysis in FG Rotating Hollow Disk and Cylinder Subjected to Thermal and Mechanical Load

A. R. Khorshidvand [1a] , M. Javadi [1b]

[1] Department of Mechanical Engineering, South Tehran Branch, Islamic Azad University, Tehran, Iran

[a] AR_Khorshidvand@azad.ac.ir [b] M_ Javadi@azad.ac.ir

Keywords: Functionally graded materials; Rotating disk and cylinder; Thermoelasticity

Abstract. In this paper, a new solution is presented for one-dimensional steady-state mechanical and thermal stresses in a FG rotating hollow disk and cylinder. The material properties for FG are expressed as nonlinear exponential functions through the radius and Poisson's ratio is taken to be constant. The temperature distribution is derived from first law of thermodynamics by solving energy equation, with a general thermal and mechanical boundary conditions on the inside and outside surfaces. Heat conduction and Navier equations are solved analytically by choosing elliptic cylinder coordinates system and the results are shown for displacement and stress components along the radial direction.

Introduction

Functionally graded materials (FGMs) are used in modern technologies as advanced structures. Mechanical and thermal stresses for FG thick hollow disk and cylinder are the subject in the theory of elasticity and thermoelasticity. Jabbari et al. [1] derived an analytical solution for one-dimensional steady-state thermoelastic problems hollow cylinders made of FGM where the material properties are expressed as power functions of radius. Reddy and Cheng [2] obtained numerically the three-dimensional solutions for FG plates by using the transfer matrix method. Tutuncu [3] used the infinitesimal theory of elasticity and obtained power series solutions for stresses in functionally graded cylinderical vessels under internal pressure. The elastic modulus of material is asummed as exponentially-varying through the thickness with constant Poisson's ratio. Zamani Nejad et al. [4] presented closed form solutions for deformations and stresses in rotating functionally graded thick hollow cylinder under thermal load. Khorshidvand et al. [5] presented the analytical solution for thermomechanical behavior in a functionally graded thick hollow rotating disk. Their study was one-dimensional, and steady-state temperature distribution with thermal and mechanical boundary conditions.

In this paper, a one-dimensional steady-state thermoelastic problem of rotating thick hollow disks and cylinders made of functionally graded material as exponential functions in radius direction is considered, under thermal and mechanical loads and temperature distribution is assumed to be the function of radius direction through the thickness. The Navier equation is obtained as a non-homogeneous ODE with constant coefficients.

Analysis

In this study the elliptic-cylinder coordinate system is used to define the cylinderical geometry. Figure(1) shows that the coordinate surfaces $\eta = constant$ are elliptic-cylinders and $\theta = constant$ are related to hyperbolic cylinders and $z = constant$ indicates planes. It would be a general case to define cylinder shells but in particular case it may be converted to cylinder with circular cross section when parameter "$\mathbf{a}$" as a distance from center of elliptic-cylinder to its focus approaches to zero, hence elliptic cylinder surface goes to cylinder surface and η values increases and it causes that $\sinh\eta = \cosh\eta$ and then the equation of cylinder can be written as $x^2 + y^2 = \mathbf{a}^2 \cosh^2\eta$ where $\mathbf{a}\cosh\eta$ is equal to radius of cylinder and each η 's value shows one cylinderical surface when "$\mathbf{a}$" approaches to zero surfaces η_1 and η_2 will show inside and outside surfaces of cylinder respectively. If u_η is displacement in radial direction, the strain-displacement relations for a hollow disk and cylinder are as follow

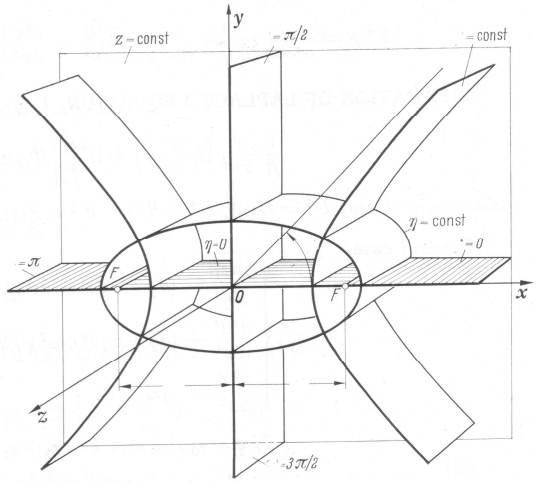

Fig.1 Elliptic-cylinder coordinate system

$$\varepsilon_{\theta\theta} = \frac{1}{\mathbf{a}\cosh\eta} u_\eta \text{ , } \qquad \varepsilon_{\eta\eta} = \frac{1}{\mathbf{a}\cosh\eta}\frac{\partial u_\eta}{\partial \eta} \tag{1}$$

where the coordinates η , θ are considered according to elliptic-cylinder coordinate. The Hooke's relations in plane stress case for a functionally graded disk are.

$$\sigma_{\eta\eta} = \lambda^* \varepsilon_{\eta\eta} + \upsilon\lambda^* \varepsilon_{\theta\theta} - \mu^* \alpha T(\eta)$$

$$\sigma_{\theta\theta} = \lambda^* \varepsilon_{\theta\theta} + \upsilon\lambda^* \varepsilon_{\eta\eta} - \mu^* \alpha T(\eta)$$

$$\sigma\eta\theta = E/(1+\upsilon)\varepsilon\eta\theta \tag{2}$$

where $\lambda^* = E/(1-\upsilon^2)$, $\mu^* = E/(1-\upsilon)$ and in plane strain case for a cylinder, hook's laws are

$$\sigma_{\eta\eta} = \lambda(\varepsilon_{\eta\eta} + \varepsilon_{\theta\theta}) + 2\mu\varepsilon_{\eta\eta} - (3\lambda + 2\mu)\alpha T(\eta)$$

$$\sigma_{\theta\theta} = \lambda(\varepsilon_{\eta\eta} + \varepsilon_{\theta\theta}) + 2\mu\varepsilon_{\theta\theta} - (3\lambda + 2\mu)\alpha T(\eta)$$

$$\sigma_{zz} = \lambda(\varepsilon_{\eta\eta} + \varepsilon_{\theta\theta}) + 2\mu\varepsilon_{zz} - (3\lambda + 2\mu)\alpha T(\eta) \tag{3}$$

where $\lambda = \upsilon E/(1+\upsilon)(1-2\upsilon)$, $\mu = E/2(1+\upsilon)$ and $T(\eta)$ is the temperature distribution determined from the first law of thermodynamics. The Navier equation in terms of displacement component can be written for disks in the following

$$\frac{1}{\mathbf{a}Cosh\eta}\left(\frac{d}{d\eta}\left(\lambda^* \frac{1}{\mathbf{a}Cosh\eta}\frac{du_\eta}{d\eta} + \upsilon\lambda^* \frac{1}{\mathbf{a}\cosh\eta} u_\eta - \mu^* \alpha T(\eta)\right) + \lambda^*(1-\upsilon)\left(\frac{1}{\mathbf{a}Cosh\eta}\frac{du_\eta}{d\eta} + \upsilon\lambda^* \frac{1}{\mathbf{a}\cosh\eta} u_\eta\right)\right) + \rho F_\eta = 0$$

and for cylinder

$$\frac{1}{\mathbf{a}\cosh\eta}\frac{\nu E'}{(1+\nu)(1-2\nu)}\left(\frac{1}{\mathbf{a}\cosh\eta}\frac{du\eta}{d\eta} + \frac{1}{\mathbf{a}\cosh\eta} u\eta\right) + \frac{1}{\mathbf{a}\cosh\eta}$$

$$\cdot\frac{du\eta}{d\eta}\cdot\frac{1}{\mathbf{a}\cosh\eta}\cdot\frac{E'}{1+\nu} + \frac{E(1-\nu)}{(1+\nu)(1-2\nu)}\frac{1}{\mathbf{a}\cosh\eta}\frac{d}{d\eta}\left(\frac{1}{\mathbf{a}\cosh^2\eta}\frac{du_\eta}{d\eta} + \frac{1}{\mathbf{a}\cosh\eta} u_\eta\right) + \rho F_\eta = \frac{1}{\mathbf{a}\cosh\eta}\frac{d}{d\eta}\left(\frac{E}{1-2\nu}.\alpha T\right) \tag{4}$$

Analysis of Energy Equation

The first law of thermodynamics applied for energy equation in the steady-state condition for one-dimensional analysis disk and cylinder in elliptic-cylinder coordinate is

$$\nabla^2 T = \frac{d}{d\eta}\left(K(\eta)\frac{dT}{d\eta}\right) = 0 \tag{5}$$

The thermal boundary conditions are assumed as a linear combination of conduction and heat flux as follows:

$$C_{11}T(\eta_1) + C_{12}T'(\eta_1) = F_1 \; C_{21}T(\eta_2) + C_{22}T'(\eta_2) = F_2 \tag{6}$$

The functions F_1 and F_2 are the known boundary conditions. By assuming $K = K_0 e^{m_3 \eta}$ and integrating Eq. (5) twice, yields

$$T(\eta) = -A1 / m3 e^{-m_3 \eta} + A2 \tag{7}$$

where A_1 and A_2 are the unknowns and can be estimated by substituting Eq.(7) into Eq.(6) follows

$$A_1 = \frac{-C_{11} \cdot F_2 + C_{21} \cdot F_1}{-C_{11}(-C_{21}/m_3 + C_{22}) e^{-m_3 \eta_2} + C_{21}(-C_{11}/m_3 + C_{12}) e^{-m_3 \eta_1}}, \quad A_2 = \frac{-F_1(-C_{21}/m_3 + C_{22}) e^{-m_3 \eta_2} + F_2(-C_{11}/m_3 + C_{12}) e^{-m_3 \eta_1}}{-C_{11}(-C_{21}/m_3 + C_{22}) e^{-m_3 \eta_2} + C_{21}(-C_{11}/m_3 + C_{12}) e^{-m_3 \eta_1}} \tag{8}$$

Analysis of Stresses

Since the material properties of disk and cylinder are assumed to be graded along the radial direction as a exponential function, modulus of elasticity, thermal expansion, and density are as follows

$$E = E_0 e^{m_1 \eta} \quad \alpha = \alpha_0 e^{m_2 \eta} \quad , \quad \rho = \rho_0 e^{m_4 \eta} \tag{9}$$

The Eq. (4) can be rewritten by substituting Eq. (7) and Eq. (9) , as follows

$$\frac{d^2 u_\eta}{d\eta^2} + A_{11} \frac{du_\eta}{d\eta} + A_{12} u_\eta = (A_3 e^{(m_2 - m_3)\eta} + A_4 e^{m_2 \eta}) \cosh \eta + A_5 e^{(m_4 - m_1)\eta} \cosh^3 \eta \tag{10}$$

where for dicks

$$A_{11} = m_1 \quad A_{12} = \upsilon m_1 - 1 \quad A3 = (1 - (m1 + m2)/m3) A1 (1 + \upsilon) \alpha 0 \mathbf{a} \quad A_4 = (m_1 + m_2) A_2 (1 + \upsilon) \alpha_0 \mathrm{a} \quad A5 = -(1 - \nu^2) / E0 \rho_0 \mathbf{a}^3 \omega^2 \tag{11}$$

and for cylinders

$$A_{11} = 1 + m_1 \quad A_{12} = (\upsilon m_1 / (1 - \upsilon) - 1) \quad A_3 = (1 - \frac{m_1 + m_2}{1 + m_3}) A_1 (\frac{1 + \nu}{1 - \nu}) \alpha_0 \mathbf{a} \quad A_4 = (m_1 + m_2) A_2 (\frac{1 + \nu}{1 - \nu}) \alpha_0 \mathbf{a} \quad A_5 = -\frac{(1 + \nu)(1 - 2\nu)}{(1 - \nu) E_0} \rho_0 \mathbf{a}^3 \omega^2 \tag{12}$$

Equation (10) is a non-homogeneous ODE with constant coefficients, the complete solution for u_η is the summation of general and particular solutions as follows

$$u_\eta^{(g)} = B_1 e^{K_1 \eta} + B_2 e^{K_2 \eta} \tag{13}$$

and for disks

$$K_{1,2} = (-m_1 \pm (m_1^2 - 4(\upsilon m_1 - 1))^{0.5}) / 2$$

and for cylinders

$$K1,2 = (-(1 + m1) \pm ((1 + m1)^2 - 8(\upsilon m_1 / (1 - \upsilon) - 1))^{0.5}) / 2 \tag{14}$$

and the particular solution is obtained as follows

$$u_\eta^{(p)} = (D_1 e^{(m_2 - m_3)\eta} + D_2 e^{m_2 \eta}) \cosh \eta + D_3 e^{(m_4 - m_1)\eta} \cosh^3 \eta \tag{15}$$

where by substituting Eq. (15) in Eq. (10), it is obtained for disk case as

$$D_1 = A_3 / [(m_2 - m_3 + 1)^2 + m_1 (m_2 - m_3 + 1) + (\upsilon m_1 - 1)] \qquad D_2 = A_4 / [(m_2 + 1)^2 + m_1 (m_2 + 1) + (\upsilon m_1 - 1)]$$

$$D_3 = A_5 / [(m_4 - m_1 + 3)^2 + m_1 (m_4 - m_1 + 3) + (\upsilon m_1 - 1)] \tag{16}$$

and for cylinder

$$D1 = A3 / [(m2 - m3 + 1)^2 + m1 (m1 - m3 + 1) + (\nu m1 / (1 - \nu) - 1)], \qquad D2 = A4 / [(m2 + 1)^2 + m1 (m2 + 1) + (\nu m1 / (1 - \nu) - 1)]$$

$$D3 = A5 / [(m4 - m1 + 3)^2 + m1 (m4 - m1 + 3) + (\nu m1 / (1 - \nu) - 1)] \tag{17}$$

Displacement component is obtained as follows

$$u_{(\eta)} = B_1 e^{K_1 \eta} + B_2 e^{K_2 \eta} + (D_1 e^{(m_2 - m_3)\eta} + D_2 e^{m_2 \eta} \cosh \eta + D_3 e^{(m_4 - m_1)\eta} \cosh^3 \eta \tag{18}$$

and by substituting Eq. (18) and (1) into Eq. (2) stress components can be obtained as follows

$$\sigma_{\eta\eta} = A\{(Ke^{(m_1+K_1)\eta}B_1 + te^{(m_1+K_2)\eta}B_2)/\mathbf{a}\cosh\eta + (pe^{(m_1+m_2)\eta} + he^{(m_1+m_2-m_3)\eta} + le^{m_4\eta})/\mathbf{a}\} + (we^{(m_1+m_2-m_3)\eta} + y)/\mathbf{a}$$

$$\sigma_{\theta\theta} = A\{(xB_1e^{(K_1+m_1)\eta} + zB_2e^{(K_2+m_1)\eta})/\mathbf{a}\cosh\eta + (ye^{(m_1+m_2)\eta} + we^{(m_1+m_2-m_3)\eta} + se^{m_4\eta})/\mathbf{a}\} \quad (19)$$

where for disk

$$A = E0/(1-\upsilon^2), \quad K = \upsilon + K_1, \quad w = ((m2-m3+1)\nu+1)D1 + (1+\nu)A1/m3.\alpha 0.\mathbf{a}, \quad p = (((m2+1)+\upsilon)D_2 - (1+\nu)A2.\alpha 0.\mathbf{a})$$

$$h = (((m2-m3+1)+\nu)D1 + A_1(1+\nu)\alpha 0.\mathbf{a}/m_3), \quad l = (((3+m4-m1)+\upsilon)\cosh^2\eta D3, \quad t = \upsilon + K_2$$

$$y = (((m2+1)\nu+1)D2 - (1+\nu)A2\alpha_0\mathbf{a}, \quad s = (((m4-m1+3)\nu+1)\cosh^2\eta D3, \quad x = \nu K1 + 1, \quad z = \nu K2 + 1 \quad (20)$$

and for cylinder

$$A = E0/(1+\upsilon)(1-2\upsilon), \quad K = \upsilon + (1-\upsilon)K_1, \quad t = \upsilon + (1-\upsilon)K_2, \quad p = (((m2-m3+1)(1-\nu)+\nu)D2 - (1+\nu)A2.\alpha 0.\mathbf{a})$$

$$h = (((m2-m3+1)(1-\nu)+\nu)D1 + A_1\alpha 0.\mathbf{a}(1+\nu)/m3), \quad l = (((4+m4-m1)\nu + (1-2\nu)(3+m4-m1))\cosh^2\eta D3$$

$$w = ((m2-m3+2)\nu + (1-2\upsilon))D1 + (1+\nu)A1/m3.\alpha 0.\mathbf{a}, \quad y = ((m2+2)\nu + (1-2\upsilon))D2 - (1+\nu)A2\alpha_0\mathbf{a}$$

$$s = (((m4-m1+4)\nu + (1-2\upsilon))\cosh^2\eta D3, \quad x = \nu(K1-1)+1, \quad z = \nu(K2-1)+1 \quad (21)$$

The boundary conditions for stresses may be used for determining the constants B_1 and B_2. By giving the mechanical boundary conditions on the inside and outside surfaces as

$$\sigma_{\eta\eta}(\eta_2) = -P_o \qquad \sigma_{\eta\eta}(\eta_1) = -P_i \quad (22)$$

The solution for B_1 and B_2 is given by the cramer's method from Eqs. (22) as follows

$$B_1 = (b_4b_5 - b_2b_6)/(b_1b_4 - b_2b_3) \quad B_2 = (b_1b_6 - b_3b_5)/(b_1b_4 - b_2b_3) \quad (23)$$

where the constants are as follows

$$b1 = \frac{1}{\mathbf{a}\cosh\eta 1}(K)e^{(m_1+K_1)\eta 1}, \quad b2 = \frac{1}{\mathbf{a}\cosh\eta 1}(t)e^{(m_1+K_2)\eta 1}, \quad b5 = -\frac{1}{A}P_{in} - \frac{1}{\mathbf{a}}(h)e^{(m_1+m_2-m_3)\eta 1} - \frac{1}{\mathbf{a}}(p)e^{(m_1+m_2)\eta 1} - \frac{1}{\mathbf{a}}(l)e^{m_4\eta 1}$$

$$b_3 = \frac{1}{\mathbf{a}\cosh\eta_2}(K)e^{(m_1+K_1)\eta 2}, \quad b_4 = \frac{1}{\mathbf{a}\cosh\eta_2}(t)e^{(m_1+K_2)\eta 2} \quad (24)$$

Results and Discussion

The results of analytical solution can be shown for two examples; thick hollow rotating disk and cylinder. In both of example, Poisson's ratio is taken 0.3 and the modulus of elasticity and the thermal coefficient of expansion at the inner surface are $E_{in} = 200\text{GPa}$ and $\alpha_{in} = 1.2e-6 \quad 1/^oc$ respectively.

For different values of m, radial displacement, radial and hoop stresses along the radial direction are plotted. The mechanical and thermal boundary conditions are taken as $P_{in} = 50MPa, P_{out} = 0$ and $T_{in} = 10^oC$, $Tout = 0^oC$. The results for disk are shown in Ref. [5]. Here, for the rotating cylinder, with $Rin = 1(m)$, $Rout = 1.2(m)$ and having angular velocity values around central axis, results are shown in Figs. (2) to (5). It is assumed that m values for modulus of elasticity (m_1), coefficient of thermal expansion (m_2), and heat conduction coefficient (m_3) are identical to m, ranging from -2 to 2. It can be observed from figures, the results are in good agreement with the same results from Ref. [1], for $\omega = 0$. Figure (2) shows radial displacement decreases for a constant angular velocity, with increasing values of m, and for a $m's$ value with increasing of angular velocity, increases. Figure (3) represents the radial stress along the radial direction for each angular velocity and decreases as m increases. The hoop stress versus the radial direction is shown in Fig. (4). It is seen that for $m < 1$ the hoop stress decreases along the radial direction, whereas the hoop stress increases for $m > 1$ along the radial direction. The curve associated with $m = 1$ shows that the variation of circumferential stress radial direction is minor, and is almost uniform across the radius, and also uniformity of circumferential stress occurs in smaller radius with increasing ω. Radial displacement for a constant angular velocity $(\omega = 50rad/\sec)$, $R_{out}/R_{in} = 1,1.15,1.2$ with increasing values of m, are plotted in Fig. (5).

Conclusion

In this paper, analytical solutions of deformation and stresses for symmetric thick hollow rotating disk and cylinder made of functionally graded material are presented in elliptic-cylinder coordinate system. It is shown that Navier's equations are converted to non-homogeneous ordinary differential equation with constant coefficients. The material properties are assumed to be graded along the thickness direction according to the exponential law function .

Acknowledgment

The present research work was supported by Islamic Azad University – South Tehran Branch.

References

[1] M. Jabbari, S. Sohrabpour, M. R. Eslami, "Mechanical and Thermal Stresses in a Functionally Graded Hollow Cylinder Due to Radially Symmetric Loads", Int. J. Pressure Vessel and Piping, vol. 79 (2002), PP. 493-497.

[2] JN. Reddy, ZQ. Cheng, "Three-dimensional Solutions of smart functionally graded plates", Journal of Applied Mechanics, vol. 68 (2001), PP. 234-41.

[3] N. Tutuncu, "Stresses in thick-walled FGM cylinders with exponentially-varying properties", Engineering Structures, vol.29 (2007) , PP. 2032-2035.

[4] M. Zamani Nejad, G.H. Rahimi, "Deformations and stresses in rotating FGM pressurized thick hollow cylinder under thermal load," Scientific Research and Essay, vol. 4 (2009), PP. 131-140.

[5] A.R. Khorshidvand, M. Jabbari, "Thermomechanical Analysis in FG Rotating Hollow Disk", (Trans Tech Publications, Switzerland), Journal of Applied Mechanics and materials, vols. 110-116 (2012), PP. 148-154.

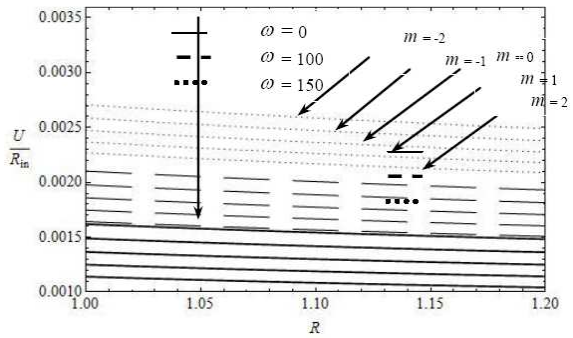

Fig. 2 Dimensionless displacement distribution through the of FG rotating cylinder

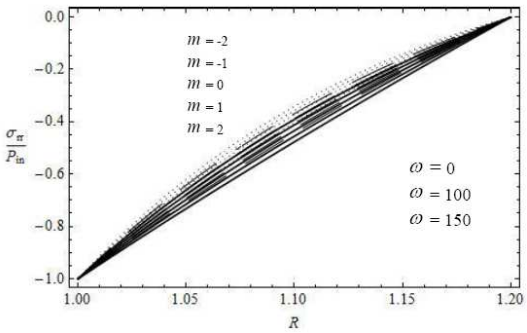

Fig. 3 Dimensionless radial stress through the thickness of FG rotating cylinder

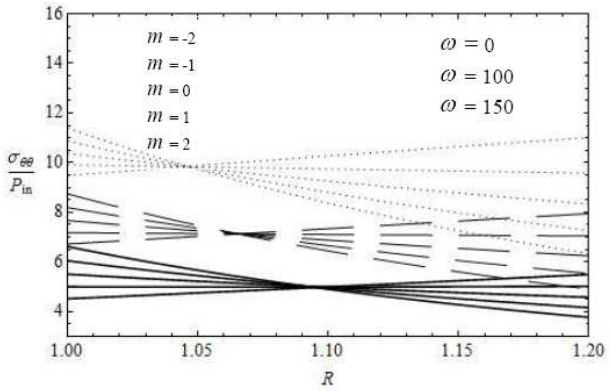

Fig. 4 Dimensionless hoop stress through the thickness of FG rotating cylinder

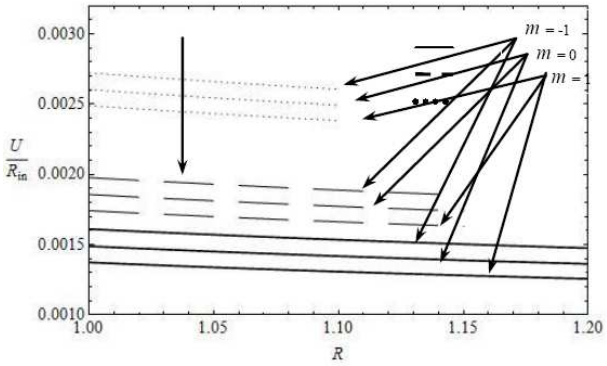

Fig. 5 Dimensionless displacement distribution through the radius of FG rotating cylinder ($\omega = 50 rad/\sec$)

© (2012) Trans Tech Publications, Switzerland
doi:10.4028/www.scientific.net/AMM.187.74

Test and numerical analysis of underwater explosion on circular plates

Sheikhi Koohsar A.A.[1,a],Nasereddini S.M.S. [2,b],Bazrafshan E.[3,c]

[1,2,3] Faculty of Material and Production Technologies, Malek Ashtar University of Technology-Tehran, Iran, P. O. Box 15875-1774

[a]kohsar@gmail.com, [b]nasereddinimehdi@yahoo.com, [c]bazrafshan_es@yahoo.com

Keywords: Underwater Explosion Loading, Strain Rate Effects, Numerical Analysis, LS-DYNA

Abstract. Underwater explosion is a complex discussion because it has two phase environment including shock waves, bubble effects, cavitation, high strain rate, geometric and material non linearity. Results of underwater explosion tests on the circular steel plates have been discussd. Test results compared with numerical analysis results which it is done by LS-DYNA code. LS-DYNA is the software which is used to analyze large dynamic deflections by use of explicit method. We found that this code has good accuracy to predict the maximum deflections. Strain rate effects included in the program by use of Cowper-Symonds relation.

Introduction

One of sea war strategies is to concentrate on underwater explosion to destroy ships and other sea structures. So an important problem which designers are encountered is to design a resistant structure against blast. To do this job properly they should understand behavior of structures against underwater exlplosion loading. In 1859 Besant started this branch of science by analyzing an empty bulb in infinite fluid [1,2]. Later tries have done on this subject by others. For many years noticeable works on loading of air blast on structures have been done. Complexity of underwater explosion because of shock wave, bulb, cavitation, reloading effects and high strain rate effects, geometric and analytical non linearities will cause to some difficalty of analytical solution [1, 3,4,5,6,7,8]. Considering the complete problem will result in simultaneous solving of dynamic response of structure and spreading of the shock wave in the fluid. So solving this problem will cost a lot. There have been various approximations for separating of structure displacement from fluid [9]. Mindlin plane wave approach and Bleich [10] and Geers approchs [11, 12] are samples of conventional models. Combinations of these models with finite element methods lead to produce some computer codes such as SA-STAGS [13], USA-VAST [14] and LS-DYNA. Therefore numerical methods as a good method is using. In this paper we used of LS-DYNA code which it is an explicit code and it uses explicit integration. The specific use of this code is to analyze large dynamic deformations.

Explaining the test and results

Tests did in a pool with length, width and height 290 [cm], 190 [cm] and 220 [cm] respectively. The charge was C4 in the form of sphere. Plates were circular from St37 with thickness of 2.8[mm] and diameter of 240 [mm]. No.8. standard detonator was used. The outer edge of plate was fixed by using 12 screws. Fig.1 represents the arrangement of C4 and plate. 30 [gr] C4 placed in 30 [cm] of a plate which is clamped with 12×M8 screws. Detonator wire fastened to the bars.

In Fig. 2 plastic deformation of a plate is displayed which a 30 [gr] charge is placed in distance of 10 [cm] and maximum deflection accured. Top and front views are shown respectively.

Fig. 1 Fixing the charge at specified distance.

Fig. 2. Deformation of plate by exploding 30 [gr] charge at distance of 10[cm].

Fig. 3- Rupture of plate at test no.5.

Fig.3 shows top view of broken plate. In this case 20 [gr] charge is placed in 5[cm] of plate. Plate has broken from edges and its deflection couldn't be measured. Summery of test results are displayed in Table 1.

Table 1- Experimental results

Test no.	Plate no.	Stand off (R) [m]	Charge weight (W) [Kg]	Shock factor (SF) (0.45*W^0.5/R)	Maximum permanent def.[m]	Failure mode
1	No.1	0.3	0.03	0.26	0.02039	I
2	No.2	0.15	0.03	0.52	0.04177	I
3	No.3	0.1	0.03	0.78	0.05955	I
4	No.4	0.1	0.015	0.55	0.0421	I
5	No.5	0.05	0.02	1.27	*	II

I: large plastic deformation II: Tearing at supports *: Impossible to measure

There is a fator which it shows the strength of shock and is proportional with square root of charge weight also it has a reverse proportion with stand off. In SI system it is as below formula.

$$SF = 0.45\frac{\sqrt{W}}{R}. \quad (1)$$

For simplicity this factor has been used for reporting the results and discussions.

Finite element formulation for axisymmetric plates

Now the basic formulas which this code (LS-DYNA) uses are discussed. Considering an element of circular plate, using virtual work equation of motion for that element is [9]

$$\int_V \rho_s \{\tilde{u}\}^T \{\ddot{u}\} dV + \int_V \mu_s \{\tilde{u}\}^T \{\dot{u}\} dV + \int_V \{\tilde{\varepsilon}\}^T \{\sigma\} dV = \int_A \{\tilde{u}\}^T \{F\} dA. \quad (2)$$

In Eq.2 ρ_s is density of the plate, μ_s is the parameter of structural damping, V and A are volume and area of the element respectively. $\{\tilde{u}\}$ and $\{\tilde{\varepsilon}\}$ are virtual displacement and strain vectors correspondingly. $\{\dot{u}\}$ and $\{\ddot{u}\}$ are velocity and acceleration vectors. $\{\sigma\}$ Is the vector of internal stress and $\{F\}$ is the force vector which applied to the surface, but in underwater explosion this vector is unknown. So Eq.2 will not solve until using a model for interaction of fluid-structure. Substituting the displacements and strain vs. virtual displacements relations into Eq.2 then have:[9]

$$[\mathrm{m}]\{\ddot{\delta}_c\}+[\mathrm{c}]\{\dot{\delta}_c\}+\{\gamma^{\mathrm{int}}\}=\{\gamma^{\mathrm{ext}}\}. \quad (3)$$

In Eq. 3 parameters are as below:

$[N]$: shape functions matrice , $[N]^T$: transpose of shape functions matrice

$\{u\}=[N]\{\delta_c\}$:finite element interpolation relation , $[c]=\int_V \mu_s\{N\}^T\{N\}dV$:damping matrix

$[m]=\int_V \rho_s\{N\}^T\{N\}dV$: mass constituting matrix , $\{\gamma^{\mathrm{int}}\}$:internal force vector, $\{\gamma^{ext}\}$: interaction force vector

and $\{\dot{\delta}_c\}$, $\{\ddot{\delta}_c\}$ are, respectively, the element and nodal velocity and acceleration vectors. Once the equation of motion for each element is defined, the global equation of motion is then obtained by the systematic assemblage of all element contributions. The final form can be expressed as

$$[\mathrm{M}]\{\ddot{\Delta}\}+[\mathrm{C}]\{\dot{\Delta}\}+\{\Gamma^{\mathrm{int}}\}=\{\Gamma^{\mathrm{ext}}\}. \quad (4)$$

Where the capital symbols represent the global quantities of those defined in Eq. 3.

Numerical analysis

According to the geometry, axisymmetric method and lagrangian coordinates are used. Four major elements (explosive, water, plate and air) were defined. For explosive,*MAT_HIGH_EXPLOSIVE_BURN (ρ=1.601,D=0.819,P_{cj}=0.28) was used as material model and *EOS_JWL as equation of state (A= 6.0977,B=0.12950,R1=4.5,R2=1.4,ω=0.25). For water and air, *MAT_NULL was used as material model and *EOS_GRONEISEN was as equation of state for water (C=0.15). For plate *MAT_PLASTIC_KINEMATIC was chosed as material model. *EOS_LINEAR_POLYNOMIAL(C_4=C_5=0.4) was used as equation of state for air. In order to achieve a stable solution, time steps (Δt) should be less the time it takes for a wave to pass through the smallest element of the model. In other words:

$$\Delta \mathrm{t} \le \frac{\mathrm{l}}{\mathrm{v}}. \quad (5)$$

Where l is the minimum element length and v is wave speed. It is Courant-Friedrich-levy condition that should be satisfied in numerical solution. In case of impact problems such as projectile penetration and explosion loading, where deformations are considered large, Δt will change through the simulation process. Therefore:

$$\Delta \mathrm{t} = \alpha \frac{\mathrm{l}}{\mathrm{v}}. \quad (6)$$

Where α is usually considered less than 0.9. In this case, based on LS-DYNA suggestion $\alpha = 0.67$ was used in analysis. Strain rate effects has taken into account by using the Cowper-Symonds relation: [1]

$$\sigma_{\mathrm{dy}} = \sigma_{\mathrm{y}}\left(1+\left|\frac{\dot{\varepsilon}}{\mathrm{D}}\right|^{1/\mathrm{n}}\right). \quad (7)$$

In Eq.7 σ_y is the static yield stress and “D” and “n” are constants which differ for materials. For instant for St37 they are 40, 5 respectively. [15] Units which are used in the analysis are [gr], [cm], [μs], [1e7N] and [Mbar]. In Table 2 mechanical properties of steel plates is shown.

Table 2- Mechanical properties of test speciments

No.	Property	Value
1	Elastic modulus (E) [Mpa]	2.10E+05
2	Poisson s ratio (γ)	0.3
3	Mass density (ρ_s) [kg/m^3]	7800
4	Tangent modulus (E_t) [Mpa]	1700
5	Static yield stress (σ_y) [Mpa]	296
6	Ultimate tensile stress (σ_{ult}) [Mpa]	432
7	Rupture strain (ε_{rup})	0.34

Fig. 4 shows y-displacement of node 41 which it is in the center of plate in two cases with and without considering the strain rate effects. (SF=0.26)

Considering the Fig. 4 this notes can be resulted:

1- Approximately until 180 [μs] there is no deflection. If the velocity of the shock wave is calculated, it is found that it is equal to the velocity of sound in the water.
2- Because of primery shock wave deflection has a constant rate until 550 [μs]. After that as reloading effects appears a jump in the graf is seen. To explain this it is important to know that in underwater explosion primery shock wave and reloading effects are important in deformation of the plate.
3- As displayed in the graf after 600 [μs] there is a reduction in deformation. This can because of reflecting wave.
4- If strain rate effects are not considered there will be an error about 4.2 percent in maximum deflection. Because with considering the strain rate effects the plate will be strengthen.

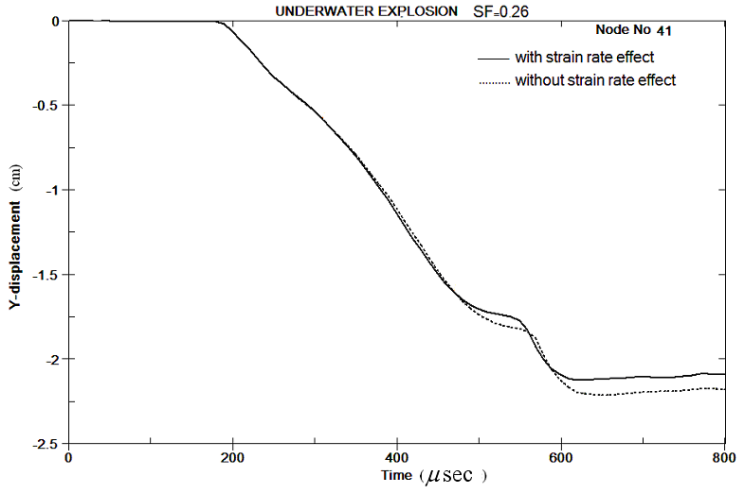

Fig. 4. Comparison of y-displacement of node 41 with and without considering the strain rate effects is presented. (SF=0.26)

In Table 3 the maximum deflections of plates in numerical analysis has been displayed. In this Table strain rate effects considered.

Table 3. The maximum deflections of plates in analysis considering the strain rate effects.

Analysis no.	Plate no.	Stand off (R) [m]	Charge weight (W) [Kg]	Shock factor (SF) (0.45*W^0.5/R)	Maximum permament def.
1	NO.1	0.3	0.03	0.26	0.02084
2	NO.2	0.15	0.03	0.52	0.04216
3	NO.3	0.1	0.03	0.78	0.05925
4	NO.4	0.1	0.015	0.55	0.04183
5	NO.5	0.05	0.02	1.27	*

* Rupture occurred.

Considering the test results, LS-DYNA with good accuracy predicts the maximum deflections. However there were small errors because of numerical errors, mesuarement errors, etc. boundary conditions were so important to get a good result. As see in Fig. 5 results of analysis with considering the strain rate effects with so obtained from tests are the same. Therefore this code predicts the maximum deflections of plates so close to the test results. Another result that can be observed from Fig. 5 is the greater the SF the greater influence of strain rate effects.

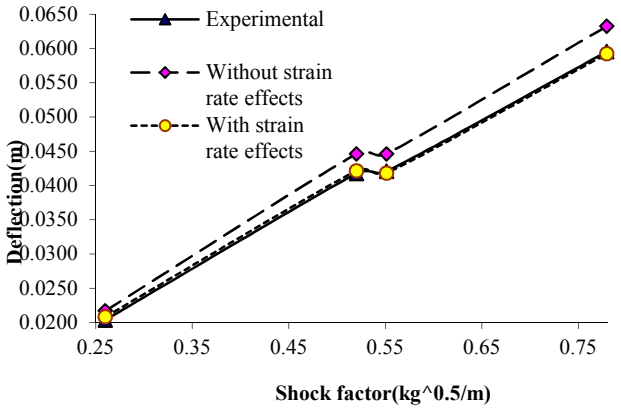

Fig. 5-Comparision of maximum deflections of plates with numerical results.

Summary

Although there was the possibility of comparisons between all points, maximum deflections were compared. From Table 3 it can be seen that LS-DYNA with a good accuracy predicts the maximum deflections. Defining the boundary conditions and selecting the appropriate parameters are important to get good results also this code shows rupture of plates correctly. So with good mesh and appropriate parameters this code with high accuracy will be useful to predict the maximum deflections. Also St37 plates are so sensitive to strain rate effects. In similar tests on Al 5010 plates it is shown that they are less sensitive to strain rate effects. [15] Another result is in high SFs the effects of strain rate are more important. Reloading effects are very important in explosive forming this has been showed in Fig.4.

References

[1] Ramajeyathilagam K. Vendhan C. P. Bhujanga Rao V.: *Non-linear transient dynamic response of rectangular plates under shock loading*, International Journal of Impact Engineering Vol. 24 pp. 999-1015 (2000).

[2] Besant, W. H. :*Hydrostatics and Hydromechanics*, G. Bell, London (1959), p. 158.

[3] Gupta AD, Gregory FH, Bitting RL, Bhattacharya S.: *Dynamic analysis of an explosively loaded hinged rectangular plate*, Comput Struct. (1987), pp. 26-339.

[4] Klaus MH.: *Response of a panel wall subjected to blast loading*, Comput Struct (1985) pp. 21-129.

[5] Houlston R, Slater JE, Pegg N, DesRachers CG.: *On analysis of structural response of ship panels to air blast loading*, Comput Struct 1985. pp. 21-273.

[6] Koko TS, Olson MD. : *Non-linear Transient Response of Stiffened plates to Air Blast loading by a super element Approach*, Compute Methods Appl Mech Eng 1991. pp. 90-737.

[7] Santiago JM, Klaus MH, Wisniewski HL.: *Finite element dynamic analysis of a blast loaded cylinder*, ASME Proc, Conference on Pressure Vessels and Piping and Exhibition, Chicago, IL, (1986).

[8] Jones N.: *Structural impact*, Cambridge University Press, (1989).

[9] Jiang J., Olson M.D.: *Non-linear transient analysis of submerged circular plates subjected to underwater explosions*, Compute. Methods Appl. Mech. Eng. Vol. 134, (1996) pp. 163-179.

[10] Mindlin R. D. and Bleich H. H.: *Response of an elastic cylindrical shell to a transverse, step shock wave*, J. Appl. Mech. vol. 20 (1953) pp. 189-195.

[11] Geers T. L.: *Residual potential and approximate methods for three-dimensional fluid-structure interaction problems*, J. Acoust. Soc. Am. vol. 49 (1971), pp. 1505-1510.

[12] Geers T. L.: *Doubly asymptotic approximations for transient motion of submerged structures*, Acoust.Soc.Am. Vol. 64 (1978) pp. 1500-1508.

[13] DeRuntz J. A. and Dragon F. A.: *Underwater shock analysis of non-linear structure*, A Reference Manual for the USA-STAGS code (Version3), DNA 5545F, Defense Nuclear Agency, Washington, DC, (1980).

[14] Slater J. E. and Norwood M. E.: *Naval ship structure analysis for underwater explosions*, Proc. 2nd Canadian Marine Dynamics Conf, UBC, Vancouver (1993) pp. 176-184.

[15] J.Zamani, H. Motamed al shariati, A. K. Ghamsari, A. Sheikhi Koohsar: *Investigation of Strain rate in Circular Plates under Dynamic Loading by Introducing Dynamic to Static Collapse Pressure Ratio*, Journal of Energetic Materials Vol.5, No.2, pp.73-79. Tehran (2011).

© (2012) Trans Tech Publications, Switzerland
doi:10.4028/www.scientific.net/AMM.187.80

Comparing of The Welding Atmosphere Moisture Effect on Hydrogen Distribution in TI-6AL-4V, Pure Commercial Titanium and TI-15V-3CR-3SN-3AL Weld Joints

Nasereddini S.M.S.[1,a], Sheikhi Koohsar A. A.[2,b], Bazrafshan E.[3,c]

[1,2,3] Faculty of Material and Production Technologies, Malek Ashtar University of Technology-Tehran, Iran, P. O. Box 15875-1774

[a]nasereddinimehdi@yahoo.com, [b]kohsar@gmail.com,[c]bazrafshan_es@yahoo.com,

Keywords: Welding atmosphere, Moisture, Hydrogen absorption, Hydrogen distribution, Titanium weld joints.

Abstract. Welding-titanium and titanium alloys must be performed with special precautions because these materials are very reactive to contamination from atmosphere gases. One of the important technological considerations in welding titanium and its alloys is protection of the molten weld pool and HAZ from atmospheric gases such as nitrogen, oxygen, carbon dioxide and moisture and contamination. Absorption of the atmospheric gases affects the mechanical and metallurgical properties and may cause embrittlement, lake of fatigue strength and hydrogen cracking of titanium welds. In this paper, the effect of welding atmosphere moisture on hydrogen absorption and distribution in Ti-6Al-4V, pure titanium and TI-15V-3CR-3SN-3AL TIG welds has been studied. The experimental results indicated that hydrogen distribution which was symmetrical with respect to the weld axis had maximum and minimum points. It was also observed that heat treating the joints after welding resulted in reduction of the magnitude of the maximum and minimum points as well as redistributed the hydrogen in the welds in such a way that the distance of the maximum and minimum points got farther from the weld axis. This distribution is affected by type of titanium alloy and degree of annealing .in this investigation we used vacuum welding chamber with TIG welding apparatus and a special metal sampling and composition detecting systems for joining the samples and detecting the amount of hydrogen in the weld metal .the aim of this investigation was to increase the level of our knowledge about harmful effect of diffusion the hydrogen in the different titanium alloys.

Introduction

Some basic properties which make titanium alloys the natural choice for a specific range of applications are low density (about 60% relative to steel), appreciable strength at intermediate temperatures and corrosion resistance in marine environment and in chemical process operations. Commercial applications are numerous due to their corrosion resistance to a variety of agents present in chemical plants and to seawater for marine applications. Titanium and its alloys have found wide applications in areas such as medical sciences, aerospace and chemical industries, etc. All these applications are due to favorable properties of this metal like high strength to weight ratio, high temperature resistance, good corrosion resistance, good formability, etc. Although titanium and most of its alloys can be welded almost easily; but certain precautions must be taken to ensure production of sound and high – quality welds. Titanium like other reactive metals has a high affinity for atmospheric gases , and the welding processes that employ a flux or expose the heated metal to the atmosphere are not used because of contamination and embrittlement of the weld [1,2,3,4,5, 6] . Similarly, cleanliness of both base and filler metal is important in welding titanium. Titanium alpha alloys can be strengthened only by cold work (called also strain hardening) (not by heat treatment), are weldable in annealed condition and retain their strength at high temperature. Titanium alpha-beta alloys can be welded in certain conditions but with limited weld ductility or heat affected zone ductility; however they can be strengthened by heat treatment. Welding-titanium of beta alloys is performed in the annealed condition, and then, if necessary, they can be cold worked and heat treated to preserve ductility in the weld. Hydrogen which is absorbed from moisture of the shielding

gas , residual oils , cleaning agents and dirt on the joint surfaces plays an important role in causing embrittlement and cracking of titanium welds . The observations made by Fromin [7,8,9,10,11] for hydrogen absorption in titanium welds indicates that water dissociation reaction up to a temperature of 450 °C is :

$$H_2O \leftrightarrow H_2 + \tfrac{1}{2} O_2 \quad (1)$$

At higher temperatures:

$$H_2O \leftrightarrow H + OH \quad (2)$$

$$H_2O \leftrightarrow 2H + O \quad (3)$$

The last two reactions occur in the central zone of the welding arc. At zones near the surface of the molten metal (farther from arc center) ; reactions (2) and (3) are reversed and as a result of this phenomenon the atomic oxygen and hydroxyl don't react with the molten titanium. Due to water vapor dissociation, the atmosphere surrounding the welding arc gets saturated with oxygen and hydrogen. At a later stage, the following reactions occur:

$$Ti\ (molten) + H_2O \leftrightarrow TiO\ (molten) + H_2\ (gas) \quad (4)$$

$$Ti\ (molten) + H_2O \leftrightarrow TiO\ (gas) + H_2\ (gas) \quad (5)$$

Fromin has concluded that reaction (5) is more probable to occur i.e. the probability of the formation of titanium oxide and hydrogen absorption in the weld metal is more. Hydrogen absorption in weld metals of more commercial metals has attracted more attention than titanium welds [12]. Although this phenomenon in titanium welds is an important problem which needs more investigations but because of certain difficulties; little work has been done or reported on this subject. This is especially true for Ti–6 Al– 4 V and TI-15V-3CR-3SN-3AL welds.

Experimental Details

Base Metal. 3*16 Ti – 6 Al – 4 V ,pure commercial titanium and) TI-15V-3CR-3SN-3AL sheets of 100 mm X 80 mm X 3 mm size having the chemical composition given in (Table 1-2) were used as the base metal .They were placed in acetone , hot water and ethyle alcohol and dried prior to welding.

Table 1 .Chemical composition (%) of the (α + β) Ti – 6 Al – 4 V alloy.

Al	C	Fe	H	N	O	V
5.5 – 6.75	0.08	0.03	0.012	0.05	0.2	3.5 – 4.5

Table 2. Chemical composition (%) of the (β) TI-15V-3CR-3SN-3AL alloy.

O	C	Fe	N	H	Al	Sn	Cr	V
0.22	0.08	0.04	0.04	0.01	2.5-3.5	2.5-3.5	2.5-3.5	14.5-15.5

Welding Chamber and the Shielding Gas. A welding vacuum chamber of 0.8 m^3 capacity was used for this work. A vacuum pump was used to create the necessary vacuum in the chamber and then the chamber was filled with argon as the shielding gas at a pressure of 133 Kpa. Table 3 gives the details of the shielding gas.

Table 3. Details of the argon shielding gas

Gas purity, %	Dew point , ° C	Max. O, %	N ,%	CO_2+CnHm	Moisture vol. %
99.821	-15	0.002	0.01	0.0002	0.166

Welding Procedure. An automatic TIG welding power source in DCEN mode using the following welding parameters was employed for this work:Welding current :195 A , Welding speed :11 cm / min., Voltage :12 v , Electrode diameter :2.4 mm Arc length : 1.6 mm.
The prepared titanium sheets were square - butt welded. A total of eight joints were made between these sheets in a vacuum welding chamber that prepared for titanium welding.[10,13].

Weld joint Metal Hydrogen Measurement. Out of the eight joints, four were used for hydrogen measurement without annealing and the other four were used after annealing the joints. The joints were annealed at a temperature of 800 ºC for two hours and were cooled in the furnace. There are different methods to determine hydrogen distribution in metals [14]. In this investigation for determination of the hydrogen content of welds, samples of 2 x 10^{-3} gr were removed using a probe of 0.3 mm diameter at the intersection of lines as shown in (Figure 1). These samples were placed in a furnace which was air vacuumed to a pressure of 1.33 x 10^{-3} Pa and then filled with a high purity oxygen gas to a pressure of 133 Kpa . After burning the samples in the furnace, the hydrogen content could be measured from the amount of moisture formed. The furnace temperature was 1600 ºc.

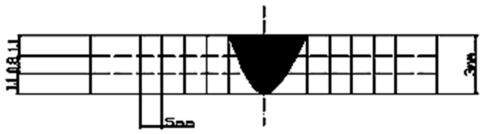

Figure 1- Points of sample removal

Experimental Results and Analysis

In(Figure 2) ;three samples of different Ti- alloys weld joints that studied in this paper are shown. In (Figure 3); the magnitude and distribution of hydrogen content of the weld metals are shown with and without annealing. It is seen that this symmetrical distributions with respect to the weld axis consist of peak and valley points. The occurrence of the maximum and minimum points (peak and valley points) of hydrogen content in the weld metal is due to the opposing effects of diffusion coefficient (Q) and hydrogen concentration (C [H]). Increase in temperature (Figure 4) decreases hydrogen concentration and causes an increase in diffusion coefficient [7, 10, 14,15,16,17]. Without annealing these points had a high magnitude and were close to the weld axis whereas after annealing their magnitude decreased and their distance also got farther from the weld axis. Vacuum annealing of the specimens causes a decrease in the magnitude of hydrogen contact due to degasification. In addition to this since the hydrogen concentration in the base metals is low, the peak and valley points move towards the base metal due to annealing procedure for all of three alloys are presented in the Table 4.

Table 4. Annealing procedures of materials

Material	Annealing procedure
Commercially pure titanium	650-815°C,15-120min
Ti-6Al-4V	705-870°C,15-60min
Ti-15V-3Cr-3Sn-3Al	760-815°C,3-30min

A: Pure Commercial Titanium

B:Ti-6Al-4V

C: TI-15V-3CR-3SN-3AL

Figure 2- Samples of different weld joints

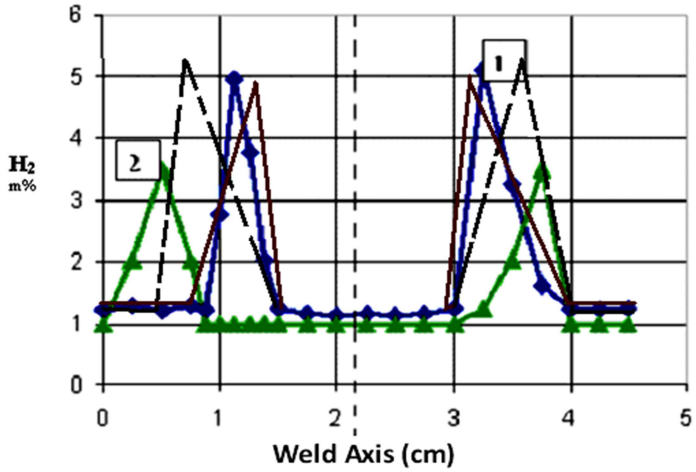

Figure 3- (1) hydrogen distribution in the weld metal for■ : without annealing for Ti-6Al-4V, **(_ _ _):**for TI-15V-3CR-3SN-3AL and (_____ **):** for pure commercial titanium, and (2)▲: for Ti-6Al-4V with annealing .

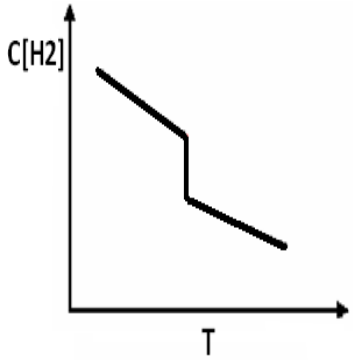

Figure 4- Schematic of change of hydrogen concentration in titanium with temperature

Conclusion

Based on this investigation the following conclusions could be drawn:

1. Hydrogen distribution in titanium welds had peak and valley points.
2. Annealing caused redistribution of hydrogen in the weld specimens in such a way that the distance of peak and valley points got farther from the weld axis.
3. For all of three alloys in this work, Annealing also resulted in reduction of the magnitude of peak and valley points. This heat treatment also reduces 30% of magnitude of each peak.
4. Fast movement of hydrogen atoms in titanium crystal lattice and the rapid change of its solubility with temperature cause a relatively heterogeneous distribution of hydrogen in the weld metal.
5. peaks of hydrogen concentration in the weld metal for the pure titanium welds are more closer to the weld axis and peaks of hydrogen concentration for the TI-15V-3CR-3SN-3AL weld joints are less closer to the weld axis .also peaks of hydrogen concentration for TI-15V-3CR-3SN-3AL weld joints is the highest and for pure commercial titanium weld joints is the lowest.
6. Non-uniform heating of different zones of the weld specimens causes different solubilities of hydrogen in these zones and as a result directional diffusion of hydrogen takes place.

References

[1] Otani: Welding Technology. 54, 87(2006)

[2] Otani: Titanium Welding Data sheets. Ver.2, 2005

[3] Nishikawa et al.: Preprints of the National Meeting of J.W.S. Vol.65, 1999, p.276

[4] Nishikawa et al.: Preprints of the National Meeting of J.W.S. Vol.65, 1999, p.278

[5] Nadkarni S V, 1988, Modern arc welding technology, Oxford and IBH publishing CO.

[6] Lancaster J F,1999,Metallurgy of welding,Sixth edition,Woodhead publishing limited.

[7] Welding handbook, Volume 2, Eighth edition, AWS.

[8] Kolachev B A, Livanov V A and Bokhanova A A, 1974, Mechanical properties of titanium and its alloys,Metallurgia (in Russian).

[9] Bratoukhina M, 1997, Forging,welding,brazing and heat treatment of titanium and its alloys, Mashinostraienie (in Russian).

[10] Zamkov V N, 1984, Titanium science and technology.

[11] Nikifrova G D, 1973, Fusion welding technology and equipments, Mashinostraienie (in Russian).

[12] Harwig D D, Longenecker D P, Cruz J H, Sep. 1999 , Effects of welding parameters and electrode atmospheric exposure on the diffusible hydrogen content of gas shielded flux - cored arc welds, 314s-321s.

[13] Goorevich S M, 1990,Nonferrous metals welding handbook,Naouka doumka (in Russian).

[14] Smith II R D, et al, Supplement to the welding journal May 2001 , The determination of hydrogen distribution in high-strength steel weldments, Part 1 and 2.

[15] Cheosnutt J C, Rhodes C G and Williams J C , 1976, Relationship between mechanical, microstructure and fracture topography in (α+β) titanium alloys, Fractography-microscopic cracking processes, 99-138.

[16] Collins E W,1984,The physical metallurgy of titanium alloys, ASM , Metals park.

[17] Harrigan M J, Kaplan M P and Sommer A W, 1974, Effect of chemistry and heat treatment on fracture properties of Ti-6Al-4V alloy, Fracture prevention and control, 225-254.

CHAPTER 3:

Chaotic States and Analysis of Systems

© (2012) Trans Tech Publications, Switzerland
doi:10.4028/www.scientific.net/AMM.187.87

Design and Research of Electric Vehicle Driving System based on SOPC

Zhao Ya[a], Qi Hui[b]

Department of Electronic Information and Control Engineering. Beijing University of Technology

Beijing, China

[a]zhaoya@emails.bjut.edu.cn, [b]qihui@bjut.edu.cn

Keywords: electric vehicle; SOPC; PMSM

Abstract: Motor driving system is a key technology for electric vehicle (EV), and brake energy feedback technology which benefits to prolong driving rang is typical feature of electric vehicle driving system. Hardware logic realization of permanent magnet synchronous motor (PMSM) driving control algorithm for EV in some sense contributes to the integration of EV controller. This paper mainly researches on vector control and energy feedback algorithm for PMSM, constructs digital high performance algorithm test platform for low power PMSM, and completes driving control of PMSM based on this platform.

Introduction

Although traditional vehicle brings tremendous convenience to people's life, at the mean time it does harm to environment. According to the statistics, over 60% pollutions derived from the emission of transportations at present. To decrease the amount of emission and protect environment development of EV is appealed by the whole vehicle industry.

The primary problems of EV are high initial cost and low driving range so far [1]. On the basis of constant battery capacity, the main method for increase driving range is to improve driving efficiency which includes using high efficient driving motor-PMSM, and introducing brake energy feedback control strategy. When the vehicle is braking, the inertia energy of the vehicle transfers to motor through transmission system, and the motor works as a generator to charge and reuse brake energy which may be wasted in mechanical brake.

To improve driving efficiency, electronic control system of EV becomes more and more complex. With main driving motor transforming from direct current (DC) motor to alternate current (AC) motor, the complexity of driving system increases accordingly. Correspondingly, brake energy feedback technology lead to an increasing difficulty of brake force distribution (BFD) [2][3]. These talked above restrict the possibility of integration manifold algorithms into a single chip, increase the number of system controller, and aggravate the burden of communication bus. To figure out this problem, this paper puts forward a comparatively new electronic control system structure of EV based on SOPC, which benefits integration. Based on that, using hardware logic to realize PMSM driving control algorithm for EV achieves the rapidity of driving control and does not disturb the algorithm of BFD existing as form of software in the same chip.

The second part of this paper puts forward an easily integrated electronic control system structure of EV. The third part describes algorithm of brake force distribution. The fourth part illustrates realization method of PMSM controller on the basis of SOPC and implements vector control and field-weakening algorithm with hardware. The fifth part verifies the feasibility and validity of the PMSM driving control algorithm based on hardware logic.

Electronic Control System Structure of EV

EV controller is generally separated into three controllers (Fig.1) or even more according to different function of control algorithm [4]-[6]. Every controller commonly adopts DSP or MCU as main chip, and CAN bus is used in data transmission between controllers.

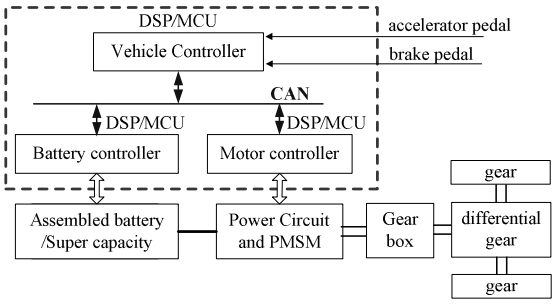

Figure1. Traditional structure of EV control system

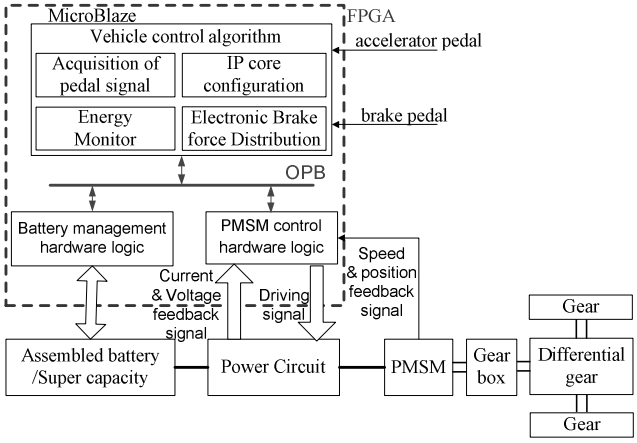

Figure 2. Structure of EV control system proposed by the paper

The function of each controller is described as follows. EV controller is responsible for signal acquisition of accelerator pedal and brake pedal, energy monitor, *BFD* and so on. Motor controller drives motor according to the signal provided by the EV controller. Battery controller is responsible for the detection of battery capacity and coordination between super capacity and storage battery.

In this paper, an easily integrated electronic control system structure of EV (Fig.2.) is put forward, in which FPGA is used to realize the function of three controllers and CAN bus in Fig.1 is replaced by OPB bus inside this chip to simplify complexity of system. Vehicle control algorithm is designed using software, in the MicroBlaze of FPGA, to maintain flexibility. Whereas, PMSM control algorithm is designed using hardware logic, because PMSM that used in this test system pertains AC motor demanding complex control algorithm and rapid response (approximately 100*us*). Furthermore, hardware logic will not disturb the operation rapidity of software in the MicroBlaze.

Brake force distribution and the request for motor controller

Brake force distribution. Brake force distribution (*BFD*) is part of vehicle control algorithm. Its aim is to realize brake energy recycle and limit charge current to protect battery. Therefore, vehicle brake force is offered by reasonable distribution of mechanical brake and electric brake which is generated by motor on the basis of the position of brake pedal, speed of vehicle, state of charge (*SOC*) and the maximum brake torque generated by motor. If the control object is an EV driven by rear wheel, brake force can be distributed using (1).

$$\begin{cases} T_{br} = F_{br}/r_b \\ T_e = \begin{cases} T_{br} & T_{br} \le T_{\max} \\ T_{\max} & T_{br} > T_{\max} \end{cases} \\ F_{regen_br} = T_e \bullet r_d \\ F_{mech_br} = F_{br} - F_{regen_br} \end{cases} \tag{1}$$

Brake force of rear wheel (F_{br}) combines electric break force (F_{regen_br}) and mechanical break force (F_{mech_br}), based on serial brake strategy of best brake feel [7].Where r_d is the radius of tire, and T_e is electric brake torque, and T_{max} is maximum brake torque of PMSM. When brake torque of rear wheel (T_{br}) is less than T_{max}, only electric brake is applied. When T_{br} is more than that, electric brake force reaches peak, and the remanent brake force is satisfied by mechanical brake system.

PMSM electric brake force is also restricted by T_{max} and *SOC*. When PMSM angular velocity (ω) is lower than the base velocity (ω_n), T_{max} is rated torque (T_n). When ω is higher than ω_n, T_{max} decreases as hyperbola along with ω [8], shown in (2).

$$T_{\max} = \omega_n T_n / \omega \tag{2}$$

When *SOC* exceeds the standard, T_e should be restricted to protect battery and bus capacity. Reference [9] is used in EV driving control with the modification to restrain the fluctuation of bus current and voltage aroused by the limitation of T_e. According to the maximum *SOC* (soc_{max}) and minimum *SOC* (soc_{min}), new electric brake torque (T_{e_c}) is calculated, and mechanical brake force is revised based on T_{e_c}.

$$T_{e_c}=\begin{cases} T_e & SOC < soc_{\min} \\ T_e \bullet \dfrac{SOC - soc_{\min}}{soc_{\max} - soc_{\min}} & soc_{\min} \le SOC \le soc_{\max} \\ 0 & SOC > soc_{\max} \end{cases} \tag{3}$$

BDF needs the support of precise torque control for PMSM realized by motor controller and precise mechanical brake system to obtain the aim of best brake feel.

Request for Motor Controller. The crucial distinctions between motor controller for EV and general controller are shown as follow: 1) Vector control is introduced to guarantee torque track performance because *EFD* will be ineffective and even do harm to the brake system without precise torque control. 2) The mode of PMSM brake should be regenerated brake to implement energy feedback under the condition of EV brake. 3) Field-weakening control is used to elevate torque performance at high speed, and acquire more feedback current under the condition of EV declivity. The implement of vector control, regenerated brake and field-weakening control are described in the fourth part.

Design of Pmsm Controller Based on FPGA

Overview of Hardware Logic for PMSM Drive Control. Hardware logic for PMSM drive control (*HLPDC*) based on FPGA produced by Xilinx is showed in Fig.3. Vehicle control algorithm, in MicroBlaze, could configure *HLPDC* by writing register and acquire state and data from *HLPDC* by reading register. To be specific, software sends instruction (reference torque T_e^*) to *HLPDC*, and this hardware output PWM signal in order to drive power circuit and complete drive and brake control of PMSM.

HLPDC is divided into seven modules: current regulation, position and speed calculation, current feedback detection, voltage feedback detection, *Park* transform, field-weakening and SVPWM. Field-weakening module adopts floating-point formation to insure control precision because real values of motor parameter, current and voltage are used during the calculation. The rest of these modules adopt fix-point formation because range of data is narrow comparatively, and could be calculated before design easily.

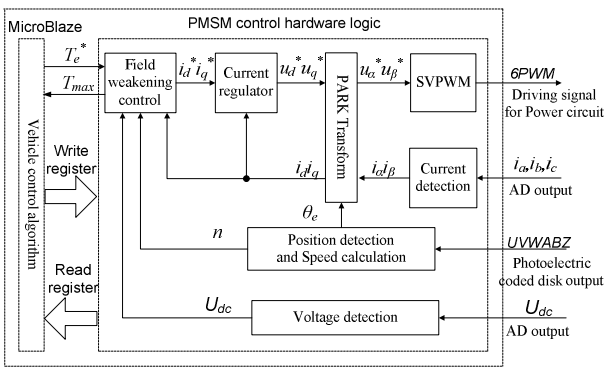

Figure 3. Hardware logic for PMSM drive control

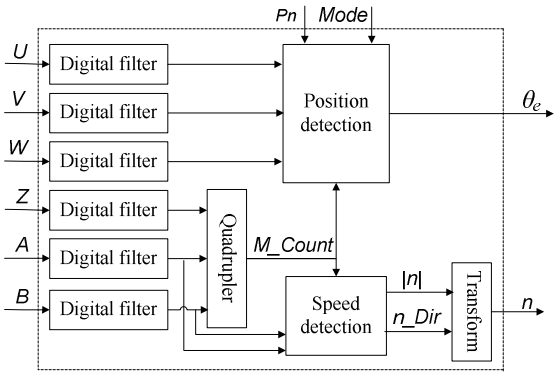

Figure 4. Hardware structures of position and speed calculation module

Position and speed calculation. The position of rotator and speed calculation in real time is necessary for achieving PMSM vector control. This function could be implemented through correspondingly hardware logic of processing the output signal from photoelectric coded disk [10] fixed on PMSM, and the hardware structure is showed in Fig.4.

U,V,W signals, generated by photoelectric coded disk, have absolute information which is used to estimate initial position. Counter (*M_count*), which takes count of two pulses (*A,B*), is used to judge the direction of rotator and calculate position and speed. Position angle $\theta_e(k)$ can be obtained using (6)

$$\theta_e(k)=p_n \bullet M_count \bullet R_1 / Z_1 \tag{6}$$

Where Z_1 is the number of pulse with one rotation output by quadrature; R_1 is the data rang of position angle; p_n is pole pair. What's more, *M/T* method is adopted to detect speed and the equation can be arranged as follows:

$$n = 60 M_1 f_0 / Z_1 M_2 = (60 f_0 / Z_1) \bullet M_1 \bullet (1/M_2)(r/\min) \tag{7}$$

Where M_1 is the number of pulse of quadrature output during T_c (speed sample period), and M_2 is the number of f_0 (high frequency pulse) from the start of T_c to rising edge of the quadrature output after the end of T_c. The state diagram of speed calculation is showed in Fig.5. When the speed is so low that long waiting time for rising edge will lead to an overflow of M_2, speed should be set to zero and restart next period speed detection.

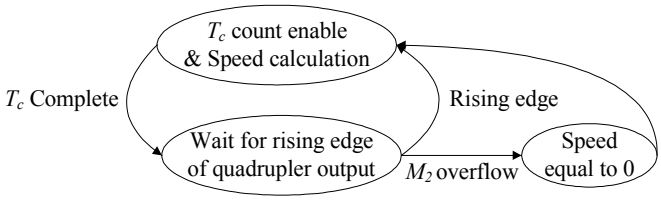

Figure 5. M/T speed calculation

Current and voltage feedback detection. AD7862, of which highest sample frequency is 250KSPS (Sample per Second) [11], is adopted to translate analog signal of current and voltage sensor into 12*bit* digital signal. Current and voltage feedback detection module input current (i_a, i_b) and bus voltage (U_{dc}) of PMSM from AD7862, and output feedback signal after digital filter.

Field-weakening. A method of field-weakening is put forward for smooth transition from normal condition to field-weakening condition, using field-weakening equation as in [12]. Field-weakening current i_{d2}^* can be obtained directly from (8), according to feedback angular velocity ω_e, bus voltage U_{dc} and feedback current i_q which contains the information of load torque. In addition, limitation of current is adopted to provide a normal current output [13][14]. Implement structure of field-weakening under the L_d=L_q condition is showed in Fig.6. Where L_d and L_q are stator inductance in *dq* axis.

$$i_{d2}^* = f(i_q, U_{dc}, \omega_e) = -\frac{\psi_f}{L_s} + \sqrt{\frac{3}{8}\left(\frac{U_{dc}}{L_s \omega_e}\right)^2 - (i_q)^2} \tag{8}$$

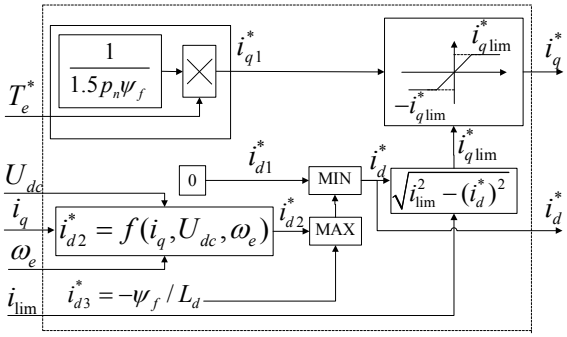

Figure6. Implement structure of field-weakening under the Ld=Lq condition

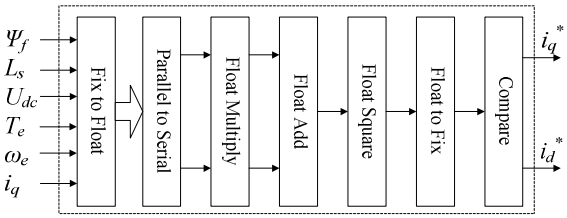

Figure 7. Hardware Structure of field-weakening module

This method could adapt to the fluctuation of bus voltage, and judge the necessity of field-weakening according to load and speed at present. MAX avoids field-weakening current exceed the maximum power curve, and MIN is to realize a smooth transition between normal control and field-weakening control. According to torque reference T_e^*, pole pair p_n and rotator flux ψ_f, torque current i_q^* is acquired, and it is limited by i_d^*.

Field-weakening module uses floating-point to acquire more precision of calculation and adapt to wider parameter range. This module transfers parallel input data into serial data, and repeatedly uses multiplication and addition module for decrease logic resource. Pipeline mode is not necessary in this module because calculation needs only once in each current sample period, and the hardware structure of field-weakening module is showed in Fig.7.

The parameters of motor for simulation are as follows: stator inductance (L_d=L_q) equals to 0.00343H and rotator flux (ψ_f) is 0.171Wb. The sequence diagram of field-weakening is showed in Fig.8, and under this condition, the output result of simulation is corresponding to the calculation result according to field-weakening equation. When the speed of motor exceeds rated speed (3000*r/min*), current reference of flux (*Id_Ref*) increases gradually, and current reference of torque (*Iq_Ref*) is restricted by *Id_Ref*.

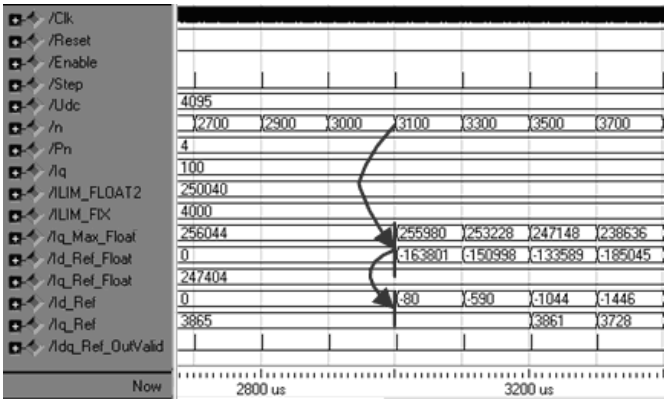

Figure 8. Field-weakening sequence diagram

SVPWM. SVPWM module is designed to output six PWM signal driving inverter to output voltage to control PMSM. Eight static voltage vectors linearly compose rotated voltage space vector U_{out} showed in Fig.9(a). Where U_{000} andU_{111} are zero vectors for inefficacy to stator flux, and work period of inverter is divided into six sectors by the rest of the six voltage vectors (U_{100}, U_{110}, U_{010}, U_{011}, U_{001}, U_{101}).

Hardware structure of SVPWM module is showed in Fig.10. Firstly, this module uses voltage reference (u_α^*, u_β^*) to calculate the sector of U_{out} for selecting the right constant matrix ($M_{2\times2}$). Secondly, voltage vectors (U_{cmp1}, U_{cmp2}, U_{cmp0}) are calculated according to (9), and the duty cycles of SVPWM (*Cmpr1, Cmpr2, Cmpr3*) are obtained. Finally, six SVPWM signals are generated after passing through comparator and dead zone generator.

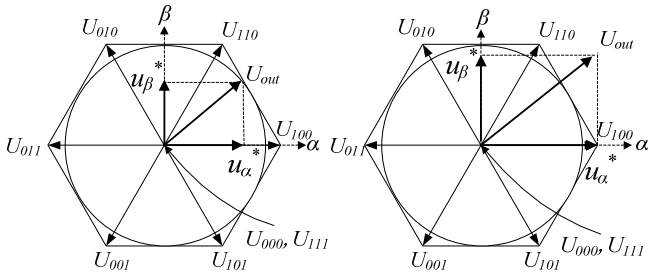

a) Normal b) Over modulation

Figure 9. Composition of voltage space vector

$$\begin{cases} \begin{pmatrix} U_{cmp1} \\ U_{cmp2} \end{pmatrix} = T1per \times M_{2\times 2} \times \begin{pmatrix} u_\alpha^* \\ u_\beta^* \end{pmatrix} \\ U_{cmp0} = (T1per - U_{cmp1} - U_{cmp2})/2 \end{cases} \tag{9}$$

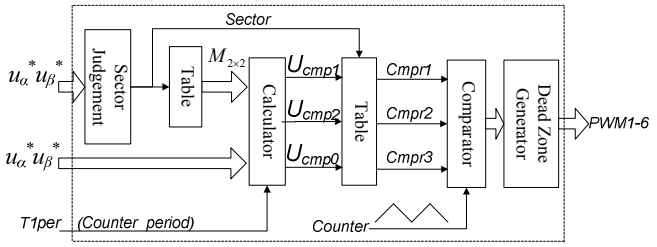

Figure 10. Hardware structure of SVPWM module

When U_{out} is in the inscribed circle showed in Fig.9(a), the sequence diagram of SVPWM duty cycle calculation is illustrated in Fig.11. Where *Uarfa* and *Ubeta* are the input voltage reference (u_α^*, u_β^*), and *Cmpr1, Cmpr2* and *Cmpr3* represent the duty cycle under the condition of normal modulation.

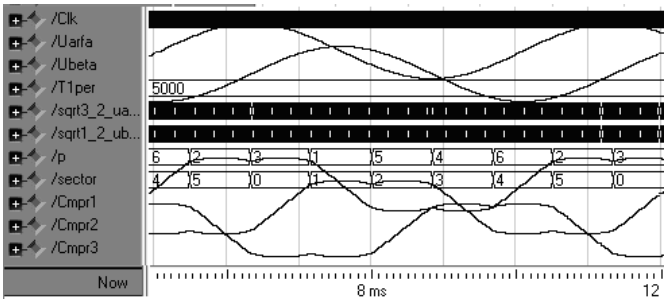

Figure 11. SVPWM duty cycle calculation sequence diagram (normal modulation)

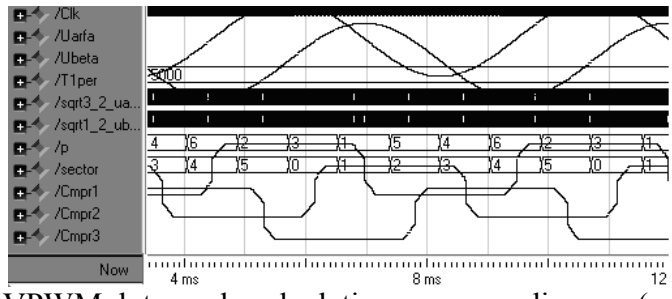

Figure 12. SVPWM duty cycle calculation sequence diagram (over modulation)

When U_{out} exceeds the hexagon showed in Fig.9(b), U_{out} should be dragged back into hexagon with over modulation technique, and the sequence diagram of SVPWM duty cycle calculation is illustrated in Fig.12.

Experiment and Result

Experiment platform of low power PMSM based on FPGA is constructed to test performance of *HLPDC*. This platform comprises PMSM (rated current 2.6A), DC motor, hardware circuits and dynamometer. Hardware circuits include control circuit based on XC3S1500, signal adjust circuit and power circuit.

Speed response graph of PMSM in vector control algorithm, observed by monitoring software on PC, is showed in Fig.13. The adjust time is less than 6*s*, static error is less than 1%, and overshoot is less than 10%, so the performance of speed track is well. What's more, speed and bus current response graph of PMSM is showed in Fig.14. During brake from 1500 *r/min* to 0 *r/min*, bus current is reverse (-0.2A), so brake current passes from motor to the bus capacity, and energy feedback is realized.

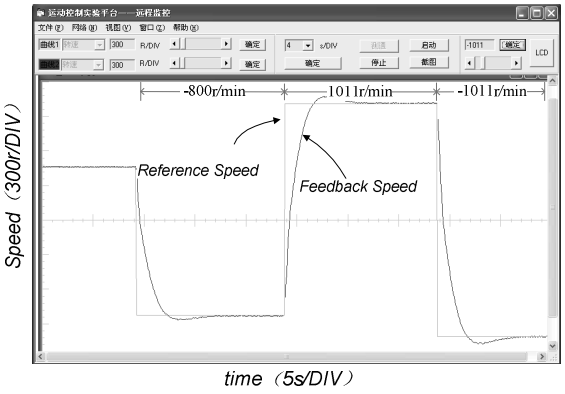

Figure 13. Speed response graph of PMSM

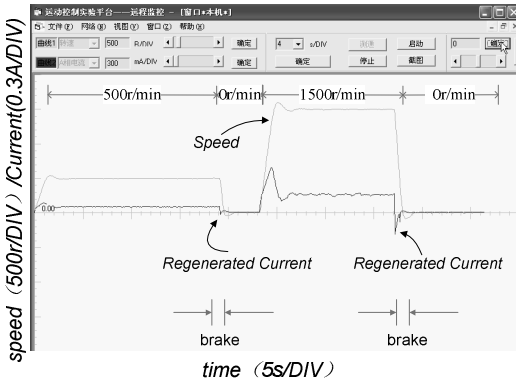

Figure 14. Speed and bus current response graph of PMSM

Conclusion

In this paper, vector control and energy feedback algorithm for PMSM used by EV is mainly studied. A comparatively new electronic control system structure of EV based on SOPC is put forward. Additionally, digital high performance algorithm test platform is constructed for low power PMSM based on FPGA. Driving control of PMSM based on this platform is completed.

To complete the integration of brake controller and PMSM controller, software of brake force distribution should be realized, and integrated into FPGA with the IP core of PMSM vector control. In addition, driving tests of high power motor should be accomplished to further verify the reliability of the system.

References

[1] Zhao Hou-Cai, "The design and realization of regenerative braking system for electric vehicles based on DSP" Guangdong University of Technology .2007, pp. 11-13

[2] Liu Bo, "Research and implementation of braking-energy recovery system based on pure electric vehicle",Tsinghua University. 2004, pp. 23-29

[3] Zhang Pei-Bin, "Research and simulation of electric vehicle's regenerative braking control",WuHan University of Technology.2006, pp. 21-22

[4] Wang Kui, "Development of Control strategy and software for power train system of pure electric automobiles", TianJin University, 2004, pp.11-15

[5] Xiao Jing-Yi, "The electronic control system for electric vehicle", Beijing Jiaotong University, 2007, pp. 35-40

[6] Wu Ying-Jie, Wang Jun-Yan, “Application of power feedback brake of brushless DC motor to electric vehicle”, Journal of Shanghai Dianji University.2006,3(9), pp. 52-55

[7] He Ren, Hu Qing-Xun, “Braking course of city bus with regenerative braking system”, Journal of jiangsu university(natural science edition), 2005,5(26),pp. 389-392

[8] Mehradad Ehsani,Yimin Gao,Sebastien E.Gay ,Ali Emadi. “Modern electric, hybrid electric, and fuel cell vehicles fundamentals, theory, and design” ,China machine press.2008, pp. 18-25

[9] Feri Yusivar,Kenji Uchida,Takahiro Kihara,Shinji Wakao, “An anti oscillation strategy for the regenerative braking control of permanent magnet synchronous motor with insufficient load power consumption” , The 27the Annual Conference of the IEEE Industrial Electronics Society (IECON’01),2001, pp. 1457-1461

[10] Wu Qian-Kun, “Study on some problems of single chip AC servo control system”, Harbin University of Science and Technology ,2004, pp. 35-47

[11] Analog Devices.AD7862 datasheet.1996, pp. 1-16

[12] Leng Zai-Xing, Ma Zhi-Yuan, “Space vector field-weakening control of IPMSM drives”, Micromotors Servo Technique.2006, pp. 11-14

[13] Sang-Hoon Kim,Seung-Ki Sul, “Voltage Control Strategy for maximum torque operation of an induction machine in the field weakening region”. *IEEE Transactions on Industrial Electronics*. 1994, pp. 599-604

[14] Bon-Ho Bae,Nitin Patel,and Steven Schulz,Seung-Ki Sul.New, “Field weakening technique for high saliency interior permanent magnet Motor”, *IEEE*,2003, pp. 898-904

© (2012) Trans Tech Publications, Switzerland
doi:10.4028/www.scientific.net/AMM.187.95

Study on the Temperature Filed of Wet Dual Clutch Transmission during Starting Process

Xi Liu, Xiusheng Cheng[a], Yan Li, Qiang Gu, Yinshu Wang

College of Automotive Engineering, Jilin University, Changchun, China

[a]xiusheng_cheng@yahoo.com.cn

Keywords: Dual clutch transmission, Wet clutch, Matlab, Temperature field, Numerical simulation

Abstract. Based on the analysis of starting process of wet dual clutch transmission, dynamic rules for piston pressure and relative angular velocity of wet clutch were determined, According to the unsteady heat exchanging theory and the heat exchanging process of clutch engagement, a two dimensional heat conduction model of wet clutch was developed with reasonable initial conditions and boundary conditions. Matlab/PDE toolbox was used to solve the established model. The temperature distribution of friction pairs along the axial and radial direction were revealed in the Simulation results. Testing program had been designed, and real vehicle test was done to the temperature field on friction interface of wet dual clutch transmission in starting process. The test result indicated that the temperature field model and its solution were reliability, and it was instructive to optimize the design of wet clutch and its engaging control in starting process.

Introduction

Dual clutch transmission (DCT) is a kind of newly developed mechanical automatic transmission, and its power is transferred by two clutches connected separately to two coaxial shafts. One of the shafts is hollowed so that the other shaft can run through its center. The driven gears of contiguous shifts on the output shifts meshed with the corresponding gears on the two input shafts. Power-shift can be obtained with the attendance of two clutches so as to shorten the shifting time and improve the gear-shifting quality effectively [1].

For wet clutch has the advantages of stability working, high torque driving and progressive attaching point, it enable the driving more comfortable. At present time, wet clutch has been adopted into the industrial production of dual clutch transmission. The dual clutch transmission with wet clutches would produce slippage among their friction pairs when starting. Because the heat produced by slippage is very high, and the engagement time is short, the temperature of friction pairs will increase instantaneously, generating a high gradient temperature field. The overlarge temperature gradient leads to warp and fissure of friction plates and dual steel plates, and aggravates the friction, deforming and thermal failure, which results in the decreasing of the reliability and service life of clutch [2][3]. For these reasons, it becomes a necessity to study the dynamic temperature field of the friction pairs of clutch.

The transit temperature field when wet clutch friction pairs meshing together were modeled based on the analysis on the starting condition of vehicle assembled with dual clutch transmission in this essay. Matlab/PDE toolbox was used to solve the temperature model, and experiment was adopted to verify the viability of the model.

The starting process of wet dual clutch transmission

The Control of Clutch in Starting Process. The control for clutch of starting process is largely dependent on the road conditions and the intentions of drivers. In order to start the vehicle as the intentions of the driver, the engagement of clutch should be controlled reasonably. The control of clutch should meet the requirement as followed:

- Avoiding engine miss.
- Avoiding the shaking and impaction which are uncomfortable to passengers.

- Avoiding too much dynamic load caused by drive system.
- Extending the work life of clutch.
- Reflecting the intention of the driver.

Jerk is one of the key evaluating indicators of starting quality, which is quantized riding comfort. It reflects the rate of change of vehicle longitudinal acceleration. Theoretically, the jerk is controlled by adjusting the rate of change of torque transmitted by clutch. For wet dual clutch transmission, the torque transmitted by clutch can be changed by controlling the rate of change of clutch pressure.

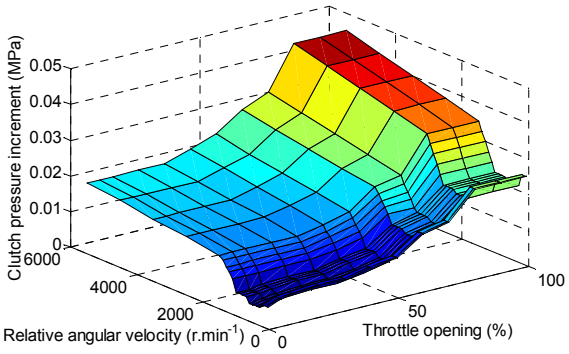

Fig. 1 Clutch pressure increment graph in starting process

The slipping work is another key evaluating indicator of starting quality. It is related to difference between speed of driving disc and driven disc, slipping moment and slipping time. It is used to evaluate the friction work produced by clutch engagement. In the process of clutch engagement, slipping work is mainly converted into heat, increasing the temperature of clutch friction pairs. According to the reliability and security of clutch assembly, the slipping work should be as low as possible to meet the requirement of jerk.

The throttle percentage is an important indicator of driver intention. In the starting process, the larger the throttle opens, the quicker the driver wants the auto to start. And the driver is preparing to bear relevant large impaction. In this case, the jerk could be decided by the throttle percentage so that the clutch pressure increment of each control period in the starting process could be obtained. Combined with speed difference of driven disc, the engagement work index was amended [4]. The amended results were shown as Fig.1.

The Coupling Process of Clutch. Multiple discs wet clutch is used in dual clutch transmission, and the alternated dual steel plates and friction discs are fixed in it. As shown in Fig.2, p is the coupling pressure of clutch, $\omega_d(t)$ is the rotate speed of driving disc, and $\omega_s(t)$ is the rotate speed of driven speed. A friction pair is made up of one dual steel plate and one friction disc. The friction disc comprises a core disc and two friction linings, while the friction disc is the driving disc, which is connected to input shaft by internal spline and the separator disc is the driven disc, which is fixed to clutch hydrocylinder by external spline to connect with the output shaft.

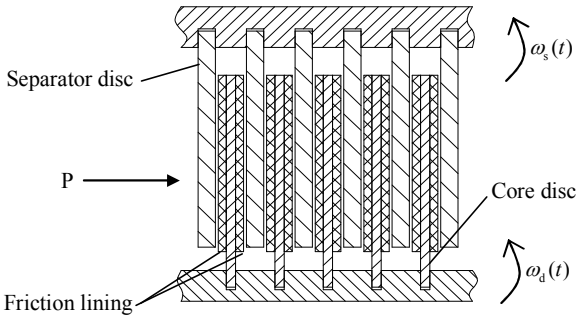

Fig. 2 Schematic of wet clutches

From the moment the driving disc and the driven disc begin to contact with each other to produce relative sliding work, until the moment the driving disc and the driven disc rotating together is called a coupling process. The work produced by sliding is converted into heat, and increases the temperature of friction pairs during the coupling procedure.

The model of temperature field of clutch

The Model of Heat Exchanging. In the process of clutch coupling, relative sliding emerges due to difference between rotate speed of friction disc and rotate speed of separator disc. Part of the input power is consumed in the sliding process transformed into kinetic energy to improve the temperature of friction pairs.

Ignoring the influence of the groove in the friction disc, it is considered that the clutch friction pairs have the mechanism of axial symmetry, and the temperature field is related to radial position r and normal direction z, but has nothing to do with circumferential direction [5][6]. The assumptions are as followed:

- The heat given away by lubricating can be ignored because the coupling process is short.
- The physical parameters don't change while coupling, for the material of the friction pairs are even.
- A pair friction discs temperature condition is needed to be analyzed considering the heat conducting of each friction disc is the same.
- The radiating of friction pair can be ignored for the coupling process is very short, and the produced heat is all used to increase temperature.

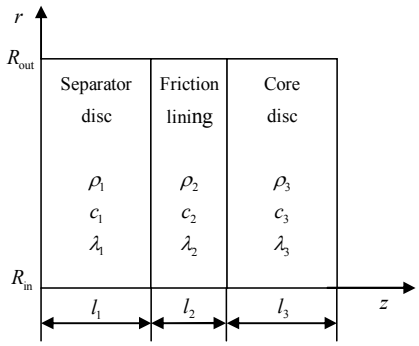

Fig. 3 Coordinate system of clutch heat conduction mode

Additionally, the differences of both ends of clutch are neglected. Due to the heat conducting symmetry and configuration of each friction pair, it is assumed that there is no heat exchange on one half of thickness of separator disc and core disc. The established frame of axes is showed in Fig.3. l_1 is half thickness of separator disc, l_3 is half thickness of core disc, l_2 is the thickness of friction lining, R_{in} is the rotating inside radius of friction pair, R_{out} is outer radius, $\rho_1 \sim \rho_3$ is density, $\lambda_1 \sim \lambda_3$ is thermo conductivity, $c_1 \sim c_3$ is specific heat capacity. The heat exchanging equations of transient temperature field on separator disc, friction lining and core disc were established using Fourier heat exchanging theory.

$$\frac{\rho_i c_i}{\lambda_i}\frac{\partial T_i(r,z,t)}{\partial t} = \frac{\partial^2 (r,z,t)}{\partial r^2} + \frac{\partial^2 (r,z,t)}{\partial z^2} + \frac{1}{r}\frac{\partial T_i}{\partial r} \tag{1}$$

where i =1, 2, 3, and it stands for separator disc, friction lining and core disc separately. $T_i(r,z,t)$ stands for friction pair temperature.

The density of heat flow and its assignment. In the process of clutch coupling, part of the kinetic energy is transformed into heat by sliding between friction linings and separator discs. The density of heat flow, where radius of sliding friction surface is, is as bellow:

$$q(r,t) = \mu(\Delta\omega)\cdot p(t)\cdot\Delta\omega\cdot r \tag{2}$$

where $\mu(\Delta\omega)$ is friction coefficient, $p(t)$ is positive pressure of friction surface, $\Delta\omega$ is relative angular velocity.

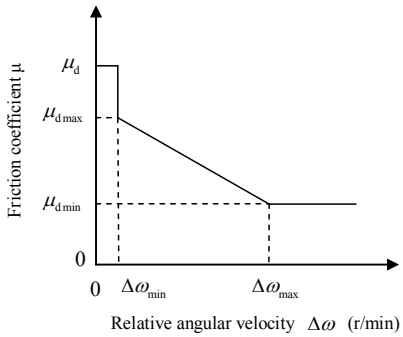

Fig. 4 Friction characteristic of wet clutch

Generally speaking, the friction coefficient of wet clutch in slipping is related to rotate speed difference, which is a dynamic parameter called kinetic friction coefficient. The kinetic friction coefficient is generally greater than static friction coefficient. In this essay, the static friction coefficient is set as constant, and the kinetic friction coefficient stands for linear function of rotate speed difference [7]. It is shown in Fig.4, and its expression is described below:

$$\mu(\Delta\omega)=\begin{cases}\mu_d & |\Delta\omega|<\Delta\omega_{\min}\\ \mu_{d\max}-\dfrac{\Delta\omega-\Delta\omega_{\min}}{\Delta\omega_{\max}-\Delta\omega_{\min}} & \Delta\omega_{\min}\le|\Delta\omega|\le\Delta\omega_{\max}\\ \mu_{d\min} & |\Delta\omega|>\Delta\omega_{\max}\end{cases} \tag{3}$$

where μ_d is static friction coefficient, μ_{dmax} is the maximum value of kinetic friction coefficient, μ_{dmin} is the minimum value of kinetic friction coefficient, $\Delta\omega_{min}$ is rotate speed difference in response to maximum kinetic friction coefficient, $\Delta\omega_{min}$ is rotate speed difference in response to minimum kinetic friction coefficient.

The assignment of density of heat flow among friction pairs is related to thermo resistance of interface among friction pairs and heat exchanging caused by lubricating oil. During the process of coupling, the lubricating oil flow and thickness of oil are very low; very little heat is absorbed by lubricating oil which could be neglected. Therefore, it is considered that all heat produced is presented to steel plates and friction discs. What's more, the relation of distribution between friction linings and separator discs of heat flow density could be obtained for the interfaces have the same temperature and total heat produced by friction equal to the sum of heat absorbed by separator discs and friction linings.

$$q_1(r,t)+q_2(r,t)=q(r,t) \tag{4}$$

$$\frac{q_1(r,t)}{q_2(r,t)}=\sqrt{\frac{\lambda_1\rho_1c_1}{\lambda_2\rho_2c_2}} \tag{5}$$

where q_1 is heat flow density assigned to separator disc surface, q_2 is heat flow density assigned to friction lining surface.

Initial Conditions. The moment (t=0) when the clutch begins to engage but not couple yet, the temperature of separator discs, friction linings and core discs all are T_0:

$$T_i(r,z,t)\big|_{t=0}=T_0(r,z) \tag{6}$$

Boundary Conditions. Boundary conditions reflect the surface characteristics of thermal conductivity system. The boundary conditions of heat exchange model during the process of wet clutch coupling are as followed:

According to the symmetry of configuration and heat conductivity, the value of heat conductivity is zero at the half thickness position of separator disc and core disc:

$$\frac{\partial T_1(r,z,t)}{\partial z}\Big|_{z=0} = 0 \tag{7}$$

$$\frac{\partial T_3(r,z,t)}{\partial z}\Big|_{z=l_1+l_2+l_3} = 0 \tag{8}$$

Because of the rotating of the friction pair, the inner surface and outer surface which parallel the radial direction have forced convection occurred with ATF in the clutch shell, and the temperature of inner portion of system is changed. It is hard to analyze accurately owing to the complexity of inner configuration of wet clutch, so the heat convection occurred on the inner and outer surface parallel the radial direction of friction pairs is simplified as bellow:

$$-\lambda_i \frac{\partial T_i(r,z,t)}{\partial r}\Big|_{r=r_{in}} = h_{i-in}(T_i - T_0) \tag{9}$$

$$-\lambda_i \frac{\partial T_i(r,z,t)}{\partial r}\Big|_{r=r_{out}} = h_{i-out}(T_i - T_0) \tag{10}$$

where h_{i-in} and h_{i-out} are convective heat transfer coefficient.

On the interface between separator discs and friction linings, temperature distribution is the same, and there is heat input generated by friction:

$$T_1(r,z,t)\Big|_{z=l_1} = T_2(r,z,t)\Big|_{z=l_1} \tag{11}$$

$$\lambda_i \frac{\partial T_i(r,z,t)}{\partial z}\Big|_{z=l_1} = q_i(r,t) \tag{12}$$

where i =1, 2.

On the boundary face of friction facings and chips, the boundary conditions are:

$$T_2(r,z,t)\Big|_{z=l_1+l_2} = T_3(r,z,t)\Big|_{z=l_1+l_2} \tag{13}$$

$$\lambda_2 \frac{\partial T_2(r,z,t)}{\partial z}\Big|_{z=l_1+l_2} = \lambda_3 \frac{\partial T_3(r,z,t)}{\partial z}\Big|_{z=l_1+l_2} \tag{14}$$

Temperature Field Computation

From the analysis above, we know that the heat exchange during the process of wet clutch coupling is a nonlinearity transient issue. Its differential equation is nonlinear parabolic equation and its solution is very complexity. The normally used numerical computation methods for temperature field are finite element meshes in spatial domain and finite difference grid in time domain. Actually, the finite difference and finite element are combined together to solve the equation. The program is hard to write for the algorithm is relative complex, and it is inconvenient to provide accurate data for the temperature field study during the process of wet clutch coupling.

The PDE Toolbox of MATLAB provides a powerful, flexible and practical platform for studying and solving the problem of two dimensional space partial differential equation. The toolbox could be used to interactively realize the thorough procedure of pretreatment, after treatment and calculation and etc to solve the partial differential equation intuitively, quickly, and accurately. The PDE Toolbox could be used to solve equations such as linear oval-type partial differential equation, parabolic-type partial differential equation, hyperbolic-type partial differential equation, intrinsical-type equation and simplified nonlinear partial differential equation[8][9]. The heat exchanging equation of transient temperature field of clutch is parabolic-type equation. The equation is in PDE Toolbox:

$$d\frac{\partial u}{\partial t} - \nabla(c\nabla u) + au = f \tag{15}$$

where d is complex variable function on domain Ω.

After transforming the heat exchanging equation of wet clutch transient temperature field into normalized parabolic equation, solve the equation of temperature field as the flow shown in Fig.5.

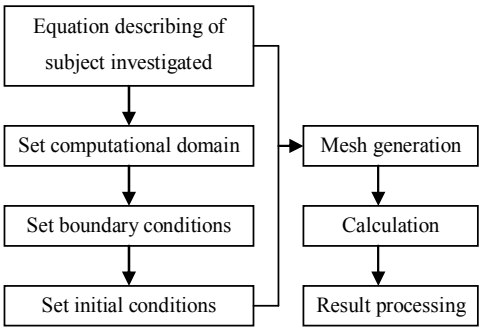

Fig. 5 Calculation process flow chart of PDE toolbox

Result and analysis

In the starting process of wet dual clutch transmission, the larger the throttle opened, the faster the driver want the car to start, which means the engaging time would be shorter. The temperature rise of clutch would be high when the car started in the condition of small throttle opening, and analysis to the temperature field of clutch would be more suitable. Hence this essay took the starting condition when the throttle percentage was 15% as the object of study.

When the throttle percentage was 15%, the curve that the clutch pressure varied with time could be obtained according to the starting control strategy in Fig.1. The curve was shown in Fig.6a. The curve that rotating speed difference between driving disc and driven disc varied with time could be acquired and it was shown in Fig.6b.

Fig.7a showed the simulation curve that the temperature changed follow the direction of thickness of separator disc when the fixed radius r was 98mm and l_1 was 1.7mm. It could be obtained that the temperature paralleled the direction of thickness dropped a little. However the temperature didn't drop too much, for the heat conductivity of steel plate was good.

The temperature curve of different position paralleled the radial direction of the friction surface at the moment the wet dual clutch transmission during starting completely (t=3.7s) was shown in Fig.7b. In order to verify the reliability of the temperature field model and the simulation result, a platinum resistance thermometer sensor (PRTS) whose diameter was 0.4mm was fixed at intervals of 5mm along the radial direction of separator disc of friction surface [10]. The PRTS temperature specifications was 0℃ to 350℃, response time was 10ms, and its error was ±0.5℃. Real car test was done assembled with wet dual clutch transmission.

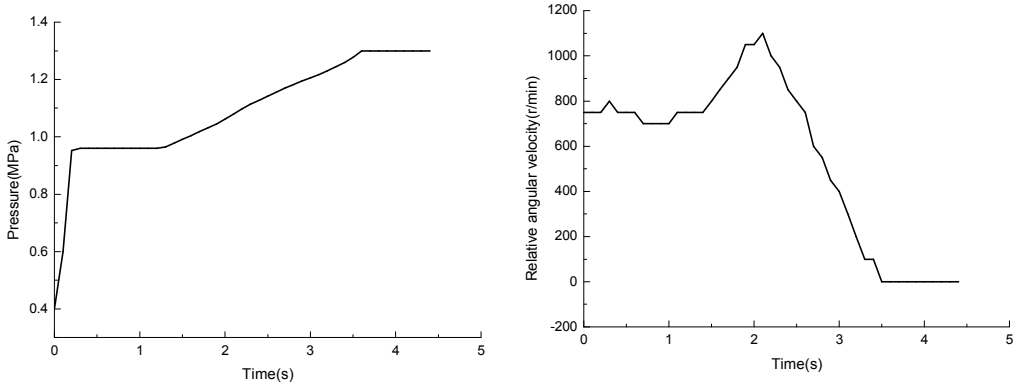

Fig. 6 (a)Piston pressure; (b) The relative angular velocity

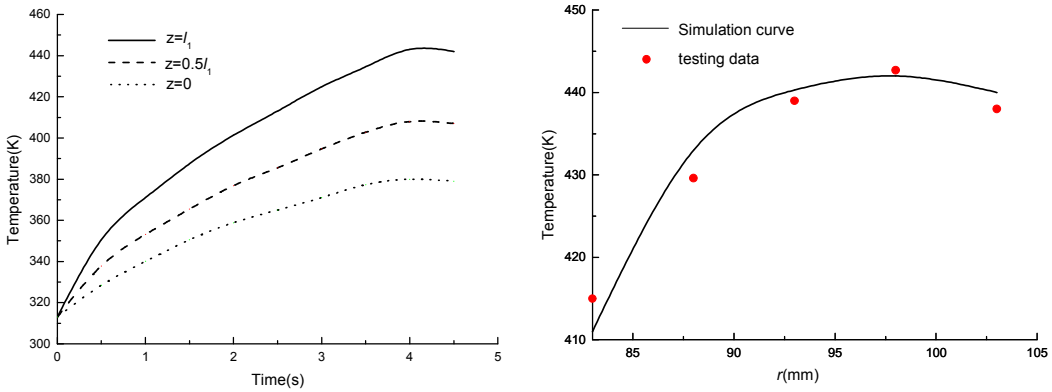

Fig. 7 (a) Temperature variety of axial different point of Separator disc; (b) Temperature of friction interface along the radius at 3.7s

As shown in Fig.7b, the temperature obtained by every sensor at the moment the clutch engaged completely was closed to the simulation curve. It was shown that there were certain errors between test result and simulation result, but their overall trend of the temperature distributions were agreed with each other. The maximum temperature appeared close to the external part of friction surface, for the reason that the slipping linear velocity was large, and heat exchanging had little influence on high energy slipping. In the real car test, the clutch pressure and the rotating speed difference between driving disc and driven disc couldn't be totally agreed with simulation process, so the temperature error was inevitable. Furthermore, the error was in the acceptable range from the compared result. Therefore, the model and its solution of wet clutch temperature field were validity.

Conclusion

After analyzing the starting process of wet dual clutch transmission, the temperature filed during the wet clutch coupling process was modeled and analyzed based on unsteady state heat exchanging theory. And relevant test had been done. The result showed that the temperature model and its solution were validity. It provided a method to study the temperature field of wet clutch in engagement, and it could be used to design and optimize the existing clutch. Additionally, it provided the theoretical foundation for drawing up control objectives of wet dual clutch transmission during starting condition.

References

[1] Zhang Deming and Wu Guangqiang, "Application of fuzzy-slide model control in electronic control clutch of DCT," Automobile Technology, Oct. 2007, pp. 1-6.

[2] M. Mansouri, M.Holgerson, M.M.Khonsari, and W.Aung, "Thermal and dynamic characterization of wet clutch engagement with provision for drive Torque," Journal of Tribology, vol. 123, Feb. 2001, pp. 313-323.

[3] Deur, J., Petric, J., Asgari, J., Hrovat, D., "Modeling of a wet clutch engagement including a thorough experimental validation," SAE paper 2005-01-0877.

[4] Cheng Xiusheng, Feng Wei, Lu Zhonghua, Liu Xi, and Gu Qiang, "Starting control of wet double clutch transmission," Journal of Jiangsu University (Natural Science Edition), vol. 31, Feb. 2004, pp. 145-149.

[5] T. M. Cameron, T. McCombs, S. Tersigni, and T.-C. Jao, "Flash temperature in clutches," SAE paper 2005-01-3890.

[6] L.Afferrante, M.Ciavarellab, P. Decuzzi, and G. Demelio, “Transient analysis of frictionally excited thermoelastic instability in m-ultidisk clutches and brakes,” Wear, vol. 254, no.1-2, 2001, pp. 136-146.

[7] M.Goetz, M.C.Levesley, and D.A.Crolla, “Integrated Powertrain Control of Gearshifts On Twin Clutch Transmissions,” SAE paper 2004-01-1637.

[8] Li Ping, Zhang Wei, “Application of MATLAB in Solving temperature field,” vol . 27, no. 3, 2005, pp. 32-35.

[9] Li Jiageng, Hu Xuxiao, Lei Jinbo, and Li Junwei, “The calculation of temperature field and displacement field of deformable body,” Machine Tool & Hydraulics, No.14, 2004, pp.59-61.

[10] Cai Dan, Wei Chenguan, and Song Wenyue, “Measurement of surface temperature distributions and calculation of surface stresses on clutch discs,” Vehicle & Power Technology, no.4, 2004, pp.7-11.

© (2012) Trans Tech Publications, Switzerland
doi:10.4028/www.scientific.net/AMM.187.103

Research on Taylor Vortices in the Wedge-shaped air gap of Evaporation cooling Turbo Generator

Gao Jinshui[1,a] and Gu Guobiao[2,b]

[1]Institute of Electrical Engineering Chinese Academy of Sciences, Graduate University of Chinese Academy of Science, Beijing, China

[2]Institute of Electrical Engineering Chinese Academy of Sciences, Beijing, China

[a]gaojs@mail.iee.ac.cn, [b]gbgu@mail.iee.ac.cn

Keywords: Evaporation cooling, Turbo Generator， Taylor Vortex, air flow.

Abstract. Cooling technique is one of the most important parts to improve the development of turbo generator. Turbo generator with evaporative cooling stator and water cooling rotor possesses many excellent qualities for mid unit. In this system the stator bars and core are immerged in evaporative coolant, which could be cooled fully. The rotor bars are cooled by water inner cooling mode. In this paper, we describe the Taylor Vortices in the Wedge-shaped air gap of Evaporation cooling Turbo Generator and present the research on gas-flow and heat-transfer with different features in the turbo generator. The CFD method is used to analyze this system, which has different features, including gap size, rotating speed, Apex angle. And the heat-transfer calculation proves the axial direction gas-flow can do well to the rotator heat-emitting.

Introduction

Evaporative cooling technique utilizes the latent heat of vaporization of coolant to cool the electrically active components of turbo generator, which is far larger than specific heat capacity of coolant. The cooling effect is reliable, and the temperature of generator is more even. Combined the superiorities of evaporative cooling technology and water cooling technology, we studied the turbo generator with evaporative cooling stator and water cooling rotor.

The evaporative coolant can be used for long time, and there is no need to monitor and maintain. This will decrease the investment and cost of maintenance. And the coolant is insulating, nontoxic, which will improve the security of generator [1]. The manufacturing of evaporative cooling turbo generator is simpler, which is similar with air cooling unit [2]. So the period of order can be shortened, consumers and equipment manufacturers are favor of this advantage.

In evaporative cooling technique self-circulation can be performed, which would decrease the loss of cooling system and improve the efficiency of generator [3]. The coolant is insulating liquid. When end windings are immerging in it, the electrical field of end windings can be improved. And the length of end windings could be shortened. This will reduce the end-connection reactance, and improve the performance of generator.

Taylor Vortices Theory. The flow between concentric rotating cylinders, is one of the most investigated problems of the motion near rotating bodies. And viscous flows between rotating circular cylinders have been of interest to many scientists [4]-[6] during the last century. The pioneering work in this field was done by G. I. Taylor [7] who described theoretically and proved experimentally the existence of regular vortices between two rotating cylinders.

Taylor vortices will occur initially in the larger part of the annulus, where the centrifugal forces are largest. As illustrated in Fig.1 and Fig.2, more vortex pairs will be generated until the whole gap is finally filled with vortices. The vortex cells travel upwords to the larger radius, their motion being caused by the imposed meridional swirl.

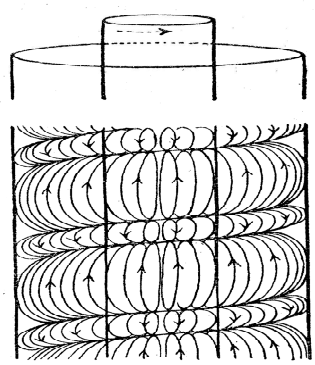

Fig.1. Flow of the taylor vortices

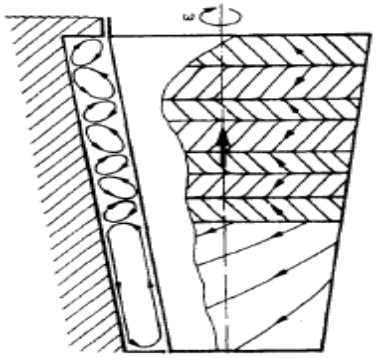

Fig.2. Taylor vortex flow between conical cylinders

Taylor vortices may also appear, however, in other geometries than circular cylinders. A simple variation of the classical Couette-Taylor geometry leads to a flow between cones and cone-cylinder combination. In changing from circular to conical cylinders, the radius changes linearly and generates a linear change of centrifugal forces. The resulting imbalance of centrifugal forces in the annulus drives the three-dimensional basic flow.

The three-dimensional basic flow together with the axially different centrifugal forces has crucial consequences on the onset. Besides observing a simultaneous existence of stable and unstable flows in the gap, we can study the conditions of travelling Taylor vortices in Turbo generator. Then regular closed vortex cells will be generated by disturbances, known as Taylor vortices, if the critical value of Taylor number reaches the set value.

$$T = r_i s^3 \omega^2 / \nu^2 \tag{1}$$

Where,

r_i : the radius of the inner cylinder;

s : the gap between the cylinders;

ω : the rotational velocity of the inner cylinder;

ν : the kinematic viscosity;

Structure Characteristics

As the increasing of unit capacity, the losses of turbo generator are sharply increasing. The cooling design is put in the most important position of turbo generator. For the mid-size turbo generator we recommend the cooling system by immerging combined with inner evaporative cooling stator and water cooling rotor The stator core and end structure are cooled by evaporative cooling technique easily. And the stator windings are cooled mainly by inner evaporative cooling technique. When the turbo generator is running in a lower load, the immerging evaporative cooling technique can perform the cooling of windings. So the pump of inner evaporative cooling system can be turn off.

In this paper, a 300MW evaporative cooling turbo generator is studied. It includes the stator, the rotor, the isolated tube, the condenser and the circulatory system. The cooling method for the rotor is the water inner cooling, while the stator adopts the immersion type and the winding interior conduit evaporative cooling way, which the stator is immerged in the evaporative coolant, and the coolant takes away heat losses by the use of latent heat.

There is a glass-fiber reinforced resin sleeve between stator and rotor in the air gap, and the outer diameter of sleeve contacts with the inner diameter of stator core [8]. The sleeve and shell of stator are connected to become a hermetic cabin and the stator components are included in it. There is also a wedge-shaped gap between the rotor and the sleeve. The gas-flow and the heat-transfer in the air gap are studied in this paper.

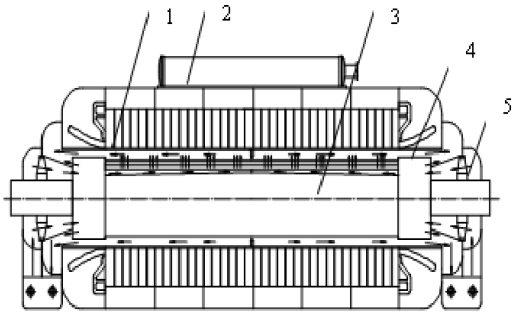

Fig.3. Turbo generator with evaporative cooling technology
1-stator 2-condenser 3-rotor 4-sleeve 5-fan

Fig.4. Immerging combined with inner evaporative cooling stator and water cooling rotor

Evaporative Cooling Stator. Turbo generator with evaporative cooling stator and water cooling rotor has a glass-fiber reinforced resin sleeve between stator and rotor in the air gap. There is a condenser lying on the top of stator shell. The general structure is shown in Fig.3 and Fig.4. The evaporative coolant is injected into the hermetic cabin. Bars and core of stator are immerged in the evaporative coolant.

The coolant absorbs heat losses of bars and core by the use of latent heat, which is larger than specific heat far from water[7]. Liquid coolant becomes into vapor keeping on the same temperature. The vapor coolant rises, and reaches into condenser. The second cooling water of condenser absorbs the heat of vapor, and the vapor lost heat becomes into liquid. Liquid coolant drops for gravity. The heat losses of stator are taken away by the second cooling water in the end, and this course is performed by self-circulation of liquid and vapor coolant. The transfer of heat does not need any accessional energy and any noises.

When the turbo generator is running, coolant in the hermetic cabin keeps on the boiling point. The boiling point is economical about between 40℃ and 60℃ according to our experiences. The heat exchange between stator and coolant is performed on the boiling point, so the temperature of stator

can keep on a uniform distribution [8]. Especially, the temperature rise of stator end structure descends greatly, compared with other gas cooling method. As well as the coolant is insulation medium, it can improve the reliability of stator electric field. The electric field of stator end winding is very complicated, and insulation of end windings.

Cooling air flow. Cooling air flows around the surfaces of heated rotor, and takes away the heat. Combined with the structure of sleeve, the cooling system introduces the axial-radial ventilation mode. Cooling air is pressured into the ends of rotor by fans. The cooling air cools the end windings of rotor, and flows into the end of air gap directly. Then cooling air flows into air gap through and flows along axial-direction. Cooling air flows into cooler at the end of air gap. In addition, there is a trapezium cylinder between the axial flow fan and end of rotor, which separates the cooled air with heated air. The cooled air from cooler is pressured into the end of rotor through the trapezium cylinder, and the fan is rotating with rotor in the same speed.

Methods Used In The research

The heat exchange equation is as follow

$$\frac{\partial}{\partial x}\left(k_x\frac{\partial T}{\partial x}\right)+\frac{\partial}{\partial y}\left(k_y\frac{\partial T}{\partial y}\right)+\frac{\partial}{\partial z}\left(k_z\frac{\partial T}{\partial z}\right)=-q \tag{2}$$

$$\frac{\partial T}{\partial n}=0 \tag{3}$$

$$-k\frac{\partial T}{\partial n}=\alpha\left(T-T_f\right) \tag{4}$$

Where,

$k_{x,y,z}$: thermal conductivity along x, y and z directions;

q : the heat flux;

T : the wall temperature;

α : the convection coefficient;

T_f : the fluid temperature.

T_f is the temperature of cooling air around heat surface in air cooling generator, and it is boiling point of coolant in evaporative cooling generator.

3-D Model of generator. According to the symmetry of generator, the 3-D model is shown in Fig 5. The glass-fiber reinforced resin sleeve and rator are separated for different heating system. The temperator of the sleeve is considered constant. For the more, the surfaces of the sleeve and rotor are slip. So the system can get some simplified.

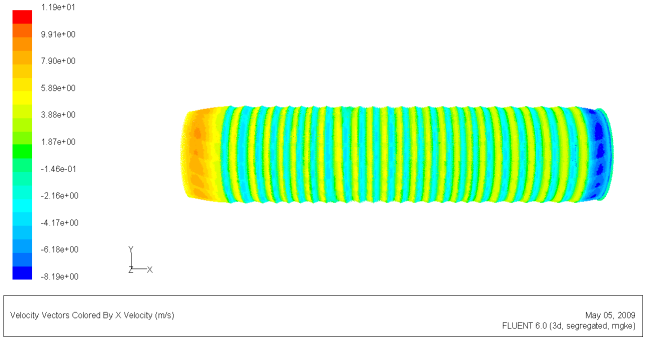

Fig. 5. Model of generator

Air Flow. To evaluate the correctness of the proposed computation method, based on the 300MW turbine generator designed by the Shanghai Generator Plant, we did the calculation of generator parameters. 300MW evaporative cooling turbo generator: rating power *PN*=300*MW*, rating rotate speed *N*=3000*rad/min*, rator outer diameter *D*=1100mm, stator core length *L*=5450mm, gas gap size s=60mm. So the taylor number is $T=r_i s^3\omega^2/\nu^2=7.6\times10^6$.

Gas-flow and heat-transfer in the wedge-shape air-gap of horizontal evaporation cooling motor is studied by numerical method. Under the assumption that the inner surface of stator sleeve and outer surface of rotor are smooth, taking the fact into account that the temperature of' stator sleeve of evaporation cooling motor keeps almost the same, horizontal evaporation cooling motor is simplified as a physical model of two coaxial sleeves, with outer sleeve (the stator) holds still and keep at constant temperature and inner sleeve (the rotor) is rotating and heated. The gas-flow in the annular cross section is study, and it is clarified that in such a physical model when rotor is rotating at high speed, the nature-flow is restrained by rotating-flow, so the actual 3D gas-flow field in the wedge-shape air-gap can be simplified to an axial symmetric quasi-3D gas-flow field.

At first the streamlines of the flow were calculated in the case. Fig.5 shows the streamlines at successive phases (as in fig.2). From fig.5, we can see the air flow is wrapped as a sprial round the rotor. It also shows that a critical speed of rotation exists, above which appears a stable, secondary mean flow consisting of regularly spaced totoidal cortices.

It can be seen from Fig 6 and Fig. 7 that the circulation in a section of the fluid by an radial-axial plane consists of a series of vortices which fill square compartments extending from the inner rotor to the outer stator.

Fig.7 illustrate alternate vortices rotate in opposite directions as though they were geared together. And the velocity of outward flow is faster than that of inward flow.

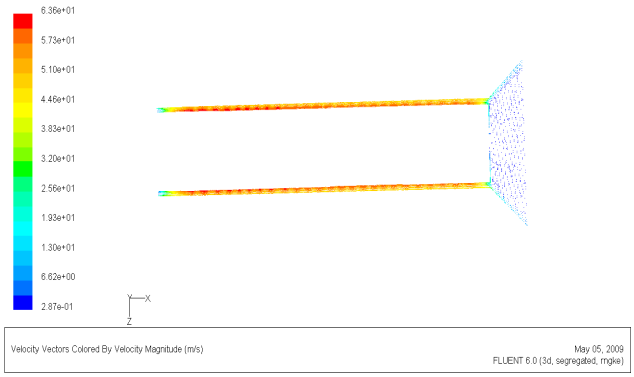

Fig.6. Velocity vectors in radial-axial plane

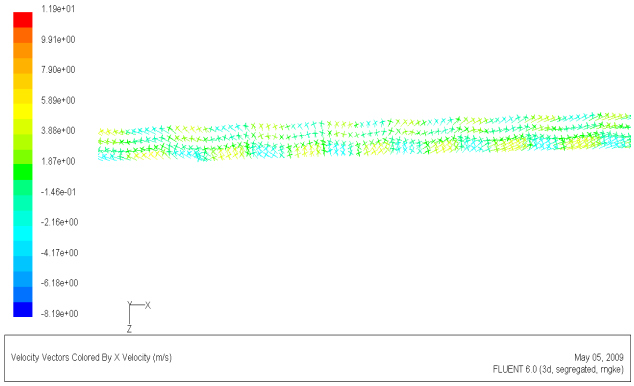

Fig.7. X velocity vectors in radial-axial plane

Heat Transfer. In our study, cooling air in the wedge-shaped gap can create gas flow without fan, which carry out the heat of rator. Table I shows the analysis results based on different conditions. The fist array demonstrates mass flow rate of 0.3887 kg/s at s=60mm. When gap size is decreased, the mass flow rate is inclined as well, as is shown in the second array. So the velocity of the travelling vortices is differernt for differernt gap sizes. For a constant Taylor number, the velocity is higher for a small gap size, as exhibited in table1. However there is even impossible with tracelling vortices if the gap size is too small. So suitable gap size and apex angle of sleeve are required. The structure of evaporative cooling turbo generator, which has a wedge-shaped gap, is available to creat air flow.

From the table I, we can see the mass flow rate will increase with a longer size. When temperature of stator is constant and rotor is at 2000W/m^2 heating loss, more mass flow could be created. We can get the conclusion the loss of rator can generate more air flow.

Table 1 Results of different conditions

	Mass flow rate (kg/s)	Volume flow rate (m^3/s)
Gap size s=60mm	0.3837	0.3184
Gap size s=10mm	0.1668	0.1384
Apex angle Φ =0	-0.4846	-0.4022
Half-length	0.1707	0.1417
Rotor Heating	0.3965	0.3290

Conclusion

The CFD method is used to analyze this system, which has different features, including gap size, rotating speed, Apex angle. Then the flow fields are calculated to keep the model correct. And the heat-transfer calculation proves the axial direction gas-flow can do well to the rotator heat-emitting. This work also provides foundation for the calculation of gas-flow and heat-transfer in wedge-shaped air gap of evaporation cooling turbo generator.

References

[1] G.B.GU, “Research and development about the application of evaporative cooling technology to 50 MW turbo-generator”, Bulletin of Institute of Electrical Engineering, Academia Sinica, July,1992,23(5),pp1-15

[2] L.W.Shen, X.H.MA, “Generator used for gas turbine combined cycle units”, *Electrical Equipment,* 2004, 5(4), pp. 24-28.

[3] Reinhard Joho, “Advances in synchronous machines”, *Proceedings of the IEEE Power Engineering Society Transmission and Distribution Conference*, Vol.1, pp.398-400, 2002.

[4] Manfred Wimmer,”An wxpermental investigation of Taylor vortex flow between conical cylinders”, J. Fluid Mech.1995, Vol. 292, pp. 205-227

[5] Dwnne B.,Wimmer M.,”Travelling Taylor vortices in closed system”.Acta Mech,133,pp.69-85,1999

[6] S.T. Wereley, R. M.Lueptow, “Spatio-temporal character of non-wavy and wavy Taylor-Coutte flow”,J. Fluid Mech,364,pp 59-80, 1998

[7] Taylor. G. I.,”Stability of a viscous liquid contained between two rotating cylinders”, Phil. Trans.Roy. Sci. A233,pp 289-343, 1923

[8] Z.W.Wen, G.B.Gu, and H.F.Wang, “Calculation of 3D thermal field in the stator of turbo-generator with immersion evaporative-cooling system and forced inner-cooling”, *Proceedings of the CSEE,* 2006, 26(23), pp.133-138

© (2012) Trans Tech Publications, Switzerland
doi:10.4028/www.scientific.net/AMM.187.109

Omni-Vision System of Intelligent Car Based on DSP&FPGA

ZHOU Yu-bin[1,a], YANG Yu-ning [2]

[1] School of Mechanical Engineering,Shanghai University of Science and Technology, Shanghai, 201620, China

[2] Dept. of Computer Science V ICM , University of Mannheim, Mannheim, German

[a]choybeen@yahoo.com

Keywords: DSP; Stereo vision; Image processing.

Abstract. In order to realize omni-vision system of intelligent car for auto wandering in real-time processing, an image processing system with 6 vision channels based on FPGA&DSP is designed. In the system, two ZBT SRAM chips are used as the input and output cache for high data transferring. A FPGA chip is responsible for the core logic controlling and video synchronous. Digital videos are sent so processing module by camlink bus. Data are exchanged by EMIF and McBSP between FPGA and DSPs. EDMA is used for data transferring between SRAM in FPGA and ZBT SRAM. The QDMA is used for 2D data transferring to 1D into DSP cache. Tasks are assigned to chips by μC/OS on master DSP. All this together, real-time data sampling and processing for multi-channel vision was realized.

Introduction

The vision system of intelligent car with one camera is efficient and practical, but the image grabbed from convex mirror limitted the enviroment information for intelligent auto wandering. In the field of digital image sequence processing system, a series of procedure such as image mosaicking, image enhancement, target tracking and recognition, etc, need to be processed simultaneously in real-time, which is always the great challenge for all scientists. The omni-vision system introduced in the paper includes 6 cameras, 5 looking around of the car and one looking upwards for the whole enviroment, each of which is running at 200 fps with the resolution of 1.3 Mpixel (1280x1024). These cameras will yield a total system data rate of 600 Mpixel/s. Simple 8-bit monochrome systems feature a data rate of 600 MBytes/s, and color systems, which typically use 24 bits to 48 bits per pixel, have a data rate that quickly reaches multi-gigabyte-per-second range. Because most machine vision algorithms are computationally expensive, even the up-to-date high-performance PC can not handle such an image data rate in real time. Special hardware resources are needed to overcome the limitations of host CPU.

As the high-definition and multi-channel requirement in the visual system development over the past years, the highly parallel in data processing for image processing, solution with high-speed FPGA and DSP is preferred to overcome the capability constraints in PC computing. And since the continuous improvement in chip speed, DSP and FPGA can finish more and more data processing per second. There are four main ways at present for real-time image processing: 1) based on a common PC [1-2]; 2) based on general-purpose DSP chips [3]; 3) based on one or more dedicated DSP chips; 4) based on programmable FPGA or DSP+FPGA [4]. The last solution based on general-purpose DSP chip for logic controlling along with the FPGA for highly parallel data processing is very appropriate for real-time processing of high-speed visual application. The advantages are not only taking the advantage of the high-speed DSP for processing control, while taking advantage of FPGA in a highly parallel data processing[5-6].

In this paper, a real-time digital image processing system is presented. The system includes 2 FPGAs and 2 high-performance DSPs: C6416, 2 ZBT SRAM chips are data input and output cache. The system works on high-speed data communication between DSPs and FPGA through the EMIF and the McBSP. The EDMA is used for data transfer among chips to meet the multi-channel visual system for real-time computing requirements.

This paper will be structured as follows: The main hardware architecture will be introduced in section 2; Section 3 is about multi-channel video grabber including data sampling and controlling logic of high speed camera by FPGA. We will describe the data communication between DSPs and FPGA in section 4; Section 5 introduces the task management by embedded OS; And the acknowledgment in last section.

Hardware System Design

The hardware platform built for multi-channel vision processing applications makes use of the state-of-the-art CMOS image sensor, FPGA and DSP technologies. Fig. 1 illustrates a high-level diagram of the hardware system. The designed hardware system consists of three modules: A high speed CMOS camera, a Camera Link image grabber, and a dedicated FPGA + Dual-DSP processing system.

The system has two FPGA, FPGA1 in image grabber module is responsible for image data grabbing and communication control, FPGA2 in data processing module is for high-speed parallel data processing. Two DSPs process the 2D image data from all the three cameras simultaneously.

The logic control chip FPGA1 is XILINX's XC3S1000L-FG456 used as the grab logic controller for video data. It is from Spartan3 low-power series with a 1M logic gates, 24 18x18 multipliers, and a wealth of on-chip storage space. Parallel computing FPGA2 is the member of XILINX's Virtex-4 series designed for parallel data processing: XC4VFX60-FF1152, within 4M on-chip RAM, 56,880 logic gate and 128 logical XtremeDSP modules. It is powerful enough for large number of high-speed data processing. The especial on-chip 18-KRAM module works in 500MHz, supporting the real dual-port simultaneous read and write operations. The 2 co-processing DSPs C6416, each has eight parallel processing units, working on 600Hz, can finish up to 4.8 thousand trillion instructions / second (MFLOPS). The system also provides rich interface resources, including a 4-lane PCI Express, Gigabit Ethernet, USB2.0, and generous purpose user IO as well as LVDS link for board communication.

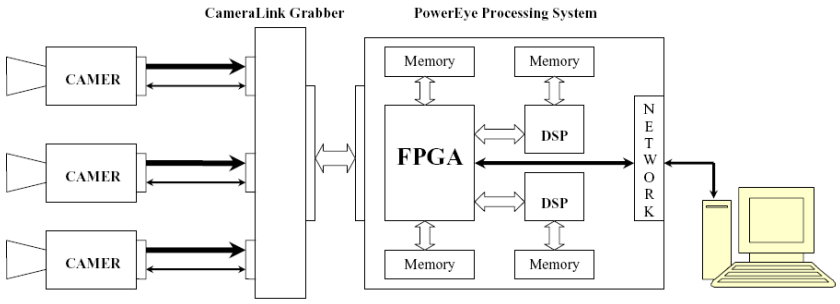

Fig. 1. Hardware block diagram

Multi-channel video grabber

As it is necessary for the system to detect fast movements in some applications, image grab rate should high enough to record the history of fast moving objects. Cameras play an essential role in an optical tracking system. With the dramatic improvement of image sensor technology, more and more high-speed image sensors are available. This provides the possibility to build a high-speed camera, which is able to capture fast moving objects.

Image Grab Module. The MT9M413 image sensor is size of 1280×1024 (1.3Mega pixel) CMOS digital sensor that is capable of 500 frames-per-second operation. This image sensor is available in both monochrome and color mode which has on-chip 10-bit analog-to-digital converters (ADCs). These ADCs require different input reference voltages for bias setting and calibration

operation. Two DAC6573 digital-to-analog (DAC) converters are used to generate the reference voltages. The sensor board contains the MT9M413 image sensor is chosen to build our high speed camera, mounted on the top of the PCB and all required external circuitry, including DACs, decoupling capacitors and Samtec connectors on the bottom.

The realized high speed camera consists of three hardware parts. The sensor module carries out the photo-electrical signal conversion sensor at a high pixel clock.

- An FPGA device, is programmed to generate the control signals for the sensor module and the interface board, which represents the last hardware module in the camera system.
- The interface board converts the digital image data to high speed LVDS signal pairs and receives control signals from the host. Camera Link standard is chosen as the camera interface.

Different circuit boards in the camera system are connected by high speed Samtec connectors(QTH-090-01-L-D-A) to increase system flexibility. Camera Link is the communication interface for connecting the camera with the main processing board for our high speed camera, because it supplies the highest data transfer bandwidth. The Camera Link Transmitter (CLinkTx) board implements the Camera Link FULL standard, It can also be configured as Camera Link Base or Camera Link Medium, due to the reprogrammability of the FPGA based control module. The main task of FPGA1 is used to track the video sync-signal, control data acquisition, and inform the FPGA2 to set the parameters such as camera frame rate, exposure time, the video window.

FPGA Control Module. The system logic controller chip is FG456, whose main task is to control the input/output frame buffer in order to inform the main processor chip to read out the image data from ZBT SRAM in time. It generates the all control signals required for the sensor, and synchronizes the output data stream from the sensor with the interface board. The on-chip programmable PLL generate the clock needed to drive the FPGA different clock. The internal counter could control the image grabbing size to XCFS04 FLASH by changing the carry signal of Adder. Fig. 2 shows the logic control block diagram.

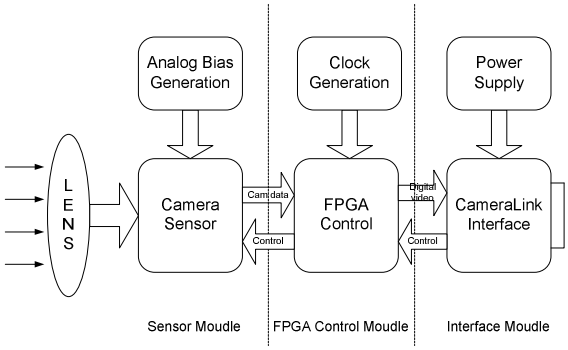

Fig. 2. Controlling Logic by FPGA1

The FPGA1 receives the digital video from the sensor, packets the raw image data into Camera Link format, and then sends them to CLinkTx board via the high speed Samtec connector. FPGA1 also receives and executes control commands from the host. These commands include the configuration of the sensor, such as exposure time, gain, frame rate, region of interest (ROI), etc.

Ping-Pong data buffer in ZBT-RAM. The acquired digital image data are stored for frame buffer through two Zero-bus turn-around(ZBT) SRAM. There is no switching time between read and write cycle, ZBT SRAM can provide the greatest throughput to the system, thus increase maximum system bandwidth, since there is no bus latency (NoBL) during data buffering, not like the DDR which need to be managed through FIFO.[15-16]. A great challenge to implement a high speed ZBT SRAM controller is how to minimize the clock skew. Clock skew potentially reduces the overall design performance by increasing setup times and lengthening clock-to-output delays-both of which increase the clock cycle time. To ensure high performance, 3 Digital Clock Managers (DCMs) inside the

FPGA1 are used in the ZBTSRAM controller as can be seen from Fig. 3: one to de-skew and generate a 2x controller clock and two to de-skew and generate a board-level 2x clock for the ZBT SRAM banks. The result is a high-speed, de-skewed clock driving the controller and the ZBT SRAM, which could satisfy all design requirements.

ZBT SRAM is well suited for image data buffering or Look-Up-Table applications that experience frequent bus turnarounds. Each ZBT SRAM can simultaneously receive full frame data from two channels. Frame rate of each channel is 60 fps, totally 120Mbytes per second. The operating frequency of ZBT SRAM is 250M, the maximum data throughput is high as 4.5GBytes/s, fully meet the speed requirement of the system data acquisition.

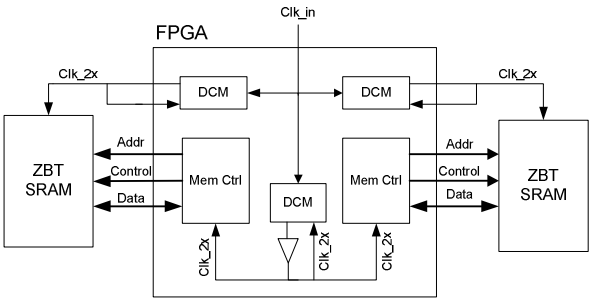

Fig. 3. FPGA and ZBT SRAM

Data communication among chips

The most important aspect of multi-chip co-processing system is the inter-chip data communication efficiency. It directly impacts on the system overall performance. Variety methods for data transmission in the system increase the system efficiency. For this reason, great attention was given to this aspect early on in the hardware architecture design and the realized multi-path scheme shown in Fig. 4 will satisfy the most demanding applications.

Data communication between FPGA and DSPs. Depending on the chip interface and application characteristics of system demanding, there are two kinds data communication style connecting the FPGA and DSPs: 32bit EMIF-A and McBSP0. The 32bit EMIF-A could run at very high rate for data transmission between DSP and FPGA which takes full advantage of EDMA controller integrated within DSP.

The FPGA internal FIFO is used as data buffer for transferring to the receiving data from DSPs. The FPGA computing core began to get data from the FIFO to receive and process as soon as receiving data over a threshold amount. On the other hand, the calculation core sends the result to the transmit FIFO buffer if it has a threshold amount of free space. DSP will start the EDMA interrupt to transfer data to the DSP on-chip Cache as soon as the data transmit FIFO data reaches the threshold amount without interrupting the CPU core. The peak data rate is up to 532 MBytes/s since the EMIF-A is working in a 32bit bus, 133 MHz.

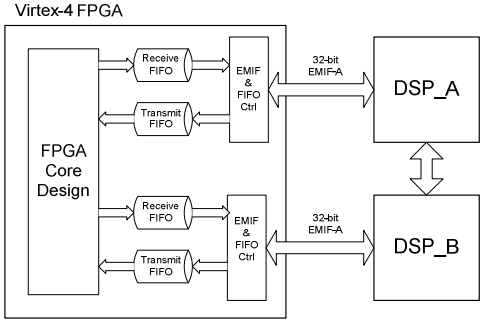

Fig. 4. Inter-processor communication between FPGA and DSPs

The second method of communication between DSP and FPGA is by McBSP. Two DSPs' McBSP0 is connected to the FPGA. McBSP is a full-multiplexed serial port, working at 125Mbps. It has independent frame sync signal: FSX, FSR and bit sync clock CLKX, CLKR, and the system clock signal CLKS. In addition, an external CLKS input allows the transmitter and/or receiver to run from an externally provided clock. Data are communicated to the McBSP port via the data transmit (DX) pin for transmission and via the data for receive (DR) pin for reception. Data receiving and transmitting is also very simple in this way. For both the transmitter and receiver, the each clock or frame may be configured independently to be driven from an external source (slave) or from the McBSP's sample rate generator (master). This sample-rate generator can program both the width and active period of internally generated frame synchronization. Because of the simplicity of the McBSP transmission protocol, this communication interface costs minimum FPGA resources.

Data communication between DSPs. There are two ways are designed for data communication between the two DSPs. In the first way, two DSPs are linked together through the two other McBSP interfaces. In order to obtain maximum data transfer rate, the two serial port of DSP: McBSP1 and McBSP2 are linked so that each DSP can be used as clock master and frame master. In other words, when one DSP's McBSP is used as a master in the communication interface generating data transmission clock, it can also generate the frame synchronization signals. In the same time, the other interface is waiting the control signals from the controller as a slave.

When the McBSP1 of DSP-A acts as the master to send data, the McBSP1 of DSP-B acts as the slave for receiving. At the same time, McBSP2 of DSP-B transmitter is configured to acts as the master to McBSP2 of DSP-A to generate the synchronization signal like clock and frame.

In addition to McBSP, the two DSPs can also be linked through EMIF-A for high-speed data exchange. This interface is implemented by the FPGA2's internal 32bit bi-directional interface through the FIFO buffer. The programmable FIFO threshold interrupts support inter-DSP data movement via EDMA. This FIFO based link architecture support higher data transfer rate and lower latency for complex exchanges of bulk data and control messages between the DSPs. The data transfer between DSPs can be achieved as high as 512 MBytes/s when the DSP's EMIF-A working on 133 MHz.

Data communication with PC. In order to control from PC or remote terminator, the system has access interface of Ethernet, USB2.0 and PCI-Express for communication purposes. Network access is provided by a 10/100/1000 Mbps Ethernet PHY, which is connected to the Virtex-4 FPGA via a standard Gigabit Multi Independent Interface (GMII). The PHY connects to the outside world with a standard RJ45 connector. General purpose I/O transfers are supported by way of the USB2.0 port. The 4 lane PCI-Express edge fingers are connected to the Multi-Gigabit Transceiver (MGT) blocks of the Virtex-4 FPGA, allowing the system to be used as a PCI-Express device.

Parallel Image Processing

Experiments of object tracking were tested on the omni-vision system. It is one of the important procedures among the auto wandering for intelligent car. During object tracking, the huge amount of data throughput and very large volume of calculation need high performance efficiency for real-time data processing. Tracking by features is implemented in our system by the following steps: 1) The current frame is firstly divided into some small blocks, features are extracted from each block with an adaptive threshold. And features are extracted from blocks of the reference frame using the same way. 2) Predicted the inter-frame motion, and find the correspondent feature in a small searching window of reference frame. 3) MVs of those features are classified from background or from moving objects by their velocity and acceleration using K-Medoids cluster. Images are stabilized by the global MVs from the feature set being identified from the background. And the motion from objects is introduced by the rest feature points. The small difference of motion among different channels implies the real motion direction in 3D world.

Since the object tracking application on the system requires the software had to support images of multi-channel been processed simultaneously, the processing procedures are also complicated, including tasks for pre- and post- processing except the feature tracking algorithm for optical tracking. The μC/OS is a kind of low-cost priority-based pre-emptive real time multitasking operating system kernel for microprocessors which could run on efficiently on C6416[7]. New version of μC/OS-II supporting C6416 could be downloaded from Micrium homepage. In our system, one of the two DSPs runs in master mode and assigns the tasks to FPGA2 and another DSP.

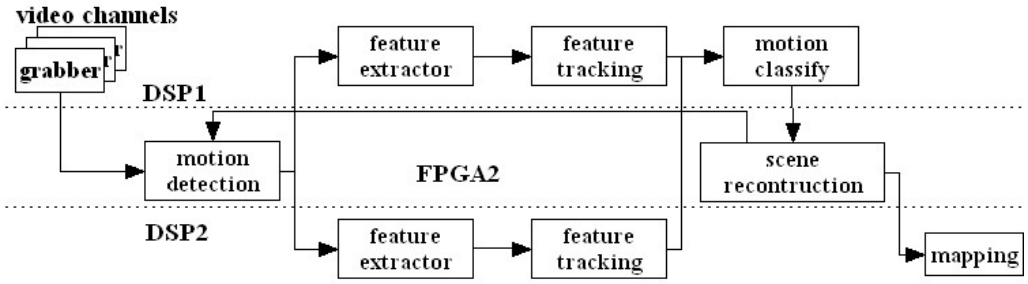

Fig. 5. Parallel tasks processing

Object tracking involving lots of parallel data processing is assigned byμC/OS to FPGA2. The two DSPs could work simultaneously on different task phase of tracking for different frames to implement the whole tracking algorithm as shown in Fig.5.

The experiment result shows the method could deal with multi-object moving in the scene along with stabilization on our system in 60fps. FPGA2 takes off much parallel data processing such as a number of the total features and clusters which make the processing speed fast enough for real-time application even though multi-channel videos are processed in the same time.

Acknowledgements

Thanks the Shanghai Education Committee for supporting the project by Science Fund of Excellent Yong Teacher (2008-2010: GJD08017).

References

[1] R. C. Chaubey. Computerized Image Analysis Software for the Comet Assay, *Molecular Toxicology Protocols, ISSN 1064-3745,*2008

[2] JinSeon Youn, JunRim Choi, Seung-Soo Han, Parallel Integer Motion Estimation Method by Using Reference Blocks Shared for HD Video Encoding, International *Conference on Electronic Computer Technology, ISBN: 978-0-7695-3559-3, IEEE Computer Soc, CA, USA*, Feb.2009: p577-581

[3] M. Fikret Ercan. Parallel Image Understanding on a Multi-DSP System. O. Gervasi and M. Gavrilova (Eds.): ICCSA 2007, LNCS 4706, Part II, pp. 1¨C12, 2007. *Springer-Verlag Berlin Heidelberg* 2007

[4] Shirvaikar Mukul1 ; Bushnaq, Tariq1 , A comparison between DSP and FPGA platforms for real-time imaging applications, *Proceedings of SPIE-IS and T Electronic Imaging - Real-Time Image and Video Processing*, 2009

[5] Davis, L.S.: Foundations of Image Understanding. *Springer, Heidelberg* (2001)

[6] Kumar, V.P., Wang, C.L.: Parallelism for Image Understanding. *In: Zomaya, A.D. (ed.) Parallel and Distributed Computing Handbook*, pp. 1042¨C1070. Mcgraw-Hill, New York (1996)

[7] HLI Ji-kuiH, HXIANG Huai-kunH, HHU HongH. Research on video image processing system based on uCOS - Ⅱ. *Journal of Harbin Institut of Technology.*H Vol.39, No.2, H2007

© (2012) Trans Tech Publications, Switzerland
doi:10.4028/www.scientific.net/AMM.187.115

Finite-time Chaos Control and Synchronization of the New Chaotic System with Unknown Parameters

Ke-e Li [a] ,Yuhua Xu [b](Corresponding author)

[a]School of Information and Mathematics Yangtze University, Hubei Jingzhou, 434023 PR. China

[b]Department of Maths, Yunyang Teachers' College, Hubei Shiyan. 442000 PR. China

yuhx2004@163.com.

Keywords- Finite-time;Chaos control;Chaos synchronization

Abstract. In this paper, a new chaotic system is discussed. Some basic dynamical properties are studied , and we also deal with the finite-time chaos control and synchronization of the new chaotic system. Based on the finite-time stability theory, the control law are proposed to drive chaos to equilibria within finite time, and the control law and the parameter update law are proposed to realize finite-time synchronization of the new chaotic system under unknown parameters. The controller is simple and robust to noise. Numerical simulations are given to show the effectiveness of the proposed controllers.

Main text

Chaos synchronization has been a hot topic since the pioneering work of Pecocra and Carroll [1], variety of method and techniques have been proposed for the control and synchronization of chaotic systems which include sliding mode control [2], adaptive synchronization [3], observer-based control [4], backstepping control [5], nonlinear control [6], impulsive synchronization [7], and so on. These methods can stabilize the chaotic system asymptotically. In practical engineering process, we may want to stabilize the system as quickly as possible. Therefore, more and more people began to realize the important role of synchronization time [8].

In[8], Wang et al. proposed a continuous controller to realize finite-time synchronization of the unified system with bounded disturb parameters to realize finite-time synchronization. In [9], Feng et al. proposed finite-time synchronization of two chaotic systems by using a terminal sliding mode controller and they adopted the Genesio chaotic system as their example. If the system has mismatched uncertainties, the state of the system can be driven to a small neighborhood of the equilibrium in a finite-time. In [10], Gilles et al. proposed finite-time global chaos synchronization for piecewise linear maps and discrete chaotic systems. In this paper, we present a controller to realize finite-time chaos and synchronization of the new chaotic system under unknown parameters. The controller is robust to noise and simple to be constructed.

The new chaotic system.A new chaotic system is proposed in this paper, the autonomy differential equations that describe the system are

$$\begin{cases} \dot{x} = a(z - x), \\ \dot{y} = bx - xz, \\ \dot{z} = cy + xy, \end{cases} \tag{1}$$

Which is chaotic for the parameters (see Fig.1.(a)).

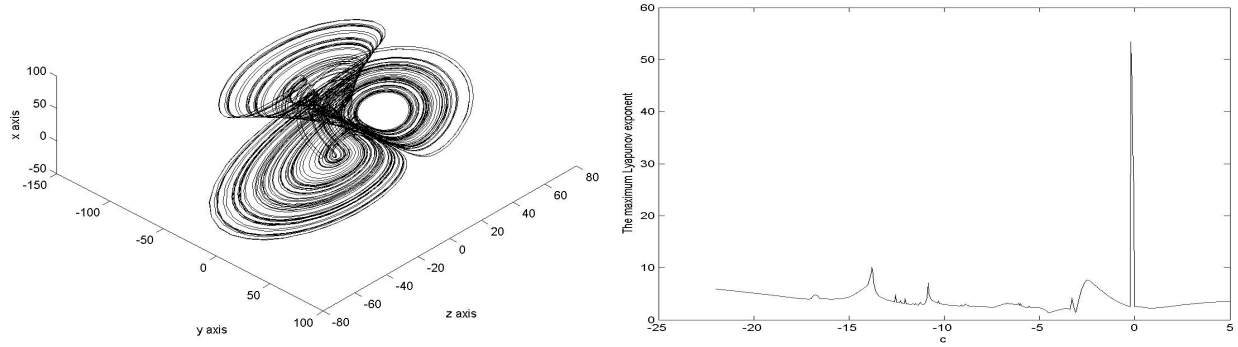

Fig.1. (a) The new chotic attractor ; (b)The maximum Lyapunov exponent spectrum

Next, we will study some basic properties of the new chaotic system.

(a) Chaotic behavior

For system (1), we have $\Delta V = \frac{\partial \dot{x}}{\partial x} + \frac{\partial \dot{y}}{\partial y} + \frac{\partial \dot{z}}{\partial z} = -a$. Therefore, as long as $\Delta V < 0$ at $a > 0$, system (1) is dissipative, and an exponential contraction of the system (1) is e^{-a} when $a > 0$. The shape of the chaotic system (1) is shown in Fig.1(a). The corresponding Lyapunov exponent is 2.2599 for the initial value . Fig.1.(b) displays the maximum Lyapunov exponent spectrum of system for . It is clear that there are some periodic windows in Fig.1.(b). However, these periodic windows are very important in the evolution of the dynamics system (1). The bifurcation diagram of system (1) shows the basic bifurcation phenomena in Fig.2(a). Figure.2(b) shows the Poincare mapping on x-y plane, with several sheets of the attractors visualized. It is clear that some sheets are folded.

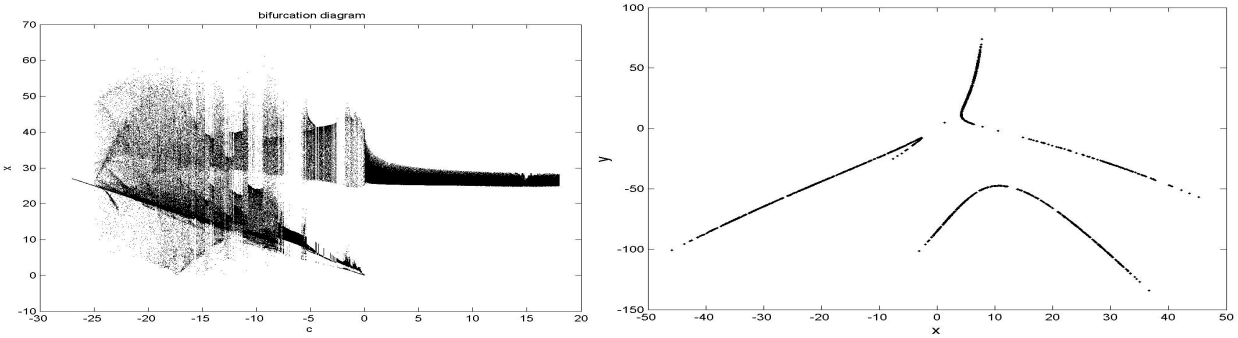

Fig.2. (a) Bifurcation diagram of system; (b) Poincare mapping on x-y plane

(b) Equilibria and bifurcations

Let

$$\begin{cases} a(z-x) = 0, \\ bx - xz = 0, \\ cy + xy = 0. \end{cases} \tag{2}$$

Eqs. (2) have two solutions as follows:

$E_1(0,0,0)$, $E_2(b,0,b)$.

Proposition 1. When $a = 20, b = 25, c = -13$, the equilibrium $E_1(0,0,0)$ is a saddle-foci point; system (1) has a Hopf Bifurcation at the equilibrium $E_2(b,0,b)$.

Proof. For equilibrium $E_1(0,0,0)$, system (2) are linearized, the Jacobian matrix is defined as:

$$J_o = \begin{pmatrix} -a & 0 & a \\ b-z & 0 & -x \\ y & x+c & 0 \end{pmatrix} = \begin{pmatrix} -20 & 0 & 20 \\ 25 & 0 & 0 \\ 0 & -13 & 0 \end{pmatrix}$$

To gain its eigenvalues, we let $|\lambda I - J_0| = 0$.

So, the corresponding eigenvalues at E_1 are

$$\lambda_1 \approx -28.1833$$

$$\lambda_2 \approx 4.0917 + 14.6250i$$

$$\lambda_3 \approx 4.0917 - 14.6250i. \tag{3}$$

From (3), the equilibrium $E_1(0,0,0)$ is saddle-foci point.

Next, linearizing the system about the nonzero equilibria E_2 yields the following characteristic equation:

$$f(\lambda) = \lambda^3 + 20\lambda^2 + 300\lambda + 6000 = 0 \ , \tag{4}$$

the corresponding eigenvalues are

$$\lambda_1 = -20, \ \lambda_2 \approx 17.3205i \ , \ \lambda_3 \approx -17.3205i \tag{5}$$

According to Eq.(4)-(5), one has

$$\lambda' = \frac{-300}{3\lambda^2+40\lambda} \approx 0.2093 + 0.1611i \quad ;$$

that is, $\mathrm{Re}\,\lambda' \neq 0$, $\mathrm{Im}\,\lambda' \neq 0$.

Hence, system (1) has a Hopf Bifurcation at the equilibrium E_2.

Finite time controlling chaos to the equilibrium. In this section, effective feedback controllers are designed to drive the chaotic trajectories to equilibria within finite time.

Definition 1. For the following controlled chaotic system:

$$\dot{x} = f(x) + u\,, \tag{6}$$

Where $x \in R^n$, $f: R^n \to R^n$ is continuous vector function, u is a controller. If there exists a constant $T > 0$ (T may depend on the initial state $x(0)$), such that

$$\lim_{t \to T} \|x(t) - E\| = 0\,,$$

and $\|x(t) - E\| \equiv 0$, if $t > T$ .The chaotic trajectories of the original system is driven to the equilibrium E, then chaos control of the system (6) is achieved within finite time, where E stand for equilibria of the original chaotic system $\dot{x} = f(x)$.

Lemma 1 [9] Assume that a continuous, positive-definite function $V(t)$ satisfies the following differential inequality:

$$\dot{V}(t) \le -cV^{\eta}(t)\,,\ \forall t \ge t_0,\ V(t_0) \ge 0,$$

where $c > 0,\ 0 < \eta < 1$ are all constants. Then, for any given t_0, $V(t)$ satisfies the following inequality:

$$V^{1-\eta}(t) \le V^{1-\eta}(t_0) - c(1-\eta)(t - t_0),\ t_0 \le t \le t_1\,,$$

and $V(t) \equiv 0\,, \forall t \ge t_1$ with t_1 given by $t_1 = t_0 + \dfrac{V^{1-\eta}(t_0)}{c(1-\eta)}$.

Lemma 2 [11] When $a,\ b$ and $c < 1$ are all positive numbers,the following inequality holds:

$$(a+b)^c \le a^c + b^c.$$

The proof of the lemma 1 and the lemma 2 is omitted here (See Refs. [8,9,11]).

Lemma 3 When a_i $(i = 1,2,\cdots,n)$ and $c < 1$ are all positive numbers, the following inequality holds:

$$(a_1 + a_2 + \cdots + a_n)^c \le a_1^c + a_2^c + \cdots + a_n^c \quad .$$

Proof. We can get the following ratiocinative process from the lemma 2, that is,

$$(a_1 + a_2 + \cdots + a_n)^c \le (a_1 + a_2 + \cdots a_{n-1})^c + a_n^c$$

$$\le (a_1 + a_2 + \cdots + a_{n-2})^c + {a_{n-1}}^c + a_n^c \le \cdots \le\ a_1^c + a_2^c + \cdots + a_n^c.$$

Consider the following controlled system of system (1):

$$\begin{cases} \dot{x} = 20(z - x) + u_1\,, \\ \dot{y} = 25x - xz + u_2\,, \\ \dot{z} = -13y + xy + u_3\,, \end{cases} \tag{7}$$

Let

$$\begin{cases} x_1 = x - m, \\ y_1 = y - 0, \\ z_1 = z - m, \end{cases}$$

where $(m,0,m)$ stand for the equilibrium of system (1).

Then system (7) yields the following system

$$\begin{cases} \dot{x}_1 = 20(z_1 - x_1) + u_1, \\ \dot{y}_1 = (25-m)x_1 - x_1 z_1 - m z_1 + 25m - m^2 + u_2, \\ \dot{z}_1 = -13y_1 + x_1 y_1 + m y_1 + u_3. \end{cases} \tag{8}$$

Step 1: Let $u_1 = -20z_1 - x_1^{\eta}$, where $\eta = q/p$ is a proper rational number. p and q are positive odd integers and $p > q$.

Substituting this control input u_1 into Eqs. (8) yields

$$\dot{x}_1 = -20x_1 - x_1^{\eta} \tag{9}$$

Chose a candidate Lyapunov function as follows:

$$V_1 = \frac{1}{2}x_1^2 \tag{10}$$

Then the differentiation of V_1 along the trajectories of (10) is

$$\dot{V}_1 = x_1(-10x_1 - x_1^{\eta}) = -20x_1^2 - x_1^{\eta+1} \le -x_1^{\eta+1}$$
$$= -2^{\frac{\eta+1}{2}}(\frac{1}{2}x_1^2)^{\frac{\eta+1}{2}} = -2^{\frac{\eta+1}{2}} V_1^{\frac{\eta+1}{2}}. \tag{11}$$

From Lemma 1, there are a $T_1 > 0$ such that $x_1 \equiv 0$ provided that $t > T_1$, that is $x \equiv m$.

Step2:Select $u_2 = (m-25)x_1 + x_1 z_1 + m z_1 - 25m + m^2 - y_1^{\eta}$,

$u_3 = 13y_1 - x_1 y_1 - m y_1 - z_1^{\eta}$

Substituting this control input u_2 and u_3 into Eqs. (8) yields

$$\begin{cases} \dot{y}_1 = -y_1^{\eta}, \\ \dot{z}_1 = -z_1^{\eta}. \end{cases} \tag{12}$$

Chose a candidate Lyapunov function as follows:

$$V_2 = \frac{1}{2}y_1^2 + \frac{1}{2}z_1^2 \tag{13}$$

Then the differentiation of along the trajectories of (13) is

$$\dot{V}_2 = \dot{y}_1 y_1 + \dot{z}_1 z_1 \quad = -y_1^{\eta+1} - z_1^{\eta+1} \le -2^{\frac{\eta+1}{2}}(\frac{1}{2}y_1^2 + \frac{1}{2}z_1^2)^{\frac{\eta+1}{2}} = -2^{\frac{\eta+1}{2}} V_2^{\frac{\eta+1}{2}}. \tag{14}$$

In the proof of (14), we have used Lemma 2 at the inequality before the last equation. Then from Lemma 1, the system (12) is to say $y_1 \equiv 0$, $z_1 \equiv 0$ after a finite-time $T_2 > 0$.

So when $t > \max\{T_1, T_2\}_1$, $x \equiv m$, $y \equiv 0$, $z \equiv m$, i.e. the systems (1) finite-timely stabilize chaos to equilibria by the controller u_1, u_2, u_3 .

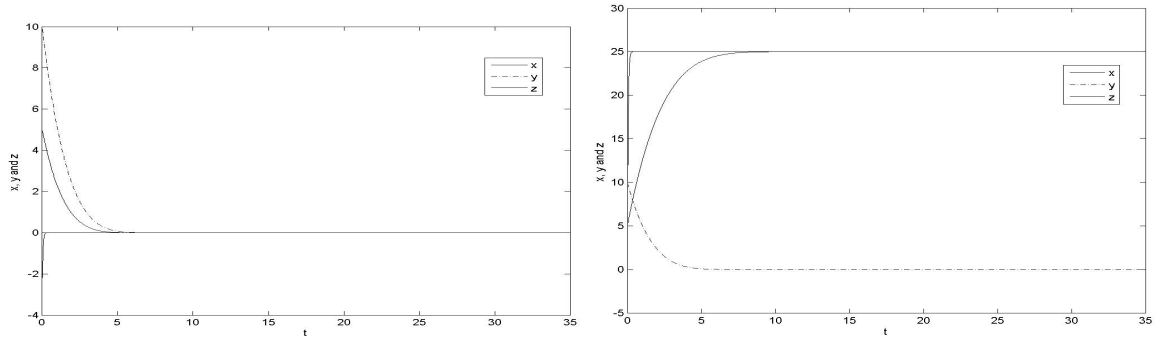

Fig.3.(a) Finite-time stabilizing chaos to the equilibrium; (b) Finite-time stabilizi(a)ng chaos to the equilibrium

For the numerical simulations, fourth-order Runge-Kutta method is used to our simulation with time step being equal to 0.001. In this control scheme, the initial values of system (1) is , we assume $\eta = 0.8$. Fig.3.(a) shows that chaos is finite-timely suppressed to the equilibrium $E_1(0,0,0)$. Fig.3.(b) shows that chaos is finite-timely suppressed to the equilibrium $E_2(25,0,25)$.

Finite-time synchronization of two identical systems with unknown parameters . In this section, effective feedback controllers are designed to realize finite-time synchronization of two identical new chaotic system under unknown parameters.

Definition 2 [8] Consider the following two chaotic system:

$$\begin{cases} \dot{x}_m = f(x_m), \\ \dot{x}_s = h(x_m, x_s), \end{cases} \tag{15}$$

where x_m, x_s are two n-dimensional state vectors. The subscripts 'm' and 's' stand for the drive and response systems, respectively. $f, g : R^n \to R^n$ are vector-valued functions. If there exists a constant $T > 0$, such that

$$\lim_{t \to T} \|e\| = \lim_{t \to T} \|x_m - x_s\| = 0 ,$$

and $\|x_m - x_s\| \equiv 0$, if $t > T$, then synchronization of the system (15) is achieved finite-time.

Consider the following controlled system of system (1):

$$\begin{cases} \dot{x}_1 = a_1(z_1 - x_1) + u_4, \\ \dot{y}_1 = b_1 x_1 - x_1 z_1 + u_5, \\ \dot{z}_1 = c_1 y_1 + x_1 y_1 + u_6, \end{cases} \tag{16}$$

where a_1, b_1, c_1 are unknown parameters of the response system which need to be estimated.

Let

$$\begin{cases} u_4 = -ae_3 - e_1^{\beta} - ke_1, \\ u_5 = x_1 z_1 - xz - be_1 - e_2^{\beta}, \\ u_6 = xy - x_1 y_1 - ce_2 - e_3^{\beta}, \end{cases} \tag{17}$$

And

$$\begin{cases} \dot{a}_1 = (x_1 - z_1)e_1 - e_a^{\beta}, \\ \dot{b}_1 = -e_2 x_1 - e_b^{\beta}, \\ \dot{c}_1 = -e_3 y_1 - e_c^{\beta}, \end{cases} \tag{18}$$

where $\beta = q/p$ is a proper rational number. and are positive odd integers and $p > q$.

Proposition 2. When $a = 20,\ b = 25,\ c = -13$ and , then synchronization of the system (1) and system (16) are achieved finite-time.

Proof. It is easy to see from (1) and (16) that the error dynamics can be obtained as follows:

$$\begin{cases} \dot{e}_1 = e_a(z_1 - x_1) + a(e_3 - e_1) + u_4, \\ \dot{e}_2 = e_b x_1 + be_1 - x_1 z_1 + xz + u_5, \\ \dot{e}_3 = e_c y_1 + ce_2 + x_1 y_1 - xy + u_6, \end{cases} \tag{19}$$

Let

$$\begin{cases} e_a = a_1 - a, \\ e_b = b_1 - b, \\ e_c = c_1 - c, \end{cases}$$

Chose a candidate Lyapunov function as follows:

$$V_3 = \frac{1}{2}e_1^2 + \frac{1}{2}e_2^2 + \frac{1}{2}e_3^2 + \frac{1}{2}e_a^2 + \frac{1}{2}e_b^2 + \frac{1}{2}e_c^2 \tag{20}$$

Then the differentiation of along the trajectories of (20) is

$$\begin{aligned}
\dot{V}_3 &= \dot{e}_1 e_1 + \dot{e}_2 e_2 + \dot{e}_3 e_3 + \dot{e}_a e_a + \dot{e}_b e_b + \dot{e}_c e_c \\
&= e_1(e_a(z_1 - x_1) - ae_1 - e_1^{\beta} - ke_1^{\beta}) + e_2(e_b x_1 - e_2^{\beta}) + e_3(e_c y_1 - e_3^{\beta}) \\
&+ e_a(e_1(x_1 - z_1) - e_a^{\beta}) - e_b(e_2 x_1 + e_b^{\beta}) - e_c(e_3 y_1 + e_c^{\beta}), \\
&= -(k + a)e_1^2 - e_1^{\beta+1} - e_2^{\beta+1} - e_3^{\beta+1} - e_a^{\beta+1} - e_b^{\beta+1} - e_c^{\beta+1}, \\
&\le -e_1^{\beta+1} - e_2^{\beta+1} - e_3^{\beta+1} - e_a^{\beta+1} - e_b^{\beta+1} - e_c^{\beta+1}, \\
&= -2^{\frac{\beta+1}{2}}((\frac{1}{2}e_1^2)^{\frac{\beta+1}{2}} + (\frac{1}{2}e_2^2)^{\frac{\beta+1}{2}} + (\frac{1}{2}e_3^2)^{\frac{\beta+1}{2}} + (\frac{1}{2}e_a^2)^{\frac{\beta+1}{2}} + (\frac{1}{2}e_b^2)^{\frac{\beta+1}{2}} + (\frac{1}{2}e_c^2)^{\frac{\beta+1}{2}}) \\
&\le -2^{\frac{\beta+1}{2}}(\frac{1}{2}e_1^2 + \frac{1}{2}e_2^2 + \frac{1}{2}e_3^2 + \frac{1}{2}e_a^2 + \frac{1}{2}e_b^2 + \frac{1}{2}e_c^2)^{\frac{\beta+1}{2}} \\
&= -2^{\frac{\beta+1}{2}} V_3^{\frac{\beta+1}{2}}.
\end{aligned} \tag{21}$$

In the proof of (21), we have used Lemma 3 at the inequality before the last equation. Then from Lemma 1, the error system (19) is finite-time stable. That is to say $e_1 \equiv 0, e_2 \equiv 0, e_3 \equiv 0$ after a finite-time $T > 0$.

So when $t > T$, $x_1 \equiv x$, $y_1 \equiv y$, $z_1 \equiv z$, i.e. the response systems (16) finite-timely synchronizes the drive system (1) by the controller u_4, u_5, u_6 .

In this synchronization scheme, the initial values of the drive system and response system are , the initial values of the parameters are , we assume $k = 2, \beta = q/p = 1/2$. Fig.4.(a) shows the error variable e_1, e_2, e_3 tend to zero, respectively. Fig.4.(b) shows that the estimated values of the unknown parameters converge to $a = 20, b = 25, c = -13$, respectively.

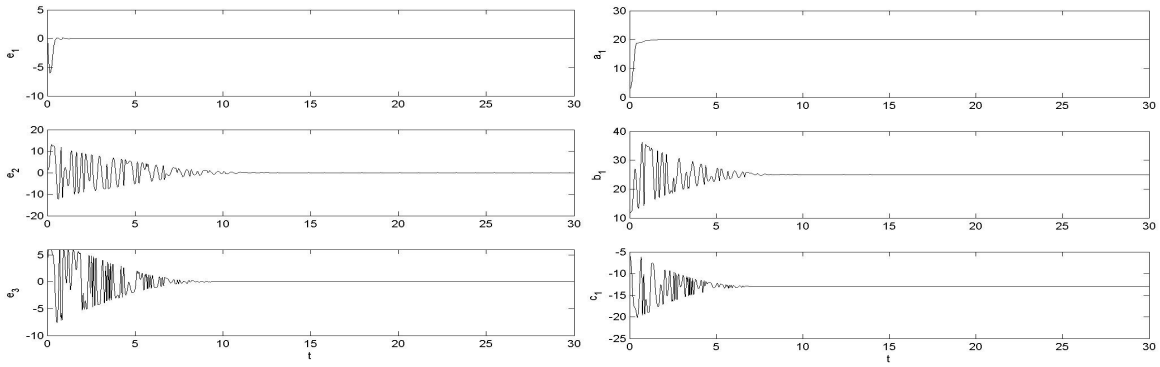

Fig.4.(a) Error signals between drive and response system; (b) The time evolution of the estimated parameters

Moreover, we verify the robustness of this method (the concept of robustness is referred in[12]), by adding noise to the response system, the response system becomes

$$\begin{cases} \dot{x}_1 = a_1(z_1 - x_1) + u_4 + rand, \\ \dot{y}_1 = b_1 x_1 - x_1 z_1 + u_5, \\ \dot{z}_1 = c_1 y_1 + x_1 y_1 + u_6, \end{cases}$$

We choose the initial values as before. Fig.5.(a) show that the error system is also a finite-time stable to zero. Fig.5.(b) shows that the estimated values of unknown parameters is also a finite-time stable to $a = 20, b = 25, c = -13$, respectively.

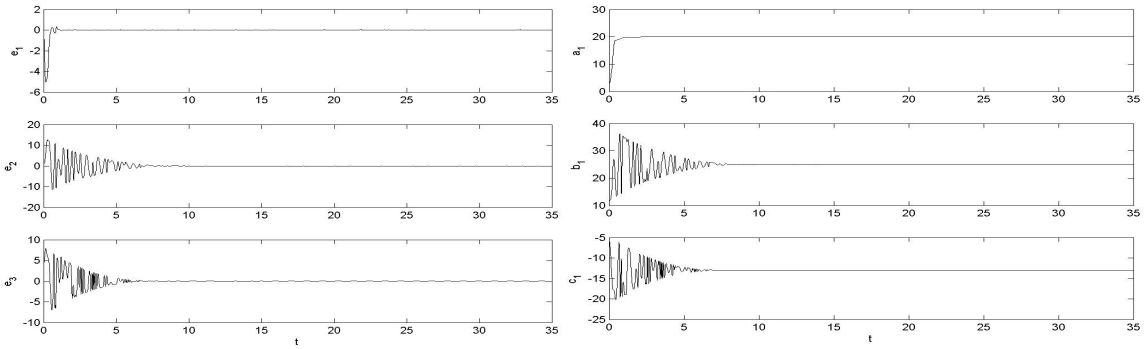

Fig.5.(a) Error synchronizationnoise; (b) The time evolution of the estimated parameters under adding noise

Conclusions

In this paper, we have constructed a new chaotic system. we also have proposed the control law and the parameter update law to realize finite-time chaos control and synchronization of the new system under unknown parameters, and the presented continuous controller has strong robustness to noise. Of course, these methods also apply to the other chaotic system from the proof process.

Acknowledgements

The authors are grateful to the Emphasis Science and Technology Research Program for the Education Department of Hubei Province of China (D20105001).

References

[1] Pecora LM, Carroll TL. Synchronization in chaotic systems. *Phys. Rev. Lett.* 64 (1900)821–4..

[2] Mohammad Haeri, Amir Abbas Emadzadeh. Synchronizing different chaotic systems using active sliding mode control. *Chaos Solitons Fractals* 31(2007)119-29

[3] Chen HH, Lee CI and Yang PH. Adaptive synchronization of linearly coupled unified chaotic systems. *Chaos Solitons Fractals* 40(2009)589-606.

[4] Mahboobi SH, Shahrokhi M and Pishkenari H.N, Observer-based control design for three well-known chaotic systems, *Chaos Solitons Fractals* 29(2006)381-92.

[5] Peng CC, Chen CL, Robust chaotic control of Lorenz system by backstepping design, *Chaos Solitons Fractals* 37 (2008)598-608.

[6] Xu.Y, Zhou.W, Fang. J, Hybrid dislocated control and general hybrid projective dislocated synchronization for the modified Lü chaotic system, *Chaos Solitons Fractals* 42 (2009) 1305-1315.

[7] Chen YS, Chang CC. Impulsive synchronization of Lipschitz chaotic systems. *Chaos Solitons Fractals* 40(2009)1221-8

[8] Wang H, Han ZZ, Xie QY, Zhang. Finite-time chaos synchronization of unified chaotic system with uncertain parameters, *Commun Nonlinear Sci Numer Simulat* 14 (2009)2239-47.

[9] Feng Y, Sun L, Yu X. Finite time synchronization of chaotic systems with unmatched uncertainties. *In: The 30th annual conference of the IEEE industrial electronics society, BusanKorea; 2004*

[10] Gilles Millerioux, Christian Mira. Finite-time global chaos synchronization for piecewise linear maps. *IEEE Trans Circuits Syst I* 48(2001)111–6.

[11] Hong Y, Yang G. Global finite-time stabilization: from state feedback to output feedback. *In: Proceedings of the 39th IEEE Conference on Decision and Control*, Sydney, Australia; 2000

[12] Guo RW. A simple adaptive controller for chaos and hyperchaos synchronization. *Phys. Lett. A* 372 (2008) 5593-7.

© (2012) Trans Tech Publications, Switzerland
doi:10.4028/www.scientific.net/AMM.187.122

Chaotic Analysis of the Velocity Signal in Impinging Stream Mixer

Jianwei Zhang, Yanfang Song*

School of Mechanical Engineering,Shenyang University of Chemical Technology ,Shenyang, China

* Corresponding author. Yanfang Song,Tel.:13602408958;
E-mail address: 272534374@163.com.

Keywords: Impinging Stream, Chaotic Analysis, Correlation dimension, Kolmogorov entropy, Lyapunov exponents, scientific computation

Abstract
The velocity signal of the flow field in Impinging Stream Mixer (ISM) was measured with Laser Doppler Anemometer. A de-noising method for velocity signal in ISM based on wavelet threshold was used. It is obtained that the attractor of the system possess infinite self-similar nested structure by comparing the strange attractor before and after de-noising, which is based on phase space reconstruction theory. It is shown that K entropy and the largest Lypunov exponents have the similar tendency in spatial distribution through scientific computation, however, the stratification of K entropy is more obvious. The value of K entropy and the largest Lypunov exponents are both positive, proving that the system is chaotic. The results indicate that K entropy and Lyapunov exponents can be increased by improving the rotating speed, the disorder and unpredictability of chaos system will increase homogeneously, so as to promote the micro-mixing and improve work efficiency.

1. Introduction

Impinging stream technology is a novel technical method .It is first proposed by the scientist Elperin of the Institute of Belarus in 1961[1], then Israel's Tamir proved [2], Impinging stream is the most effective methods to enhance the transfer processes in heterogeneous systems, especially process of external diffusion control transmission, transfer coefficients are several times to ten times greater than the general. Impinging stream has been successful in the K-T Pulverized Coal Gasifier, Stagnation Jet Mixer [3] and Trost Jet Mill [4]. On the chemical industry and other industries, the Impinging stream has great potential. ISM contains a lot of complicated information in the flow field, but the traditional linear analysis can not give a reasonable explanation. A new nonlinear analysis method based on chaotic analysis is used to study the instantaneous velocity signal in the flow field. In nonlinear systems, chaos refers to a determined but not predictable state of motion. Its unpredictability is very similar to pure random movement, but differently, there are some simple principles in complicated phenomena of chaos.

Chaos identification is divided into two methods: qualitative identification and quantitative identification. Quantitative method identifies chaotic behavior by calculating the characteristic parameters of the singular attractors in chaotic signals, which involves phase space reconstruction rationality and algorithm availability. The characteristic parameters to describe chaos are correlation dimension, Kolmogorov entropy and Lyapunov exponents.

Phase space reconstruction is the premise and tools for chaotic analysis of the time series, which reconstructs a certain high-dimensional phase space from one-dimensional time series. Time delay reconstruction method that Packard et al. [5] proposed was used to the chaotic time series for phase space reconstruction of chaotic attractor. G-P algorithm which Grassbtrger and Procacci [6] proposed was adopted for correlation dimension. To reduce computation time, correlation integral algorithm that Duan Wenfeng [7] proposed was also adopted**.** A correlation integral calculation method that Grassberger and Procassia [8] proposed was used to solve K entropy. Small Data Sets that Rosenstein [9] proposed was used for the largest Lyapunov exponents. The method is not only easy to implement, but also shows excellent robustness to embedding dimension, time delay and so on.

2. Experimental measurement

The velocity of flow field in ISM was measured with Laser Doppler Anemometer (LDA) in laboratory. The mean velocity, the fluctuating velocity and the instantaneous velocity were obtained. Distilled water was taken as the medium in experiment, hollow glass balls with density in 1.05~1.15 kg•m-3 and diameter in 10~15 μm were intermingled in water as instructing particles. Select the rectangular coordinate system ,the center was set as the original point, the axis line of two oriented tubes was Y-axis, the horizontal and vertical planes were considered as X and Z-plane. As a result of the different coordinate settings on LDA, the velocity was decomposed into orthogonal X, Y, Z directions and non-orthogonal L1, L2, L3 directions, which is shown in Fig.1.In which the L2 direction is the same with Y direction, the L1 and L3 direction present an angel of ϕ =6.8° on positive and negative Z direction, respectively. Because ϕ =6.8° is a small angel, we can ignore this angel and assume that either L1 or L3 direction can be chosen as radial direction. In this paper, L3 direction is chosen as radial direction.

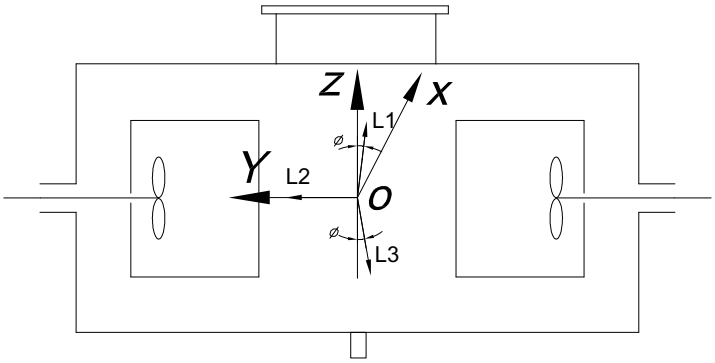

Figure.1 Schematic structure and coordinate setting of ISM

The rotating speed is 600r/min, 700r/min, 800r/min, 900r/min.In the longitudinal section which is perpendicular to axis connecting line of the two draft tubes, we take 1 / 4 mixer drum section as the object of study based on the axisymmetric structure of mixer. Set origin of the coordinate as the cut-off point, the right and left sides are decorated seven measuring surface, respectively, Y = 0, ± 2, ± 4, ± 6, ± 8, ± 10, ± 20, ± 30 mm, in total 15 surface. The spacing of each point is 4 mm, and the spacing of 4 sides surface closer to the coordinate origin is 2 mm, and the spacing of the farther 3 sides is 10 mm, and measuring points are arranged of 168 on each side.

3. Data processing and analysis

3.1. Pretreatment

LDA is a device to measure tracer particles through the probe laser Doppler signals, and then obtain the speed according to the relationship between speed and the Doppler frequency. As the observation time is different, we need to use interpolation to get the same sampling frequency. The velocity signal before and after interpolation is shown in Fig 2.It is shown that the amount of data increased obviously after interpolation, changed from 2504 to 10000. The sampling frequency is also changed from 125 into 500HZ.

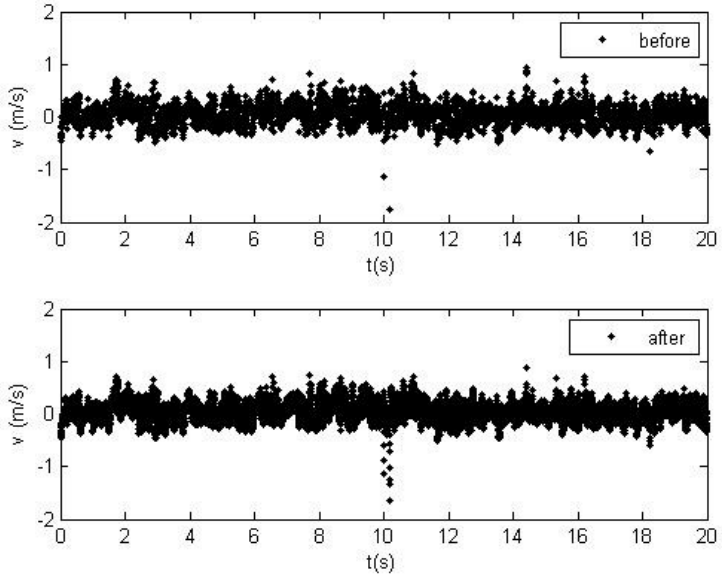

Figure 2.The velocity signal before and after interpolation

As the fluctuations of parameters, the vibration of the power system and external environment, the velocity signal included noise inevitably. The chaotic signal is very sensitive to noise, and the noise will affect the calculation of chaotic parameters directly. Therefore, the de-noising for instantaneous velocity signal is necessary. The VisuShrink method [10] that Donoho proposed in 1994 was used for the velocity signal. As shown in Fig.3, the signal after de-noising eliminated the "wild point", and almost kept the trend of the original signal.

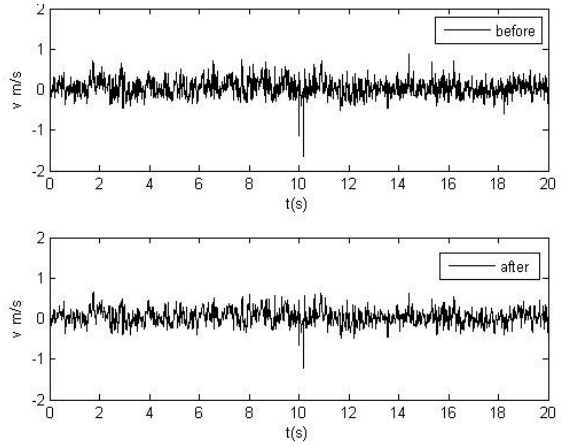

Figure 3.The velocity signal before and after De-noising

3.2. Chaotic attractor：

Chaotic attractor is the study object of chaos, which possess complicated, stretching and distorted structure. It is the product of system with overall stability and local instability. Chosen the date which the rotating speed is 700r/min and coordinates are (-24.0.-16) as an example. Phace space reconstruction was applied to the original data and the de-noising data, and we obtained the two-dimensional projection of the attractor in Fig.4 and Fig.5.The Fig.4 showed that the noise pollution destroyed the self-similarity and fractal structure of the attractor. The attractor after de-noising has the similar features with the chaotic attractor, with a very peculiar topology structure and geometry forms. Preliminarily, we considered that the reactor is chaotic as it is stretching and folding with a certain range.

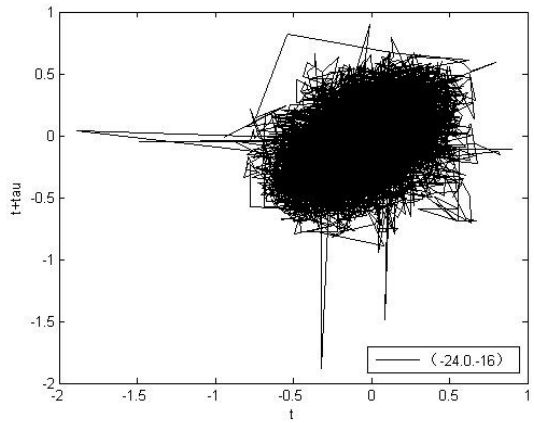

Figure.4 The attractor of original data

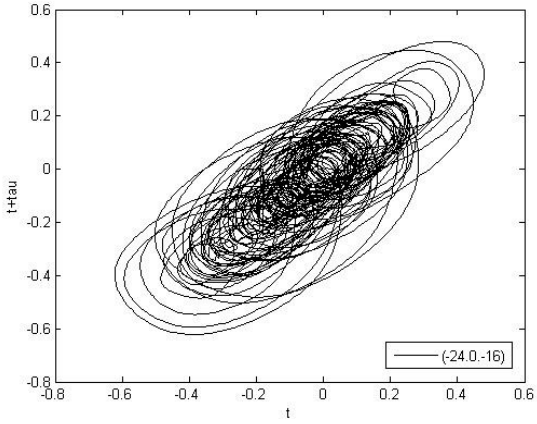

Figure.5 The attractor of de-noised data

3.3. Correlation dimension

According to the G-P algorithm mentioned before, describe as follows:

Selecting a delay time τ and embedding dimension m from a one-dimensional time series of length N, each vector in space is defined as follows:

$$Q_i = (x_i, x_{i+\tau}, x_{i+2\tau}, \ldots, x_{i+(m-1)\tau}), \quad i = 1,2,\ldots,N_m \tag{1}$$

$N_m \longrightarrow$ is the number of vector points in phase space.

A correlation integral, C(r), is then calculated using,

$$C_m(r) = \frac{1}{N_m(N_m-1)} \sum_{i \neq j}^{N_m} H(r - \| Q_i - Q_j \|) \tag{2}$$

Correlation dimension is calculated by using the fundamental definition:

$$D = \frac{d \ln C_m(r)}{d \ln r} = \lim_{r \to 0} \frac{\ln C_m(r)}{\ln r} \tag{3}$$

The correlation dimension D is the slope of $\ln C_m(r) \sim \ln r$ saturated curve. It is a measurement by which the distance of the vector reconstructing phase space alters with velocity of spherical radius. According to equation (2) we calculated a range correlation integral of different embedding dimension m, the data capacity is 10,000, and sampling time is 20 seconds. Through program composition and matlab calculation, we obtained the following log (Cr) and log (r) correlation integral curve in Fig.6.

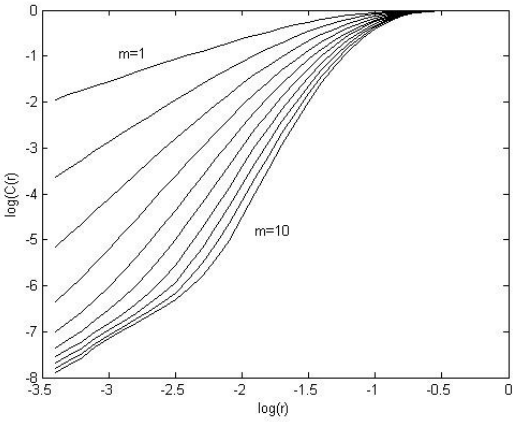

Figure 6.The curve of correlation integral

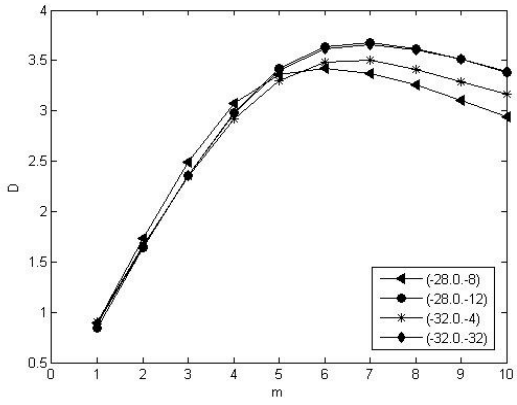

Figure 7.The correlation dimension value changes with m

The correlation dimension under the different embedding dimension m is calculated in Fig. 7.With the increase of embedding dimension, the correlation dimension is increased. However, when m = 6, the correlation dimension is almost no change. The correlation dimension is saturated in this case, and the minimum m of reaching correlation dimension saturation can be used as the embedding dimension of phase space reconstruction.

3.4. Kolmogrov entropy

Kolmogorov entropy（K entropy） is measure-theoretic entropy, which can distinguish regular motion, chaotic motion and random motion.

K entropy is defined as the average rate of information loss:

$$\begin{aligned} K &= \lim_{\Delta t\to 0}\lim_{r\to 0}\lim_{n\to\infty}\frac{1}{n\Delta t}\sum_{i=0}^{n-1}\left(K_{i+1}-K_i\right) \\ &= \lim_{\Delta t\to 0}\lim_{r\to 0}\lim_{n\to\infty}\frac{1}{n\Delta t}\left(K_n-K_0\right) \\ &= \lim_{\Delta t\to 0}\lim_{r\to 0}\lim_{n\to\infty}\frac{1}{n\Delta t}K_n \\ &= \lim_{\Delta t\to 0}\lim_{r\to 0}\lim_{n\to\infty}\frac{1}{n\Delta t}\sum_{i_0\cdots i_n}P\left(i_0,i_1,\cdots,i_n\right)\log P\left(i_0,i_1,\cdots,i_n\right) \end{aligned} \tag{4}$$

For the regular motion, $K=0$;For the random motion, $K\to\infty$;But if the system shows deterministic chaos, K is a constant greater than zero.

3.5. The maximum Lyapunov exponents

The method of small data is used to calculate the maximum Lyapunov exponents. The principle and the specific calculation process of Small Data Sets is introduced briefly as follows:

Selecting a delay time τ and embedding dimension m from the one-dimensional time series of length N, reconstruct phase space:

$$X(t)=\{x(t),x(t+\tau),\ldots,x[t+(m-1)\tau],t=1,2,\ldots,M \tag{5}$$

$M=N-(m-1)$, and then look for the recent adjacent points of each point given, that is,

$$d_t(0)=min\,\|\,X(t)-X(t^*)\,\|,|\,t-t^*|>p \tag{6}$$

Combined with Sato etc estimation equation:

$$lnd_t(i)=\ln C_t+\lambda_1(i\Delta t),t=1,2,...,M \tag{7}$$

The maximum Lyapunov exponents can be approximated as the slope of Equation.

It can be acquired by method of least squares approximate to this line.

$$y(i)=\frac{1}{\Delta t}\langle lnd_t(i)\rangle \tag{8}$$

Select a point of the flow field as an example, and get y (i) ~ i curve (Fig. 8) as follows:

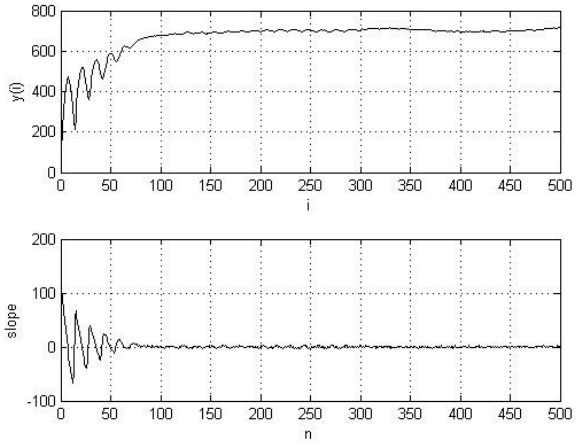

Figure 8 y (i) ~ i curve and the slope of the curve

As shown in the Fig. 8, when i = 0 ~ 71 , the slope of y (i) ~ i curve shake ups and downs significantly; When i = 71 ~ 500 , the slope of y (i) ~ i curve is relatively stable within a certain region, which is an ideal linear zone. In this set of data, the embedding dimension m=6, the delay time τ=14. The author select [71 500] as the linear zone, and make a regression curve with least square method, and gain the conclusion that the maximum Lyapunov exponent is 0.0662.

All tables should be numbered with Arabic numerals. Headings should be placed above tables, left justified. Leave one line space between the heading and the table. Only horizontal lines should be used within a table, to distinguish the column headings from the body of the table, and immediately above and below the table. Tables must be embedded into the text and not supplied separately. Below is an example which authors may find useful.

3.6. Spatial distribution and Rotating speed affection

According to the methods previously mentioned above, the authors calculated the radial K entropy and the maximum Lyapunov exponents on the plate of Y = 20, the results are shown in Fig. 9 and Fig.10.

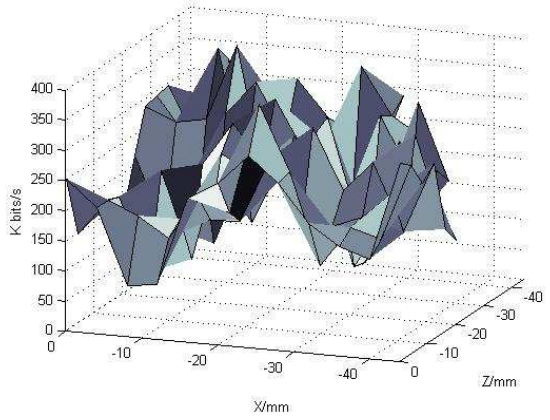

Figure.9 Radial distribution of K entropy on the plate of Y=20

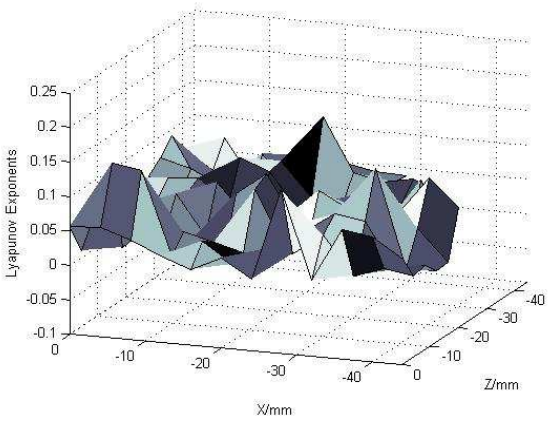

Figure.10 Radial distribution of the maximum Lyapunov Exponents on the plate of Y=20

It is obtained that K entropy range from 53 to 391, and the maximum Lyapunov exponents range from 0.0015 to 0.1580 through scientific computation. The spatial distribution is shown in Fig.9 and Fig.10.Both of them are positive and finite, indicate that the system is chaotic. The frequency of the velocity signal is high, so that K entropy of each point is large. It agrees with the previous research

results [11].As the value of K entropy is large, the unpredictability and the loss of information of the system are great. The cross section of ISM flow field can be divided into four partitions, which are central zone, impinging zone, transition zone and returning zone from inner to exterior, respectively. As shown in Fig.9, the stratification apparent of K Entropy is obvious .It is because the plate of Y = 20 is far from impaction zone, the fluid is not affected by the impaction. The speed of central zone and transition zone are lower, and have a lower K entropy; The speed of impinging zone and returning zone are larger, opposite, and the value of K entropy are larger. As shown in Fig.10, the distribution of the maximum Lyapunov exponents has a similar trend with K entropy. But the stratification of the maximum Lyapunov exponents is not as significant as K entropy, a tendency to average of the section, and the value of some point is great. It is illustrated that the chaotic system is sensitivity to initial conditions. As the effects of the impact, a little difference in initial conditions can lead to different results.

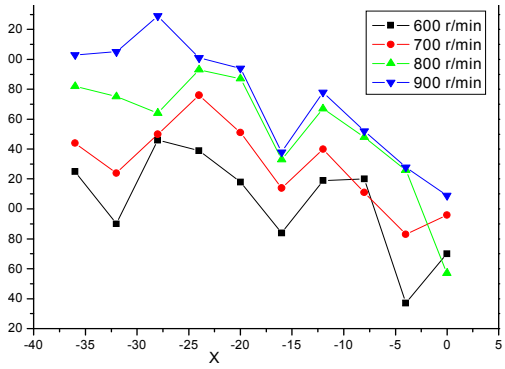

Figure .11 The K entropy change with rotary speed

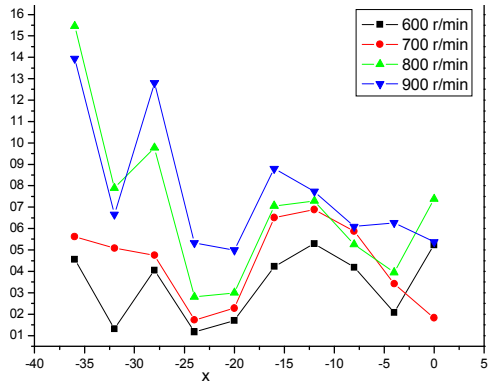

Figure.12 The maximum Lyapunov exponents change with rotary speed

To acquaint the influence of the rotating speed on K entropy and the maximum Lyapunov exponent, the authors calculated K entropy and the maximum Lyapunov exponents at different rotating speed (from 600 r/min to 900 r/min) on the cross section of Y =-10.As shown in the Fig.11 and Fig.12, the value of K entropy and the maximum Lyapunov exponents were in an upward tendency on the whole as the rotating speed increased, especially in central zone, impinging zone and transition zone. It is shown that the increment of speed can improve the system's confusion and disorder, promote the micro-mixing and improve work efficiency.

4. Conclusions

Chaos theory was used to analyses the instantaneous velocity time series of the flow field in ISM through scientific computation, the main conclusions are described as follows:

(1) The flow field of the impinging stream mixer is chaotic. The attractor of the system possesses infinite self-similar nested structure.

(2) The K entropy of the flow velocity signal range from 53 to 391, and the maximum Lyapunov exponents range from 0.0015 to 0.1580.It indicates that the extent of the system and the loss rate of the information are relatively large.

(3) The value of K entropy and the maximum Lyapunov exponents increase gradually with the increment of the rotating speed. It could improve the complexity of chaotic systems by increase the rotating speed, so as to promote the micro-mixing and improve efficiency.Section headings should be left justified, with the first letter capitalized and numbered consecutively, starting with the Introduction. Sub-section headings should be in capital and lower-case italic letters, numbered 1.1, 1.2, etc, and left justified, with second and subsequent lines indented. You may need to insert a page break to keep a heading with its text.

References

[1] Elprein I.T.“Heat and mass transfer in opposing currents”. Engng. Physics，vol.6,pp.62-68,1961

[2] Tamir A. Impinging stream reactor - theory and application. Wu Yuan translation. Beijing: Chemical Industry Press, 1996.

[3] Brauer H. Staustrahlmischer, German patent, 2900083,pp.7-23, 1980.

[4] Perry R H, Green D. Chemical Engineer’Handbook, 6th ed.New York:Mc-Graw-Hill, 1984

[5] Packard N. H . et al. “Geometry from a time series”. Phys. Rev Letters, vol.45,pp.712-716, 1980

[6] P. Grassberger, I. Procaccia. “Characterization of Strange Attractors”. Phys. Rev Lett , vol.50,pp.346-349, 1983

[7] Duan Wenfeng. “Chaotic Analysis Method and its Application to Pressure Fluctuation in Gas-Solid Fluidized Beds”,Si Chuan:Si Chuan University(China), 2001

[8] P.Grassberger and I.Procaccia, “Estimation of the Kolmogorov entropy from a chaotic signal”. Phys.Rev.A, vol.28,pp.2591-2593,1983

[9] Rosenstein M T,Collins J,and De luca C.J. “A practical method for calculating largest Lyapunov exponents from small data sets”.Physica D, vol.65,pp.117-134,1993

[10] D. L. Donoho, “De-noising by soft-thresholding”. IEEE Trans. Inform Theory, vol.41,pp.613-627,1995.

[11] Zhang Jianwei , Wang Yang , Tang Huihua , Jiao Li, “Chaotic analysis of pressure fluctuation in impinging region of SCISR”, Journal of Chemical Industry and Engineering(China), vol.12, pp.2309-2314, 2005.

© (2012) Trans Tech Publications, Switzerland
doi:10.4028/www.scientific.net/AMM.187.130

Modeling and Experiment on Active Vibration Control of Hydraulic Excitation System*

Zhang Huixian[a] , Miao Lingxia[b]

(Electronic Science and Engineering Department, Huanghuai University, Zhumadian,China)

[a]zhxsky2008@163.com, [b]Miaolx2009@163.com

Keywords: hydraulic excitation force; vibration exciter; fluid-structure interaction; finite element method

Abstract. For studying dynamic characteristics of fluid filled pipe under hydraulic excitation force generated actively by a new developed vibration exciter, at first a computer code based on the method of characteristics (MOC) was developed. Then the excitation force calculated by MOC was applied to the corresponding nodes of finite element of pipe, by using Newmark's method, the dynamic response at every cross section of pipe was obtained. The numerical simulations show that a simple harmonic motion arises at every cross section of the pipe, and the lateral vibration amplitude of every node along the pipe increases as the rising excitation force. In addition, measured data were compared with numerical simulation, which were basically consistent with each other.

Introduction

Pipe vibration in hydraulic system can usually bring bad results, such as resonance and fatigue. C Schmitt [1] established a numerical model to simulate the propagation of pressure waves in water. Jiduo Jin [2] studied stability and parametric resonance of a clamped-clamped pipe conveying fluid. The results revealed the relationships between fluid and fluid-filled pipe. Ridong Bao[3] studied dynamic characteristics of pipe conveying fluid with elastic support Almost all study above focus on how to reveal the damage factors of fluid-filled pipe and avoid it damaged. If we try to generate a kind of vibration by fluid-filled pipe, and which can be utilized and adjusted freely, then it will be an entirely new research.

System components and modeling

System components

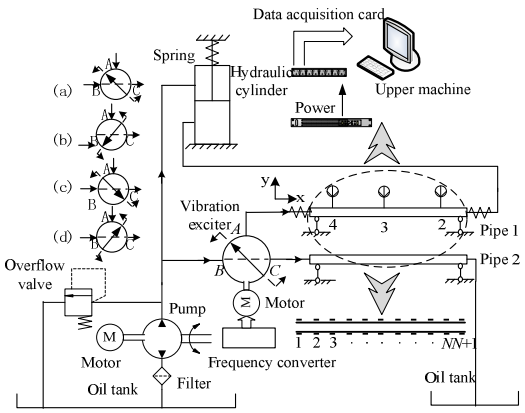

Fig.1 Experimental apparatus

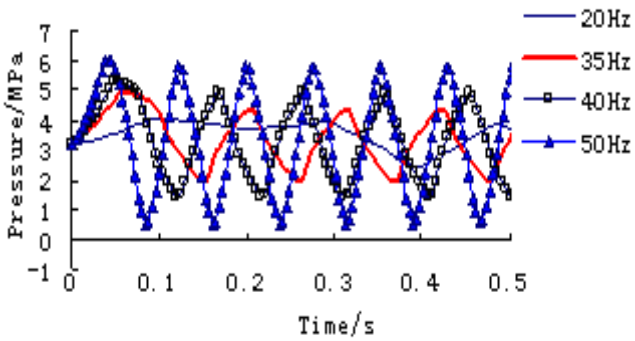

Fig.2 Excitation pressure at the vibration exciter

Hydraulic excitation system shown in Fig.1 consists of vibration exciter, pipe and hydraulic cylinder [4].Vibration exciter serves as a valve working from open to close rapidly and controlled by frequency converter. B port of vibration excitation is oil inlet.A port and C port is oil outlet, where they are connected to the excitation pipe1 and the return pipe2 respectively. With rotating of the vibration exciter, the hydraulic cylinder will move up and down, thus the pipe1 will vibrate regularly.

Mathematical model

According to analysis model illustrated in Fig.1, the basic control equations including momentum conservation equation and continuity equation can be finally deduced and expressed into two partial differential equations shown in Eq.1 and Eq.2 [5]:

$$\frac{\partial H}{\partial t}+v\frac{\partial H}{\partial x}+\frac{c^2}{g}\frac{\partial v}{\partial x}+v\sin\alpha=0 \tag{1}$$

$$\frac{\partial H}{\partial x}+\frac{1}{g}(\frac{\partial v}{\partial t}+v\frac{\partial v}{\partial x})+\frac{\lambda}{D}\frac{v|v|}{2g}=0 \tag{2}$$

$$c=\sqrt{\frac{K/\rho}{1+DK/eE}} \tag{3}$$

Where H is pressure head, t is time, v is steady flow velocity, c is pressure wave velocity of water hammer, α is included angle between pipe axis and horizontal plane, λ is fluid resistance coefficient, D is internal diameter of pipe, x is position coordinates, g is gravitational acceleration, K is elastic modulus of fluid, ρ is fluid density, e is thickness of pipe wall and E is elastic modulus of pipe.

In this paper, Eq.1 and Eq.2 can be solved with the method of characteristics.Served as first-order quasilinear hyperbolic partial differential equation, firstly, Eq.1 and Eq.2 should be converted into ordinary differential equations.Then the corresponding finite difference equations are shown as follows[6][7] :

$$c^+:\ (v_{Pi}-v_{i-1})+\frac{g}{c}(H_{Pi}-H_{i-1})+\frac{g}{c}v_{i-1}\Delta t\sin a+\frac{\lambda\Delta x}{2Dc}v_{i-1}|v_{i-1}|=0 \tag{4}$$

$$c^-:\ (v_{Pi}-v_{i+1})-\frac{g}{c}(H_{Pi}-H_{i+1})-\frac{g}{c}v_{i+1}\Delta t\sin a-\frac{\lambda\Delta x}{2Dc}v_{i+1}|v_{i+1}|=0 \tag{5}$$

Where $i=1, 2, \ldots, N$, corresponding to N nodes along the fluid-filled pipe. Through the discretized difference equations above, numerical solutions can be obtained by programming.

Fluid simulation by MOC

According to the method of characteristics, the pipe shown in Fig.1 is divided into $N+1$ sections, so section1 and section $N+1$ correspond to the hydraulic cylinder and the vibration exciter respectively. If the converter are set as 20Hz, 35Hz, 40Hz and 50Hz , and the system pressure is 3.5MPa.Through the developed program, the simulation results shown Fig.2 show the excitation pressure at the vibration exciter will rise with the increasing frequency of converter, which indicates that the vibration exciter, serving as excitation source, can generate variable and controllable pressure wave [8].

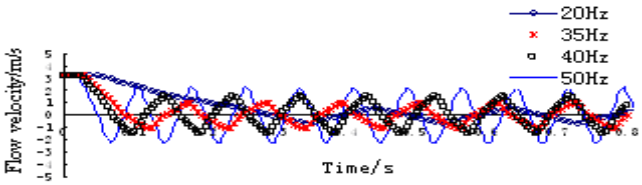

Fig.3 Flow velocity at the vibration exciter

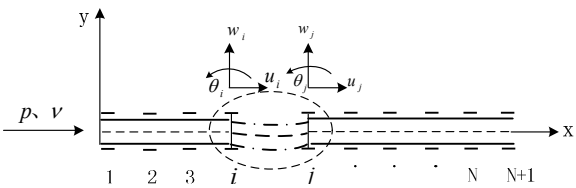

Fig.4 MOC-FEM model of fluid filled pipe

Fig.3 shows when the system pressure is a constant, the flow velocity at the vibration exciter will also rise with the increasing frequency. The computing results in Fig.2 and Fig.3 indicate that the excitation pressure and flow velocity along the pipe is simple harmonic wave.

MOC-FEM model of fluid filled pipe

The excitation pressure of fluid has been calculated, if it is applied to the pipe filled fluid, then the dynamic characteristics of pipe will be worked out. So the finite element method is used and the pipe1 is simplified as beam model shown in Fig.4.Based on Hamilton variation principle, if viscoelasticity of the pipe is omitted, then the vibration equation of fluid filled pipe is described as follows[9]：.

$$EI\frac{\partial^4 y}{\partial x^4}+(m_f\upsilon^2+AP-T)\frac{\partial^2 y}{\partial x^2}+2m_f\upsilon\frac{\partial^2 y}{\partial x\partial t}+c\frac{\partial y}{\partial t}+(m_p+m_f)\frac{\partial^2 y}{\partial t^2}=0 \quad (6)$$

Where P is fluid pressure, υ is flow velocity, x is pipe axis and y is its lateral, m_f is mass of fluid per meter, m_p is mass of pipe per meter, c is damping coefficient of pipe, E is elastic modulus of pipe, I is moment of inertia, T is axial force and A is flow area of pipe. The following is the discretized vibration equation by Galerkin method [10]

$$[M]^e\{\ddot{\phi}\}+[C]^e\{\dot{\phi}\}+[K]^e\{\phi\}=\{p(x,t)\}^e \quad (7)$$

Where $[M]^e$ is element mass matrix of fluid filled pipe, $\{\phi\}$ is displacement vector of node, $[C]^e$ is element damping matrix, $[K]^e$ is element stiffness matrix, and $\{p(x,t)\}^e$ is excitation force vector of node generated from fluid. By finite element principle, the vibration equation of fluid-structure interaction is assembled as follows.

$$[M]\{\ddot{\phi}\}+[C]\{\dot{\phi}\}+[K]\{\phi\}=\{p(x,t)\} \quad (8)$$

Where $[M]$ is general mass matrix of fluid filled pipe, $[C]$ is general damping matrix and $[K]$ is general stiffness matrix. $\{p(x,t)\}$ is general external load vector, which is equal to the excitation force generated by fluid.

Newmark method is adopted to solve the dynamic Eq.8. Fig.5 shows the lateral vibration amplitude of section2 to section4 increase in turn, indicating for each cross section along the pipe, the vibration amplitude and the excitation force are almost linear relationship. So, we can conclude from Fig.5 that the vibration amplitude of pipe can be adjusted by excitation force.

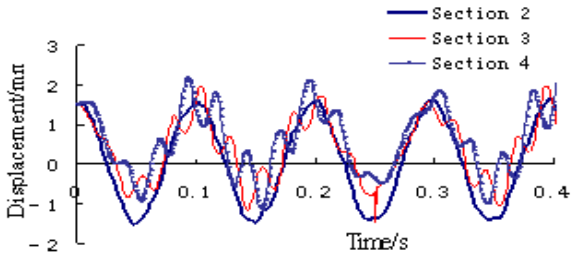

Fig.5 Time–histories of lateral vibration

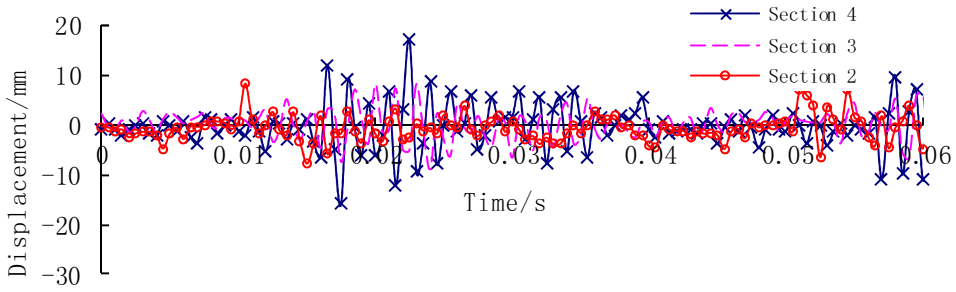

Fig.6 Measured lateral vibration amplitudes

By acceleration transducers and data acquisition card, the lateral vibration amplitude is presented by curves shown in Fig.6.Fig.6 shows the vibration amplitude at each cross section is section4> section3> section2.Compared with the simulation in Fig.5, almost identical motion laws are presented. But due to harmonic interference, the measured waveform is not quite consistent with the simulation results.

Conclusions

In this study, a new hydraulic excitation system was designed and a computer code was developed. Numerical simulation shows some interesting dynamic characteristic on pipe vibration. In addition, experimental data were acquired by transducer .Comparison between numerical simulation and experiment was basically consistent with each other, specific as follows:

(1)MOC-FEM was established and a computer code was developed to simulate the dynamic characteristics of fluid filled pipe.MOC was used to simulate pulsating fluid generated by vibration exciter. The results show that a simple harmonic motion arises at every cross section of the pipe.

(2)The vibration equation of fluid-structure interaction was established. The pipe was simplified as beam model and FEM was used to analyze its dynamic characteristics. Then Newmark method is adopted to solve the lateral dynamic response of pipe.

(3)The simulation results by MOC-FEM show the lateral vibration amplitude at every cross section is an almost linear relationship with the excitation force, indicating the lateral vibration amplitude can be adjusted actively.

Acknowledgements

The work is supported by the Natural Science Research Program of Education Department of Henan Province, China(No.2011C460003). Great appreciation also goes to Mine Fluid Control Engineering Research Center of Shanxi Province and Taiyuan-Bosch Hydraulic Engineering Co. Ltd for equipment support.

* The work is supported by the Natural Science Research Program of Education Department of Henan Province, China(No.2011C460003).

References

[1] Schmitt C, Pluvinage G.Water pipeline failure due to water hammer effects [J]. Fatigue and Fracture of Engineering Materials and Structures, 2006, 29(12): 1075~1082.

[2] Jin Jiduo, Song Zhiyong ,Yang Xiaodong. Stability and Parametric Resonances of a Clamped-ClampedPipe Conveying Fluid [J]. Journal of Vibration Engineering,2004,17(2):190~195.

[3] Bao Ridong, Jin Zhihao, Wen bangchun.Analysis of Nonlinear Dynamic Characteristics of Commonly Supported fluid conveying pipe [J].Journal of Vibration and Shock,2008,27(7):87~90.

[4] Huixian Zhang, Ziming Kou, Juan Wu, et al. Numerical Simulation and Analysis of Hydraulic Excitation System Based on Water Hammer by the Method of Characteristics [C].Advanced Material Research,2011,2210~2215.

[5] Wylie E B, Streeter V L. Fluid Mechanics[M].sixth ed. McGraw-Hill Book Co, New York,1983.

[6] Tian Wenxi, Su G H, Wang Gaopeng, et al. Numerical simulation and optimization on valve-induced water hammer characteristics for parallel pump feedwater system [J]. Annals of Nuclear Energy, 2008, 35:2280~2287.

[7] Sun Yudong, Liu Zhongzu,Liu Jianhu,etc. Application of MOC to Calculation of Fluid-structural Coupling Response of Piping System Under Impact of Water Hammer [J].Journal of Ship Mechanics,2005,9(4):130~137.

[8] Ziming Kou, Huixian Zhang, Juan Wu, et al. Numerical Simulation and Experimental Analysis of an Active Hydraulic Excitation System Based on Pulsating Flow [C].Advanced Material Research,2011,2216~2222.

[9] Jin J D, Song Z Y. Parametric resonances of supported pipes conveying fluid [J]. Journal of Fluids and Structures, 2005,20: 763~783.

[10] Wang Shizhong, Yu Shisheng. Calculation for Solid-liquid Coupling Vibration of Fluid Conveying Pipe [J].Journal of Harbin Institute of Technology,2001,33(6):816~818.

.

© (2012) Trans Tech Publications, Switzerland
doi:10.4028/www.scientific.net/AMM.187.134

The Study of Ball and Plate System Based on Non-linear PID

Shengqi Sun[a], Lin Li [b]

The Key Laboratory of Manufacturing Industrial Integrated Automation, Shenyang University, Shenyang, 110044, China

[a] Sunshengqi@sina.com, [b] lilin_52336@126.com

Keywords: ball and plate system; multivariable; nonlinear; point to point control; track control

Abstract. It is difficult to build a precise mathematical model for complex ball and plate system and many intelligent algorithms' programming are larger, so we make use of the non-linear PID controller to control actual system and realize the point to point control and circular trajectory control of the ball. The experiment results show that the control method of non-linear PID could ensure the movement accuracy of the ball, achieve the performance of control process, and have better control effect than traditional PID.

Introduction

Ball and plate system is a typical complex plant with multi-variable, nonlinear and time-delay, which is the extension of the traditional ball and beam problems. As more factors to consider, it is difficult to establish its precise mathematical model. At present there are many studies about ball and plate system[1-4], but most of them base on software simulation, many intelligent algorithms need large amount of programming, and it is difficult to apply to the actual system. In this paper, we use nonlinear PID to control motor, so the controller parameters could be adjusted dynamically, and the better track of the ball could be gotten.

Ball and Plate System Components

The hardware of ball and plate is composed of plate, bracket, camera, two servo motors, base and electrical control box, which could be seen in fig.1.

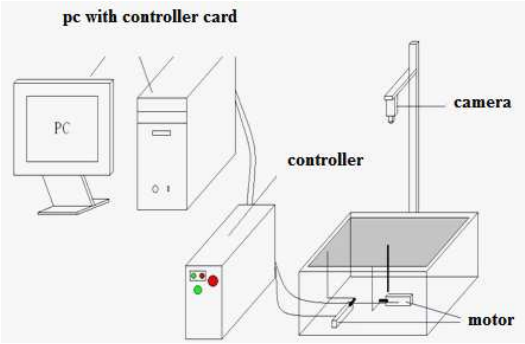

Fig.1 Hardware of ball and plate system

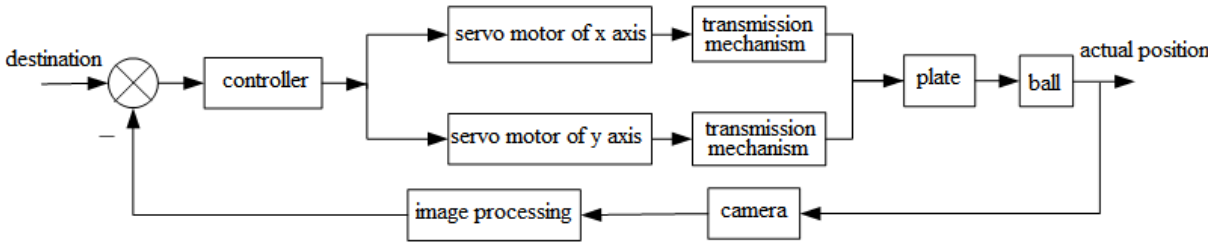

Fig. 2 Control block of ball and plate system

The location information of ball could be gotten from visual system. The image of ball and plate could be collected through camera. After image processing and recognition the center location of the ball can be gotten. We could know the present location of the ball, and compute the ball's position deviation of present location and destination. Using controller we could compute the pulses of servo motor, then the plate could incline some angle with the motor moving, and the ball will move to its destination. The control block of ball and plate system could be showed in fig. 2.

Design of Control System

Point to Point Control. If the ball is moving from one point to other, regardless of the moving track, the ball could get the destination rightly at last, we could call this way is point to point control. In this controlling method, there is not strictly required about the moving speed and track between two points. The ball not only could move along one coordinate, and then along another coordinate, but also could move along two coordinates. Point to point control aims to tilt the board to make the ball moving to the target location, and draws the track of the ball on control interface. The block diagram of point to point control is showed in fig.3.

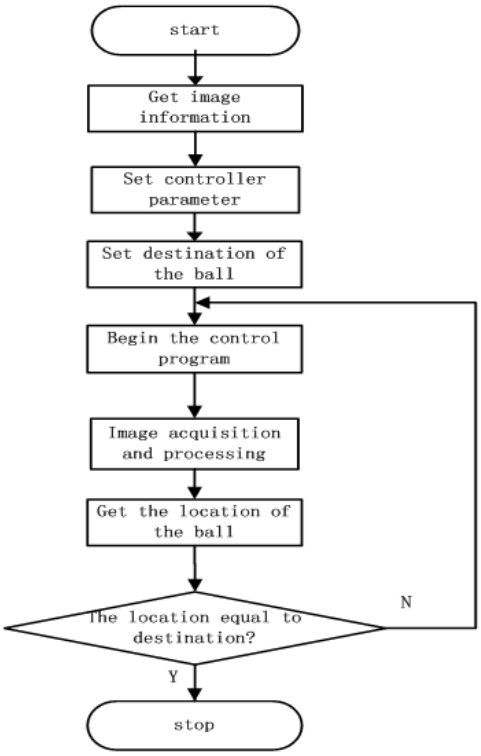

Fig. 3 The block diagram of point to point control

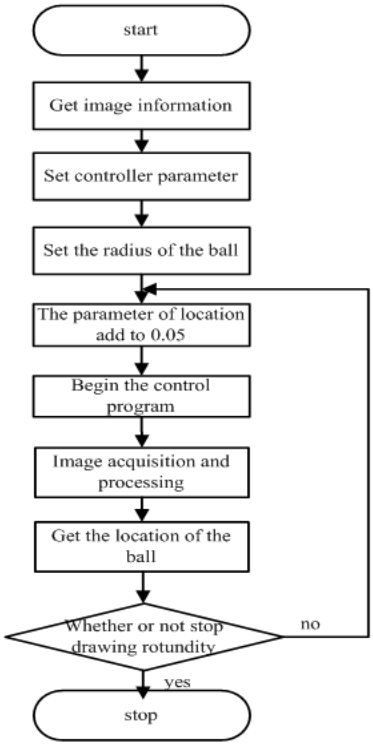

Fig. 4 The block diagram of circular trajectory control

Circular Trajectory Control Design. The circular trajectory control means to continuous path control. In this movement the location and speed of the ball could be controlled continuously on two or more than two coordinates, so the ball could do curve movement.

The circular trajectory control aims mainly to make the ball's track as a round. It takes the camera as feedback, gets the ball's moving track, and draws it on the control interface. The block diagram of circular trajectory control is showed in fig.4.

The ball's X and Y axis location can be gotten from the following formula:

$$\begin{cases} X = R \times \sin(\alpha) \\ Y = R \times \cos(\alpha) \end{cases} \tag{1}$$

Where R is the radius of circular trajectory, and α is the angle between the start and present location of the ball.

The Design of the Controller. The relation of input and output of traditional PID controller is:

$$u = K_p e + \frac{1}{T_i}\int edt + T_d \frac{de}{dt} \tag{2}$$

Where u is the linear combination of e, $\frac{de}{dt}$ and $\int edt$.

Making the relation of input and output of non-linear PID controller is[5-7] :

$$u = f(e, \frac{de}{dt}, \int edt) \tag{3}$$

For the controller function is not available or very complex, we can not give a simple and practical mathematical expressions.

Make

$$\begin{aligned} x_1 &= e \\ x_2 &= \frac{de}{dt} \\ x_3 &= \int edt \end{aligned} \tag{4}$$

So according to Taylor's theorem

$$\Delta u = \frac{\partial f}{\partial x_1}\Delta x_1 + \frac{\partial f}{\partial x_2}\Delta x_2 + \frac{\partial f}{\partial x_3}\Delta x_3 + \cdots \tag{5}$$

The following rules should be taken to approximate u:

1) Assume x_1=0, x_2=0, x_3=0, then u=0. Apparently the normal PID controller could meet this assumption.
2) The controller function should following the principle of negative feedback of control system, so Taylor expansion takes only odd powers.
3) In order to ensure simplicity of controller, power of the whole function takes up to three times. So the PID controller is:

$$u = (kp_1 + kp_2 e^2) \times e + \left[ki_1 + ki_2 \left(\int edt \right)^2 \right] \times edt + [kd_1 + kd_2 \times \left(\frac{de}{dt} \right)^2] \times \left(\frac{de}{dt} \right) \tag{6}$$

The Results and Analysis.

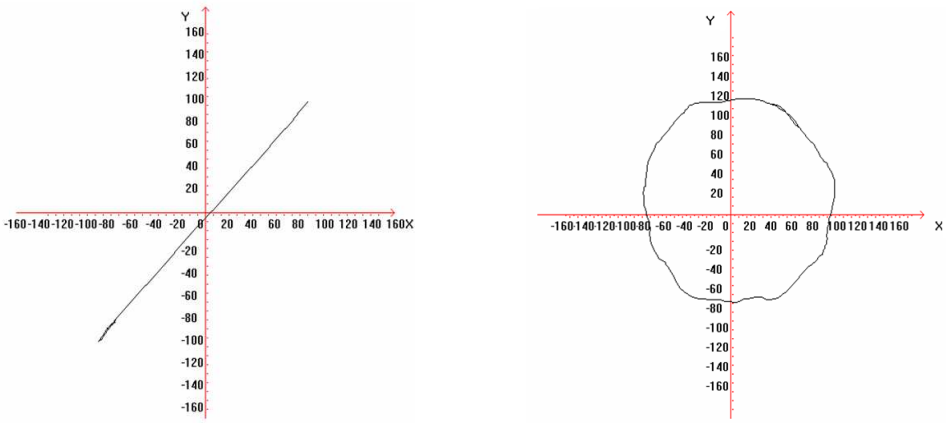

(a) point to point control (b) circular trajectory control

Fig.5 Movement track

Using zero function to make the plate get level in the control interface, and ensure the ball quiescence in any places of the plate.

Set parameters in the place of closed-loop control, adjust the parameters of k_P, k_{P1}, k_d, k_{d1}, set destination parameters of X and Y axis, and pitch on X axis and Y axis closed-loop control. The interfaces of point to point control and circular trajectory control are showed in fig.5.

As different settings of non-linear PID and traditional PID, the rise time t_s, settling time t_r and overshoot δ are list in the table 1.

Table 1 The results contrast of non-linear PID and traditional PID

controller / Setting	non-linear PID	traditional PID
ΔX=50	$t_s = 2.65s$ $\delta = 0\%$	$t_s = 1.59s$ $t_r = 0.53s$ $\delta = 4\%$
ΔX=100	$t_s = 1.59s$ $t_r = 1.0s$ $\delta = 6\%$	$t_s = 2.12s$ $t_r = 1.10s$ $\delta = 6\%$
ΔX=200	$t_s = 1.59s$ $t_r = 1.06s$ $\delta = 3\%$	$t_s = 2.65s$ $t_r = 1.59s$ $\delta = 7\%$

When the setting is increasing within a certain range, the change of performance indicators is bigger for traditional PID than non-linear PID. For non-linear PID, when ΔX is increasing within a certain range, t_s is reducing. But for traditional PID, when ΔX is increasing within a certain range, t_s is increasing too. For the same ΔX, t_r is smaller in non-linear PID than in traditional PID. So we can get the conclusion that the response speed of non-linear PID is faster than traditional PID, and the control effect is better for non-linear PID.

Conclusion

The ball and plate system takes VC++6.0 software as development platform, uses servo drive to drive servo motor, so the plate could tilt when the motor is running, and controls the ball's location on the plate. In actual system, we use non-linear PID controller to realize point to point control and circular trajectory control of the ball. This method could solve the problems of larger programming and longer computation time for other intelligent algorithm. The control error could be smaller than ±2mm, and the control effect is better.

Acknowledgement

It is a project supported by the National Natural Science Foundation of China (61004039).

Reference

[1] H Wang, Y Tian, et al., Proceedings of the 7th World Congress on Intelligent Control and Automation Piscataway, USA, 2164-2169, (2008).

[2] D Yuan, Z Zhang. IET Control Theory & Applications, Vol. 4 Issue 4, p573-589, (2010),.

[3] Chin E Lin, C C Ker. Applied Electromagnetics & Mechanics, Vol. 27 Issue 1/2, p133-151, (2008).

[4] H Wang, Y Tian, et al. Journal of System Simulation, Vol 22, NO 5, pp1251-1256, (2010).

[5] Y X Su, B Y Duan. Control and Decision, Vol 18, No 1, pp126-128, (2003).

[6] H Shang, Z M Chen, et al. Control Theory and Applications, Vol 26, No 4, pp439-442. (2009).

[7] Y.X.Su, B.Y.Duan, C.H. IEE Proceedings -- Control Theory & Applications, Vol. 151 Issue 1, p95-102,(2004),

© (2012) Trans Tech Publications, Switzerland
doi:10.4028/www.scientific.net/AMM.187.138

Finite Element Analysis of the Static/Dynamic Behavior of Wind Turbine Gearbox

Wei Jing[1, 2, a], Xu-Jian Sun[1], Wei Sun[1] and Ai-Gui Guo[3]

[1]School of Mechanical Engineering, Dalian University of Technology, Dalian, 116024, China,

[2]The State Key Laboratory of Mechanical Transmission, Chongqing University, Chongqing 400044, China

[3]Gear transmission branch, Taiyuan Heavy Industry Co., Ltd. Taiyuan, 030024, China

[a]weijing@dlut.edu.cn

Keywords: Wind Turbine Gearbox; Finite Element Analysis; Performance analysis; Static/Dynamical Behavior.

Abstract. Gearbox is a key part and is more easily over loaded and it has a high failure rate in MW-class wind turbine. It is necessary to analyze, predict and optimize its static/dynamical behavior. It presents the performance of one type wind turbine gearbox and the static analysis results of the housing, spline and gear pairs of the wind turbine gearbox are obtained using finite element method. The natural frequency and modal shape of the gearbox are analyzed. The modification data of the flank shape for each class tooth alignment and tooth profiles are obtained from the analysis. The related data on the strength and stiffness of all the parts in wind turbine gearbox are provided. It lays a foundation for the reliability assessment and optimization design of wind turbine gearbox.

Introduction

Gearbox is a key part and is more easily over loaded and it has a high failure rate in MW-class wind turbine. Wind turbines are often mounted at those complicated working conditions or offshore [1, 2]. Because of these properties, such as heavy load, high reliability, it is very important to analysis and simulates the transmission system. Elastic deformations will occur in gears and shafts in the gearbox during power transmission [3]. In addition, gearboxes are mounted at small space on tower top of wind turbines; it is very difficult to repair the gearbox once any fault occurs. Therefore, the reliability and life of the gearbox for wind turbine are more critical than ordinary machinery [4].

In order to improve the design efficiency, obtain the reasonable structure, taking high reliability, low noise and long life of the MW-class wind turbine for consideration, the housing, spline and gear pairs, etc, in one type of MW-class wind turbine gearbox are analyzed using finite element method (FEM) in this paper. The structure diagram of the wind turbine gearbox is shown in Fig.1.

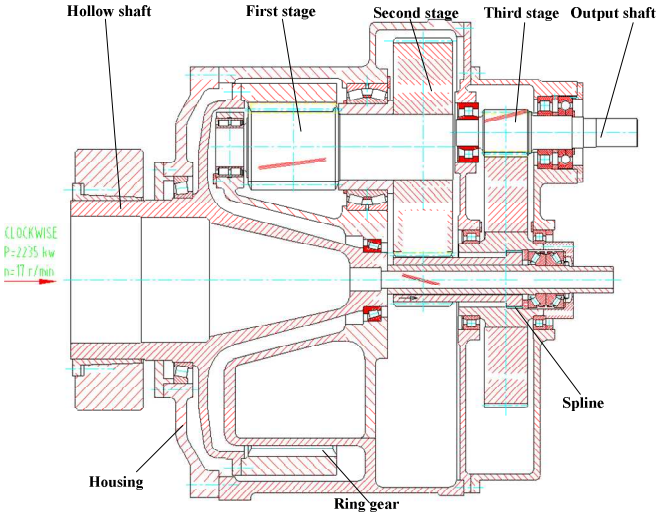

Fig. 1 Structure diagram of wind turbine gearbox

Static anslysis of housing components

The housing components is the gearbox package, meanwhile, the housing is the support of gears and shafts. Considering actual working conditions, each part of the housing components is connected together by bolts and undertakes loading together [5]. Therefore, each part of the housing is combined as a complete system to carrying out the synthetic analysis that could be further accord with the practical situation. The design of gearbox housing should meet the requirement of strength and stiffness under the rated and limited power. Therefore, static structure analysis of the housing should be carried out.

In this paper, the software ANSYS are used to perform static analysis for gearbox housing. The solid models are imported to ANSYS using 3D modeling software after solid models are built. The analysis results are shown from Fig.2 (a) to Fig.2 (d).

From Fig. 2, the maximum stress is about 73.125MPa under the rated condition (see Fig.2 (a)) and the maximum stress is about 192.42MPa under limited condition (see Fig.2 (c)). The maximum stress appears at the corner of the supporting flange. The material used for the gearbox housing is QT400 and its tensile strength limit is 400MPa and yield limited is 250MPa. The maximum stress is far less than the allowable stress under limited condition. Meanwhile, it can be seen from the equivalent stress that the stress in other areas are very low except the corner of the supporting flange. The maximum deformation appears at the back of the housing from deformation contour (see Fig.2 (b) and Fig.2 (d)). The maximum deformation is less than 1 mm. The gearbox housing can meet with requirement of strength and stiffness from the view of static structure theory.

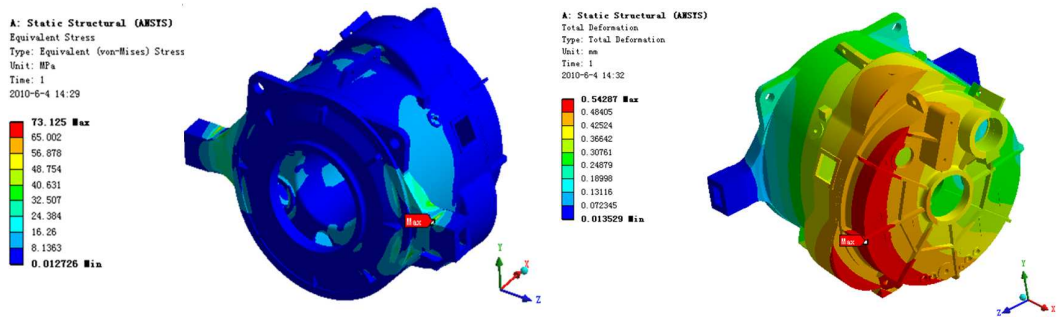

(a) Stress contour under the rated condition; (b) Deformation contour under the rated condition

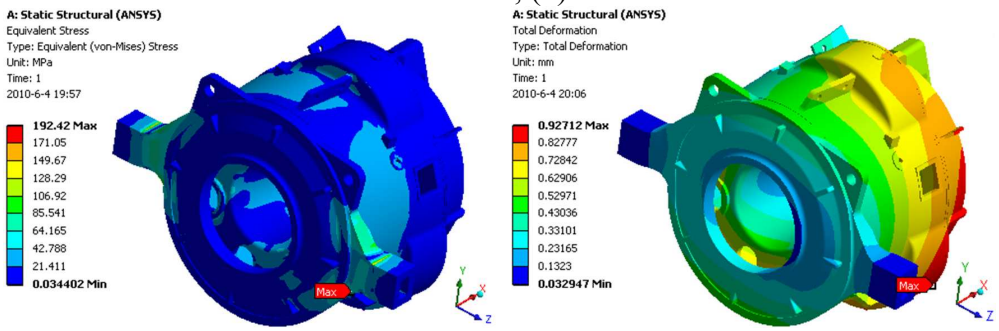

(b) (c) Stress contour under the limited condition; (d) Deformation contour under the limited condition

Fig. 2 Stress and deformation contour of housing

Modal analysis of the gearbox

Natural frequency and modal shape are very important parameters for wind turbine gearbox. The working frequency should keep away from each natural frequency of gearbox [6]. Therefore, the modal analysis of gearbox should be performed and check the design rationality.

The boundary conditions should be simplified before mode analysis is performed. In this paper, some boundary conditions are simplified as following:

(a) External force is neglected because of modal is the natural property which has nothing to do with external force.

(b) According to gear coupling dynamics theory, the stiffness of gear pairs is simplified as spring elements.

(c) The shaft and bearing hole is node coupled in axial and tangential direction. Each bearing is simulated using four spring elements distributed as cross through axle center and the spring elements is paralleled to X axis and Y axis.

The wind turbine gear box is meshed as four node and tetrahedron grid cell by I-DEAS free meshing method. The coupling gear box finite element model is shown as Fig. 3.

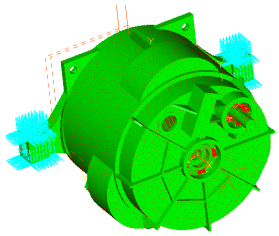

Fig.3 Coupling FE model of wind turbine gearbox

The modal analysis of the wind turbine gearbox shown in Fig.1 is performed by Lanczos method in I-DEAS Model Solution. The first ten steps of natural frequency and corresponding mode are listed in Tab.1. And the corresponding mode of the first 3 steps is shown in Fig.4.

Table 1 First ten steps of natural frequency(Hz)

Step	Frequency	Step	Frequency
1	43.3	6	96.5
2	58.7	7	103.9
3	70.9	8	115.5
4	74.4	9	120.1
5	88.0	10	128.9

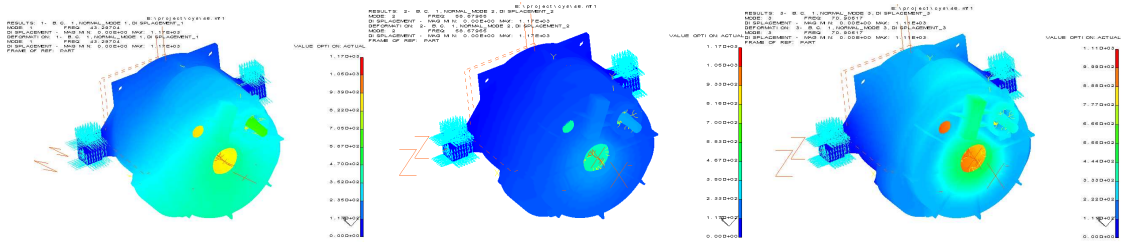

Fig.4 (a) Formation of the first step frequency;(b) Formation of the second step frequency; (c) Formation of the third step frequency

From Fig.4, we can know that the largest vibration happens at the back of gearbox and mostly appears as up and down swing trend in these first several mode shapes. The harmonic response analysis should be done because of the lower natural frequency of first several vibration modes from above modal analysis.

Contact analysis of spline

It will have some certain elastic deformation when spline transmitting torque. Meanwhile, wind turbine gearbox work under complicated conditions and heavy loads. Therefore, it's important to study the spline contact analysis.

During analysis, all the contact teeth are defined as contact pair. The internal spline is defined as target area and the external spline is defined as contact area. The spline finite element model is shown in Fig.5.

The total deformation of external spline is shown in Fig. 6 and the maximum deformation is 0.037mm. The total deformation of internal deformation is 0.0073mm.

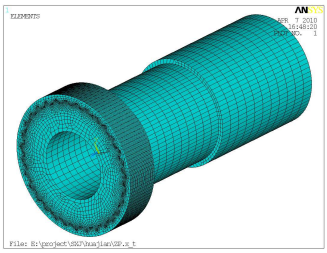

Fig.5 FE model of spline connection

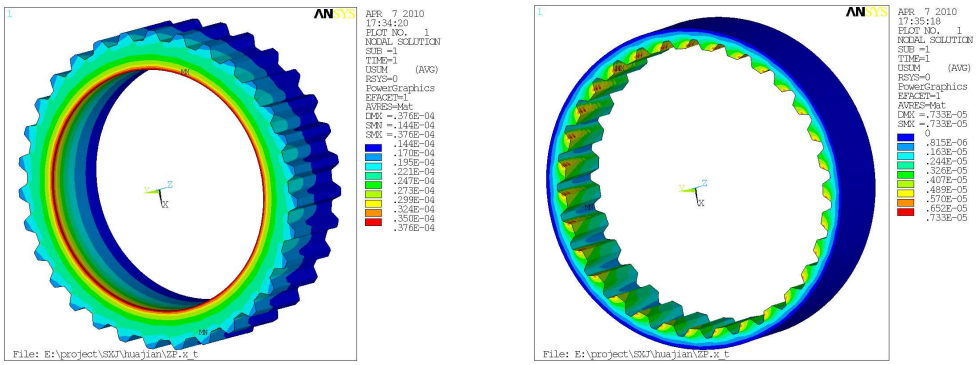

Fig.6 (a) Deformation contour of contact analysis of external spline; (b) Deformation contour of contact analysis of internal spline

Because spline is axial symmetry structure, the contact stress on one tooth surface is extracted from above results. The contact stress contour of spline is shown in Fig.7. The maximum contact stress is 176.198MPa. It appears at the root of tooth which is near to the torque input.

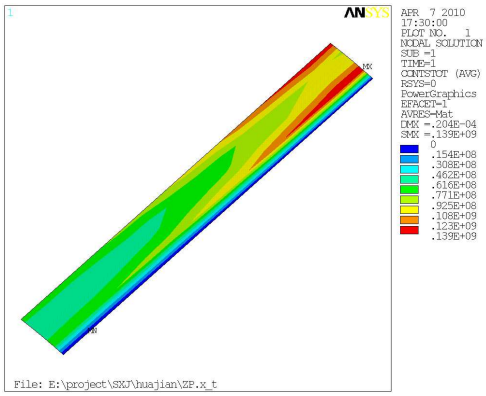

Fig.7 Contact stress contour of spline

Through above analysis, it can be seen that the maximum contact stress appears at one third position which is nearer to torque input. The deformation of external spline is greater than that of internal under the same loading. Thus, if the contact zone of spline wanted to be well-distributed, the spline flank should be corrected.

Contact analysis of gear pairs

The gear tooth is relative to impact and vibration during transmission. Moreover, contact stress and bending stress of tooth surface are relative to fatigue failure, pitting and gluing [7], [8]. Thus, it is necessary to analysis contact for wind turbine gearbox.

Contact analysis and profile relief of gear flank. In order to further investigate deformation and contact stress of each tooth surface in planetary gear and ring gear, At a given time, the contact teeth of the first stage planetary gear and ring gear are numbered as No.1 and No.2 (see Fig. 8(a) and Fig. 8 (b)).

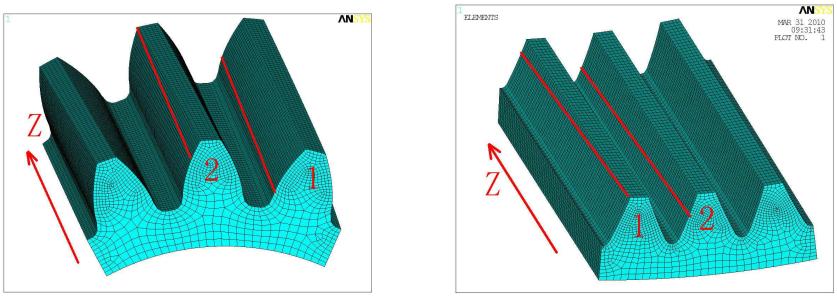

Fig.8 (a) FE model of planetary gear for contact analysis; (b) FE model of ring gear for contact analysis

The analysis results of the first stage planetary and ring gear using ANSYS are shown in Fig. 9. The maximum contact stress is 606.198MPa (see Fig. 9 (a) and Fig. 9 (b)), appears at the contact line in No.1 tooth surface. This stress is much larger than other stress and appears at the edge of gear flank. It will greatly decrease after profile relief.

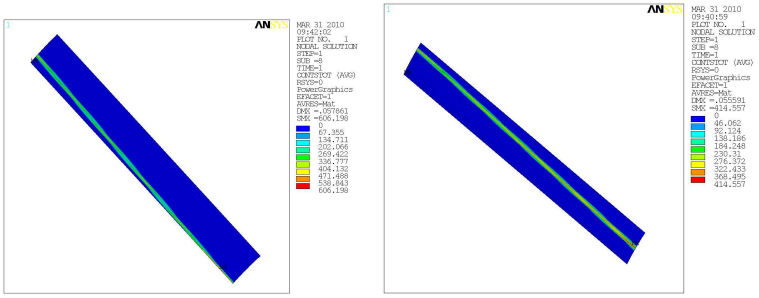

(a) Contact stress of pinion in No.1 tooth surface (b) Contact stress of pinion in No.2 tooth surface

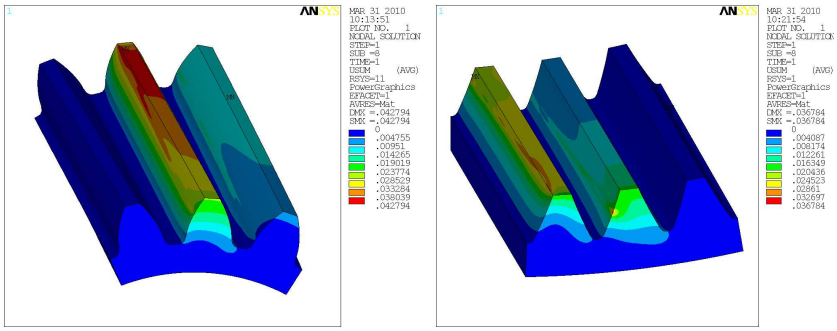

(c) Total deformation contour of pinion (d) Total deformation contour of ring gear

Fig. 9 Coontact stress and deformation of gear flank

According to the deformation contour of planetary gear and ring gear (see Fig.9 (c) and Fig.9 (d)), the deformations at the tip of planetary gear and ring gear are 0.042mm and 0.036mm, respectively. These deformations are generated by the transmitted torque. And these data can be used as the profile relief of gear flank.

FE Analysis of planetary gear and lead modification. The deformation data of planetary gear and ring gear can be used as the profile relief from above analysis. Actually, gears flank should be either modified in lead direction because of the shaft deformation (including bending and torsional deformation), surface deviation and manufacturing error, etc. Therefore, the gear shafts should be analyzed to obtain the lead modification data.

The analysis here focuses on the bending and torsional deformation of gear shafts. Some geometric features of the gear in shafts are neglected. Meanwhile, the loading and constraint are applied to the corresponding positions according to the actual bearing and torque input. The FE model of the first stage planetary gear and ring gear contains shaft is shown in Fig.10.

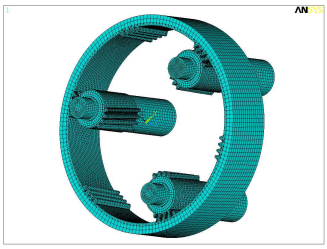

Fig.10 FE model of planetary gear system

The maximum total bending deformation in planetary gear shaft is 0.018mm, which distance from the left section of planetary gear shaft 192.72mm. The total bending deformation contour is shown in Fig.11 (a). According to the deformation of deformation between the two sides of gear in axis direction, the lead crown curve can be obtained. the lead crown of the first stage planetary gear is 0.011mm.

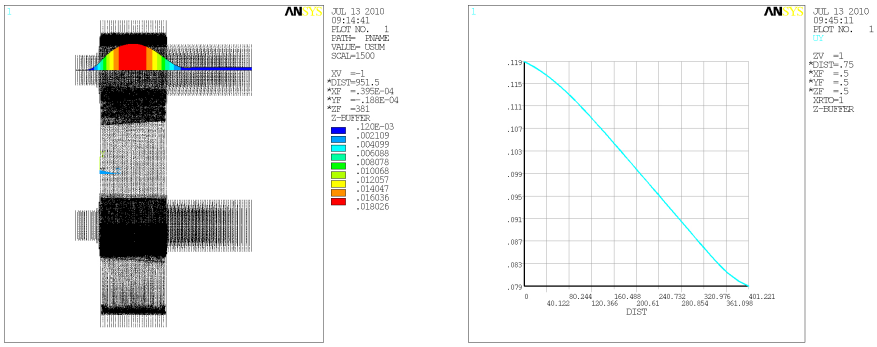

Fig.11 (a) Bending deformation contour of pinion; (b) Torsional deformation curve in dedendum circle of planetary gear

Choosing the node belong to the addendum generatrix in non-contact gear to analysis the distribution of torsional deformation, we can get the circumferential deformation differences between two terminals of the planetary gear non-contact tooth is 0.04mm, shown in Fig.11(b), The relative torsional angle of deformation in reference circle is 0.005˜, i.e., the spiral modification angle is 0.005˜.

Comparisons of FE result with DIN 3990 standard. In order to check analysis results, the strength of every gears calculated by DIN3990-1987 is listed in Tab.2. Through comparative study, it can be known that the contact stress and bending stress calculated by FE method are smaller than that calculated by DIN3990-1987 [9]. The main reason about that is the application factor, stress modification coefficients and life factor, etc, are not considered when calculate contact stress and bending stress using finite element method.

Table 2 Gear strength of the wind turbine gearbox

Gear pair	Contact stress(MPa)		Bending stress(MPa)	
	Left flank	Right flank	Left flank	Right flank
Third stage pinion	885.537	0.0000	335.1344	0.0000
Third stage wheel	885.537	0.0000	387.2273	0.0000
Second stage planetary gear	969.1584	0.0000	327.5331	0.0000
Second stage sun gear	969.1584	0.0000	307.9855	0.0000
First stage Planetary gear	812.6218	0.0000	381.7221	0.0000
First stage ring gear	0.0000	812.6218	0.0000	314.4531

Note: The values “0.0000” denote the flank is not the work side.

Dynamic analysis of gear pairs

To predict dynamic vibration, noise and other dynamics of wind turbine gearbox during transmission, it is necessary to analyze the dynamics properties [10]. ADAMS is virtual prototype software, and it has a powerful dynamic simulation and post-processing capabilities. The dynamic properties of wind turbine gearbox are simulated by ADAMS in this paper.

Parameters setting. Rotating blades of the wind turbine drive the hollow shaft, thereby drive the ring gear. According to actual rated rotation speed 17 r/m on input shaft of the wind turbine, after transform it to rotation angle 102 °/s, then impose the constant speed drive speed 102 °/s on the hollow shaft. The first stage planetary gear shaft drives the second planetary gear; the end of planetary shaft should impose a load torque which is 1.071 10^5 Nmm. To avoid load torque suddenly change and slowly increase the torque on the input shaft, a step function in ADAMS is used to apply load. The loading curve in ADAMS by step function is shown in Fig.12.

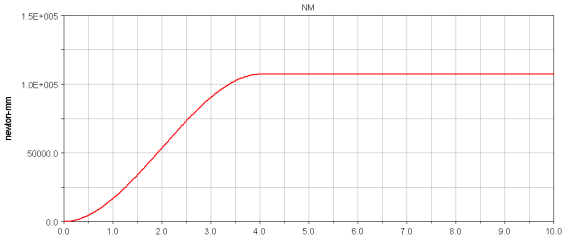

Fig.12 Loading curve in ADAMS by step function

The material of planetary gear is 17CrNiMo6 and the stiffness coefficient of collision is 1.766 106 MPa according to Hertz theory. The stiffness coefficient of collision is set as 2.2 and the embedded depth is 0.1mm; kinetic sliding friction factor is 0.05 and static sliding friction factor is 0.08 according to engineering experience.

Dynamic analysis of the gear pairs. The coordinate of the mass center of one planetary gear of wind turbine gearbox in ADAMS is(0, 584.634, 387.088). According to analysis results, it can be known that the displacement in X direction at mass center is 1.5mm (see Fig.13 (a)), the displacement in Y direction at mass center is 1.616mm (see Fig.13 (b)), while the displacement in Z direction at mass center is a constant value (see Fig.13 (c)). The displacement in X and Y directions change periodically because of contact and friction of gear tooth surface. Meanwhile, the impact force between planetary gear and ring gear decreased greatly after modification (see Fig. 13 (d) and Fig.13 (e)). It shows that the gear modification can decrease the impact force greatly and it achieves the desired purpose of reducing vibration and noise.

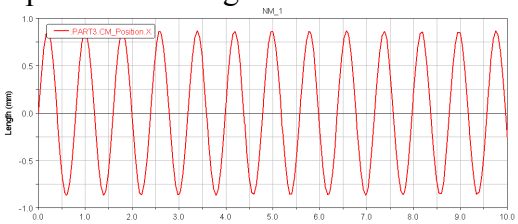

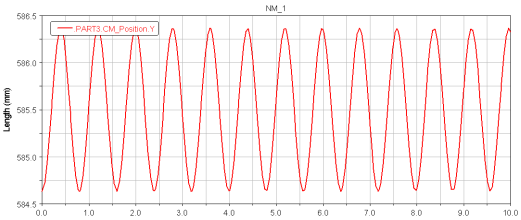

(a) Displacement in X direction at mass center; (b) Displacement in Y direction at mass center

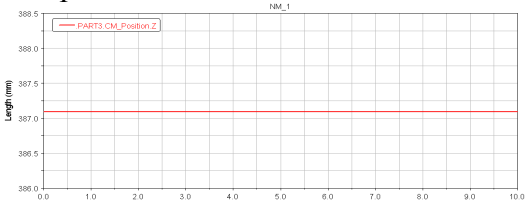

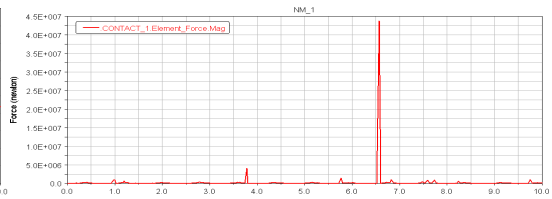

(c) Displacement in Z direction at mass center; (d) Impact force between planetary gear and ring gear before modification

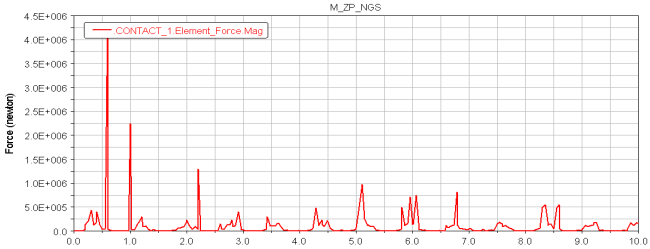

(e) Impact force between planetary gear and ring gear after modification

Fig.13 Dynamic analysis results

Conlusions

In this paper, it provide data support for designing good performance and good static/dynamic characteristics MW-class wind turbine gearbox based on finite element analysis before manufacturing. By means of experimental tests to validate the finite element analysis results showing that the analysis results are correct and reliable. Therefore, it is a feasible and effective means to design, analyze and optimize the wind turbine gearbox using finite element method.

Acknowledgments

This work is supported by China Postdoctoral Science Foundation (No.:20100471443) and China Postdoctoral Science Foundation special funded project (No.:201104560). The authors would also like to acknowledge grant No.:SKLMT-KFKT-200906 from the opening foundation of the State Key Laboratory of Mechanical Transmission, Chongqing University, China. The authors would like to take this opportunity to express their sincere appreciation.

References

[1] GL Wind Energy GmbH. Section 7.1.3. GL Wind Technical Note 068. Requirements and recommendations for implementation and documentation of resonance analysis. In Guideline for the Certification of Wind Turbines (Edition 2003 with Supplement 2004). Germanischer Lloyd Windenergie GmbH: Hamburg, Germany, 2006.

[2] ANSI/AGMA/AWEA6006-A03. Standard for Design and Specification of Gearboxes for Wind Turbines. AGMA Foundation the American Gear Manufacturers Association: Alexandria, VA, 2003.

[3] Guo Aigui, Fan Weimin, Wei Jing, Sun Wei. Finite Element Analysis of Taizhong Ⅲ Wind Turbille Gearbox. Journal of Mechanical Transmission, 2009;33(6):55-60.(In Chinese)

[4] ISO 81400-4-2005: Wind turbines-Part 4: Design and Specification of Gearboxes.

[5] Yan Kejun. Static and Dynamic Finite Element Analysis of Speed-increase Gearbox for 1.5MW Wind Generator. Journal of Mechanical Transmission, 2009;33(6):49-52. (In Chinese)

[6] Cui Zhiqin, Yang Ruifeng. Combined structure Feature Parametric model Modal analysis. Chinese Journal of Mechanical Engineering. 2008, 44(2):234-237.

[7] Peeters J., Vandepitte D., Sas P.. Analysis of internal drive train dynamics in a wind turbine. Wind Energy, 2006, 9(1):141-161.

[8] Zhu Caichao, Huang Qi, Tang Qian. Study on multi-teeth contact and load distribution of speed increase gearbox transmission system for the wind-driven generator. Transactions of the Chinese Society of Agricultural Machinery, July 2006; 37(7):86-89,.

[9] DIN 3990-1987: Calculation of load capacity of cylindrical gears—Part 3: Calculation of tooth strength.

[10] Ma Chao-Feng, Cui Ya-Hui, Liu Kai, Liang Wen-Hong. Dynamic modeling of the gearbox transmission for the wind turbine. ASME International Mechanical Engineering Congress and Exposition, Proceedings, 2010(15):179-183. Proceedings of the ASME International Mechanical Engineering Congress and Exposition 2009, Lake Buena Vista, FL, NOV 13-19, 2009.

© (2012) Trans Tech Publications, Switzerland
doi:10.4028/www.scientific.net/AMM.187.146

Design of Auto Route Identified Vehicle Model based on MC9S12XS128

ZHENG Fu

National Space Science Center, CAS, Beijing 100190, China

zhengfu11@mails.gucas.ac.cn

Keywords: Automatic identification; PID; Modulated infrared sensor; Predictive control; S12 MCU.

Abstract. A vehicle based on automatic route identification technology by using modulated infrared photoelectric sensors was introduced. Circuits for path detecting , motor drive, speed sensor and servo drive were designed. And the controlling strategy was introduced. At last, the assembled model car could run along the black line stably and fast.

Introduction

Freescale Cup National University Smart Car racing is an important race for the National Colleges, which is approved and commissioned by the Ministry of Education Automation Teaching guide sub-committee and organized by Freescale Co.. In 2006, Tsinghua University hosted the first Smart Car competition. Now the race has been successfully held for four times. And the fifth will be held this year. The structure and control strategy of how to design the car will be introduced [1] [2].

Hardware Design

A 16-bit micro-controller MC9S12XS128 was used to control the smart car. The speed of car can be gotten by counting the pulses of optical encoder. The MCU generates 2 PWM pulses to the servo and to drive the motor according to the path state detected by sensors. Figure 1 is the photo of the real car. Figure 2 is the overall control chart of Smart car.

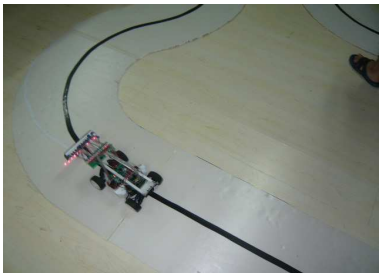

Fig.1 The photo of the real car

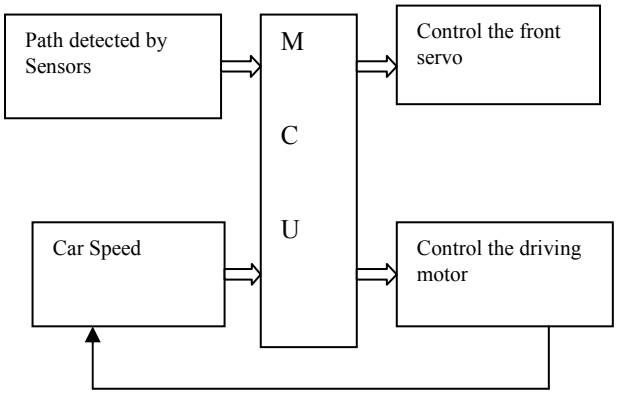

Fig.2 Schematic diagram of smart car

Path detecting module. Detecting path information can get the relative position between the smart car and the black line on the surface of white road. The MCU reads the A/D value converted from the voltage that infrared sensor receive the reflecting light in traditional smart cars. However, it is easily influenced by the environment. So the modulated infrared sensor LM567 was adopted.

LM567 is a low-cost PLL IC for audio. It can be used to construct well-performed reflective photoelectric sensor.

As shown in Figure 3, a square wave signal produced by LM567 light the LED. The photodiode receives the reflecting infrared light. The signal is amplified by the BJT and converted to voltage signal, then sent to the internal phase detector of LM567. And Lm567 outputs high or low level by comparing with the internal comparator. Parallel negative feedback circuit has a stable gain and low input impedance. So it can eliminate the photodiode junction capacitance effects and get good high frequency characteristics. The 200K potentiometer (R6, 200K adjustable) is used to adjust amplifier gain to adjust the sensitivity. The 510K resistor and the 1000p capacitor between the outi and outo are used to add 50mV comparator hysteresis to eliminate output jitter caused by frequency modulation ripple. And the 1000p capacitor is used to compensate effect of the C1 and speed up the output transition.

In order to prevent output jitter caused by overlap of the adjacent spots when the frequency of a probe is close to another, a single unit (the LM567 below in Figure 3) was used to generate oscillation to the remaining 10 units to provide synchronized clock signals to eliminate the difference shoot the problem. Only one was drawn in the figure for improving the drive capability through an inverter, such as 74ACT14. Besides the clock signal is connected to the capacitive terminal of the oscillator while driving the BJT to light the LEDs. As a result, demodulation efficiency is greatly increased. And the maximum detection range increased. There is a very small difference between the reference signal and the transmitting/receiving signals.

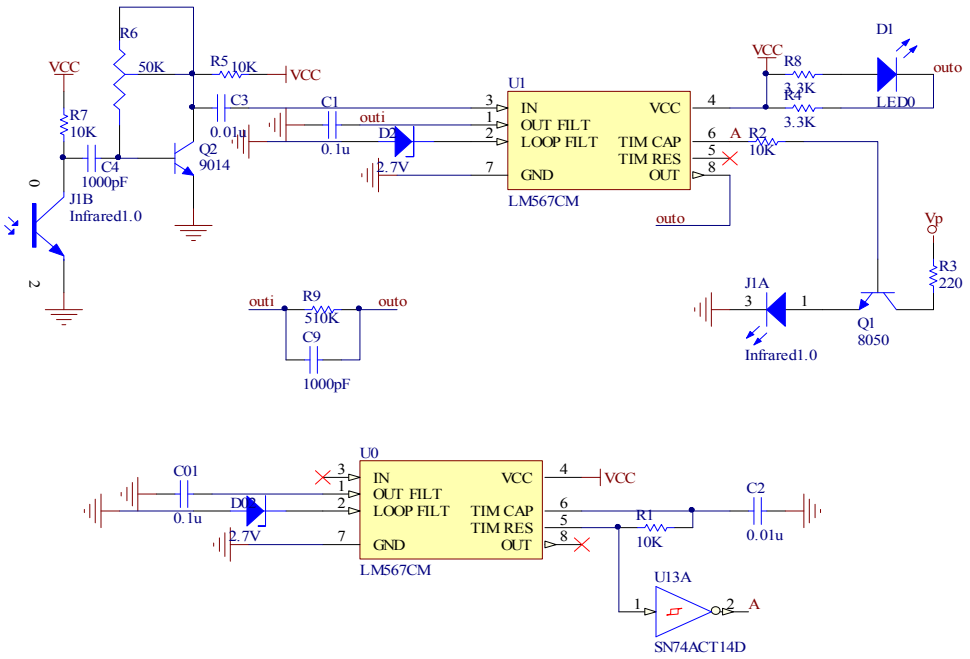

Fig.3 The schematic of sensor board with LM567

Motor speed measurement modul. To keep the car running smoothly along the track, speed of the motor and the steering system should be controlled to keep the car run on a right route. Thus, the car can not slid off the runway because of high speed. The motor speed was controlled by PWM. If it is open-loop, many factors will affect it, such as battery voltage, motor friction, uneven road friction and the front wheel steering angle etc. So through the speed test, closed loop speed control of the car models can eliminate the impact of the above factors and make car models run more accurately. And integrated optical encoder was used to test speed. The signal is connected to PT7 of the MCU[1].

Servo control module. The servo controls the direction of the smart car. And the servo is controlled by PWM. And the servo's rotation is proportional to the pulse width. There is a 50Hz reference signal inside the servo. And the servo controls the direction and rotation by comparing the reference signal with the PWM signal.

Motor drive module. With the acquirement of the competition's Organizing Committee, RS-380SH motor was used. It works at voltage 7.2V and no-load current of 0.5A. Specified rotating speed is 16200 r / min. MC33886 was used to drive the motor. It's a monolithic H-Bridge ideal for fractional horsepower DC-motor and bi-directional thrust solenoid control. The schematic of the MC33886 is shown in Figure 4.

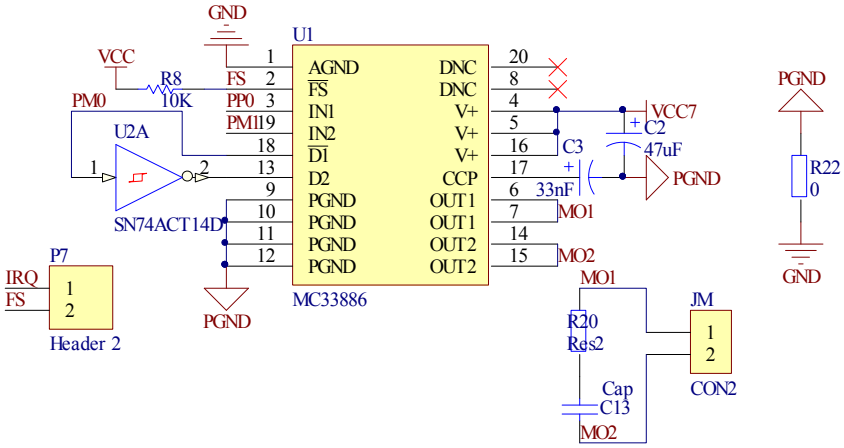

Fig.4 The schematic of the MC33886

Software Design. The software development tool is CodeWarrior compiler developed by MetroWerks. First, the relative position with the black line was gotten by analyzing the signals of the sensor board. So the path status was decided.

Judging the relative position between the black line and the car. Sensors layout is shown in Figure 5. There may be one or two sensors above the black line at the same time. Then, the relative position can be gotten between the car and the black line as the numbers in the figure. 10ms timing can be achieved with the RTI module of the S12. And the S12 reads the value of the sensors every 10ms. Besides, the deference between adjacent second sensor values can not exceed 4. Thus it can remove the random interference and exclude the impact of the background of track.

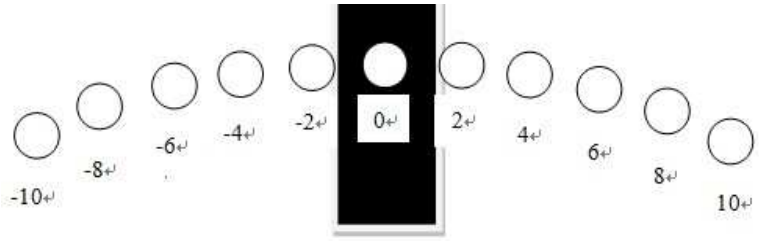

Fig.5 Sensors layout chart

Servo control. First the length of the servo rod can be adjusted to a optimal value. If it's too long or too short, it may lead to a tense state. So the car can not steer flexibly. The relationship between the turning radius of the car models and steering angle of the servo is not linear. The relationship between them can be obtained by experiment, as shown in Table 1. It is proportional control. Some derivative control can be added to improve the dynamic performance.

Table 1. Relationship between the turning radius of the car and steering angle of the servo

Left radius（mm）	Servo angle（° ）	Right radius（mm）	Servo angle（° ）
450	15	1300	98
500	17	1200	101
600	20	1100	108
700	31	1000	116
800	43	900	124
900	52	800	131
1000	68	700	144
1100	71	600	149
1200	77	550	157
1300	80	500	164
∞	90	450	170

Motor control. Traditional PID control was used to control the speed of the motor, as Figure 6. In the experiments, the integral part leads to integral overshoot easily. So PD control was used.

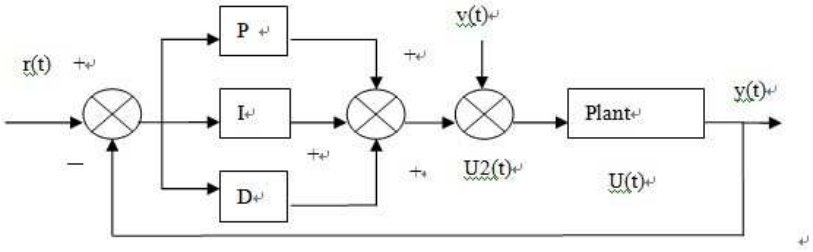

Fig.6 PID control block diagram

Predictive control. There are straight line, small S curve, and big curve in the track. In the straight line the car should be running at maximum speed. In large curve it should be based on the speed of the slowest driving; in small S curve, medium speed driving. Path testing requires testing path center, path direction, path curvature. By reading 3-5 points in the vertical direction of the track, the above features of the track can be gotten, as shown in Figure 7.

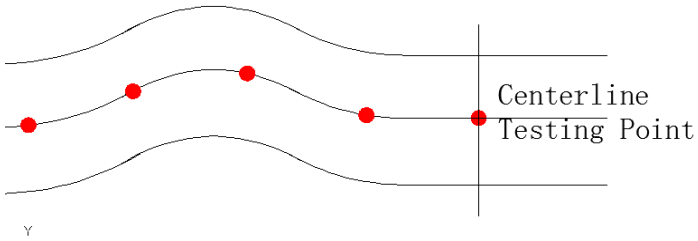

Fig.7 Predict the path diagram

Conclusion

Based on the MC9S12XS128, the schematic was designed. And PCB board was made with Altium Designer. PID control was adopted to control the smart car. And the smart car achieved the requirements of the smart car competition.

Acknowledgment

This paper was supported by Chinese Universities Scientific Fund (BJFU-YX2010-8).

References

[1] Zhuo Qing, Huang Kaisheng, and Shao Beibei, "*Learn to make smart cars.*" Press of Beijing University of Aeronautics & Astronautics,2007.

[2] G. Yue-hua, "Design of Autonomous Tracing System in Intelligent Vehicle Based on Infrared Photoelectric Sensor," *Semiconductor Optoelectronics,* vol. 1, 2009.

[3] X. W. Hao and H. F. Sun, "Tracking Control Algorithm Based on Photoelectric Sensors for Smart Car System," *Iccsse 2009: Proceedings of 2009 4th International Conference on Computer Science & Education,* pp. 587-591, 2009.

[4] T. Schweers, "Smart hyper - a hybrid concept-car with high innovative potential," *Vehicle Concepts for the 2nd Century of Automotive Technology,* vol. 1653, pp. 243-254, 2001.

[5] P. K. Chang*, et al.*, "Integrated smart car navigation and voice control system design," *Iecon 2006 - 32nd Annual Conference on Ieee Industrial Electronics, Vols 1-11,* pp. 23-28, 2006.

[6] Z. H. Wang and Y. Y. Ye, "Image Recognition Technology and Optimized Control Algorithm of the Self-tracing Smart Car Based on CMOS Camera Sensor," *Icems 2008: Proceedings of the 11th International Conference on Electrical Machines and Systems, Vols 1- 8,* pp. 2096-2101, 2008.

[7] X. Q. Wang*, et al.*, "Route Identification and Direction Control of Smart Car Based on CMOS Image Sensor," *2008 Isecs International Colloquium on Computing, Communication, Control, and Management, Vol 2, Proceedings,* pp. 176-179, 2008.

[8] M. F. Wang and Z. J. Jiang, "The Design and Comparison of DC Motor Drive Circuit in Smart Car Competition," *2009 Ieee International Conference on Intelligent Computing and Intelligent Systems, Proceedings, Vol 2,* pp. 325-328, 2009.

[9] S. H. Ma and W. Li, "Non-linear PID Control Method with Feed-forward in Smart Car," *Ccdc 2009: 21st Chinese Control and Decision Conference, Vols 1-6, Proceedings,* pp. 462-465, 2009.

[10] Z. L. Lu*, et al.*, "Intelligent Control Research based on the Smart Car," *2nd Ieee International Conference on Advanced Computer Control (Icacc 2010), Vol. 2,* pp. 292-297, 2010.

[11] Freescale Semiconductor,Inc. MC9S12XS128 Device User Guide.

© (2012) Trans Tech Publications, Switzerland
doi:10.4028/www.scientific.net/AMM.187.151

Finite Element Analysis of Flextensional Transducer with Slotted Shell

Si Chen*, Yu Lan

Harbin Engineering University, Nantong Street, No.145-1, Harbin 150001, China
* Corresponding author.E-mail address: chensi_83@126.com.

Keywords: SLOTTED SHELL, LOW FREQUENCY, SMALL SIZE, TRANSDUCER

Abstract. The study of low frequency, small size transducer was an important aspect for the development of the underwater acoustic transducer. The Class Ⅳ flextensional transducer was a typical low frequency, high-power and small size transducer. For decreasing its resonant frequency in the case of small size, a flextensional transducer with slotted shell was analyzed using finite element software ANSYS. A comparison between the flextensioanl transducer with slotted shell and the Class Ⅳ flextensional transducer was made. The maximum size of the shell is 200mm. The transmitting voltage response of the transducer reaches to 131dB with resonant frequency 600Hz in water. The transducer could radiate at low frequency with small size of the shell.

1. Introduction

Along with the continual enlargement of modern sonar application, higher demands are put forward to sonar equipment. One of the demands is to decrease the working frequency and reduce the size of the transducer. At present, the low frequency and small size transducer is the main research direction of underwater acoustic transducer. The Class Ⅳ flextensional transducer is a typical low frequency, high-power and small size transducer and widely used in the field of underwater acoustics. The resonant frequency of the flextensional transducer is closely related to the stiffness of the shell. If the working frequency of the transducer can be decreased farther in the case of small size, it would be favorable to the miniaturization of the flextensional transducer, also to the arraying.

Based on the application requirements above, a flextensional transducer with slotted shell was analyzed using finite element software ANSYS based on the Class Ⅳ flextensional transducer.

2. Structure of the transducer

The typical Class Ⅳ flextensional transducer usually has a closed oval-shaped cylindrical shell as shown in Figure1.

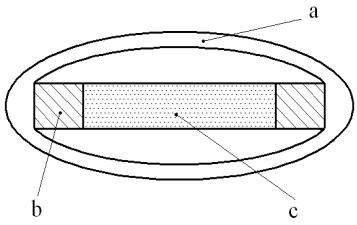

Fig.1. The configuration of a typical Class Ⅳ flextensional transducer a: shell, b: transition structure, c: actuator.

The shell is driven along its major axis by a driver which could be either a ceramic stack or magnetostrictive material resulting in a magnified motion of the shell in the minor axis to radiate energy into the water [1-2]. The flextensional transducer has the advantages of low resonant frequency due to the flexural mode. It could achieve high-power radiation due to the large volume displacement resulting from the magnified motion of the shell.

The resonant frequency of the flextensional transducer is closely related to the resonant frequency of the shell and the actuator. The resonant frequency of the shell has more significant influence on the resonant frequency of the transducer [3]. For decreasing the resonant frequency of the transducer, the stiffness of the shell should be reduced. One of the methods to reduce the stiffness of the shell is to increase its size. The larger the shell is, the lower the resonant frequency of the transducer would be. The size and the weight of the transducer will be increased due to the larger size of the shell which will cause great difficulties to the application.

Based on the consideration above, a flextensional transducer with slotted shell was analyzed [4-6]. The configuration of the transducer is shown in Figure2.

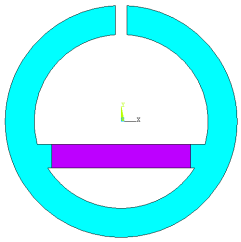

Fig.2. The configuration of the flextensional transducer with slotted shell

The main features of the structure are as follows: the shell is slotted which is helpful to decrease the resonant frequency of the transducer. The actuator is not placed on the horizontal axis of the transducer as the Class Ⅳ, but below the horizontal axis. It is helpful to make full use of the displacement amplification of the shell. The cross-section of the shell is circular not oval which is helpful to decrease the resonant frequency of the transducer further.

Next, the transducer will be analyzed using finite element software ANSYS.

3. Finite element analysis of the transducer

The finite element model of the transducer is builded in finite element software ANSYS. The flextensional transducer is constituted of the shell, the transition structure (made of hard aluminum) and the actuator (made of piezoelectric ceramic PZT-4). Only the 1/4 finite element model is needed due to the space symmetry of the flextensional transducer as shown in Figure3. The shell is 25mm thick, 100mm high. The radius of the shell is 100mm.

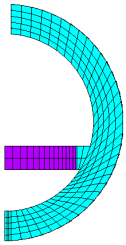

Fig 3. The 1/4 finite element model of the transducer

Modal analysis of the transducer in air is made. The natural frequencies and mode shapes of the transducer are obtained. The displacement vector of the first mode is shown in Figure4. The natural frequency of the transducer in air is 712Hz.

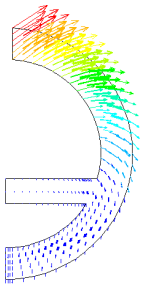

Fig 4. The displacement vector of the first mode

Then harmonic response analysis of the transducer in air is made. Alternating current at different frequencies is imposed on the actuator resulting in the vibration of the transducer. In this type of transducer, the vibration of the shell plays a major role in the radiation. The physical quantities of interest are extracted. Then according to the basic definitions, some important parameters of the transducer can be obtained such as the admittance, the transmitting voltage response and so on.

The admittance curves of the transducer in air are shown in Figure5. The transducer resonates at 712Hz in air at which the conductance value is 3.1mS.

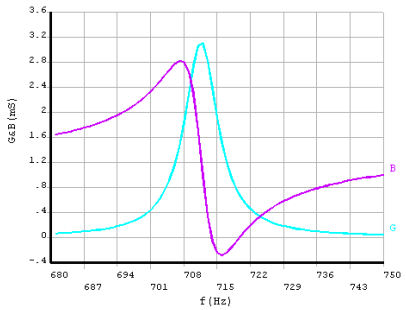

Fig.5. The admittance curves of the transducer in air

The finite element model of the transducer in water is established as shown in Figure6.

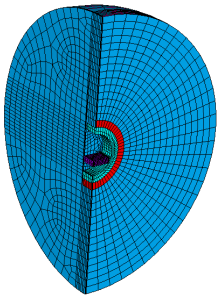

Fig.6. The 1/4 finite element model of the transducer in water

Harmonic response analysis is made. The admittance curves of the transducer in water and the transmitting voltage response (TVR) curve were obtained as shown in Figure7, Figure8 respectively. The resonant frequency of the transducer in water is 600Hz. The conductance value of the transducer is 0.28mS at resonance. The transmitting voltage response of the transducer reaches to 131dB.

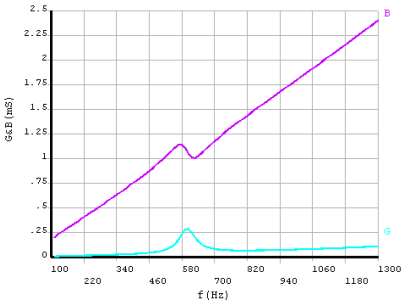

Fig.7. The admittance curves of the transducer in water

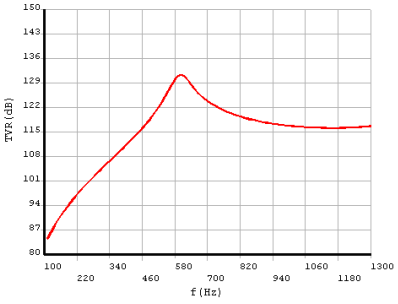

Fig.8. The transmitting voltage response of the transducer

Meanwhile the Class Ⅳ flextensional transducers are simulated, a comparison is made as shown in Table 1.

Table 1. The comparison between the two kinds of flextensional transducers

	maximum size of the shell (mm)	resonant frequency in water (Hz)	maximum transmitting voltage response (dB)
flextensional transducer with slotted shell	200	600	131
Class Ⅳ flextensional transducer (a)	200	3200	140
Class Ⅳ flextensional transducer (b)	590	600	133

In the case of the same maximum size (200mm), keeping the thick of the shell and the actuator unchanged, the resonant frequency of the Class Ⅳ flextensional transducer in water is 3200 Hz, the resonant frequency of the flextensional transducer with slotted shell in water is only 600 Hz. The TVR of the slotted one is a little lower than that of the Class Ⅳ. In order to obtain the same low resonant frequency, the maximum size of the Class Ⅳ flextensional transducer should increase to 590mm. Thus, the flextensional transducer with slotted shell has certain advantages in radiating acoustic energy at low frequency with smaller size.

4. Conclusions

In this paper, a flextensional transducer with slotted shell was analyzed. The transducer can radiate at low frequency in the case of small size due to the low stiffness of the slotted shell and the displacement amplification of the shell. The maximum size of the transducer is 200mm. The resonant frequency of the transducer is 600Hz with maximum transmitting voltage response 131dB. The assembly process of the transducer will be studied and a prototype of the transducer will be developed in further work.

References

[1] L. H. Royster. Flextensional Underwater Acoustics Transducer. *J. Acoust. Soc. Am*;45:671-682.

[2] G. A. Brigham. Analysis of the Class-Ⅳ Flextensional Transducer by Use of Wave Mechanics. *J. Acoust. Soc. Am*;56:31-39.

[3] K. D. Rolt. History of the Flextensional Electroacoustic Transducer. *J. Acoust. Soc. Am*;87:1340-1349.

[4] J. C. Debus, J. N. Decarpigny, B. Hamonic. Analysis of A Class Ⅳ Flextensional Transducer Using Piece-Part Equivalent Circuit Models. *Proc. of the Third International Workshop on Transducers for Sonics and Ultrasonics*, 1992;181-197.

[5] P. F. Flanagan. Electro-acoustic Transducers. *U. S. Patent*, 1993; 5,268,879.

[6] R. Porzio. Longitudinally Driven Slotted Cylinder Transducer. *U. S. Patent*, 2008; US 7,466,066 B2.

CHAPTER 4:

Vibrational Analysis and Mechanics of Structures etc.

© (2012) Trans Tech Publications, Switzerland
doi:10.4028/www.scientific.net/AMM.187.157

Experimental Study on Bending Capacity of Plain Wall System

Hooi Min YEE[1, a], Kok Keong CHOONG[2,b] and Rohamezan ROHIM[1,c]

[1]Faculty of Civil Engineering, Universiti Teknologi MARA Pulau Pinang, 13500 Permatang Pauh, Pulau Pinang, Malaysia.

[2]School of Civil Engineering, Engineering Campus, Universiti Sains Malaysia, 14300, Nibong Tebal, Penang, Malaysia

[a]minyh@ppinang.uitm.edu.my, [b]cekkc@eng.usm.my, [c]rohamezan627@ppinang.uitm.edu.my

Keywords: Plain wall system, reinforced concrete and bending capacity

Abstract. Plain wall system is highly suitable to be used with reinforced concrete as its building material. Concrete vertical walls may serve both architecturally partitions and structurally to carry gravity and lateral loading. Moment transfer of joint is an important aspect for proper structurally functioning of plain wall system. Hence, the aim of this study is to investigate experimentally the effect of reinforcement details in the wall on bending capacity for support stiffness in plain wall system in Malaysia. A total of six wall specimens were tested. Three of this specimens consisted single layer of rebar while another three specimen consisted of double layer of rebar. The size of the plain wall's specimens is 1000mm in length, 1080mm in width, 1000mm in height and 80mm in thickness. The average concrete strength was 23.49MPa with Grade 30N/mm^2 and the average yield strength of R5 bar was 817MPa. The bending capacity at failure for single layered of rebar in wall for specimen 1, 2 and 3 were found to be 3.59kNm, 3.81kNm and 3.15kNm, respectively. The bending capacity at failure for double layered of rebar in wall for specimen 1, 2 and 3 were 5.50kNm, 6.31kNm and 7.00kNm, respectively. Based on the results, specimens consisted of double layered of rebar in wall is found to provide higher bending capacity to the joint of plain wall system in the range from 56.25% to 98.86% compared with single layered of rebar in wall.

Introduction

In concrete high rise building, the repetition in the use of formwork is almost a necessity to optimize construction speed of cast in place. In this case, the most suitable building system will be the use of plain wall system. Plain wall structural system is a system suitable for use in the field of high-rise building where the main load resisting system is in the form rigidly connected plain wall. It is also sometimes called box system or plain wall system. Plain wall structural system is highly suitable to be used with reinforced concrete as its building material. Plain wall system which is composed only of reinforced concrete walls and slabs has been widely used in many countries since this type of structure not only can facilitate construction speed but also can reduce the construction cost with the use of suitable and repetitive system formwork. Fig 1 shows the plain wall structural system.

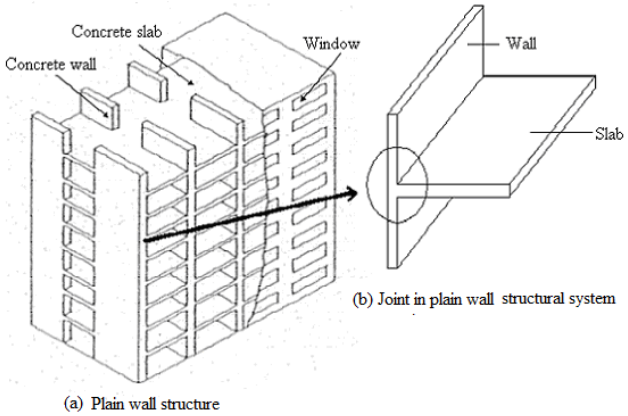

Fig. 1 Plain wall structural system

Yeoh [1] has carried out a comparison between behaviour of plain wall system and using the conventional moment resisting frame. Liu and Abdhassan [2] have studied the moment-rotation parameters for composite shear tab connections in steel frame buildings. Arlekar and Murty [3] have used finite element analysis of 18 strong-axis steel welded beam-column subassemblages with connection reinforcement. Liu et al [4] have studied the effects of the inner and outer stiffeners and splice plates jointed with high-strength bolts on the stability bearing capacity and the failure mode of the steel box column and an axial compression model tests have been carried.

For plain wall system, the vertical element i.e. concrete wall is designed to carry the load transfer from slabs. Proper understanding of strength and stiffness of joint is crucial for the design and analysis of plain wall system. Among the factors, the reinforcement details play an important role, since concrete has negligible tensile strength. This study has been carried out with the objective to understand the effect of reinforcement details in wall part on the strength and stiffness of joint in plain wall system.

Methodology

The following works were involved : determination of suitable scaled down size of joint of plain wall system to be investigated and numbers of sample of joint to be cast, load testing of joint samples, rebar tensile test and concrete cube test. A total of six specimens were tested. Three specimens consisted single layered of rebars (denoted as 1(S), 2(S) and 3(S)) and another three consisted of double layered of rebars in the wall (denoted as in 1(D), 2(D) and 3(D)). The size of the sample of plain wall used was length, L = 1000mm, width, W = 1080mm, height, H = 1000mm and thickness, T = 80mm as shown in Fig. 1b The sketch of slab with single and double layers shown in Fig. 2. Two different arrangement of rebars in wall segment have been chosen : single layer and double layer; as shown in Fig. 2a and 2b, respectively. 5mm mild steel bars were used for all the rebars.

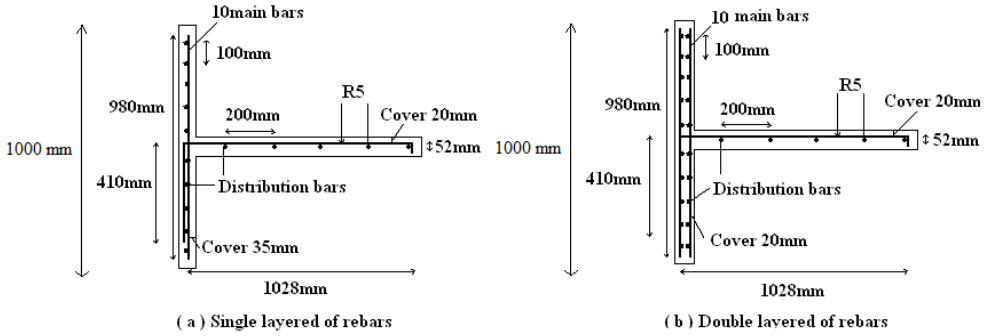

Fig. 2 Details of test specimens

The preparation of the concrete specimens including installation of rebars, preparation of the timber formwork, concrete casting and curing were carried out in the laboratory at the Faculty of Civil Engineering, Universiti Sains Malaysia. The concrete was prepared by the mixer in the lab. The experiment setup is shown in Fig. 3. The specimen was placed by the hydraulic jack that was loaded at a distance of a 580mm from the wall face. The test consisted of two loading cycles. The load was applied gradually in small increment with vertical deflection at A and B recorded. The load applied was measured using a 40kN proof ring. The applied load was halted at load level of 2kN. Then, the specimen was unloaded and recovery of deflection was recorded. After that, the specimen was once again reloaded until the maximum loading was reached. The readings of deflection were taken at every 0.5kN of load increment. Deflection and relevant data at that stage were recorded. The specimen was considered fail when the load was observed to decrease with further increase in deflection.

Fig. 3 Test setup

Results and Discussion

The six specimens of the test results for bending moment at failure are observed to be less than their corresponding predictions. The actual tensile test results of the three rebars samples were consistent with each other with an average value of 817MPa. The cube test results of the six specimens were also found to be consistent with each other in the range from 22MPa to 26MPa. The actual cover had checked by actual dismantling of one plain wall specimen and using cover meter on the remaining five samples. Table 1 shows a summary of all the test results, corresponding predictions based on BS 8110 [5] and the theoretical based on actual concrete cover of the six specimens.

Table 1 Summary of comparisons with theoretical calculation

Specimen	Bending Moment (kNm) at failure			
	Theoretical (actual concrete cover)	Theoretical	Actual	% Difference
1 (S)	5.84	8.41	3.59	-57.31
2 (S)	6.16	8.41	3.81	-54.70
3 (S)	6.80	8.41	3.15	-62.54
1 (D)	5.36	8.41	5.50	-34.60
2 (D)	7.12	8.41	6.31	-24.97
3 (D)	6.16	8.41	7.00	-16.77

The value of concrete cover will influence the effective depth of tension rebar. For the particular structure stiffness, by increasing the stiffness of effective depth will reduce and subsequently contribute to bending capacity. It is due to effective depth, d = thickness - cover - (rebar diameter/2). Specimens with double layered of rebars were found to exhibit bending capacity at failure compare to specimens with single layered of rebars. The crack pattern can be seen in Fig. 4. The cracks were observed to be extending and propagating along with the appearance of new cracks.

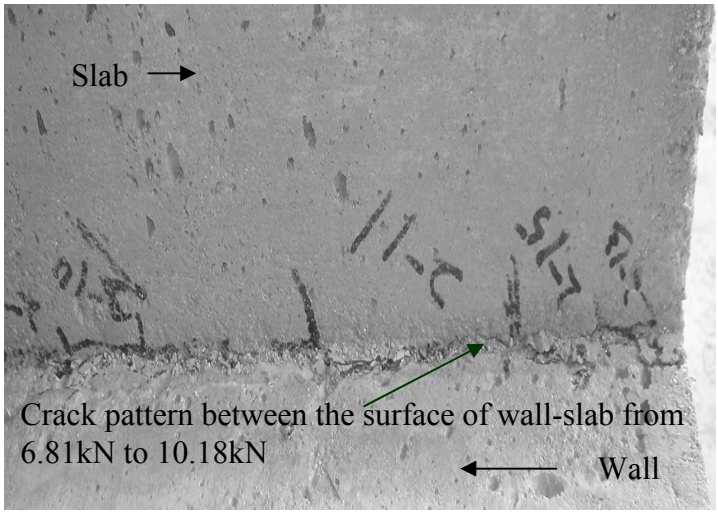

Fig. 4 Crack pattern of specimen 3 (D) at intersection of wall and slab loaded from 6.81kN to 10.18kN

Conclusion

Based on experimental results, specimen which consisted of double layered of rebars in wall provide in the range from 56.25% to 98.86% higher bending capacity to the plain wall system compared with single layered of rebars in wall.

References

[1] S.L. Yeoh: A Computational Study on Plain wall System Considering Floor Slab Flexural Stiffness. (MSc Dissertation, School of Civil Engineering, Universiti Sains Malaysia 2006).

[2] J. Liu and A.A. Abolhassan: Moment-Rotation Parameters for Composite Shear Tab Connections, Journal of Structural Engineering, Vol. 130 (2004), p. 1371-1379.

[3] J.N. Arlekar and C.V. Murty: Approved Truss Model for Design of Welded Steel Moment-Resisting Frame Connections, Journal of Structural Engineering Vol. 130 (2004), p. 498-510.

[4] Y. Liu, J. Zhang, G. Zhang, H. Xu and Y.Gao: Experimental Research on Stability Bearing Capacity of Spliced Segments of Steel Box Column, Journal of Building Structures Vol. 31 (2010), p. 23-27.

[5] British Standard Institution, 1997. BS 8110 : Part 1 : 1997, Structural Use of Concrete, Part 1. Code of Pratice for Design and Construction. British Standards Intitution, p. 21 and 65.

© (2012) Trans Tech Publications, Switzerland
doi:10.4028/www.scientific.net/AMM.187.161

Gear Vibration Monitoring System Based on Virtual Instruments

Chuanhui Wu, Yu Guo (Corresponding author), Yajun Fan

Kunming University of Science and Technology,Kunming 650093, China

kmgary@163.com.

Keywords: condition monitoring and faults diagnosis, vibration analysis,LabVIEW, visual instruments;

Abstract. Vibration analysis is widely used for gear faults diagnosis. A gear vibration monitoring system based on virtual instrument developing platform LabVIEW and vibration analysis technology is developed and introduced in this paper. It satisfies the requirements of machinery condition monitoring and supports function expansion. Online and offline monitoring of gear running states can be realized though this system in both time domain, frequency domain and joint time –frequency domain. Experiments showed that this gear vibration monitoring system can be widely employed in gearbox. System not only guarantees the accuracy of the test results but also provides a friendly user interface for users' easy operation.

Introduction

Signal processing is an efficient tool for gear faults diagnosis, which can analyze gear vibration signal in both time domain, frequency domain and joint time–frequency domain, so it has greatly improved the accuracy of gear faults diagnosis [1]. Machine condition monitoring systems so far, are mainly designed for sophisticated key equipments in enterprises. By stressing full function, versatile, these condition monitoring systems are featured with a large and complex structure, which make the system costly. Thus, they cannot adapt to the condition monitoring requirements of general running equipments and also cannot suit the practical aspects of fault diagnosis education at school. A low-cost rotating machinery condition monitoring system is introduced in this paper to solve these problems mentioned above. It is developed based on virtual instruments developing platform LabVIEW and signal acquisition related hardware. The development of this system is of good academic research value and potential engineering application foreground.

Hardware architecture

For virtual instruments, hardware is the physical foundation. As a result, choosing and installation of hardware parts is very important. The hardware architecture included in the presented vibration monitoring system, shown as Fig.1, is briefly introduced as follows: acceleration sensors (the piezoelectric sensors 4520,4527,4530 series are used in the experiments of this paper) for acquiring vibration signals, charge amplifier (VM-27M, 6 channels) for signal conditioning, such as filtering and amplifying signal, eddy probe (DWQZ) and the corresponding probe adapter for generating RPM pulses, data acquisition card (NI USB-9215) for signal acquisition.

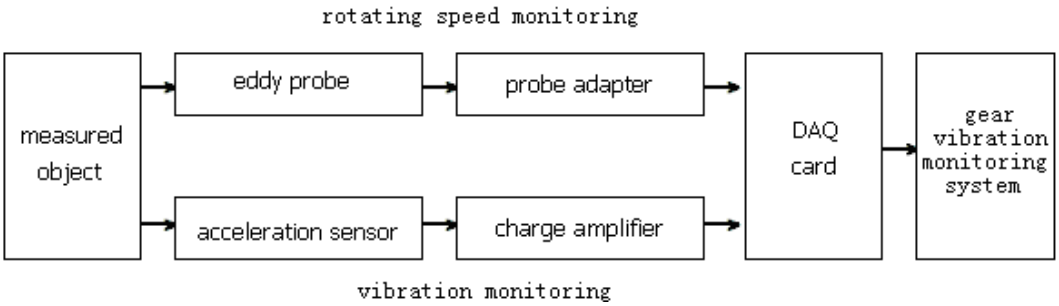

Fig. 1 System hardware architecture

Software architecture

Software of a virtual instrument is the soul of the whole test system. According to the test demands of gear vibration monitoring, the software architecture of the presented system is illustrated as Fig. 2. The system includes two main parts, thus the online analysis and offline analysis. And each part separately use online analysis guide and offline analysis guide to help users to finish online and offline test. Meanwhile, each part has three function modules, time domain analysis module, frequency domain analysis module and joint time–frequency (JTF) domain analysis module. Different analysis methods are included in each module.

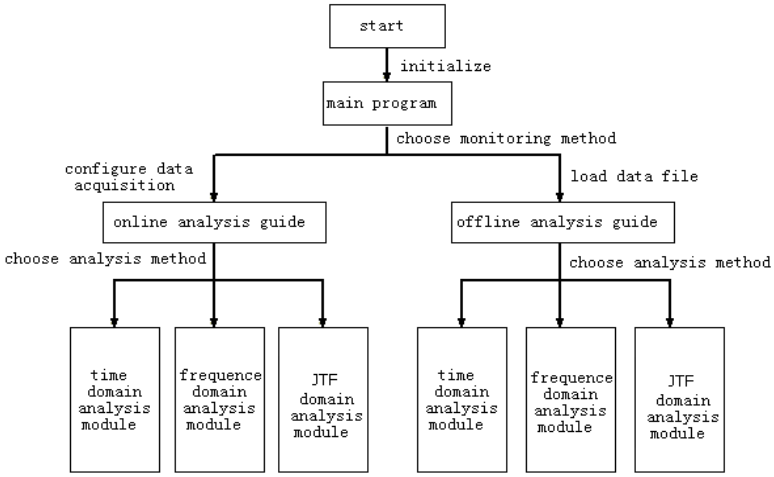

Fig. 2. Software architecture of gear vibration monitoring system

Online monitoring

The basic requirements for online monitoring are, on the one hand, the data acquired has to be completed and real –time; on the other hand, signal analyzing methods used must be effective, the raw data has to be stored in time based on the rules that we assign. To reach these goals, many creative methods have been utilized in this system as list below.

- To ensure data completeness when they are acquired with high sampling rate. As the frequency-band of a gear vibration signal can reach 10 kHz, the sampling frequency of the DAQ device should be at least 25.6 kHz. Therefore, a sampling rate of 40 kHz is used in following experiments. To solve this problem, a so called producer/consumer design pattern of LabVIEW is employed in the micro system. The producer acquires data and then put it into a queue; the consumer reads data from the same queue established before by producer. At the same time, the consumer deal with data analysis and storage too. Thus, the acquiring data are complete and of real-time in the micro system
- Data storage. It includes the format of data to be stored, and the attribute information of data that should be added to the data file. For data storage format, the TDMS format of LabVIEW is selected, because it has quite high storing speed and of small files size. For the attribute information, it provides more test environment information for offline analysis, such as, the title of measured object, the organization of test etc. The information have to be acquired previously when user try to configure a test, then the only thing one has to do is to add those information to the TDMS data file.
- Data transfers between different analysis modules. The use of producer/consumer design pattern makes data transferring much more easily. When online analysis call different function modules, just add a queue operation to read these data in the queue established in online guide.
- In online analysis, a user guide interface is provided to guide user to finish online gear vibration test (see Fig. 3), which includes three steps: viz. data acquisition parameter configure, online analysis parameter choose, analysis method choose. When all three steps are done, one can view the test result. For example, the vibration severity and real time alarming can be obtained in time domain analysis and the STFT can be performed in JTF domain analysis.

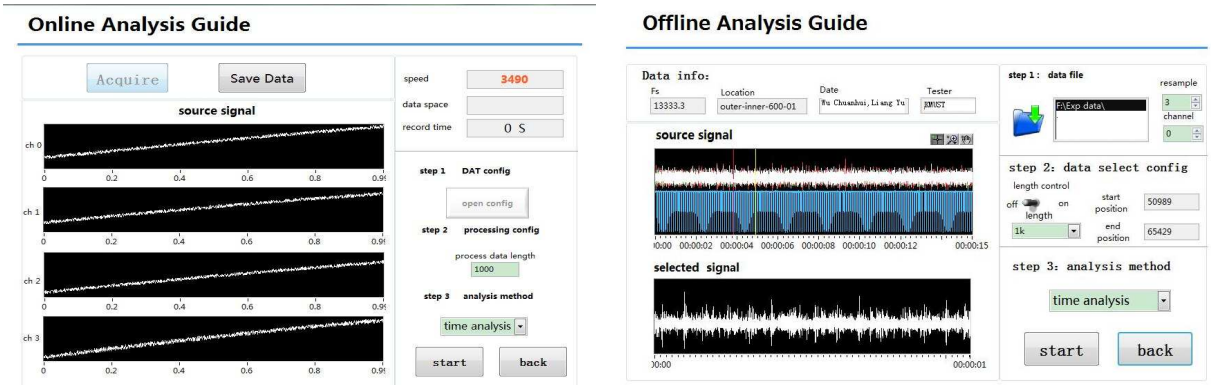

Fig. 3. (a) Online analysis guide interface; (b) Offline analysis guide interface

Offline analysis

Offline monitoring is provided for analyzing the data that have been acquired before and stored in data files. Compared with online analysis, offline analysis is more accurate. Because the data is static, so it is better for gear faults diagnosis. Offline analysis also includes three steps to guide user to finish offline monitoring process.

Step one, user should specify a file path and assign the channels to a multi-channel acquisition data for loading a data file. Step two, truncate the loaded data to suit the following analysis, since the data loaded from file may be too huge for JTFA computation; Step three, an analysis approach is assigned for time domain analysis, frequency domain analysis or joint time frequency domain analysis, which is introduced as follows.

Time domain analysis. By analyzing time history of signals directly, it provides a qualitative judgment on the periodicity and randomicity of vibrations. Then, the running condition of the observed devices can be estimated. Time domain analysis functions include: statistical parameters, such as vibration severity, mean, root mean square, peak value, variance, dimensionless characteristic factors (crestfactor, shapefactor, impulsefactor, clearancefactor, skewness, kurtosisfactor) and the probability density distribution analysis etc. It is worth mentioning that vibration severity is also employed to realize the alarm function automatically for the monitored machinery in the condition monitoring system according to ISO10186-3 standard.

Frequency domain analysis. By transferring the signal in time domain into frequency domain, the frequency components consisted in the signal is highlight, which make the inferring of the sources of vibrations obviously. The advantages of frequency domain analysis make it widely used in faults diagnosis. The spectral analysis of gear faults mainly focus on the side-band frequency. Besides the amplitude spectrum and power spectrum, the cepstrum analysis method and the envelope analysis method are included in the frequency domain analysis of the monitoring system.

Joint time-frequency domain analysis. One of the most prominent features of this system is its joint time-frequency analysis (JTFA) module. JTFA is an efficient tool for nonstationary signal processing with an insight to the signals' time–varying characteristics, which can be generated by most machinery faults[3]. For example, the Short Time Fourier Transform (STFT) is one of the widely used JTFA functions, which is defined in [4]. The result of JTFA actually represents a one dimension time signal with two dimensions time–frequency density function, aiming at revealing how much frequency components are there in the signal, and how these components change with time. There are STFT, Wigner-Ville Distribution (WVD), Choi-Williams Distribution (CWD), Empirical Mode Decomposition (EMD), Self-adaptive time–frequency analysis etc. are integrated in this monitoring system for nonstationary vibration analysis. It is worth mentioning that only STFT is designed for online analysis in all the JTFA functions.

System integration and test.

System integration. According to the system architectures mentioned above, function modules and interfaces are programmed in LabVIEW. Then, all modules and interfaces are integrated to the monitoring system. The event structure is the key to perform the dynamic call subroutines (or subvis in LabVIEW) corresponding to different analysis functions. The property nodes techniques in LabVIEW are employed to display or hide different interfaces. By these way, not only the

running efficiency of the mornitoring system is improved, but also the users' misoperation can be avoided as far as possible. All these considerations ensure that the monitoring system can run efficiently and reliably in any condition monitoring duties.

Test example. An example of gear fault test is introduced here to show the ability of this monitoring system. The test rig is shown as Fig. 4 (a)The test details are listed as follows: the test object is a 41 teeth gear with a spalling fault; the speed of the shaft is 600r/min; the sampling ratio is 40 kHz with corresponding anti-aliasing filtering. The test result of offline JTFA (STFT) is shown as in Fig. 4 (b).

Move the cursor in the frequency spectrum (left hand side) and read the values of peaks, then, the frequency of each peak is around 409 Hz, 820 Hz, 1232 Hz, 1633 Hz. Theoretically, gear-mesh frequency should be 410Hz, and the 2×, 3×, 4× harmonic frequencies should be 820Hz, 1230Hz, 1640Hz respectively. It is clear the peakvalues in the spectrum are well matched with the characteristic frequencies of the gear mesh. The spectrogram shows that the peaks are more stable. By evaluating all these characteristic frequencies and the rotating parts in the monitored object comprehensively, a fault diagnosis conclusion can be reached that the fault is corresponding to spalling.

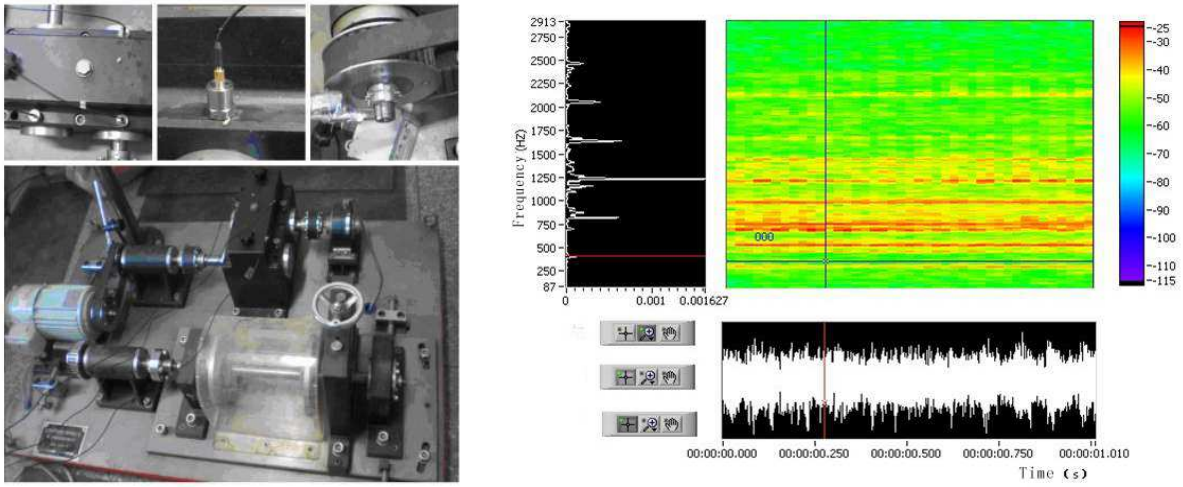

Fig. 4. (a)Test rig; (b) JTFA test result

Conclusion

This paper discussed a gear vibration monitoring system based on virtual instrument. The system can be used for signal acquisition, signal storage, signal online and offline analysis in time domain, frequency domain and joint time-frequency domain. Tests verified the validity of this system. It takes the advantages of short developing time, low cost, reliability and good expansibility, which make it have a good application foreground in educational training and the low cost condition monitoring for general machinery.

Acknowledgement

The Project sponsored by National Undergraduates Innovating Experimentation Project (Grant no. 091067410).

References

[1] Shi Guangfan, Yan Guangming, Li Jigang. The design and implement of virtual instrumentbased on computing technique and USB platform. ICITA'05.

[2] John Wiley, Sons Ltd, Signal Analysis.1999

[3] Shie Qian, Dapang Chen. Joint time-frequency analysis. IEEE signal processing magazine; Mar,1999.

[4] Igor Djurovic, LJubisa Stankovic. A virtual instruments for time –frequency analysis. IEEE transactions on instrumentation and measurement ;vol.48,no.6,Dec.1999

© (2012) Trans Tech Publications, Switzerland
doi:10.4028/www.scientific.net/AMM.187.165

Design and Dynamic Walking Control of Humanoid Robot SCUT-*I*

Bi Sheng[a], Zhuang Zhongjie, Min Huaqing,Mo Huaxi

South China University of Technology,Guangzhou 510006,China

[a]picy@scut.edu.cn

Keywords: Humanoid robot, Dynamical walking, Control system structure, Sensor fusion.

Abstract. The basic configuration and control method of the humanoid robot SCUT-I are presented. SCUT-I, developed by the Robot and Intelligent Software Laboratory in South China University of Technology, 58.2 centimeter tall and 3.9 Kg weight with 21 degree of freedom (DoF), was designed to be humanlike including two legs, two arms, a trunk and a head. The mechanical design, hardware description, sensor fusion and motion control schemes of SCUT-I are represented, and a kind of dynamical walking control schemes based on linear inverted pendulum model (LIPM) and attitude sensor feedback control is proposed.

Introduction

Humanoid robots are expected to take an important role in assisting human activities in human daily environments because of their flexibility and friendly appearance. There are a number of humanoid robots that have been recently built throughout the world. The prototypes WABIAN [1], Honda [2], HRP-2 [3], Johnnie [4] have been designed for performing static and dynamic walking in several environments.

The control of a humanoid is a challenging task due to many degrees of freedom involved and the non-linear model, and it is hard to stabilize dynamics [5]. Compared with other legged robots, a humanoid biped robot is more difficult to design and control[6] . Compactness, lightness, high joint torques, large joint range, low backlash and friction need to be considered for mechanical design. Control of such a naturally unstable system is not an easy project. Without efficient and safe control algorithm and reliable hardware, the humanoid robot may fall down and the damage is fatal.

SCUT-I robot is designed by Robot and Intelligent Software Laboratory of South China University of Technology. It won the champions of RoboCup China Open 2008 in RoboCup Soccer Humanoid League. It also got champion in 2009 Cross-strait Exchanges Robot Competition in the humanoid soccer games.

Fig.1. SCUT-I Robot in Robocup Soccer game

SCUT-I robot can fulfill all kinds of basic bipedal walking, such as walking, climbing stairs[7]and so on. It can also receive commands from keyboard or remote computer via wireless LAN. Several kinds of sensors are used to help robot to feel the world.

Mechanical Design

The robot has a height of 582mm, and only weights 3.9 Kg, including batteries. The detailed dimensions are shown in Fig.2. The robot has 21 servo motors: 6 in each leg, 3 in each arm, 2 in the head, and 1 in the trunk. The 3DoF orthogonal hip joint and 2DoF orthogonal ankle joint altogether make the bipedal walking possible, and the joint in the trunk allows the robot to execute various kinds of movements, such as kicking, goal keeping, getting up from the ground and etc.

For SCUT-I robot, three types of actuators are used: Dynamixel RX-64[8], RX-28 and RX-10 servo motors produced by Robotis Company. RX-64 actuators are used in the joints that are important for bipedal walking such as hips, knees, ankles, and the trunk. RX-28 actuators are used in elbows and the Shoulder where less torque is needed. RX-10 actuators are used in head where least torque is needed (shown in Table1).

Table 1. DoF assignment for SCUT-I robot

Joint	DoF	Angle Range	Actuator
Head	Yaw×1	-80° ～ 80°	RX-10
	Pitch×1	-5° ～ +80°	RX-10
Shoulder	Pitch×2	-90° ～ +180°	RX-28
	Yaw×2	-20° ～ +180°	RX-28
Elbow	Pitch×2	-5° ～ +130°	RX-28
Trunk	Pitch×1	0° ～ +130°	RX-64
Hip	Roll×2	-30° ～ +60°	RX-64
	Yaw×2	-45° ～ +70°	RX-64
	Pitch×2	-60° ～ +120°	RX-64
Knee	Pitch×2	-12° ～ 0°	RX-64
Ankle	Pitch×2	-60° ～ +45°	RX-64
	Yaw×2	-60° ～ +70°	RX-64
Total	21 actuators		

The mechanical structure SCUT-I robot and DoF assignment in the whole body can be seen in Fig.2.

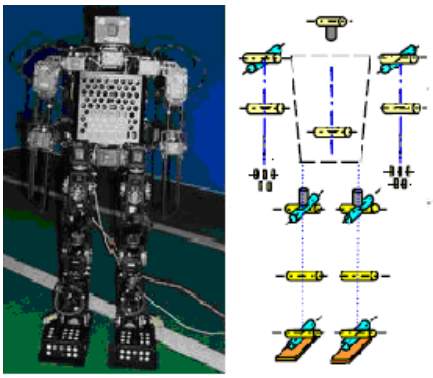

Fig.2. The structure of SCUT-I robot

Electrical Design and Sensors

Electrical Design. SCUT-I robot can receive commands from keyboard and remote computer. It can also communicate with other robots via wireless LAN. The block diagram of electrical system for SCUT-I robot is described in Fig.3. The main computer, which is PC-104 with 500MHz processor (AMD GeodeLX 800), 256MB DDR RAM and 2G ROM, is used in SCUT-I robot. The PC-104 board computer receives information from the CCD camera via the USB port. It computes the walking path and sends locomotion command to the motion control board. Motion control board, which is STM32 MCU sub control board with 70MHZ processor (STM32F103ZCT), can control motor via RS485 port and receive information from IMU (Inertial Measurement Unit) sensor.

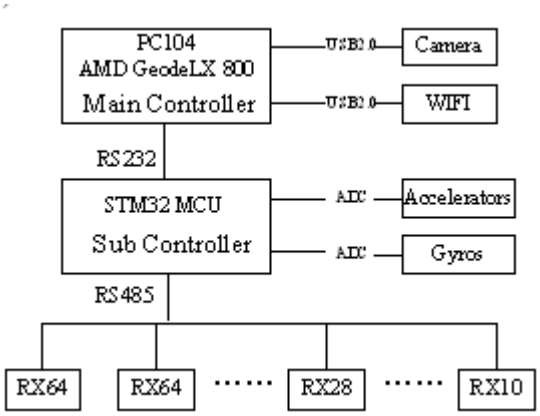

Fig.3. The block diagram of electrical system

Sensors. SCUT-I robot has image processing system so that it can recognize objects. So it need image sensors.

It is necessary for biped robots to estimate the absolute attitude for controlling the absolute posture, so that biped robots can continue dynamically stable walking. For estimating attitude, it need IMU sensor.

Our robot is equipped with image sensors and IMU sensor.

(1) Image sensors

A Logitech Pro 5000 web camera is used as the vision sensor, and the field of view is about 51°×37°. As the field of view is not wide enough, the robot has to rotate its head to scan the environment. The Logitech Pro 5000 camera is connected to the main controller via a USB cable. And image series of a resolution of 640×480 can be provided in real time by 30 frames per second.

SCUT-I robot can track objects by image sensor. In RoboCup Soccer, image sensors are used in SCUT-I robot to track football, white line and goal etc. The whole process is as follows:

(a) Color Segmentation.

We implemented a fast method of color segmentation based on a color look-up table[9]. Firstly, images of objects, such as goal, ball, beacon and etc, are captured and stored. Then the pixels in the images are manually labeled as the color it belongs to. And the color look-up table is generated when the program initializes. Since it is necessary that the look-up table covers the whole color space (HSI), which consists of 256×256×256 pixels, the storage size of the look-up table will be huge.

(b) Object Recognition

Object recognition is retrieved from left to right, and from top to bottom. During the scanning, each pixel is classified using the color look-up table. A characteristic series of colors or a pattern of colors, are used for object recognition.

(2) Inertial Measurement Unit (IMU)sensor

IMU has two kinds of sensor: gyroscopes, accelerators.

Gyroscopes estimate attitude through integrating the angular velocity. But the error of estimated attitude is accumulated by the integration in this case.

Accelerators can also estimate the attitude by the direction of gravity. Outputs of Accelerators contain the acceleration by motions and the gravity acceleration. When the direction of gravity acceleration is estimated, the acceleration other than the gravity acceleration becomes the factor of the error.

The problem in SCUT-I robot is overcome by Kalman filtering, shown in Fig.4. The data which are obtained from these sensors are generally fused, so that the accuracy of the attitude estimation is improved[10-11].

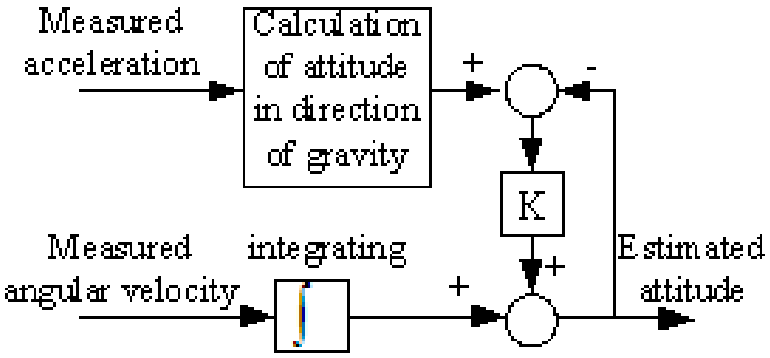

Fig.4. The block diagram of sensors fusion

K is Kalman gain in Fig.4.

On SCUT-I robot, acceleration chip is ADXL204[12], which is a kind of Dual-Axis chip produced by ADI company. Gyroscopes chip is IDG-300[13], which is a kind of Dual-Axis chip produced by InvenSense company.

We selected appropriate noise covariance Q and R as follows:

$$Q = \begin{bmatrix} 0.8 & 0 \\ 0 & 0.7 \end{bmatrix} \quad R = [0.5]$$

According to kalman filtering equation[11], the result in Fig.5 is gotten when SCUT-I robot is walking forward. Gyroscope data and accelerometer data are fused. Before the fusion the Gyroscope measurement is quite noisy. The fusion result becomes more stable after the gyroscope data is fused with accelerometer.

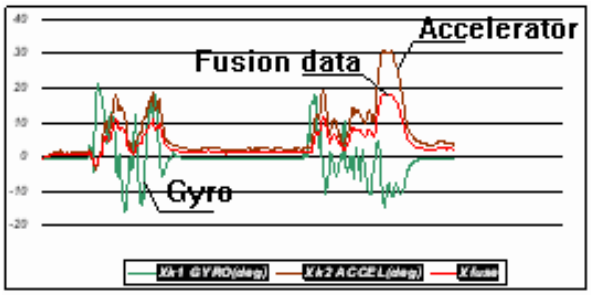

Fig.5. Fusion IMU data from robot forward walking

Dynamic Control And Stability

Dynamic Walking Control Scheme. The adopted walking control scheme is classified into two parts (shown in Fig.6): (a) The walking pattern is pre-generated by the pattern generation which ensures the biped robot's stable walk on the flat surface. (b) The sensory feedback controller works in real-time to modify the generated pattern to adapt to unexpected disturbances and the uncertainty of the surfaces according to the information of sensors implemented in the biped robot.

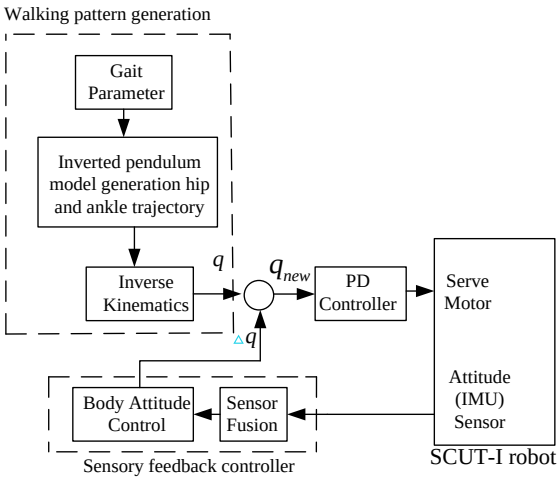

Fig.6 Architecture of the walking controller

(1) Walking pattern generation

Humanoid walking is a periodic motion which alternates between the single support phase and the double support phase. In the single support phase, only one foot is in contact with the ground to support the humanoid, and the other leg swings forward. In the double support phase, both of the humanoid feet are in contact with the ground.

The process of walking pattern generation is shown in Fig.6.

We select 5 parameters to control SCUT-I robot to walk (seen as Eq. (1)). Where s is step length, $T_{\sup}$ is one walking cycle period, T_d is double support-phase time, h_{foot} is the height of swing foot, h_c is the height of Center of Mass(CoM).

$$P_{robot} = f(s, T_{\sup}, T_d, h_{foot}, h_c) \tag{1}$$

According to these 5 parameters and linear inverted pendulum model, all the joints trajectory can be designed.

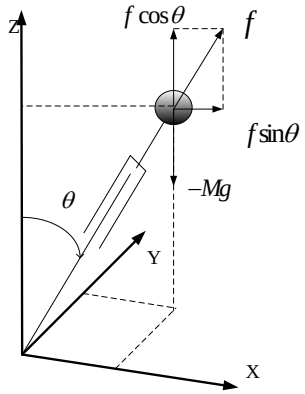

Fig.7. The model of linear inverted pendulum

The linear inverted pendulum model is shown in Fig.7 and described by the Eq.(2) and Eq.(3) [14]. Where $T_c = \sqrt{g/h_c}$.

$$x(t) = x(0)\cosh(t/T_c) + T_c\dot{x}(0)\sinh(t/T_c) \tag{2}$$

$$y(t) = y(0)\cosh(t/T_c) + T_c\dot{y}(0)\sinh(t/T_c) \tag{3}$$

According to Eq.(2) and Eq.(3), we can get the hip joint trajectory and ankle joint trajectory. Then we use Inverse Kinematics method to get the other joint trajectory. At last we get all the joints trajectory and generate SCUT-I robot walking gait.

(2) Sensory feedback controller

According to IMU sensor, we can get attitude of the robot. The walking motion is stabilized by the attitude feedback controller for SCUT-I robot. The controller is designed using PD controller and shown in Eq.(4).

$$q_{new} = q + k_p * \Delta q + k_d * \frac{d\Delta q}{dt} \tag{4}$$

Where q and q_{new} represent the angles in foot pitch, foot roll, hip pitch, hip roll, waist pitch, shoulder roll and shoulder pitch; Δq is the adjustment value of body attitude control, k_p and k_d are the hand optimized control parameters and t is the time.

The improvement of stability is achieved by the attitude controller.

Walking Stability Analysis. Walking stability of Humanoid is very important. Zero Moment Point (ZMP)[15] is used as the criterion for walking stability of SCUT-I robot. The ZMP equation is shown as follows:

$$x_{zmp} = \frac{\sum_{i=1}^{13}(m_i(\ddot{z}_i + g)x_i - m_i(z_i - z_{zmp})\ddot{x}_i}{\sum_{i=1}^{13} m_i(\ddot{z}_i + g)} \tag{5}$$

$$y_{zmp} = \frac{\sum_{i=1}^{13}(m_i(\ddot{z}_i + g)y_i - m_i(z_i - z_{zmp})\ddot{y}_i}{\sum_{i=1}^{13} m_i(\ddot{z}_i + g)} \tag{6}$$

where (x_i , y_i, z_i) is the position of the mass center of link i, m_i is the mass of link i and n is the number of link, z_{zmp} is the height of ZMP point.

The ZMP position of Humanoid robot is used to estimate the stability of the robot. The distance between ZMP and the center of support polygon (shown in Fig.8) is used to decide the stability of the robot, seen as in Eq.(7) and Eq.(8)

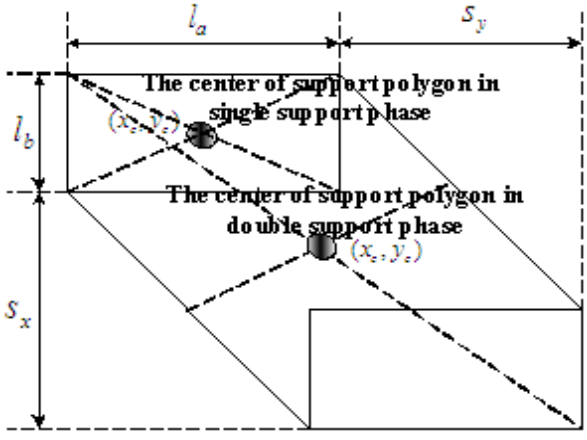

Fig.8. Supporting polygon area

$$\Delta zmp_x = x_{zmp} - x_c \tag{7}$$

$$\Delta zmp_y = y_{zmp} - y_c \tag{8}$$

In double support phase, Δzmp_x and Δzmp_y should be satisfied with Eq.(9) and Eq.(10) when humanoid robot walking stably.

$$-(l_a + s_x)/2 \le \Delta zmp_x \le (l_a + s_x)/2 \tag{9}$$

$$-(l_b + s_y)/2 \le \Delta zmp_y \le (l_b + s_y)/2 \tag{10}$$

Where s_x is the step length in x axis, s_y is the step length in y axis, l_a is the length of foot, l_b is the width of foot.

In single support phase, Δzmp_x and Δzmp_y should be satisfied with Eq.(11) and Eq.(12) when humanoid robot walking stably.

$$-l_a/2 \le \Delta zmp_x \le l_a/2 \tag{11}$$

$$-l_b/2 \le \Delta zmp_y \le l_b/2 \tag{12}$$

Experiments. In humanoid robot walking experiments, the adopted walking control planning algorithm has played an important role.

According to Eq.(9)-(12) and some parameters(s_x = 0.1m, s_y =0.1m, l_a =0.138m, l_b =0.08m), when $-0.119 \le \Delta zmp_x \le 0.119$, $-0.09 \le \Delta zmp_y \le 0.09$ in double support phase, and $-0.069 \le \Delta zmp_x \le 0.069$, $-0.04 \le \Delta zmp_y \le 0.04$ in single support phase, SCUT-I robot can walk stably.

The results Δzmp_x and Δzmp_y of SCUT-I robot walking forward is given in Fig.9 and Fig.10.

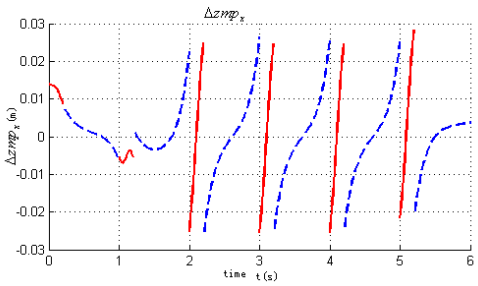

Fig.9. The curve of Δzmp_x

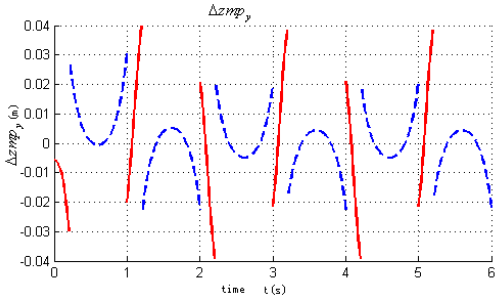

Fig.10. The curve of Δzmp_y

In Fig.9 and Fig.10, solid line represents double support phase and dashed line represents single support phase. According to the curve Δzmp_x and Δzmp_y, SCUT-I robot walks stably.

Conclusion

In this paper the design of the 58.2cm tall, autonomous SCUT-I robot has been described. SCUT-I robot is a self-autonomous humanoid robot, with 1 camera, 1 Dual-Axis accelerator and 1 Dual-Axis Gyroscope and 21 actuators integrated on its body, controlled by a PC 104 computer system.

The specifications and functions of SCUT-I robot, some related works on gait planning, sensor fusion and vision are presented. A kind of dynamical walking control scheme based on linear inverted pendulum model is proposed, which helps SCUT-I robot walk stably. Meanwhile, attitude sensor feedback control techniques are integrated into this gait tuning process, which will be the focus of our future work.

References

[1] Yamaguchi Jin-ichi and Takanishi Atsuo, “Development of a biped walking robot having antagonistic driven joints using nonlinear spring mechanism,” IEEE International Conference on Robotics and Automation,1997,vol.l, pp.18-192.

[2] Hirae K and HiroseM, “The development of Honda robot.” Proceedings of the 1998 IEEE International Conference on Robotics and Automation , USA:IEEE, 1998, pp. 1321-1326.

[3] Kaneko Kenji, Kanehiro Fumio and Kajita Shuuji, et al. Ota, “Design of prototype humanoid robotics platform for HRP.” IEEE International Conference on Intelligent Robots and Systems, 2002, vol.3, pp.2431-2436.

[4] K. Löffler, M. Gienger and F. Pfeiffer, “ Sensors and control concept of walking "Johnnie".” The International Journal of Robotics Research, 2003, Vol. 22, pp. 229-239.

[5] Marc Raibert, Legged robots that balance, MIT Press,Cambridge, MA, 1986.

[6] Jian Wang, Tao Sheng , Hongxu Ma ,et al, “Design and dynamic walking control of humanoid robot Blackmann,” Proceedings of the 6th World Congress on Intelligent Control and Automation, CHINA:IEEE, 2006, pp. 8848-8852.

[7] Bi Sheng, Min Huaqing, Liu Qifeng, et al, “Multi-objective optimization for a humanoid robot climbing stairs based on Genetic Algorithms, ” 2009 IEEE International Conference on Information and Automation. CHINA: IEEE,2009,pp.66 -71.

[8] Robtis company, “Dynamixel RX-64 user’s manual v1.10,” pp.1-49

[9] James Bruce, Tucker Balch, Manuela Veloso, “Fast and inexpensive color image segmentation for interactive robots,” International Conference on Intelligent Robots and System. Japan:IEEE,2000,pp. 2061-2066.

[10] Masato Takahashi,Koichi Nishiwaki,Satoshi Kagami, et al, “Development and evaluation of an attitude measuring system that uses acceleration information of walking for biped robots,” IEEE SENSORS 2007 Conference.IEEE,2007,pp.292-295.

[11] Greg Welch and Gary Bishop, “An introduction to the Kalman filter,” unpublished,2006,pp.1-16.

[12] Analog Device, “ADXL204 datasheet,”2006,pp.1-12.

[13] InvenSence Device, “IDG-300 datasheet,”pp.1-17.

[14] Shuuji Kajita, Fumio Kanehiro, Kenji Kaneko, et al. “The 3D linear inverted pendulum mode: A simple modeling for a biped walking pattern generation,” Proceedings of IEEE/RSJ, International Conference on Intelligent Robots and Systems:IEEE, 2001,pp.239-246.

[15] Miomir Vukobratovic, “Zero-moment point -thirty five years of its life,”International Journal of Humanoid Robotics,vol.1, no.1,2004,pp.157-173.

© (2012) Trans Tech Publications, Switzerland
doi:10.4028/www.scientific.net/AMM.187.173

Maximum bending moment and maximum additional bending moment for high vertical vessels under wind pressure

Tian Jian, Zhang Zhongning[a]

School of Mechanical Engineering Shenyang University of Chemical Technology, Shenyang, 110142, China

[a]zhongningzhang@126.com.

Keywords: High vertical vessels; maximum bending moment; wind load; weight

Abstract. On the basis of analyzing all forces on the self-supported vertical vessels, the superposition method in mechanics of materials and a MATLAB program are used to calculate the maximum wind bending moments of the high vertical vessels caused by both weight and linear distributed wind pressure. The results show that the effect of weight to wind bending moments of the heavy weight high columns can not be ignored. And a special formulation for calculating the maximum wind bending moment is deduced which can be directly used for strength and/or stability calculations.

Introduction

With the continuous emergence and development of large-scale petrochemical enterprises, the number of high vertical vessels with larger slenderness ratio is also increasing. Under wind loads such vertical vessels will have large static deflections [1], bending moments, and additional bending moments arising from the eccentric gravity, which will eventually form large stresses in vertical vessel body and skirt leading to strength and/or stability failure. The vertical vessels design standard in China steel vertical vessels supported by skirt [2] ignored the additional bending moments.

The following shows the analysis and calculations of the maximum bending moment and the maximum additional bending moment to the vertical vessels caused by weight using the superposition method of mechanics of materials and a MATLAB program created by us.

Analytical Mechanics Model

A vertical vessel of height H is subjected to a horizontal distributed wind load as shown in Fig 1. The total mass of the vertical vessel M is evenly distributed along the column of the same cross-section. The stiffness of the vertical vessels is EI.

Assume that the total mass is evenly distributed on the n-particles, then the mass of each particle m = M/n occupying a height of h = H/n. The height of a particle with number i, j (counting from the top of the vertical vessel) is

$$H_i = H + \frac{h}{2} - h \cdot i = H \cdot (1 + \frac{1}{2n} - \frac{i}{n}) = a_i H$$

$$H_j = H + \frac{h}{2} - h \cdot j = H \cdot (1 + \frac{1}{2n} - \frac{j}{n}) = a_j H \quad (1)$$

The vertical vessel subjected to a horizontal linear distributed wind load will be bended into a curve as shown in Fig 1 in the shape of a solid line. Under such condition, the gravity mg acting on each particle becomes an eccentric load causing further deformation of the vertical vessel in the shape of a dotted line as shown in Fig 1. The influences of weight on the deflections and bending moments can be calculated by the superposition principle of mechanics of materials. It is easy to see from Fig 1 that the greater the value of n, the closer the analytical mechanics model to the actual vertical vessel and the higher the accuracy of calculation results.

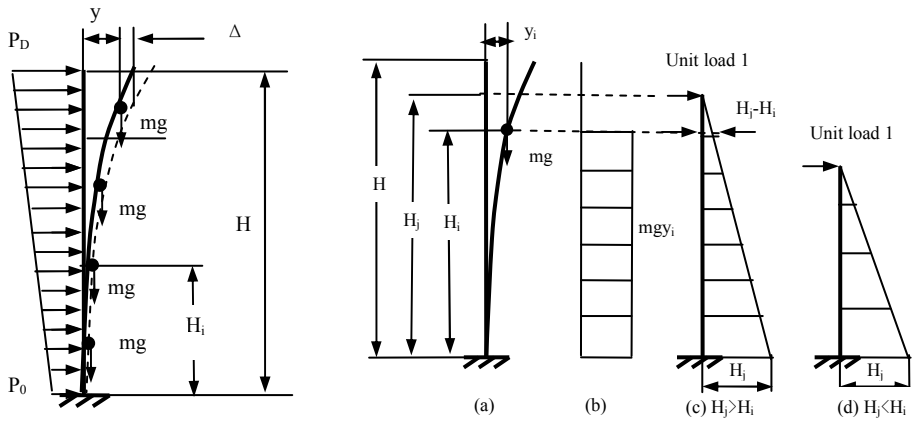

Fig. 1. Analytical Mechanics Model

Fig. 2. Deformation and Bending Moment Diagrams for Calculation

The deflection calculation

The vertical vessel subjected to a horizontal wind load will be bended into a curve as shown in Fig 1 in the shape of a solid line. The deflection of a particle with number i counting from the top of the vertical vessel [see Fig 2 (a)] is [3, 4]

$$y_i = \frac{P_0 H_i^{\,2}}{24\,EI}(H_i^{\,2} - 4HH_i + 6H^2) + \frac{(P_D - P_0)H_i^{\,2}}{120\,EIH}(20H^3 - 10H^2 H_i + H_i^{\,3}) = b_i \frac{P_0 H^4}{EI} + c_i \frac{P_D H^4}{EI} \tag{2}$$

This is the eccentric distance of the particle from the vertical vessel axis. With such an eccentric gravity mg the vertical vessel will undergo a combined deformation of bending and compression. The bending moments will be mgy_i [see Fig 2 (a)]. Fig 2 (b) is the bending moment diagram under applied force. The height of a particle j counting from the top of the vertical vessel is H_j. Fig 2 (c) is the bending moment diagram under a horizontal unit load on the particle j (when j < i). Fig 2 (d) is the bending moment diagram under a horizontal unit load on the j particle (when j ≥ i). The deflection of the particle j due to the eccentric gravity of the particle i can be calculated by multiplying the quantity on these bending moment diagrams (using unit load method [3, 4] of Mechanics of Materials).

$$\Delta_{ji} = \frac{w\overline{M_C}}{EI} = \frac{\frac{1}{2}H_j H_j \cdot mgy_i}{EI} = \frac{mg \cdot H^6}{E^2 I^2}(b_i \cdot P_0 + c_i \cdot P_D)\ a_j^{\,2}/2) = \frac{mg \cdot H^6}{E^2 I^2}(d_{1i}P_0 + dd_{1i}P_D) \qquad \text{(where } j \geq i\text{)} \tag{3}$$

$$\Delta_{ji} = \frac{w\overline{M_C}}{EI} = \frac{\frac{1}{2}(H_j - H_i + H_j)\cdot H_i \cdot mgy_i}{EI} = \frac{mg \cdot H^6}{E^2 I^2}(b_i \cdot P_0 + c_i \cdot P_D)(a_j - a_i/2)a_i$$

$$= \frac{mg \cdot H^6}{E^2 I^2}(d_{2i}P_0 + dd_{2i}P_D) \qquad \text{(where } j < i\text{)} \tag{4}$$

Due to the fact that there are n particles that are uniformly distributed over the vertical vessel height, when analyzing the effect of weight on the deflection of the particle j, a superposition of deflections, which are caused by individual particles on the particle j due to each eccentric gravity, must be made to obtain the additional deflection of the particle j.

$$\Delta_j = \sum_{i=1}^{n}\Delta_{ji} = \frac{mg \cdot H^6}{E^2 I^2}[(\sum_{i=1}^{j} d_{1i} + \sum_{i=j+1}^{n} d_{2i})P_0 + (\sum_{i=1}^{j} dd_{1i} + \sum_{i=j+1}^{n} dd_{2i})P_D] \tag{5}$$

Recalling for Eq. (2), the total deflection on the j particle is

$$\omega_j = y_j + \Delta_j = b_j \frac{P_0 H^4}{EI} + c_j \frac{P_D H^4}{EI} + \frac{mg \cdot H^6}{E^2 I^2}[(\sum_{i=1}^{j} d_{1i} + \sum_{i=j+1}^{n} d_{2i})P_0 + (\sum_{i=1}^{j} dd_{1i} + \sum_{i=j+1}^{n} dd_{2i})P_D] \tag{6}$$

Where the a_i, a_j, b_i, b_j, d_{1i} , d_{2i} , dd_{1i} , dd_{2i} in the above formulations and e_1, e_2 , ee_1, ee_2 in the latter formulations are constants which can be calculated by a MATLAB program.

The calculation of maximum bending moment and maximum additional bending moment caused by weight

By each particle's deflections, it is easy to obtain the maximum wind moment

$$M_{\max}=\sum_{j=1}^{n}mg\omega_j=\sum_{j=1}^{n}[b_j\frac{mgP_0H^4}{EI}+\frac{m^2g^2P_0H^6}{E^2I^2}(\sum_{i=1}^{j}d_{1i}+\sum_{i=j+1}^{n}d_{2i})]+\sum_{j=1}^{n}[c_j\frac{mgP_DH^4}{EI}+\frac{m^2g^2P_DH^6}{E^2I^2}(\sum_{i=1}^{j}dd_{1i}+\sum_{i=j+1}^{n}dd_{2i})]$$

$$=e_1\frac{MgP_0H^4}{EI}+e_2\frac{M^2g^2P_0H^6}{E^2I^2}+ee_1\frac{MgP_DH^4}{EI}+ee_2\frac{M^2g^2P_DH^6}{E^2I^2} \quad (7)$$

Where the maximum additional wind moment caused by weight is

$$M_{add}=e_2\frac{M^2g^2P_0H^6}{E^2I^2}+ee_2\frac{M^2g^2P_DH^6}{E^2I^2} \quad (8)$$

Based on the above analysis, a computational program is developed using MATLAB language to solve the problems. For the number of segments n = 1, 2, 3, 4, 6, 8, 10, 20, the following results are obtained from the computations using the MATLAB program.

It can be seen from the Table 1 that as long as the vertical vessel is divided into more than three segments for calculating the maximum wind moment in a similar manner, the precision in engineering calculation will be met. For high vertical vessels with the same cross-section, the maximum wind moment and the effect of weight on the maximum wind moment under linear wind load can be calculated by the following formula which can be used in engineering calculations

$$M_{\max}=\frac{MgH^4}{EI}(0.1271P_D-0.0771P_0)+\frac{M^2g^2H^6}{E^2I^2}(0.0149P_D-0.0071P_0)$$

$$=\frac{MgH^4}{EI}[0.1271P_D-0.0771P_0+\frac{Mg\cdot H^2}{EI}(0.0149P_D-0.0071P_0)] \quad (9)$$

$$M_{add}=\frac{M^2g^2H^6}{E^2I^2}(0.0149P_D-0.0071P_0) \quad (10)$$

This formula shows that the effect of weight on the maximum additional wind moment depends on the total weight of the vertical vessel, the height of the vertical vessel, the distributed wind load, and the stiffness of the vertical vessel. When the vertical vessel is heavy in weight and larger in slenderness ratio, the influence of weight on the wind bending moments must be considered.

Table 1. Computational Results from the MATLAB Program.

n	1	2	3	4	6	8	10	20
e_1	-0.0818	-0.0785	-0.0777	-0.0774	-0.0772	-0.0772	-0.0771	-0.0771
Error	6.10%	1.82%	0.78%	0.39%	0.13%	0.13%	0%	0%
ee_1	0.1260	0.1268	0.1270	0.1270	0.1271	0.1271	0.1271	0.1271
Error	0.87	0.24%	0.08%	0.08%	0%	0%	0%	0%
e_2	-0.0102	-0.0081	-0.0076	-0.0074	-0.0072	-0.0072	-0.0071	-0.0071
Error	43.7%	14.1%	7.04%	4.23%	1.41%	1.41%	0%	0%
ee_2	0.0158	0.0153	0.0151	0.0150	0.0150	0.0149	0.0149	0.0149
Error	6.04%	2.68%	1.34%	0.67%	0.67%	0%	0%	0%

References

[1] Tian Jian, Duan Xinqun, Zhang Zhongning, Weng Li. A new method of calculating the top deflection of uniform high columns. *J Pressure Vessel Technology* November 2006; p. 26-28. (in Chinese)

[2] JB/T 4710-2005, *Steel vertical vessels supported by skirt* [S]; 2005. (in Chinese)

[3] Tian Jian, *Mechanics of Materials*. Beijing: China Petrochemical Press; 2006. (in Chinese)

[4] Liu Hongwen, *Mechanics of Materials*. 4th ed. Beijing: Higher Education Press; 2004. (in Chinese)

© (2012) Trans Tech Publications, Switzerland
doi:10.4028/www.scientific.net/AMM.187.177

Experimental Research on Trajectory Control of Walking Rehabilitation Training Robot

Zhong Wen, Jinwu Qian, Linyong Shen and Yanan Zhang

School of Mechatronics Engineering and Automation Shanghai University

Shanghai,China

e-mail:wenzhong1002@sina.com

Keywords: Walking Robots; Rehabilitation Training; Impedance Control; Adaptive Control

Abstract. In order to improve the effect of smooth motion, the impedance control is introduced into the control system of walking rehabilitation training robot. An impedance control strategy for active rehabilitation training model is proposed and analyzed, and an adaptive control algorithm is proposed on that basis. The experimental tests of three control methods including PD position servo control, impedance control and adaption control are implemented on the robot prototype. The experimental results show that the robot can continuously adjust its gait trajectory according to the human-robot interaction force to meet the expected gait characteristics under the latter two control strategies. The feasibility and validity of the two control strategies is proved, which will be used in active rehabilitation training.

Introduction

In recent years, the amount of patients with locomotor misfunctions in the lower limbs resulting from spinal cord injuries (SCI), stroke and other central nervous system diseases increases steadily, which seriously endangers human health. Body weight support treadmill training has become a major rehabilitation method in improving walking ability of the patients. Numerous clinical studies support the validity of the method [1-3]. Developing an automated lower limbs exoskeleton orthosis to replace traditional manual assistance training becomes the current research focus by integrating robotics and rehabilitation medicine. University Hospital Balgrist of Switzerland, Mechanical Systems Laboratory of Delaware University and the other groups have developed related research work, which all made some valuable research results [4-7].

On how to effectively control the robot-assisted walking rehabilitation training， some researchers have conducted extensive exploration research. The impedance controller was designed for active training model of Lokmat [8], and the hybrid force/position adaptive control method was also designed based on human-robot collaborative idea [9]. An adaptive collaboration control algorithm was proposed on the basis of researching impedance control [10-11]. It can achieve the LOPES with different stiffness and flexibility by adjusting impedance parameters. In addition, some control methods of upper limbs exoskeleton rehabilitation robot can be used for reference. The fuzzy logic and PID control were incorporated into the hybrid force/position control to achieve rehabilitation training that upper limb moved along a straight line or circular path [12]. The neural network technology was used to adjust PID control gain in real time so that the end of rehabilitation robot provided auxiliary force to adapt the changes of patient's condition [13]. Since all of the above control method for different controlled objects, each has advantages and disadvantages, and most of them are at the experimental stage, which needs further research.

A walking rehabilitation training robot (WRTR) system is being developed in our research group [14], which has achieved a fixed gait trajectory locomotor function. In order to improve the effect of rehabilitation, the rehabilitation training with active subject participation is developed.

On the basis of previous work, two control algorithms are developed for active rehabilitation training model in this paper. In both passive and active working models, the trajectory control experiments are implemented on the physical prototype, respectively.

Experimental System Structure and Function

The WRTR system (Fig.1) mainly comprises powered gait orthosis (PGO) which is attached to the patient' s legs, a treadmill, a body-weight support system and a control system. The core component is PGO which is a two-leg gait orthosis with six degree-of-freedom (DOF) in an exoskeleton structure. Each hip, knee and ankle joint has a rotational DOF and can realize flexion and extension movements in the sagittal plane simulating human walking. Each joint is equipped with a linear actuator to drive the orthosis, a rotary angle sensor to measure the joint angle and a one DOF force sensor behind the linear actuator to measure the driving force. There are two cuffs and a rehabilitation boots on each single leg orthosis. The gait orthosis can move only upward and downward in the vertical direction while the patient's center of gravity is fixed on parallelogram linkage. In order to meet different subject characteristics, the lengths of the thigh and shank of the PGO are adjustable, and the space between the two legs is also adjustable. The control system hardware consists of an industrial computer (IPC), a motion control card (PCI-8158), a multi-function DAQ card (DAQ-2204), driving circuit and signal processing circuit. The control block diagram is shown in Fig.2.

Fig.1 Walking Rehabilitation Training Robot

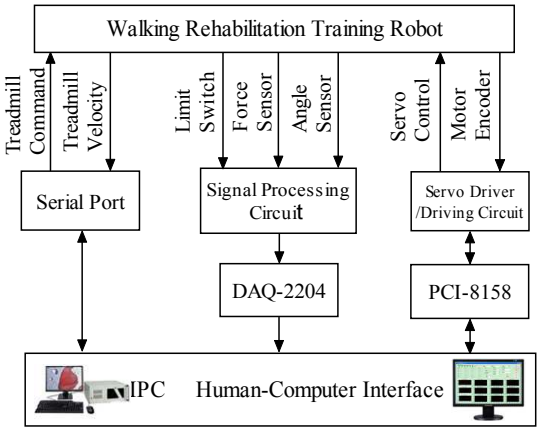

Fig.2 Block diagram of control system hardware

During rehabilitation training process, a patient is suspended by the body-weight support system over the treadmill to relieve part of his body weight. Their leg is attached on the PGO at the position of the cuff, and dressed rehabilitation boots. When the IPC sends an order, the motion control card can output command signal to driving circuit. And the servo driver will receive the command to control the motor to achieve the function that PGO guides the subject rehabilitation training. Meanwhile, the IPC sends command signal to the treadmill by serial port to realize coordinated movement. During the training process, joint angle, driving force, limit switches and other signals are collected in real-time by DAQ-2204 and feedback to the controller to achieve gait trajectory controlled in different models.

There are passive and active training models in the system according to rehabilitative stages of the patient. During passive training model, the robot can guide the patient's legs to move in a fixed physiological gait pattern, which stimulates the patient's sense of the right movement. The patient's muscle spasm and abnormal movement are completely inhibited. During active training model, the

patient's limited abnormal movement is inhibited. The gait trajectory is adjusted in real time by continuous detecting patient's intention so that the robot provides part auxiliary force, zero auxiliary force and resistance force indirectly, aiming to enhance the effect of rehabilitative training.

Control Strategies

Impedance Control Impedance control can make the robot having certain stiffness and damping by adjusting the ideal dynamic relationship between the force and position, which can effectively solve the robot-environment interaction problems. During walking rehabilitative training, PGO drives patient's legs walking on treadmill. When human-robot coupling as resulting from muscle spasms occurred, the excessive traction of PGO will result in the patients' secondary injury. An effective solution to human-robot interaction is particularly important. Each patient has his own gait characteristics, and a single fixed gait trajectory can not meet the requirements of various stages of rehabilitation. However, the impedance control allows a variable deviation from predefined gait trajectory during rehabilitative training, which makes the training gait changeable according to the patient's intention. This amount of deviation depends on the human-robot interaction force and impedance parameters. The impedance relationship can be represented as follows:

$$\boldsymbol{F} = \boldsymbol{B}_d(\dot{\boldsymbol{\theta}}_r - \dot{\boldsymbol{\theta}}) + \boldsymbol{K}_d(\boldsymbol{\theta}_r - \boldsymbol{\theta}) \tag{1}$$

Or expressed as：

$$\boldsymbol{F} = (\boldsymbol{B}_d S + \boldsymbol{K}_d)(\boldsymbol{\theta}_r - \boldsymbol{\theta}) = Z(s)\Delta\boldsymbol{\theta} \tag{2}$$

Where $\boldsymbol{B}_b, \boldsymbol{K}_d$ are the 3×3 damping and stiffness coefficient matrix, respectively, reflecting the energy consumption and contact stiffness. $\boldsymbol{F}$ is the 3 × 1 general human-robot interaction force. $\boldsymbol{\theta}_r, \dot{\boldsymbol{\theta}}_r$ are desired angle and angular velocity vector in joint space, respectively. $\boldsymbol{\theta}, \dot{\boldsymbol{\theta}}$ are actual angle and angular velocity vector, respectively.

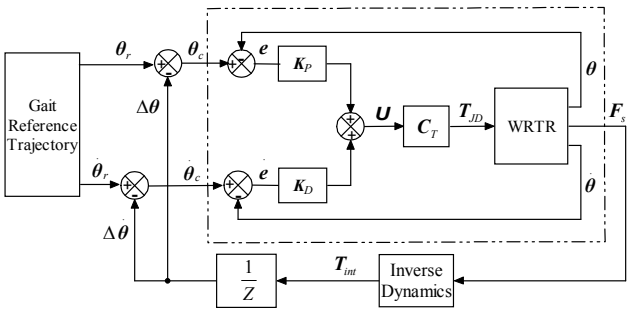

Fig.3 Position-based impedance control schematic

Fig.3 shows position-based impedance control schematic. The inner PD position control loop is in the dashed-line box, and the impedance control loop is added to the position control system to generate desired trajectory modified values. The principle of work is as follows:

1) When human-robot interaction torque $\boldsymbol{T}_{int} = 0$, impedance control based force loop is opened, the system works in position servo control model. $\boldsymbol{\theta}_c, \dot{\boldsymbol{\theta}}_c$ are the PGO controlled joint angle trajectory position and velocity, respectively. $\boldsymbol{K}_P$, $\boldsymbol{K}_D$ are the positive definite proportion and differential gain matrix, respectively. $\boldsymbol{C}_T$ is the dynamic model based torque controller. The control law for the system then equals:

$$\boldsymbol{T}_{JD} = [\boldsymbol{K}_P(\boldsymbol{\theta}_c - \boldsymbol{\theta}) + \boldsymbol{K}_D(\dot{\boldsymbol{\theta}}_c - \dot{\boldsymbol{\theta}})]\boldsymbol{C}_T = (\boldsymbol{K}_P\boldsymbol{e} + \boldsymbol{K}_D\dot{\boldsymbol{e}})\boldsymbol{C}_T \tag{3}$$

At this point, the robot works in passive training model. The patient is guided by PGO walking in a predefined gait trajectory. The gait trajectory of the robot can track $\boldsymbol{\theta}_r, \dot{\boldsymbol{\theta}}_r$ perfectly.

2) When human-robot interaction torque $\boldsymbol{T}_{int} \neq 0$, the outer force loop is closed automatically, $\boldsymbol{\theta}_r, \dot{\boldsymbol{\theta}}_r$ become the controlled variables of desired trajectory. According to the linear actuator driving force $\boldsymbol{F}_s$ measured by the force sensor, the inverse dynamics model is used to extract the human-robot

interaction torque $\boldsymbol{T}_{int}$, and feedback to impedance controller, resulting in corresponding position and velocity deviation $\Delta\boldsymbol{\theta},\Delta\dot{\boldsymbol{\theta}}$ which continuously modify the predefined reference trajectory. The control law is as follows:

$$\boldsymbol{T}_{JD} = [\boldsymbol{K}_P(\boldsymbol{\theta}_r - \Delta\boldsymbol{\theta} - \boldsymbol{\theta}) + \boldsymbol{K}_D(\dot{\boldsymbol{\theta}}_r - \Delta\dot{\boldsymbol{\theta}} - \dot{\boldsymbol{\theta}})]\boldsymbol{C}_T \tag{4}$$

$$\Delta\boldsymbol{\theta} = \frac{1}{Z}\boldsymbol{T}_{int} \tag{5}$$

At this point, the robot works in active training model. The gait trajectory of PGO will gradually adapt to the patient's gait characteristics under the condition of patient's active force, thus the control of human-robot interaction force is achieved indirectly. At the same time, it can change the gait trajectory offset and response speed by adjusting impedance parameters $\boldsymbol{B}_d, \boldsymbol{K}_d$ to adapt different stages of rehabilitation, achieving certain degree compliant motion. When the impedance parameters are very large, the resulted deviation will be close to zero, which can be considered as passive training model. Therefore, the impedance parameters can be adjusted to adapt different patients and different stages of rehabilitation.

In practice, when $\boldsymbol{T}_{int}$ less than certain value, we consider $\boldsymbol{T}_{int} = 0$ to overcome the influence of mechanical structure vibration and so on. When $\boldsymbol{T}_{int}$ is larger than certain limit due to outside interference or patient's factors, such as muscle spasms, the control program will immediately stop the walking training, which avoids excessive trajectory deviation harm to the patient.

Adaptive Control The above control strategy is always in a fixed reference trajectory, and the change of trajectory deviation is only on the basis. It is difficult to adapt the adjustment of different individuals gait trajectory, which needs therapists according to the case of the patients and clinical experience to manual regulation. This problem can be solved by the following adaptive algorithm. It can continuously modify the reference trajectory of PGO according to the patient's active force. Adjustment of the reference trajectory is realized by trajectory parameters on-line adaptive optimization. Firstly, the reference joint angle trajectories are parameterized as follows:

$$\theta_{r,j} = a_j \cdot \theta_{r,gen,j}(\omega_j t) + b_j \tag{6}$$

Where j=1,2,3 is corresponding to hip, knee or ankle joint, respectively. The parameter a_j represents the amplitude scaling factor of the joint angle, parameter ω_j is the scaling factor of gait cycle and parameter b_j is the offset of the joint angle to change the hip joint flexion and extension, knee joint flexion amount and ankle joint plantar flexion and bending. In order to realize synchronization of the three joint movements, the parameters $\omega_1, \omega_2, \omega_3$ which are used to calculate the new scaling factor of gait cycle by the weighted average are not completely independent. New ideal reference trajectories $\boldsymbol{\theta}_r = (\theta_{r,hip}, \theta_{r,knee}, \theta_{r,ankle})^T$ are generated by trajectory parameters adjusted on-line. When $a_j = 1, \omega_j = 1, b_j = 0$, $\boldsymbol{\theta}_r = \boldsymbol{\theta}_{r,gen}(t)$ is a standard physiological joint angle trajectory function. Fourier series expansion is used to fit the above joint angle trajectory, obtaining a good fitting result, the expression as follows:

$$\theta_{r,gen,j} = \sum_{n=1}^{\infty} A_n \sin(n\omega t + \varphi_n) + A_0 \tag{7}$$

Where $A_n, \omega, \varphi_n, A_0$ are parameters in Fourier series.

In the impedance control strategy, the inharmonious features of muscle strength caused by lower limbs muscle spasm and muscle tension, mechanical structure vibration and the other reasons will influence the change of driving force $\boldsymbol{F}_s$, which will make the changed value of human-robot interaction torque too large or too small. And then the trajectory deviations calculated by the impedance controller are also too large or too small, the modified gait trajectory will not conform to physiological law. It will certainly affect the effect of rehabilitative training. Therefore, on the basis of impedance control model and gait trajectory parameterized, an adaptive control algorithm is developed. It is based on a normal physiological gait trajectory to fit the modified gait trajectory, and obtained a new desired trajectory resulting from overall effect of patient's intention in one cycle. Fig. 4 shows the adaptive control block diagram.

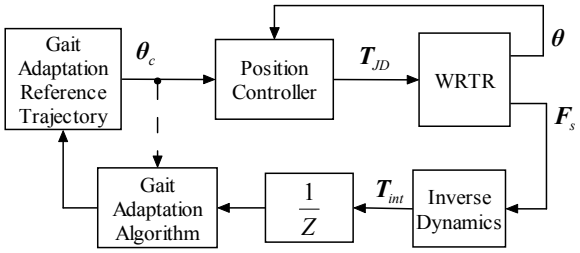

Fig. 4 Adaptive control block diagram

Every moment position deviation is calculated by the impedance relationship as follows:

$$\Delta\boldsymbol{\theta} = \frac{1}{\boldsymbol{B}_d \boldsymbol{s} + \boldsymbol{K}_d} \Delta\boldsymbol{T}_{int} \tag{8}$$

Modified gait trajectory:

$$\boldsymbol{\theta}_{c,new} = \boldsymbol{\theta}_{r,old} - \Delta\boldsymbol{\theta} \tag{9}$$

Then using the best square approaching of Euclidean norm of the joint trajectory deviation, the objective function is established. Calculating the optimal trajectory parameters pN can be achieved by the following equation:

$$P(\boldsymbol{p}_N) = \int_{(N-1)T}^{NT} \left\| \boldsymbol{\theta}_{c,new}(t) - \boldsymbol{\theta}_r(t) \right\|_2^2 dt \tag{10}$$

The results of the minimization of the objective function in [(*N-1*) *T*, *NT*] is Nth trajectory parameters $a_{j,N}, \omega_{j,N}, b_{j,N}$ updated every gait cycle *T*, which produces the adaptation of reference trajectory.

Experimental Research

Programming The control methods are programmed by integrating VC++6.0 and Matlab, using dialog-based MFC project. The two control algorithms are compiled by MATLAB language into functions of “impedence.m” and “adaptation.m”, respectively. Enter “mcc -v -B csharedlib:algorithmlib impedence.m adaptation.m**”** command in command window of matlab software to create shared libraries, generating four documents "algorithmlib. dll "" algorithmlib.h "" algorithmlib.lib "" algorithmlib.ctf", copy them to the current folder of VC project, and use implicit link method to call dynamic link library in VC. It can realize calling the function of the algorithms. In the modules of data acquisition and motion control, it can call the function by configuring the project in the same method above using the supplier provided function database. The serial communication between IPC and treadmill is realized by ActiveX control “MSComm” initialized in the program. According to the communication protocol of the treadmill, IPC can send and receive control commands. During the force sensor signal acquisition process, there are various kinds of interference factors which make the data fluctuated largely. Therefore, a function of weighted recurrence average method is programmed by C language to process the data before it feedback to the control algorithms. The development environment of system control program is VC++6.0. The user interface is programmed using controls in VC and ActiveX control package “DAQBench” which is ActiveX component software developed for measurement and automation applications. Human-computer interface of the control system is shown in Fig.5. The training time, walking speed, joint angle, joint driving force and other information are displayed and recorded in real time, which will help the therapists determining the patient's recovery status.

Fig.5 Human-computer interface of the control system

Experimental Research According to the analysis of control algorithm and programming above, three groups experiment are implemented on the psychical prototype of WRTR including position servo control, impedance control and adaptive control model. In experiments, manually applying force on thighs and shanks of PGO realizes the patient's active force, which tries to change the gait trajectory. This will result the change of each measured joint driving force, and the extracted Human-robot interaction torques will be changed, too.

During position servo control model, by removing outer impedance control loop which is depicted in Fig.2, it becomes PD controller based passive rehabilitative training. In actual experiment, training gait cycle is 4.6s, applying active force at the sixth cycle. The experimental results of hip joint are shown in Fig. 6 and Fig. 7. Fig. 6 shows the desired (dashed line) and measured (solid line) gait trajectory. Fig. 7 shows a measurement of hip driving force. As can be seen from the figure, when the active force applied, the measured force increases obviously, but the hip joint trajectory which is the same as before has not been affected obviously. The maximum trajectory deviation is 1.92 °. It has realized gait trajectory tracking control effectively.

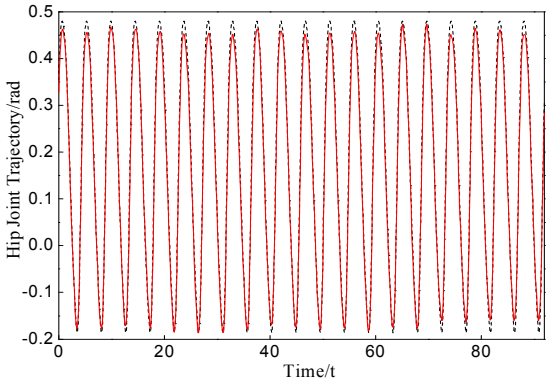

Fig.6 Hip joint trajectory in position control model

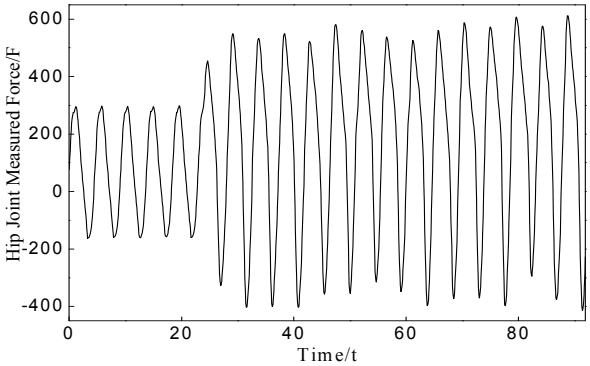

Fig.7 The changing curve of the hip joint measured force

During the impedance control model, the impedance parameters is adjusted to $\boldsymbol{B}_d$ = diag [80 20 15], $\boldsymbol{K}_d$ = diag [360 96 48] via the computer simulation and experimental debug, its units are Nms/rad and Nm/rad, respectively. The training gait cycle is 4.6s. Applying active force which changes in certain regularity at the fourth cycle tries to increase the training stride. The experimental results are shown in Fig. 8 and Fig. 9. Fig. 8 shows the desired (dashed line) and measured (solid line) gait trajectory. Fig. 9 shows the measurement of hip driving force. The results show that the measured force changes continuously after applying active force. The impedance controller generates corresponding trajectory deviation to modify hip joint trajectory which changes correspond with the expected one, increasing the hip extension and flexion. The maximum trajectory deviation is 8.26°. The measured force has certain decreased trend during the adjustment process of hip joint trajectory, which shows certain impedance characteristic.

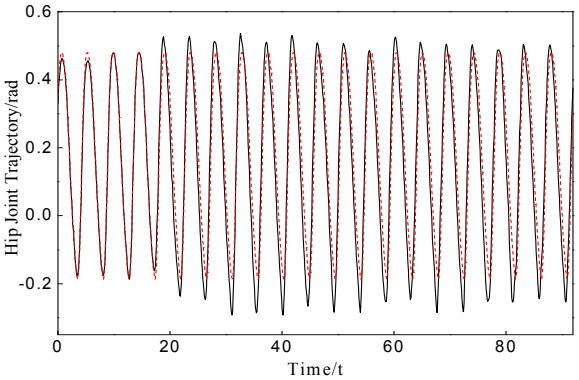

Fig.8 Hip joint trajectory in impedance control model

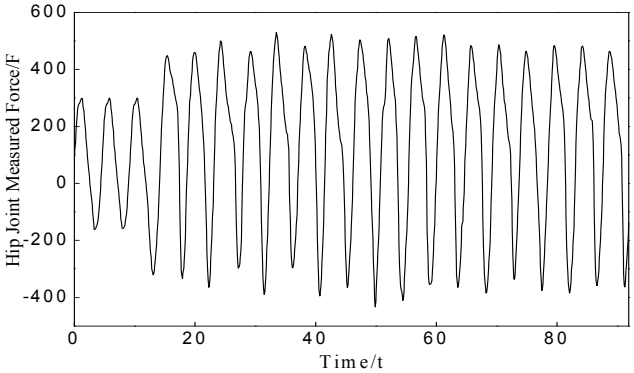

Fig.9 The changing curve of the hip joint measured force

During adaptive control model, at the same experimental conditions, the hip joint experimental results are shown in Fig.10, Fig.11 and Fig.12. At the former ten cycles, the robot works in passive training model and walks in a fixed gait trajectory, applying active force at the 11th cycle trying to increase walking stride greater than the former. The adaptation of the three trajectory parameters is shown in Fig.10. After thirteen gait cycles adjustment, the trajectory parameters a_1, ω_1, b_1 fluctuate at 1.12, 0.98, -0.03, respectively. The training gait cycle has increased appreciably due to ω_1 decreased, and the hip joint trajectory tends towards stability. Relative to passive training model, the former ten cycles, as shown in Fig.11, the extension angle and flexion angle of adjusted gait trajectory increased by 2.7 ° and 3.1 °, respectively. Fig.12 shows that measured force firstly increases, then decreases and reaches a certain level, which achieves the purpose that PGO provides rehabilitation training auxiliary force indirectly.

According to the experimental results above, it is known that the PD position controller can achieve the track of desired trajectory well in passive training model. The trajectory deviation in impedance control model is larger than in position control model obviously at the same active force, which proves the algorithm meeting the requirement of active rehabilitation training, allowing deviated from the desired trajectory. During adaptive control model, the adaptation of the trajectory parameters has realized the reference trajectory modified to meet different gait characteristics. Both of the two control algorithms can make the robot adjusting its gait trajectory according to the amount of active force to adapt desired gait. The results prove the feasibility of both control algorithms applied to active rehabilitation training. However, there are certain trajectory fluctuation and control error in experiments, mainly because applying active force manually can not simulate the patient's perfectly, and the mechanical structure has vibration. The experimental method and optimization of control algorithm should be further studied.

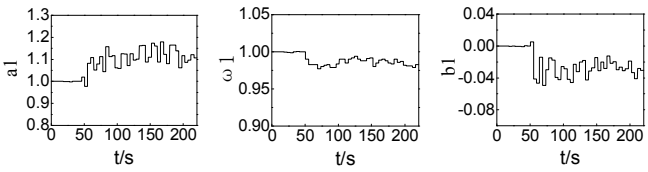

Fig.10 The adaptation of hip joint trajectory parameters

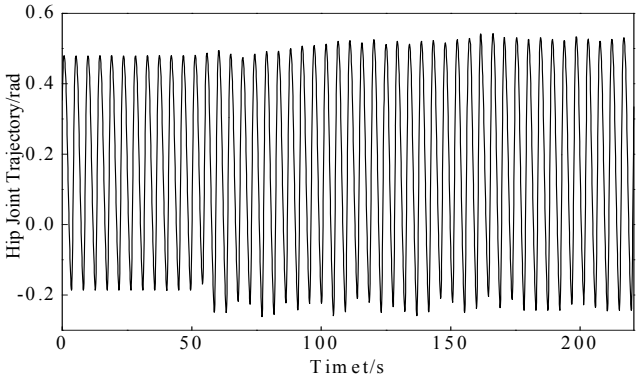

Fig.11 Hip joint trajectory in adaptive control model

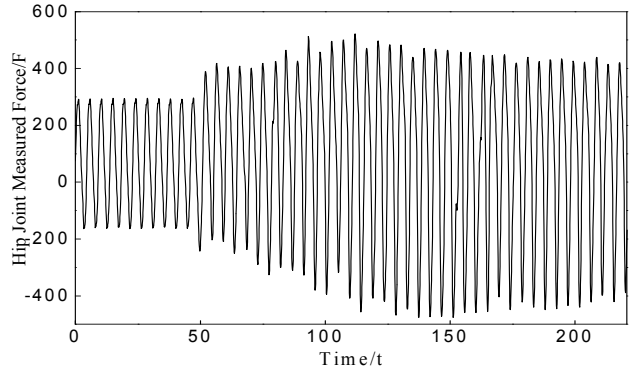

Fig.12 The changing curve of the hip joint measured force

Conclusion and Future Work

In this paper, both impedance control and adaptive control are developed for active rehabilitation training model, tested on the physical prototype, and compared with the PD position servo control. The experimental results show that the two control algorithms can make the robot adjusting its gait trajectory according to the amount of active force continuously to adapt expected gait trajectory, which shows certain impedance characteristic and achieves the purpose that the robot provides rehabilitation training auxiliary force indirectly. In conclusion, preliminary results showed that the feasibility and validity of both control algorithms will be used for active rehabilitative training, which provides foundation for further study of the project.

However, these are only the early tests of the control algorithms. The experiments also have some control error, and both algorithms lack of a full evaluation of undergoing patient research and clinical trials. In the near future, more experiments will be implemented using the two control algorithms to verify its performance, the program will be modified to consummate the algorithm. The method of extracting the human-robot interaction torque will be also improved and the mechanical structure will be perfected, so as to better realize the active rehabilitation training.

Acknowledgment

This work is jointly supported by National High-Tech R&D Program (No. 2006AA04Z224); National Science Foundation (No. 50975165); Shanghai Leading Academic Discipline Project (No. 10XD1401900); Innovation Group Project from Shanghai Education Commission; Graduate Innovation Fund of Shanghai University.

References

[1] S. Hesse, C. Bertelt, A. Schaffrin, M. Malezic, and K. H. Mauritz,"Restoration of Gait in Nonamulatory Hemiparetic Patients by Treadmill Training with Partial Body-weight Support," Arch. Phys. Med. Rehabil.,vol. 75, no. 10, Oct.1994. pp. 1087–1093,

[2] M. Visitin, H. Barbeau, N. Korner-Bitensky, and N. E. Mayo, "A New Approach toRetrain Gait in Stroke Patients through Body Weight Support and Treadmill Stimulation," Stroke, vol. 29, no. 6,Jun. 1998, pp. 1122–1128.

[3] Y. Laufer, R. Dickstein, Y. Chefez, and E. Marcovitz, "The Effect of Treadmill Training on the Ambulation of Stroke Survivors in the Early Stages of Rehabilitation," J. Rehabil. Res. Dev., vol. 38, no. 1, Jan-Feb. 2001, pp. 69–78.

[4] G. Colombo, J. Matthias, S. Reinhard and M. Volker. "Treadmill Training of Paraplegic Patients Using a Robotic Orthosis," Journal of Rehabilitation Research and Development,vol. 37, no. 6,Nov.-dec., 2000, pp. 693-700.

[5] S. K. Banala, A. Kulpe and S. K. Agrawal, "A pwered Leg Othosis for Gait Rehabilitation of Motor-Impaired Patients," Proc. IEEE International Conferrence on Robotics and Automation, IEEE Press, Apr. 2007,pp. 4140-4145,doi: 10.1109/ROBOT.2007.364115 .

[6] K. K. Mankala, S. K. Banala and S. K. Agrawal, "Passive Swing Assistive Exoskeletons for Motor-Incomplete Spinal Cord Injury Patients," Proc. IEEE International Conferrence on Robotics and Automation, IEEE Press, Apr. 2007,pp. 3761-3766,doi: 10.1109/ROBOT. 2007. 364055 .

[7] C. Fang, W. Rencheng and J. Xiaohong, "The Progress of Partial Body Weight Support Treadmill Robots," Chinese Journal of Rehabilitation Medicine, vol. 31, no. 2, Apr. 2008, pp. 366-368.

[8] R. Riener, L. Lünenburger and S. Jezernik, "Patient-cooperative Strategies for Robot-Aided Treadmill Training: First Experimental Results," IEEE Transactions on Neuronal Systems and Rehabilitation Engineering, vol. 3, no.13, Mar. 2005, pp.380-394,doi: 10.1109/TNSRE.2005.848628.

[9] M. Bernhardt,M. Frey, G. Colombo and R. Riener, "Hybrid Force-Position Control Yields Cooperative Behaviour of the Rehabilitation Robot LOKOMAT," Proc. IEEE 9th International Conference on Rehabilitation Robotics, IEEE Press, Jun. 2005. pp. 536-539,doi: 10.1109/ICORR.2005.1501159 .

[10]E. H. Asseldonk, J. F. Veneman, R. Ekkelenkamp,et al, "The Effects on Kinematics and Muscle Activity of Walking in a Robotic Gait Trainer during Zero-force Control," IEEE Transactions on Neural Systems and Rehabilitation Engineering, vol. 16, no.4, Aug. 2008, pp.360-370,doi: 10.1109/TNSRE.2008.925074.

[11]R. Ekkelenkamp, J. F.Veneman, H. Kooij van der, "LOPES: Selective Control of Gait Functions during the Gait Rehabilitation of CVA Patients," Proc. IEEE 9th International Conference on Rehabilitation Robotics, IEEE Press, Jun. 2005,pp. 361-364,doi: 10.1109/ICORR.2005.1501120.

[12]J. Ming-Shaung, K. Chou-ching, L. Dong-Huang, H.Ing-Shiou and C. Shu-Min, "A Rehabilitation Robot with Force-position Hybrid Fuzzy Controller: Hybrid Fuzzy Control of Rehabilitation Robot," IEEE Trans Neural Syst Rehabil Eng, vol. 13, no.3, Sep. 2005, pp.349-358,doi: 10.1109/TNSRE.2005.847354 .

[13]D. Erol, N. Sarkar. "Intelligent Control Framework for Robotic Rehabilitation after Stroke," Proc. IEEE International Conference on Robotics and Automation, IEEE Press, Apr. 2007, pp. 1238-1243, doi: 10.1109/ROBOT.2007.363154.

[14]Feng Zhiguo, Qian Jinwu, Zhang Yanan, etal. "Biomechanical Design of the Powered Gait Orthosis," Proc. Proceedings of the 2007 International Conference on Robotics and Biomimetics, IEEE Press, Dec. 2007, pp. 1698-1702, doi: 10.1109/ROBIO.2007.4522421.

© (2012) Trans Tech Publications, Switzerland
doi:10.4028/www.scientific.net/AMM.187.186

Kinematics Simulation and Control System Design of Serial Robot Based on ADAMS and Pro/E

Hongmei Fan

School of Automation, Nanjing Institute of Technology, Nanjing 211167, P R China

zdhxfhm@njit.edu.cn

Keywords: Robot, Adams, Simulation, Virtual Prototype

Abstract. Mechanic dynamic analysis software ADAMS was used to build a virtual prototype of a 6-D serial robot, and the kinematics simulation was performed. The virtual prototype model provides the theoretic foundation and main parameters for the control system design, production and application in experiment.

Introduction

The virtual prototype technology is the dynamic simulation technology in the mechanical systems. This technology, from the viewpoint of analyzing and solving the whole product performance and the relative problems, is a computer-aided engineering technology, it solves the shortcomings of traditional design and production. The engineer constructs the prototype model in the computer, then analyzing its dynamic performance, according to the analyzing result, the prototype design is improved. Using the virtual prototype technology, the design and development procedure of mechanic products can be simplified consumedly; the product development cycle is shorten; the development fee and cost is decreased; and the product quality and performance is improved[1],[2].

ADAMS is a famous virtual prototype analyzing software, developed by Mechanical Dynamic Inc.. On the one hand, the user can analyze the statics, kinematics, and dynamics performance of the virtual prototype, on the other hand, the ADAMS is an opening software, it provides many interfaces, it is also a secondary development platform.

This paper is organized as follows: Section I gives a brief introduction of virtual prototype and ADAMS. In section II, we present the simulation model of the 6-DOF serial robot. The kinematics simulation is introduced in section III. In section IV, the realization of the control system and its function is presented and finally, section V concludes this paper.

The simulation model of robot

The principle of constructing the virtual prototype model is the same as the physical prototype model. It requires simplify the model as much as possible, that is to say, under the condition of satisfying the kinematics simulation, the part number of the virtual prototype should be the least.

3-D solid model in Pro/E The 3-D solid model of the robot is constructed in Pro/E, in this paper, the robot is a 6-D serial robot, it has 6 joints and the motion part is the base, the waist, the upper arm, the forearm, the wrist and the manipulator. In order to decreasing the trouble of adjustment, the start moving position of the motion part should be considered at the beginning of assembling it. If the assembly drawing is finished, then the document can be imported into the ADAMS by using the function of Mechanism/Pro.

Constructing virtual prototype in ADAMS After completing the 3-D model drawing, then the virtual prototype can be constructed in ADAMS. In order to ensuring the accuracy of the virtual prototype, the motion part is remained, the gear，the bearing, and other part are omitted. The simplifying model is imported into the ADAMS. Before simulation in ADAMS, the motion restriction should be ordained firstly. The base and the earth adopts fixed joint, all the motion joints adopt revolute joint. The motion rules about the base and the waste, the waist and the upper arm, the upper arm and the forearm, the forearm and the manipulator is set then. Providing the velocity of every motion part is regularity. If the velocity parameter of each joint is set, then the kinematics simulation, analysis and comparison is done, this is the so-called robot positive kinematics problem.

On the contrary, providing the end trajectory of the robot is known, according to the set end point, doing the kinematics simulation, analysis and comparison, this is the inverse kinematics problem. The 3-D model of the robot and its virtual prototype is shown in fig. 1.

Fig. 1. (a) 3-D model of the robot; (b) the virtual prototype

Kinematics simulation

If the virtual prototype is completed, the mechanical kinematics function of the robot system is formed automatically by the ADAMS/Solver modular, the static kinematics, and dynamics analysis can be performed in this modular. The other modular ADAMS/Postprocessor can output the high performance animation, all kinds of data curves, etc. The simulation analysis is done by using the two modules[3],[4],[5].

The motion control is achieved by the function step(), its expression is:

$$\text{Step}(x,x_0,h_0,\text{x}_1,h_1)$$

Where x is the independent variable, it cam be time or the user-defined variable, normally it is the function of time; x_0 is the start vale of x; h_0 is the variable value of x_0, ,x_1 is the end value of x; h_1 is the variable value of ,x_1. If the variable value is focus, then the value is added alphabetic d which represents degree.

The ADAMS also provides many kinds measuring functions, the displacement, velocity, and acceleration curves of the motion part can all be measured. It also provides data processing modular. By processing the curve data, the positive kinematics solution and the inverse kinematics solution can be solved, it is very useful to helping the robot design. Fig. 2 is one of the kinematics simulation curves.

Fig. 2. The manipulator displacement and velocity curve

Control system design

The robot control system is composed of computer, servo(step) motor, motion control card, actuator, and the power. The motion control card, which control the position, velocity, accelerate of the servo motor, is made up of high performance DSP processor, CPLD programmable device and servo interface. The actuator transforms the low power pulse provided by the motion control card to a high power electric signal, which can drive the motor rotate with the load.

Considering the real time and stability of the system, the robot control system is developed by EVC, We explored 5 control functions[6]:

Space calculation Space calculation includes kinematics positive & reverse solution for the 6 DOF serial robot, the interface is depicted in fig.3. The top frame is the position and posture of the end effector, the bottom frame is the 6 joints' angle. In fig. 3, the first 3 ranks in the top frame is the posture parameter, the forth rank is the position parameter. If we input the 6 joint' angle and click the positive solution button, the relative position and posture of the end effector will be displayed in the top frame, vice versa.

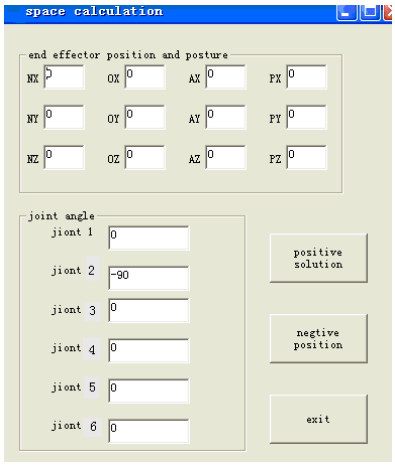

Fig. 3. Space calculation

Joint motion The 6 joints can be tested respectively, the interface is shown in fig. 4. Choice a joint in the joint choice frame, the joint orientation, the motion mode and the start mode first, then set the motion parameters(the motion velocity, the target position), finally, click the start button, observe whether the joint moves as expected. When the stop button is clicked during the motion period, the joint motion will stop immediately. If the manipulator open button is clicked, the manipulator will open and the button will become "manipulator close", and click this button again, the manipulator will close.

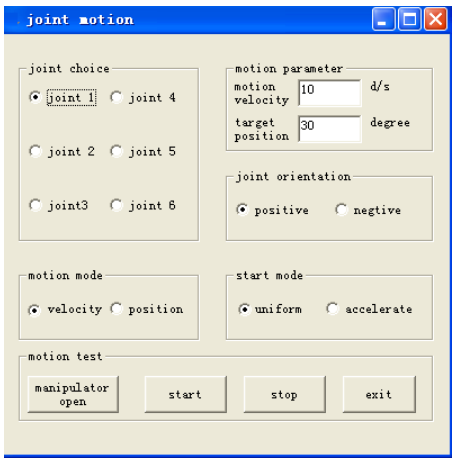

Fig. 4. Joint motion

Robot teach programming The state and the coordinate of each joint can be displayed and saved as a teach programming. The interface is shown in fig. 5, the procedure is as follows:

- Start the control software, observe whether every joint of the robot is the zero position, if not, click the reset button, reset the robot.
- Click the "+" or "-" button in the joint motion frame, control the joint move to the target position, then click the "record" button, record this point, this record also be added to the teaching list.
- If all the teaching is finished, then click the "save" button, the teaching file is saved.

- Click the “open” button, the teaching file saved before can be loaded in the teaching list, then choice the teach mode, “single”, teaching only once, “continuous” teaching repeatedly until the “stop” button is clicked.

Robot reset When the user clicks the robot reset button, the robot returns the zero position.

Robot urgent stop If there is any wrong movement, the user can click the robot urgent stop button, the power of the main driven motor circle is cut off.

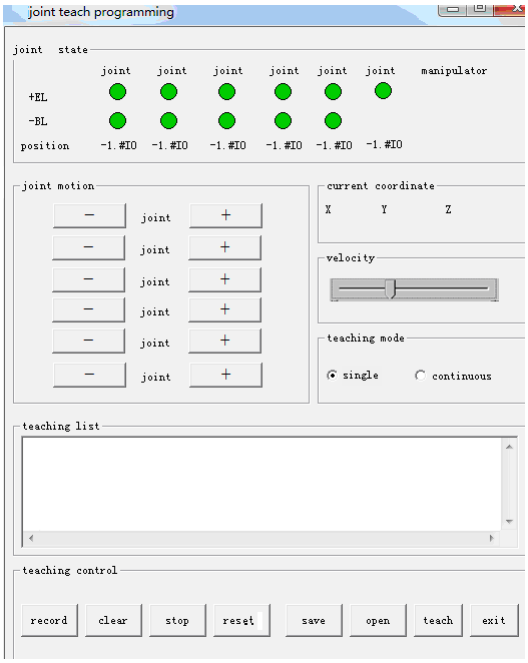

Fig. 5. Joint teach programming

Conclusions

This paper presents a method of robot virtual design and simulation. The model, which is constructed in the Pro/E, is imported in the ADAMS, if the motion restriction is built, then the kinematics analysis and simulation can be done in ADAMS. The displacement and velocity curves of the motion part can be obtained too, the simulation curves offer data and parameters for controlling robot movement and planning path by the inverse kinematics analysis of the robot.

Acknowledgements

This is supported by Nanjing Institute of Technology foundation of China(QKJB2009008).

References

[1] Huo Guozhu, Zhang Xiaofeng. “Virtual design and simulation of a robot based on Pro.e and ADAMS” [J]. Mechinery Design & Manufacture, 2009(3), pp. 183-185.

[2] Jia Xiaogang, Yuan Liye, Shen Dong. “Kinematics simulation of parallel machine tool based on ADAMS and Pro/E[J]. Machine Tool & Hydraulics,2009,vol. 37, no. 2, pp.138-140

[3] ADAMS/VIEW User’s Reference Manual. MSC. Software,2003.

[4] ADAMS/Solver Reference Manual. MSC. Software,2003.

[5] ADAMS/Control Reference Manual. MSC. Software,2003.

[6] Hongmei Fan. “The robot remot monitoring and fault diagnosis system based on wireless network”.IEEE International Conference on Computer Application and System Modeling, 2010, in press.

© (2012) Trans Tech Publications, Switzerland
doi:10.4028/www.scientific.net/AMM.187.190

Design of an Adaptive Terminal Dynamic Sliding Mode Controller for Anti-ship Missiles

He Peng-cheng[1a], Jia Lin-sheng[1], Wang Yu-lin[2] and Zhang Wen-guang[2]

[1]Department of Control Engineering Naval Aeronautical and Astronautical University

Yantai 264001, China

[2]Eighth Elements of 91006 troops Feidong 231614, China

[a]Email: hpc19851230@163.com

Keywords: Overload Control; Termianal Sliding Mode; Variabl Estructure Systems; Adaptive; Chattering;

Abstract. Adaptive dynamic sliding mode control strategy for the overload control of anti-ship missiles using Lyapunov stability theory is proposed. By using a function augmented sliding hyperplane, it is guaranteed that the output tracking error converges to zero in finite time. In addition, an adaptive method is adopted to attenuate the uncertainties. The simulation shows validity of the proposed method.

Introduction

A new generation of anti-ship missiles is known as supersonic flight, high mobility, and long-range attacks. However, the missile in large airspace will be affected by external disturbances. During the recent years, considerable efforts have been made to deal with the design of the overload system known as high mobility and simple design for anti-ship missiles [1-6]. The missile overload control system is designed based on variable structure control method in [4]. A fuzzy backstepping method is adopted in [5], and the fuzzy item is used to keep the track performance of the overload control system. An adaptive backstepping method is applied for a missile system with unknown parameters and uncertainties in [7], the method gives the adaptive scheme guaranteeing uniform ultimate boundedness. However, this approach ignores the effect of the item $a_{35}\delta_z$ on the system.

The general attention is paid to sliding mode control because of its robustness at home and abroad, and the control method has been applied to the missile's control, which obtains satisfactory results [7-9]. However, in the ordinary sliding mode control, because the output tracking errors can not converge in finite time to zero. In order to get better performance, some of experts proposed a terminal sliding mode control strategy [10-11], the nonlinear term is introduced into the design of the sliding mode such that the state variable of the sliding mode tends to zero in the finite time in the phase of sliding mode motion. For the Anti-shi missile, the second overload control system, the paper presents an adaptive dynamic terminal sliding mode control method, which not only makes the system error in finite time converges to zero, but also the uncertainty on the parameters is attenuated, thus the performance of sliding mode control system is improved.

Model of missile VERTICAL channel

After single-channel decoupling process, the missile model can be simplified to second-order system in applying the overload control technology. Take the vertical channel of the anti-ship missile as example, and select the state variables as follows

$$\begin{cases} x_1 = e = n_y^d - n_y \\ x_2 = \dot{e} = -\dot{n}_y \end{cases} \tag{1}$$

where n_y is missile vertical overload, and n_y^d is missile expected overload.

Rewrite (1) as follows

$$\begin{bmatrix}\dot{x}_1\\ \dot{x}_2\end{bmatrix}=\begin{bmatrix}0 & 1\\ -a_1 & -a_2\end{bmatrix}\begin{bmatrix}x_1\\ x_2\end{bmatrix}+\begin{bmatrix}0\\ 1\end{bmatrix}u \tag{2}$$

where x_1 and x_2 are the state variables of system, u is the control input variable of system, a_1 and a_2 are system parameters.

Consider the disturbance, (2) can be written as

$$\begin{cases}\dot{x}_1=x_2\\ \dot{x}_2=-a_1x_1-a_2x_2-bu+d(x,t)\end{cases} \tag{3}$$

where $x=\begin{bmatrix}x_1 & x_2\end{bmatrix}$.is system state variables, $d(x,t)$ is the system outer disturbance.

Control Law Design

Define the tracking error

$$E=x-x_d=\begin{bmatrix}e & \dot{e}\end{bmatrix}^T \tag{4}$$

where $e=x_1-x_{1d}$, x_{1d} is the expected value of x_1.

Then, define terminal switching function

$$s(x,t)=CE-W(t) \tag{5}$$

where $C=\begin{bmatrix}c_1 & c_2 & \cdots & c_n\end{bmatrix}$, $c_i\,(i=1,2,\cdots,n)$ is positive constant and $c_n=1$, Define $W(t)=CP(t)$, then we can get

$$s(x,t)=C(E-P)=\sum_{l=1}^{2}c_l\left(e^{(l-1)}-p^{(l-1)}\right) \tag{6}$$

where $P(t)=\begin{bmatrix}p(t) & \dot{p}(t) & \cdots & p^{(n)}(t)\end{bmatrix}^T$ and it is satisfied the following assumption.

Assumption 1: design Terminal function $p(t):R_+\to R, p(t)\in C^n[0,\infty), \dot{p},\ddot{p},\cdots,p^{(n)}\in L^\infty$, for $T>0$, $p(t)$ is limited in $[0,T]$, and $p(0)=e(0)$, $\dot{p}(0)=\dot{e}(0)$, …, $p^{(n)}(0)=e^{(n)}(0)$, where $C^n[0,\infty)$ is all the differentiable function defined in $[0,\infty)$.

Assumption 2: The external disturbance of the system is bounded and slowly varying, that is $|d(x,t)|\le D_{max}$, $\dot{d}(x,t)=0$, where $D_{\max}$ is positive.

Define dynamic Terminal sliding mode as follows

$$\sigma(x,t)=\dot{s}(x,t)+\lambda s(x,t) \tag{7}$$

where λ is positive constant.

Clearly, according to assumption 1, the Terminal function $p(t)$ can be described as follows

$$p(t)=\begin{cases}e_0+\dot{e}_0t+\frac{1}{2}\ddot{e}_0t^2-\left(\frac{a_{00}}{T^3}e_0+\frac{a_{01}}{T^2}\dot{e}_0+\frac{a_{02}}{T}\ddot{e}_0\right)t^3+\\ \left(\frac{a_{10}}{T^4}e_0+\frac{a_{11}}{T^3}\dot{e}_0+\frac{a_{12}}{T^2}\ddot{e}_0\right)t^4-\left(\frac{a_{20}}{T^5}e_0+\frac{a_{21}}{T^4}\dot{e}_0+\frac{a_{22}}{T^3}\ddot{e}_0\right)t^5 \;if\quad 0\le t\le T\\ 0\quad if\quad t>T\end{cases} \tag{8}$$

With assumption one, $p(t)$ is continuously differentiable function when $t=T$, and so terminal function $p(t)$ and its derivative $\dot{p}(t)$, $\ddot{p}(t)$ are zero when $t=T$.

According to the results above, it is easy to get the value of $a_{ij}\left(i,j=0,1,2\right)$.

$$\begin{cases} a_{00}=-10 \\ a_{10}=15 \\ a_{20}=-6 \end{cases},\begin{cases} a_{01}=-6 \\ a_{11}=8 \\ a_{21}=-3 \end{cases},\begin{cases} a_{02}=-1.5 \\ a_{12}=1.5 \\ a_{22}=-0.5 \end{cases} \tag{9}$$

Define Lyapunov function

$$V\left(t\right)=\frac{1}{2}\sigma^{T}\sigma \tag{10}$$

With (6) ~ (7), the derivative of σ can be gotten as follows

$$\dot{\sigma}=c_2\left(e^{(3)}-p^{(3)}\right)+c_1\left(\ddot{e}-\ddot{p}\right)+\lambda\sum_{l=1}^{2}c_l\left(e^{(l)}-p^{(l)}\right) \tag{11}$$

We can simplify the every term of the (13) as follows

$$\begin{aligned} &c_2\left(e^{(3)}-p^{(3)}\right) \\ &=c_2\left(\dddot{x}_2-\dddot{x}_{2d}-p^{(3)}\right) \\ &=c_2\left(-a_1\dot{x}_1-a_2\dot{x}_2-\dot{b}u-b\dot{u}\right)+ \\ &c_2\left(\dot{d}\left(x,t\right)-\dddot{x}_{2d}-p^{(3)}\right) \end{aligned} \tag{12}$$

$$c_1\left(\ddot{e}-\ddot{p}\right)=c_1\left(\dot{x}_2-\dot{x}_{2d}-\ddot{p}\right)$$

$$=c_1\left(-a_1x_1-a_2x_2-bu+d\left(x,t\right)-\dot{x}_{2d}-\ddot{p}\right) \tag{13}$$

$$\begin{aligned} &\lambda\sum_{l=1}^{2}c_l\left(e^{(l)}-p^{(l)}\right)=\lambda c_1\left(\dot{e}-\dot{p}\right)+\lambda c_2\left(\ddot{e}-\ddot{p}\right) \\ &=\lambda c_1\left(x_2-x_{2d}-\dot{p}\right)+ \\ &\lambda c_2\left(-a_1x_1-a_2x_2-bu+d\left(x,t\right)-\dot{x}_{2d}-\ddot{p}\right) \end{aligned} \tag{14}$$

then

$$\begin{aligned} &\dot{\sigma}=\left[-c_2\dot{b}-\left(c_1+\lambda c_2\right)b\right]u+\left(c_1+\lambda c_2\right)d\left(x,t\right) \\ &+c_2\left(-b\dot{u}+\dot{d}\left(x,t\right)\right)+c_2\left(-a_1\dot{x}_1-a_2\dot{x}_2-\dddot{x}_{2d}-p^{(3)}\right) \\ &+\lambda c_1\left(x_2-x_{2d}-\dot{p}\right)+ \\ &\left(c_1+\lambda c_2\right)\left(-a_1x_1-a_2x_2-\dot{x}_{2d}-\ddot{p}\right) \\ &=L_1u+\left(c_1+\lambda c_2\right)d\left(x,t\right)-c_2b\dot{u}+L_2 \end{aligned} \tag{15}$$

where

$$\begin{aligned} &L_1=-c_2\dot{b}-\left(c_1+\lambda c_2\right)b \\ &L_2=c_2\left(-a_1\dot{x}_1-a_2\dot{x}_2-\dddot{x}_{2d}-p^{(3)}\right)+ \\ &\left(c_1+\lambda c_2\right)\left(-a_1x_1-a_2x_2-\dot{x}_{2d}-\ddot{p}\right)+ \\ &\lambda c_1\left(x_2-x_{2d}-\dot{p}\right) \\ &L=c_2b \end{aligned} \tag{16}$$

Finally, the control law is given as follows

$$\dot{u}\left(t\right)=L^{-1}\left[L_1u+L_2+\left(c_1+\lambda c_2\right)\left(D+\eta\right)\mathrm{sgn}\left(\sigma\right)\right] \tag{17}$$

It is known to us that when missiles are in flight, especially in the large airspace, the aerodynamic parameters change rapidly, so we need to estimate the variables L_1, L_2.

Define

$$\begin{aligned}\tilde{L} &= L - \hat{L} \\ \tilde{L}_1 &= L_1 - \hat{L}_1 \\ \tilde{L}_2 &= L_2 - \hat{L}_2\end{aligned} \tag{18}$$

Then we design

$$\dot{u}(t) = \hat{L}^{-1}\left[\hat{L}_1 u + \hat{L}_2 + (c_1 + \lambda c_2)(D + \eta)\operatorname{sgn}(\sigma)\right] \tag{19}$$

where

$$\begin{aligned}\dot{\hat{L}}_1 &= k_{c1}\sigma u \tanh(\frac{\sigma u}{\varepsilon_{s1}}) - \Gamma_1(\hat{L}_1 - \hat{L}_1(0)) \\ \dot{\hat{L}}_2 &= k_{c2}\sigma \tanh(\frac{\sigma}{\varepsilon_{s2}}) - \Gamma_2(\hat{L}_2 - \hat{L}_2(0)) \\ \dot{\hat{L}} &= k_{c3}\sigma \dot{u} \tanh(\frac{\sigma}{\varepsilon_{s3}}) - \Gamma_3(\hat{L} - \hat{L}(0))\end{aligned} \tag{20}$$

We can redesign the sliding mode controller as

$$\begin{aligned}u_c = \hat{L}^{-1}\Big(&-\hat{h}_1 n_y - \hat{h}_2 w_z - \hat{h}_3 \delta_z - \Delta_1 - \\ &\lambda(\sigma + \beta\operatorname{sgn}(\sigma))\Big)\end{aligned} \tag{21}$$

in addition, we can also get

$$\dot{u}(t) = L^{-1}\left[L_1 u + L_2 + (c_1 + \lambda c_2)(D + \eta)\operatorname{sgn}(\sigma)\right] \tag{18}$$

with (15) ~ (18), rewrite (15) as follows

$$\dot{\sigma} = (c_1 + \lambda c_2)\left[d(x,t) - (D + \eta)\operatorname{sgn}(\sigma)\right] \tag{22}$$

With (10) ~ (19), the derivative of V can be gotten as follows

$$\begin{aligned}\dot{V}(t) &= \sigma\dot{\sigma} = (c_1 + \lambda c_2)\left[d(x,t)\sigma - (D + \eta)\operatorname{sgn}(\sigma)\sigma\right] \\ &\le -(c_1 + \lambda c_2)\eta|\sigma|\end{aligned} \tag{23}$$

$$\begin{aligned}\dot{V} &= S\dot{S} - \frac{1}{k_{c1}}\tilde{L}_{12}\dot{\hat{L}}_{12} - \frac{1}{k_{c2}}\tilde{L}_{22}\dot{\hat{L}}_{22} - \frac{1}{k_{c3}}\tilde{E}\dot{\hat{E}} \\ &= S\left(\tilde{L}_{12}Z + \tilde{L}_{22}O_1 + \tilde{E} - \beta\,\mathrm{sgn}(S)\right) - \\ &\quad \frac{1}{k_{c1}}\tilde{L}_{12}\dot{\hat{L}}_{12} - \frac{1}{k_{c2}}\tilde{L}_{22}\dot{\hat{L}}_{22} - \frac{1}{k_{c3}}\tilde{E}\dot{\hat{E}} \\ &= -\beta S\,\mathrm{sgn}(S) + \tilde{L}_{12}ZS - \frac{1}{k_{c1}}\tilde{L}_{12}k_{c1}ZS + \\ &\quad \tilde{L}_{22}O_1S - \frac{1}{k_{c2}}\tilde{L}_{22}k_{c2}O_1S + S\tilde{E} - \frac{1}{k_{c2}}\tilde{E}k_{c2}S \\ &= -\beta S\,\mathrm{sgn}(S) < 0\end{aligned} \tag{24}$$

The stability of the system is proofed, if we make $\xi(t) = E(t) - P(t)$, it is easy to get

$$\begin{aligned}s(x,t) &= CE(t) - W(t) \\ &= CE(t) - CP(t) = C\xi(t)\end{aligned} \tag{25}$$

It is shown that if proper $P(t) = 0, \forall t \geq T$ is chosen, the tacking error converges to zero within finite time T.

Simulaiton

The parameters of missile model are as follows: $b = -7638.7$, $a_1 = 141.73$, $a_2 = 2.63$, $c_1 = 1.2$, $\lambda = 3$, $k_{c1} = 9.810$, $k_{c2} = 1.2$, $k_{c3} = 2.3$, $d = 130 + 0.1*\cos(t)$.

The actual and desired trajectories are shown in Figure 1. The solid yellow line represents the actual trajectory, and the solid black line shows the desire done. From this figure, one can easily know that the actual output converges to the desired trajectory within 1.6s.

Figure 2 shows the output tracking error. As can be seen in this figure, the output tracking error converges to zero in 1.6s. In other words, after the relaxation time, that can be set arbitrarily, the system output tracks the reference trajectory perfectly.

It is shown that the dynamic control input signal always shows the chattering phenomena in figure 3. However, in figure 4, we can see that the chattering phenomena is eliminated in control input.

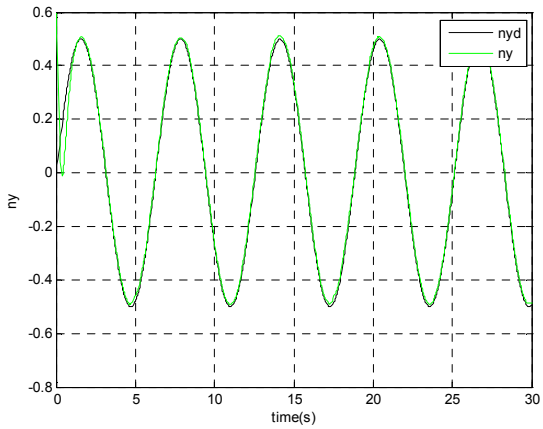

Fig.1 Reference and actual trajectories

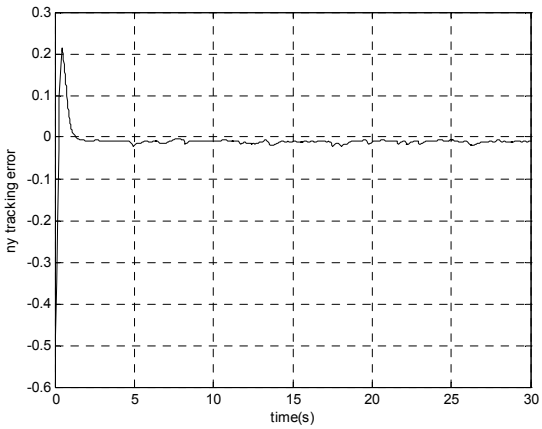

Fig.2 Taajectory tracking error

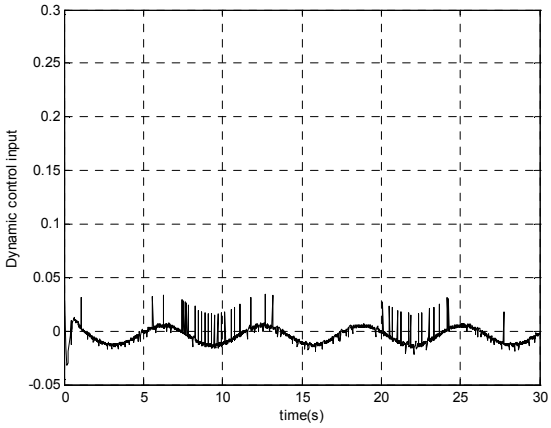

Fig.3 Dynamic control input

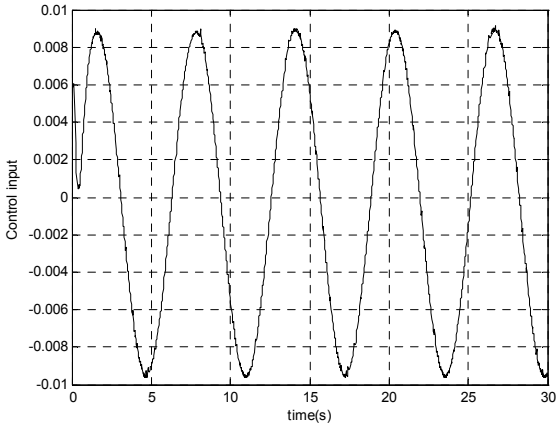

Fig.4 Control input

Conclusion

The terminal sliding mode control scheme using the function augmented sliding hyperplane has been proposed for overload control systems. By using the proposed sliding hyperplane, it was guaranteed that the reaching phase problem is overcome and the output tracking error converges to zero in finite time, and the relaxation time can be set arbitrarily.

References

[1] Gu Wenjin, Wang Shixing, Zhang Yifei, “Overload control for achieving great control over the airspace motor,’’ Naval Aeronautical Engineering Institute, vol. 15, 2000, pp. 401-404.

[2] Gu Wenjin, Yu Jinyong, Zhang An, “Design of Missile Control System overload of nonlinear backstepping design,’’.Missiles and Guidance Journal, 2004, pp. 110-112

[3] Gu Wenjin, Zhao Hongchao, Wang Fenglian., “Fuzzy variable structure control design for anti-ship missiles,’’Journal of System Simulation, vol. 4, 2005, pp. 944-946

[4] Zhao HongChao, Gu Wenjin, Madden Wu, “Output-redefinition-based variable structure control for aerodynamic missiles,’’ Ordnance Sinica, 2005, pp. 783-786

[5] Wang Ran, Zhang An, “Overload control system design for winged missile using fuzzy dynamic backstepping,’’Missiles and Guidance Journal, 2006, pp. 10-12

[6] SH Kim, YS Kim, C Song, “A robust adaptive nonlinear control approach to missile autopilot design,’’Control engineering practice, vol. 12, 2004, pp. 149-154

[7] Song JianHai, Zhang TianJiao. “Application of sliding mode control in the missele contol”. Control jounal, vol. 19, 1999, pp. 32–38

[8] Gu WenJin, Zhang YiFei, Li ChangPing, “composite control of linear/adaptive variable structure control’’, Chinese Tournal of Astronautics, vol. 14, 2001, pp. 49–56

[9] Hung J Y, Gao W, Hung J C, “Variable Srtucture Control: A Survey,’’IEEE Trans.Industrial Electronics, vol. 40, 1993, pp. 2–22.

[10]Wu Y，Man Z.Terminal sliding mode control design for uncertain dynamic systems[J]. Systems&Control Letters, 1998, 34(5):281-287.

[11]Park K B，Lee J.Comments on “A robust MIMO terminal sliding mode control scheme for rigid robot manipulators”[J]. IEEE Trans Automatic Control, 1996, 41(5):761-762.

© (2012) Trans Tech Publications, Switzerland
doi:10.4028/www.scientific.net/AMM.187.196

Seismic Analysis for the Suspended Converter Valve Tower of the UHV

Q.G. Sun[a], X.F. Wu, J.J. Di, Y.C. Zhou

Department of Mechatronic Engineering, North China University of Technology , Beijing 100144, China

[a]E-mail: qgsun@ncut.edu.cn

Keywords-Finite Element Model; Mode; Response Spectrum Method; Earthquake Response; UHV

Abstract: Based on the ANSYS software, a finite element model of a single converter valve tower of the UHV (Ultra High Volt) is built, the structure dynamic characteristics of the converter valve tower is analyzed by the modal analysis method, the earthquake response of the converter valve tower is calculated by the response spectrum analysis method. The prestress effect and the large deformation effect are taken into account in the calculation process, and the seismic responses under some complex loads which combine the earthquake loads and the gravity load are calculated. The results show that lots of natural frequencies of the converter valve tower, which is designed as a flexible structure, very low. The fundamental vibration modes are pendulum sways in X- and Y-direction. The displacements of the horizontal sway response of the converter valve tower are larger than other direction displacements. This conclusion must be considered in the reasonable arrangement design of the valve hall.

Introduction

The UHVDC (Ultra high Voltage Direct Current) transmission is one of the hot trend measures in the power transmission project. As one of key equipments, the converter valve tower is often taken into account a certain degree of earthquake resistance in its structure design. A lots of research work in this area had been done in some companies, such as, Siemens and ABB, and also many scholars in China have been engaged in the research on the earthquake resistance of the converter station valve hall. Y. J. Ma [1], Z. H. Liu[2], L. J. Huang[3] *et al* researched on the dynamic characteristics and the earthquake responses of the whole hall by the FEM and the interaction of the valve tower and the valve hall was also discussed in their papers. But the finite element model of the converter valve tower is complicated, and there is a large calculated amount and a hard work in the seismic analysis. A detailed finite element model for the 800KV single valve tower is built, and its static analysis, modal analysis and response spectrum analysis are done based on the ANSYS software in this paper.

The suspended valve tower

The Construction. The valve is the core part of the HVDC power transmission system. Now the suspended structure of valve tower is widely employed in the HVDC transmission project. Here we take the 800KV single valve tower as an example to illuminate the construction of the suspended valve tower, as shown in Fig. 1. The suspended valve tower is arranged in the hall. Every valve tower has four layers. Every layer has two thyristor modules and two reactor modules. Layers are connected by some M30 epoxy studs. The valve tower is hanged by 4 strings of long-rod insulator. Every string of insulator has 5 parts of long-rod insulator. Every part of insulator is connected flexibly by the axle pin. The valve tower adjoins an arrester. The total weight of a valve tower is about 1.2 ton.

The Finite Element Model. A finite element model for the 800KV single valve tower is modeled using the ANSYS version 11.0, based on the appropriate simplified principle and actual distribution of the structure mass. A right-hand Cartesian co-ordinate system has been adopted, as shown in Fig. 1. X axis is horizontal parallel to module short side. Y axis is horizontal parallel to module long side. Z axis is vertical upwards. The model has been restrained at the roof fixity

positions, where UX=0, UY=0, UZ=0, ROTZ=0. SHELL63, BEAM188, MASS21 and MPC184 elements are used in the finite element model. SHELL63 elements are used to model the thyristor and reactor modules. BEAM188 elements are used to model the M30 epoxy studs and long-rod insulators. MASS21 elements are used to develop the actual distribution of the structure mass. MPC184 elements are used to model the flexible axle pin connection. There are 8751 nodes and 8903 elements total in the finite element model. The element plot of the valve tower is shown in Fig. 1.

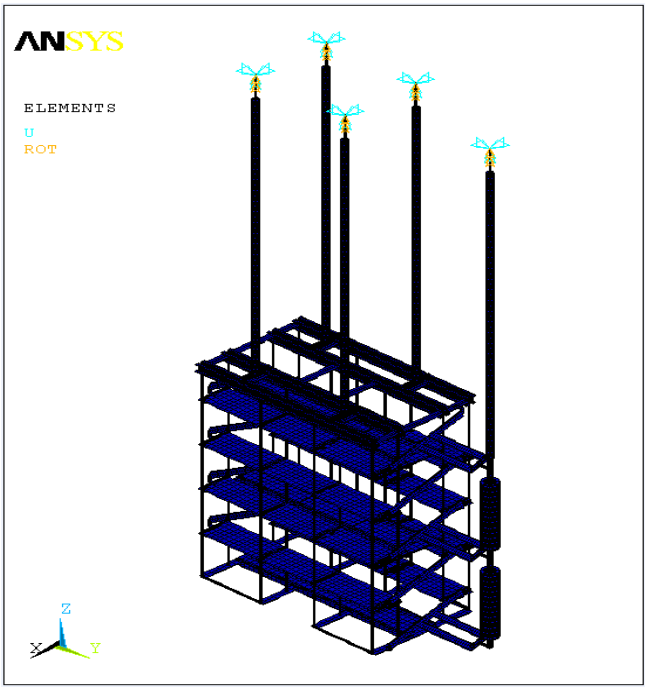

Figure 1. Finite element model of the converter valve tower

Hypothesis

We suppose that the earthquake response of the valve tower and the hall are independent each other, or their interaction can be ignored completely in this paper. In the paper [1] the first horizontal natural vibration frequency of the hall is about 5Hz, the first vertical natural vibration frequency of the hall is about 4Hz, and the first horizontal natural vibration frequency of the valve tower is about 0.08Hz, the first vertical natural vibration frequency of the valve tower is about 10Hz. These results tell us that the interaction of valve tower and hall is very small. The same conclusion was obtained in the paper [2] and the paper [3]. Therefore this hypothesis is reasonable, and we just aim to analyze the earthquake response of the valve tower in this paper.

Computation method

There are the static method, response spectrum method and time history method in the seismic design theory and calculation method. The response spectrum method and the time history method are recommended in the Code for Seismic Design[4]. The response spectrum method is easy to operate, and be used widely, and it is adopted in this paper.

The three direction seismic and static loads are subjected to the model, and the prestress effect and large deformation effect are included. The load combination method is used in the calculation. Every load is as a special calculation case. Then every case combines together based on the worst combination principle[5]. In calculation process the three direction earthquake responses are combined using the SRSS method, and then the absolute value of static load response is superimposed.

The computation procedures of the response spectrum analysis are as follows: a) obtain static load solution with the prestress effect and large deformation effect; b) obtain the modal solution; c) obtain the spectrum solution; d) expand the modes; e) combine the modes; f) write the results to the mode combination file and write the load case to a load case file.

The static analysis solution and the modal analysis solution can be obtained from the response spectrum analysis solution. The static analysis solution also is written to the load case file. Then every load case is read out from the database, and is combined. All results are read out from the database and review them finally.

Modal analysis

The valve tower vibration characteristics which include the natural frequencies and the mode shapes are determined using the modal analysis. The Block Lanczos Method is used in the modal extraction. The partial solution procedure is used to calculate the eigenvalues and eigenvectors. There are lots of low natural frequencies in this kind of flexible valve structure. The fundamental vibration modes are the pendulum sways (X- and Y-direction) both at about 0.18 Hz. The solution results are shown in Table 1 and Fig. 2.

TABLE I. EIGENFREQUENCIES AND MODAL PARTICIPATION FACTORS

Mode	Mode Description	Frequency /Hz	Part -X	Part -Y	Part -Z
1	X-sway	0.1774	106.2000	-12.9900	-0.0004
2	Y-sway	0.1778	-12.9700	-106.2000	0.0011
3	Z-torsion	0.2372	-1.0970	-1.1780	0.0009
4	X-wave	0.9701	12.6100	0.3084	0.0051
5	Y-wave	1.0860	0.3223	-13.2400	-0.0057

Seismic analysis

The Earthquake response spectrum. Reference to Technical Rule for Designing HVDC Converter Station[6], the valve hall building belongs to group B. The earthquake response spectrum is designed using a basic ground motion acceleration, 0.15g, and seismic fortification intensity is 8 degree, and site classification is Class Ⅱ, and the earthquake occurs frequently. The horizontal direction maximum seismic influence coefficient is 0.24, the vertical direction maximum coefficient is 0.12, the characteristic period is 0.40s [4]. A damping ratio is assumed as 2%. The seismic coefficient curves are shown in Fig. 3.

The Earthquake response. The seismic induced forces, displacements and accelerations have been assessed, and the worst load combinations have been calculated in this paper. Some results of the seismic analysis are summarized in Table 2, Table 3, Fig. 4 and Fig. 5.

TABLE II. MAXIMUM RESPONSE FORCE AND MINIMUM SAFETY FACTOR

Items	Maximum Axial Force/ Stress /Bending Moment	Ultimate Resistance	Minimum Safety Factor
Long-Rod Insulators	30.4KN	300KN	9. 9
Top Main Beam	18.6MPa	170MPa	9.1
M30 Epoxy Studs	0.24 KN·m	1.3KN·m	5.4

TABLE III. MAXIMUM RESPONSE DISPLACEMENT AND ACCELERATION

Items	Maximum Response Displacement /M	Maximum Response Acceleration /M·S-2
X-Direction	0.416	1.242
Y-Direction	0.397	4.889
Z-Direction	0.004	2.384

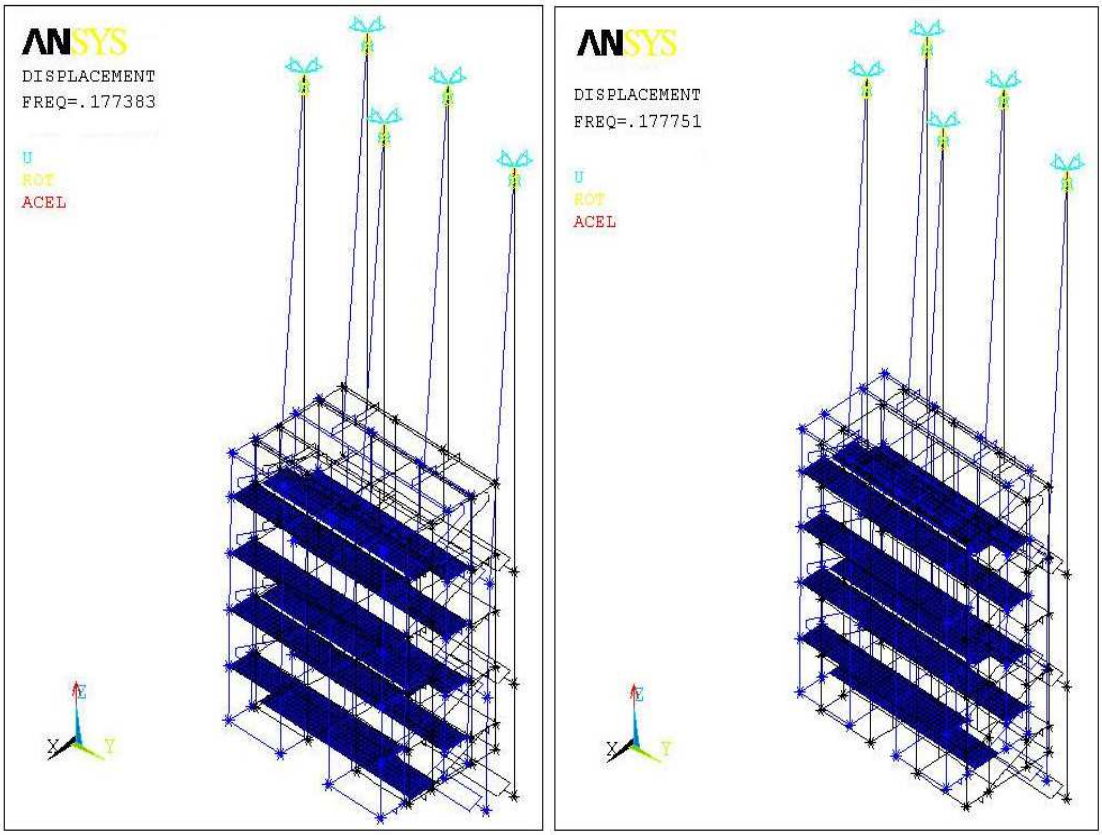

a) The first mode b) The second mode

Figure 2. Modal of the converter valve tower

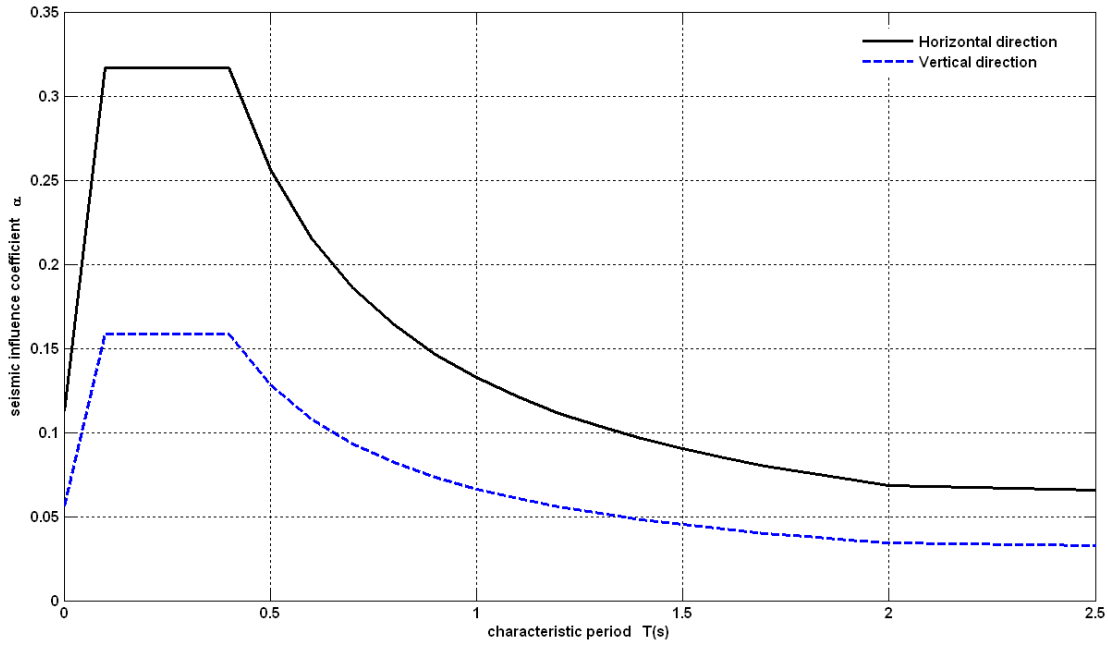

Figure 3. Seismic coefficient curves

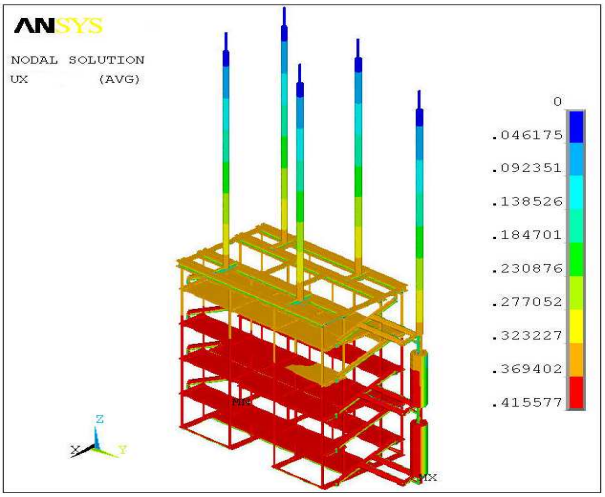

a) X-direction

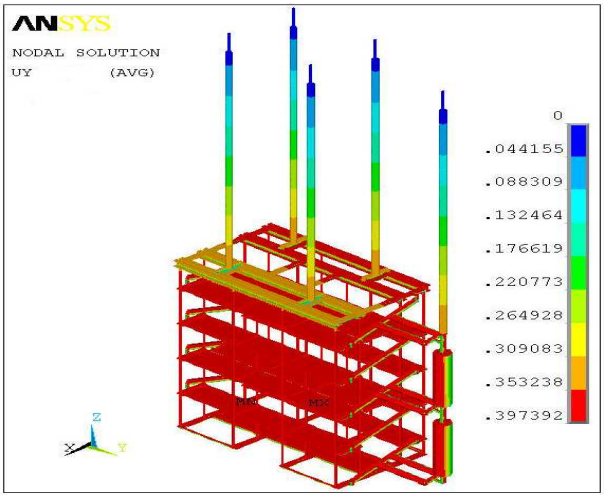

b) Y-direction

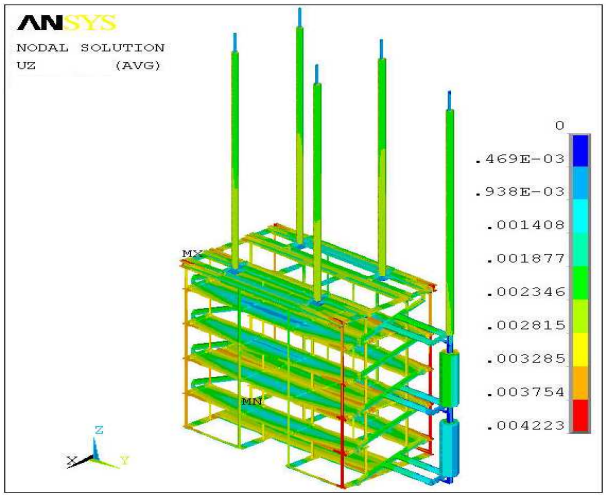

c) Z-direction

Fig 4. Displacement distribution in the worst combination

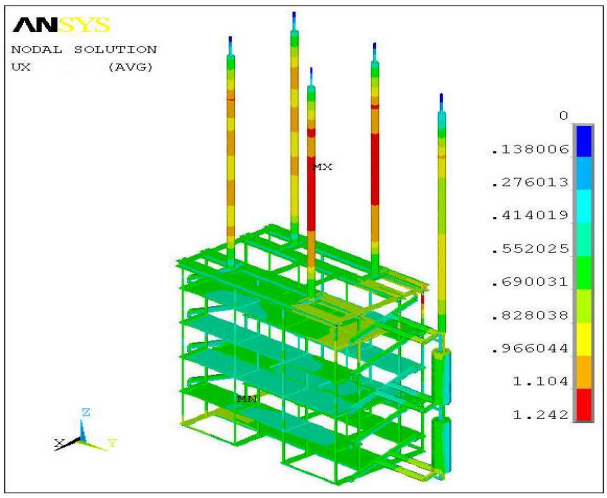

a) X-direction

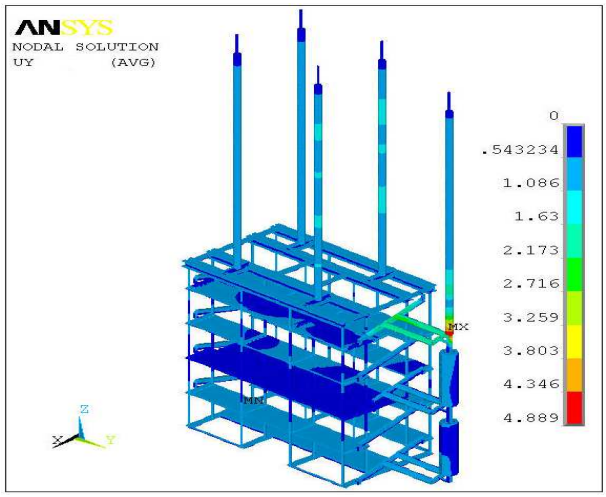

b) Y-direction

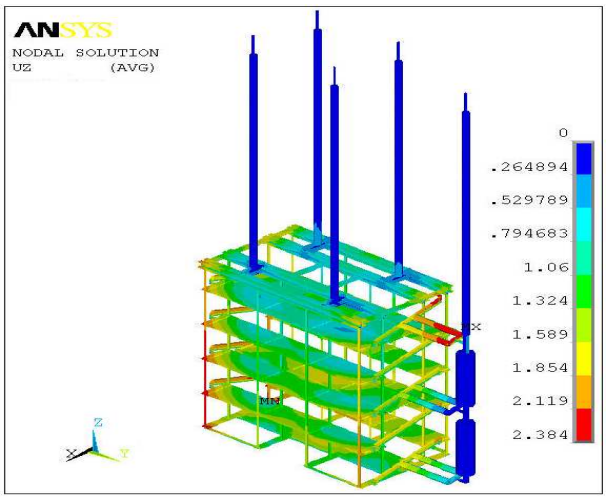

c) Z-direction

Fig 5. Displacement distribution in the worst combination

Conclusions

Based on the ANSYS software, and under some hypothesis conditions, the seismic characteristics of the 800KV single converter valve tower is analyzed by the modal analysis method in this paper, the results are as follows,

1) Lots of natural frequencies in calculation are low in this kind of flexible valve structure. The fundamental vibration modes are pendulum sways in X- and Y-direction both at about 0.18 Hz.

2) Under some calculation conditions, such as the seismic fortification intensity is 8 degree, and based on the worst combination principle, the maximum horizontal response displacement of the 800KV single converter valve tower is 0.416m in X-direction, the most response accelerations of the thyristor and the reactor modules are within 0.3-0.6m·s^{-2}, the axial force of long-rod insulators is 30.4kN, the maximum bending moment of M30 epoxy studs is 0.24 kN·m.

References

[1] Y. J. Ma, “Structural Selection and Anti-quake Analysis of Converter Station Valve Hall, ” Electric Power Construction, 2009, vol. 30, pp. 37-40.

[2] Z. H. Liu, H. H. Zhu, and S. Ye, “Research of Seismic Response of Suspending Valves in Converter Station,” Southern Power System Technology, vol. 3, 2009, pp. 24-26.

[3] L. J. Huang, “The Vibration Test and Nonlinear Dynamical Analysis Study of the Valve Hall Structure,” WuhanUniversity of Technology, 2007.

[4] GB/J50011-2001: Code for Seismic Design of Buildings, 2001.

[5] C. G. Zhang, “Application of Ansys to Analysis of Vibration Type Decomposition Response Spectrum of a Concrete Gravity Dam,” Yunnan Water Power, vol. 25, 2009, pp. 24-27.

[6] DL/T5223-2005: Technical Rule for Designing HVDC Converter Station, 2005.

CHAPTER 5:

Materials Science and Technologies

© (2012) Trans Tech Publications, Switzerland
doi:10.4028/www.scientific.net/AMM.187.205

Electronic Structures of X level due to Indium-Carbon Dimers in Silicon

Hiroyuki Kawanishi[a] and Yoshinori Hayafuji[b]

[a,b]Graduate School of Science and Technology, Kwansei Gakuin University,

2-1 Gakuen, Sanda, Hyogo 669-1337, Japan

E-mail: [b]hayafuji@kwansei.ac.jp

Keywords: semiconductor, silicon, ULSI, shallow junction, codoping, dimer codopant, *ab initio* calculation, electronic structure, dopant energy level, DV-Xα

Abstract. Electronic structures of silicon with carbon, indium, or indium-carbon dimers were calculated to investigate the interaction between indium and carbon in X center due to the indium-carbon dimers. Ab initio calculations were carried out mainly for basic $Si_{71}H_{60}$, C-$Si_{70}H_{60}$, In-$Si_{70}H_{60}$, and InC-$Si_{69}H_{60}$ clusters. The results showed that : (i) the X level was observed at E_{HOMO} + 0.42 eV in the InC-$Si_{69}H_{60}$, which was a little bit shallower than E_{HOMO} + 0.44 eV of the corresponding substitutional In in the In-$Si_{70}H_{60}$, (ii) dominant constituents of density of states of the X level were the partial densities of states of In and Si, and (iii) the X level had the antibonding nature between In and C.

Introduction

Ultra-large scale integration (ULSI) applications, where the critical dimensions of transistors are less than 0.01μm, inevitably require steep doping profiles and ultra-shallow source/drain junctions. Shallow n^+ source/drain areas can be formed by low energy implantation of the column VA heavy ions such as arsenic As and antimony Sb ions. However, formation of shallow p^+ source/drain areas is difficult even by low energy ion implantation, because of the lack of the column IIIA heavy ion. Indium In might potentially replace boron B commonly used as an acceptor dopant in silicon Si[1]. This is because shallow and steep doping profiles can be obtained by low energy ion implantation of heavy In ions. The reason why In has not been used as an acceptor dopant is due to its deep ionization energy of 0.156 eV. Another reason comes from its low solid solubility of $1\text{-}2\times10^{18}$ atoms/cm^3 in Si[2]. In recent years, a new doping method called codoping has been developed as a valence control method for semiconductors by using simultaneous doping of both n- and p-type dopants[3]. It was demonstrated that the existence of codopants increases the carrier mobility and the dopant solubility, but decreases the dopant ionization energy. More recently, one of the authors has reported that the trimer complexes In_2D (D=phosphorus P, As, Sb, or bismuth Bi) act as shallower acceptors with smaller ionization energies than an In acceptor[4]. More than thirty years ago, a few pioneers reported some works on a different type of codoping. Baron et al. observed a new shallower acceptor level having the strong correlation with the existence of In complexes than the level of the substitutional In acceptor[5]. Jones et al. pointed out that these In complexes were carbon C-In dimers and that all the C-IIIA column element (B, Al, Ga, In or Tl) dimers called the X centers also acted as shallower acceptos with ionization energies approximated 80% of the corresponding substitutional IIIA ionization energies[6]. Recent interest has arisen in the use of X centers as an alternative to B, because of the more practical simplicity of dimer formation process than the trimer formation process in ULSI applications. Some space, however, remains for a complete understanding of the electronic characteristics of the X centers. In this paper, we present *ab-initio* calculation results of electronic structures of silicon clusters with In, C or an InC dimer to investigate atomic interactions among In, C and matrix Si atoms in the X level due to the InC dimer.

Calculation methods

Ab initio calculations were carried out using the discrete variational-Xα (DV-Xα) molecular orbital method to investigate localized quantum structures of Si clusters with In, C or an In-C dimer and to evaluate the ionization energies of the dopants[7]. In this *ab initio* real-space calculations, the Slater exchange potential was employed as the exchange-correlation term V_{xc} of one-electron Hamiltonian. The atomic orbitals used in the calculations were 1s-3d for Si, 1s for hydrogen H, 1s-2p for C and 1s-5p for In. Mulliken overlap population analysis was performed, giving the subtotal bond overlap population Q^i_{AB} between an A and a B atoms at any molecular orbital φ_i [8]. A Si cluster Si_{71} was extracted from an ideal Si crystal to make a basic $Si_{71}H_{60}$ cluster with H terminators, having the T_d symmetry. The interatomic distance is 0.235 nm for Si-Si and 0.147 nm for Si-H. Modified clusters of In-$Si_{70}H_{60}$, C-$Si_{70}H_{60}$ and InC-$Si_{69}H_{60}$ were used to investigate the electronic structures of the clusters with dopants. For the In-$Si_{70}H_{60}$ and the C-$Si_{70}H_{60}$ having T_d symmetry, the Si atom at the center of the $Si_{71}H_{60}$ was replaced with In or C, respectively. For the InC-$Si_{69}H_{60}$ having C_{3v} symmetry, the Si atom at the center of the $Si_{71}H_{60}$ was replaced with In, and one of the three Si atom located at the nearest neighboring substitutional site of the In atom was replaced with C. In this study no structural relaxation was carried out.

Results and discussions

Dopant energy levels in band gaps and their ionization energies. Figure 1 shows four energy level diagrams for the clusters, (a) $Si_{71}H_{60}$, (b) C-$Si_{70}H_{60}$, (c) In-$Si_{70}H_{60}$, and (d) InC-$Si_{69}H_{60}$. Solid and broken lines represent occupied and unoccupied energy levels, and chain double-dashed lines in the gaps represent the dopant energy levels, respectively.

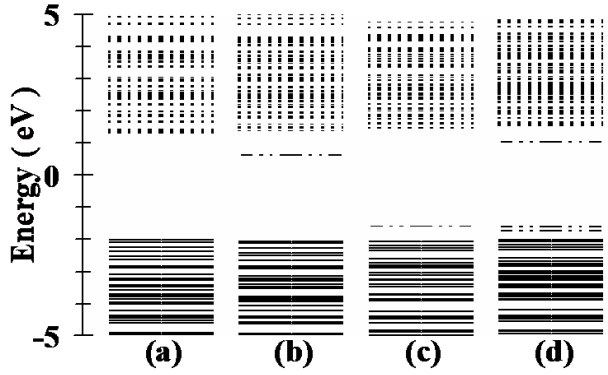

Fig.1. Energy level diagrams for (a) $Si_{71}H_{60}$, (b) C-$Si_{70}H_{60}$, (c) In-$Si_{70}H_{60}$ and (d)InC-$Si_{69}H_{60}$ clusters. Solid and broken lines represent occupied and unoccupied energy levels, and chain double-dashed lines in the gaps represent the energy levels due to the dopants

The highest occupied molecular orbital (HOMO) and the lowest unoccupied molecular orbital (LUMO) shown in Fig. 1(a) for the $Si_{71}H_{60}$ correspond to the valence band top and the conduction band bottom in a band structure of crystalline Si, respectively. For the $Si_{71}H_{60}$, the band gap energy, defined as the energy difference between the HOMO and the LUMO, is 3.35 eV, which is far from the experimental band gap energy of 1.21 eV of crystalline Si at 0K. This large difference between the experimental and calculated band gap energies is due to quantum confinement effects resulting from the cluster size of nm[9]. In Fig. 2(b) for the C-$Si_{70}H_{60}$, we can see unoccupied deep acceptor energy level just below the LUMO due to doping of C. We will discuss doping of C and its dopant ionization energy in the next section of this paper. In Fig. 2(c) for the In-$Si_{70}H_{60}$, we can see a shallow dopant energy level at E_{HOMO} + 0.44 eV due to doping of In. This energy level was determined to be threefold degenerate with T_d symmetry. Two of three orbitals in the level are filled with two electrons, while the other orbital is occupied by a single electron, so that the orbital can act as a single acceptor. In Fig. 2(d) for the InC-$Si_{69}H_{60}$, we can see three energy levels due to codoping

of C and In. An unoccupied energy level just below the LUMO is related with C, as described later. The upper level of two level just above HOMO was determined to be twofold degenerate, and the lower one was to be nondegenerate. One of the upper twofold level and the lower one are filled with two electrons. The other of the upper twofold level is occupied by a single electron, so that the orbital can act as an single acceptor. This level is called the X level. The ionization energy of the X level was determined to be E_{HOME} + 0.42 eV. Experimental acceptor ionization energies for In and InC are 0.15 eV and 0.11 eV, respectively. There exists large difference in the ionization energy of between the calculated value in the cluster Si and the experimental value in crystalline Si both for doping of In and the InC dimer. This is also due to quantum confinement effects of the carriers, already mentioned[9]. We should point out from Fig. 2 that dopant energy levels due to the codoping were formed by combining the dopant energy levels due to the single dopings, and that the atomic interaction of C and In solved the degenerate level.

Energy levels in band gap due to C doping. The energy level diagram of Fig. 1(b) shows that doping of C induces the dopant energy level in gap, as mentioned in the former Section. Doing of C into crystalline Si never induces an extra energy level in band gap, because C is isovalent to Si. In compound semiconductors such as GaP, however, it has been found that even isovalent atoms may act as dopants[10]. When C replaces Si in a Si cluster, the electronegativity of C is so great that it attracts an extra valence electron to itself, and becomes negatively charged. This makes C an isovalent acceptor in the Si cluster. The Coulomb field of the negatively charged C atom can weakly bind a hole, and this hole can be ionized to make it available to carry current if the energy level of the isovalent acceptor is shallow. We suppose that the appearance of the dopant energy level induced by doping of C might be due to the size of infinite clusters in which the movement of the additional carrier is confined. Figure 2 shows the cluster size dependence of the dopant energy

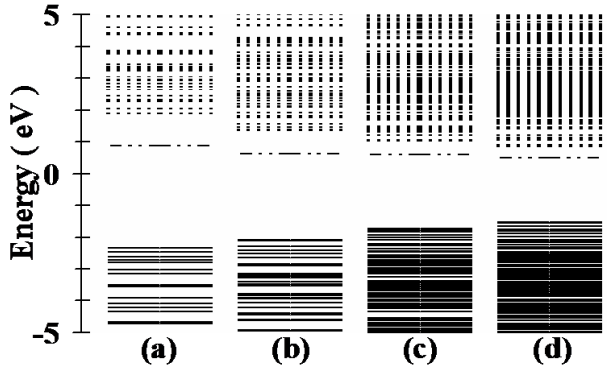

Fig.2. Energy level diagrams for (a) C-$Si_{34}H_{36}$, (b) C-$Si_{70}H_{60}$, (c) C-$Si_{164}H_{100}$ and (d) C-$Si_{264}H_{140}$ clusters. Solid and broken lines represent occupied and unoccupied energy levels, and the chain double-dashed lines in gaps represent the levels induced by doping of C, respectively.

levels for (a) C-$Si_{34}H_{36}$, (b) C-$Si_{70}H_{60}$, (c) C-$Si_{164}H_{100}$ and (d) C-$Si_{264}H_{140}$, all of which are unrelaxed. The band gap energies were determined to be 4.22, 3.48, 2.74, and 2.42 eV, respectively. The dopant energies from the LUMO were also determined to be 1.00, 0.73, 0.44, and 0.37 eV for the C-$Si_{34}H_{36}$, the C-$Si_{70}H_{60}$, the C-$Si_{164}H_{100}$ and the C-$Si_{264}H_{140}$, respectively. Both the gap energy and the dopant energy decrease as the number of Si atoms in the clusters increases. The ratios of the dopant energy to the gap energy for the corresponding cluster were calculated to be 0.24, 0.21, 0.16, and 0.15, respectively. Extrapolating the plot of the cluster size dependence of the ratios, we can get the ratio of zero value at the number of Si atoms of 1500, at which the dopant energy becomes zero. In sufficiently large Si clusters such as crystalline Si, the dopant energy level of C may reach and be beyond the LUMO.

Densities of state of In, C or InC in doped Si clusters. Figure 3 shows three pictures of densities of state (DOS) for the clusters, (a) In-$Si_{70}H_{60}$, (b) C-$Si_{70}H_{60}$ and (c) InC-$Si_{69}H_{60}$. Vertical dashed lines correspond to the dopant energy levels in the gap, shown in Fig. 1(b)-(d). Figure 3(a) shows (I) total DOS, (II) partial DOS of In, and (III) partial DOS of Si located at the nearest

neighboring In. Figure 3(b) shows (I) total DOS, (II) partial DOS of C, and (III) partial DOS of Si located at the nearest neighboring C. Figure 3(c) shows (I) total DOS, (II) partial DOS of In, (III) partial DOS of C, and (IV) partial DOS of Si located at the nearest neighboring In. From these pictures, we can see that the dominant constituents of the In and C acceptor level are the partial DOS's of In and Si, and the partial DOS's of C and Si, respectively, and that the dominant constituents of the X level are the partial DOS's of In ,C and Si.

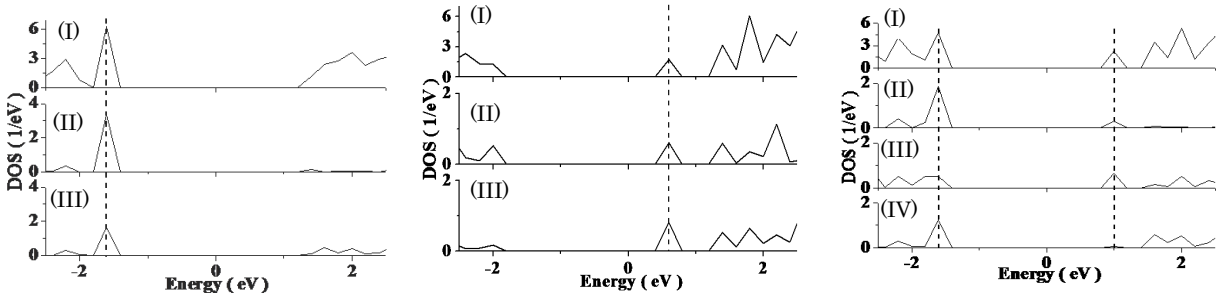

Fig. 3. Total and partial densities of states for (a) In-$Si_{70}H_{60}$, (b) C-$Si_{70}H_{60}$ and (c) InC-$Si_{69}H_{60}$. The vertical broken lines correspond to the dopant energy levels by doping of In or C, and to the X level by doping of In and C.

Bonding nature of X level. The subtotal bond overlap population Q^i_{InC} at some molecular orbital φ_i serves as an index of bonding nature. A positive or a negative value of Q^i_{InC} indicates bonding or antibonding nature of molecular orbital φ_i between In and C in InC-doped clusters. Figure 4 shows a diagram of energy levels and a picture of subtotal bond overlap population Q^i_{InC} for a InC-doped cluster. As described previously, we can see two energy levels just above the HOMO. The upper energy levels including the X level with twofold degeneracy have the antibonding interaction between the In and C, and the lower energy level with nondegeneracy has the bonding interaction between the In and C. The energy level just below the LUMO due to the doping of C has also the antibonding interaction between the In and C.

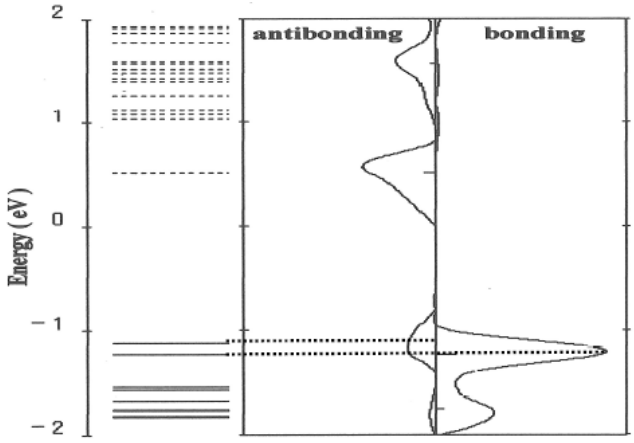

Fig. 4. A picture of the subtotal bond overlap population Q^X_{InC} at some molecular orbital φ_X, corresponding to energy level X, showing bonding and antibonding interaction between the In and C atoms in a InC-doped cluster.

Conclusion

Electronic structures of Si with C, In, or InC dimers were calculated to investigate the interaction between In and C in the X center due to the InC dimers using the discrete variational–Xα molecular orbital method mainly for basic $Si_{71}H_{60}$, C-$Si_{70}H_{60}$, In-$Si_{70}H_{60}$, and InC-$Si_{69}H_{60}$. The calculation results were as follows; (i) the In- and the InC-induced dopant levels were observed at E_{HOMO} + 0.44 eV for the In-$Si_{70}H_{60}$ and E_{HOME} + 0.42 Ev for the X level in the InC-$Si_{69}H_{60}$, respectively. The ionization energy of the X level was a little bit smaller than that of the corresponding substitutional In. (ii) dominant constituents of densities of states for the X levels were the partial densities of states of In and Si with a small part of C. (iii) subtotal bond overlap population analysis showed that the X level had an antibonding nature between In and C in the InC-$Si_{69}H_{60}$. (iv) the antibonding interaction mainly among the orbitals of In and C lowers the corresponding In acceptor level to form the shallower X level.

References

[1] I. C. Kizilyalli, F. A. Stevie, and J. D. Bude, IEEE Electron Device Lett. **17**, 46 (1996).

[2] O. Dokumaci, P. Ronsheim, C. D'emic, A. G. Domenicucci, S. Hegde, P. Kozlowski, and H. S. P. Wong, Mater. Res. Soc. Symp. Proc. **568**, 205 (1999).

[3] H. Katayama-Yoshida, T. Nishimatsu, T. Yamamoto, and N. Orita, J. Phys.: Condens. Mattre **13**, 8901 (2001).

[4] E. Atoro, Y. Ohama, and Y. Hayafuji, Appl. Phys. Lett. **83**, 3051 (2003).

[5] R. Baron, M. H. Young, J. K. Neeland, and O. J. Marsh, Appl. Phys. Lett. **30**, 594 (1977).

[6] C. E. Jones, D. Schafer, W. Scott, and R. J. Hager, J. Appl. Phys. **52**, 5148 (1981).

[7] H. Adachi, M. Tsukada, and C. Satoko, J. Phys. Soc. Jpn. **62**, 266 (1993).

[8] R. S. Mulliken, J. Chem. Phys. **23**, 1841 (1955).

[9] Y. Hayafuji, K. Ohmori, K. Igei, and N. Kambara, Int. J. Quantum Chem., **109,** No.12, 2764 (2009).

[10] A. Baldereschi and J. J. Hopfield, Phys. Rev. Lett. 28, 171(1972).

© (2012) Trans Tech Publications, Switzerland
doi:10.4028/www.scientific.net/AMM.187.210

IMPROVEMENT OF CORROSION RESISTANCE OF RARE EARTH ELEMENT (REE)-BASED ANODIC OXIDATION COATING ON AZ91D MAGNESIUM ALLOY

M. Z. M. Zain[1,a], S. Illias[1,b], M. Mat Salleh[1,c], K. A Ismail[1,d], Z. Nooraizedfiza[1,e]

[1] School of Manufacturing Engineering, Universiti Malaysia Perlis, Kampus Tetap Pauh Putra, Jalan Arau-Changlun, 02600, Arau, Perlis, Malaysia

[a]mzamzuri@unimap.edu.my, [b]suhaimi@unimap.edu.my, [c]mokhtarms@unimap.edu.my, [d]k.azwan@unimap.edu.my, [e]nooraizedfiza@unimap.edu.my

Keywords: Magnesium alloy, Rare earths element, Anodization, Corrosion resistance

Abstract. Anodization is a useful technique for forming protective films on magnesium alloys and improves its corrosion resistance. Based on the rare earth metal (REE) salt solution, the optimum parameter was selected by comparing the anti-corrosion property of anodic film. The structure, component and surface morphology of anodic film and cross-section were analyzed using X-ray diffraction (XRD) and scanning electron microscopy (SEM) coupled with Energy Dispersive Spectroscopy (EDS). The corrosion behavior was evaluated by immersion test. In this paper, a dense anodic film approximately 20 μm thick was prepared on a AZ91D magnesium alloy through anodic oxidation coating. The results show that the anodic films were mainly composed of $Mg_{17}Al_{12}$, $Mg_{17}La_2$, MgO and amorphous compounds. The best corrosion resistance was obtained with specimen anodized in solution containing both lanthanum nitrate and magnesium, whose corrosion resistance is approximately 3 times higher than that of as-received AZ91D magnesium alloy.

Introduction

Magnesium and its alloys have some excellent properties, such as the lowest density of industrial metals, a high strength-to-weight ratio, vibration absorbency, and electromagnetic wave shield characteristics. Because of these properties, magnesium and its alloys can be applied in the manufacture of components for motor vehicles, in housing for electronics, and in the manufacture of sporting goods. In addition, magnesium and its alloys are more easily recycled than synthetic resins [1], which make these materials eco-friendly.

However, the poor resistance of magnesium and its alloys to corrosion has limited the application of these materials in corrosive environments [2]. Thus, surface treatments are needed to improve the corrosion resistance of magnesium and its alloys. Anodization is a popular surface-protective treatment for magnesium and its alloys. In contrast to other surface treatments for magnesium, anodization produces a relatively thick, hard, adherent and abrasion-resistant film [3]. The most effective anodic coatings are the commercially available HAE [4] and DOW17 [5]; however, toxic substances, such as chromate and fluoride, are present in the electrolytes used in these products, and the materials treated using these methods appear green and brown, respectively, limiting their decorative use.

Recently, a few new environmentally friendly anodizing electrolytes have been developed [6]. Some researchers reported that the corrosion resistance of magnesium was bettered by the formation of a surface oxide film containing rare earth elements (REs) [7]. Besides, previous investigation has indicated that the corrosion resistance of magnesium metal was particularly improved in the solution containing both lanthanum nitrate and magnesium nitrate [8]. However, previous works was mainly focus on magnesium metal.

In the present study, Mg $(NO_3)_2$ and/or La (NO_3) were used to form anodic films on AZ91D magnesium alloy with satisfactory anti-corrosion properties by anodizing. The effects of treatment condition on the properties of the anodic film on AZ91D magnesium alloy were investigated.

Experimental

The commercial Mg-based AZ91D alloy, whose chemical composition is shown in Table 1, was employed and mounted with epoxy resin leaving an area of 10 mm x 10 mm exposed. The specimen was polished with emery paper #1000 and rinsed with distilled water.

Table 1 Chemical composition of specimen

Material AZ91D	Chemical composition (wt %)							
	Al	Zn	Mn	Si	Cu	Ni	Fe	Mg
	2.93	0.73	0.205	0.004	0.004	<0.001	0.002	bal.

The specimens were anodized in 500 mL solutions containing 0.1 mM $La(NO_3)_3$, and/or 0.1 mM $Mg(NO_3)_2$ at ambient temperature. In the electrolytic cell, a stainless steel plate was used as the cathode, while magnesium alloy was used as the anode. The specimens were anodized in various current density ranging from 10 -50 mA/cm^2 under constant treatment time. After anodization, the specimen was washed with distilled water, and then was dried in hot air. The anti-corrosive properties of the anodic films were examined against salt water. The corrosion rate of the specimen was measured in the accordance with JIS H 0541. The specimen was immersed in NaCl solution of 0.5 dm^3 for 72 hours. The NaCl concentration was 50 g/dm^3, and the pH was set as 10-11 by $Mg(OH)_2$. The corrosion test was conducted at 35°C in an incubator. The salt water was kept stirring by magnetic stirrer. The specimen was rinsed with distilled water, and the corrosion product on the surface was removed with a hard plastic brush. The specimen was weighted, and the corrosion rate, R (mm/y) was calculated by the following equation;

$$R = \frac{8.76 \times 10^4 W}{ADt} \quad (1)$$

Where W, A, D and t are weight change (g), active area (cm^2), density (g/cm^3) and immersion time (h), respectively.

The surface morphologies and cross-section of the specimen were examined using a Joel JSM-6300 scanning electron microscope (SEM) and analyzed by EDS (Shimadzu, ED AX DX-4). The structure and composition of the film are examined by XRD (Rigaku, RINT- 2500).

Results and Discussion

The surface morphologies of as-received and anodized specimen in La $(NO_3)_3$ and Mg $(NO_3)_2$ solution at 20 mA/cm^2 are shown in Fig. 1. It can be seen from Fig. 1(a) that polishing flaws still can be seen on the surface of as-received specimen. On the contrary, SEM image (Fig. 1(b)) obtained of specimen anodized in La $(NO_3)_3$ and Mg $(NO_3)_2$ solutions show that oxides are porous. In addition, obvious extended microcracks can be seen on the surface. These microcracks are caused by overlarge thermal stress in fast solidification of melts when the film surface contacts with the solution [9]. The existence of microcracks in the film may reduce the corrosion resistance of the specimen. However, the microcracks is filled with a substance with the same composition of the oxide film as revealed in Table 2.

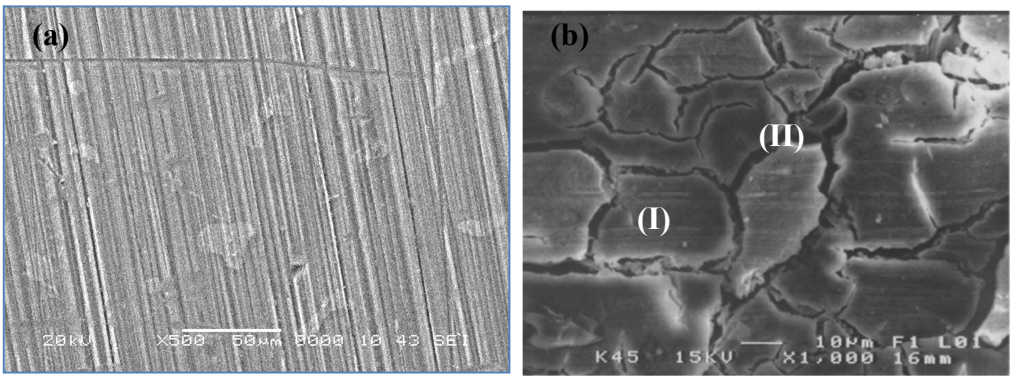

Figure 1. SEM images of (a) as-received specimen and (b) specimen anodized in La $(NO_3)_3$ and Mg $(NO_3)_2$ solution at 20 mA/cm^2 .

The oxide particles are incorporated into the coating, as proved by EDS analysis that detects elements such as oxygen, magnesium, aluminum and lanthanum. Table 2 shows the results of quantitative analysis of the anodic film surface formed in La $(NO_3)_3$ and Mg $(NO_3)_2$ solutions with different regions examination. The result show that a slightly change of amount of anodic film composition in both surface and microcracks, which indicated that the microcracks is filled with Oxygen and lanthanum originated from La $(NO_3)_3$ and Mg $(NO_3)_2$ solution.

Table 2 EDS result of different region examination of the anodic film formed in lanthanum nitrate and magnesium nitrate solution at 20 mA/cm^2 as labeled in Fig. 1(b).

	Element content (wt %)			
	O	Mg	Al	La
(I)	47.67	39.97	8.19	0.61
(II)	45.80	43.30	6.51	1.34

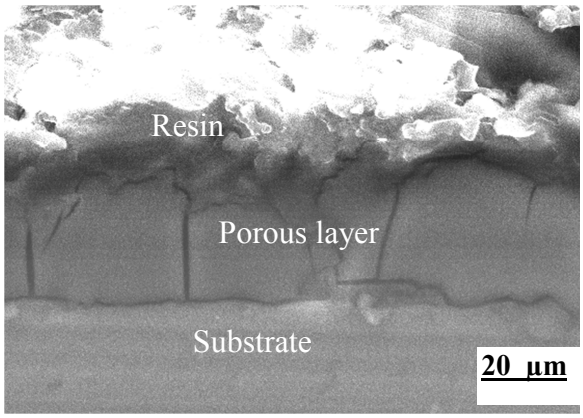

Figure 2. SEM image of the cross-section of specimen anodized in in lanthanum nitrate and magnesium nitrate solution at 20 mA/cm^2.

Fig. 2 shows the SEM image of the cross-section of specimen anodized in lanthanum nitrate and magnesium nitrate solution at 20 mA/cm^2. The oxide thickness is in the range 20-25 µm for specimen anodized in both lanthanum nitrate and magnesium nitrate solution. Conversely, the oxides produced in independent solution are thinner.

XRD analyses were carried out on the specimens coated with La $(NO_3)_3$ and Mg $(NO_3)_2$ solution to investigate the chemical composition of the different elements presented on the surface. Fig. 3 shows the XRD patterns of specimen anodized in La $(NO_3)_3$ and Mg $(NO_3)_2$ solution at 20 mA/cm^2. The result shows that β-$Mg_{17}Al_{12}$ was the main compound existing in the anodic film. It is noticed that peaks associated with MgO, and $Mg_{17}La_2$ were also identified.

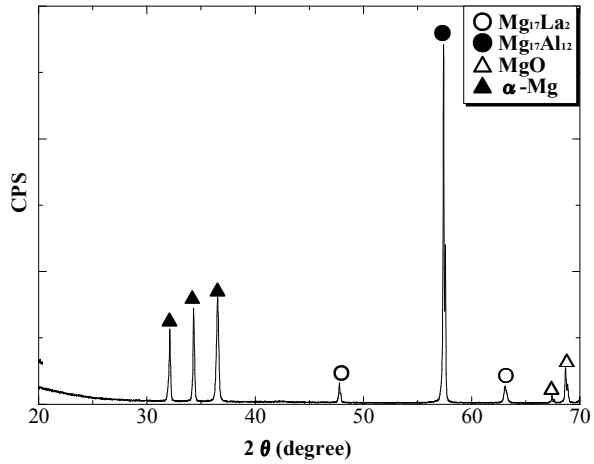

Figure 3. XRD pattern of specimen after anodized in lanthanum nitrate and magnesium nitrate solution at 20 mA/cm^2 .

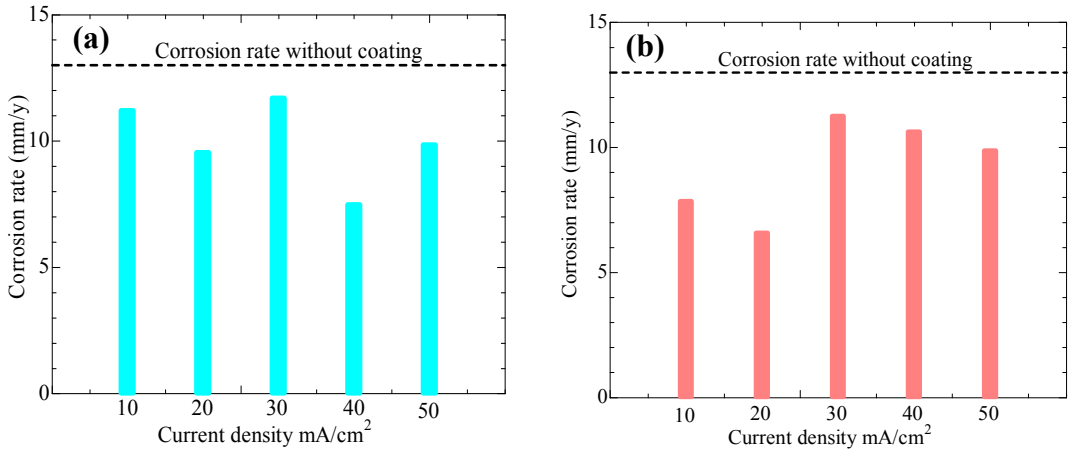

Figure 4. Corrosion rate of specimens after anodized in a) magnesium nitrate b) lanthanum nitrate solution at different current density.

The corrosion resistance of specimen was improved by anodizing in solution containing Mg $(NO_3)_2$ to some extent as shown in Fig. 4(a). The corrosion rates of all specimens are varied depending on the treatment condition. The specimen anodized in solution containing La $(NO_3)_3$ showed good corrosion resistance under some condition, but the corrosion resistance got worse under other conditions as shown in Fig. 4(b). However, the corrosion resistance of the specimen was remarkably improved when anodizing in both Mg $(NO_3)_2$ and La $(NO_3)_3$ solutions at 20 mA/cm^2 as shown in Fig. 5. The corrosion resistance of as-received specimen is about 13 mm/y, but the corrosion resistance of specimen anodized in solution containing both Mg $(NO_3)_2$ and La $(NO_3)_3$ solutions has increased to 3.7 mm/y. The coating conditions strongly affect the improvement in the corrosion resistance.

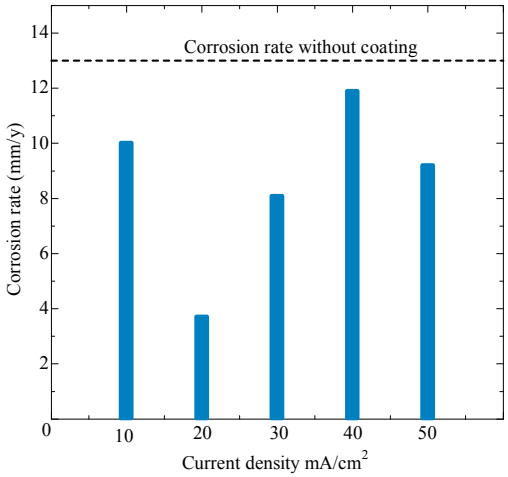

Figure 5. Corrosion rate of specimens after anodized in in lanthanum nitrate and magnesium nitrate solutions at different current density.

Conclusions

A new anodic oxidation coating was designed and produced on AZ91D magnesium alloy by anodizing aqueous solutions containing lanthanum nitrate and magnesium nitrate at ambient temperature. SEM and XRD analyses showed that the lanthanum-based anodic oxidation coating exhibited good quality with some closed microcracks. The chemical composition was uniform and the coating was enriched with β - $Mg_{17}Al_{12}$, MgO, and $Mg_{17}La_2$ compounds. The corrosion resistance of AZ91D magnesium alloy was significantly improved by the anodic oxidation coating in the solution containing both lanthanum nitrate and magnesium nitrate solution at current density 20 mA/cm^2. Thus, it is an interesting alternative to the environmentally undesirable Cr^{6+}-based coatings for all standard magnesium alloys.

References

[1] D.L. Albright, J.O. Haagensen, Life cycle inventory of magnesium, 54th Annual World Magnesium Conference, 1997.

[2] G.L. Makar and J. Kruger, Corrosion studies of rapidly solidified magnesium alloys, *J. Electrochem. Soc.* **137** (1990), p. 414.

[3] G. Song, A.Atren, D.St. John, X. Wu and J. Nairn, The anodic dissolution of magnesium in chloride and sulphate solutions, Corros. Sci. 42 (2000), p.1433.

[4] H.A. Evangelides, Method of Electrolytically Coating Magnesium and Electrolyte Therefor, U.S. Pat. 2,723,952 (1955).

[5] The Dow Chemical Company, Bath for and Method of Producing a Corrosion Resistant Coating upon Light Metals, G.B. Pat. 762,195 (1956).

[6] O. Khaselev and J. Yahalom, The anodic behavior of binary Mg–Al alloys in KOH–aluminate solutions, *Corros. Sci.* **40** (1998), p. 1149.

[7] K. Brunelli, M. Dabala, I. Calliari and M. Magrini: Corros. Sci. 47 (2005) 989-1000.

[8] T. Takenaka, T. Ono, Y. Narazaki, Y. Naka, and M. Kawakami: Electrochim. Acta 53 (2007) 117-121

[9] Xue Wenbin, Deng Zhiwei, Thin Solid Films 372 (2000) 114

© (2012) Trans Tech Publications, Switzerland
doi:10.4028/www.scientific.net/AMM.187.215

Enhancement of Mica Paper Insulation Strength with Surface Modification

ZHANG Xiaowei[1,2], LIU Shupeng[1], QIAN Yupeng[2], ZHU Yingbo[2]

[1]School of Gemology and Material technology, Shijiazhuang University of Economics, Shijiazhuang, 050031, China

[2]School of resources and environmental Engineering, Wuhan University of Technology, 430070, China

[a]liushupeng2000@163.com

Keywords: Mica paper; Strength; Surface modification; Modifier.

Abstract. Mica paper is made as one kind of insulation material, but low strength limits its applications. Surface modification is proved to be an effective way to enhance its strength. In this paper modifier like ethylene diamine tetraacetic acid, cationic polyacrylamide, cationic starch, ethylene diamine tetraacetic acid plus cationic polyacrylamide and ethylene diamine tetraacetic acid plus cationic starch are introduced to improve strengths of mica paper. Finally ethylene diamine tetraacetic acid plus cationic starch is chosen as modifier of mica flakes. After modification mica paper can reach high tensile strength of 19.84N/cm, which is more than six times high than mica paper without any modification.

Introduction

Mica is broadly used as insulation in the form of mica paper [4]. Mica paper is a paper like material made of finely flaked mica pressed together into cohesive sheets held together by van der Waals forces, without the intervention of any binders. But when mica paper is applied in the production binders and reinforcement materials are needed to enhance strength of mica paper [5]. However, binders and reinforcement materials can cut down insulation and temperature resistant of mica paper [6]. Therefore how to reduce the dosage of binders and reinforcement materials is important to the enhancement insulation property of mica paper [7].

Mica raw material, water quality, surface property and other factors affect strength of mica paper. When raw materials are chosen, one important thing for the enhancement of mica paper strength is effective decreasing of impurity ions and surface forces improvement of mica flakes [1]. Water used for mica paper production always contains large quantity of calcium and magnesium which called hard water. It is harmful to the strength of mica paper. Ways of decrease contents of calcium and magnesium is the effective way to improve the strength of mica paper. Ethylene diamine tetraacetic acid is used as titrant of calcium and magnesium when hardness of water is measured. Ethylene diamine tetraacetic acid is one kind of metal cation complexing agent which can form complex with metal cation [2]. When ethylene diamine tetraacetic acid used as modifier water can be purified, meanwhile the improvement of mica paper strength [3].

Another important way to improve strength of mica paper is using of polymer modifier. According to the paper making industry, many polymer modifiers are used to enhance the strength of papers. The most commonly used ones are polyacrylamide and starch. They are divided in cationic, anionic and non-ionic types according to the actually use. Mica has a surface with negative charge; therefore modifier with positive charge is appropriate for mica surface modification. Modifiers can improve the surface property of mica flakes; add hydrogen bonding between mica flakes, so as to improve the strength of mica paper and its insulation, heat resistant property.

Experiment

Experimental materials. Indian muscovite is chosen to do experiment. After X-ray fluorescence analysis main content of Indian muscovite is gotten like $SiO_2$48.07%; $Al_2O_3$32.73%; K_2O10.27%; $Fe_2O_3$1.92%; $TiO_2$0.28%. Combined with X-ray diffraction analysis (Fig.1) muscovite is proved to be high purity one. Before mica paper making, mica pulp should be prepared firstly. Mica pulp is prepared by calcined chemical pulp making way, so as to burn mica flakes under the temperature of 760 Degrees Celsius for 50 minutes. After calcined mica flakes are emerged into sulfuric acid with concentration of 4 percent, meanwhile violent agitation is needed to obtain fine mica flakes.

Other agents also need to be prepared. They are analytically pure calcium chloride; analytically pure ethylene diamine tetraacetic acid; cationic polyacrylamide with molecular weight of ten millions; cationic starch with 0.08 degree of substitution. One percent concentration of cationic polyacrylamide solution is prepared under the temperature of 60 Degrees Celsius while agitation. One percent concentration of cationic starch is prepared under the temperature of 95 Degrees Celsius pasting for 30 minutes.

Test of Zeta potential. Mica surface potential in pure water is tested by GSL-101B Zeta potential test equipment, and also potential in water contain calcium, ethylene diamine tetraacetic acid, cationic polyacrylamide and cationic starch.

Mica paper making. Mica pulp is pulp with fine mica flakes which are used to form mica paper depend on forces between them by ZQJ-B paper making machine. Mica pulps modified by those modifiers are also making paper by the same way. Basis weight of mica paper is 100 g/m^2. Thickness, tensile strength, dielectric strength of mica paper is tested in the experiment.

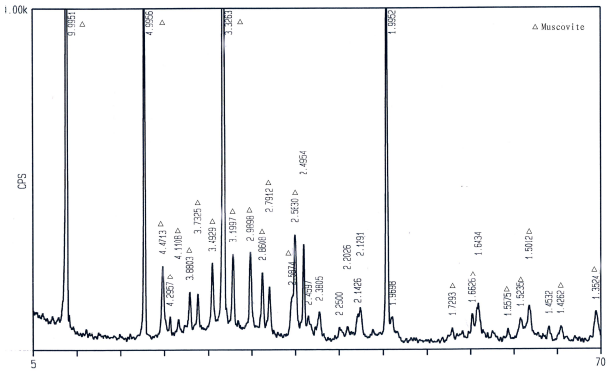

Fig. 1 XRD of muscovite

Results and discuss

Modifiers of mica flakes in pure water. Different modifiers show different effects to modification of mica surface. In this paper different modifiers ethylene diamine tetraacetic acid, cationic polyacrylamide, cationic starch, ethylene diamine tetraacetic acid plus cationic polyacrylamide and ethylene diamine tetraacetic acid plus cationic starch are chosen to modify the mica flakes. Through the changes of Zeta potential and properties of mica paper proper modifier is chosen to enhance the strength of mica paper. In the experiment mica pulp concentration is chosen as 20%, dosage of modifier is 1%, modification time 1 hour. When those are ready results as table 1 are gotten.

Table 1. Modifiers of mica flakes in pure water

Modifier	Zeta potential/mV	Basis weight/g/m^2	Thickness /mm	Tensile strength/N/cm	Dielectric strength/KV/mm
None	-21.392	101.1	0.062	5.01	22.62
Ethylene diamine tetraacetic acid	-22.016	100.6	0.061	5.36	22.66
Cationic polyacrylamide	-15.527	102.0	0.061	10.25	22.65
Cationic starch	-11.342	100.7	0.060	20.68	22.73
Ethylene diamine tetraacetic acid plus Cationic polyacrylamide	-15.466	100.4	0.060	10.31	22.59
Ethylene diamine tetraacetic acid plus Cationic starch	-11.541	100.1	0.060	20.74	22.77

Through table 1 conclusion can be gotten as follows. When ethylene diamine tetraacetic acid is added as modifier, Zeta potential of mica flakes almost didn't have any change, tensile strength of mica paper improved a little but not so obviously. When cationic polyacrylamide is added as modifier, parts of negative charge of mica surface are neutralized by the positive change of cationic polyacrylamide. Also the mica paper made from mica flakes after cationic polyacrylamide modification has higher tensile strength from 5.01N/cm to 10.25N/cm, about two times higher than before. Cationic polyacrylamide has a significant effect to improve strength of mica paper. When comes to cationic starch, more negative charges are neutralized by positive of cationic of cationic starch than cationic polyacrylamide. After cationic starch modification mica paper almost has four times higher tensile strength. It is much higher than other modifiers. When modifier ethylene diamine tetraacetic acid used together with cationic polyacrylamide or cationic starch almost same results are gotten compare to cationic polyacrylamide or cationic starch only. It means ethylene diamine tetraacetic acid almost doesn't work when mica flakes in pure water.

Table 2. Influence of impurity ions on modification

Modifier	Zeta potential/mV	Basis weight /g/m^2	Thickness /mm	Tensile strength/N/cm	Dielectric strength/KV/mm
Pure water	-21.392	101.1	0.062	5.01	22.62
Water contains calcium	-18.159	100.9	0.064	3.11	20.62
Ethylene diamine tetraacetic acid	-21.317	101.2	0.063	5.14	22.70
Cationic polyacrylamide	-12.116	100.8	0.062	7.36	21.11
Cationic starch	-8.655	99.7	0.062	16.98	21.20
Ethylene diamine tetraacetic acid plus Cationic polyacrylamide	-14.103	100.4	0.062	10.09	22.68
Ethylene diamine tetraacetic acid plus Cationic starch	-10.985	102.1	0.062	19.84	22.74

Modifiers of mica flakes in pure water. Water contain impurity ions especially metal cations are harmful to the property of mica paper and modification of mica flakes. In this experiment 1.0×10^{-3}mol/L calcium chloride is added to water to increase the hardness of water. While mica flakes and modifiers are immersed by this kind of water its property will be changed.

Table 2 shows the potential changes of mica flakes and properties changes of mica paper when hard water used. Compared to pure water hard water decreases the surface forces of mica flakes so as to the decrease of tensile strength and dielectric strength of mica paper. The existence of calcium neutralizes parts of negative charge of mica flake and compresses the thickness of electric double layer, reduced Van der Waals force between mica flakes, and increases thickness of mica paper. Those all reasons cause the decreases of tensile strength and dielectric strength of mica paper. While modifiers like cationic polyacrylamide and cationic starch are added to the water, calcium react on the surface of mica flake together with modifiers which decrease modification effects so as to get lower strength than pure water. But when ethylene diamine tetraacetic acid is added to the water, complex of calcium and ethylene diamine tetraacetic acid formed quickly makes the content of calcium decreased or vanished. Water can be pure water again [8]. Very similar data were obtained when cationic polyacrylamide and cationic starch are used combined with ethylene diamine tetraacetic acid as in pure water. So we make a conclusion that in hard water combination of modifiers is useful. When ethylene diamine tetraacetic acid removed the influence of calcium cationic plays its full role as in pure water.

Influence of modifier dosage on modification. Ethylene diamine tetraacetic acid plus cationic starch have shown excellent performance as modifier of mica flakes. As shown in the experiment 1% concentration of ethylene diamine tetraacetic acid almost can remove the calcium in water. Maintain the dosage of ethylene diamine tetraacetic acid, different dosage of cationic starch is added to modify mica flakes. Modification effects data are shown in table 3 and fig 2.

Tensile strength of mica paper improves while dosage of modifier increases. However, more than 1% of cationic added is not so useful for the improvement of mica paper tensile strength. Therefore, 1% of dosage for cationic use is suitable.

Table 3. Influence of modifier dosage on modification

Dosage of modifier /%	Zeta potential/mV	Basis weight /g/m2	Thickness /mm	Tensile strength /N/cm	Dielectric strength /KV/mm
0.6	-13.125	100.5	0.061	15.28	22.70
0.8	-12.991	101.2	0.060	17.42	22.68
1.0	-11.541	100.1	0.060	20.74	22.77
1.2	-11.054	102.1	0.060	21.03	22.76
1.4	-11.006	100.9	0.060	21.14	22.70

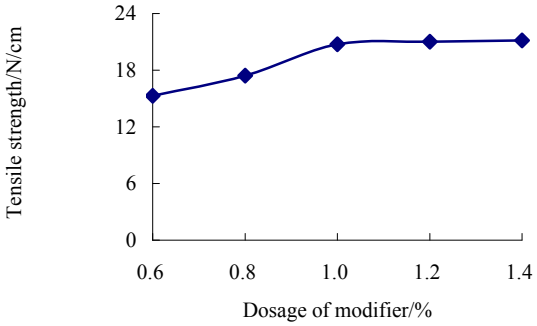

Fig 2 Influence of modifier dosage on modification

Mechanism of combination modifier. Firstly, calcium and magnesium of hard water can form complex with ethylene diamine tetraacetic acid which can remove the impurity ions before mica flakes are immersed into water. Without impurity ions modifiers can work just the same as in pure water. Then cationic starch solution is added as the modifier that can attract to surface of mica paper depending on the attraction between positive charge of cationic starch and negative charge of mica surface[9]. The starch attracted on the mica surface existing large quantity of units which can provide strong hydrogen bonding to form Hydrogen Bridge between mica flakes [10]. Cationic starch improves surface force between mica flakes, providing much higher tensile strength and humidity resistance of mica paper.

Conclusions

- According to the data of experiment modification of mica flakes can effectively improve strength of mica paper.
- Modifier used in water not so hard could be cationic only. After modification tensile strength of mica paper might be as high as 20.68N/cm, about three times higher than without any modification.
- When used in hard water cationic starch modifier only can't catch perfect effect. Cationic starch combined with ethylene diamine tetraacetic acid can solve the hardness of water problem. Modified mica flakes can make mica paper with 19.84N/c tensile strength which is more than five times than the flakes without modification.
- While dosage of ethylene diamine tetraacetic acid is determined to be 1% dosage of cationic starch choose 1.0% will be more economical.

Mica flakes used for mica paper making after modification can reach a high strength, no need of binders to be added. Mica paper insulations made from those kind of mica paper has the properties of high strength and high content of mica that can provide higher insulation strength, heat resistance and moisture resistance. Mica paper can be made materials which can't afford before.

References

[1] M. Ashraf Chaudhry, Rew K Jonscher, “The Dielecteric properties of Mica Paper in Variable Temperature and Humidity,” Journal of materials science, vol. 20, Oct. 1985, pp. 3581-3589, doi:10.1007/BF01113764.

[2] H.K Christenson, “Adhension and Surface Energy of Mica in Air and Water,” Journal of Physical Chemistry, vol.97, Nov. 1993, pp. 12304-12041, doi:10.1021/j100148a032.

[3] Lei Xu, Miquel Sameron, “Effects of Surface Ions on the Friction and Adhesion Properties of Mica,” Langmuir, vol.14, Mar. 1998, pp. 2187-2190, doi:10.1021/la9713659.

[4] REN Yaowu, “Industrial Used and Development of Crushing Mica,” Geology of Inner Mangolia, vol.3, Mar. 1998, pp. 17-21, doi: ISSN:1007-7715.0.1998-03-002.

[5] YUAN Chuxiong and TIAN Zhongkai, “Mica and Intensive Processing,” Metallic Ore Dressing Abroad, vol.33, Apr. 1996, pp. 42-45, doi: ISSN:1003-4129.0.1996-04-013.

[6] GONG Xianzheng and ZU Zhanliang, “Mica Processing Technology Status and Development Trend,” China non-metallic mining industry Herald, vol.17, May. 2000, pp. 42-45, doi:ISSN:1007-9386.0.2000-05-005.

[7] XU Wenxin and GUO Tuozhu, “Research of mica materials and Its Prospect,” Mineral Resources and Geology, vol.15, Mar. 2001, pp. 42-45, doi: ISSN:1001-5663.0.2001-03-010.

[8] SUN Chuanyao and Yin Wanzhong, Principles of Silicate Minerals Flotation, 1st ed., vol. 1. Beijing, 2001, pp.93–105.

[9] HUANG Bofen and SHANG Xiaoqin, “Application of C-3 Cationic Starch as strengthening Auxiliary in Packet Paper s Production,” Chemical Industry Times, vol.6, Mar. 2002, pp. 47-49, doi: ISSN:1002-154X.0.2002-06-015.

[10] ZHONG Guangquan, “Effects of Conductivity and Degree of Substitution of Cationic Starch on the Dry Strength Improvement of Paper,” Paper Science & Technology, vol.28, Apr. 2009, pp. 42-44, doi: SUN:GDZZ.0.2009-02-010.

© (2012) Trans Tech Publications, Switzerland
doi:10.4028/www.scientific.net/AMM.187.220

Index Loss Analysis of YBCO Coated-conductor Coils by Means of Simulation

Xiu Li[a], Yinshun Wang, Yangrui Zhang

North China Electric Power University Beijing, 102206, China

[a]liixiu@126.com

Keywords: Critical Current; Index Loss; N-Value; Weibull Distribution

Abstract. The high temperature superconducting (HTS) tape has low index value compared with the 1st generation superconductor based on the power-law model of V-I characteristics because of its intrinsic characteristics of weak-link and low pinning potential. So, there is potential drop resulting in joule heat called index loss when it operates below quench. To search a way for researching, the Weibull distributions of critical current and n-value in turns of a model double-pancake (DP), made of coated conductor, are numerically calculated based on anisotropic empirical models obtained by fitting the experimental data in the temperature of 77 K. And also the index loss of double-pancake (DP) is also calculated. Then, the double-pancake is tested at 77 K, furthermore the simulative results are quietly approaching the experimental results. Finally the optimal operation current for this DP is discovered.

Introduction

With development of high temperature superconductor, great progress on HTS application has been achieved as the magnet which is made of HTS coils. Due to its higher critical current density, weak anisotropic properties and potential low cost, YBCO coated-conductor so called 2nd generation HTS tapes become the important candidate for magnet application in mid- and low temperature and electrical application in 77 K. Since the technology of YBCO coated conductor tape has achieved tremendous development, km length of the coated conductor can be obtained as in superconducting cable and magnet [1]. It is promising for application of electrical engineering although there are some problems [2].

However, though the coated conductor has less anisotropic than the 1st generation Bi2223/Ag tapes in perpendicular magnetic field [3], its anisotropy still needs to investigate in design of HTS devices.

Due to its weak averaged pinning potential which results in relative flat V-I curve compared with the conventional superconducting wire or tape, there is non-ignorable joule loss (so called index loss) if operating close but below critical current.

In HTS coil, the critical current and *n*-value of each turn are not uniform because magnitude and orientation of magnetic field in each turn is different. So the end-to-end test for the critical current and n-value of the coil can not reflect local characteristics in detail since there are distributions of the critical currents and *n*-values in the whole coil. It is necessary to make statistic analysis according to the Weilbull distribution of critical currents and *n*-value on each turn of the coil. Regard to the Weibull distribution which was first used in 1939 by Wallodi Weibull, there are three parameters called shape, scale and location. Furthermore, shape parameter is the key which determines the basic shape of the distribution density curve just as its name implies. Simultaneously, analysis on the index loss of the double-pancake at different transport current is significant for stable operation of the high temperature superconducting coil. In this paper, the index loss of a HTS double-pancake model is calculated by use of power-law models, and tested in liquid nitrogen temperature of 77 K. Then the optimal operation current can be determined, which is useful for practical application of HTS coils.

Calculation Model

The effects of perpendicular and parallel external field on the critical current and *n*-value are not identical due to anisotropic property which is the intrinsic characteristics of HTS. By fitting the experiment data shown as Fig. 1 and Fig. 2, the calculation models of critical current and *n*-value are obtained which are shown in (1) and (2).

$$I_c(B_{//},B_{\perp}) = I_{c0}/(48-6.8\exp(-B_{//}/B_0)-40.2\exp(-B_{\perp}/B_0)) \quad (1)$$

In the critical current model (1), I_{c0} is the critical current at self field in temperature of 77 K, $B_{//}$ and $B_{\perp}$ are the parallel and perpendicular field components, respectively, and B_0 is the constant of 12T. Correspondingly, the *n*-value for the conductor is determined as (2) where n_0 is the *n*-value at 77 K and self-field, B_0 is the 0.7 T. Obviously, Fig. 1 and Fig. 2 prove that the models are accurate and suitable in the experiment and the following calculation although there is little distance.

$$n(B_{//},B_{\perp}) = n_0/(30.8-7.5\exp(-B_{//}/B_0)-22.3\exp(-B_{\perp}/B_0)) \quad (2)$$

The other coefficients in (2) are different from (1) because the effect of parallel and perpendicular field on critical current and *n*-value are different. Generally, the critical current and n-value of HTS tape can be obtained by fitting *V-I* curve to power-law (3)

$$E = E_c(I/I_c)^n \quad , \quad (3)$$

Where E_c is the criterion of 1 μv/cm and E is the voltage per centimeter length of the tape with transporting current I.

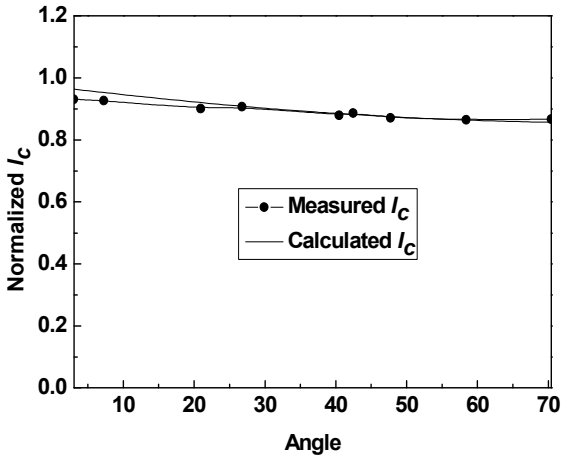

Fig.1. The Relationship of Normalized Ic and Angle.

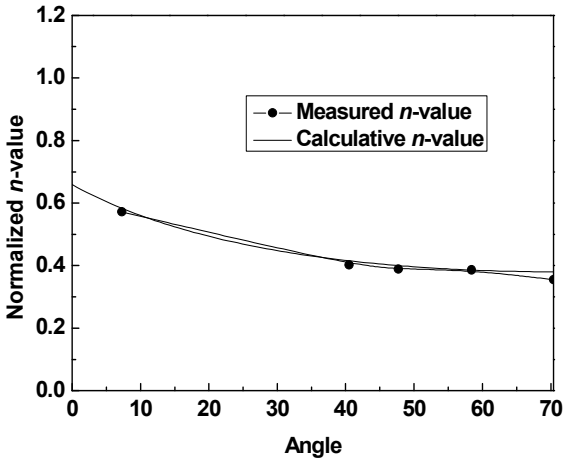

Fig.2. The Relationship of Normalized N-Value and Angle.

The index loss of the double-pancake is calculated by the sum of joule loss in each turn shown in (4), where I is the transport current in the double-pancake.

$$P_{index} = 2 \times I \times \sum_{j=1}^{225} E_c \times (I / I_{c,j})^{n_j} \times L_j \tag{4}$$

$I_{c,j}$ and n_j can be obtained from (1) and (2), which are the critical current and n-value of the j^{th} turn in the single-pancake respectively, L_j is the length of the turn which is equal to $2\pi r_j$, r_j is the radius of the j^{th} turn.

DP Fabrication and Experiment

The high temperature superconducting double-pancake is wound by the coated conductor YBCO tape produced by *SuperPower*. The dimension of the tape is 0.1 mm×4.0 mm. The main parameters of the DP are shown in Table 1. The tape is insulated by wrapping of insulation films.

Firstly, the short sample is tested by traditional four-probe method for measuring the *V-I* relation in liquid nitrogen temperature of 77 K and self field, its critical current and *n*-value are 85.0 A and 11.9, respectively. And then the double-pancake is tested.

Table.1 Main parameters of The DP

Parameters	Value
Turns	450
Inner radius	26.765 mm
Outside radius	105.52 mm
Total length	201 m
DP height	11.17 mm

Results and Discussion

The magnetic field distribution of the DP is calculated by the finite element method (FEM), Fig. 5 and Fig. 6 show the perpendicular and parallel magnetic field distribution at operating current of 15 A, respectively. Fig. 7 shows the schematic configuration of the coil turns. The first turn is the innermost layer, as well as the 225^{th} turn is the outermost layer. The perpendicular field increases from the 1^{st} to 148^{th} turn and then decreases. Simultaneously, the parallel component reduces from 1^{st} to 186^{th} turn, then it increases.

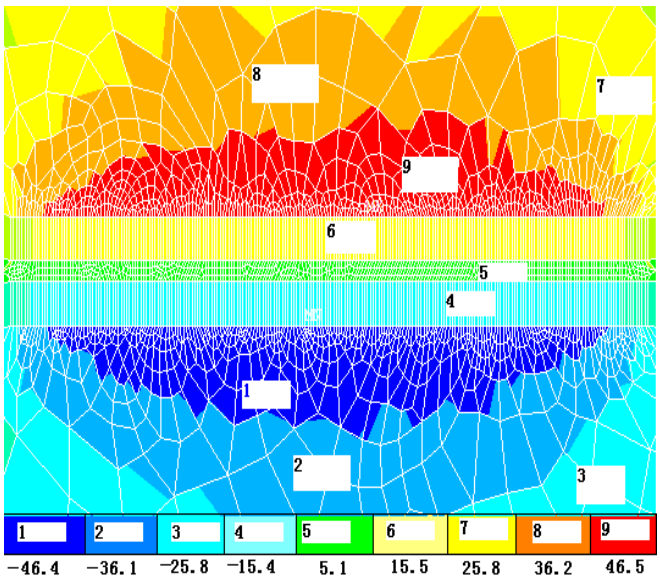

Fig.5. The Distribution of the Perpendicular Field in the Double-Pancake.

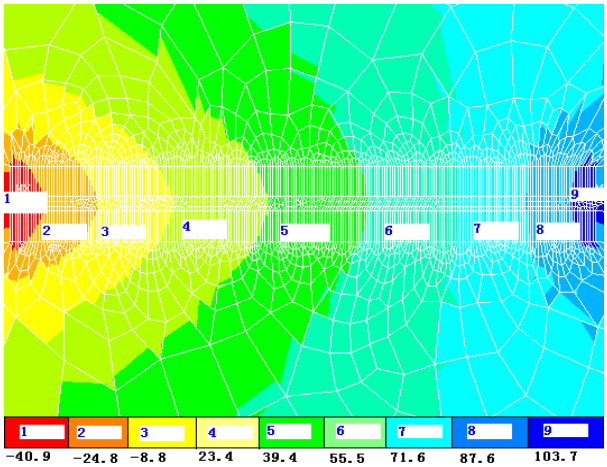

Fig.6. The Distribution of the Parallel Field in the Double-Pancake.

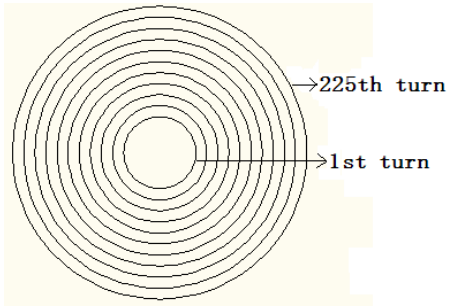

Fig.7. Schematic Configuration of the Coil Turns

It is obtained that the strongest perpendicular field component is round the 148th turn, and the weakest one occurs on the inner and outer edge. Also there is little disparity between them. Simultaneously, the strongest parallel component of the field presents on the inner edge, and the weakest one is near the 186th turn, and there is larger disparity range between the minimum and maximum.

Based on empirical models of (1) and (2), the distributions of critical current and *n*-value in each turn at different transport current are calculated, the results are shown in Fig. 8 and Fig. 9.

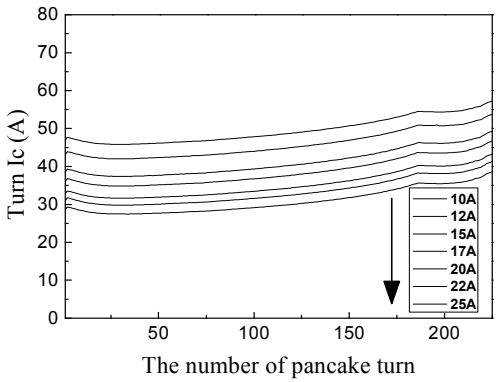

Fig.8. The Critical Current Distribution of Each Turn with Different Current.

With different transporting current, the I_c of around 30th turn is the lowest. For example, the I_c of 28th turn is the lowest in the total coil when the current is 10 A. In Fig. 8, the lines from top to bottom show I_c -*N* with the current 10, 12, 15, 17, 20, 22 and 25 respectively. By the way, N is the number of turn. Variation trend of the critical currents is qualitatively agreed with the *n*-value.

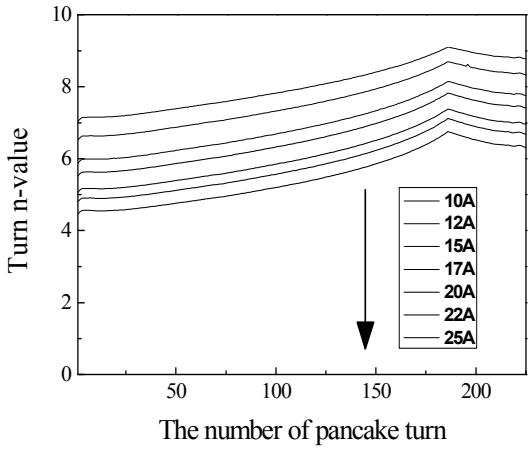

Fig.9. The N-Value Distribution of Each Turn with Different Current.

In Fig. 9, the lines from top to bottom show *n*-*N* with the current 10, 12, 15, 17, 20, 22 and 25 respectively. The lowest n-value presents at the inner end of the DP. Additionally, the measured Ic and n-value of the DP by end-to-end can not accurately reflect the overall performance because the property of the DP is mainly determined by the weakest point in turns of DP. So the overall performance can be analyzed by the statistical method which is a useful tool for analyzing the distributions of the critical current and *n*-value in the whole DP. The parameters of the Weibull function including the scale parameter *a* and the shape parameter *b* can be acquired by fitting the I_c-*N* and *n*-*N* curves respectively [4]. I_c-*N* and *n*-*N* mean different turn is with different critical current and *n*-value. When the transport current is 15 A, the Weibull function of the critical current is described by (5)

$$\begin{cases} F = 1 - \exp(-((I_c - I_{c\min})/a)^b) \\ f = ba^{-b}(I_c - I_{c\min})^{b-1}\exp(-((I_c - I_{c\min})/a)^b) \end{cases}, \tag{5}$$

where the *a* and *b* are equal to 3.6050 and 0.8831, the $I_{c\min}$ is the minimum critical current among all of the turns in a single- pancake which is 37.4 A.

Fig. 10 shows the Weibull function and probability of critical current distributions in the DP. It presents that most of the turns are with low critical current close to the minimum which indicates that the part of low critical current has major contribution to the global critical current of the DP. So the average critical current of the DP is about 38-40 A. It can be calculated by the integral formula (6), Where the variable I_{ci} is the critical current of every single turn, $f(I_{ci})$ is the probability density and $I_{c,coil}$ is the global critical current of the DP. And the $I_{c\max}$ is the maximum critical current for all of the turns.

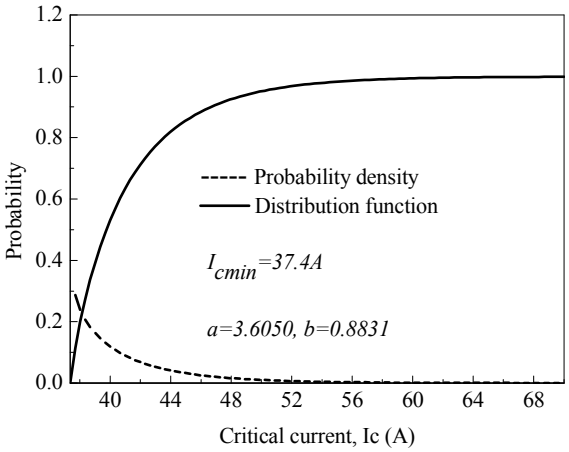

Fig.10. The Weibull Distribution of the Critical Current for the Single-Pancake Coil.

$$\int_{I_{c\min}}^{I_{c\max}} I_{ci} \cdot f(I_{ci}) dI_{ci} = I_{c,coil} , \tag{6}$$

Weibull function of the *n*-value is given by (7)

$$\begin{cases} F = 1 - \exp(-((n - n_{\min})/a)^b) \\ f = ba^{-b}(n - n_{\min})^{b-1} \exp(-((n - n_{\min})/a)^b) \end{cases} , \tag{7}$$

where a and b are 1.1701 and 1.4332, the $n_{\min}$, i.e. the minimum *n*-value among the all of the turns in the single-pancake, is 5.9.

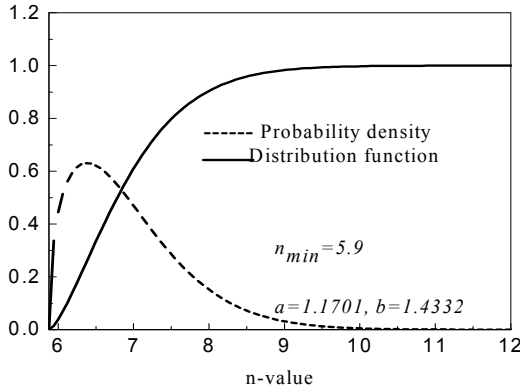

Fig.11. Weibull Distribution of the N-Value in the Single-Pancake.

With transport current *I* 15A, Weibull function of the *n*-value is shown as in Fig. 11. It shows that the probability of *n*-value below 7 is near 0.5. The *n*-value of turns mostly even all is below 9. Similarly, part of the low *n*-value has major distribution to the global *n*-value of the DP. It can be calculated by the integral formula (8)

$$\int_{n_{\min}}^{n_{\max}} n_i \cdot f(n_i) dn_i = n_{coil} , \tag{8}$$

Where the variable n_i is the exponent n of every single turn, $f(n_i)$ is the probability density and n_{coil} is the average *n*-value of the DP. The $n_{\max}$ is the maximum *n*-value for the single-pancake.

So when the applied current is given, the critical current and *n*-value of the magnet consisting of several pancake coils can be simulated.

The loss of each turn is very different since the different I_c's and *n*-values result in different voltage drop. With transport current is 10 A, 12 A, 15 A, 17 A, 20 A, 22 A and 25 A, the index losses of the DP were simulated and experimentally tested in liquid nitrogen temperature of 77 K. Fig. 12 presents the experimental and the calculated losses. It shows that the calculative loss is good agreed with the experimental loss if the transport current is below 22 A although the experimental results are little more than the calculated ones. The reason is that generation heat in inner turns can not be transferred to liquid nitrogen in time and then it induces the local temperature rise resulting in the reduction of local critical current and the *n*-value. Both of them intersect at 21 A. When transport current is higher than 22 A, the difference between them is serious, calculated results are much more than the experimental ones, which results from the fact that simulation still follows the power law model with $n>1$, but when the YBCO quenches, it gradually transfers into normal state, then it observes conventional Ohm law with $n=1$. Therefore, it is estimated that the optimal operation current for this DP should be determined below 21 A considering the margin for stably applying although it does not quench near 25A. The detailed and exact simulation should consider the heat transfer equation and the dependence of critical current on temperature in near future.

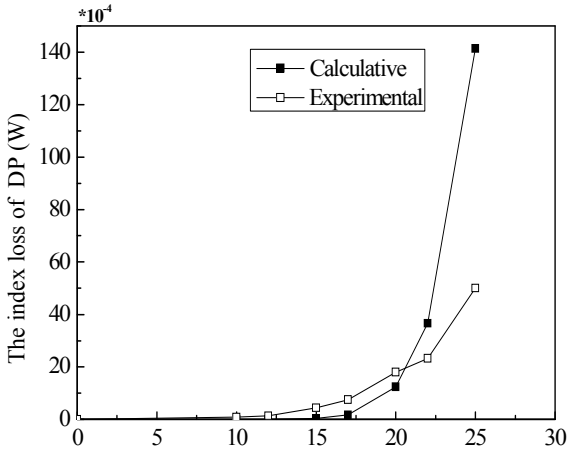

Fig.12. Index Loss of the DP at Different Operation Currents.

Conclusion

The distributions of local critical currents I_c's and n-values of a double-pancake made of YBCO coated conductor are numerically calculated and fitted by the three-parameters Weibull function based on their empirical anisotropic models. The index loss for the double-pancake is also simulated and tested in liquid nitrogen temperature of 77 K, both of them are good qualitatively agreement with each other below 21 A below which is determined to be the optimal operation current. This estimation possibly provides useful method for practical operation of HTS magnet.

References

[1] O. O. Ige, D. Aized, D. Bushko, A. Curda, R. Medeiros, and G. Snitchler, "A demonstration HTS magnet for minesweeping application (Periodical style)," IEEE Trans. Appl. Supercond. vol. 10, no. 1, pp. 482-485, March 2000.

[2] Yuri Lvovsky, "limiting length in cooling design of HTS magnets (Periodical style)," IEEE Trans. Appl. Supercond. vol. 11, no. 1, pp. 1840-1843, March 2001.

[3] J. Yates Coulter, Jeffrey O. Willis, Monikka M. Mann, Paul C. Dowden, Stephen R. Foltyn, Paul N. Arend et al., "Magnetic-field anisotropy of high-critical current YBCO coated conductors (Periodical style)," IEEE Trans. Appl. Supercond. vol. 9, no. 2, pp. 1487-1489, June 1999.

[4] K Ogawa and K Osamura, "The Weibull distribution function as projection of two-dimensional critical current distribution in Ag/Bi2Sr2Ca2Cu3O10+δ tapes (Periodical style)," Supercond. Sci. Technol. vol. 20, no. 5, pp. 479-484(6), May 2007.

© (2012) Trans Tech Publications, Switzerland
doi:10.4028/www.scientific.net/AMM.187.227

The Synthesize and Properties of Aquosity Polyester Acrylate Nanoemulsion

Cui Yan, Ma Changzheng, Zhang Guangcheng and Qi Fengjun

(Armored Force Technology Institute ,Changchun 130117,China)

Keywords: Nanometer emulsion, block type, nanometer paint

Abstract*:* A new type of polymer nanoemulsion has been synthesized by molecular self-assembly technique. The emulsion particle size that can be clearly observed by CENT is less than 100nm. The results of these measurements support the idea that polyacrylate molecular segments assemble with polyester segments. Then based on the polymer nanoemulsion, waterborne block type exterior architectural nanopaints have been prepared. The waterborne coatings behave good water-resistance, physics-mechanical properties and decorative and protective performance. Scrub resistance improves greatly which can reach 10000 times.

At present, most nanometer paints were modified paints, they were produced by traditional emulsion and nano-fillers. Due to the big particle size of the polymer latex, harder polymer, and higher temperature of the film, the paint is difficult to form a whole film, and resistance to water is bad, adhesion is lower, gloss is not good, etc. [1-8] We have synthesized unsaturated fatty acid modified metacrylic acid polyester nanoemulsion by molecular self-assembly polymerization without emulsifier. The particle size are between 1~100 nm. Paints were prepared using this nanoemulsion, adhesion, washability, weather ability and barrier propterty were improved.

The Synthesize of Unsaturated Fatty Acid Modified Metacrylic Acid Polyester Nanoemulsion

Reagents and instruments. benzoic acid, soya fatty acid, phthalic anhydride, pentaerythrite, trimethylolpropane, dimethylbenzene, methacrylic acid, methyl methacrylate, butyl methacrylate, benzoyl peroxide, three-neck flask, etc.

Synthesize. Unsaturated fatty acid modified metacrylic acid polyester nanoemulsion were synthesized by high shear emulsion process after the reaction of hydrophobic polymer and hydrophile methyl methacrylate, volatility amine as neutralizer in water, tru-sealer as assistant.

The synthesize of hydrophobic unsaturated fatty acid modified silicone polyester resin. Benzoic acid, soya fatty acid, phthalic anhydride, pentaerythrite, trimethylolpropane, dimethylbenzene were put into the reactor by the resipe. This mixer is heatd with stirring and keep 1.5h at 160-170°C. Then heating-up again keep 6h at 230±2°C. and ester water is removed by steam-stripping. Then cooling the mixture, add dimethylbenzene and titanic isopropyl ester at 180°C, after reaction for 6h at 170±2°C,cooling to reserve. The properties showed in table1.

TABLE I. THE PROPERTIES OF HYDROPHOBIC UNSATURATED FATTY ACID MODIFIED SILICONE POLYESTER RESIN

item	properties
product appearance	Water white yellowish resin liquid
solid content %	50±2
acid value ≤	9

50 parts dimethylbenzene and 50 parts butanol were put into reactors, the mixture is heated to 115±2°C with stirring under nitrogen protection. Under this temperature, hydrophobic unsaturated fatty acid modified silicone modified polyester resin were add into the mixture at dropwise within 3h, then cooling the mixture to reserve. The properties showed in table2.

The synthesize of hydrophile methyl methacrylate.

TABLE II. THE PROPERTIES OF HYDROPHILE METHYL METHACRYLATE

item	properties
product appearance	Water white transparent liquid
solid content %	15.0
acid value ≤	50±2

The synthesize of unsaturated fatty acid modified silicone metacrylic acid polyester nanoemulsion. Hydrophile methyl methacrylate copolymer and hydrophobic unsaturated fatty acid modified silicone polyester resin were mixed with the same quantity and stirring to blend. At 100±2°C, organic solvent was removed by vacuum. When solid content % is achieved 85%, mixture were pumped into high shear reactor with stirring, PH value regulator AMP-95 and 3% tru-sealer soft water were put into the reactor at first. Under the condition of 75±5°C, 1400-1600rpm, 40-60min, aquosity block unsaturated fatty acid modified silicone metacrylic acid polyester nanoemulsion were synthesized. The properties showed in table3:

TABLE III. THE PROPERTIES OF UNSATURATED FATTY ACID MODIFIED SILICONE METACRYLIC ACID POLYESTER NANOEMULSION

item	properties
product appearance	Transparent water dispersion liquid
solid content %	30±2
acid value ≤	9.5±0.5
particles size nm	30±10

Test of polymer emulsion particles size. Transmission electron microscope(TEM): the emulsion were diluted by deionized water(concentration is about 0.1%), the particles size were tested by capillary electrophoresis nanoparticlesTEM.

Results and Discussion

TEM analyze. Particles size of polymer emulsion were tested at the University of Hong Kong, the results are showed in table4 .

TABLE IV. PARTICLES SIZE OF POLYMER EMULSION

item	index
1．average diameter	72nm
2．range	54 ~ 89nm
3．standard deviations	10nm

TEM picture of polymer emulsion are showed in figure1 :

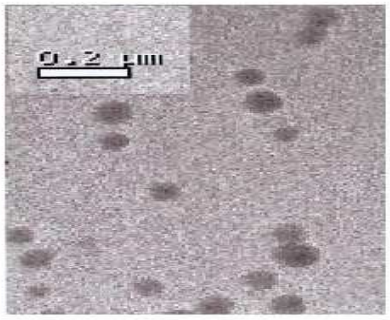

Figure 1. TEM picture of unsaturated fatty acid modified silicone metacrylic acid polyester nanoemulsion

From Fig.1, we can see that the particles size of unsaturated fatty acid modified silicone metacrylic acid polyester nanoemulsion is nanometer. The structure of the particles is nuclear shell structure, the size is smaller, the film is more compact contrast to the traditional emulsion. As a result erosion protection of this emulsion is more effective.

The film were prepared according to the Chinese Standard, the film were put into the oven at 120℃ for 20min after the surface were dried, then preserve under room temperature for one week, the film front surface and cross section were characterized by TEM JXA-840, the pictures are showed in fig.2 and fig.3.

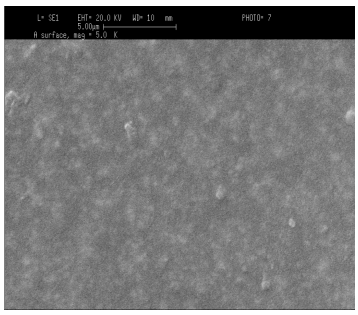

Figure 2. The front surface of the film

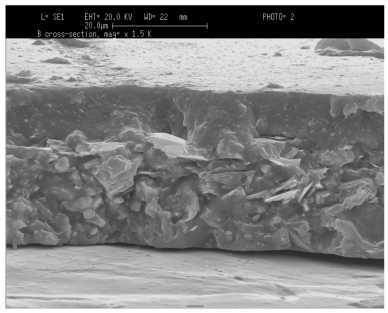

Figure 3. Cross section of the film

The properties of the film are determined by the particles size. The properties of the nanoemulsion and the traditional emulsion are showed in table 5

TABLE V. THE PROPERTIES OF THE NANOEMULSION AND THE TRADITIONAL EMULSION

properties	traditional emulsion(D>100nm)	nanoemulsion(D<100nm)
adhesion	0.5MPa	>1.5Mpa
Viscosity T-4 cup	13-15s	40-120s
resistance to water	<8h	<12h
resistance to salt spray	<500h	>1000h
washability	1000 times	>10000 times
stain resistane	bad	good

Conclusions

From the picture of front surface and cross section of the film, nanoemulsion can form the film with more density, more smooth, higher adhesion strength contrast to the traditional emulsion, due to small-size effect and bigger specific surface area. The film prepared using the nanoemulsion can resistance to water, oxygen and ions more effectively, and washability and stain resistane can satisfied the performance requirements.

References

[1] ZHANG Li-de, MU Ji-mei. Nanomaterial and Nanostructure. Beijing: Science Press, 2001, 51~67

[2] XU Guo-cai, XIN Hong-fei. Paint & Coatings Industry, 1999, (7): 3~5

[3] Schlarb B, Rau M G, Haremza S. Progress in Organic Coatings, 1995, 26: 207-215

[4] Schlarb B, Haremza S, et al. Progress in Organic Coatings, 1996, 29: 201-208

[5] Peng Y X, Zheng Z H, et al. Progress in Organic Coatings, 2003, 48: 161-163

© (2012) Trans Tech Publications, Switzerland
doi:10.4028/www.scientific.net/AMM.187.231

A Novel Anti-fuse Based on (Ba, Sr)TiO_3(BST) and Pb(Zr, Ti)O_3 (PZT) Thin Films

TANG Qianying[a], YUAN Liu, HE Yafan, LI Ping, XIE Xiaodong, WANG Gang

State Key Laboratory of Electronic Thin Films and Integrated Devices, University of Electronics Science and Technology of China, Chengdu, China

[a]tang_qanying@hotmail.com

Keywords: Anti-fuse; PZT; BST.

Abstract. This paper presents a new application of (Ba, Sr)TiO_3(BST) and Pb(Zr, Ti)O_3 (PZT) thin films in anti-fuse and their resulting anti-fuse behaviors. Compared with amorphous silicon, BST and PZT anti-fuses demonstrate distinct advantages: lower on-state resistance and lower breakdown electric field. With the sandwich-like structure of Pt/Ferroelectric Ceramics/Pt, the devices exhibit an apparent anti-fuse behavior. The resistivity of BST structure switches from 6.7 MΩ to 12.3 Ω at the average breakdown electric field of 0.3 MV/cm, while the PZT structure switches from 106 MΩ to 10.7 Ω at the average breakdown electric field of 1.3 MV/cm. Finally, the prospect of using BST and PZT is discussed and suggestions for their improvements are proposed.

Introduction

Anti-fuse is a device that is widely applied in FPGA, PROM and EPROM chips. This paper presents a sandwich-like structure of anti-fuse, with the bottom and top electrodes being the two metal layers and the layer between the electrodes being dielectric. The non-programmed anti-fuse operates like a capacitor with a high off-state resistance. However, when the voltage applied on the anti-fuse exceeds the threshold value, the device will experience an irreversible thermal breakdown and form a fusible interconnection. This programming process results in a sudden switch of resistivity from at least several mega ohms to several ohms.

In BST- and PZT-based FRAMs, the above breakdown phenomena have been observed in the cells [1, 2]. This characteristic is coincident with the programming principle of anti-fuse. Thus, it makes BST and PZT which are usually applied in FRAMs prospective materials as anti-fuse dielectric. This paper aims at discussing the metal/dielectric/metal (MDM) anti-fuses based on BST and PZT. We are primarily concerned with the following features of the anti-fuse: off-state resistance, leakage current, programming voltage and on-state resistance. Finally, the prospect of applying BST and PZT thin films in the anti-fuse is discussed.

Process and Experiment

Si/SiO_2/Ti structures were used as substrates for the metal/dielectric/metal anti-fuse. The thickness of the SiO_2 layer is 650 nm. A 15 nm thick Ti film was deposited using Sputtering System For Ferroelectric Thin Film followed by 110nm of Pt. The PZT film was then deposited with $PbZr_{0.53}Ti_{0.47}O_3$ ceramic using the same instrument. The sputtering condition was prepared with a base pressure of ~10-5 Pa, wafer temperature of 400℃ and Ψ(Ar：O_2)=50:1. Under such condition, a PZT thin film with the thickness of ~300nm was deposited and then annealed at the temperature of 650℃.

The BST ($Ba_{0.6}Sr_{0.4}TiO_3$) film was sputtered in the Multi-workpiece RF Magnetron sputtering System with a base pressure of ~10^{-4}Pa, wafer temperature of 400℃ and Ψ(Ar：O_2)=2:1. Finally, another Pt layer was deposited on top of the BST and PZT films.

The test was conducted on the probe station, with Agilent's Semiconductor Parameter Analyzer 4155B applying swept voltage on the top electrode. According to the test results and the I-V characteristic, the leakage current and programming voltage could be derived. The sweep voltage was then exerted on the electrode and measured the I-V characteristic after programming. The test data was processed by linear regression to obtain resistance. Statistical software SPSS was used to compute the mean and standard deviation of programming voltage and leakage current.

Results and Comparison

The typical BST and PZT anti-fuses programming processes are shown in Fig. 1 and Fig. 2 respectively, which indicate obvious anti-fuse behaviors in both cases.

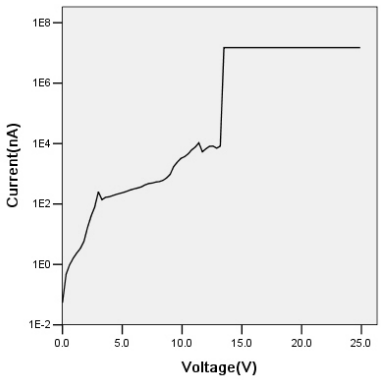

Fig. 1. The I-V characteristic of a non-programmed BST anti-fuse structure

The BST (thickness: ~500 nm) and PZT (thickness: ~200 nm) anti-fuses are studied in this paper. The test results are listed in Table 1 and the electrical characteristic of an amorphous silicon anti-fuse is also listed and discussed as follows.

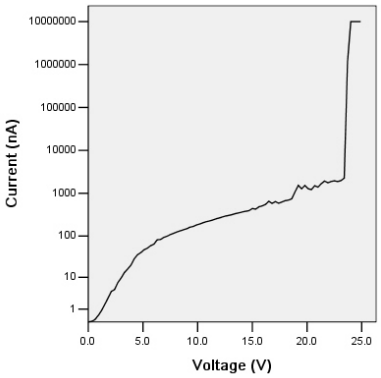

Fig. 2. The I-V characteristic of a non-programmed PZT anti-fuse structure

Table 1. A comparison between different types of anti-fuses

Dielectric Material	**Thickness (nm)**	**Breakdown Electric Field**		**On-state Resistance**		**Leakage Current Density (A/cm2)**	**Off-state Resistance (MΩ)**
		Mean (MV/cm)	*Coefficient of Variation*	*Mean (Ω)*	*Coefficient of Variation*		
Amorphous Silicon	150	1.1	12.3%	61.8	25.0%	7×10^{-4}	145
	250	1.0	16.1%	69.5	33.9%	9.16×10^{-6}	1.11×10^{4}
BST	500	0.3	5.9%	12.3	8.6%	2.8×10^{-3}	6.7
PZT	200	1.3	17.4%	10.7	5.8%	8×10^{-5}	1146.4

In the literature, amorphous silicon anti-fuses have been reported [3, 4, 5, 6]. According to [6], the breakdown electric field and on-state resistance of a typical amorphous silicon anti-fuse is approximately 1 MV/cm and 55 Ω respectively, which is in accordance with what we observed in our experiment. Furthermore, the conformities of breakdown voltage and on-state resistance are also similar, which validate the test results of amorphous silicon anti-fuses we fabricated.

On-state Resistance. Table 1 indicates that BST and PZT anti-fuses have smaller mean values of on-state resistance compared with amorphous silicon anti-fuse. Anti-fuses with smaller on-state resistance applied in FPGAs are more approaching the ideal short-state and result in lower power consumption and higher speed. The coefficient of variation expresses the variation as a percentage of the mean, and is calculated as follows:

$$CV\% = (SD/Mean)\times 100\% \quad (1)$$

In this equation, CV stands for coefficient of variation, SD stands for standard deviation. (1)provides a general estimation of the conformity of devices. As the table illustrated, the conformities of the BST and PZT are better than the other type. When anti-fuses are applied in practical circuits, higher conformity will result in better circuit performance and meet the designers' expectation more closely. Furthermore, the reliability of a circuit receives better assurance with higher conformity.

Breakdown Electric Field. Breakdown electric field (BEF) is calculated as programming voltage divided by thickness as follow:

$$BEF= V/d \quad (2)$$

Here in (2), V stands for programming voltage, and d stands for thickness. Compared with the concept of breakdown voltage, it is better for the comparison between distinctive types of dielectric anti-fuses when thicknesses are different. According to Table 1, lower breakdown electric field is observed in BST, making the anti-fuse attractive for future FPGAs, in which lower working and programming voltages are highly desirable with the downsizing of devices. Dielectric materials with lower breakdown electric field make a low programming voltage easier to obtain by adjusting the thickness. It is also obvious that the conformity of the breakdown electric field is superior to amorphous silicon ones.

Leakage Current. The leakage current of the BST and PZT are still not ideal, but some papers [7] and experiments show that the depositing and annealing temperature affect the leakage current significantly and the ratio of elements in BST and PZT also play an important role. Thus, the characteristic of leakage current performance could be improved by adjusting the growth condition: process, growing temperature, annealing temperature etc.

On-state Reliability. During the test, the switch-off performance was observed in the amorphous silicon anti-fuse. However, no such phenomena exhibited in the BST and PZT anti-fuses with the same sample size. These results indicate a higher on-state reliability of the BST and PZT, which imply a better performance when applied in practical circuits. However, further experiments are still needed to investigate the breakdown processes of different types of materials.

Conclusion

According to the comparison between distinctive anti-fuses, the BST and PZT ones have generally lower off-state resistance. The BST anti-fuse has a relatively lower breakdown field which is advantageous when applied in the small size and low power FPGAs. Furthermore, the anti-fuse structures based on BST and PZT could also be applied in FRAMs where one time programming (OTP) is necessary for the sake of safety. By using such anti-fuse, the fabrication process is well compatible with the FRAMs'.

More studies and experiments are still needed to better understand the breakdown mechanism and the on-state stability. The time-dependent dielectric breakdown (TDDB) is also an important indicator of anti-fuse's off-state performance which deserves further researches.

Acknowledgment

The authors would like to thank the support from State Key Laboratory of Electronic Thin Films and Integrated Devices Innovation Fund (CXJJ200905), University of Electronic Science and Technology of China for providing the facilities for fabricating the devices, Dr. Luo for technical support on depositing TiO_2 and Dr. Huo for assistance on sputtering the PZT and BST thin films.

References

[1] WANG Binsheng, AN Weiguang, ZHANG Dan. "Electrical Breakdown Mechanics and Reliability Analysis for PZT Piezoelectric Ceramics" Journal of Harbin Engineering University, 2008 29(4): pp. 337-341

[2] ZHOU, Zhigang; WU, Yugong; ZHANG,Yalin; LU0,Jinling. "The Thermo-mechanical Breakdown of Ferroelectric Ceramics. Proceedings of the 3rd International Conference on Properties and Applications of Dielectric Materials" July 8-12, 1991 Tokyo, Japan.

[3] Yosi Shacham-Diamand. "Filament Formation and the Final Resistance Modeling in Amorphous-Silicon Vertical Programmable Element" IEEE Transactions on Electron Devices, Vol. 40, No. 10, Oct. 1993.

[4] ZHANG Bang-wei. "High k Gate Dielectric and Materials Si Nanotransistor" Micronanoelectric Technology, 2006(3)

[5] T. Busania, R. A. B. Devine. "Nonvolatile memory and anti-fuse behavior in Pt/a-TiO2 /Ag structures" J. Vac. Sci. Technol. B, Vol, 26, No. 5, Sep/Oct 2008.

[6] A. J. LaDuca. "Amorphous Silicon Based Anti-Fuse" IEEE 1993 Bipolar Circuits and Technology Meeting 1.2.

[7] S. Maruno, T. Kuroiwa, N. Mikami, K. Sato, S. Ohmura, M. Kaida, T. Yasue, T. Koshikawa "Model of leakage characteristics of (Ba, Sr)TiO3thin films" Applied Physics Letters, Vol. 73, No.7 17 August

© (2012) Trans Tech Publications, Switzerland
doi:10.4028/www.scientific.net/AMM.187.235

Fiber-optic Electric Field Sensor Based on Electrostriction Effect

Juan Zhao[a], Huiyuan Zhang, Yinshun Wang and Hongwei Liu

School of Electrical and Electronic Engineering. North China Electric Power University. Beijing 102206, China

[a] zhaojuan_5516503@126.com

Keywords: ELECTROSTRICTION, ELECTRIC FIELD SENSOR, FIBER BRAGG GRATING.

Abstract. This paper presents a new method for measuring AC field strength, with application of electrostriction effect of electrostrictive ceramics and technology of fiber Bragg grating. We use electrostriction effect to design the fiber-optic electric field sensor. This device turns the strain of electrostriction material influenced by electric field into the strain of fiber Bragg grating, then wavelength of feedback changes. We can get the strain of electrostriction material through the comparison between initial wavelength and wavelength of feedback, then measurement of electric field strength can be achieved by detecting the strain of electrostriction material. Experiments indicate that fiber-optic electric field sensor based on electrostriction effect is of effective value for measuring electric field strength, and the response of measuring system to AC electric field is linear. We apply an effective method for the research of measuring electric field strength.

Introduction

Measurement of high voltage & strong electric field is always a key research area in high- voltage measurement, one is frequency field measurements, such as electromagnetic fields near the transmission lines or ground, electric field measurement in the surface of insulator, voltage loop, switch and other high voltage equipment; the other is transient field measurement, such as pulsed power technology, lightning or gap discharge, substation switching processes etc [1]. Ever since a long time ago, when the piezoelectric phenomenon of some crystalloid came to light, researchers have focused on the research and application of piezoelctric function of piezoelectric material. Designing a kind of fiber-optic electric field sensor which exchange energy through piezoelectric material to detect electric field strength is of effective value [2]. Sensor technology has been one of mainstays of modern information technology [3, 4]. Fiber Bragg grating sensor has become the perfect choice in electric power industry, because of its ability to be transmited through long distance with low loss, owing to its character of prevention to interference of electromagnetic field. Fiber Bragg grating sensor has a wide prospect. Fiber Bragg grating sensor has numerous advantages, such as prevention to interference of electromagnetic field, small size(the net size of standard optical fibre is 125um), light weight, high tolerance of temperature(the maximum working temperature can reach 400 to 600 centidegree), long transmmission distance, rustproof ability, high sensitivity, easily changed shape. In electric power industry, the change of electric field strength turns to changement of voltage, which leads to a shape change of PZT. The shape change can be easily obtained by means of wavelength drift of fiber Bragg grating sticked on the piezoelectric ceramics, then the electric field strength can be measured. This is a method with low cost; moreover, complicated electric isolation is not needed.

This paper describes a new kind of measuring method, with application of electrostrictive ceramics, which can meet the need for measuring high electric field strength in elctric power system of high voltage, such as measurement of electric field strength of area near ultra high voltage transmmission line, research of character of all kinds of air gap under impulse voltage [4]. Experiments indicate that this system has high sensitivity and resolution.

The measurement system

As shown in Fig. 1, measurement system consists of the following components: electric field probe, optical fiber, fiber Bragg grating demodulator.

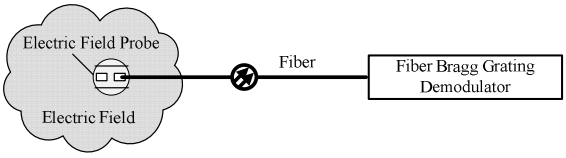

Fig. 1.The measurement syetem

Electric field probe receives and outputs laser, the laser is then transmitted to the fiber Bragg grating demodulator with optical fiber. Comparing the initial wavelength with the feedback wavelength under the electric field, the fiber Bragg grating demodulator would get the strain of electrostrictive ceramic. The electric field strengh can be measured according to the electrostrictive ceramic strain.

Design and working principle of electric field probe

Schematic of the probe is shown in Fig. 2.

The metal spherical shell is divided into two parts in average, the middle of the two hemispheres installed a flat body, on the flat body fixed a signal amplification, conversion circuit and a rectangular electrostrictive ceramics, electrostrictive ceramics including specifications for the 8 mm×8 mm×20 mm. The two metal hemispheres are placed in the electric field, two metal cables are soldered to the upper and lower inner shell surface respectively, the metal line at the other end receives the circuit board, then the electric signal of the electric field can load on the circuit. This signal is amplified, transformed, filtered by the circuit. And then the circuit produces DC voltage. Positive and negative leads of electrostrictive ceramics attach to DC voltage produced by circuit. Bragg grating glues to the side of electrostrictive ceramics direction, that is the elongation of the direction of shortening. Upper and lower surface of the ceramic is electrode surface. Positive and negative leads of electrostrictive ceramics extract from both sides. Optical fiber extracts from the upper and lower ball cracks and comes to fiber Bragg grating demodulator.

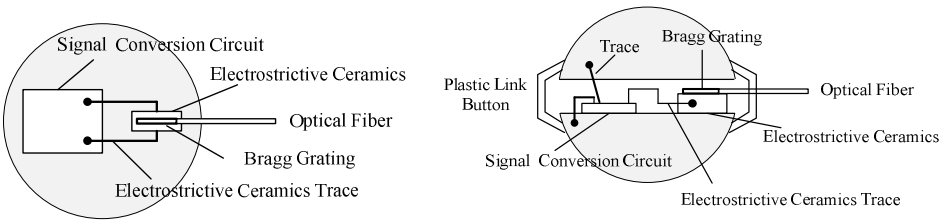

Fig. 2. (a) Top view inner electric field probe; (b) Cutaway view of electric field probe

Transducer is one of the core components of the sensor [5], so selecting the appropriate transducer material is important. Electrostriction is the fundamental electromechanical coupling in all materials—everything is electrostrictive [6]. Elastic strain in the material results from distortion of the bond lengths, electron distribution functions, or electric dipoles with an applied electric stress. Electrostriction is a phenomenon that the stress and strain are proportional to the square of electric field. Some polyurethane elastomers and perovskite-type ceramics can produce large deformation under applied electric fields. In engineering these electrostrictive materials are used as transducers and actuators. So their strength and electric field distribution should be considered [7].Schematic diagram of PLZT piezoelectric of stacked piles is show in Fig. 4 [8].

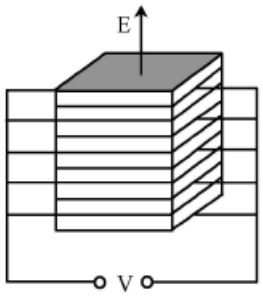

Fig. 3. Schematic diagram of PLZT piezoelectric of stacked piles

The fundamental requirements of electrostrictive materials for transducer applications are as follows:

a) Large field-induced polarization for obtaining large induced piezoelectric coefficients.

b) High dielectric constant for enabling a good electrical impedance matching to the system electronics, especially for small element size of phased arrays.

c) Low electrical loss tangent to reduce the amount of heat generated on transmit and improve signal-to-noise ratio on receive.

d) Wide operating temperature range.

e) Fast polarization switching speed (turn ON/OFF time), and zero remanent polarization when E-field is removed for achieving the complete OFF state on elevation aperture control [9].

Electrostriction material experiments used is developed by China Electronic Science and Technology Corporation 26th Research Institute called WTYD0808020 type material. PLZT, PMN, PZN ferroelectric ceramics are the most used electrostrictive materials [10-12]. The material of rectangular block is encapsulated of epoxy by PLZT thin multi-layer stack , the volume of 8mm×8mm×20mm. The material has the feature of short response time, withstanding the maximum blocking force large, electric field perpendicular to the direction of displacement and the displacement of high output. And its displacement hysteresis loop is long and narrow which contains a very small area [13]. In the operating voltage range of 0V-200 V, the voltage - displacement curve diagram is shown in Fig. 4. In a small low voltage, the loop line introduced by hysteresis effect changes little. According to the type curve of PLZT material [13-15], its hysteresis within the voltage range of 0V-10 V is not obvious. Displacement and electric field strength form a well quadratic curve [16].

Provide a functional relationship between the induced dielectric displacement and the applied electric field that can be used to define electrostriction. An electrostrictive ceramic excited by an E-field given by $E = Edc + E\omega \cos \omega t + E\Omega \cos \Omega t$,where $E\omega$ is amplitude of the carrier , $E\Omega$ is amplitude of the low frequency field and Edc is the dc bias, produces strains (using e = ME2),

$$e_{\omega} = (2ME_{dc}E_{\omega})\cos \omega t \tag{1}$$

$$e_{\omega \pm \Omega} = ME_{\omega}E_{\Omega}\cos(\omega t \pm \Omega) \tag{2}$$

Along with strains edc, $e\Omega$ and higher harmonics [4].The strain of dielectric materials under the electric field and the applied electric field strength is as follows:

$$e = dE + ME^2 \tag{3}$$

In the formula, e is strain, d is piezoelectric coefficient, M is electrostrictive coefficient (m2/V2) (M may change with the external environment situation such as temperature); E is electric field strength (V/m) [13]. Electrostriction and piezoelectricity are both electromechanical properties that can be linked via thermodynamic formalism [17]. In ferroelectric ceramics, electrostrictive

coefficient is much larger than the piezoelectric coefficient, the later plays a leading role [16]. To this kind of ferroelectric ceramics, the deformation in the electric field is followed by the formula: e≈ME2. The magnitude of electrostriction can be improved by: increasing the drive field or increasing the M coefficient. Materials with large values of dielectric displacement have much larger values of useful electrostrictive strain [17]. The low hysteresis and high strain achievable with unipolar excitation of electrostrictors is advantageous. In addition, because the electrostrictive spontaneous does not exist polarization, making such material even at high operating frequencies can still showed no or very small hysteresis losses [13].

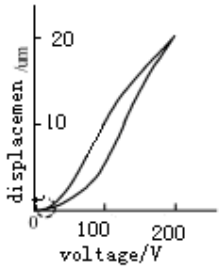

Fig. 4. Voltage - displacement curve of electrostriction material

From the electrostrictive ceramics characteristic simulation, Fig. 6 and Fig. 7 show that the strain of electrostrictive ceramics directly placed in the electric field is small.

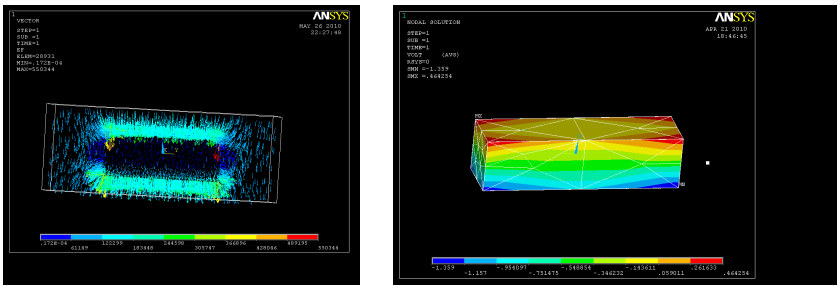

Fig. 5. (a) Power line distribution around electrostrictive ceramics in electric field; (b) Potential distribution of electrostrictive ceramics in electric field

When electrostrictive material is placed between two metal circular plates which simulate a uniform electric field environment, because the electrostrictive material dielectric constant is so large and induced potential difference of the upper and lower electrode surface is too small, if the material placed directly in the field, the material deformation is small. But telescopic effect is obvious when directly add voltage source on the material. Fig. 5 shows the relationship between voltage and strain to the electrostrictive material if directly adding voltage source on that. When the voltage is very low, the material deformation is still very apparent. Therefore, this paper adopts the method of voltage signal load to realize the impact of strain on the material.

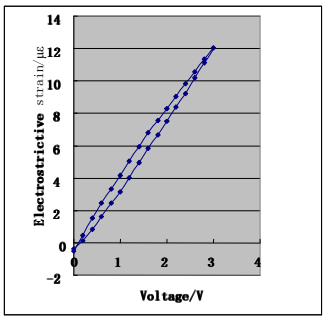

Fig. 6. Relations between the load voltage of electrostrictive material and stretching strain

When the electric field to be tested acting on the metal spherical shell, the metal spherical shell will induce the consistent electric signals as the electric field strength. With the processing of circuit amplification, conversion, filtering, the induced signals transform to the DC voltage signals. Apply the DC voltage to the electrostrictive material on the positive and negative terminal; electrostriction material will be deformed according to the size of DC voltage signals. The Bragg grating linked to the electrostriction material is deformed too. The feedback wavelength to fiber Bragg grating demodulation changes too. Fiber Bragg grating demodulator compares wavelength back from the electric field with the initial state to calculate the strain of Bragg grating or electrostriction material. Micro-strain relations with the wavelength as:

$$e = (ID - \lambda_0) * 1000 / 1.2 \tag{4}$$

In the formula, e is strain, ID is feedback wavelength for the tested electric field, λ0 is the initial state wavelength, and 1.2 is the conversion factor between wavelength and micro-strain with unit pm/με. The strain and the two ends voltage of the material are square relationship. Through the modulation of the circuit, the electric field strength and the output of the direct voltage of the circuit is in the square relationship too. And then we can see that the strain of the material and the electric field strength are in the linear relationship.

Through the detection of micro-strain, electric field strength can be achieved. Enable the measurement of the electric field.

Experimental results and analysis

Use the system shown in Fig. 1.

With two smooth circular metal plate's analog external electric field, electric field strength ranges 0kV/ m ~ 200kV / m. Outputing system response according to the electric field strength is as the curve shown in Fig. 8. Two kinds of test method type that AC field amplitude increases and decreases respectively, the results are of linear line. It shows that the system response according to the external electric field has good linearity. And the system output increases with the AC field amplitude increasing, decreases with the decreasing, indicating the electrostrictive ceramics hysteresis effect is not obvious, the impact to the experiment is negligible. Repeating experiments is to compare the experimental results. Observation of Fig. 8, from three lines of the overlapping situation, overlapping, which indicates good repeatability measurement system, the experimental results is high reliability.

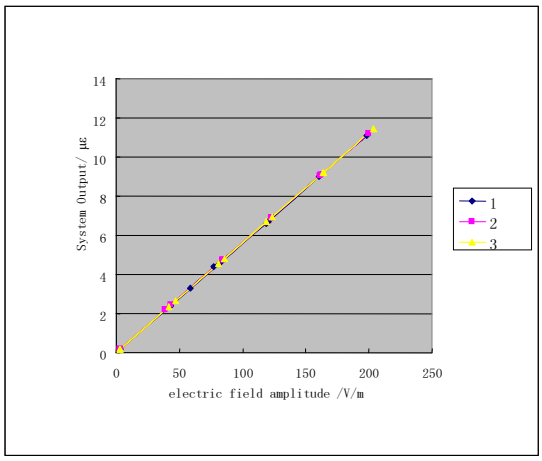

Fig. 7. The relationship between electric field amplitude and the system output

Conclusion

This paper is about a new fiber-optic electric field sensor design. The system has good stability, high sensitivity, good linearity etc. This paper shows the theoretical analysis and process implementation. Experimental results show that the system has good performance. It can meet the measurement of electric power system.

References

[1] Rong Zeng, Weiyuan Chen, etal. Study on Optical Electric Integrated Electric Field Measurement System and Appl ication in High Voltage Measurement[J]. High Voltage Engineering, 2006, 32(7):1-5.

[2] Fabiny L, Vohra S T A F B. High-Resolution Fiber-Optic Low-Frequency Voltage Sensor Based on the Electrostrictive Effect [J]. IEEE Photonics Technology Letters, 1993, 5.

[3] Yoshifumi Amemiya. Sensor Entry [M].Science Press, 2000.

[4] Yong He. Photoelectric Sensor and Its Application [M]. Chemical Industry Press, 2004.

[5] Changhai Shi, Jianping Chen, etal. A novel configuration for the transducer of magnetostrictive fiber-optic interferometric sensors[J]. Proceedings of SPIE - The International Society for Optical Engineering, v 6019 I, Passive Components and Fiber-based Devices II, 2005.

[6] A. F. Devonshire, "Theory of ferroelectrics," Philos. Mag., vol . 3, no. 10, pp. 85–130, 1954.

[7] Quan JIANG. General Solution of Stress Fields in an Electrostrictive Material with point charge [J]. SPAWDA 2008, 2008.

[8] Xiao-yang Wang. Design of Interferometric Fiber-Optic Weak DC Electric-Field Sensor[J]. Chinese Journal Of Sensors And Actuators, 2008, 21(5): 765-768.

[9] Jie Chen & T. R.(Raj) Gururaja. Dc-biased Electrostrictive Materials and Transducers for Medical Imaging [J]. Ultrasonics Symposium, 1997. Proceedings., 1997 IEEE, 1997,2(2):1651-1658.

[10] Wen-zhuo Li, Wan-sheng Zhao, etal. New Technologies and Applications of Piezoelectric and Electrostrictive Materials and Actuators[J]. Piezo Electric &Acoustoopttics, 2001, 23(4): 259-264.

[11] PARK S E, SHROUT T R. Ultrahigh strain and piezoelectric behavior in relaxo r-based ferrolectric single crystals [J]. Journal of Applied Physics, 1997, 82 (4): 1804-1811.

[12] PARK S E, SHROUT T R. Characterist ics of relaxo r-based piezoelectric signle crystals for ultrasonic transducers [J]. IEEE Trans. on Ultrasonics, Ferroelectric and Frequency Control Special Issue on Ultrasonic Transducers, 1997, 44 (5): 1140-1147.

[13] Rui-qing Zheng. A Study of the Vibration Characteristics of an Active Control Hydraulic Mount with Electrostrictive Actuator [D]. Jilin University, 2004.

[14] CETC No.26 Research Institute. WTYD0808020 Voltage - displacement curve [S]. 2007.

[15] Yun Ou. Study of Design Theories and Control Methods of Engine Active Mount with Piezoelectric Actuator [D]. Jilin University, 2003.

[16] Liming Wang, Suchun Mao, Zhicheng Guan. Sparkover of rod-plane gap for composite alternating or direct/impulse voltages [J].J Tsinghua Univ(Sci&Tech), 2002, 42(3): 285 -287.

[17] Steven M. Electrostrictive Ceramics for Low-Frequency Active Transducers [J]. IEEE Transactions on Ultrasonics, Ferroelectrics, and Frequency Control, 2000, 47(4) :861-876.

© (2012) Trans Tech Publications, Switzerland
doi:10.4028/www.scientific.net/AMM.187.241

Life Prediction for Silicon Pressure Sensor Based on SVR

Zhihua ZHAI, Pingli WU

Yellow River Conservancy Technical Institute,Kaifeng 475003, China

zhihuazhai@163.com

Keywords: life prediction; silicon pressure; support vector regression; sensor

Abstract. In order to improve the reliability of silicon pressure sensor, life prediction for silicon pressure sensor should be performed. Life prediction for silicon pressure sensor based on support vector regression is proposed in the paper. Grid method is used to determine the parameters of support vector regression in the process of training support vector regression model. Life for silicon pressure sensor under the conditions of different pressures is given in the experimental analysis. The comparison of the errors and mean errors between support vector regression and BP neural network indicates that life prediction accuracy of support vector regression for silicon pressure sensor is higher than that of BP neural network.

Introduction

Life prediction for electronic products can gain the state change of electronic products and avoid the economic loss. Silicon pressure sensor is one of the most popular sensors[1-3]. In order to improve the reliability of silicon pressure sensor, life prediction for silicon pressure sensor should be performed. BP neural network is one of the most popular prediction methods[4,5]. The life prediction results for silicon pressure sensor by using BP neural network may be unsatisfactory due to the over-fitting of BP neural network. In the study, life prediction for silicon pressure sensor based on support vector regression is proposed. Support vector regression is a nonlinear kernel-based regression technology, which possesses good function approximation and nonlinear prediction ability. In order to solve the problem of the parameters selection, the parameters of support vector regression are determined by Grid method in the process of training support vector regression model. Life for silicon pressure sensor under the conditions of different pressures is given in the experimental analysis. By the comparison of the errors and mean errors between support vector regression and BP neural network, the prediction performance of life for silicon pressure sensor by the two prediction models indicates that life prediction accuracy of support vector regression for silicon pressure sensor is higher than that of BP neural network.

Theory of Support Vector Regression

It is well-known that support vector regression is a kind of support vector machine with prediction function. Support vector regression is a nonlinear kernel-based regression technology. The technology can locate a regression hyperplane with small risk in the high dimensional feature space[6],which possesses good function approximation and nonlinear prediction ability. The theory of support vector regression is introduced in the section.

The form of support vector regression is described as followings:

$$F(x) = w \cdot \eta(x) + b \tag{1}$$

where w denotes the weight vector, b denotes the offset.

By positive slack variables ξ_i^*, ξ introduced, the objective function and constraints for support vector regression are described as followings:

Minimize

$$\frac{1}{2}\|w\|^2 + C\sum_{i=1}^{n}(\xi_i + \xi_i^*) \tag{2}$$

with constraints,

$$y_i - (\omega, x_i) - b \le \varepsilon + \xi_i$$
$$(\omega, x_i) + b - y_i \le \varepsilon + \xi_i^*$$
$$\xi_i^{(*)} \ge 0, i = 1,2,\cdots,n$$

where C is a regulation parameter, ε denotes a precision parameter which represents the radius of the tube located around the regression function.

By using Lagrange multipliers α_i, the dual Lagrange form is obtained as followings:

Maximize

$$\sum_{i=1}^{n} y_i(\alpha_i - \alpha_i^*) - \varepsilon\sum_{i=1}^{n}(\alpha_i + \alpha_i^*) - \frac{1}{2}\sum_{i=1}^{n}\sum_{j=1}^{n}(\alpha_i - \alpha_i^*)(\alpha_j - \alpha_j^*)k(x_i, x_j) \tag{3}$$

with constraints,

$$\sum_{i=1}^{n}(\alpha_i - \alpha_i^*) = 0$$
$$0 \le \alpha_i \le C, i = 1,2,\cdots,n$$
$$0 \le \alpha_i^* \le C, \quad i = 1,2,\cdots,n$$

Finally, the regression function of support vector regression can be obtained as followings:

$$F(x) = \sum_{i=1}^{n}(\alpha_i - \alpha_i^*)k(x_i, x) + b \tag{4}$$

where $k(x_i, x) = \eta(x_i)\ \eta(x)$,which denotes the kernel function.

In order to solve the problem of the parameters selection, the parameters of support vector regression are determined by Grid method in the process of training support vector regression model. In the process of using Grid technology, the search scopes of the parameters C and ε of support vector regression are defined as [1 10000] and [0.0001 0.1].

Application Analysis

Life for silicon pressure sensor under the conditions of different pressures is given in Fig.1.As shown in Fig.1, the life for silicon pressure sensor is increasing with the increasing of pressures. The life data for silicon pressure sensor in T1~T6 are used as the training data of support vector regression and the life data for silicon pressure sensor in T7~T9 are used as the testing data of support vector regression. In the process of training support vector regression model, the parameters of support vector regression are determined by Grid method. The prediction results by using support vector regression are shown in Fig.2.Fig.3 shows the prediction results by using BP neural network. In order to show the superiority of support vector regression, the errors and mean errors of support vector regression and BP neural network are computed, whose results are shown in Fig.4.By the comparison of the errors and mean errors between support vector regression and BP neural network, the prediction performance of life for silicon pressure sensor by the two prediction models is shown. It can be seen that life prediction accuracy of support vector regression for silicon pressure sensor is higher than that of BP neural network.

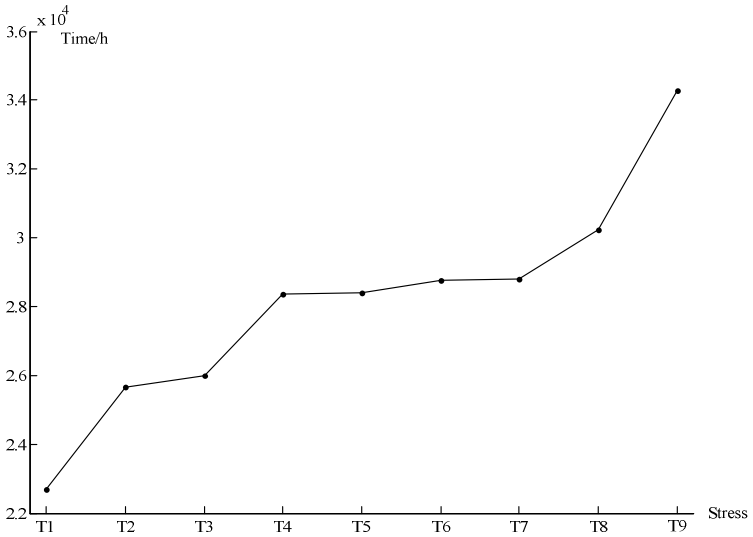

Fig.1. Life for silicon pressure sensor under the conditions of different pressures

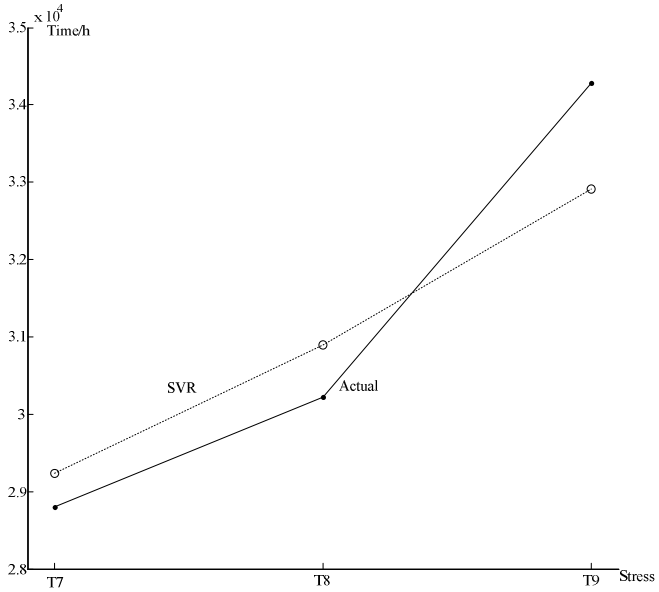

Fig.2. The prediction results of silicon pressure sensor by using support vector regression

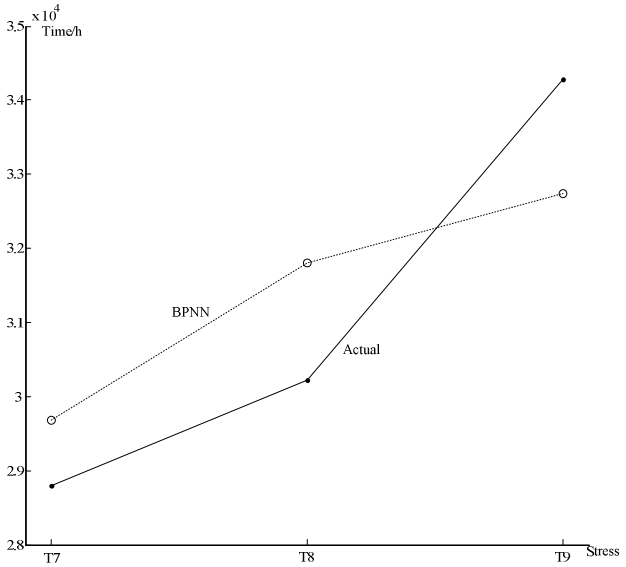

Fig.3. The prediction results of silicon pressure sensor by using BP neural network

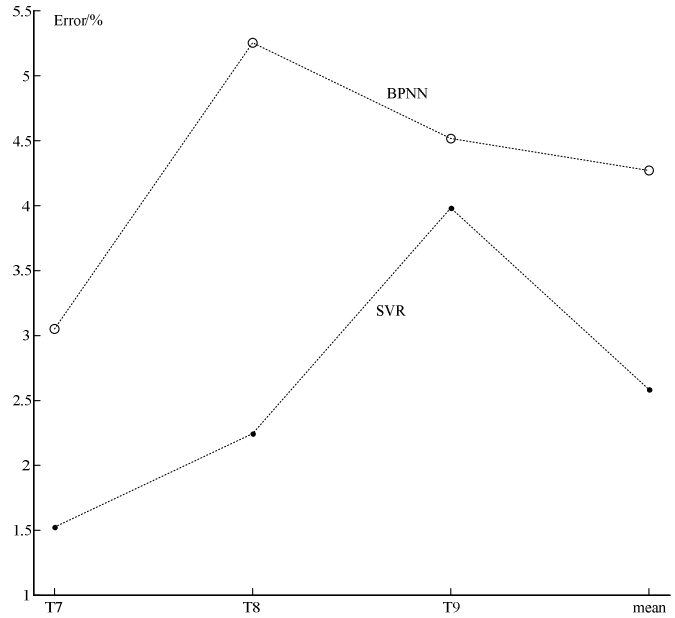

Fig.4. The errors and mean errors of support vector regression and BP neural network

Summary

In the study, life prediction for silicon pressure sensor based on support vector regression is proposed. Support vector regression is a nonlinear kernel-based regression technology. In order to solve the problem of the parameters selection, the parameters of support vector regression are determined by Grid method in the process of training support vector regression model. By the comparison of the errors and mean errors between support vector regression and BP neural network, it is indicated that life prediction accuracy of support vector regression for silicon pressure sensor is higher than that of BP neural network.

References

[1] Bo-Na Lee, Kun-Nyun Kim, Hyo-Derk Park, Sang-Mo Shin,Calibration and temperature compensation of silicon pressure sensors using ion-implanted trimming resistors, Sensors and Actuators A: Physical Vol.72(1999),p.148-152

[2] M. Maeda, A. Sato, M. Yuyama, M. Kosuge, F. Matsumoto, H. Nagai,Characteristics of a silicon pressure sensor in superfluid helium pressurized up to 1.5 MPa, Cryogenics Vol.44(2004), p.217-222

[3] Raluca Muller, Paula Obreja, V. Banu, I. Pavelescu, D. Dascalu,Silicon-compatible waveguides used for an integrated opto-mechanical pressure sensor, Optical Materials Vol.17 (2001), p.255-258

[4] Eva Kaslik, Stefan Balint,Complex and chaotic dynamics in a discrete-time-delayed Hopfield neural network with ring architecture, Neural Networks Vol.22(2009),p.1411-1418

[5] Shengyuan Xu, James Lam,A new approach to exponential stability analysis of neural networks with time-varying delays, Neural Networks Vol.19(2006),p.76-83

[6] Ankit B. Gandhi, Jyeshtharaj B. Joshi,Estimation of heat transfer coefficient in bubble column reactors using support vector regression, Chemical Engineering Journal Vol.160(2010), p.302-310

© (2012) Trans Tech Publications, Switzerland
doi:10.4028/www.scientific.net/AMM.187.245

Research on Ytterbium Doped Phosphate Glasses

Lidan Fan[1, a] and Lihua Wu[2,b]

[a] College of Mechanical Engineering Jilin Teacher s' Institute of Engineering & Technology Changchun, China

[b] Meihekou vocational education center, Meihekou, China

[a]email: fanlidan111@163.com

Keywords: laser glass, ytterbium, optical, thermal.

Abstract. Ytterbium doped laser glasses is generally preferred in the updating of various laser material because it have excellent mechanical and stability of thermal and optical properties. In this paper, experiments are performed through changed the concentrations of laser glasses medium and Ytterbium ions based on current research. The different of the concentrations and thickness of Yb3+ doped phosphate glasses have been investigated in order to gain best spectroscopic properties and stability of thermal and optical properties.

Introduction

Laser material had played an important role in the history of the laser. It was still the key on the laser development in the 21st century. Laser technology would be a fundamental change with the birth of new materials. It greatly facilitated the technological development and application. Laser glass has a series of merit, for example, great energy storage, easy to make a big size, higher optical through, high optical quality uniformity and high thermal stability.

Years of research show that great energy beams rely mainly on the laser. Up to now, neodymium doped glasses of laser is the most mature in technical, but ytterbium doped glasses will be generally preferred in the updating of various laser material. Yb^{3+} electron configurations is $4f^{13}$,it has two electric station[1]. The energy gap between the ground state and the excited state（2F7/2,2F5/2）is $10000\,cm^{-1}$,it generate Start fission under ligand field and formed on the quasi four levels of the laser running institutions Yb^{3+} . have many advantages relative to conventional rare earth ions such as Nd^{3+} and Er^{3+} [2].

- More appropriate to laser diode double-pumped solid-state laser.
- Wavelength pumped and wavelength operated by laser are very closed, quantum efficiency amounting to 90%.
- The heat load is lower on the material.
- No existed excited state absorption, high conversion efficiency.
- There is no concentration quenching out in the case of high concentration doped.
- The fluorescence lifetime is long and easily stored energy.

On account of above reasons, development and research on Ytterbium doped laser glasses have important theoretical meaning and practical value [3], especially for high power laser weapon that must have excellent mechanical, stability of thermal and optical properties [4]. In this paper, experiments are performed through changed the concentrations of laser glasses medium and Ytterbium ions based on current research [5][6]. The different of the concentrations and thickness of Yb^{3+} doped phosphate glasses have been investigated. A variety of spectroscopic properties and stability of thermal and optical properties were discussed.

Preparation Ytterbium Doped Phosphate Glasses

The composing parts ytterbium doped phosphate glasses are listed in the table. All materials are high purity materials.

Table 1. Composition of Ytterbium doped phosphate glasses

Component	P_2O_5	Al_2O_3	K_2O	Yb_2O_3	La_2O_3	BaO	Sb_2O_3	Y_2O_3
content	70	6	7～11	3.5～7.5	2.2	5	0.3	2

A set of will be produced in this experiment. The melting process was shown in Fig.

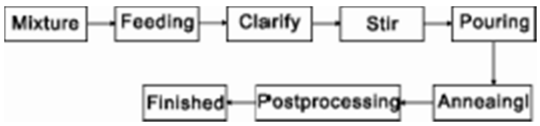

Fig 1. Glass melting process

Experiment equipment

Melting furnace

As shown in Fig.2, the furnace used in this experiment is resistance heating furnace in which the pyrogen is silicon carbide [7]. Platinum crucibles are used for glass melting. The high temperature Clarify process which can eliminate the air bubble in the melting glass is carried out by a platinum leaf blade which can circumrotate in the glass liquid.

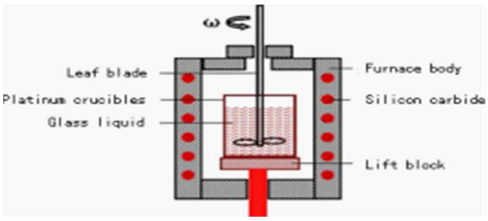

Fig 2. Structure of platinum crucible melting furnace

Casting molds

Casting mold used in this experiment is made of cast iron. The styles and size of the mold can be adjusted depending on the glass casting size.

Anneal furnace

The anneal furnace used in this experiment be shown in Fig.3.

Fig 3. Heat Treatment Equipment

Fabrication process

Getting uniform powder by porphyrizing and mixing the mixture after scaled and put them into the Petri dish

Put the 100 ml platinum crucible into the silicon carbide rod electric furnace whose temperature accuracy is ±2 and fusion temperature is 1400~1480.Take out the crucible, put 1/3 of the powder into it then put back the crucible. Take out the crucible and put 1/3 of the powder into it again after the powder has smelted and then put back. Put the left powder into the crucible after the powder has smelted and put back. Put little powder into the crucible mainly to avoid the phosphate glass corroding the crucible. Observe fusing, exhausting and homogenization at any time by getting out

little vitreous humor using nickel-chromium alloy wire when heating up. There have clear vitreous humor of medium degree viscosity in the crucible and the smelting and producing process is ending after on hour.

Take out the smelted vitreous humor and put into the heated iron pattern. After modeling put it into the annealing furnace of 600℃.And then after grind and polishing, the glass are made into samples for the use of performance test.

Performance Test

The tested samples come from different concentration of ytterbium ions phosphate glass,which were made into different thickness. Samples will be the following tests.

Refractive index The refractive index of the glass can be tested by using V-prism refractor meter offered by Optical instrument garage in shanghai. The measured precision is 5×10^{-5} .

Test of complex ions density The test of doped rare earth ions density, according to the formula as follows:

$$N = \left(A \times \rho \times 6.022 \times 10^{23}\right) \Big/ B \tag{1}$$

Where N is doped density, piece/ cm3;

A is the introduction volume of laser ion oxides, wt%;

ρ is density, g/cm3;

B is molecular weight of Oxide compound;

Test of absorption spectrum The test of spectrum is carried out under normal temperature, absorption spectrum of the sample is determined by using Lambda 900UV/VIS/NIR Spectrometer (produced by PerkinElmer Corporation USA), as shown in Fig.4.Wavelength range measured by Instrument: 175 ～ 3300nm[8]; bandwidth: 0.05 ～ 5.0nm; precision of wavelength: +0.08nm; wavelength Repeatability: <0.02nm; photometer accuracy: +0.003A; Photometer duplication: <0.0004A; baseline drift: <0.0002A/h; base straight: +0.001A.This instrument is provided with two groups of different optical devices which include different light sources (deuterium lamp and halogen lamp), diffraction gratings and detectors (Multiplier phototube and PbS).

Fig 4. Lambda 900UV/VIS/NIR Spectrometer

Test of fluorescence spectrum As shown in Fig.5, the test of fluorescence spectrum of glass is executed by using TL9000 spectrometer made from UK, during the proceeding of the test, Coherent FAP System 980nm Peninsula laser is used as excitation source.

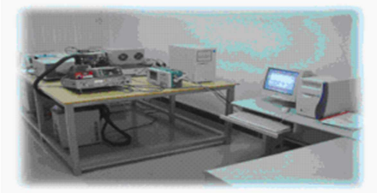

Fig 5. TL9000 Spectrometer

The glass sample will be grinded and its size will be $\phi 6\times 30mm$. The test will be carried on by using expansion coefficient tester made by Laboratory. The heating rate modulates 10degrees/min. The temperature of the test ranges from normal temperature to 500 degrees. When the temperature rises from t1 to t2, the length of glass sample changes from l1 to l2, linear expansion coefficient α can be elaborated by the following formula.

$$\alpha = \frac{\frac{l_2 - l_1}{t_2 - t_1}}{l} = \frac{\frac{\Delta l}{\Delta t}}{l} \quad (2)$$

Test Result

The density of ytterbium doped glasses increases with the Yb203. The relationship between them is closely linear. The essential structure of the ytterbium doped glasses is three-dimensional network of [P04] tetrahedron. The importation of A1203 can be concerned with [A104] tetrahedron. However, the bond of P-0-P will rupture when K20 and BaO are imported. When Yb2O3 is imported, the atomic weight of Yb3+ is bigger and the electric charge is higher. The structure of glass is compact. The result is that the density of glass will increase when the number of Yb203 increases.

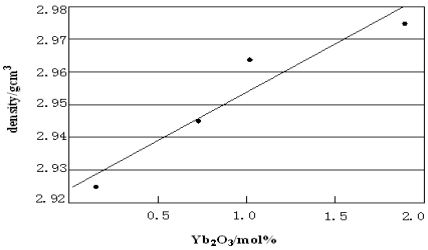

Fig 6.The relation between density and Yb2O3

When the density of laser glass increases, the refractive index will increase. The stacking density and polarizability decide the refractive index. As the amount of Yb203 increases, the stacking density will increase, and the density of glass will be accretion. Because that Yb3+ is non-inert gas and the polarization force is bigger. The two reasons induce that the refractive index increases when the density increases.

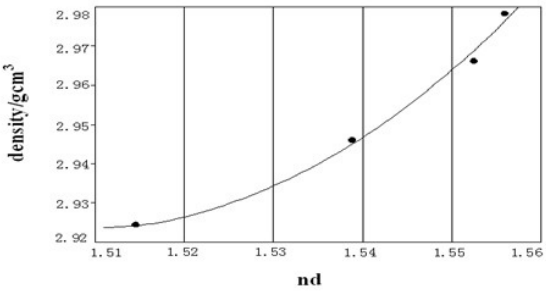

Fig 7. The relation between refractive index and density

As we can see from the Fig.8, the transition temperature (Tg) of the glass is 605.5°C, the fusion temperature (Tf) is 680°C. Under the transition temperature, the coefficient of thermal expansion is direct proportion of the temperature. It is affected by nonego little. At the transition temperature, the curve sharply turns to the area of molten temperature. When the temperature keep on increasing, the coefficient of thermal expansion is still invariability. So the Al2O3 in the host glass can largely reduce the coefficient of thermal expansion of the glass. It is because that under the accustomed dosage, the Al2O3 becomes the tetrahedron, which can repair the short net. The result is that the coefficient of thermal expansion of the glass reduced.

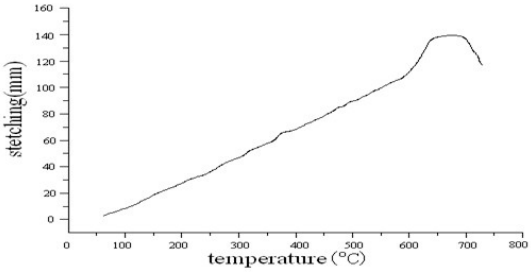

Fig 8.The curve of thermal expansion

Fig.9 is the absorption spectrum curve of the different Yb3+ ions concentration (the thickness of the sample is 5mm).

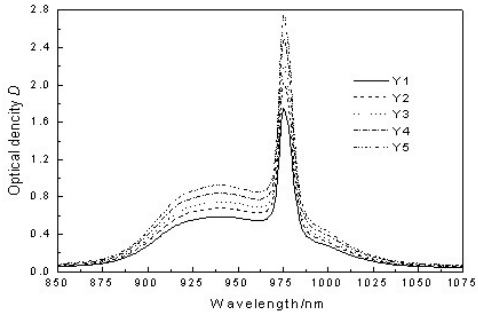

Fig 9. The curve of absorption spectrum

Fig.10 is the fluorescence spectrum curve of different Yb3+ ions concentration (the thickness of the sample is 5mm)

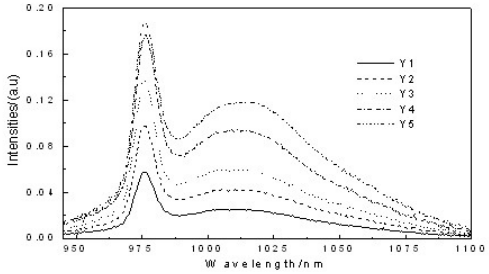

Fig 10. The curve of fluorescence spectrum

Fig.11 is the curve of absorption spectrum and fluorescence spectrum of the same Yb3+ ions concentration which is the sample Y5 in above figure (the thickness of the sample is 5mm).

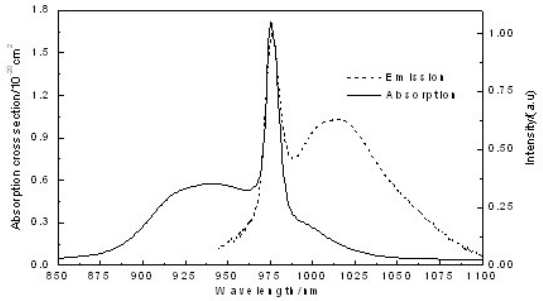

Fig 11. The curve of absorption spectrum and fluorescence spectrum

Conclution

This paper produced different of the concentrations of ytterbium ions phosphate glass, tested and analyzed physical properties and optical character. We have some conclusions as follow:

a) Absorption spectrum is changed with the content of the network former and network modifier. The non-symmetry field of Yb3+ ion ligand field is changed by the different glass structure, it would cause dissimilar Stark energy level splitting.

b) Fluorescence spectra showed that when the concentration of Yb3+ is increased, the secondary peak intensity and the peak intensity of fluorescence are increased in the same thickness, and the spectrum is gradually broadened, λp and λs are shifted to longer wavelength. In the same doping concentration, the secondary peak intensity and the peak intensity of fluorescence are increased with the increase of sample thickness, and λp and λs are shifted. The analysis results show that the shape of fluorescence spectra is affected by radiation trapping effect, it would bring error for stimulated emission cross section,the measurement of fluorescence lifetime and calculation.

c) The secondary peak intensity and the peak area of fluorescence calculated by F-L and RE are increased with the concentration of Yb3+.The result of F-L is greater than RE. The analysis results show that the error is caused by Yb3+ ground state reabsorption. The stimulated emission cross section calculated by RE is reasonable.

d) The measurement fluorescence lifetime τf is longer than the calculated fluorescence lifetime τrad. The doping concentration and the thickness of glass samples wouldn't affect the result. The analysis results show that there is radiation trapping effect in the different concentration Yb3+of silicate glass, and radiation trapping effect is increased with the concentration of Yb3+ and thickness of sample increased.

e) Comprehensive performance experiments show that the best concentration of Yb2O3 is about 2mol% in the system.

Acknowledgements

The authors gratefully acknowledge the support of Hydrodynamic Transmission and Automatic Transmission Research office of Jilin University.

References

[1] Orth C,et al.Engineering and modeling progress in building mercery, a diodepumpedsolid state laser(DPSSL) for ICF application[C]. 3rd ICF international conference, June 1998.Monterey, CA, USA.

[2] Deng peizhen, Jiang Chun,Ying Hongbing,et al.Yb3+ion doped glass with high stimulated cross section at near IR[J].Proceedings of SPIE,1998,3416:99-103

[3] C. C. Robinson. Multiple sites for Er3+ in alkali-silicate glasses. J.Non-Cryst Solids, 1974, 15 : 1～9

[4] P. M. Peters, H. N. Houde Walter, Local structure of Er3+ in multi-component glass, J.Non-Cryst. Solids,1998,239(1/3):162～165

[5] KrupeW F, Chase LL. Ground-state depleted solid-state laser principles, characteristics and scaling. Opt Quantum Electron, 1990,22: 1

[6] Lacovara P, Chai H K, Wang c A, et al.Room-temperature diode-pumped Yb: YAG laser. Opt Letter, 1991,16:1089

[7] Liu Zhuping, Qi Changhong, Dai Shixun, et al. Spectra and laser properties of Er3+, Yb3+: phosphate glasses. Optical Matertials, 2003,21: 789～794

[8] Dai Shixun, Sugiyama A, Hu Lili, et al. The spectnun and laser properties of ytterbium doped phosphate glass at low temperature. Journal of Non-Crystal Solids, 2002, 311: 138～144M. Young, The Technical Writer's Handbook. Mill Valley, CA: University Science, 1989.

© (2012) Trans Tech Publications, Switzerland
doi:10.4028/www.scientific.net/AMM.187.251

Synthesis of an Oxidation Resistant Coating for Ni-based High Temperature Structural Materials by Dip Coating

Wan-Ting Chen[1, a], Rudder T Wu[1,b], Karen Chien[1,c], Liberty T Wu[1,d], Hong Gao[1, e], Hiroshi Harada[1,f]

[1] National Institute for Materials Science, 1-2-1 Sengen, Tsukuba Science City, Ibaraki Prefecture, 305-0047, JAPAN

[a] chen.wanting@nims.go.jp, [b]wu.rudder@nims.go.jp, [c] hsuehfen.chien@utoronto.ca,

[d] liberty.wu@postgrad.manchester.ac.uk, [e]gao.hong@nims.go.jp, [f]harada.hiroshi@nims.go.jp

Keywords: Dip-coating; oxidation; oxidation resistant coating; high temperature structural materials

Abstract. High temperature structural materials are becoming increasingly important under the growing demand for stronger materials to work under the aggressive operating conditions of modern gas turbine engines. Alongside the mechanical strength, surface protectiveness of these materials is also of great importance in order to maintain the originally designed microstructure and chemistry. For coating scientists and engineers, a simple and effective method of making surface oxidation- and corrosion- resistant is always preferred. In this study, oxidation resistance of a coating system prepared by means of dip coating is investigated. Cross-sectional morphologies of the dip coated specimens before and after thermal cycling are also characterized using a scanning electron microscope.

Introduction

In gas-turbine engines, the hot gas stream generated by compressed air with fuel and ignited in combustor is used for aircraft propulsion and land-based power generation. Turbine engine components in such high temperature environment must have the ability to withstand the extreme operating temperature. Therefore, developing high temperature structural materials, such as nickel-based single-crystal superalloys with improved temperature capability [1] can improve the engine efficiency and performance [2-4], which also contributes to fuel saving and carbon emissions [5].

In order to protect these high temperature structural materials from oxidation, oxidation resistant coating is applied onto the surface. There are various methods of preparing oxidation resistance coatings, such as chemical vapor deposition (CVD), electroplating and air plasma-spray (APS) [6-9]. Dip coating is a cost-effective method which can be operated in open atmosphere and carried out in low temperature to obtain thin layers. During the procedure involving dip coating, well cleaned substrates were immersed in the coating solution before being withdrawn slowly in a steady speed to achieve film formation of uniform thickness [10-11]. The research presented in this paper focuses on using a dip coating approach to prepare an oxidation resistant coating on a nickel-based single crystal superalloy.

Experimental Details

The chemical compositions of the nickel-based single crystal superalloy and the Ni-based oxidation resistant coating powder are shown in Table 1. The dip coater shown in Figure 1 was used to prepare Ni based oxidation resistant coating on the surface of the substrate material. The chemical solution for dip coating prepared by adding 50g coating power into Polyethylene Glycol (PEG) and magnetically stirred for 3 hours.

Before dip coating, a substrate specimen was clipped to a sample holder and dipped in the prepared dip coating solution. The solution was being constantly stirred and the specimen was being slowly withdrawn at the speed of about 25μm per second.

The obtained specimens were then dried in an oven at the temperature of 80°C for 48 hours. After drying, two coated samples and a reference specimen were placed in alumina crucibles. The samples together with crucibles were then subjected to cyclic oxidation testing. Each thermal cycle involved 1 hour at a furnace temperature of 1135°C, after which the specimens were removed automatically from the rig and cooled for 1 hour.

The mass changes at different cycles resulted from oxidation were measured. A scanning electron microscope (SEM) machine was used to characterize the microstructure and the morphology of oxide scales.

Table 1. Chemical compositions of nickel-based superalloy and coating

Element [wt%]	Ni	Al	Cr	Other alloying elements
Ni-based superalloy	62.6	5.7	3.2	Bal.
Ni-based coating	65.8	8.1	4.0	Bal.

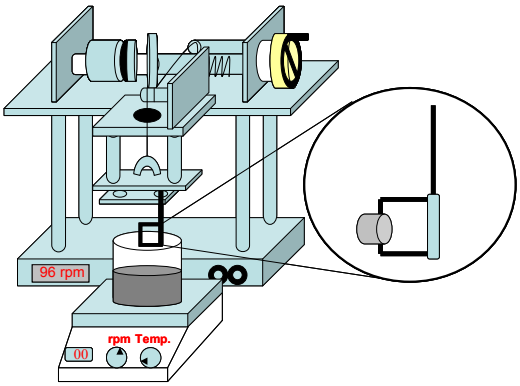

Fig. 1. Schematic illustration of a dip coater.

Result and Discussion

Cross-sectional observation of an as-coated specimen. From the SEM micrograph shown in Figure 2, the dip coated layer was quite evenly distributed on the substrate. It can be seen that the coated layer was approximately 20μm thick with many pores, which were likely resulted from the drying and evaporation of organic solvent. It is believed that by decreasing the particle size and increasing the size distribution, it would be possible to make more densely coated layer by dip coating. If the particle size is too large, the existence of excess pores may induce difficulty for the sintering process. Small particles, on the other hand, would allow denser packing and their excess surface area could assist the subsequent sintering process.

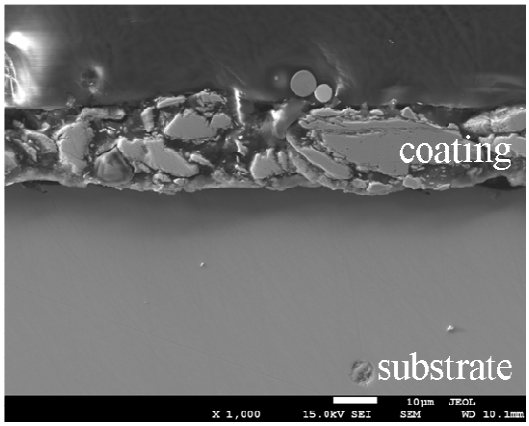

Fig. 2. A SEM micrograph showing the coating layer prepared by dip-coating on the surface of the Ni-based alloy substrate.

Cyclic oxidation testing. Oxides formed on the surface from the reaction between oxygen and elements of the coating and substrate as well as spallated pieces collected in the crucible were together weighted. The mass change per area of two dip coated samples and a reference substrate sample at different cycles is shown in Figure 3. The mass change of all specimens increased slightly in the early cycles but later dropped with increasing thermal cycling. It is clear that the difference of mass change with increasing thermal cycling indicated that the dip coated samples offered better oxidation resistance than the base substrate.

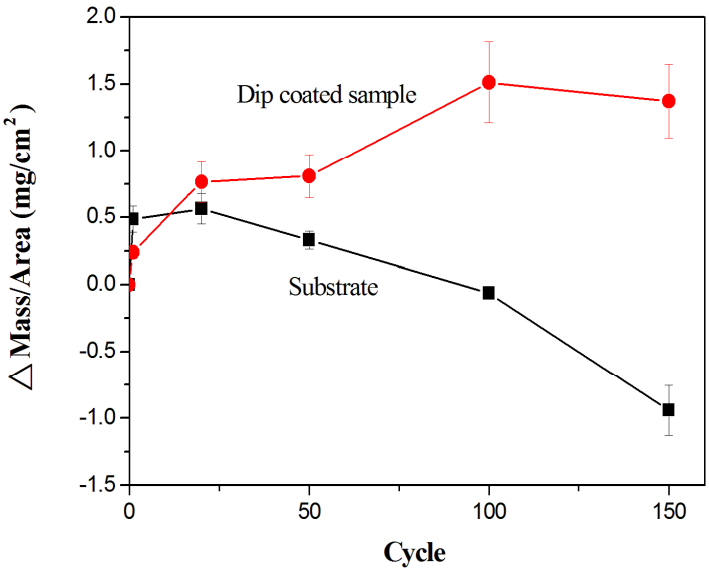

Fig. 3. The mass change of substrate and dip coated samples at different thermal cycles.

Cross-sectional characterization of specimens after 200 thermal cycles. Until now, there has been little work reported on preparing oxidation resistant coatings using dip coating. As shown in Figure 4, the oxide grown on the substrate was twice thicker than that on the dip coated specimen. It is believed that with the dip coating, oxidation resistance was improved, which might be due to the formation of more protective oxides, such as alumina and chromia. In addition, the morphology of oxides grown on the surface of the substrate revealed interesting multi-layer structures, which were not observed in the case of dip coated specimen.

Suggested future work. In this experimentation, the effect of surface roughness of substrates was not studied. The beneficial effect of employing a sintering step was also not evaluated. It is expected that sintering can help achieving a more dense and protective coating layer. All these factors remain to be clarified and are prioritized tasks for future studies.

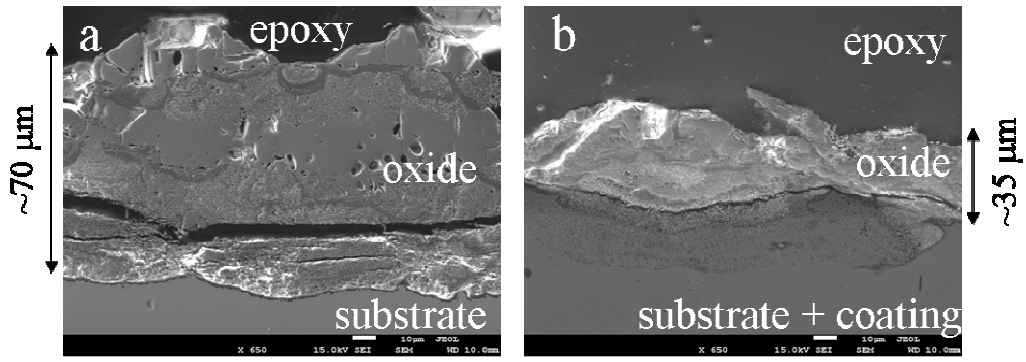

Fig. 4. SEM micrographs of a) substrate without coating, and b) dip coating sample after 200 thermal cycles.

Conclusion

In this experiment, preparation of an Ni-based oxidation resistant coating on a nickel-based superalloy has been carried out.The following points can be summarized:

1. SEM analyses indicated that approximately 20μm thick coating had been deposited on substrates by dip coating.
2. From the observation of the mass change after thermal cycling test, it appeared that the coating layer prepared by dip coating helped improving the oxidation resistance and oxide adhesion.
3. Based on SEM analyses, the oxide grown on the substrate was noticed to be twice thicker than that on the dip coated specimen.

References

[1] R.C. Reed, *Superalloys: fundamentals and applications*, Cambridge University Press, Cambridge (2006).

[2] K.A. Green, R.M. Pollock, H. Harada, T.E. Howson, R.C. Reed, J.J. Schirra, S. Walston, (eds.), *Superalloys 2004, Tenth International Symposium*, The Minerals, Metals, and Materials Society, (2004), pp.401-408.

[3] D. Furrer, H. Fecht, *Ni-based superalloys for turbine discs*, JOM Journal of The Minerals, Metals and Materials Society, 51, 1, (1999), pp.14-17.

[4] H. Xu and H. Guo, *Thermal Barrier Coatings*, Woodhead Publishing Limited (2011).

[5] H. Harada, *High temperature materials for reduction of CO_2 emission*, Journal of The Materials Science Society of Japan, 44, 6, (2007), pp.236-242.

[6] S. Bose, *High Temperature Coatings*, Butterworth-Heinemann Elsevier (2007).

[7] T.E. Strangman, *Thermal barrier coating for turbine airfoils*, Thin Solid Films, 127, (1985), pp.93-105.

[8] J.R Nicholls, M.J Deakin and D.S Rickerby, *A comparison between the erosion behaviour of thermal spray and electron beam physical vapour deposition thermal barrier coatings*, Wear, 233-235, (1999), pp.352-361.

[9] R.T. Wu and R.C. Reed, *On the compatibility of single crystal superalloys with a thermal barrier coating system*, Acta Materialia, 56, (2008), pp.313-323.

[10] H. Tikkanena, C. Suciub, I. Wærnhusb, A.C. Hoffmanna, *Dip-coating of 8YSZ nanopowder for SOFC applications*, Ceramics International, 37, 7, (2011), pp.2869-2877.

[11] L.E. Scriven, *Physics and applications of dip coating and spin coating*, Better Ceramics through Chemistry III, (1988), pp.717-729.

© (2012) Trans Tech Publications, Switzerland
doi:10.4028/www.scientific.net/AMM.187.255

The Study of TiCN Coating Based on Vacuum arc ion Plating and its Performance

Lijing ZOU [1, a]

[1] Binzhou Polytechnic,Binzhou China

[a] zoulijing@126.com

Keywords: coating, multi-arc ion plating, performance, pulse bias.

Abstract. This article provides an overview of the basic properties of the TiCN hard film, preparation methods, influencing factors, and application development trend. Magnetron sputter ion plating, radiofrequency sputtering method and multi-arc ion plating three coating preparation techniques are introduced. In this paper, with the coating by multi-arc ion plating method as the study object, an overview of the impact of C and N flow to its structure, as well as temperature, coating thickness, the pulse bias, the arc current to its performance is provided. Compared to other hard coatings, the improvement in its performance is showed and the future direction of technology development of TiCN is briefly discussed.

Introduction

Arc ion plating (AIP) is a low temperature physical vapor deposition (PVD) technology developed in recent years, mainly used for thermal barrier anti-oxidation and wear-resistant coating (such as TiN and TiC, TiCN, etc) deposition. TiN is a wear-resistant hard coating widely researched and applied in domestic and international. However, in high temperature condition, the TiN coating has poor antioxidant, anti-diffusion wear ability, limiting its further development. To solve this problem, new nano-composite coating technology are started to develop in domestic and international, combining the nitrides, carbides and oxides to form a wide variety of complex solid coating ,for example, (Ti, Zr) N, (T, Si) N. TiN film has excellent film performance, but for tools and abrasive and etc. in machinery field, its hardness seem lower; TiC has high hardness, but the toughness of the film is poor, under the impact of high load or non-continuous cutting, the film is easy to fracture [1-2]. TiCN coating with high hardness, resistance to pitting corrosion, high temperature resistance, erosion, combined with the matrix and low friction coefficient good mechanical properties are widely used in cutting tools, drills, and mold. Coating material reduces the diffusion and chemical reaction between the props and the work piece, thereby reducing wear and tear, a better solution to the conflict between the tool strength and toughness.

By optimizing the lattice structure of the coating, adding alloying elements and multi-layer coating composition can further improve the strength and toughness of the coating to greatly improve the durability and cutting speed of the tool, making the tool life increased by three to five times, the cutting speed increased by 50% to 70%, the processing accuracy increased by 0.5 to 1 level, the tool consumption costs reduced by 30% to 50%. TiCN composite film has a higher hardness than the TiN film and better toughness and chemical stability than TiC film, having broad application prospect and more and more attention [2-4]. This article provides an overview and study of TiCN film preparation methods, coating performance, influencing factors and the development status quo.

Preparation methods of the TiCN coating

Since 1985, After Knotke first published research on the TiCN coating technology, People expressed great interest to its excellent high temperature oxidation resistance and good application performance, and so far had developed a variety of physical vapordeposition technology [5]. At present, there are

three methods of preparation of TiCN coating, which are magnetron sputter ion plating method, radiofrequency sputtering method and multi-arc ion plating method, in which the magnetron sputter ion plating method and multi-arc ion plating method are most widely used and low cost.

Magnetron sputter ion plating. Magnetron sputtering technique was developed in the early 1970s, as the deepening of technology and research, it has been widely used in the industrialization field of electrical, optical film and energy, mechanical industrial etc. and become one of the most widely used preparation of TiCN film methods. In coating process, Ti ions are generated by using Ar ions generated by Ar gas glow discharge to bomb the Ti target, and by electrostatic acceleration fly to the work piece and thus deposition film. This method has high deposition rate, uniformity film thickness, and the ion plating can improve the combining ability of coating and substrate interface and make film organization dense. At the same time, the targets susceptible to pollution, and low deposition rate in the coating process are its main weakness. It has been found [6], when carbon and nitrogen partial pressure increases, the deposition rate will slow down.

Multi-arc ion plating. Multi-arc ion plating belongs to an improved ion plating method [7], first developed by the Soviets, in the early 1980s, first practical by the U.S. Multi-Arc. The basic principle is taking the metal target source as the cathode, discharging by arc between the anode shell and making the target evaporation and ionization, forming space plasma, and then depositing coating on the work piece. Compared to other membrane technologies, the advantage is that the cathode produces plasma directly, and the cathode target can be arbitrarily arranged, which greatly simplifies the sample fixture. In addition, the multi-arc incident particle energy is high, the ionization rate can reach 60% ~ 80%,the density of membrane is high, the strength and durability are good, the interface of film and matrix is easy to produce atomic diffusion and the film adhesion is good.

Vacuum arc ion plating technique uses plasma electromagnetic field to filter, which can effectively reduce or eliminate large particles, shown in Figure 1. Martin etc. [4] made comprehensive summary of the filtered arc, and used the arc-type filtered arc in a variety of substrate coating. The filter arc was first used by Aksenov etc. [8] , and it has been successfully used for the film of deposition semiconductors, various types of metal and alloy etc.. Compared with conventional arc ion plating coating, arc-type filtered arc coating macro-particle is no impurities, homogeneous, dense structure, and able to meet the requirements of the optics, microelectronics film. There are also some disadvantages to the filtered arc source, that is, the beam diameter is small, usually less than 200nm, and difficult to form multi-arc source array, making the mass production of large area can not be achieved, and the transmission efficiency is not high, the maximum transmission efficiency of the bend structure approximately about 30%, the ion current just 2% to 3% of the arc current [9-10].

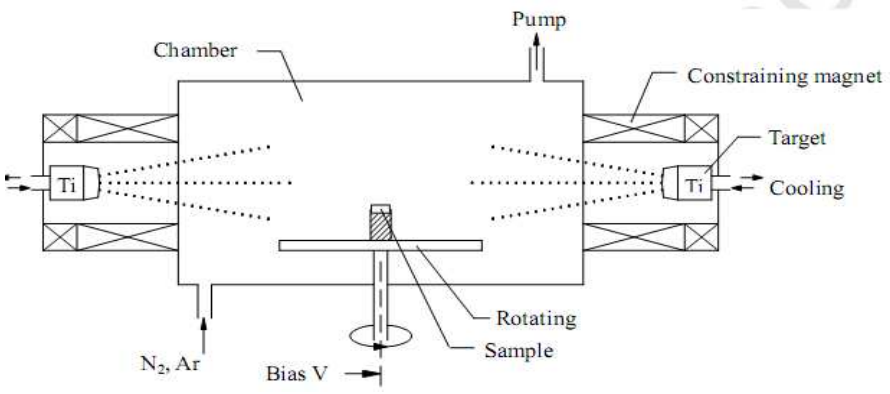

Figure 1 Multi-arc ion plating method schematic diagram

Influence of gas flow on the coating structure

Change of the N2 partial pressure (flow) will cause the sputtering nitrogen ion density and energy change, impacting the combining with the metal atom, making the preferred growth orientation change, thus affecting the coating performance. BYShew, etc. [5] found that under the condition of

total pressure 0.8Pa and Ar flow 20sccm, when the nitrogen flow is less than 6sccm preferred orientation is (111), when the nitrogen flow is greater than 6sccm, (111) peak intensity decreases, and (200) peak intensity increases, mainly because in the structure of fcc-TiCN, (111) plane surface energy is low, under low nitrogen flow atoms are migration to (111) plane, with the increase of nitrogen flow, the atomic migration rate decreases, but (200) crystal surface with high surface energy has high step density, and the diffusion distance away from the low-energy grid points is short, benefit the crystal preferential growth along the (200) crystal surface [6]. BYShew etc. [11] found that when the nitrogen flow is 1sccm, samples obtained are amorphous structure, when the nitrogen flow is more than 2sccm, there is columnar structure in the film, grain boundary existing, when nitrogen flow increases to 6sccm, the film becomes dense, and respectively prefers to the microstructure of the isotropic and the grain refinement, mainly as the increase of nitrogen flow, the atomic migration rate is reduced, the membrane surface changes in local chemical potential. The researchers found that with nitrogen flow increasing, the grain gathered in the film is less, the surface becomes dense and smooth, the roughness decreases gradually until constant.

Now the carbon source used by the researchers' preparation of TiCN is the C2H2 or CH4 gas [3-4] mainly, because TiN and TiC are NaCl-type face-centered cubic structure, the radius of N atom and C atom is very close, N is 0.071nm, C is 0.077nm, the two can be mutually replacement to form a single-phase material TiC (N) or of TiN (C). Under certain condition, there may be two-phase structure appeared. In the XRD diffraction spectrum the peaks of them are very close, and even some overlap, resulting in the phase analysis complexity, so it is commonly written as TiCxN1-x. Figure 2 shows the X-ray diffraction spectrums of TiCxN1-x films of different components, the Ti (C, N) peak covers the TiN peak and TiC peak. It can be seen from the figure, the film that x is less than 0.6 film has similar diffraction information with TiN, the preferred orientation is still (111) direction, but the peak position is slightly offset to the left, this is because after the C atoms which atomic radius are larger replace part of N atoms which atomic radius are smaller the lattice constant is bigger. Figure 3 shows the Ti (C, N) (1 1 1) orientation diffraction peak intensity with the increase of C content gradually weakens, when x = 0.9, (220) preferred orientation appears, which is the result of the surface energy and the distortion working together [6].

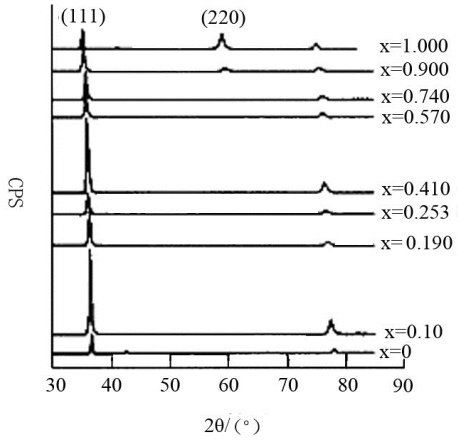

Figure 2 Changes of C content in XRD diffraction spectrums

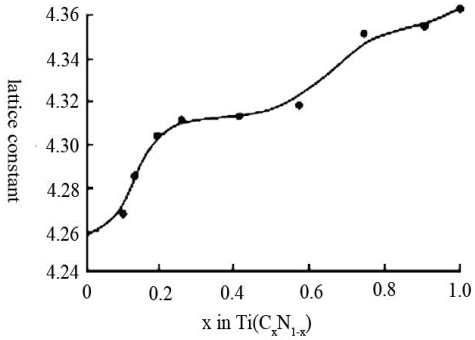

Figure 3 Lattice constant changes with C content

Influence factors of TiCN coating performance

Temperature. The quality of TiCN coating is mainly affected by the process factors like composition, temperature and atmosphere. Different matrix temperature will cause the coating's grain size, shape, structure are completely different. The deposition temperature too high and deposition rate too fast will cause the coated crystal show thick branched, affecting the quality of the coating; the deposition temperature too low, it tends to form porous, loose sediments, affecting the binding strength of the coating and matrix. Therefore, a reasonable choice of temperature is a necessary condition to obtain

high quality coating. Mc.Cormell etc. [9] deposited TiCN coating on stainless steel with PVD method, including that its hardness, bond strength and coefficient of friction will not change when the temperature is below 250℃. After 450℃ heat treatment to samples, TiCN coating friction coefficient is 0.2 before 250℃,and up to 0.3 at 250℃, but still lower than the friction coefficient of TiN, it is because in TiCN coating C has played a lubricant role. Studies [10] show that when the temperature is below 200 ° C, the coefficient of friction and wear rate of TiCN coating increases with increasing temperature.

Pulsed bias. The existence of pulsed bias plays a very important role to reduce the droplet and improve the coating quality. Negative bias attracting positive charge sputter work piece can make the titanium ions near the cathode target accelerate the fly, increase the chance of collision with nitrogen in the plasma and droplet, and at the same time increase the bonding strength of the titanium and nitrogen. If maintain the vacuum pressure constant, the nitrogen flow increases with increasing negative bias, but nitrogen content in the film decreases with the increasing of negative bias [4]. This is mainly the Ti-Ti bonding ability is stronger than Ti-N, and with the increasing of negative bias, the re-sputtering ability of the titanium stronger than nitrogen. In addition, with the increasing of bias the plasma particles make the energy particles fly to the matrix change, affecting the organizational structure of the film.

Arc current. The experimental results found [5], in certain film thickness scale and certain process condition, the relationship of arc current and hardness is shown in Figure 4. Considered from the perspective of industrial production application, increasing arc current can improve productivity and film hardness and wear resistance.

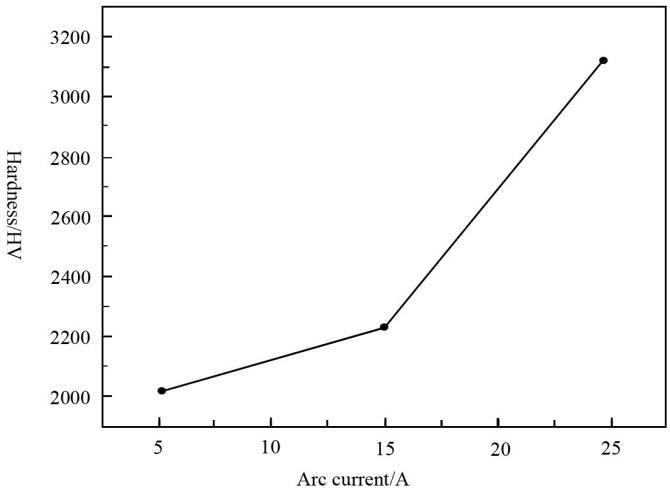

Figure 4 The relationship of arc current and hardness

Increasing arc current, means that the target overall temperature increases, corresponding droplets will increase, and the droplet size will increase too. Increasing of droplets and droplet size will inevitably lead to the decline of corrosion resistance of the film, especially large diameter droplets, with about 1/3 buried in the film in height direction and the irregular small holes at the bottom. When encounter corrosive substances like acid and alkali etc., these holes first corrupt and form needle-shaped holes [5], therefore, their existence is the main reason that the corrosion resistance of the coating reduces. Therefore, in practical application, for the coordination of the contradiction between increasing arc current and droplet, some optimized ways can be used, such as to increase the evaporation area of the target, strengthen the cooling effect of target or design new arc source which can inhibit droplets produce.

TiCN coating technology trend

With the large capacity of power plant steam turbine, steam turbine blade is the key component of the gas steam turbine engine, the most direct part conversing thermal energy into mechanical energy. In engine working process, the working environment of the turbine blade is very bad, not only to withstand high temperature, high pressure, the impact of high-speed air flow and composite role of centrifugal load and vibration load, but also fall under the high-temperature gas corrosion. In particular, the pitting corrosion resistance will decline rapidly, making the life of the turbine blade greatly reduce, or even cause catastrophic damage [12-13]. At present, only relying on the advanced cooling technology, the development of new high-temperature alloy materials and improvement of turbine blade manufacturing process is difficult to meet the industrial demand in a short period, and therefore strive to improve the pitting corrosion resistance of advanced turbine blade is essential . Coating at blade surface can greatly improve the blade anti-erosion performance, extending its life. In view of the superiority of the physical and chemical performance of TiCN coating, there is great potential on the surface protection of turbine blade.

Conclusion

For the excellent performance of TiCN coating and considerable research prospect, TiCN coating is a thriving film field. In addition to the requirements of the traditional performance, preparation of more thick and a lower friction coefficient and wear rate of TiCN coating is the future direction of development with countries around the world increasing more capital investment and technical research to the super hard quality film. Today, the resources, cost, ergonomics increasingly stringent required, coating scientists should look squarely at the difference of domestic and international, and guide to accelerate the development of hard coating of TiN and TiCN.

References

[1] Yanfa Mao, Weiguo Tang, Jinliang Liu. Technical progress of the TiAlN nanocomposite coating. Tool Engineering, 2006, 40(1): 20-24

[2] Y Y Gu, J F Lin, C F Ai. The tribological characteristics of titanium nitride, titanium carbonitride and titanium carbide coatings[J]. The Solid Films, 1997, 302: 193-200

[3] L Larlsson, L Hultman, M P Johansson, et al. Grouth, microstructure and mechanical propertis of are evaporated TiCxN1-x films[J]. Surface and Coatings Technology, 2000, 126: 1-14

[4] H M Gabriel, H K Kloos. Morphology and structure of ion-plated TiN, TiC and Ti(C,N) coatings[J]. Thin Solid Film, 1984, 118: 243-254

[5] Yu Xin, Shuping Fan, Jianxin Wu. The study of the impact of C2H2/N2 flow rate to deposit Ti(C,N) film. Vacuum Science and Technology, 1997, 17(5): 351-354

[6] Mukong Wang, Ruixin Ma, Wei Lin. The research progress of TiAlN hard film / coating material. Cemented Carbide, 2008, 25(3): 186-191

[7] G S Fox-Rabinovich, J L Endrino, et al. Impact of annealing on microstructure properties and cutting perform ance of an TiAlN coating[J]. Surface and Coatings Technology, 2006, 201: 3524-3529

[8] Lishi Wen. Surface deposition technology [M]. Beijing:China Machine Press,1989: 162-168

[9] A Richthofen, R C Remer, et al. Composition binding states structure and morphology of the corrosion layer of an oxidized TiAl0.54N0.46 film[J]. Thin Solid films, 2006, 312: 190-194

[10] Chengming Li, Xiaojun Sun, Yong Zhang. Observation of the the particle size of arc ion coating and the scanning electron microscopic effected [J]. Journal of Chinese Electron Microscopy Society, 2004, 23(3): 252-256

© (2012) Trans Tech Publications, Switzerland
doi:10.4028/www.scientific.net/AMM.187.260

A New Design of Underwater Robot Fish System Using Shape Memory Alloy

Peihua HUANG[1,a], Jian WANG[2,b]

[1]Binzhou University department of Computer and Science Shandong, China
[2]The Sencond Artillery Petty Officer School Shandong, China
[a]huangqrnu@126.com, [b]ustc009@hotmail.com

Keywords: Shape Memory Alloyt; Underwater; Robot Fish

Abstract. The bionic structure of an oscillatory propulsion system was discussed in this paper, This structure was contrived from sufficient analysis by the anatomical structure of a fish, Shape Memory Alloy was used to apply its power. Of course, we simplified the oscillatory propulsion system. Finally, we established the quantitative relationship among parameters depending on the torque balance equation.

Introduction

Propellers for underwater vehicles are not very efficient, their efficiency being no more than 40 percent[1]. The main cause is the production of vortices perpendicular to the direction of motion. Due to their orientation, these vortices do not produce thrust, though they increase power consumption. An alternative apparatus for thrust development is the oscillating foil. The production of thrust is based on the formation of a reverse Karman vortex street in the flow wake[2]. Thrust generation and its sensitivity to the Strouhal number is similar to the efficient propulsion of fish.

At present, most fish-like propulsion system is driven by motor. It has at least the following three drawbacks:

1)Noisy

2)Low power/weight ratio

3)Hard to realize mini or micro oscillatory propulsion system.

The best way to solve these problems is to use intelligent materials such as Piezoelectric (PZT), Shape Memory Alloy(SMA), Ionic Polymeric Metal Composites(IPMC). There are many reasons why the SMA is the most attractive material. The SMA is a device with lightweight and small Volume[3]. The miniaturization of robotic systems needs powerful compact and lightweight actuators. The SMA has a high strength-to-weight ratio, which makes it ideal for miniature applications. Moreover, the SMA works quiet without any pollution[4]. So it is widely applied in biomimetic engineering. For example, Toshio Fukuda e.g. (Nagoya University) used SMA thin film to simulate the wave form of swimming fish by controlling the electric schedule[5]; Othon K. Rediniotis achieved SMA wire driven biomimetic autonomous underwater vehicle actuator; Nagahiko Shinjo and Geoffrey W. Swain designed an SMA-based oscillating propulsive system .

However, the response frequency of the above actuators are rather slow, this restricts the development of oscillatory propulsion system. besides, the SMA controlled between martensite and austenitic phases has three limitations: non-linear,hysteresis and small strain.

In this work, an underwater oscillatory propulsion system is developed, characterized by：

1) An efficient oscillating propulsion mechanism.

2)Low cost so that the possibility of losing does not make its use prohibitive.

3)High response frequency, reaching up to 1.5Hz.

4)Biomimetic design according to anatomical structure of a vivid fish.

5)Large rotation angle and elastic soft motion.

This paper discusses machine structure, dynamics and control arithmetic related to the development of this vehicle. First, a biomimetic design structure is introduced. Then its dynamics is analyzed. Moreover, a Fuzzy Logical Control(FLC) arithmetic is designed to solve the control problem of SMA. At last, some experimental results of the underwater oscillatory propulsion system are given.

Bionic Machine Design

Before designing the underwater oscillatory propulsion system, a detailed anatomical analysis of a fish(take crucian as an example) was done.

Swimming motion is generated by activating alternate sides of segmented muscles in a sequential manner. An anterior muscle is activated first and a wave of activation propagates from head to tail, producing a backward traveling wave of body bending. The locomotor musculatures in fish are arranged in a segmental manner and each segment or myomere forms a complex three-dimensional structure. The general shape of a crucian anatomic structure is shown in Fig.1.

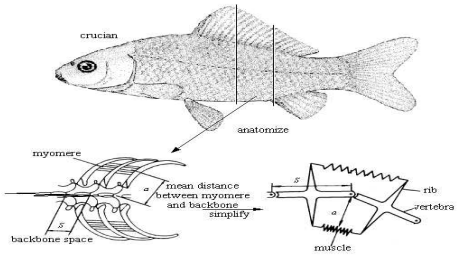

Fig.1.Anatomic structure of the middle part of crucian

A myomere is composed of two distinct types of muscles: oxidative red and glycolitic white muscles. Red muscles are primarily for low-intensity and long-duration activities such as steady swimming; thus, it is the primary focus of this study. The red muscles are generally located along the mid lateral line just under the skin in a wedge formation (superficial red muscle). The remaining muscle volume is occupied by white muscles, which are used for short bursts of high-intensity activities, such as sprinting and escape maneuvers.

Fish swimming is classified as anguiliform, subcarangiform, carangiform, thunninform and ostraciform, depending on the percentage of their body that contributes to thrust production through undulatory motions.

The traveling wave method is used by aquatic animal with slender-long body such as eel. However this style is abandoned due to the required joints that complicate the design and increase friction losses. The oscillating wing method is used by most aquatic animals, but it is also complicate for initial design. As a result we choose oscillating plate method as our design model despite the fact that this design style has the worse hydrodynamic performance because of the rigid body. However it provides the simplest design: less joints, less mechanical losses due to friction, simple and inexpensive construction, simple control and finally less weight.

According to the above analysis, we finally design the underwater oscillatory propulsion system as follows(the head is just for aesthetic feeling or imply one use of the oscillatory propulsion system) see Fig.2.

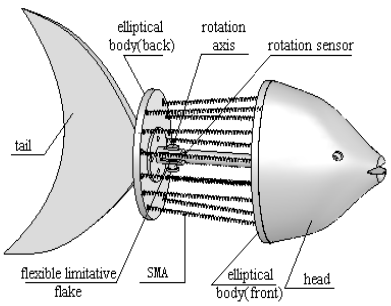

Fig.2.The structure of underwater oscillatory propulsion system

In order to increase the SMA working journey, we choose SMA spring instead of SMA wire. To imitate the distribution of red muscle and strengthen the driven force, six parallel SMA springs are arranged along each side of the inside surface of the elliptical body. The elastic limitative dead block has two functions, one is to avoid over rotate; the other is to store energy transformed from kinetic energy to potential energy, which can reduce energy waste. The surface is covered with elastic film instead of hermetic materials due to the fact that the SMA springs need water to cool them in order to fasten working frequency. We use lunate caudal fin to produce maximal thrust. Rotation sensor is used for closed loop control. The working Mechanism of the underwater oscillatory propulsion system can be described as follows see Fig.3.

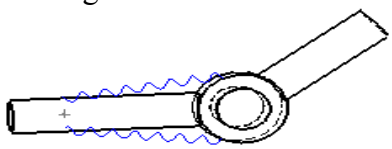

Fig.3. The different-type of SMA actuator

When one side SMA is within the Martensitic phase, the other SMA can be heated into the Austenitic phase by electric current, it begins to contract and forces the joint to rotation; contrarily, it will rotate towards the other direction. The motion of the joint can be described by equation (1),

$$\theta(t) = \theta_{aver} + \theta_{\max} \sin(\omega t + \varphi)$$

$$\omega = 2\pi f \tag{1}$$

where θ(t) is the angle between the tail and the longitudinal axis of the vehicle, is the mean of θ(t) during one period and f is the frequency of the oscillating foil, φ is the initial phase. If the oscillatory propulsion system keeps straight at the beginning, then φ=0. If the oscillatory propulsion system does symmetrical movement, then θ_{aver} =0.

DYNAMIC ANALYZE

Simplified model. The underwater oscillatory propulsion system model (Fig.4) is simplified to dynamic analysis.

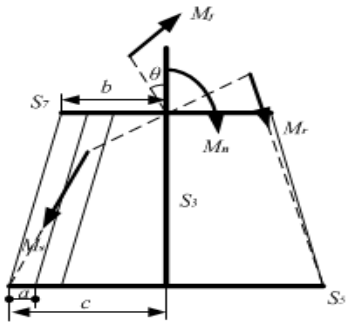

Fig4. Simplified model of underwater oscillatory propulsion system

The red declining wire represents the SMA spring distributing on one side. MS--the SMA driven torque; Mγ-- the SMA resistant torque; Mf--the damping torque; Mn--mass inertia torque; a--the projection distance between two SMA springs; b and c --the distance between the outermost SMA and the center.

Establish dynamic function. There are three main forces: the SMA force, the damping force and mass inertia force. Therefore, we can establish the torque balance equation as follows:

$$M_s - M_r = M_f + M_n \tag{2}$$

The parameters are calculated below.

1) M_s and M_r

$$M_s = \sum_{i=1}^{3} M_{si} \tag{3}$$

$$M_r = \sum_{i=1}^{3} M_{ri} \tag{4}$$

i=1, 2, 3 .

Equation(3)(4) means that the total one side SMA torque is the sum of every SMA spring torque. In order to simplify the calculation we use the mean distance between SMA spring and the center (b' and c')instead of b and c. see Fig.5.

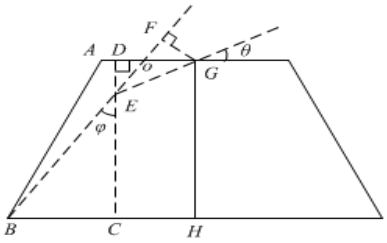

Fig.5 Geometry model

While the rotation angle equals to θ, we calculate the vertical length from pivot to force $L_s$and L_r

Known quantity:

EG=b', BH=c', $\angle$DGE=θ， Request for:

GF namely Ls

Suppose: $\angle$BEC=$\angle$DEO=φ

then ΔDEO$\backsim\Delta$FOG $\Rightarrow$ $\angle$FGO=φ

for $DE = b' \sin\theta \quad DG = b' \cos\theta$

then $BC = c' - b' \cos\theta \quad EC = S_3 - b' \sin\theta$

$tg\varphi = (c' - b' \cos\theta)/(S_3 - b' \sin\theta)$

In ΔDEO use the law of tangents then OG=DG-DO

$$DO = tg\varphi \times b' \sin\theta = \frac{c' - b' \cos\theta}{S_3 - b' \sin\theta} \times b' \sin\theta$$

In ΔFOG use law of cosines

$$L_s = b' \left(\cos\theta - \sin\theta \frac{c' - b' \cos\theta}{S_3 - b' \sin\theta} \right) \times \frac{1}{\sqrt{\left(\frac{c' - b' \cos\theta}{S_3 - b' \sin\theta} \right)^2 + 1}} \tag{5}$$

Because of the symmetry, we can get the conclusion： $L_s = L_r = L$ (6)

the SMA relative strain

$$\varepsilon = \frac{\Delta l}{l} = 1 - \sqrt{\frac{\left(S_3 - b' \sin\theta\right)^2 + \left(c' - b' \cos\theta\right)^2}{S_3{}^2 + \left(c' - b'\right)^2}} \tag{7}$$

l is the original length of the SMA spring.

Now

$$M_s = L_s \times n(\varepsilon, T_1) \tag{8}$$

$$M_r = L_r \times n(\varepsilon, T_2) \tag{9}$$

here $n(\varepsilon, T_i) = A\sigma(\varepsilon, T_i)$ (10)

A is the cross area of SMA spring; $\sigma(\varepsilon, T_i)$ is the inner stress, which can be concluded from the strain-stress curve of SMA spring.

According to (8) (9), we can infer that

$$\begin{aligned} M_s - M_r &= L \times n(\varepsilon, T_1, T_2) \\ &= L \times A(\sigma(\varepsilon, T_1) - \sigma(\varepsilon, T_2)) \end{aligned} \tag{11}$$

2) The damping torque M_f

In order to calculate the damping torque, caused by hydrodynamic drag on the tail, the tail is segmented into two segments. See Fig.6.

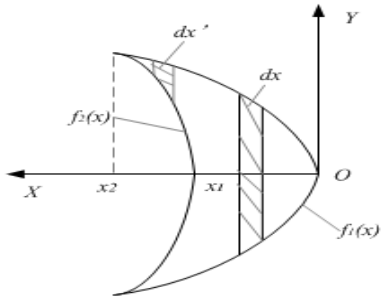

Fig.6 Mathematical model of tail

According to

$$F_{hydro} = 0.5 \times \rho_w \times C_D \times A \times U^2 \tag{12}$$

where A is the area of the surface. The drag coefficient C_D is found in tables to be 0.27 for laminar flow and 0.13 for turbulent flow, while a transition occurs at Reynolds number Re =105($R_e = U \cdot L / V$).

$$dF_{damp} = \begin{cases} 0.5 \cdot \rho_w \cdot C_D \cdot (2 f_1(x)) \cdot dx \cdot u^2 \\ 0 < x < x_1 \\ 0.5 \cdot \rho_w \cdot C_D \cdot [2 \left| f_2(x) - f_1(x) \right|] \cdot dx \cdot u^2 \\ x_1 < x < x_2 \end{cases} \tag{13}$$

where $u = W_L \cdot x$

As a rough approximation, it is assumed that the tail is perpendicular to the flow and therefore the drag coefficient is $C_D = 2$The elementary torque with respect to the tail's joint axis dMf generated by dFdamp is dMf = xdFdamp. Integrating the elementary torques along the radial direction provides the total damping torque:

$$\begin{aligned} M_f &= \rho_w \cdot C_D \cdot \int_0^{x_1} f_1(x) W_L^2 x^3 dx \\ &+ \rho_w \cdot C_D \cdot \int_{x_1}^{x_2} [f_2(x') - f_1(x')] W_L^2 x'^3 dx' \end{aligned} \tag{14}$$

where $f_1(x)$ and $f_2(x)$ are design in advance.

3) The mass inertia torque M_n

The equivalent inertia of the tail I_y with respect to the tail's joint axis equals the sum of the mass inertia of the tail I_{ym} and the inertia of the accelerated water I_{yw}. The later is calculated through the corresponding added mass coefficient.

However $I_{ym} << I_{yw}$,so I_{ym} can be omitted.

$$I_{yw} = \int_0^{x_1} z^2 \cdot \rho_w \cdot \pi / 2 \cdot (2 \cdot f_1^2(x) + b^2) dz + \int_{x_1}^{x_2} z^2 \cdot \rho_w \cdot \pi / 2 \cdot [2 \cdot (f_2(x) - f_1(x))^2 + b^2] dz \tag{15}$$

then M_n can be expressed as

$$M_n = I_{yw} \cdot \dot{W}_L \tag{16}$$

here

$$\dot{W}_L = \frac{d^2\theta}{dt^2} = 4\pi^2 f^2 \theta_{\max} \sin(\omega t + \varphi) \tag{17}$$

Motion Control Algorithm

In this section, a Fuzzy Logic Control (FLC) algorithm is introduced to solve the non-linear and hysteresis problem of SMA. Meanwhile a Pulse Width Modulation (PWM) is used to heat the SMA spring to reduce the energy waste. The FLC consist of a set of linguistic rules.

For the oscillatory propulsion system, the input linguistic variables are the joint angles error $\Delta\theta$ and joint velocities $\Delta\dot{\theta}$. The output linguistic variable is PWM modulation ratio Q.

The input linguistic variable $\Delta\theta$ is characterized by fuzzy sets and scaled with the fuzzy sets{ NB(Negative Big), NM(Negative Medium), NS(Negative Small), NO(Negative Zero), PO(Positive Zero), PS(Positive Small), PM(Positive Medium), PB(Positive Big)} and the linguistic variable Q and $\Delta\dot{\theta}$ are scaled with the fuzzy sets{NB(Negative Big), NM(Negative Medium), NS(Negative Small), ZO(Zero), PS(Positive Small), PM(Positive Medium), PB(Positive Big)}.

We use the triangle-type membership functions for the linguistic variables respectively.

Experimental Results and Conclusion

In the experiment, the modulation factor (MF) of the PW modulator is defined as the ratio of the on-time to the period and is described by equation(18).

$$MF = T_{on} / (T_{on} + T_{off}) \tag{18}$$

First we test the extent and velocity of oscillation under different MF, we just heat one side SMA spring by PWM and do nothing with the other side. Fig 7 shows the experiment result under 16V voltage.

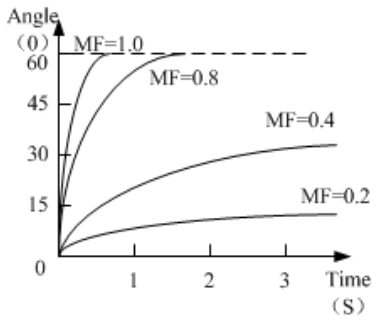

Fig.7 Extent and velocity of oscillation under different MF

From the picture we can clearly see that the extent and velocity of oscillation are both increased with MF under the same heating time. The maximal oscillatory angle is about 600 because of the mechanical design. When MF below a certain value, it is impossible to drive SMA spring to it's maximal constriction. We also test the maximal oscillatory frequency under different supplying voltages (MF=1, $\theta = 30^0$). See Fig8.

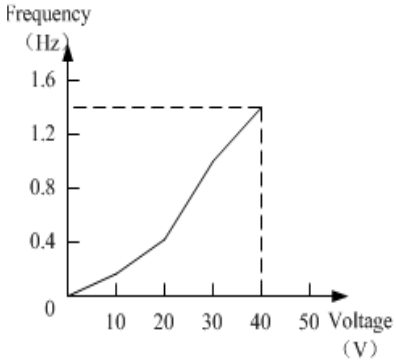

Fig.8 Maximal oscillatory frequency Under different voltages

With the increase of supply voltage, the oscillatory frequency is greatly increased. The maximal frequency can reach almost 1.5Hz at 40V. It is a very exciting result for SMA actuator. But more energy is needed.

In this paper, a biomimetic underwater oscillatory propulsion system is developed and the dynamic equation is established. Meanwhile an experimental closed-loop control system for the oscillatory propulsion system has been developed based on the proposed simplified propulsive mode. The experimental results have demonstrated the good performance of the joint driven by the SMA spring However, our proposed motion control algorithms did not take the dynamics into account, only the motion kinematics was considered, which has to be improved in the future.

Acknowledgment

Thanks my cooperators,thanks binzhou University and The Sencond Artillery Petty Officer School,The paper was supported by binzhou University fund(Code number:BZXYG0904).

References

[1] Triantafyllou, M. S, "An Efficient Swimming Machine", Scientific American, March 1995, pp. 40 – 48.

[2] ELIOT G. DRUCKER1,LAUDER2"A HYDRODYNAMIC ANALYSIS SPEED: WAKE STRUCTURE AND LOCOMOTOR FORCE IN SLOW " The Journal of Experimental Biology 203, 2379–2393 (2000)

[3] K.lkuta, "Micro/Miniature Shape Memory Alloy Actuator" in Proceedings of IEEE International Conference on Robotics and Automation, Vol.3.pp. 2156-2161, Los Alamitos, CA, May. 1990

[4] KojiIkuta. Sh-ape memory ally actuator[A]. Proc 1990 IEEE Int Conf on Robotics and Automation[C]. Cincinnati, Ohio: IEEE Computer Society Press, 1990. 2156～2161.

[5] Toshio Fukuda, et al. Distribution Type of Actuators by Shape Memory Alloy and its Application to Underwater Mobile Robotic Mechan-ism. IEEE 1990. 1316～1321.

© (2012) Trans Tech Publications, Switzerland
doi:10.4028/www.scientific.net/AMM.187.267

Au plating failure prevention on the electronic industry

Xiaogang Liu[1], Ping Liu[1,2,a], Xiaolong Gu[1], Xinbing Zhao[2]

[1]Zhejiang Province Key Laboratory of Soldering & Brazing Materials and Technology, Zhejiang Metallurgical Research Institute, Hangzhou 310011, PR China

[2]Department of Materials Science and Engineering, Zhejiang University, Hangzhou 310027, PR China

[a]liuping_davy@yahoo.com.cn

Keywords: Au plating, selective plating, Au embrittleness, tombstone, Mercury attack

Abstract. Au plating was widely used to the function of soldering, contact/connection, and decoration, rendered by the extremely good solderability, customer favorite noblest appearance, excellent corrosion resistance, high electrical conductivity, etc. while Au plating thickness and quality are critical to influence the function performance and reliability after service in field. In this paper, soft gold, hard gold and selective gold plating processes were introduced in different application aspects. Some typical failure analysis cases related to Au plating such as passives tombstone, contact philosophy and mercury attack were exemplified to make clear the correct application and proper Au thickness requirement. The prevention solutions were also recommended.

Introduction

The applications of gold plating in electrical and electronic components are many and varied as shown in Fig. 1. The quantity used is growing steadily especially with the growth of consumer electrical and electronic products. Generally, Au plating was adopted to the function of soldering, contact/connection, and decoration, rendered by the extremely good solderability, customer favourite noblest appearance, excellent corrosion resistance, high electrical conductivity, etc. while the plating thickness and quality are critical to products' function performance and reliability after served in field.

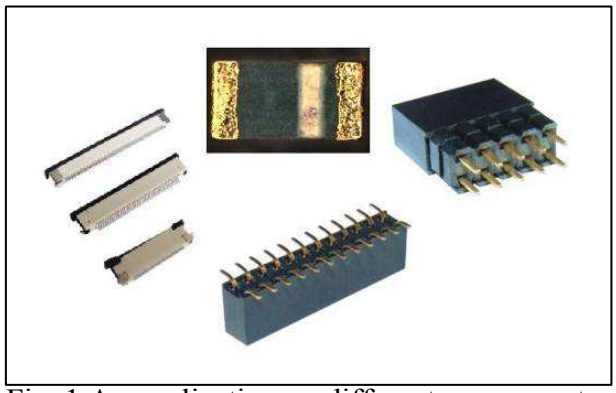

Fig. 1 Au application on different components.

In this paper, based on our failure analysis experience, some challenges of Au plating application were summarized. It is expected to provide the benefit for SQE, SMT, Process, SDE and FA engineers to understand the proper principle of Au plating application, to identify the real root cause, to take correction action and prevent quality issues.

Gold plating

Gold plating can be divided into two types: soft gold and hard gold. Soft gold can be soldered easily and die bonded, mainly adopted in the semiconductor industry. It is ultra-pure gold, less bright, 15uinch thickness. The baths used to deposit this gold must not only be extremely pure, but must be kept pure in production, to avoid rejects in subsequent manufacturing operations. Monitoring the solutions is necessary to insure no build-up of base metals such as iron, nickel, copper and lead [1].

Hard gold generally was plated on contacts and connectors. This plating contains complex cobalt or nickel in small quantities about 3 wt%, to improve hardness and brightness of the deposit, while interfere with die bonding. Hard, bright gold baths, if operated with good housekeeping and chemical control, have very long life, often three years and more.

Immersion plating of gold is actually older than gold electroplating. It is practiced mostly in applying low-cost decorative finishes. Its usefulness is limited by the extreme thinness and by the lack of permanence of the deposit.

Selective plating

In electronic assembly process, many components required the soldering terminal as well as contact terminals. Whereas, the plating thickness for two terminals is different; otherwise Au embrittleness [2] can be easy to occur (See Fig. 2). Therefore, the selective plating process [3], which is a method of electroplating a specific plating material onto a selected surface area without the use of immersion tanks or baths, was brought out. Ideally, the component should be selectively plated with 0.1-0.2 microns of Au in the solder terminal area and 1 micron of Au in the contact area, with a Ni barrier region, exposed Ni area, in between to prevent excessive solder wicking. If the selective plating is not feasible, then a compromised plating of 0.4-0.6 microns should be evaluated. That needs to be confirmed that this amount of plating would be acceptable for the contact performance as well.

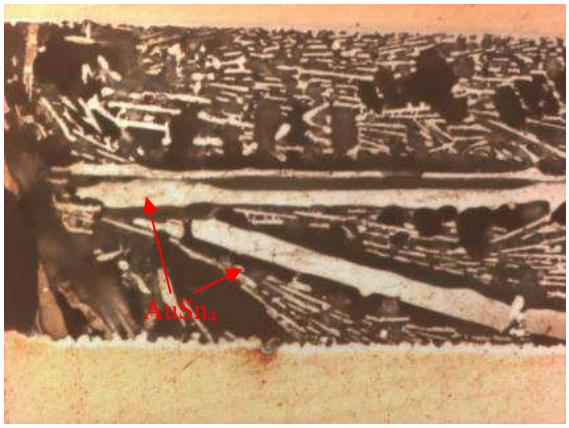

Fig. 2 Large $AuSn_4$ IMC in the solder bulk to occur Au embrittleness

Passives tombstone

High failure rate 1.4% of inductor tombstone [4] was issued at Factory Front-end process as shown in Fig. 3. The inductor terminal was plated by gold, while those resistor/capacitors with Sn plated terminals rarely appeared similar failure. Moreover, the tombstone issue can be reduced largely after changing the solder paste from current one to another brand. Upon the wetting solder height on the terminal (shown in Fig. 4), it is possible the inductor has a little skew or misaligned placement in pre-reflow process. The excellent solderability rendered by Au plating made the occurrence of tombstone failure on Au plated components more than that of Sn plating once there is a little bit difference on wetting force, induced by a misalignment placement, part tilt, higher active flux, etc. As a solution, it is recommended that the Tin plating replace Au plating because Tin plated terminal has acceptable solderability as well, no such susceptible to minor wetting force difference between two terminals.

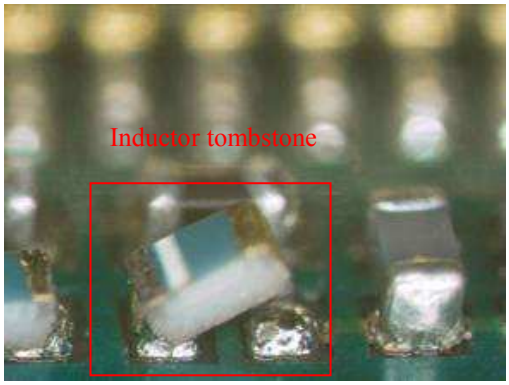

Fig. 3 Inductor tombstone after SMT process

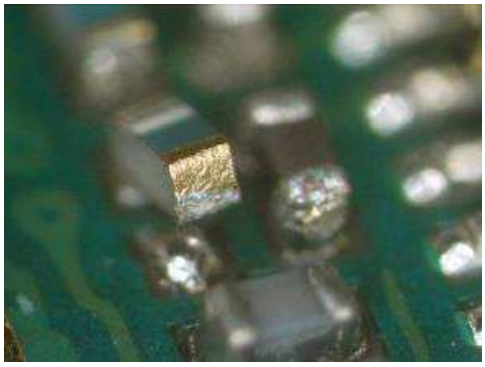
Fig. 4 Side view for the tombstoned component

Au-Au contact philosophy

Gold is used on connectors and contacts because it has excellent corrosion resistance, high electrical conductivity and, alloyed with small amounts of nickel or cobalt, has good wear resistance. For low voltage, low current and low contact force applications, gold is the best material. Table 1 list the evidence [5].

Table 1 Resistivity and contact resistance of contact materials

Contact Material	Resistivity Ωcm	Contact Resistance(2)mΩ
Pure gold	$2.4x10^{-8}$	0.8
Cobalt hardened gold	$2.4x10^{-8}$	2.6-2.8
Palladium on nickel	$1.08x10^{-7}$	3.1-5.8
Silver	$1.6x10^{-8}$	Not determined

It was reported that a GPS antenna failure occurred in an engineering evaluation of a new product. The failed sample had a brighter finish, but a higher contact resistance, which influenced the GPS function. The EDX analysis indicated a higher O concentration on the Antenna contact surface of the failed sample, which is induced by an exposed Ni surface. However, the contact surface was specified as 0.2 microns of selective Au plating. The absence of Au plating in the contact area would certainly be expected to result in an increase on the contact resistance, attributed to the friction. The contact couple of Antenna Ni surface and PCB Au surface (simplified as Ni-Au contact) also make it easier to produce Galvanic Corrosion at a moisture environment. Therefore, the antenna supplier needs to verify that parts are selectively Au plated as specified to ensure Au-Au robust contact.

Mercury Attack

Gold presents the noblest appearance and was coated onto a wide variety of substrate and jewellery. However, when a thermometer was broken, the mercury will quickly migrate into the gold surface, similar to a splash of water migrating into dry wood in our ordinary life. Immediately, the Gold

surface will turn into silver appearance. Any cleaner can not clean it up, which puzzle the wedding ring owner for a long time. Recently, on a gold-decorated phone housing, the surface shows some silver spots (see Fig. 5), EDX analysis in 20kV mode indicated Hg element as Table 2 indicated, which is obviously attacked by Hg evaporation and our project team indeed duplicated this failure. That gave some clues and actions to be taken, i.e. to avoid using Mercury-thermometer, replacing by electronic meter in monitoring human body temperature during the period of preventing SARS and H1N1 flu in electronic assembly company.

Fig. 5 Silver spot on phone housing

Table 2 Elemental analysis of silver spots

Composition (wt.%)						
		C	O	Ni	Au	Hg
Silver spots	1	14.27	1.34	41.17	28.68	14.54
	2	21.76	-	33.47	28.22	16.56
Normal surface		2.47	-	3.08	94.45	-

Conclusion

In this paper, the two gold plating types were introduced firstly. Then based on our failure analysis experience, the selective plating for terminals with the function of contact and soldering was proposed, combined with proper Au thickness (0.1-0.2microns for soldering and above 1 micron for contact). It was expected to eliminate contact issue and Au emibrittleness failure. For preventing small size passive component tombstone failure, we recommended to adopt Sn plated terminal, but not Au plating. The philosophy of Au-Au contact structure is proved as a good way to eliminate the contact intermittent as a result of the galvanic corrosion and abrasion oxidation. Finally, the Mercury attack on Au-finished surface was published at the first time.

Acknowledgements

The authors would like to acknowledge the financial support provided by Zhejiang Provincial Natural Science Foundation of China under Grant No. Y4100809, Zhejiang Science and Technology Commission of China under Grant No. 2010F20002 and thank Motorola Material Failure Analysis Laboratory for cases sharing.

References

[1] Alfred M. Weisberg, Gold plating, Metal finishing, 2001, 99, 248-262

[2] C.E. HO, R. ZHENG, G.L. LUO, A.H. LIN, and C.R. KAO, Formation and Resettlement of (AuxNi1-x)Sn4 in Solder Joints of Ball-Grid-Array Packages with the Au/Ni Surface Finish, Journal of electronic materials, 2000, 29(10), 1175-1181

[3] Selective plating of gold without environmental hazards, materials & design, 1991, 12(5), 289

[4] John R. Ellis and Glenn Y. Masada, Dynamic behaviour of SMT chip capacitors during solder reflow : 1992, 32(1-2), 286

[5] Paul Goodman, Current and future uses of gold in electronics, Gold Bulletin, 2002, 35(1), 21-26

© (2012) Trans Tech Publications, Switzerland
doi:10.4028/www.scientific.net/AMM.187.272

Thermodynamic evaluation and assessment of the Ti-U binary system

Zhanmin Cao [1, a], Kunpeng Wang [1,b], Guangwei Du [1,c], Zhiyu Qiao [1,d]

[1]State Key Laboratory of Advanced Metallurgy, School of Metallurgical and Ecological Engineering, University of Science and Technology Beijing, Beijing 100083, P. R. China

[a]zmcao@ustb.edu.cn, [b]kunpengwang@yeah.net, [c]dgw710619@126.com, [d]zyqiao@metall.ustb.edu.cn

Keywords: CALPHAD, thermodynamic properties, evaluation, ion-bonding model, Miedema model

Abstract. The thermodynamic description of the Ti-U binary system is obtained by the CALPHAD method using Thermo-Calc software and based on the estimated thermodynamic properties using ion-bonding model and Miedema model as well as the experimental phase diagram information. The liquid, αU, βU, δTi, and γ phases are assumed to be substitutional solutions with Redlich-Kister formula for the expressions of their excess Gibbs energy. The intermetallic compound TiU_2 is treated as a stoichiometric compound. The calculated phase equlibria are in good agreement with the estimated and available experimental phase diagram data.

Introduction

The Ti-U system is an important system for multi-component alloy systems which are of great interest for the development of high strength and plastic materials. The phase relations in the Ti-U system have been established experimentally. However, no experimental information about the thermodynamic properties of the system was reported up to now. In this paper, we give an estimation of thermodynamic properties about TiU_2 and the liquid phase, and the thermodynamic description of the Ti-U system is developed here.

Preparation before assessment

The experimental data of Ti-U system. Buzzard et al[1] examined alloys in the range 0 to 30 at.% titanium by thermal analysis, microscopic examination, and X-ray methods. Their results show a peritectic reaction which occurs at 1180℃, and two solid solution phases which decompose eutectoidally, one at 718℃ and 5 at.% titanium, the other at 830℃ and 18.3 at.% titanium. The αU→βU transformation occurs at 657-667℃and the βU→γU transformation is at 765 to 718℃. Udy and Boulger[2,3] have investigated the whole composition range of the Ti-U system by means of heat treatment, metallographic examination, and X-ray examination. They have found complete solid solubility above 890℃ between the γU and βTi. The liquidus curve rises smoothly from the melting temperature of uranium to that of titanium. The diagram shows that the γ solid solution decomposed at 890℃ and 33 at.% titanium into a hexagonal phase, TiU_2. This phase TiU_2 forms eutectoids at 620 ℃, 72 at.% titanium with αTi, and at 718℃, 5 at.% titanium with βU. The compound TiU_2 is reported to exist over a wide composition range with a maximum of 28-40 at.% titanium at 720℃. Knapton[4] examined the Ti-U system using X-ray methods, metallographic examination, and dilatometry. In the Knapton's results, the liquidus and solidus in the Ti-U system show a smooth increase from the melting point of uranium to that of titanium. A continuous series of the solid solutions is formed between the γU and βTi. The addition of titanium lowers the β→γ transformation from 771℃ in pure uranium to a eutectoid with the intermediate TiU_2 phase at 723℃, 4 at.% titanium. TiU_2 phase separates at 898℃ from the γ solid solution. A eutectoid is formed between TiU_2 and αTi at 655℃, 83 at.% titanium. The maximum solubility of uranium in αTi is about 0.8 at.-% at the eutectoid temperatures 723℃ and that of titanium in αU is 1 at.%. at 655℃.

The experimental results in the literatures of [2,3,4] are in reasonable agreement, except for the data given by Buzzard et al[1]. The latter values have not been used in the assessment because of the probability of specimen contamination.

The equilibrium phases in the Ti-U system are: the liquid, αU, βU, δTi, γ and the intermetallic compound TiU_2. The phase relations are shown in Table. 1.

Evaluation of the partial thermodynamic properties of the Ti-U system. As mentioned, no experimental thermodynamic data is reported. To give a reasonable thermodynamic description of the Ti-U system, we evaluate the thermodynamic properties of the liquid phase and TiU_2 using ion-bonding model[5] and Miedema model[6], respectively.

The standard formation enthalpy of TiU_2. The thermodynamic property P of a binary intermetallic compound can be described by ion-bonding model as follows:

$$P = \sum_i P_i + P_r \tag{1}$$

where P_i is the contribution of i-th ions, and P_r is the interaction term between ions.
Based on the above-mentioned model, the standard formation enthalpy of binary intermetallic compounds A_mB_n can be written:

$$-\Delta H_f^\theta = 4.186\times(x_A E_A + x_B E_B + \frac{1}{2}C_A C_B) \tag{2}$$

where x_i is the mole fraction of component i, $1/2C_AC_B$ is the interaction term, E_i and C_i are the parameters which are evaluated from the experimental data using least-squares method. Applying E_i(U)=2.08, E_i(Ti)=5.44, C_i(U)=1.77, C_i(Ti)=4.28 in the literature of [7] to the expression, the standard formation enthalpy of TiU_2 gives -29.24 kJ/mol.

Mixing enthalpy of liquid. Miedema and co-workers[6] developed a simple semi-empirical scheme for predicting the enthalpy of formation of binary metallic alloys. In the Miedema's model, the mixing enthalpy of liquid in the Ti-U binary system can be expressed as:

$$\Delta H^\theta_{\text{Ti-U}} = V_{\text{Ti}}^{2/3}V_{\text{U}}^{2/3}[-(\Delta\phi)^2 + \frac{Q}{P}(\Delta n_b^{-1/3})^2 - (\frac{S}{P})]\frac{2P}{n_b^{-1/3}(\text{Ti}) + n_b^{-1/3}(\text{U})} \times \frac{x_{\text{Ti}}[1+\mu_{\text{Ti}}\mu_{\text{U}}(\phi_{\text{Ti}}-\phi_{\text{U}})]x_{\text{U}}[1+\mu_{\text{U}}\mu_{\text{Ti}}(\phi_{\text{U}}-\phi_{\text{Ti}})]}{x_{\text{Ti}}V_{\text{Ti}}^{2/3}[1+\mu_{\text{Ti}}\mu_{\text{U}}(\phi_{\text{Ti}}-\phi_{\text{U}})] + x_{\text{U}}V_{\text{U}}^{2/3}[1+\mu_{\text{U}}\mu_{\text{Ti}}(\phi_{\text{U}}-\phi_{\text{Ti}})]} \tag{3}$$

Where $V_{\text{Ti}}^{2/3}$ and $V_{\text{U}}^{2/3}$ are the molar volume of metallic titanium and uranium, respectively; n_b(Ti) and n_b(U) electron densities of titanium and uranium at the boundary of Wigner-Seeitz atomicell as derived for the pure elements in the metallic state; ϕ_{Ti} and ϕ_{U} the electronegativity of titanium and uranium; $\Delta\phi$ the difference of electronegativities between titanium and uranium; x_{Ti} and x_{U} the mole fractions of titanium and uranium in liquid phase, respectively; and P, Q, S, μ are specific constants. Here, $\Delta n_b^{1/3} = n_b^{1/3}(\text{Ti}) - n_b^{1/3}(\text{U})$,and all the parameters are taken from the references[6,8]. The calculated results are shown in Fig. 2.

Thermodynamic models and optimization

Pure elements. As reference states for the investigated system, the pure solid elements in their stable states at 298.15 K and 10^5 Pa (stable element reference, SER) were chosen. The Gibbs energy of the element i (i=Ti,U) with ϕ phase appears in the following form:

$$^oG_i^\Phi(T) = G_i^\Phi(T) - H_i^{SER}(298.15K) = a + bT + cT^2 + dT^3 + eT^{-1} + fT\ln T + gT^{-9} \tag{4}$$

where $H_i^{SER}(298.15K)$ is the enthalpy of the element i in its standard reference state (SER) at 298.15K and 10^5Pa, T the absolute temperature in K, $G_i^\phi(T)$ the molar Gibbs energy of the element i with the structure of ϕ, $^0G_i^\phi(T)$ the Gibbs energy of the element i referred to the enthalpy of its stable state at

298.15 K and 10^5Pa and denoted by GHSER*i* in this study. Different sets of coefficients *a* to *g* used in different temperature ranges in Eq.(4) compiled by the SGTE database[9] were chosen. The lattice stability parameters for Ti and U are summarized in Table. 2.

Stoichiometric intermetallic compound. Even solubility of Ti in TiU_2 was reported[2,3], TiU_2 was approximately treated as intermetallic compound. The Gibbs energy per molar of TiU_2 is given as:

$$^{0}G_{\mathrm{m}}^{\mathrm{TiU_2}}(T) = mG\mathrm{HSERTi}+nG\mathrm{HSERU}+\Delta G_f^{\mathrm{TiU_2}} \quad (5)$$

where $^{0}G_{\mathrm{m}}^{\mathrm{TiU_2}}(T)$ denotes the standard Gibbs energy of formation per mole formula of TiU_2. Due to the lack of experimental data of heat capacities, by applying to the Neumann-Kopp rule, $\Delta G_f^{\mathrm{TiU_2}}$ can be given as follows,

$$\Delta G_f^{\mathrm{TiU_2}} = a + bT \quad (6)$$

where the parameters *a* and *b* were to be evaluated in the present work.

Solution phases. There are five solution phases in the Ti-U system, i.e., liquid, αU, βU, δTi and γ. The Gibbs energy of the solution phase in the Ti-U system is described as follows:

$$^{0}G_{\mathrm{m}}^{\varphi} = x_{\mathrm{Ti}}\,{}^{0}G_{\mathrm{Ti}}^{\varphi}(T) + x_{\mathrm{U}}\,{}^{0}G_{\mathrm{U}}^{\varphi}(T) + \mathrm{RT}(x_{\mathrm{Ti}}\ln x_{\mathrm{Ti}} + x_{\mathrm{U}}\ln x_{\mathrm{U}}) + {}^{\mathrm{E}}G_{\mathrm{m}}^{\varphi} \quad (7)$$

where $^{\mathrm{E}}G_{\mathrm{m}}^{\varphi}$ is excess molar Gibbs energy, which can be expressed by Redlich-Kister polynomial[10] as,

$$^{\mathrm{E}}G_{\mathrm{m}} = x_{\mathrm{Ti}}x_{\mathrm{U}}\left[L_0 + (x_{\mathrm{Ti}} - x_{\mathrm{U}})L_1 + (x_{\mathrm{Ti}} - x_{\mathrm{U}})^2 L_2\right] \quad (8)$$

where L_i (i=0, 1, 2,…) are the *i* order interaction parameters of solution phase in the Ti-U system and are expressed as temperature dependent terms as follows,

$$L_i = a_i + b_i T + c_i T\ln T \quad (9)$$

where a_i, b_i, and c_i are model parameters to be optimized based on the experimental data in this study.

Optimization—procedure and results

Based on the evaluated thermodynamic properties and the experimental phase diagram data, all the values of the model parameters for the phases in the Ti-U binary system were optimized using the PARROT module[11] by means of CALPHAD method, and a set of self-consistent parameters for the thermodynamic descriptions of the phases in the Ti-U system are obtained.

The optimized thermodynamic parameters for the condensed phases in the Ti-U system are summarized in Table. 3. The calculated temperatures of invariant reactions are compared with the experimental data in table 1. The calculated phase diagram compared with the experimental data is shown in Fig. 1. The optimized standard formation enthalpy of TiU_2 is -28.5 kJ/mol, which is very close to the evaluated value -29.24 kJ/mol by ion-bonding model. The calculated mixing enthalpies of liquid phase by the present thermodynamic description are compared with the estimated data using Miedema model in Fig. 2. The comparisons show that the current thermodynamic description the Ti-U system can reproduce the experimental phase diagram data and evaluated properties well.

Acknowledgements

This work was supported by National Nature Science Foundation of China (NSFC) (Grant No.50934011) and by the Fundamental Research Funds for the Central Universities.

Table. 1 Main invariant reactions of the Ti-U system

Reaction	Reaction Type	References[2,3,4]	This work
$\gamma \leftrightarrow \alpha + TiU_2$	Eutectic	928±5	938
$\gamma \leftrightarrow \beta + TiU_2$	Eutectic	993±5	1000
$\beta \leftrightarrow \alpha + TiU_2$	Eutectic	~941	938
$TiU_2 \leftrightarrow \gamma$	Congruent	1171±5	1174

Table. 2 Lattice stability parameters for Ti and U[9]

Element	Phase		Lattice stability parameters ($J \cdot mol^{-1}$)	T/K
Ti	L	${}^0G_{Ti}^L - {}^0H_{Ti}^\delta$	$=4134.494+126.63427T-23.9933Tln(T)-4.777975\times10^{-3}T^2+0.106716\times10^{-6}T^3+72636T^{-1}$	298.15-900
			$=4382.601+126.00713T-23.9887Tln(T)-4.2033\times10^{-3}T^2+0.090876\times10^{-6}T^3+42680T^{-1}$	900-1155
			$=13103.253+59.9956T-14.9466Tln(T)-8.1465\times10^{-3}T^2+0.202715\times10^{-6}T^3-1477660T^{-1}$	1155-1300
			$=369519.198-2554.0225T+342.059267Tln(T)-163.409355\times10^{-3}T^2-12.457117\times10^{-6}T^3-67034516T^{-1}$	1300-1941
			$=-19887.066+298.7367T-46.29Tln(T)$	1941-4000
	δ	${}^0G_{Ti}^\delta - {}^0H_{Ti}^\delta$	$=-8059.921+126.63427T-23.9933Tln(T)-4.777975\times10^{-3}T^2+0.106716\times10^{-6}T^3+72636T^{-1}$	298.15-900
			$=-7811.815+132.988068T-23.9887Tln(T)-4.2033\times10^{-3}T^2+0.090876\times10^{-6}T^3+42680T^{-1}$	900-1155
			$=908.837+66.976538T-14.9466Tln(T)-8.1465\times10^{-3}T^2+0.202715\times10^{-6}T^3-1477660T^{-1}$	1155-1941
			$=-124526.786+638.806871T-87.2182461Tln(T)+8.204849\times10^{-3}T^2-0.30474\times10^{-6}T^3+36699805T^{-1}$	1941-4000
	γ	${}^0G_{Ti}^\gamma - {}^0H_{Ti}^\delta$	$=-1272.064+134.71418T-25.5768Tln(T)-0.663845\times10^{-3}T^2-0.278803\times10^{-6}T^3+7208T^{-1}$	298.15-1155
			$=6667.385+105.366379T-22.3771Tln(T)+1.21707\times10^{-3}T^2-0.84534\times10^{-6}T^3-2002750T^{-1}$	1155-1941
			$=26483.26-182.426471T+19.0900905Tln(T)-22.00832\times10^{-3}T^2+1.228863\times10^{-6}T^3+1400501T^{-1}$	1941-4000
U	L	${}^0G_U^L - {}^0H_U^\alpha$	$=3947.766+120.631251T-26.9182Tln(T)+1.25156\times10^{-3}T^2-4.42605\times10^{-6}T^3+38568T^{-1}$	298.15-955
			$=-10166.3+281.797193T-48.66TlnT$	955-3000
	α	${}^0G_U^\alpha - {}^0H_U^\alpha$	$=3947.766+120.631251T-26.9182Tln(T)+1.25156\times10^{-3}T^2-4.42605\times10^{-6}T^3+38568T^{-1}$	298.15-955
			$=-22521.8+292.121093T-48.66Tln(T)$	955-3000
	β	${}^0G_U^\beta - {}^0G_U^\alpha$	$=-5156.136+106.976316T-22.841Tln(T)-10.84475\times10^{-3}T^2+0.027889\times10^{-6}T^3+81944T^{-1}$	298.15-955
			$=-14327.309+244.16802T-42.9278Tln(T)$	955-3000
	γ	${}^0G_U^\gamma - {}^0G_U^\alpha$	$=-752.767+131.5381T-27.5152Tln(T)-8.35595\times10^{-3}T^2+0.967907\times10^{-6}T^3+204611T^{-1}$	298.15-955
			$=-4698.365+202.685635T-38.2836Tln(T)$	955-3000

Table. 3 Optimized thermodynamic parameters of the Ti-U system

Phase	Temperature range/K	Model	Parameters
Liquid	300-3000	(Ti,U)	L_0= -7000+4T
α	300-3000	(Ti,U)	L_0= 45000，L_1= -9000
β	300-3000	(Ti,U)	L_0= 12000
γ	300-3000	(Ti,U)	L_0= -3000
δ	300-3000	(Ti,U)	L_0= -1000+6T
TiU_2	300-3000	$(Ti)_{0.333}:(U)_{0.667}$	G^{TiU2}=-28500+17.7T+0.667*GHSERU+0.333*GHSERTi

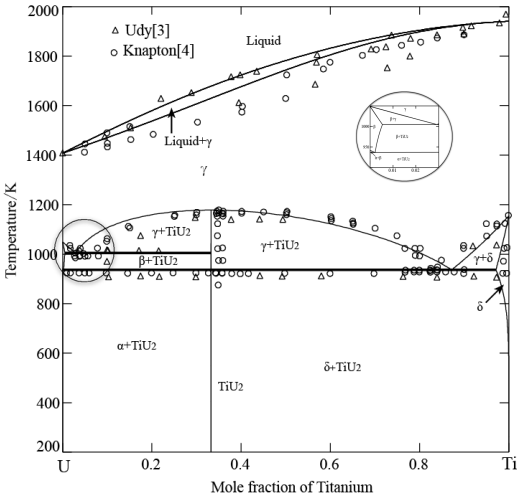

Fig. 1 The Ti-U phase diagram calculated by the present thermodynamic description with the experimental data.

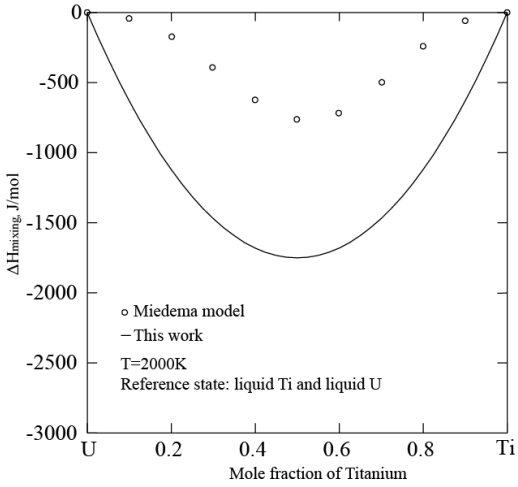

Fig. 2 The mixing enthalpy of liquid calculated by the present thermodynamic description with the Miedema model.

References

[1] R. W. Buzzard, R. B. Liss, and D. P. Fickle. Journal of Research of the National Bureau of Standards, vol. 50(4)(1953), p. 209

[2] M. C. Udy, F. W. Boulger. Journal of Metals,vol.2(1954), p. 207

[3] M. C. Udy, F. W. Boulger . Transactions of the American Institute of Mining Engineers. vol. 200(1954), p. 207

[4] A. G. Knapton, B. Sc., Ph.D., Junior Member. Journal of the Institute of Metals, vol. 83(1954-55), p. 497

[5] M. L. Huggins. The Journal of Physical Chemistry, vol. 74(2)(1970), p. 371

[6] F. R. de, Boer, R. Boom, W. C. M. Mattens, A. R. Miedema. Cohesion in metals. Amsterdam: North-Holland, 1988.

[7] Z. Y. Qiao, Z. H. Xu, H. L. Liu Computerized Physical Chemistry of Metallurgy and Materials. Beijing: Metallurgical Industry Press, 1999.

[8] A. R. Miedema. Journal of the Less-Common Metals, vol. 32(1)(1973), p. 117.

[9] A. T. Dinsdale. CALPHAD ,15(4) (1991), p. 317.

[10] Redlich, O.; Kister, A. T. Ind. Eng. Chem. vol. 40(2)(1948), p. 345.

[11] B.Sundman, B. Jansson, J. O. Anderson. CALPHAD vol. 9(1985), p. 153.

CHAPTER 6:

Mechanical/ Automotive Systems and Allied Topics

© (2012) Trans Tech Publications, Switzerland
doi:10.4028/www.scientific.net/AMM.187.281

Design and Implementation of SCM-based Smart Cars

Mei Lin[a], Yumei Zhang and Ligong Cui

School of Electrical Engineering

BinZhou Polytechnic, ShanDong, 256603, China

[a]linq_0324@163.com

Keywords: smart cars; STC89C52; single-chip microcomputer; intelligent control

Abstract. With the background of the higher vocational college students' innovative of 2010 national test plan, This paper introduces an intelligent controlling system of smart car. Which takes the STC89C52 single-chip Microcomputer as the core of control and black and white line sensors as sensing component. At the same time, the light signal is transmited by using sensors and voltage comparator lm393 to detect the black line on the road; meanwhile this detection signal is transmited to microcontroller signal port, with analysising by Microprocessor control . The smart car can travel by black line. This project involves control technology, the sensor technology, computer and power electronics and other professional domain knowledge, make the car can imitate human thought complete scheduled tasks.

Introduction

Facing the shortage of resources and traffic safety issue,how to develop a smart car not only can achieve no exhaust gas or no pollution but also can intelligence surveillance. So this problem deserves research deeply. In this paper the smart car in the curve of the black road mainly adopts the following three means of control:twice obstacle avoidance, speed control and automatic lighting system. After many practice has proved that this smart car can keep a high speed and accuracy.

Hardware Design

The smart car uses the front-wheel drive, which is executed by two DC motors. Meanwhile two front wheels can control steering by adjusting the speed of them. the rear wheels can rotate 360 degrees,which play a support role for the smart car. the photoelectric trace of pipe are installed in the body of both sides: When detecting the black line to the left sensor, the main control chip control motor stops revolver, car left correction, when right sensor detect under the black line, the main control chip control right wheel motor stops, the car to right fixed.

Based on this, this smart car system hardware mainly by the single chip microcomputer control unit, tracing module, obstacle avoidance module, and motor driver module, obstacle avoidance module, Phototaxis module, LED display module and power module.

Single-chip microcomputer control unit. This system used the STC89C52 monolithic integrated circuit as the microprocessor. The functions of this unit as follows: scanning input signal of wireless or buttons,starting or stoping smart car. During smart car driving it will read each sensor constantly to collect data,processing get data, empty PWM pulses to control motor speed by different conditions of get data, at the same time the related data to send LCD display. Among them, the P2 port used for liquid crystal display, P1.0 and P1.3 port control two motors, P1.4,P1.5, P1.6 for three button interface, P0 port connection 8 road sensors, P3.2 by black and white and grating yards of plate output signal, P3.3 take iron signal detection, P3.7 connection the acousto-optic alarm, P3.5, P3.6, P3.7 connection LED, R/W of the control and EN. The schematic diagram of smart car as Fig.1.

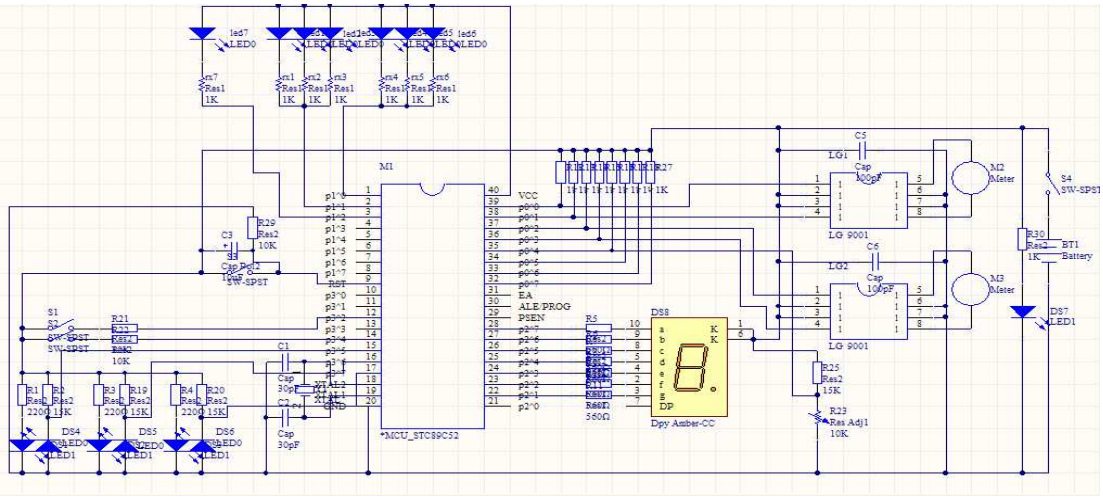

Fig. 1 The schematic diagram of smart car

Tracing module. The smart car driving on road which has black line on white paper, due to the different light reflection coefficient on black and white paper, it can judge the black road according to receiving the strength of the reflected light. In order to keep driving along the black line, detection signal can be fixed direction by the single-chip microcomputer control driver modules. the black line width is about four cm. Using infrared in different colors of physical surface has a different reflection properties of characteristics, we choose Infrared sensor to scan the black line.

Its principle is that when driving, the smart car continually launch infrared ligh to the ground, when infrared meet white ground,Infrared happen aimless launch,The reflected light was receiving by tube;but when infrared meet black ground, Infrared is completely absorbed, so no light can be received by tube;then LM393 as comparators for acquisition high and low level. It is low power dual voltage comparator, DIP8 packages, collector output, output high level need to connect to external resistance, if only use a group of comparator, another one must be grounded in LM393.Through this process, it realize the signal detection. The circuit diagram of tracing module as follow Fig.2

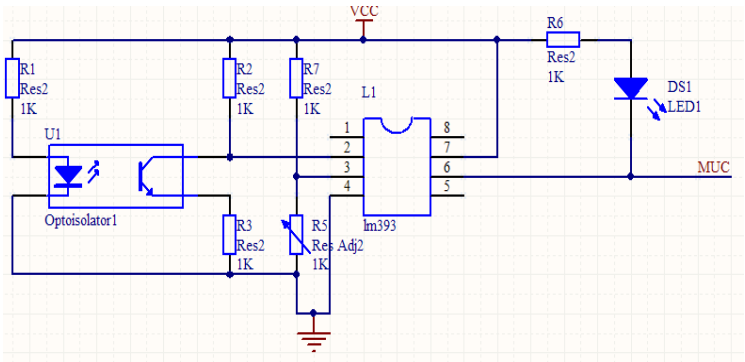

Fig. 2 The circuit diagram of tracing module

Motor driver module. This system choose the DC motor to drive wheels moving, DC motor will always turn after power supply, and pervert the power of the motor or the ground the motor rotation direction changing,The chip L9110 is for control and drive motor design application-specific integrated circuit device, will be integrated circuit in single chip division of IC, make peripheral devices cost reduction, the reliability. The chip has two TTL/CMOS compatible level of input, have good anti-jamming; Two output terminal can direct drive the rotary motion, it has large current drivers ability, each channel can through the 750 ~ 800 mA of continuous current, current peak capacity of 1.5 ~ 2.0 A; At the same time it has low output saturation pressure drop; The built-in clamping diode can release the perceptual load reverse current impulse, to make it in the drive relay, dc motors, step motor or switch power tube on the use of safe and reliable. L9110 widely sUsed for toy car motor drive, stepping motor drive and switch power tube on electricity. The circuit diagram of LG9110 as follow Fig.3

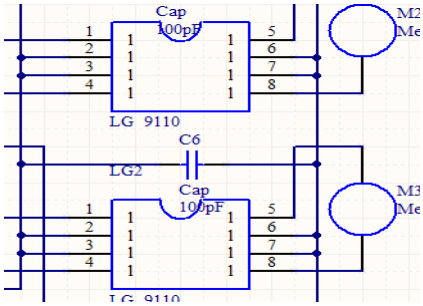

Fig. 3 The circuit diagram of LG9110

Obstacle avoidance module. In this system, we use infrared to judge obstacles,when infrared light meet the obstacles in front,the emitting signals will bounce back, than Infrared receiver tube output TTL level,these will Convenient this signal processing . The launch of the distance regulates by RW. Single Chip Microcomputer will control the motor,make car turn a corner when encounters barriers. The four groups of infrared transceiver to pipe, and the program using interrupt way obstacle avoidance turn, the car can correct judgment left or right turn. Outside of infrared signal interference are small, cost-effective.

Phototaxis module. With identical parameters on the photoconductive resistance in front of the car, through slide rheostat series output voltage and benchmark voltage comparison, then gives the command to single chip microcomputer to control motor,so as to achieve the goal. This plan even though relatively simple, but in the light of the different strength to the collection and comparison, flexible operation.

LED display module. Display Circuit has adopted the LED display pieces. Using them to achieve speedometer display . The LED consists of 8- Digital tube which are overcast . Duing to the small voltage in SCM, LED display normal display normal which not only need eight resistances link 8-Digital tube to pull voltage in p0 port,but also the public overcast pin of digital tube need to link p2 port. On the other hand, P2 port work need the current limit resistance when digital tube is dynamic display. So to provide digital pipe of the current will be reduced, cannot make digital tube light. In order to solve the problem, each public overcast pin should to link PNP transistor, seven transistor's base electrode link the current limit resistance, then the collector ground.

Transistor will enlarge output current amplification from P2 port before providing power to digital tube, Then in the single chip microcomputer programs running digital tube will light up. Ds8 integrated digital tube will light, Display speed from right to left.

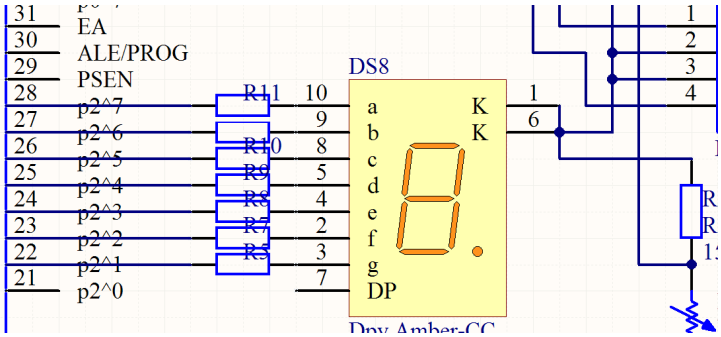

Fig. 4 The circuit diagram of LED

Power module. Generally, the scheme has the following kinds: scheme I: cable power voltage power supply by voltage regulator chip, its advantage is to provide stability of 5 V voltage, but take up too much resources.scheme II: The 1.5 V battery with four single power supply, but 6 V voltage is too low to supply power for single-chip computer or motor power .scheme III: The 1.5 V battery with eight single power supply,this way can solve problem of scheme II, Let the car to complete its function, But the battery change frequency and battery trucks are also the problem that should be considered.

consider all these factors, we choose AC regulator, change primary voltage of phase, then make the output voltage stability, as the circuit diagram, The power supply consists of transformer, rectification bridges and several power converter modules.As the Fig.6 show, total power from a 220 V AC power supply, transformer T1 make step-down for AC power, then Rectifier bridge D1 realize AC voltage into DC voltage, To prevent power supply interfere 0.1 uF filter capacitance C1 and C2 add. U1 is mainly used to get 5 V power, to supply power in the related circuit . Because the electrical machinery in the running of the power to bring great interference, so use Ds1 to isolate, so that each part of the relatively independent power supply, avoid interference.

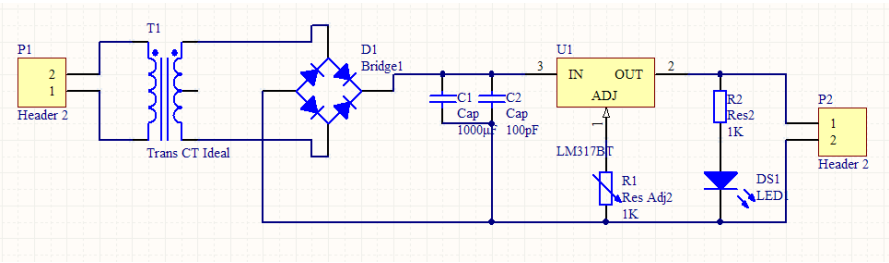

Fig. 5 The circuit diagram of power module

Software Design

System software written in C completed, the main program consist of timer service procedure, avoid barrier of procedure, Photonic program, Liquid crystal display subroutine, key and repair Change procedure, speed ranging procedure. These programs can realize main function: tracking, twice obstacles for Measure, storage, number display; speed display, Simulation lights around and so on.

The car adopt modular design which make each module independence. The core control parts of the online programming STC89C52 microcontroller which can achieve secondary development without any increase in the hardware under the condition of the system.

After power on, first test system achieve initialization, motor start.The clock starts and tracking module circuit also start;then when driving, constantly testing line to adjust the car direction; Simultaneously detection, clock, calculation, display distance, according to distance and detect metal position judgment site position. the system flow chart diagram as follow:

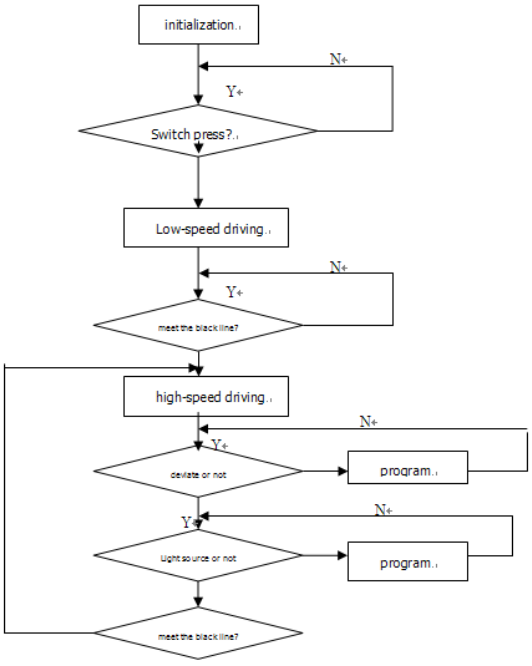

Fig. 6 The flow chart diagram

Conclusion

After the implementation of hardware and software design and commissioning many times repeatedly, has successfully developed the samples Machine.Fig. The smart car in a laboratory setting has the very good recognition and track specific goals, obstacles avoiding and site dock function which all reached the expected effect. smart car is an advanced subject relate to multi-discipline comprehensive, and has a very broad prospect of application. But to get the height of the idea of intelligent is still a long way from its development and image processing, pattern recognition, test, control and other technology to further improve closely related, the unremitting efforts of exploration and research.

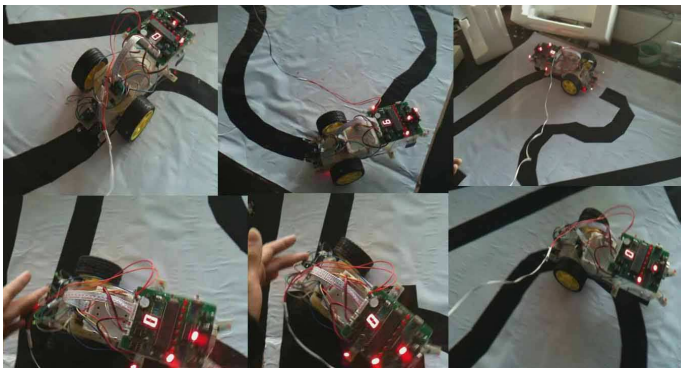

Fig. 7 The flow chart diagram

References

[1] GE Guang-ju, Design of intelligent car control system based on single-chip microcompute, Journal of Henan University of Urban Construction

[2] Van SchyndeIR, Trickle A, Osborne C. ADigital Watermark[C]// IEEE International Conference on Image Proceessing, 2009: 13-16

[3] WangWen-hu, The Design of Intelligent Car Based on80C51, Shanxi electronic technology, 2010, 4

[4] YU Lian-guo1, LI Wei2, WANG Yan-wei2, Design of SCM-based Smart Cars, FORESTRY MACHINERY & WOODWORKING EQUIPMENT, 2010, 5

© (2012) Trans Tech Publications, Switzerland
doi:10.4028/www.scientific.net/AMM.187.286

Traction Control for a Fuel Cell Hybrid Vehicle (FCHV)

Woo-Joo Yang[a] and Young-Bae Kim[b]

Dept. of Mechanical Engineering, Chonnam National University, Gwangju, Republic of Korea

[a]ywj3831@naver.com; [b]ybkim@chonnam.ac.kr

Keywords--Fuel Cell Hybrid Vehicle; Time Delay Control; Dynamic Evolution Control; Sliding Mode Control

Abstract: Traction control for the proton exchange membrane (PEM) fuel cell hybrid vehicle is studied. The traction control denotes the anti-slipping action when the vehicle meets sudden road surface friction changes. Slip ratio is utilized to analyze the slipping action, and optimum value is chosen for controlling the motor speed to prevent the slip. A one-dimensional longitudinal model of a fuel cell vehicle is constructed to prove the traction control effectiveness. The model includes a fuel cell system, a battery, an inverter and permanent synchronous motor, a bi-directional converter and a vehicle dynamics. Two three-phase permanent magnet synchronous motors (PMSM) are utilized to generate the required power for the vehicle traction. Maximum transmissible torque estimation (MTTE) control and sliding mode control are utilized for the PEM fuel cell vehicle traction control algorithms. The simulation results show that the proposed control algorithm effectively prevents vehicle slipping when a PEM fuel cell vehicle meets a sudden road friction change by distributing appropriate powers between battery and fuel cell.

Introduction

Fuel cells provide an environmentally friendly, highly efficient power source without Carnot's limitation of efficiency. The fuel cell hybrid vehicle (FCHV) is considered one of the most promising technologies for application in hybrid vehicles due to its high power density, zero pollution, low operating temperature, a certain level of rather quick startup capability, and long life time. In compared with the electrical vehicle (EV), it has the advantages of much lighter weight and longer traveling distance coverage. Therefore, in near future, FCHV will be the best solution to pollution free and energy saving transportation tool [1].

In this paper, a thorough FCHV model will be constructed including a PEMFC, battery, bi-directional converter, inverter, permanent magnet synchronous motor (PMSM) and vehicle dynamics. The PEM fuel cell model equips with the compressor, humidifier and purge valve. The battery RC model will be used in this paper, and bi-directional converter topology will be adopted for a buck-boost control. Three-phase inverter topology will be modeled interfaced with the PMSM. Finally, one-plane vehicle dynamics is modeled for regulating the vehicle longitudinal control action when the FCHV meets a sudden road friction changes. Overall configuration can be referred as shown in Fig. 1. To prevent the chattering of SMC and to improving convergence rate, alternative sliding plane can be used [2]. For proving the effectiveness of the proposed method, the maximum transmissible torque estimation (MTTE) method and PI control method will be employed as a comparison.

Modeling for Fchv

A FCHV power train model is mainly constructed based on the Simulink™ (Registered trademark of the MathWorks, Inc.) blocks in Matlab/Simulink/SimPower. Each subsystem is modeled separately, and then according to the power transfer implemented by control strategy the overall simulation model is obtained.

Fuel Cell Stack Modeling. The fuel cell stack model shown in Fig.1 represents a particular fuel cell when the parameters such as pressures, temperature, compositions, and flow rates of fuel and air vary. These variations affect the open circuit voltage E_{oc} as well as the Tafel slope A_{fc}. The E_{oc} and A_{fc} are modified as follows:

$$E_{oc} = N\left(E_n - A_{fc}\ln(i_o)\right) \tag{1}$$

$$A_{fc} = \frac{RT}{z\alpha F} \tag{2}$$

Many research papers and literatures have concerned the dynamics modeling of fuel cell stack [3-4]. Among them [3], the rate of utilizations of hydrogen and oxygen which concern electric chemical principle, the Nernst voltage and the exchange current density can be determined.

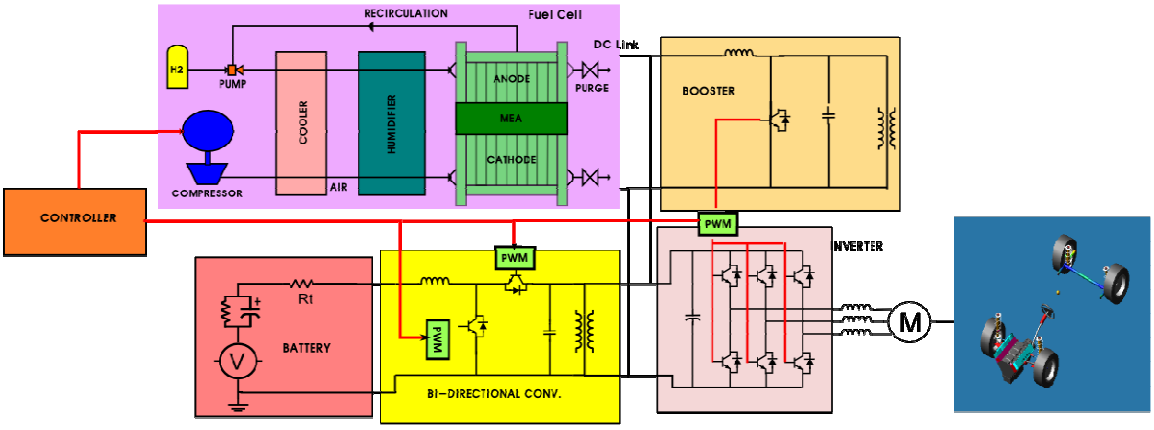

Figure 1 Configuration of FCHV System

Battery Modeling. The major issue in battery modeling is to dynamically represent the battery capacity and SOC. Battery capacity is an indication of the capability of the battery for the sustained discharge of battery current. It is usually defined in terms of Ah capacity, which is defined as the time integration of the battery current. Using the battery block in MATLAB/Simulink, a generic model parameterized to represent one type of NiMH rechargeable batteries is modeled with following assumptions: the internal resistance is supposed constant during the charge and the discharge cycles and does not vary with the amplitude of the current, the parameters of the model are deduced from discharge characteristics and assumed to be the same for charging, the capacity of the battery does not change with the amplitude of current, the temperature does not affect the model behavior, the self-discharge of the battery is not represented and the battery has no memory effect.

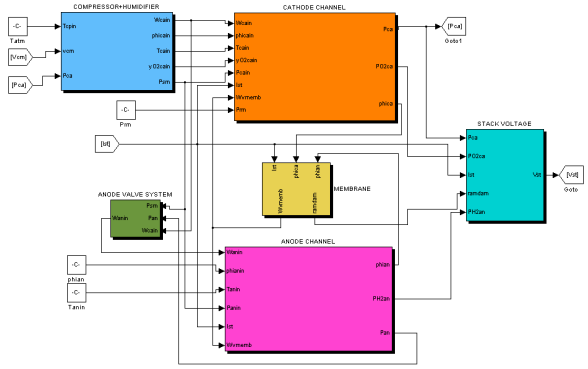

Figure 2 Fuel Cell Model

In this model, the *SOC* for a fully charged battery is 100% and for an empty battery is 0%. The *SOC* is calculated as:

$$SOC = 100\left(1 - \frac{Q \bullet 1.05}{\int idt}\right) \tag{3}$$

Motor Modeling. A three-phase permanent magnet AC synchronous machine (PMSM) with its inverter and vector control drive AC6 block of Simulink™ is illustrated in Fig.3. The electrical and mechanical parts of the PMSM are each represented by a second-order state-space model [5]. The PMSM operation mode is dictated by the sign of the mechanical torque, positive for motor mode and negative for generator mode.

Vehicle Dynamics. For the mechanical configuration, the half-vehicle model is illustrated in Fig. 4. Generally, vehicle dynamic characteristics strongly depend on the forces and torques generated between tire and road surface. The tire deforms due to the vertical load of the vehicle, and it contacts with the road through a small contact area called "contact patch." [6]. Two contact forces of longitudinal, and lateral directions, and one aligning torque are generally used to represent the tire contact mechanism. For the complete analysis and design of the vehicle dynamics, all these tire forces and torque should be considered. However, only the longitudinal motion of the vehicle is discussed in this paper to show the effectiveness of the traction control method.

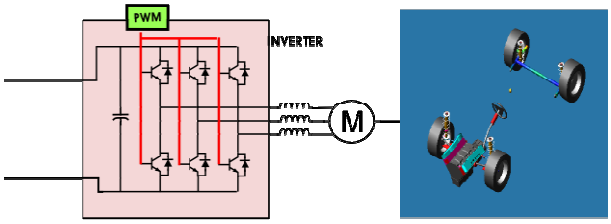

Figure 3 Inverter and PMSM

Based on Fig. 4, the dynamic differential equations for the calculation of the longitudinal motion of the half-vehicle model are described as follows:

$$\dot{V} = -\frac{\mu(m_f + m_r)g}{m} = -\frac{\mu m_f g}{m} - \frac{\mu m_r g}{m} = -F_f - F_r \tag{4}$$

$$\dot{\omega}_f = \frac{\mu m_f g r}{2J_f} - \frac{\mu m_r g r \dot{V}}{2J_f} \tag{5}$$

$$\dot{\omega}_r = \frac{T}{2J_r} + \frac{\mu m_2 g r}{2J_r} - \frac{\mu m_3 g r \dot{V}}{2J_r} \tag{6}$$

$$\lambda_f = \frac{V - r\omega_f}{V} \tag{7}$$

$$\lambda_r = \frac{V - r\omega_r}{V} \tag{8}$$

where $m_1 = \frac{b}{a+b}m$, $m_2 = \frac{a}{a+b}m$ and $m_3 = \frac{m_f h_f + m_s h_s + m_r h_r}{a+b}$. The driving forces of $F_{f,r}$ are strongly dependent upon the dynamic friction coefficient of μ and the slip condition between tire and road surface. The inter-relationship between the slip ratio and the friction coefficient can be described by various formulas. In the paper, the widely adopted Magic formula is applied to build a vehicle model [7].

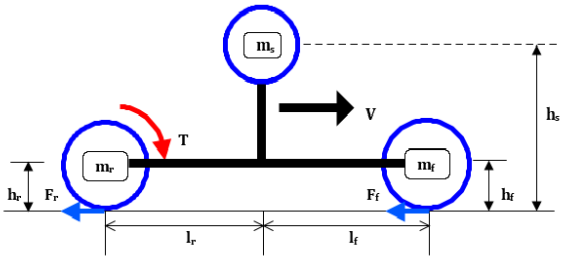

Figure 4 Longitudinal Vehicle Dynamics

To keep the optimum slip ratio on all road surfaces, road surface information is compulsory. In the present vehicle technology, however, sensing the state of the road surface friction is still limited in real-time. In most road conditions, the relationship between the slip ratio and the friction coefficient shows large deviations depending on the road surface conditions, that is, dry, rainy, snowy, and icy. The maximum friction coefficient, however, can be observed with the slip ratio between 0.1 and 0.2 regardless of the road conditions. Therefore, in the present paper, the optimum slip ratio is selected to have the value of 1.4 to satisfy the maximum friction between tire and road surface..

Traction Control

Sliding Mode Control. MTTE is a powerful technique to prevent vehicle slipping, and it has been well applied to the highly non-linear vehicle dynamics environments. However, results show some fluctuations of the motor torque. To prevent this drawback, the sliding mode control with chattering minimization is considered. It is widely applied in the strong non-linear dynamical environment, and its stability is guaranteed by selecting an appropriate sliding mode plane and by satisfying the Lyapunov stability criteria. In addition, chattering or oscillation can be avoided by selecting an appropriate sliding surface. For the torque control of FCHVs, the controlled torque T in the sliding mode should consist of an equivalent control torque T_{eq} and a switching control torque T_{sw}. The equivalent torque can be interpreted as a control that makes the system state ($\lambda, \dot{\lambda}$) move along the desired sliding surface. As the vehicle is driven by the rear motors, the slipping dynamics is considered only at the rear wheels, that is $\lambda = \lambda_r$. The equivalent torque is determined by the wheel dynamics in Equations 1-3 and the slip ratio represented by equations 4 and 5. The switching control torque ensures that the trajectory of the system is reached at the desired sliding surface and its magnitude can analytically be obtained by using the Lyapunov stability condition. Similarly, the sliding surface of $\sigma = \lambda_d - \lambda$ is selected. In this design, the controlled torque appears at the first derivative of the slip ratio tracking error, which is defined as the difference between a current slip ratio and a target one. The detailed explanation of each torques is discussed as follows:

1) Equivalent control torque T_{eq}: The equivalent control for this sliding surface design is determined from the conditions where $\dot{\sigma} = 0$, in which a target slip ratio λ_d is assumed constant ($\dot{\lambda}_d = 0$). As the first derivative of σ is zero, the following equation can be obtained from the wheel dynamic equation

$$\dot{\lambda} = \frac{r}{VJ}(T - Fr) - \frac{(1+\lambda)}{V}\dot{V} = 0 \tag{9}$$

From above equation, the equivalent torque can be easily calculated as

$$T_{eq} = Fr + \frac{J(1+\lambda)}{r}\dot{V} \tag{10}$$

In the real vehicle application, the value of the equivalent motor torque is difficult to determine from direct measurement. In FCHV, however, the T_{eq} can be estimated by measuring the stator current and voltage of PMSM. This is the advantage of the FCHV in compared with the combustion engine vehicle.

2) Switching control torque T_{sw}: The role of a switching control torque is to drive the system states to the sliding surface (σ=0). By defining the switching control torque as $T_{sw} = -K\,\mathrm{sgn}(\sigma)$, where K is a switching control gain and sgn(σ) is a sign function, a controlled motor torque becomes

$$T = T_{eq} + T_{sw} = T_{eq} - K\,\mathrm{sgn}(\sigma) \tag{11}$$

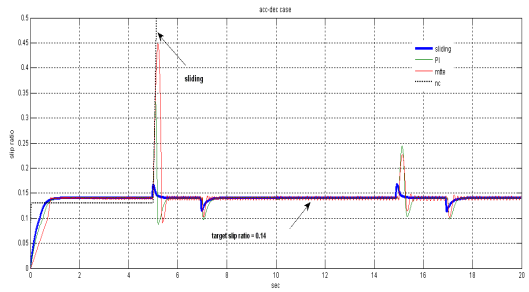

Figure 5 Slip Ratio Comparison

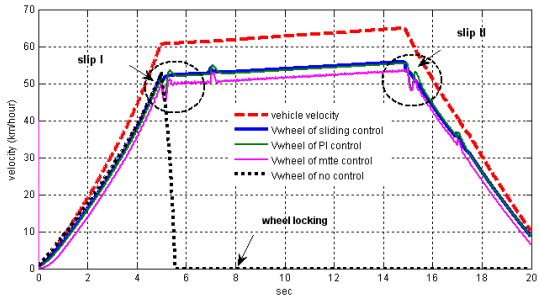

Figure 6(a) Velocity Profile Comparison

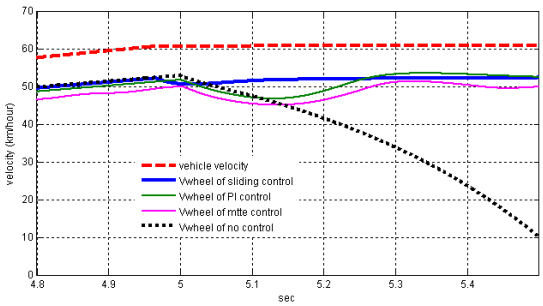

Figure 6(b) Velocity Profile Comparison (Expanded)

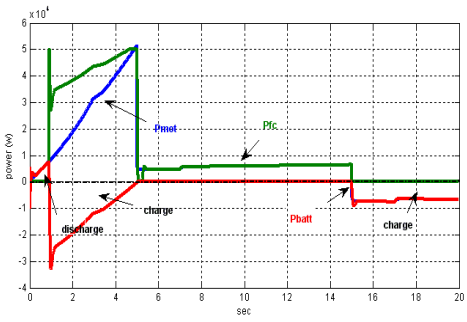

Figure 7 Power Distribution

The switching control gain K shown by the above equation can be chosen by considering a stability condition and the limitation of the motor. The stability condition can be determined by the Lyapunov stability criteria. For the given sliding surface design, the stability condition can be expressed as $\sigma\dot{\sigma} \le -\eta\,|\,\sigma\,|$, where η is a strictly positive constant.

The Lyapunov stability criteria can be rearranged as

$$\sigma\left[\frac{r}{VJ}(T_{eq} - K\,\mathrm{sgn}(\sigma) - rF) - \frac{(1+\lambda)}{V}\dot{V}\right] \le -\eta\sigma \tag{12}$$

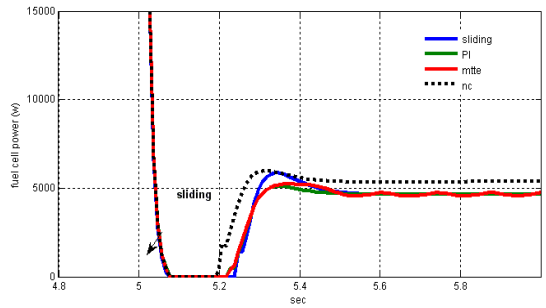

Figure 8 Fuel Cell Power Comparison

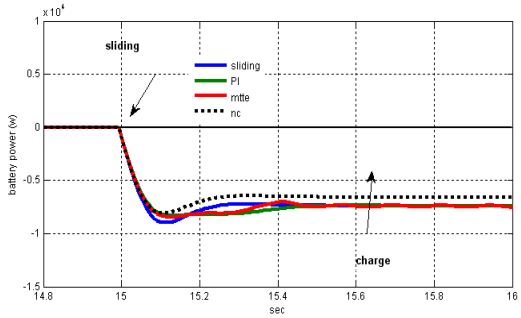

Figure 9 Battery Power Compariso

To obtain the switching control gain, let $K = \frac{VJ}{r}(F+\eta)$ to satisfy the stability condition in (41) and to substitute K into the above equation. After applying triangular inequality, the switching control gain can be written as

$$K \ge r\,|\,F\,| + J\frac{(1+\lambda)}{r}\,|\,\dot{V}\,| + \frac{VJ}{r}\eta \tag{13}$$

.

Simulation Results and Analysis

The PEM fuel cell, battery, bi-directional DC/DC converter, PMSM with inverter and vehicle were modeled using Matlab/Simulink/Simpower. If the vehicle velocity is larger than 10 km/h and SOC is larger than 30 %, the fuel cell starts working to deliver main power to the FCHV. If the velocity is negative, which means the vehicle decelerates, the fuel cell does not operate unless SOC is less than 30 %. The battery is used to start the FCHV if the SOC is larger than 30 %. The discharging battery current was set to 45 A, and charging battery current was set to 20 A. The battery charge was done if the fuel cell power exceeds the required power. The SOC of the battery was initially assumed to be 45 %.

To demonstrate the usefulness of the proposed control method, a sudden change in the road friction is applied when the vehicle accelerates. As shown in Figs. 5, the vehicle suddenly encounters a slippery road at t=10 s while traveling. In the simulation, the normal asphalt road is used before the vehicle meets the slippery wet road. As expected for an uncontrolled vehicle, the slip ratio abruptly increases causing the vehicle to slip. Fig. 6 shows the vehicle velocity and wheel velocity profiles of FCHV when it encounters a sudden slippery road at t=10 s. In the figure, PI, MTTE, sliding mode control and without control are applied and simulated for their effectiveness in the sudden slippery encounter when the vehicle accelerates. From the figure, it is known that the wheel speed should be increased to prevent the wheel slipping if the wheel locking happened when no control action takes. As the motor torque cannot increase to compensate the slipping of the vehicle, the wheel speed does not catch up with the vehicle speed. Therefore, the slip ratio suddenly becomes large with no control case, as shown in this figure.

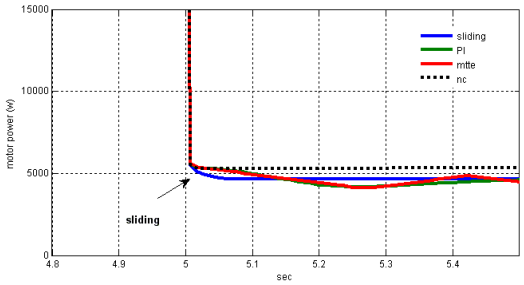

Figure 10 Motor Power Comparison

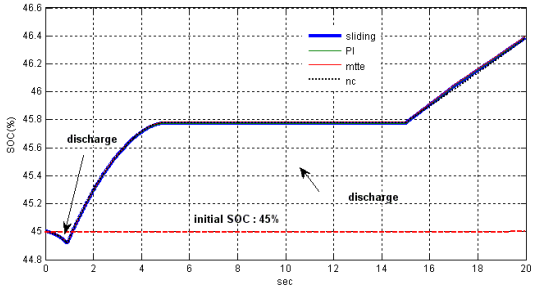

Figure 11 SOC Comparison

Fig. 7 shows the power distribution between the battery and the fuel cell. As shown from the figure, the supervisory controller can divide required motor power well with battery and fuel cell power. Fig. 8 shows the fuel cell power comparison for three control cases. Although sliding mode control has little power variations and quicker recovery than other two control methods, the difference is not noticeable.

Fuel cell power, battery power and motor power comparisons with three control actions are simulated in Figs. 8-10. Even though all three control actions show very similar power provisions, the sliding model control shows the best power supply ability with fast rising and minimal ripple. Specially as shown in Fig. 10, the sliding control action shows better transient performance in the FCHV traction control. One of the purposes of the supervisory control is to maintain the battery SOC with a certain level. Fig. 11 shows the variation of the SOC while FCHV travels. The SOC does not change much in this simulation, and three control actions show no large variation of the SOC. Even though the present simulation covers very short duration of time (about 20 s) for the FCHV operation, it is suffice that the proposed algorithm can provide appropriate power distribution and maintain the SOC with a certain level at the same time, while relevant sliding prevention is satisfied.

Conclusion

In this paper, a FCHV model is constructed including a PEM fuel cell system, a battery, a bi-directional converter, an inverter with PMSM and a vehicle dynamics. For proper working of the FCHV, two control parts are introduced: a supervisory control and component one. Adequate power distribution between the battery and fuel cell can be obtained through a supervisory control, while FCHV's components are controlled by each component control. As component control algorithms, TDC is utilized for a PEM fuel cell stoichiometry control, DEC is for a bi-directional converter, SVPWM for an inverter control. To achieve longitudinal FCHV stability when the vehicle meets a sudden slippery road, a traction control using MTTE or sliding control method is designed and applied. Two simulations are performed for showing the effectiveness of the proposed control methods. By analyzing the slip ratio, torque requirement, DC link voltage and current and SOC, the sliding control method gives the best performance for preventing the FCHV slip when it encounters a sudden slippery road. The result also reveals that the proposed supervisory control can distribute required motor power adequately into a fuel cell and a battery power without degrading the battery SOC.

References

[1] C.E. Thomas, "Fuel cell and battery electric vehicles compared," International J. of Hydrogen Energy, vol. 34, 2009, pp. 6005-6020.

[2] T.H. Shim, S. Chang and S. Lee, "Investigation of sliding-surface design on the performance of sliding mode controller in antilock braking systems," IEEE Vehicular Technology, vol. 57(2), 2008, pp. 747-759.

[3] J.T. Pukrushpan, P. Huei and A.G. Stefanopoulou, "Control-oriented modeling and analysis for automotive fuel cell systems," ASME *Journal of Dynamic Systems, Measurement and Control*, vol. 126 2004, pp. 14-25.

[4] J.C. Amphlett, R.M. Baumert, R.F. Mann, B.A. Peppley and P.R. Roberge, "Performance modeling of the ballard Mark IV solid polymer electrolyte fuel cell," *Journal of the Electrochemical Society*, vol. 142, 1995, pp.1-8.

[5] D. Grenier, L.A. Dessaint, O. Akhrif, Y. Bonnassieux and B. LePioufle, "Experimental nonlinear torque control of a permanent magnet synchronous motor using saliency," *IEEE Transactions on Industrial Electronics*, vol. 44(5), 1997, pp. 680-687.

[6] D. Foito, M. Guerrerio and A. Cordeiro, "Anti-slip wheel controller drive for EV using speed and torque observer," Proc. 2008 International Conference on Electric Machines, paper ID 1282.

[7] Gillespie, T.D., Fundamentals of vehicle dynamics, Warrendale, PA; SAE,1992.

© (2012) Trans Tech Publications, Switzerland
doi:10.4028/www.scientific.net/AMM.187.293

Kinematic Analysis of an Anthropomorphic Robot Hand

Pramod Kumar Parida[1, a], Bibhuti Bhusan Biswal[2,b] and Dhirendra Nath Thatoi[3,c]

[1]National Institute of Technology, Rourkela, Odisha, India

[2]National Institute of Technology, Rourkela, Odisha, India

[3]SOA University, Bhubaneswar, Odisha, India

[a]pramodparida71@yahoo.com, [b]bbbiswal@nitrkl.ac.in, [c]massthatoi@gmail.com

Keywords: robot hand, anthropomorphic, kinematic analysis, manipulation, simulation.

Abstract. There has been a continuous effort by researchers to develop multi-fingered robot hands for variety of applications. Some of these hands are meant for industrial applications while thers are used for orthopedic rehabilitation of humans. However the degree of success to develop an anthropomorphic robot hand in close resemblence with a typical human hand has not been satisfactory. In the present work an attempt has been made to design a robot hand having five fingers with 25 degrees of freedom by closly following the anatomy of human hand.The kinematic analysis of the hand offers confirmative results for effective graspingand manipulating objects.

Introduction

A robotic hand is one that can mimic the movements of human hand in operation.Stable grasping and fine manipulation with the multi finger rodot hands are playing an important role in the field of manufacturing, rehabilitation and other applications that require precision and dexterity[1].Dexterous grasping is the specific task and it has been accepted and adopted by many researchers as apriority issue while designing the hands. The essential modifications related to the robotic grippers such as improved force sensing capacity and improved flexibilities at the gripping are to be implemented.The multi-fingered robot hand acts as a multipurpose gripping device for various tasks with multiple-degrees-of-freedom. Some important multi-fingered hands are, WENDY hand [2], Utah/MIT hand [3], DLR hand [4], Shadow Dexterous Hand [5], Robonaut hand[6]. Such type of hand has advantage that the hand can be used with various type of robot arms because the robot hand has independant structure. Most of this type of robot hand has equal or less than four fingers. Even those with five fingers are not equal with human hand because they have less number of joints or degrees of freedom.The robot hands with five fingers and anthropometric structure are helpful for the patients who are partially paralyzed due to neurological or orthopedic impairment. The need for improving the muli-fingered robot hand arises from the desire forhandling objects of complicated shapes effectively.Therefore the mechanical design plays an importtant role in the development of the present hand.In this paper we only concentrate on the kinematic analysis of the anthropomorpphic robot hand and consider the wrist as a fixed. The hand is an articulated structure. All fingers in the model have the same essential structure, having different degrees of freedom,so the same convention is applied to all fingers. The fixed coordinate system with respect to which the whole motion is analyzed is placed outside of the hand's areai.e. at wrist. DoFs in CMC area is different with thumb having two DoFs, the ring and little fingers have two DoFs and index and middle fingers have no motion. The skeleton of a hand is abstracted as a stick figure so that the dimension of each sub-object is reduced to its link length. Each finger is modeled as a kinematical chain with the palm as its base reference frame. The model does not consider the radio carpal articulation (wrist). Each fingertip is considered to be the end-effecter of the respective finger kinematical chain.The aim of the present study is to obtain a kinematic model of the anthrpomorphic robot hand, as natural as possible and to make it capable of realizing various tasks in 3D environment. The analysis of the forward kinematics of the proposed model is studied by representing the active space as a complex surface (reach envelope) with respect to wrist.

Kinematic Model of Anthropomorphic Robot Hand

The multi-fingered robot hand acts as a multipurpose gripping device for various tasks. Since it is designed to mimic the human hands, most anthropomorphic robot hands duplicate the shape and functions of human hands. The structure of the anthropomorphic hands is almost the same as that of a human hand as shown in Fig. 1. The finger segments in human hand gives us the inspiration to design an independently driven finger segment to construct a whole finger. The segmental lengths of the thumb and fingers are taken proportionately to hand length and hand breadth with a fixed wrist.Typically the hand motion is approximated to have 27 DoFs.In thepresent study only 25 DoFs are considered. The thumb is modeled with 5 DoFs.The index and middle fingers are modeled with 4 DoFs each. The ring and little fingers are modeled with 6 DoFs each considering two degrees of freedom each at Carpometacarpel(CMC) joint for palm arch. The Trapeziometacarpal (TM) joint, all five Mecapophalangeal (MCP) joints and two CMC jointsare considered with two rotational axes each for both abduction-adduction and flexion-extension. The Interphalangeal (IP) joint on the thumb, the Proximal-Interphalangeal (PIP) and Distal- Interphalangeal (DIP) joints on the other four fingers possess 1 DoF each for the flexion-extension rotational axes. Fig.1 illustrates the proposed hand model while the parameters of the thumb and other fingers are tabulated in Table 4 and Table 5 respectively.

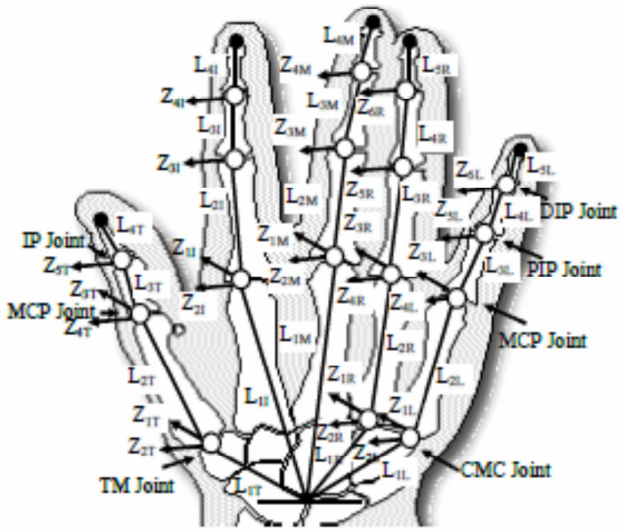

Fig.1 Kinematic model of hand

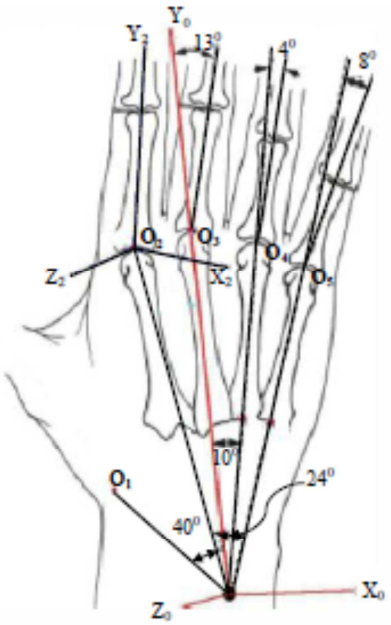

Fig.2 Global co-ordinate system

Table 1 DH table of thumb

Link(i)	Link twist angle(α_{i-1})	Link length(a_{i-1})	Joint Distance(d_i)	Joint angle(θ_i)
1T	0^0	L_{1T}	0	θ_{1T}
2T	-90^0	0	0	θ_{2T}
3T	90^0	L_{2T}	0	θ_{3T}
4T	-90^0	0	0	θ_{4T}
5T	0^0	L_{3T}	0	θ_{5T}
ε_T	0^0	L_{4T}	0	0

Table 2 DH table of index and middle fingers

Link(i)	Link twist angle(α_{i-1})	Link length(a_{i-1})	Joint distance(d_i)	Joint angle(θ_i)
1F	0^0	L_{1F}	0	θ_{1F}
2F	-90^0	0	0	θ_{2F}
3F	0^0	L_{2F}	0	θ_{3F}
4F	0^0	L_{3F}	0	θ_{4F}
ε_F	0^0	L_{5F}	0	0

Table 3 DH table of ring and little fingers

Link(i)	Link twist angle(α_{i-1})	Link length(a_{i-1})	Joint Distance(d_i)	Joint angle (θ_i)
1F	0^0	L_{1F}	0	θ_{1F}
2F	-90^0	0	0	θ_{2F}
3F	90^0	L_{2F}	0	θ_{3F}
4F	-90^0	0	0	θ_{4F}
5F	0^0	L_{3F}	0	θ_{5F}
6F	0^0	L_{4F}	0	θ_{6F}
ε_F	0^0	L_{5F}	0	0

Anthropometric Data and Joint Limits. As there were no exact anthropometric data for the segmental lengths of the human hand, the estimated measurement are made following standard formulae, where HL is Hand Length and HB is Hand Breadth[7] simillarly the angle limits for different joints considered from work of Parsuramna and Zuen[8] .

Table 4 Segment Length for Thumb

Finger	Metacarpal bones	Length
Thumb	$0.251*HL$	L_{2T}
Index	$\sqrt{(0.374*HL)^2+(0.126*HB)^2}$	L_{2I}
Middle	$0.373*HL$	L_{2M}
Ring	$\sqrt{(0.336*HL)^2+(0.077*HB)^2}$	L_{2R}
Little	$\sqrt{(0.295*HL)^2+(0.179*HB)^2}$	L_{2L}

Table 5 Segment length for fingers

Fingers	Proximal	Length	Middle	Length	Distal	Length
Thumb	$0.196*HL$	L_{3T}	-	-	$0.158*HL$	L_{4T}
Index	$0.265*HL$	L_{3I}	$0.143*HL$	L_{4I}	$0.097*HL$	L_{5I}
Middle	$0.277*HL$	L_{3M}	$0.170*HL$	L_{4M}	$0.108*HL$	L_{5M}
Ring	$0.259*HL$	L_{3R}	$0.165*HL$	L_{4R}	$0.107*HL$	L_{5R}
Little	$0.206*HL$	L_{3L}	$0.117*HL$	L_{4L}	$0.093*HL$	L_{5L}

Kinematics Analysis. Forward kinematics is used to determine the position and orientation of the proposed hand model with respect to fixed point i.e. wrist. For this purpose a kinematic model is developed using the given joint angles, the fingertip position in the palm frame is calculated with respect to MCP joints of Middle and Index finger, TM joint of thumb and CMC joint of ring and little finger. The origins are located at the respective joints marked as O_1, O_2, O_3 ,O_4 and O_5 as shown in Fig. 2.The DH method is implemented to determine the DH parameters for all the fingers which are tabulated in Table 1, Table 2 and Table 3. The global coordinate system for hand is located in the wrist as shown in Fig.2. The transfer from a reference frame to the next one the general expression of the matrix can be written as follows:

$$ {}^{i-1}T_i = \begin{bmatrix} \cos q_i & -\sin q_i \cos\alpha_i & \sin q_i \sin\alpha_i & L_i \cos q_i \\ \sin q_i & \cos q_i \cos\alpha_i & -\cos q_i \sin\alpha_i & L_i \sin q_i \\ 0 & \sin\alpha_i & \cos\alpha_i & d_i \\ 0 & 0 & 0 & 1 \end{bmatrix} \quad (1) $$

$$ {}^{0}T_n = {}^{0}T_1\,{}^{1}T_2\,{}^{2}T_3 \cdots\cdots {}^{n-1}T_n \quad (2) $$

By multiplying the corresponding transfer matrices written for every finger as in Eq. 2, the kinematical equations describing the fingertip motion with respect to the general coordinate system can be determined. It is now possible to develop a model using Eq.1 and Eq.2. A computer program using these equations in MATLAB is developed to capture the motion of the fingers. Every joint variable range as per data is divided to an appropriate number of intervals in order to have enough fingertips positions to give confident images about the spatial trajectories of these points. By connecting these positions and the complex surface bordering the active hand model workspace is obtained. The complex surface could be used to verify the model correctness from the motion point of view, and to plan the hand motion by avoiding the collisions between its active workspace and obstacles in the neighborhood.

Results

Using the Eq.1and Eq.2 along with the parametric data of human fingers presented in Table 4 and Table 5 the complex surface described by each finger tip is generated. In all the cases each angular range is divided into equal divisions. The profiles generated through the simulation of the independent finger tips are spatial. The different colour specifies for different fingers i.e. red for thumb, blue for Index finger, magenta for middle finger, green for ring finger and black for little finger. However, for the purpose of understanding and simplicity, these are presented in X-Y, X-Z and Y-Z planes in Fig. 3, Fig. 4 and Fig. 5 respectively. The profiles of the five finger tips in the 3-D plane are presented in Fig.6.

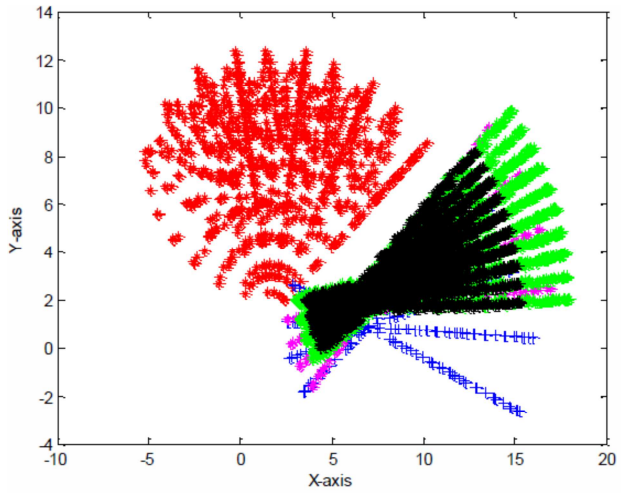

Fig. 3 Profile of fingertips in the X-Y plane

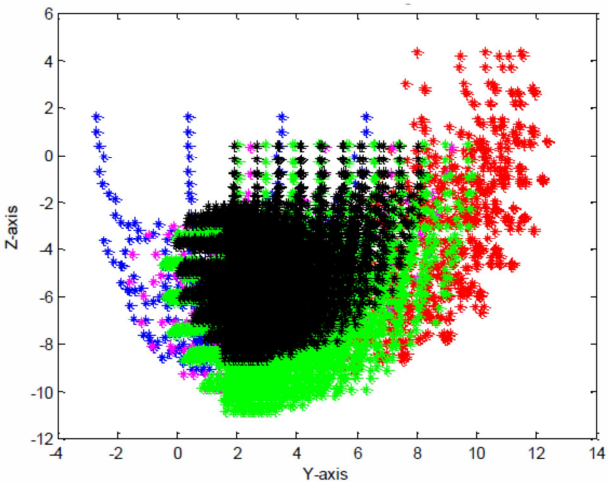

Fig. 4 Profile of fingertips in the Y-Z plane

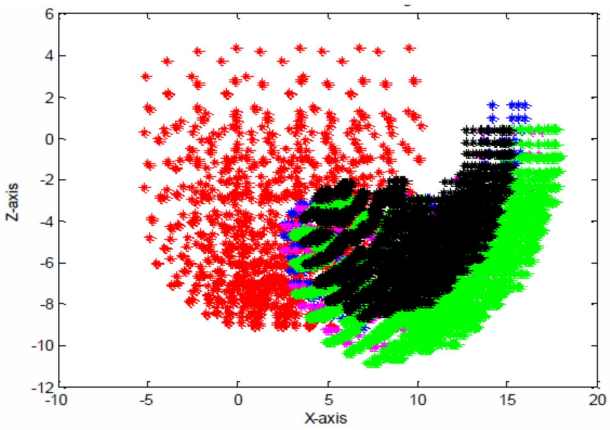

Fig. 5 Profile of fingertips in the X-Z plane

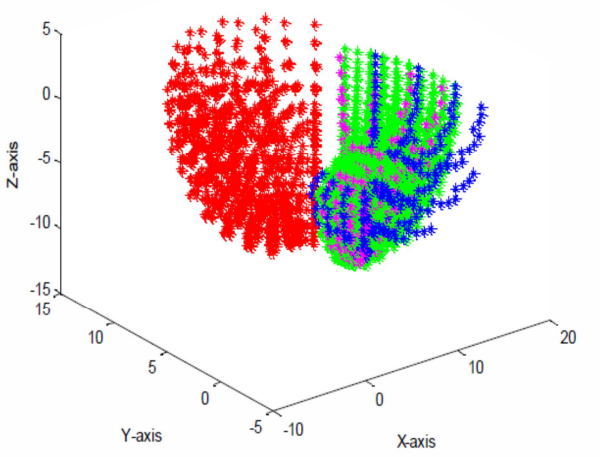

Fig. 6 Profile of fingertips in the 3-D space

Conclusion

The present work aims at developing a kinematic model of an anthropomorphic robot hand and assessing it effectiveness. The hand in question may find its potential applications in industries and other work places for manipulation of irregular as well as soft objects. It can also be used for orthopaedic rehabilitation of human hands. The model considers five fingers similar to human hand for manipulating objects securely. The joints, links and other kinematic parameters are chosen in such a way that they replicate a human hand. The kinematic simulation is carried out to estimate the work volume and assess motion constraints of the designed hand. The study shows that the kinematic behavior of the hand is suitable for the intended purpose.

References

[1] Kazuo Tanie: Design of Robot Hands, Industrial Robotics, Ed, S. Y. Nof, John Wiley & Sons, pp.112-137, (1982).

[2] Toshio Morita, Hiroyasu Iwata, Fhingeki Sugano, *Human Symbiotic Robot Design based on Division and Unification of Functional Requirement* , Proceedings of the IEEE International conference on Robotics and Automation,pp.2229-2234,(2000).

[3] S.C. Jacobsen, J.E. Wood, D.F. Knutti, and K.B. Biggers, *The UTAH/M.I.T dexterous hand: Work in progress*,Int. J. Robot. Res.,vol.3, no.4, pp.21–50(1984).

[4] J. Butterfass, M. Grebenstein, H. Liu, G. Hirzinger, *DLR-Hand II: next generation of a dextrous robot hand*,Proc. IEEE International Conference onRobotics and Automation, Taibei, Taiwan, pp.109-114(2003).

[5] R.Walkler, *Developments in dexterous hands for advanced robotic applications*, Proc. the Sixth Biannual World Automation Congress, Seville, Spain, pp.123-128(2004).

[6] C.S.Lovchik, M.A.Diftler, *The Robonaut hand: a dexterous robot hand for space*, Proc. IEEE International Conference on Robotics and Automation," Detroit, USA, pp.907-912, (1999).

[7] B.Buchcholz, T.Armstrong and S.Goldstein., *Anthropometric data for describing the kinematics of the human hand* , Ergonomics, 35(3): 261-273, (1992.)

[8] S. Parasuraman and C. Zhen, *Development of Robot Assisted Hand Stroke Rehabilitation System*, International Conference on Computer and Automation Engineering, Mar., pp. 70-74,(2009).

© (2012) Trans Tech Publications, Switzerland
doi:10.4028/www.scientific.net/AMM.187.298

The Fuzzy Comprehensive Evaluation of Laser Weapon System Combat Effectiveness

Hui Li [1,2,3, a] and Lihong Guo[1]

[1]Changchun Institute of Optics, Fine Mechanics and Physics, Chinese Academy of Sciences Changchun, China

[2] Graduate School of the Chinese Academy of Sciences Beijing, China

[3] North University of China Taiyuan, China

[a] lihui5698@163.com.

Keywords: Combat effectiveness;Fuzzy synthetic Evaluation;analytical Hierarchy process;Laser weapon system

Abstract. To evaluate the laser weapon system's combat effectiveness, which is related with so many factors, is a very complex issue. In this paper, by analyzing the factors which influence the laser weapon system, an index system for the laser weapon system comprehensive evaluation of the combat effectiveness is built up. The method of calculating weight, the improved analytic hierarchy process is introduced. The evaluation model of improved fuzzy-AHP is established and the feasibility and the validity of the proposed evaluation method is validated through a practical example.

Introduction

Laser weapon system is a new concept weapon, it is the weapon which makes use of the directional emission of the laser beam to destroy the targets and make the targets invalid. It has the characteristic of fast attack speed, flexible steering, accurate strikes, non-recoil, free from electromagnetic interference and vulnerable suffering impact from weather and environmental [1]. To evaluate the combat effectiveness of the weapon system is not only the urgent need of the modern war but also the important issue during the design, development, procurement, use and maintenance of the laser weapon system.

Fuzzy comprehensive evaluation method considers the impact of various factors and makes an integrated judge or decision of a thing among the fuzzy environment. It can handle the fuzzy information while the other methods can not [2]. However, there are still some problems: the traditional model of solving the weights of the efficiency index usually uses AHP approach, but the concordance test in AHP is essential. Only when the comparison matrix has satisfactory consistency, the conclusion based on AHP is reasonable. In the actual evaluation, we generally rely on rough estimates to adjust the comparison matrix, so as to meet compliance requirements, such method has great blindness. To overcome this shortcoming, this paper proposed to improve on the AHP. When the comparison matrix is determined, then the optimal transfer matrix based on its optimization, which naturally satisfy the consistency requirement. Process is simple, which have finally come to the right of the relative importance of each index value, can assess the combat effectiveness of laser weapon system to provide basis for decision making.

Comprehensive evaluation index system

Principle of the Index System.

Comprehensive and integrated. Index system should include every index which constitutes the system in order to fully reflect the merits or shorts of the object;

Structed and clear. Evaluation index system should accurately reflect the dominance relationship between the various levels, each index has a clear meaning, according to the relationship between the level of progression to form a structured, structured as a whole, excluding the compatibility indexes, ensure that the evaluation scientific;

Concise and science. The size of the index system should be appropriate and the calculating meaning should be definite.

Comprehensive Index System. Through careful analysis the various factors which impact the combat effectiveness of the laser weapon system, compiling and summarizing, we establish a comprehensive evaluation index system such as Table 1 [3].

Fuzzy comprehensive evaluation model

Sub-level Comprehensive evaluation Model. Make the factor set U into s subsets, denotes $U_1, U_2, \cdots, U_s$, which should satisfy the condition [4].

$$U = \{U_1, U_2, \cdots, U_s\}, \quad U_i \cap U_j = \phi \quad (i \neq j)$$

Assume the factor of the number i subset is U_i, which should satisfy the condition

$$U_i = \{U_{i1}, U_{i2}, \cdots, U_{in_i}\}, \quad i = 1,2,\cdots,s$$

Among $n = n_1 + n_2 + \cdots + n_s$, n is the number of the factor of U, n_i is the number of the factor of U_i.

Make each factor set U_i a comprehensive evaluation of single factor. Assume evaluation set $V = \{v_1, v_2, \cdots, v_m\}$. The weight of each factor among U_i which is relative to U_i is $A_i = \{a_{i1}, a_{i2}, \cdots a_{in_i}\}$, which should satisfy $a_{i1} + a_{i2} + \cdots + a_{in_i} = 1$. If R_i is the fuzzy evaluation matrix that U_i maps to V, then

$$R_i = (r_{ij,k})_{n_i \times m}, \quad i=1,2,\cdots,s \ ; \ j=1,2,\cdots,n \ ; \ k=1,2,\cdots,m$$

Table 1 Comprehensive Evaluation index system

Factor U (Weight)	Internal factor	Fuzzy Relation				Weight
		Very good	Good	Common	Poor	
Main Battle System U_1 (0.538)	Beam Quality	3	5	2	0	0.467
	Capture Ability	3	4	3	0	0.149
	Transmit Power	7	3	0	0	0.228
	Aiming Accuracy	6	4	0	0	0.086
	Damage Effect	4	6	0	0	0.070
War Guarantee U_2 (0.305)	Weather Forecast	2	6	2	0	0.110
	Electronic Warfare	3	4	3	0	0.243
	C3I Ability	3	5	2	0	0.445
	Camouflage Ability	2	5	3	0	0.202
Equipment and Technology Guarantee U_3 (0.157)	Fault Detection Ability	3	4	3	0	0.526
	Measurement Ability	2	4	3	1	0.208
	Maintenance Ability	3	5	2	0	0.266

In the formula $r_{ij,k}$, the factor U_{ij} is evaluated to the membership of v_k. As no single factor existing membership function to refer to, this paper use an expert evaluation method to determine. The Specific approach is that every expert is asked to evaluate the internal factors of objects in Table

I, which is very good, good, ordinary and poor , play tick in the corresponding blank, must play only one, further statistics and normalization on all the valid data, then we will get the corresponding membership.

So the first-class comprehensive evaluation vector is

$$R_i = (r_{ij,k})_{n_i \times m}, \quad i = 1,2,\cdots,s \quad ; \quad j = 1,2,\cdots,n \quad ; \quad k = 1,2,\cdots,m$$

Make the factor U the second class comprehensive evaluation. See each U_i as a factor of U. Make B_i as the single factor evaluation vector, then we will get the fuzzy evaluation matrix which is U mapping to V.

$$R = \begin{bmatrix} B_1 \\ B_2 \\ \vdots \\ B_s \end{bmatrix} = \begin{bmatrix} b_1 & b_{12} & \cdots & b_{1m} \\ b_2 & b_{22} & \cdots & b_{2m} \\ \vdots & \vdots & & \vdots \\ b_{s1} & b_{s2} & \cdots & b_{sm} \end{bmatrix}$$

Each U_i is a part of U, which reflect Some properties of U .We can give the weight distribution according to the importance of each U_i. The formula is $A = (a_1, a_2 \cdots, a_s)$.

Then the second-class comprehensive evaluation vector is

$$B = A \bullet R = (b_1, b_2, \cdots, b_m)$$

The Choice of Fuzzy Comprehensive Evaluation. As the impact factor of the laser weapon system combat effectiveness, in order to avoid the loss of information, we should take into account various factors. Then we use the operator $M(\bullet,+)$. Comprehensive evaluation model for the first class is

$$b_{ik} = \sum_{j=1}^{n_i} a_{ij} \bullet r_{ij,k}, \quad k = 1,2,\ldots,m$$

Comprehensive evaluation model for the second class is

$$b_k = \sum_{i=1}^{s} a_i \bullet r_{ik}, \quad k = 1,2,\ldots,m$$

Determine Weight of Each Factor in the Comprehensive Evaluation. In the assessment process, determining of the weights is very important, it directly affects the comprehensive evaluation results. In this paper, we mainly assess the combat effectiveness. Making use of AHP we can get the weights which impact the combat effectiveness of the system. The consistency test is essential in the AHP, and only when the comparison matrix has satisfactory consistency, the conclusion based on AHP is reasonable. In the actual evaluation, we generally rely on rough estimates to adjust the comparison matrix, so as to meet compliance requirements. Then this has great blindness, and can not rule out the possibility which need to be adjusted several times by the consistency test. To overcome this drawback, the following concept of the optimal transfer matrix of AHP is improved to meet the compliance requirements of nature, directly calculate the weight value, without further consistency test. Here's the method:

- According to the general objective ,we can establish the level hierarchical structure model (such as Table 1)
- Compare the factor of the same level and quantization them, then we get the judge matrix $A = (a_{ij})_{n \times n}$ .During the comparisons, we should quantitative parameters, this uses 1-9 ratio scale method. Its specific meaning as follows: For the parameters i and j : 1 means factors i and factors j are equally important; 3 means factors i is slightly more important than factor j ; 5 means

that the factors i more important than the factors j ; 7 means that factors i is very important than the factors j ; 9 means that factors i is absolutely important than the factor j ; 2,4,6,8 is between the two judgments, and the intermediate scale corresponding of the value [5].

Obtain the Optimal transfer matrix. Assume the real matrix $A=\lfloor a_{ij} \rfloor$, $B=\lfloor b_{ij} \rfloor$, $C=\lfloor c_{ij} \rfloor$, $A,B,C \in R^{n\times n}$. Now assume A to be constructed judge matrix, then A clearly meets $a_{ij}=a_{ji}^{-1}$ (known as the reciprocal matrix). In order to make A meet the consistency testing requirement, $a_{ij}=\dfrac{a_{ik}}{a_{jk}}(i,j,k=1,2,\cdots,n)$ (known as consistent matrix). Assume B meets $b_{ij}=-b_{ji}$ (known as Symmetric matrix). Obviously, if A is consistent matrix, then: $B=\lg A\left(b_{ij}=\lg a_{ij},\forall i,j\right)$, meets $b_{ij}=b_{ik}+b_{kj}$ (known as transfer matrix). In order to make A have satisfactory consistency, we can achieve the intended priority delivery of A by seeking the optimal transfer matrix C of B (so making $\sum_{i=1}^{n}\sum_{j=1}^{n}\left(c_{ij}-b_{ij}\right)^2$ the minimum is met). Obviously, if A is a reciprocal matrix, $B=\lg A$, C is the optimal transfer matrix of B , then: $A^*=10C$. We can consider that A^* is the intended optimal consistent matrix of A , which satisfy $\sum_{i=1}^{n}\sum_{j=1}^{n}$ the minimum. While C can be obtained through the following method: Because C is transferring, we can get $x_1,x_2,\cdots x_n\geq 0$, $c_{ij}=x_i-x_j$. In order to make C satisfy $\sum_{i=1}^{n}\sum_{j=1}^{n}\left(c_{ij}-b_{ij}\right)^2$ the minimum, namely making $J=\sum_{i=1}^{n}\sum_{k=1}^{n}\left(c_{ik}-b_{jk}\right)^2=\sum_{i=1}^{n}\sum_{k=1}^{n}\left(x_i-x_k-b_{jk}\right)^2$ minimum, require $\min J$, namely require $\dfrac{\partial J}{\partial x_i}=0$, $\forall i$, then

$$\frac{\partial J}{\partial x_i}=2nx_i-2\sum_{k=1}^{n}(x_k+b_{ik})=0,x_i=\frac{1}{n}\sum_{k=1}^{n}\left(x_k+b_{ik}\right)$$

$$c_{ij}=x_i-x_j=\frac{1}{n}\sum_{k=1}^{n}(b_{ik}-b_{jk})$$

Then the optimal transfer matrix of judge matrix is obtained, which satisfy the requirement of consistency test.

Application Examples

Application the fuzzy-AHP evaluation and the expert evaluation method to evaluate the combat effectiveness of the laser weapon system. Making use of the MATLAB to statistic and calculate the effective evaluation result feeding back from 10 experts, we can get the evaluation matrix and the corresponding weight vector. Evaluation matrixes are:

$$R_1=\begin{bmatrix}0.3 & 0.5 & 0.2 & 0\\ 0.3 & 0.4 & 0.3 & 0\\ 0.7 & 0.3 & 0 & 0\\ 0.6 & 0.4 & 0 & 0\\ 0.4 & 0.6 & 0 & 0\end{bmatrix}$$

$$R_2 = \begin{bmatrix} 0.2 & 0.6 & 0.2 & 0 \\ 0.3 & 0.4 & 0.3 & 0 \\ 0.3 & 0.5 & 0.2 & 0 \\ 0.2 & 0.5 & 0.3 & 0 \end{bmatrix}$$

$$R_3 = \begin{bmatrix} 0.3 & 0.4 & 0.3 & 0 \\ 0.2 & 0.4 & 0.3 & 0.1 \\ 0.3 & 0.5 & 0.2 & 0 \end{bmatrix}$$

Use the improved AHP method to calculate the weight of each level. Make $U_1 - U_{1j}$ judge matrix A_1 as an example:

$$A_1 = \begin{bmatrix} U_{11} & U_{12} & U_{13} & U_{14} & U_{15} \\ 1 & 3 & 2 & 3 & 5 \\ 1/3 & 1 & 1/2 & 3 & 2 \\ 1/2 & 2 & 1 & 2 & 3 \\ 1/3 & 1/3 & 1/2 & 1 & 2 \\ 1/5 & 1/2 & 1/3 & 1/2 & 1 \end{bmatrix}$$

According to the above algorithm, we can get every index weight vector.

$$W = [W_1, W_2, W_3, W_4, W_5]^T = [0.467, 0.149, 0.228, 0.086, 0.07]$$

After calculation, we believe that this comparison matrix has satisfactory consistency. Similarly, we can calculate the weight of other factors, such as shown in Table I. Then the first level for the comprehensive evaluation is

$$B_1 = A_1 \bullet R_1 = (0.4240 \quad 0.4379 \quad 0.1381 \quad 0)$$
$$B_2 = A_2 \bullet R_2 = (0.2688 \quad 0.4867 \quad 0.2445 \quad 0)$$
$$B_3 = A_3 \bullet R_3 = (0.2938 \quad 0.4557 \quad 0.2952 \quad 0.0281)$$

Make the above evaluation vector as a fuzzy evaluation matrix of the above level. Then the second class comprehensive evaluation is

$$B = A \bullet R = (0.3562 \quad 0.4556 \quad 0.1952 \quad 0.0044)$$

Conclusion

This paper presents the application of improved fuzzy-AHP comprehensive evaluation method to solve the laser weapon system's combat effectiveness assessment. In the evaluation process, by considering many factors, from the shaping of fuzzy relationship matrix and determining of the weights are fully attention to the expert's qualitative analysis. Through quantitative and scientific computing estimates, we arrive at a reasonable evaluation results at last. This method has a positive role in guiding and highly practical use in the comprehensive and scientific evaluation of the combat effectiveness of the laser weapon system.

References

[1] Zhongjie Liu, “New Concept Weapon”, Beijing: National Defense Industry Press, 2005

[2] Jijian Xie, “Fuzzy Mathematics and Its Applications”, Wuhan: Huazhong University Press, 2005.

[3] Yuheng Wang, Taijiao Du, “The System Evaluation Method of Laser Weapon”, Journal of Sichuan Ordnance, vol.29, pp.1-3, April 2008

[4] Hongxing Li, “Engineering Fuzzy Mathematics and Its Application”, Tianjin: Science and Technology Press, 1993

[5] Shubai Xu, “AHP Introduction”, Beijing: China Renmin University Press, 1990

© (2012) Trans Tech Publications, Switzerland
doi:10.4028/www.scientific.net/AMM.187.304

Reasearch on A Nonlinear Fuzzy Comprehensive Assessment Method for Oil & Gas Pipeline Failure Based on Fault Tree Analysis

Xue Wu, Ci-Yuan Xiao, Xue-Yan Xu

Postgraduate Department, Southwest Petroleum University ,swpu, Chengdu 610500,China
School of Science, Southwest Petroleum University ,swpu, Chengdu 610500,China
Postgraduate Department, Southwest Petroleum University ,swpu, Chengdu 610500,China
email:iamiamwuxue_ren@126.com, email:xcytlm2003@163.com, email:373988408@qq.com

Key Words-oil & gas pipeline ;failure analysis ;fault tree analysis ;nonlinear fuzzy comprehensive assessment

Abstract—The combination method of fault tree analysis and nonlinear fuzzy comprehensive assessment method was proposed to make research of oil & gas pipeline failure .The common factors influencing oil & gas pipeline failure could be determined with fault tree analysis .However , the practical operated oil & gas pipeline often have some individual factors and fuzzy ones .Nonlinear fuzzy comprehensive assessment method could evaluate objectively based on evaluated factors sets and weight sets provided by fault tree analysis .The new model steps were listed by taking the example of oil & gas pipeline failure .The result indicates that the method is more reasonable and easier for engineering application , and the evaluation result is more with the objective reality.

I. Introduction

During the operation process of oil and gas pipeline system , because of the long acrrossing path , the much and complicated topography ,and the influence of various factors such as internal and external corrosion , the third damage , operation and material defects , the pipe become invalid partially and entirety which caused huge pecuniary loss and bad influence in social to the state and enterprises . How to do gas transmission pipeline failure analysis scientifically and effectively? It has become the major research topic in oil&gas industry. The authors in the previous paper established the oil-gas pipeline fault tree by using the fault tree analysis method , and did the qualitative and quantitative analysis in detail , found out the failure reason , put forward the corresponding measures to improve , and evaluated the occurrence probability of the bottom event using the method of combining the fuzzy set theory and expert judgment on the basis of the traditional FTA method , etc .But the "fault" or "failure" of the oil&gas pipeline system itself has the fuzziness , this is a dynamic variation process . The fault tree analysis can describe the logical causal relationship between the various factors which causing the failure of the pipe system , and establish the oil&gas transmission pipeline failure tree with the tip event "pipeline failure" , obtain the minimum cut set , pipeline failure probability and each basic event's probability importance degree coefficient and the critical importance degree coefficient of the fault tree through qualitative and quantitative analysis , and then find out weak links of pipeline system and formulate rational management and maintenance plan , etc . But which the fault tree analysis given is some common factors which have influence on oil&gas transmission pipeline failure , and has more difficult in the personality and fuzzy factors in the actual operation . Therefore , it needs to introduce fuzzy theory . And the traditional fuzzy comprehensive assessment method are often linear ones while

the prominent impact in some indicators is a kind of non-linear characteristics . So this paper proposed an integrated method combining the fault tree analysis and non-linear fuzzy comprehensive assessment analysis , and hope to the objective analysis .

II. FTA and non-linear fuzzy comprehensive assessment integrated method

A. The fault tree analysis of oil&gas transmission pipeline failure

For oil&gas pipeline , the fault tree tip event is "pipeline failure" . And the pipeline system failure mainly includes the pipeline leak and fracture . Also, take the two reasons as tip events and do top-down analysis , it can be found that pipeline leakage is caused by internal and external corrosion and existed defects and pipeline rupture is caused by the third damage , corrosion cracking , incorrect operation , bad material mechanical properties . Turn on , until the decomposition is the basic event of each fault form , namely , the decomposition cannot be subdivided into or don't have to be subdivided into . Based on the research results in literature [3] , the transmission pipeline fault tree has 24 logic gates and 40 basic reasons . Its structure form is shown in literature [3] .

Through the qualitative analysis , the fault tree is combined by 21 first-order minimum cut set and 21 fourth-order minimum cut set . Because the less the order of the cut set is , the greater the occurrence probability is . So the first-order minimum cut set(X1,X2,X3,X3,X4,X5,X6,X7,X8,X9,X10, X11, X12, X13, X14,X15,X16,X17,X18,X19,X20,X21)which have greater occurrence probability or greater chanciness and the basic reason event (X6)appeared in all fourth-order minimum cut set can be considered . Quantitative analysis often includes the calculation of occurrence probability of tip events and the importance degree analysis of bottom events (including probability importance degree analysis and critical importance degree analysis). Importance degree analysis is an important component in fault tree analysis , appears as the contribution that a bottom event failure do to the occurrence probability of tip events in the system . Based on the analysis of the probability importance degree of basic events , the quantitative assessment of the influence degree that the occurrence probability of basic events do to the occurrence probability of tip events . When using the limited manpower and material resources to reduce the accidents occurrence , the basic events having greater probability importance degree should be considered firstly . And the critical importance degree appears as the ratio of the change of the occurrence probability of basic events to the change of the occurrence probability of tip events . It combines the results of structure importance degree and probability importance degree . It can be seen in literature [4] , the basic reason events having greater probability importance degree in oil&gas pipeline fault tree are:X1, X2, X3, X3, X4, X5, X14, X15, X16, X17, X18, X19, X20, X22, X29, X30, X31, X32, X33, X34,X35,X36,X3,X4,X5,X22,X32,X33,X34; the basic reason events having greater critical importance degree in oil&gas pipeline fault tree are : X14,X15, X16,X17, X18,X19, X29, X30, X31, X35, X36,X3,X4,X5,X22,X32,X33,X34 . It can be obtained by combining the probability importance coefficient and critical importance coefficient that X14, X15, X16, X17, X18, X19, X29, X30, X31, X35,X36,X3,X4,X5,X22,X32,X33 and X34 the 18 basic reason events should be taking as the main evidence for preventing pipeline failure. This is consistent with the conclusion that the minimum cut set having smaller order is the most important cut set .

B. oil&gas transmission pipeline failure multi-level non-linear fuzzy comprehensive assessment method

1) Comprehensive assessment indicator system

For the factors of oil&gas pipeline failure , we determine the first order indicator : the third damage , incorrect operation and existed defects . But the too general goal layer factors increase the difficulty and the uncertainty of the failure assessment , so it is necessary to analysis the secondary factors of oil&gas transmission pipeline failure . Because of the difference of the particular case of oil&gas transmission pipeline failure , there will be different secondary assessment factors in assessment process and should be confirmed according to the particular case . Oil&gas transmission pipeline failure comprehensive assessment indicator system is shown in figure 1.

2) Non-linear fuzzy matrix synthesis operator

In fuzzy comprehensive assessment model

$$B = A \bullet R = (a_1, a_2, \cdots, a_n) \bullet \begin{bmatrix} r_{11} & r_{12} & \cdots & r_{1m} \\ r_{21} & r_{22} & \cdots & r_{2m} \\ & & & \\ r_{n1} & r_{n2} & \cdots & r_{nm} \end{bmatrix} = (b_1, b_2, \cdots, b_m)$$

define fuzzy matrix synthesis operator . Firstly define indicator prominent impact degree coefficient vector Λ , mark $\Lambda = (\lambda_1, \lambda_2, \cdots, \lambda_n)$, in which $\lambda_i \geq 1$. The greater prominent impact degree the indicator u_i do to assessment results , the bigger λ_i is .When the indicator u_i has no prominent impact , then take λ_i to 1 . For convenience , take λ_i to integer which bigger than or equal to 1 . Order $\lambda = \max\{\lambda_1, \lambda_2, \cdots, \lambda_n\}$, the form of non-linear fuzzy matrix synthesis operator defined in fuzzy comprehensive assessment model is

$$f(a_1, a_2, \cdots, a_n; x_1, x_2, \cdots, x_n; \Lambda)$$

$$= (a_1 x_1^{\lambda_1} + a_2 x_2^{\lambda_2} + \cdots + a_n x_n^{\lambda_n})^{\frac{1}{\lambda}}$$

, $\lambda_i \geq 1$, $i = 1, 2, \cdots, n$.

Mark $A = (a_1, a_2, \cdots, a_n)$, in which $a_i > 0$ and $\sum_{i=1}^{n} a_i = 1$; $X = (x_1, x_2, \cdots, x_n)$,where $x_i \geq 1$ (for $\forall 0 < i < n$) . Because there is always degree of membership $r_{ij} \in [0,1]$ in fuzzy comprehensive assessment , when using this operator to do fuzzy matrix synthesis , it must do transformation for membership matrix of assessment object , transform the value of membership to number larger than 1 , such as $r_{ij}^{'} = e^{r_{ij}}$.

3) Multi-level non-linear fuzzy comprehensive assessment method

The steps of multi-level non-linear fuzzy comprehensive assessment method are as follows:

Step one : Divide factor set $U = (x_1, x_2, \cdots, x_n)$ into s factor sets $U_1, U_2, \cdots, U_s$ according to some property , in which $U_i = (x_{i1}, x_{i2}, \cdots, x_{in})$, $i = 1, 2, \cdots, s$ and satisfy to : ① $n_1 + n_2 + \cdots + n_s = n$; ② $U_1 \bigcup U_2 \bigcup \cdots \bigcup U_s = U$; ③For any $i \neq j$, $U_i \bigcap U_j = \varnothing$;

Step two: For every factor set U_i , do comprehensive assessment respectively . Set $V=\{v_1,v_2,\cdots,v_m\}$ as comment set, the weight that every factor in U_i relative to V is A_i : $A_i=(a_{i1},a_{i2},\cdots,a_{in})$. If R_i is single factor assessment matrix , then first-order assessment vector B_i is :

$$B_i=A_i\bullet R_i=(b_{i1},b_{i2},\cdots,b_{in}),\ i=1,2,\cdots,s \quad . \tag{1}$$

Based on the fault tree analysis results, in accordance with the critical importance coefficient , the weight of every important basic reason event A_i is :

$$A_i=I_i^{CR}\left[\sum_{j=1}^{10}I_i^{CR}\right]^{-1} \quad . \tag{2}$$

In form (2) , I_i^{CR} expresses the critical importance degree of the i th basic reason event , and $I_i^{CR}=q_i/Q_sI_g(i)$; q_i expresses the probability of the i th basic reason event , Q_s expresses the probability of the tip event , and $I_g(i)$ expresses the probability importance degree of the i th basic reason event .

Step three: Take U_i as a factor, mark $R=\{U_1,U_2,\cdots,U_s\}$. Like this, the single factor assessment matrix of R is:

$$R=\begin{bmatrix}B_1\\B_2\\\vdots\\B_s\end{bmatrix}=\begin{bmatrix}b_{11}&b_{12}&\cdots&b_{1m}\\b_{21}&b_{22}&\cdots&b_{2m}\\&&\vdots&\\b_{s1}&b_{s2}&\cdots&b_{sm}\end{bmatrix} \tag{3}$$

Take transformation $r_{ij}^{'}=2^{r_{ij}}$, process original fuzzy relationship matrix by using non-linear fuzzy comprehensive assessment method in 2.2.2 , then $R^{'}$ can be obtained .

U_i reflects some property of U , so the weight A can be given according to their importance: $A=(a_1,a_2,\cdots,a_s)$; and then the secondary assessment vector B is :

$$B=A\bullet R^{'}=(b_1,b_2,\cdots,b_m) \quad . \tag{4}$$

Step four : In order to do comparison and sorting , do quantizing for the secondary assessment vector obtained from the model . The marks V for all grade are given according to ranking , shown in table 1 .

Table 1 Reliability ranking rating form

Fraction	0.9	0.8	0.6	0.3	0.1
Reliability ranking	good	preferably	medium	worse	bad

Set V as conversion matrix , then $C=B\bullet V^T$ is the value of fuzzy comprehensive assessment . Based on the ranking , in accordance with comment grade V , the reliability ranking of the pipeline can be known .

III. Calculation example

The 18 basic reason events having greater critical importance degree in oil&gas pipeline transmission failure fault tree analysis are listed in sheet 2 , and on this account to do the basic factors of non-linear fuzzy comprehensive assessment , namely :

$$U = \{u_1, u_2, \cdots, u_{18}\},$$

in which, U expresses factor set; and u_i expresses the i th factor in factor set. Namely, X14,X15,X16,X17,X18,X19,X29,X30,X31,X35,X36,X3,X4,X5,X22,X32,X33 and X34
the 18 basic reason events should be taking as the main evidence for preventing pipeline failure.

The weight set can be calculated according to formula (2) as follows :

$A = (a_1, a_2, \cdots, a_{18}) = (0.0700, 0.0700$

$0.0700, 0.0700, 0.0700, 0.0700, 0.0700,$
$0.0700, 0.0700, 0.0700, 0.0700, 0.0328,$
$0.0328, 0.0328, 0.0328, 0.0328, 0.0328, 0.0328)$ The comment set is divided into five grade ,namely V={good , preferable , medium , worse , bad };

Record it as

$V = \{v_1, v_2, v_3, v_4, v_5\} = \{0.9, 0.8, 0.6, 0.3, 0.1\}$.

Thus , the weight sets which mainly affect factors can be obtained according to fault tree analysis , and the comment set can be determined based on experience . For some practical oil&gas transmission pipeline , do classifying according to the actual measurement value of experts and on site working staff , determine the assessment matrix on account of the membership every factor do to the five grade of the comment . According to the transformation $r_{ij}^{'} = 2^{r_{ij}}$ we can obtain $R^{'}$ from R , $R^{'}$ and R are shown in figure 2.

And then , the result of non-linear fuzzy comprehensive assessment B is

$B = A \bullet R^{'} = (1, 0.610, 0.967, 0.279, 0.238)$;

The result of non-linear fuzzy comprehensive assessment C is : $C = B \bullet V^T = 1$, it can be known from table 1 that the reliability of the evaluated oil&gas transmission pipeline belongs to level “good” .

If using linear fuzzy comprehensive assessment , there is
$B = A \bullet R = (0.5790, 0.2420, 0.1313, 0.0309, 0.0239)$

Table 2 Separate results in oil&gas transmission pipeline fault tree quantitative analysis

Serial number	The basic event code(minimum cut set)	The basic event name	Probability importance degree $\Delta I_g(i)$	Key importance degree ΔI_i^{CR}
1	X14	Unreasonable design of strength	1.000	0.067022
2	X15	Improper material choice	1.000	0.067022
3	X16	Operator training	1.000	0.067022
4	X17	SCADA communication system	1.000	0.067022
5	X18	Equipment	1.000	0.067022
6	X19	Instrument	1.000	0.067022
7	X29	Uneven metallographic structure	1.000	0.067022
8	X30	Tube containing impurities	1.000	0.067022
9	X31	Coarse grains	1.000	0.067022
10	X35	Poor quality of pipeway	1.000	0.067022
11	X36	Mechanical damage	1.000	0.067022
12	X3	Layer moving near the pipe	1.000	0.031446
13	X4	Drilling , steal oil / gas	1.000	0.031446
14	X5	Enormous pressure on pipe in-line	1.000	0.031446
15	X22	Poor quality of anti-corrosion layer	1.000	0.031446
16	X32	Poor quality in processing	1.000	0.031446
17	X33	Poor quality of installation	1.000	0.031446
18	X34	Poor quality of welding	1.000	0.031446

And the result of the comprehensive assessment is $C = B \bullet V^T = 0.8051$, and the reliability of the pipe belongs to level "preferable" .

On earth which type of assessment result is more reasonable ? The original data analysis may easily draw : the result obtained by non-linear fuzzy comprehensive assessment method can reflect the actual situation better .

IV. Epilogue

- The integrated method combining the fault tree analysis and non-linear fuzzy comprehensive assessment analysis is reasonable for the analysis and assessment of oil&gas transmission pipeline failure , and the calculation example shows that the method is simple , intuitive , and evaluation .
- The fault tree analysis and non-linear fuzzy comprehensive assessment method are both very mature assessment methods , make full use of their advantages to process combination and integration is not simple gather them together . This method not only gives play to the advantages of fault tree analysis , but also makes up the shortage of linear fuzzy comprehensive assessment method .

[1]. Xiao,C.:Fuzzy System of Engineering. Science Press,Beijing74-86,2004.

[2]. Zhang,X.Feng,Y.:A Noe-linear Fuzzy Comprehensive Assessment Model.Systematic Engineering Theory and Practice,2005.

[3]. Dong,Y.Gao H.:Fuzzy Fault Tree Analysis on Transmission Pipeline Failure Situation,Petroleum Journal,2002,23(2):85-89.

[4]. Yan,F.Dong,Y.:The Fault Tree Analysis Method in Oil&Gas Pipeline,Xi'an Petroleum Journal,2003,18(1):47-50.

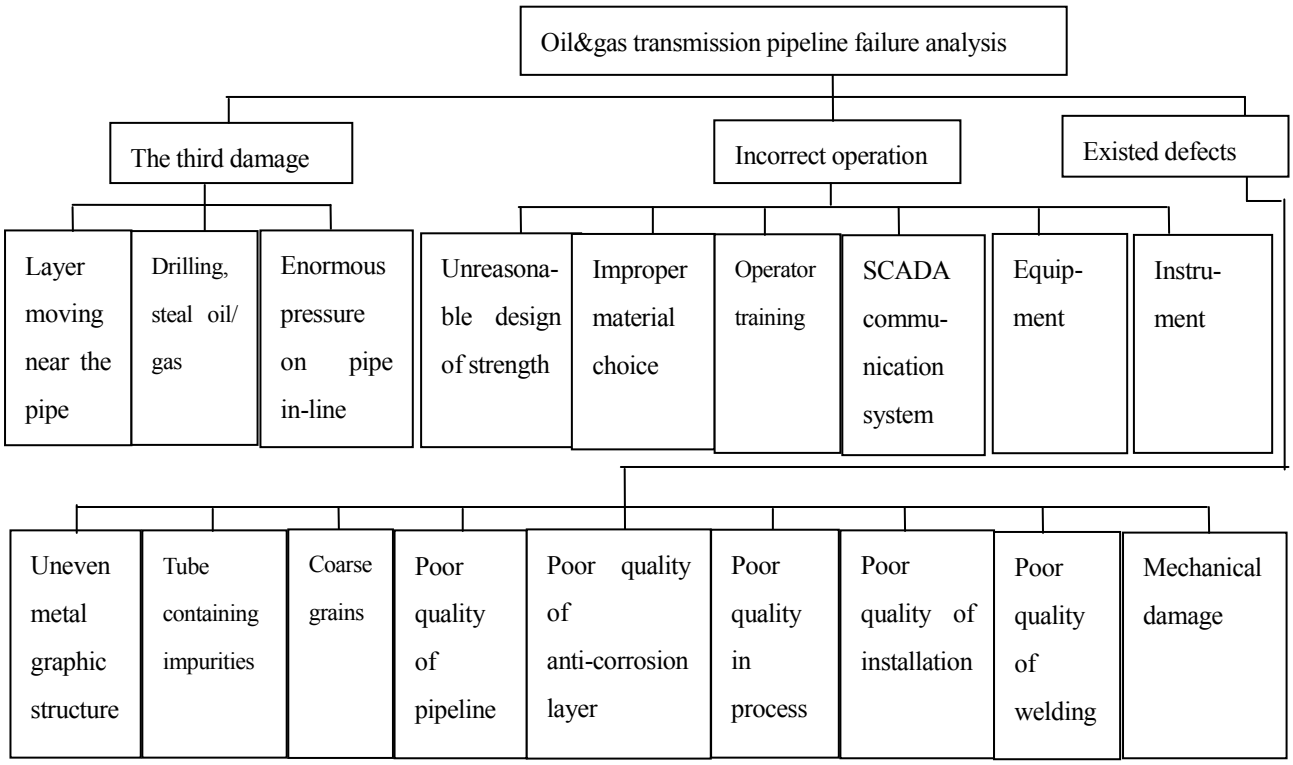

Figure 1 Oil&gas transmission pipeline failure comprehensive assessment indicator system

$$R=\begin{bmatrix} 0.6 & 0.4 & 0.8 & 0.6 & 0.7 & 0.5 & 0.6 & 0.4 & 0.6 & 0.4 & 0.7 & 0.8 & 0.7 & 0.6 & 0.3 & 0.5 & 0.7 & 0.6 \\ 0.2 & 0.4 & 0.1 & 0.2 & 0.1 & 0.2 & 0.3 & 0.4 & 0.2 & 0.4 & 0.2 & 0.1 & 0.2 & 0.3 & 0.5 & 0.1 & 0.1 & 0.1 \\ 0.1 & 0.1 & 0.1 & 0.2 & 0.1 & 0.2 & 0.1 & 0.2 & 0.2 & 0.2 & 0 & 0.1 & 0.1 & 0.1 & 0.1 & 0.1 & 0.2 & 0.1 \\ 0.1 & 0 & 0 & 0 & 0 & 0.1 & 0 & 0 & 0 & 0 & 0.1 & 0 & 0 & 0 & 0 & 0.2 & 0 & 0.1 \\ 0 & 0.1 & 0 & 0 & 0.1 & 0 & 0 & 0 & 0 & 0 & 0 & 0 & 0 & 0 & 0.1 & 0.1 & 0 & 0.1 \end{bmatrix}^T$$

$$R'=\begin{bmatrix} 1.5 & 1.3 & 1.7 & 1.5 & 1.6 & 1.4 & 1.5 & 1.3 & 1.5 & 1.3 & 1.6 & 1.7 & 1.6 & 1.5 & 1.2 & 1.4 & 1.6 & 1.5 \\ 1.1 & 1.3 & 1 & 1.1 & 1 & 1.1 & 1.2 & 1.3 & 1.1 & 1.3 & 1.1 & 1 & 1.1 & 1.2 & 1.4 & 1 & 1 & 1 \\ 1 & 1 & 1 & 1.1 & 1 & 1.1 & 1 & 1.1 & 1.1 & 1.1 & 0 & 1 & 1 & 1 & 1 & 1 & 1.1 & 1 \\ 1 & 0 & 0 & 0 & 0 & 1 & 0 & 0 & 0 & 0 & 1 & 0 & 0 & 0 & 0 & 1.1 & 0 & 1 \\ 0 & 1 & 0 & 0 & 1 & 0 & 0 & 0 & 0 & 0 & 0 & 0 & 0 & 0 & 1 & 1 & 0 & 1 \end{bmatrix}^T$$

Figure 2 R' and R

© (2012) Trans Tech Publications, Switzerland
doi:10.4028/www.scientific.net/AMM.187.311

Damping Force analysis of Magnetorheological (MR) dampers

Haijun Xing

School of Mechanical Engineering, Shijiazhuang Tiedao University, Shijiazhuang, Hebei 050043, P.R. China

xinghj@stdu.edu.cn.

Keywords: Magnetorheological Damper, Herschel-Bulkley Model, Damping Force, Approximate Root

Abstract. In this paper, utilizing Herschel-Bulkley model, the equation of MR fluid pressure gradient is derived in order to predict MR damper's force-velocity behavior. The equation, showing as a complicated nonlinear algebraic expression including various parameters, is then simplified to a nondimensional equation. This is followed by the analysis of the root of this nondimensional equation and an approximate root closely corresponding to numerical result is given.

Main Text

Over the past several decades, there has been a sustained interest in MR dampers which is one of the most promising new devices for semi-active vibration reduction systems. The damping force is produced by the movement of the MR fluid through a magnetic valve. The most widely used configuration of MR damper valve is an annular duct. In order to simplify analysis, this annular duct is usually simplified to a rectangular duct. Experimental test shows that MR damper's force-velocity behavior has an complicated nonlinear hysteresis phenomenon, and several dynamic models of MR dampers have been presented [1-3]. While not sufficient to describe the dynamic behavior of MR dampers, Quasi-static model is very useful for device design. Several efforts have been made to develop analysis of Quasi-static models. Phillips [4] developed a set of non-dimensional variables and a corresponding quintic equation to determine the pressure gradient of flow through a parallel duct. Yang G et al.[5] derived a quasi-static axi-symmetric model to predict the damper's force-velocity behavior and made a comparison between the axi-symmetric and parallel-plate models.

Bingham model is extensively utilized to describe MR fluid field-dependent characteristic, but it can not consider MR fluid shear thinning or thickening effects. In order to describe the shear thinning or thickening effects of MR fluid at higher velocity, Herschel-Bulkley model is utilized. In this paper, following a procedure similar to what utilized by Yang G et al., the quasi-static parallel-plate model utilizing Herschel-Bulkley model of MR fluid is derived and the pressure gradient expression which can predict the MR damper's force-velocity behavior is presented. Because the pressure gradient expression is very complicated, it is then simplified to a nondimensional equation. By analyzing the root of this nondimensional equation, an approximate root closely corresponding to numerical result is given.

MR Damper Configuration

Fig.1 shows a schematic diagram of the MR damper under study in this paper. The cylinder has two chambers, and the upper chamber houses a piston and MR fluid. The piston has an annular duct and a magnetic coil, and divides the upper chamber into two parts, namely: the rebound space, which is above the piston, and the compression space which is below the piston. When the piston moves up and down along the upper chamber, the MR fluid is pressurized to flow through the annular duct. The supplied current drives the coil to generate magnetic field, and the magnetic flux is along a closed loop shown as Fig.1. In order to minimize loss of flux, the piston rod is made from stainless steel. By adjusting the supplied current, the strength of the magnetic field can be controlled, and therefore the resistance to the flow of the MR fluid through the annular duct can be varied as

expected. The lower chamber is an accumulator filled with pressurized air which can compensate for volumetric changes in the upper chambers induced by the upward and downward motions of the piston.

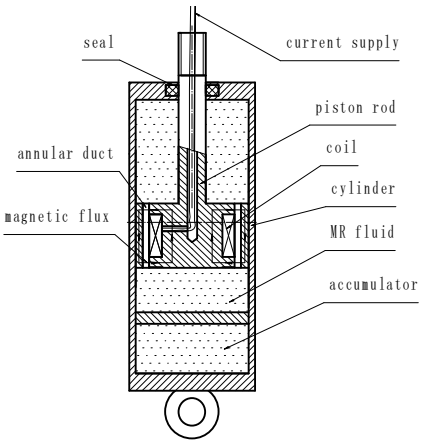

Fig. 1. Schematic diagram of the annular duct MR damper

Quasic-Static Analysis of MR Dampers

The relationship between the shear and the shear strain rate for the Herchel-Bulkley model fluid is

$$\tau = [\tau_0(H) + K|\dot{\gamma}|^{1/m}]\mathrm{sgn}(\dot{\gamma}) \tag{1}$$

where τ is the total shear stress; $\tau_0(H)$ is the yield stress due to the applied magnetic field; H is the magnitude of the applied magnetic field; $\dot{\gamma}$ is shear strain rate; m , K are fluid parameters and m , K >0.

When the size of the annular duct is small relative to the mean radius of the annulus, the annular duct can be considered as a parallel duct[4]. In parallel-plate model , the pressure gradient along the flow is resisted by the fluid shear stress, and the free body diagram of MR fluid is shown as Fig.2. The fluid shear stress and velocity profile of MR fluid in the parallel duct are illustrated in Fig.3

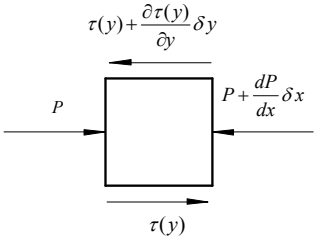

Fig. 2. Free body diagram of MR fluid through a parallel duct

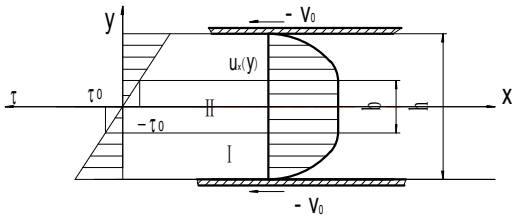

Fig. 3. The fluid shear stress and velocity profile of MR fluid in a parallel-duct

The relationship between the pressure gradient and the fluid shear stress is governed by[4]

$$\frac{dp}{dx} = \frac{d\tau(y)}{dy} = \text{constant} \tag{2}$$

Integrating this equation in terms of y yields

$$\tau(y) = \frac{dp}{dx}y + C \tag{3}$$

where C is zero because of symmetry.

In region Ⅰ of Fig.3, the shear stress has exceeded the yield stress, therefore the fluid flows. In region Ⅱ, the shear stress is lower than the yield stress, so no shear flow occurs, this un-sheared portion of fluid moves as a solid plug. Note that $\tau(-b/2) = \tau_0$, according to Eq.(3), the size of the solid plug is

$$b = -2\tau_0 (\frac{dp}{dx})^{-1} \tag{4}$$

In region I, the shear strain rate $\dot{\gamma} = du_x(y)/dy > 0$, therefore, the shear stress $\tau(y)$ given by equation (1) becomes

$$\tau(y) = \tau_0 + K(\frac{du_x(y)}{dy})^{\frac{1}{m}} \tag{5}$$

Substituting Eq.(5) into Eq.(3) and integrating once with respect to y by imposing the boundary condition that the flow velocity at $y = -h/2$ is $u_x(-h/2) = -v_0$ yields

$$u_x(y) = \frac{1}{(m+1)\frac{dp}{dx}} (\frac{1}{K})^m [(\frac{dp}{dx} y - \tau_0)^{m+1} - (-\frac{dp}{dx}\frac{h}{2} - \tau_0)^{m+1}] - v_0 (-h/2 \le y \le -b/2) \tag{6}$$

Substituting $y = -b/2$ into Eq.(6), the constant flow velocity in region Ⅱ can be obtained

$$u_x(y) = u_x(-b/2) = \frac{-1}{(m+1)\frac{dp}{dx}} (\frac{1}{K})^m (-\frac{dp}{dx}\frac{h}{2} - \tau_0)^{m+1} - v_0 (-b/2 \le y \le 0) \tag{7}$$

The velocity profile of MR fluid is symmetric to x axis, then the expression for the volume flow rate is given by

$$Q = 2w\int_{-h/2}^{0} u_x(y)dy = \frac{-2w}{(m+1)(m+2)(\frac{dp}{dx})^2} (\frac{1}{K})^m (-\frac{dp}{dx}\frac{h}{2} - \tau_0)^{m+2} - \frac{wh}{(m+1)\frac{dp}{dx}} (\frac{1}{K})^m (-\frac{dp}{dx}\frac{h}{2} - \tau_0)^{m+1} - whv_0 \tag{8}$$

Defining nondimensional variables

$$P = \sqrt[m]{\frac{wh^2}{Q + whv_0}} \frac{1}{K} (-\frac{dp}{dx}\frac{h}{2}) \tag{9}$$

$$T = \sqrt[m]{\frac{wh^2}{Q + whv_0}} \frac{1}{K} \tau_0 \tag{10}$$

Eq.(8) is simplified to a nondimensional equation

$$(P - T)^{m+1}[(m+1)P + T] = 2(m+1)(m+2)P^2 \tag{11}$$

There is no common analytical solution for Eq. (11), but it can be solved numerically. Eq. (11) have several roots, but the root of Eq. (11) corresponding to physical issue must satisfy $P > T$ which is derived from $b < h$, Eq. (4), Eq. (9) and Eq. (10) . Considering that the solid plug size b increases to h as the yield stress $\tau_0 \to \infty$ which means that $P \to T$ as $T \to \infty$, and at $T = 0$ the solution is $P = \sqrt[m]{2(m+2)}$, the approximate root of it is assumed to be in the form of

$$P = [f(m,T) + 1]T + \sqrt[m]{2(m+2)} \tag{12}$$

Where $f(m,T) \to 0$ as $T \to \infty$ .Large numeration verifies that an approximate solution can be used to estimate the desired root for $0.5 \le m \le 2$ and $0 \le T \le \infty$ which encompasses most practical conditions.

$$P = [\frac{0.09m^2 - 0.45m + 0.93}{10^{(-0.03m^2 + 0.16m - 0.03)\sqrt[3]{T}}} + 1]T + \sqrt[m]{2(m+2)} \tag{13}$$

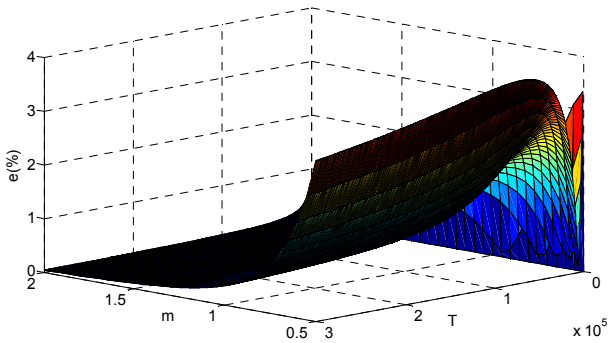

Fig. 4. Error comparison of solution between the numerical result of Eq. (11) and Eq. (13)

Fig.4 shows the error comparison in terms of the percentage of solution between the numerical result of Eq. (11) and Eq. (13) for $0.5 \le m \le 2$ and $0 \le T \le 300000$ .The results indicate that the maximum error is less than 4% .

The rebound damping force is given by

$$F_{reb} = (p_0 + \sqrt[m]{\frac{(A-A'+wh)v_0}{wh^2}}\frac{2K}{h}PL)(A-A') - p_0 A \tag{14}$$

Where p_0 is the intensity of pressure of the accumulator, A is the cross section area of the piston head, A' is the cross section area of the piston rod and L is the effective axial piston length which is exposed to the applied magnetic field.

The compression damping force is given by

$$F_{com} = p_0 A - (p_0 - \sqrt[m]{\frac{(A-A'+wh)v_0}{wh^2}}\frac{2K}{h}PL)(A-A') \tag{15}$$

Conclusion

Utilizing Herschel-Bulkley model of MR fluid, the quasi-static parallel model of MR dampers is developed and the pressure gradient expression is derived which is then simplified to a nondimensional equation. An approximate solution of the nondimensional equation is obtained to predict the damping force.

Acknowledgements

This work is Supported by National Natural Science Foundation of China (Granted No. 10972146), Program for Changjiang Scholars and Innovative Research Team in University (No. IRT0971) and Key Project of Chinese Ministry of Education(Granted No. 210023).

References

[1] Shaopu Yang, Shaohua Li, Xiaojie Wang, Gordaninejad F, Hitchcock G. A Hysteresis Model for Magneto-rheological Damper. International Journal of Nonlinear Sciences and Numerical Simulation 2005;(6)2:139-144.

[2] Shuqi G, Shaopu Y, Cunzhi P. Dynamic Modeling of Magnetorheological Damper behaviors. Journal of Intelligent material systems and structures 2006;(10)1: 3-14.

[3] Kwork NM, Ha QP, Nguyen TH, Li J, Samali B.A novel hysteretic model for Magnetorheologocal fluid dampers and parameter identification using particle swarm optimization. Sensors and Actuators A 132(2006): 441-451.

[4] Phillips RW. Engineering applications of fluids with a variable yield stress. Ph.D thesis, University of California, Berkeley, United States, 1969.

[5] Yang G, Spencer BF Jr, CarlsonJD, Sain MK. Large-scale MR fluid: modeling and dynamic performance considerations. Engineering Structures 24(2002): 309-323.

© (2012) Trans Tech Publications, Switzerland
doi:10.4028/www.scientific.net/AMM.187.315

Numerical Investigation of a Blade Riblet Surface for Drag Reduction Applications with Large Eddy Simulation Method

Wu Nanhuo[1,2,a], Tang Youhong[1,2,b], Zhao Chengbi[1,2,c],
Lin Wei[1,2], Chen Xiaoming[3], Li Runheng[1,2]

[1] Department of Naval Architecture and Ocean Engineering, School of Civil Engineering and Transportation, South China University of Technology, Guangzhou 510641, China

[2] Naval Architecture and Ocean Engineering Technology R&D Center of Guangdong Province, Guangzhou 510641, China

[3] The 602 Research Institute of CSIC, Beijing, 100024, China

[a] nanhuowu@gmail.com ,[b] ctyhtang@scut.edu.cn ,[c] tccbzhao@scut.edu.cn

Keywords: Riblet, Large eddy simulations, Drag reduction, Turbulence control

Abstract. Fully developed turbulent channel flow with a blade riblet surface has been simulated numerically at Reynolds number $\mathrm{Re}_\tau \approx 210$ by Large Eddy Simulations (LES). The blade riblet is shown to provide a total viscous drag reduction approximately 9% with the riblet spacing $s^+ = 16.9$ and the cross section $A_g^{+1/2} = 11.6$. For the sake of investigating the interaction of the turbulent flow with riblets, the mean velocity profiles, velocity fluctuations, and instantaneous flow visualization have been analyzed. It has been found that the riblet of certain size reduces drag by damping the dynamics and weakening the cross motions in the near-wall boundary layer, revealing beneficial turbulence controlling.

Introduction

Successful managing and controlling of turbulent boundary flows can achieve significant financial benefits in engineering applications [1]. Riblets, which are micro-grooves on the bounding surface and aligned to streamwise direction, have successfully reduced the net drag of turbulent layer. Different shapes of riblets, such as sawtooth, trapezoidal, and scalloped and blade riblets, have been tested experimentally and numerically to optimize the riblet size and shape for maximum drag reduction achievement. Many numerical approaches have been developed to study the flow characteristics of riblet surfaces. Choi et al. [2] applied a finite volume DNS (Direct Numerical Simulations) method to clarify the mechanism of drag reduction of riblets. They proposed that the riblets with proper spacing restrict the streamwise vortices, and that drag reduces since only a limited area above the tips exposed to the down-wash motion. Goldstein et al. [3] adopted an immersed boundary method (IBM) to model the riblets, and reported that riblets reduce drag for cross-flow damping. Horsten [4] also used IBM to find that the sharp riblet's tips attribute more drag reduction effect than that of blunt ones. Recently, a combined numerical and experimental study has been carried out to investigate the drag reduce capability of a quasi-3D riblet structure, which called wavy riblets with sinusoidal patterns, and 10.1% drag reduction is reported [5]. The experiment is conducted in an oil channel [6], which requires high accurate measurement techniques to capture the flow characteristics; while the cells of the DNS are up to 11 million, indicating a very large computational cost.

The limitations of experimental and numerical studies have motivated the researchers to provide tractable mathematical models that can accurately predict properties of turbulence with riblet surface using LES method, for example. Peet et al. [7] obtained pressure losses reduction by a sinusoidal riblets with triangular cross-section. In LES, the large-scale turbulent motions are directly resolved, whereas the small-scale motions are modeled to constrain the closure of the Reynolds equations. To our knowledge, most LES applications are reliable for examining the details and providing sufficient information of the flows in moderate computational requirements including memory (RAM) and CPU time.

We employ an LES method with Localized Dynamic Kinetic Energy Subgrid Model (LDKM) [8], whose localized model coefficients are determined dynamically so as to deal with general inhomogeneous flows, for better understanding the turbulence structure caused by the blade riblets. Furthermore, the hydrodynamic characteristics and the drag properties have been analyzed to investigate the interaction of a blade riblet with wall-bounded turbulence, and to study the drag reduction mechanism.

Numerical Approach and Computational Details

In the present study, an LES is performed in a fully turbulent channel. The governing equations employed for LES are obtained by filtering the time-dependent Navier-Stokes equations (N-S equations). To separate the large scale motions from the small ones, a filtering operation is defined to decompose the velocity $\mathbf{U}(\mathbf{x},t)$ into the sum of a filtered (or resolved, or large-scale) component $\overline{\mathbf{U}}(\mathbf{x},t)$ and a residual (or subgrid-scale, SGS) component $\mathbf{u}'(\mathbf{x},t)$ [9].

The LDKM model computes two model coefficients C_k and C_ε without recourse to *ad hoc* procedures. The subgrid-scale turbulence can be better modeled by accounting for the transport of the subgrid-scale turbulence kinetic energy. This method is very suitable to the wall-bounded flows. When the flow is fully resolved, the model automatically drives the eddy viscosity to zero [10]. It also has been successfully applied to various turbulent flows including anisotropic turbulent flows, turbulent mixing-layer, and high Reynolds number flows. Hence, the LES with LDKM is feasible and reliable to the turbulent flows with complex riblet surface boundary condition.

The no-slip boundary conditions are applied to the top smooth surface and the bottom riblet surface. The remaining streamwise and spanwise sides are periodic boundaries. For the computational details of a turbulent channel flow, three factors should be considered. First, the computational domain should be large enough to make sure that the artificial boundary conditions do not influence the resolution statistics. According to the researches of Kerho [11] and Chu and Karniadakis [12], we choose the Friction Reynolds Number $\mathrm{Re}_\tau \approx 210$, $\mathrm{L_x}$=3.0H, $\mathrm{L_z}$=3.0H (H is the height of the channel), and the computational domain is plotted in Fig. 1. Secondly, the mesh size should be small enough to resolve the important scales dynamics in the turbulent flows. Thirdly, the normalized time step is of about $\mathrm{T}^+ \approx 0.4$ in order to enhance convergence and maintain stability during calculating. The total calculation time will be longer than $\mathrm{t}^+ = 2200$ to obtain a fully turbulent channel flow.

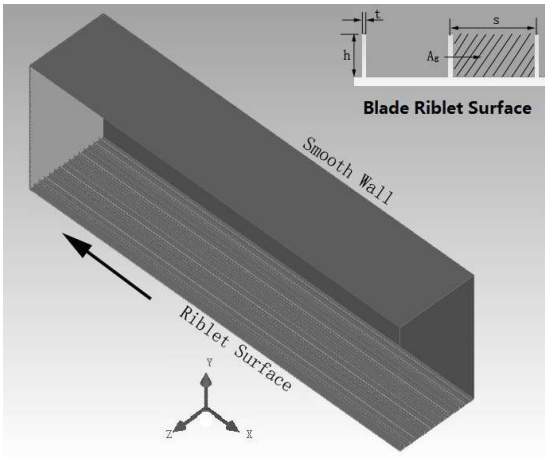

Fig. 1 Computational domain

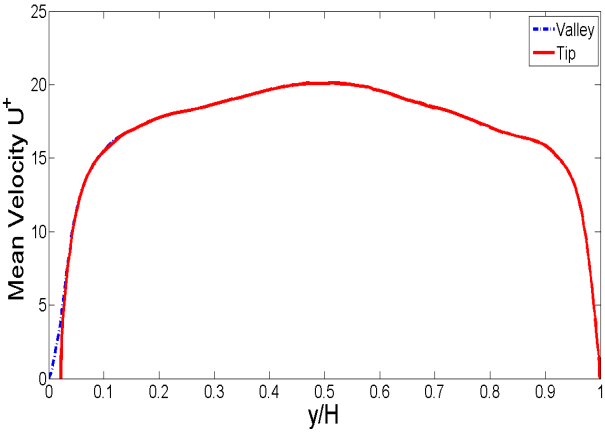

Fig. 2 Mean velocity profiles

Results and Discussions

Starting from the initial velocity field, the N-S equations were iterated forward in time until the turbulent quantities reached statistically steady states. After adequacy calculation, the statistical quantities were taken over the riblet tips and within the valleys between riblets as well.

Drag Characteristics. Typical drag reductions of 6 to 10% compared to smooth wall by two-dimensional riblets have been obtained both experimentally and numerically. If τ_{w0} is the skin friction for the smooth surface, the drag reduction can be defined as $DR = -\Delta\tau_w/\tau_{w0}$. Bechert et al. [13] have studied the blade riblets using experiments in the oil channel, and achieved a 9.9% drag reduction by blade riblets with the optimized dimensions of $s^+ = 17$, $h/s = 0.5$ and $t/s = 0.02$, finding that drag reduces with the blade thickness to spacing ratio t/s drops. In this study, the thickness to spacing ratio $t/s = 0.05$ is set, and a drag reduction of 9% is achieved by the riblets spacing $s^+ = 16.9$, which is in good agreement with the previous studies. Caria-Mayoral et al. [14] found that the viscous regime breaks down near $s^+_{opt} \approx 15$, and that the riblet cross section A_g^+ is a better characterization for the optimal riblet size, with an optimum $A^{+1/2}_{g,opt} \approx 10.7 \pm 1$. In the present work, $A_g^{+1/2} = 11.6$ is just within the optimum range.

Mean Velocity. The mean velocity profile of fully developed channel flow is defined by $U^+ \equiv \langle U \rangle / u_\tau$, and u_τ is the friction velocity at the top smooth wall. Mean velocity magnitude over the valleys and over the riblet tips are presented in Fig. 2. It can be seen that the gradient of velocity above the tip is smaller than that above the valley. However, as the tip is thin, i.e., it has a small wetted area, a minor total skin friction induced by the steeper gradient increases. The other finding is that, the two velocity profiles coincide beyond the outer layer, indicating that the riblets effect occurs majorly in the wall-bounded region.

Velocity Fluctuations. The normalized root mean square (RMS) of velocity fluctuations is shown in Fig. 3. The velocity fluctuations of all the three directions over riblets valleys and tips decrease compared to the smooth surface, at least in the region of the peak RMS values. Note that the RMS peak values in wall-normal and spanwise reduce much more than that in the streamwise. This observation is in accordance with findings of Choi et al. [2]and Chu and Karniadakis [12] who suggested that in the drag-reducing configuration, the velocity fluctuations of all the components should decrease above the riblets.

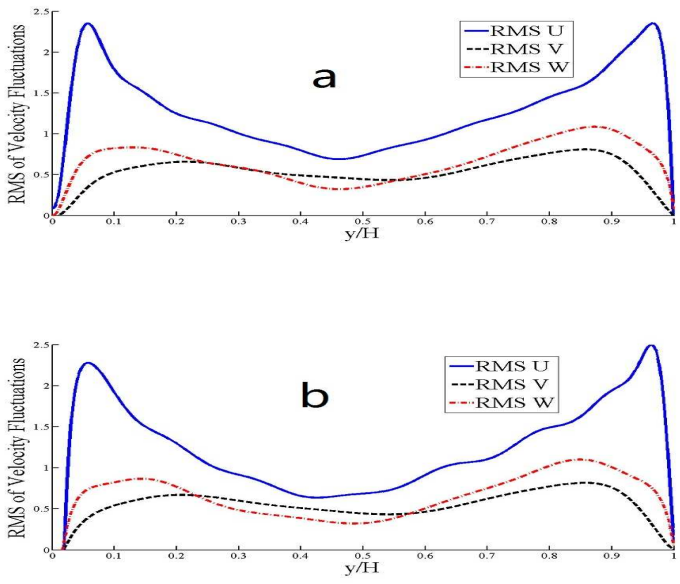

Fig. 3 RMS velocity fluctuations:
(a) over the valleys; (b) over the tips

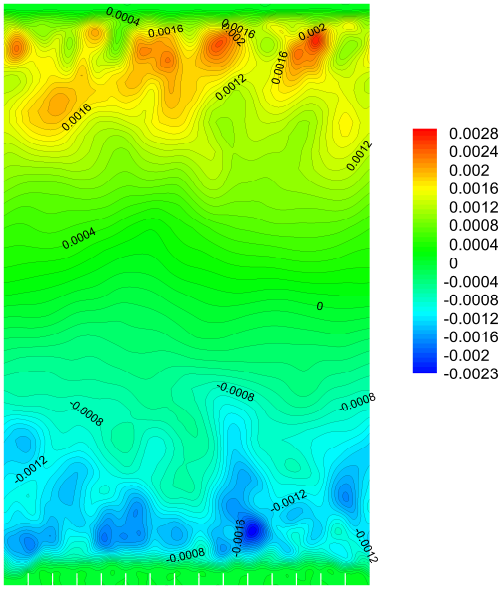

Fig. 4 Instantaneous Reynolds shear stress contours in spanwise plane

Flow Visualization. In this section, we focus on the turbulent structures by realizing the instantaneous visualization of the flows. The resolved Reynolds shear stress $\overline{u'v'}$ contours are plotted in Fig. 4. As we have seen, the Reynolds shear stress above the valleys and the tips do not differ much. But the absolute peak above the riblets is small than that above the smooth wall, thus the turbulent intensity decreases for the riblets pushing away the high chaotic perturbations from the bottom wall. According to the instantaneous cross-flow velocity contours and vectors over the riblets as shown in Fig. 5, although the tips of the blade are exposed to the flow, the producing vortices are still small and likewise few eddies can reside in the valleys. It has been shown that the spanwise motions of turbulence are impeded. The turbulence structures or quasi-coherent structures in channel flows and boundary layers have been investigated by Robinson [15] to explain the behavior of wall-bounding turbulent flows. Fig. 6 portrays the low and high streaks in wall-parallel plane above the riblet surface and the smooth wall. Low-speed streaks at $y^+ \approx 10$ are long compared with that at $y^+ \approx 30$, and the streaky structure length is up to 1000 wall units in Fig. 6 (b). It is clearly visible that the turbulent dynamics above the riblets are quite quiescent in terms of the profitable interaction with the turbulence.

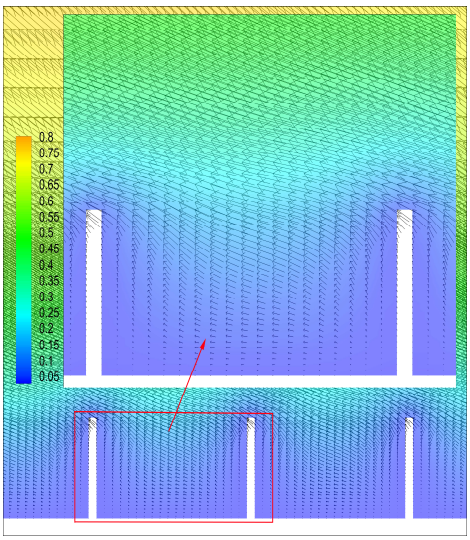

Fig. 5 Instantaneous cross-flow velocity contours and vectors over the riblets

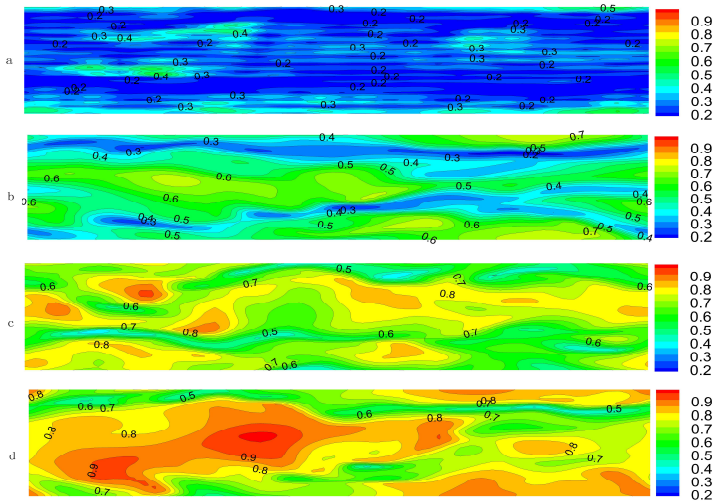

Fig. 6 Streaks in turbulent layers in wall-parallel plane; (a) riblets at $y^+ \approx 10$; (b) smooth wall at $y^+ \approx 10$; (c) riblets at $y^+ \approx 30$; (d) smooth wall at $y^+ \approx 30$

Conclusions

A significant gain in drag reduction can be expected by the passive technique - riblet surface. In this work, we investigated a blade riblet surface for viscous drag reduction in the turbulent flow using an LES method with an LDKM model, with particular emphasis on the interaction of riblets and the near-wall boundary layer. We have shown that a 9 % drag reduction is achieved with the riblet spacing $s^+ = 16.9$ as a conventional optimization characteristic riblet size and the cross section $A_g^{+1/2} = 11.6$ as a novel geometric parameter.

In this drag reduction case, the interaction between the blade riblets and the turbulent flow lodges in the near-wall boundary region, and does not penetrate further into the outer layer. The turbulence intensities are damped down by the riblet effect due to the low peak values of velocity fluctuations and the Reynolds shear stress. As can be seen, the riblet surface pushes away the flows from the boundary layer, impedes the spanwise turbulence motions, and weakens the dynamics near the wall-bounded region, thus, a skin friction reduction is obtained by a blade riblet surface.

Acknowledgements

This work was supported by the National Natural Science Foundation of China (51009069) and the 3rd Key Construction Program of the National "985" Project - South China University of Technology.

References

[1] Pollard A. Near-Wall Turbulence Control. *Flow Control*. In: Gad-el-Hak M, Pollard A, editors.: Springer Berlin / Heidelberg; 1998. p. 431-66.

[2] Choi H, Moin P, Kim J. Direct numerical simulation of turbulent flow over riblets. Journal of Fluid Mechanics 1993;255.

[3] Goldstein D, Handler R, Sirovich L. Modeling a no-slip flow boundary with an external force field. Journal of Computational Physics 1993;105.

[4] Horsten BJC. A Numerical Study on Laminar and Turbulent Flow over Sharp and Blunt Sawtooth Riblets. 2005.

[5] Kramer F, Gruneberger R, Thiele F, Wassen E, Hage W, Meyer R. Wavy riblets for turbulent drag reduction. 5th Flow Control Conference, June 28, 2010 - July 1, 2010. Chicago, IL, United states: American Institute of Aeronautics and Astronautics Inc.; 2010.

[6] Bechert DW, Hoppe G, van der Hoeven JGT, Makris R. The Berlin oil channel for drag reduction research. Experiments in Fluids 1992;12.

[7] Peet Y, Sagaut P, Charron Y. Pressure loss reduction in hydrogen pipelines by surface restructuring. International Journal of Hydrogen Energy 2009;34:8964-73.

[8] Menon W-W, Kim S. Application of the localized dynamic subgrid-scale model to turbulent wall-bounded flows AIAA, Aerospace Sciences Meeting & Exhibit, 35th, Reno, NV; UNITED STATES 1997.

[9] Pope SB. *Turbulent Flows*. Cambridge ; New York : Cambridge University Press, 2000.

[10] Ghosal S, Lund TS, Moin P, Akselvoll K. A dynamic localization model for large-eddy simulation of turbulent flows. Journal of Fluid Mechanics 1995;286:229-55.

[11] Kerho M. Active reduction of skin friction drag using low-speed streak control AIAA Aerospace Sciences Meeting & Exhibit, 40th, Reno, NV; UNITED STATES:4.

[12] Chu DC, Karniadakis GE. A direct numerical simulation of laminar and turbulent flow over riblet-mounted surfaces. Journal of Fluid Mechanics 1993;250.

[13] Bechert DW, Bruse M, Hage W, VanderHoeven JGT, Hoppe G. Experiments on drag-reducing surfaces and their optimization with an adjustable geometry. Journal of Fluid Mechanics 1997;338:59-87.

[14] Garcia-Mayoral R, Jimenez J. Drag reduction by riblets. Philosophical Transactions of the Royal Society a-Mathematical Physical and Engineering Sciences 2011;369:1412-27.

[15] Robinson SK. Coherent motions in the turbulent boundary layer. Annual Review of Fluid Mechanics 1991;23:601-39.

© (2012) Trans Tech Publications, Switzerland
doi:10.4028/www.scientific.net/AMM.187.320

The design and manufacture of the intelligent electric cars for firefighting based on SCM

Minli Tang, Ling He[a], Hengyu Wu, Wei Wang and Lisha Cai

Department of Electronic Engineering, Hainan Software Profession Institute, Qionghai, Hainan, 571400, China

[a]heling_2818@126.com

Keywords: AT89S52; Photoelectric Sensor; Flame Sensor; Design.

Abstract. With the AT89S52-SCM as the control core, the system is made up of DC, steering gear, photoelectric sensor, flame sensor, power circuit and so on. The system makes the car move and turn through the I/O of AT89S52. The RPR220-optical on the tube helps tracing. Infrared flame sensor helps flame scanning. At the same time, the buzzer and the LED make the alarm function. The LCD monitor and three buttons help to make the real-time status display and start control. The system is flexible and easy to control, tracing fast, accurate and stable operation, and lower costs, while the software of the controlling system could be improved further to expand its functionality, but does not require additional hardware costs, thereby enhancing the smart car's cost performance.

Introduction

With the AT89S52-SCM as the control core, the system is made up of forward steering motor drive module, flame sensor module, tracing senor module, car display module, obstacle avoidance module, fire fan and drive module, speed odometer module and power module circuit module. The system is capable of setting the ground track, automatically search for light, automatically avoiding obstacles and putting out the fire, including obstacle avoidance model to software. And with the buzzer and LED alarm function, the system has the LCD and three buttons for real-time status display and start control. The design block diagram is shown in Figure 1.

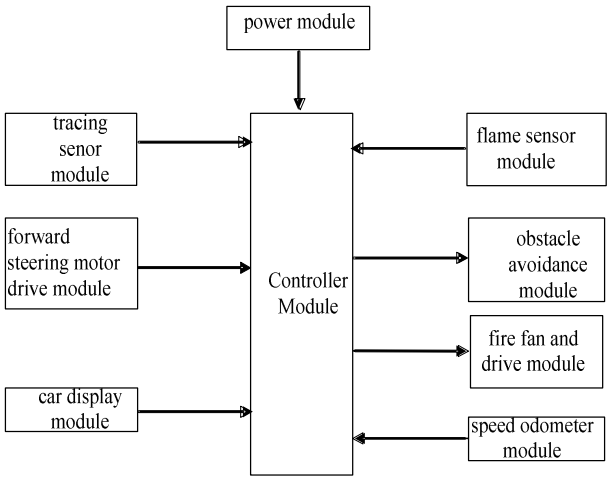

Fig.1The design block diagram

Design for modules

Selection of body. We select the car which has three wheels that can turn freely so that it can change directions flexibly and make 90-degree and 180-degree turn easily.

Analysis and Selection of tracing module. We select the RPR220-optical on the tube. RPR220 is an integrated reflective photoelectric detector. Its transmitter is a gallium arsenide infrared emitting diode. Its receiver is a high-sensitive, silicon planar optical transistor. The characters are as follows: Firstly, the plastic lenses can increase the sensitivity. Secondly, the built-in visible light filter can reduce the impact of discrete. Finally, it has a small size and a compact structure. When the LED light is reflected back, the transistor turns out low. The optical on the tube can control the circuit easily and has a stable performance.

Analysis and Scheme Comparison of the flame sensor. The system uses far-infrared sensor. By experiments, the flame sensor can test a long distance and a good linearity. It can exactly test even with a small body. In the design of the flame sensor, we set a far-infrared sensor on each of the head and both sides which are at the height of 15-20cm from the ground that is as much as the height of the fire from the ground. For the reason that the flame sensor can test a long distance, we encase the sensors on each side with black plastic papers in order to make errors of the flame ahead. By experiments, the sensor treated in the way as above only can test the flame in a distance of a square but .has no response to the farther flame so that we can reduce errors. As soon as testing the flame, the car will move to the flame and turn to fire it.

Comparative Analysis of the Obstacle avoidance scheme. Thanks to the stable location of the obstacle, we select the software obstacle avoidance mode, in order to save the source of SCM and reduce the cost.

Motor Module. It's a smart electric car. The selection of the driving motor is very important to a electric car. In order to achieve accurate positioning and precise measurement of the path, we consider the use of DC gear motor. The DC gear motor has a big rotational torque and simple assembly even with a small and light body. It's convenient to work. The original impetus provided by high-speed motors inside drive the variable speed (slowing-down) gear unit to make enough torque.

Analysis of the Display option. We select the LCD1602 for the appropriate characters, volume and weight. It can show in Chinese so it's intuitional.

Design of systematic hardware

Master-control Circuit. The master-control circuit selects AT89S52-SCM as the core control chip[2][3]. The AT89S52 is a kind SCM of 51 kernel and 8-bit COMS with low-power but high-performance. It has a FLASH-ROM inside with a space of 8k and that can be rewritten for 1000 times. It also has a RAM with 256 bytes, 32 IO ports and two 16-bit programmable counters. What's more, this kind of 51-SCM can directly download files through serials or parallels without HT-WRITER. The Minimal (AT89S52) System is shown in Figure 2.

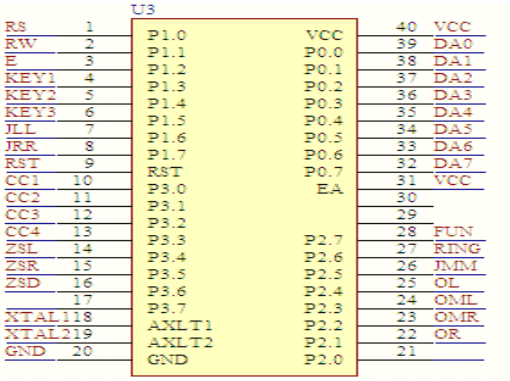

Fig.2.The Minimal (AT89S52) System

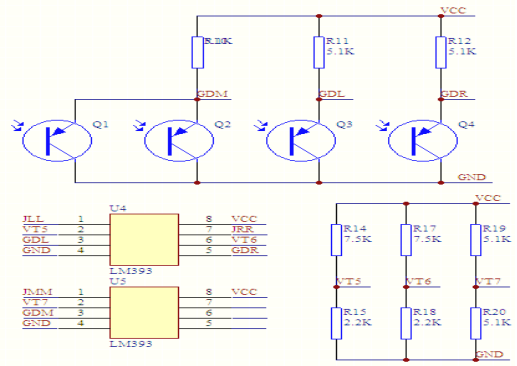

Fig.3.The flame sensor circuit

Flame Sensor Circuit. The system selects LM393-comparator. It is a packaged DIP8-intergrated chip by 8 leads[1]. What's more, it has two comparators integrated inside. In this circuit, the flame sensor won't break over but the positive pull-up resister will be in high level and export after the filter shape by the comparator, when the flame sensor can not test the fire. On the contrary, the flame sensor will break over and export in low level[3]. The flame sensor circuit is shown in Figure 3.

Tracing Circuit. The basic theory of the design of tracing circuit is the same as that of the flame sensor circuit. The tracing circuit is shown in Figure 4. Other circuits are omitted.

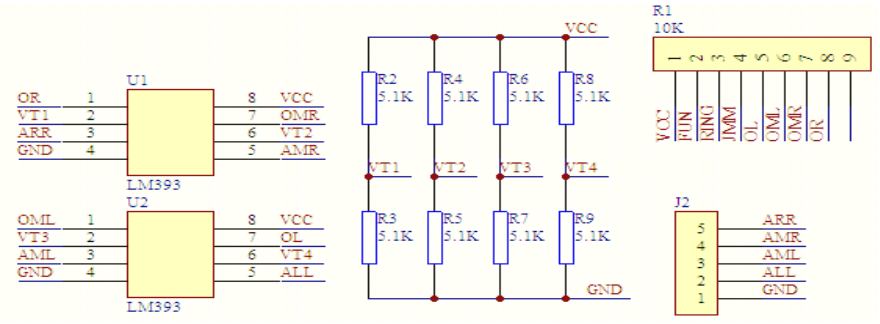

Fig.4.The tracing circuit

Design of the system software

The master program makes three methods to work[4]: the first, the car goes straight; the second, the car goes along the track, the last, traces along the custom. In the event that the car goes straight, when the car steps into the work area, it firstly will make a judgment on whether there is a white track between two wheels. If there is the white track, the car will go along the track and move 1.8m in 10 seconds with the route and time cost on the LCD. If not, the car will change the track and finish the program as above. In the event that the car goes along the track, when the car steps into the work area, it will moves along the track and make a judgment on whether there is fire in the front. If there is fire in the front, the car will put out the fire and go back to its track with the route, the time cost of movement, the coordinates of the fire and the time cost of putting out the fire on the LCD. In the event that the car traces along the custom, the car steps into the work area and finds the two flames so that it will put them out and move back to safe area as soon as possible. The LCD will display the distance of the round trip and the time cost. The flow chat of the master program is shown in Figure 5.

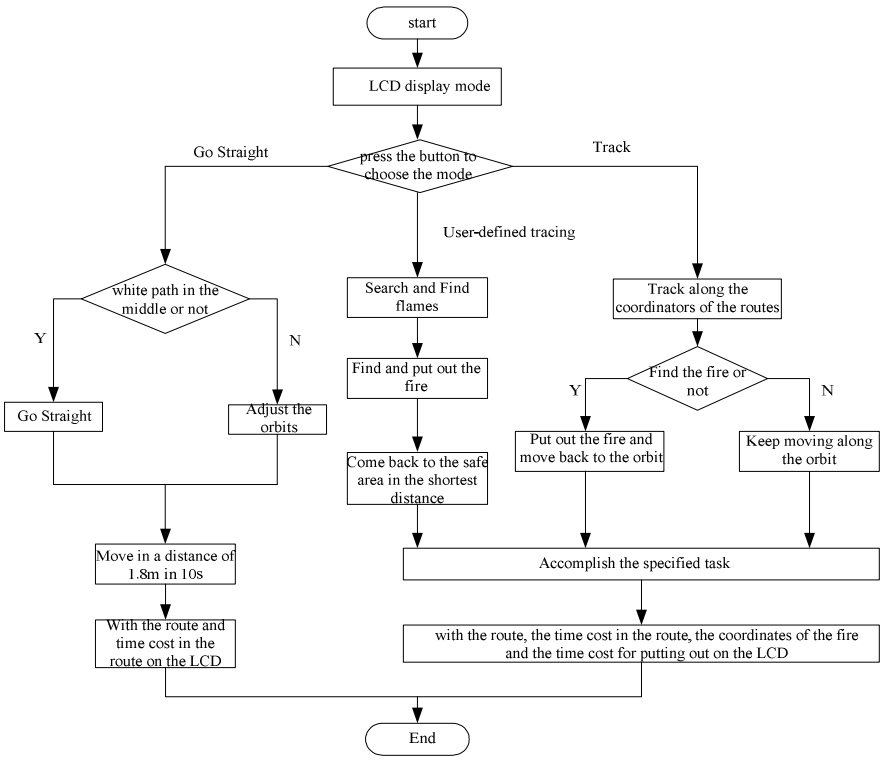

Fig.5.The master program

Conclusion

Our design is a control system of the intelligent electric cars for firefighting based on AT89S52-SCM as the core. The system has a simple circuit and compact structures. The price is lower but the performance is higher. The system has three methods to work as mentioned above and makes the intelligent control of the electro car come true, including tracing of the route, testing the fire, intelligent obstacle avoidance, measurement of the route, putting out the fire intelligently, digital tube display, audio alert and so on.

Acknowledgment

This work is sponsored by the National Natural Science Foundation of Hainan(No.610230) and the National Natural Science Foundation of Hainan(No.611127).

References

[1] Shi Yan.. Fundamentals of Digital Electronics[M]. Bai Jing:Higher Education Press.1998.

[2] Youwen Yv. Principle and application of sensor[M].Xi An:Xidian University Press.2003

[3] Hongwei Sen. MCU-based intelligent system design and implementation[M].Bei Jing: Electronics Industry Press.2005

[4] Zhongmei Ma. MCU C language application programming[M].Bei Jing: Beijing Aerospace University Press.2003

© (2012) Trans Tech Publications, Switzerland
doi:10.4028/www.scientific.net/AMM.187.324

Investigation of the Temperature Distribution in the Lithium-ion Battery for Pure Electric Vehicles

Liang Zheng [1, a], Bin Wu [1, b], Guo-qing Xu [2, c]

[1] Harbin Institute of Technology Shenzhen Graduate School

University Town of Shenzhen, HIT campus, Shenzhen, China

[2] Shenzhen Institutes of Advanced Technology, Chinese Academy of Sciences, Shenzhen, China

[a] liangzheng@hitsz.edu.cn, [b] wubin5652005@163.com, [c] gq.xu@siat.ac.cn

Keywords: Pure electric vehicle, lithium-ion battery, finite element method, thermal analysis.

Abstract: Lithium-ion batteries have more excellent performance than other types of batteries, thus it is widely used in electric vehicles. Using batteries as the main power supplier does inevitably generate a lot of heat which not only deteriorates the batteries, but endangers the safety of the vehicle. In this paper, the temperature distribution of the batteries in the pure electric vehicles was investigated to minimize the heat generated in the batteries. The finite element formulations of the 3-D heat conduction equation of the battery were established for both steady and transient states. Then the finite element simulations were developed to investigate and optimize the temperature distribution of the battery and the battery pack. A parametric study was completed such that the heat generated in the battery pack can be minimized.

Introduction

The lithium-ion batteries have much more excellent performance than the other types of batteries so that they are widely used in the electric vehicles (EVs) [1-3]. However, the Li-ion battery is very sensitive to the temperature variation. One needs to consider not only the temperature range of the batteries, but the temperature difference of each battery in the pack. Low temperature can result in insufficient electrochemical reaction inside the battery, whereas high temperature will affect the working condition so that it shortens the life of service of the battery. Furthermore, the overshoot or overdischarge may be happened in some batteries if the temperature distribution among the battery pack is nonuniform. In order to minimize the heat generated in the battery pack, the temperature distributions in the battery and the battery pack utilized in EVs are investigated and parameters are optimized to lower the temperature and non-uniformity of the temperature distribution.

Finite Element Formulations of the Heat Conduction Equation of the Li-ion Battery

The heat conduction equation in the Cartesian coordinates is given as [4]:

$$\rho C\frac{dT}{d\tau}=\frac{\partial}{\partial x}(k_x\frac{\partial T}{\partial x})+\frac{\partial}{\partial y}(k_y\frac{\partial T}{\partial y})+\frac{\partial}{\partial z}(k_z\frac{\partial T}{\partial z})+\phi_v \tag{1}$$

where ρ is the density and C is the heat capacity.

The Galerkin method is employed to obtain the finite element forms of the heat conduction equation. For the steady-state heat conduction equation, the finite element form is expressed as [5]:

$$K\phi=P \tag{2}$$

and the finite element form for the transient heat conduction equation can be written as [5]:

$$K\phi+C\dot{\phi}=P \tag{3}$$

where:

$$K_{ij}=\sum_e\int_\Omega(k_x\frac{\partial N_i}{\partial x}\frac{\partial N_j}{\partial x}+k_y\frac{\partial N_i}{\partial y}\frac{\partial N_j}{\partial y}+k_z\frac{\partial N_i}{\partial z}\frac{\partial N_j}{\partial z})d\Omega+\sum_e\int_{\tau_3}hN_iN_jd\tau \tag{4}$$

$$P_i = \sum_e \int_{\tau_2} N_i q d\tau + \sum_e \int_{\tau_3} hN_i \phi_a d\tau + \sum_e \int_{\Omega} N_i \rho Q d\Omega \tag{5}$$

In Eqs. (2)-(5), K is the heat conduction matrix, ϕ is the nodal temperature matrix, P is the temperature load matrix, C is the heat capacity matrix, and $\dot{\phi}$ represents the derivative of ϕ with respect to time. In addition, N_i denotes the shape function, and k_x, k_y, k_z represents the thermal conductivity along three axes.

Finite Element Simulations of the Li-ion Battery

Equivalent Material Properties of the battery. Figure 1 illustrates the rectangular Li-ion battery employed in this research. It has the height of 280 mm, the depth of 71 mm, and the width of 182 mm. The internal structure of the Li-ion battery mainly includes three parts: the shell, the contact layer and the central area. The central area is the heating zone of the battery since most reactions are occurred in the central area.

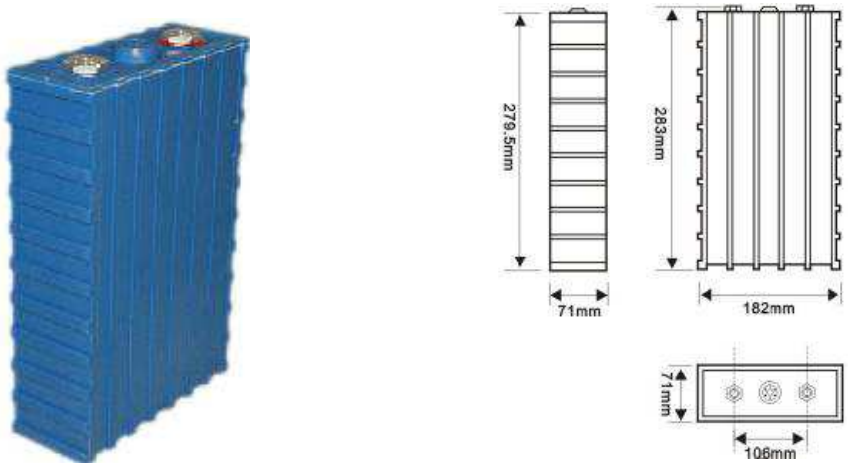

Fig. 1. Internal Structure of the rectangular Li-ion battery

The central area is the most complex area of the battery since it is stacked with hundreds of layers made of different materials. Therefore it is essentially infeasible to generate and implement finite element models of the entire battery incorporating the actual structures. Consequently, equivalent modeling techniques must be developed to investigate the temperature distribution of the battery while circumventing the time and intense computational requirements. In other words, equivalent material properties need to be calculated and utilized in the finite element models. Eqs. (6)-(8) represent the calculations of the equivalent material properties of the battery:

Density:
$$\rho = \frac{m}{V} = \sum_{i=1}^{n} \frac{m_1 + m_2 + m_3 + \cdots + m_n}{V_1 + V_2 + V_3 + \cdots + V_n} \tag{6}$$

Specific heat:
$$C = \sum_{i=1}^{n} \frac{C_1V_1 + C_2V_2 + C_3V_3 + \ldots + C_nV_n}{V_1 + V_2 + V_3 + \ldots + V_n} \tag{7}$$

Thermal Conductivity:

Serial Connection: $K = \dfrac{\sum_{i=1}^{n} l_i}{\sum_{i=1}^{n} \frac{l_i}{k_i}}$ Parallel Connection: $K = \dfrac{\sum_{i=1}^{n} A_i k_i}{\sum_{i=1}^{n} A_i}$ (8)

where l_i denotes the length of each battery along the heat flux, whereas A_i denotes the cross-sectional area of each battery along the heat flux. Both serial and parallel connection cases have been considered and the thermal conductivity of both cases were calculated (as shown in Eq. (8)).

The material properties of the lithium-ion battery used in this research are listed in Table 1, including thermal conductivity, specific heat, density, etc.

Table.1 Material properties of the Lithium-ion battery

	Anode	Anode current collector	Negative electrode	Negative collector	Diaphragm	Contact layer	Shell
Material	$LiCoO_2$	AL	Graphite	Cu	Polyethylene	Electrolyte	AL
Thickness	0.014	0.002	0.0116	0.0014	0.0035	0.05	0.07
Thermal conductivity	1.58	238	1.04	398	0.3344	0.6	238
Specific heat	1269.21	903	1437.4	385	1978.16	2055.1	903
Density	2328.5	2702	1347.33	8933	1008.98	1129.95	2702

Based on the values of the parameters provided in Table 1, the equivalent material properties of the central area in the battery can be determined:

Equivalent Density $\rho = 2123.83$ kg/m^3 Equivalent specific heat $C = 1165.91$ J/(kg·K)

Thermal conductivity: $k_x = 1.022$ W/(m·K) $k_y = 25.746$ W/(m·K) $k_z = 26.364$ W/(m·K)

Discussion of Boundary Conditions. The Li-ion battery used in this paper has a rectangular shape, which means it is under the natural convection if there is no dissipation source. Under the natural convection, the heat transfer is mainly generated by the buoyancy of the air, so different boundary surfaces may have different convection coefficients. the convection coefficient for each boundary surface needs to be calculated separately. Setting the constant temperature of the wall of 30 °C, the thermal conductivity k = 2.63×10^{-2} W/(m·k), the kinematic viscosity $\nu = 15.53\times10^{-6}$ m^2/s, and the Prandtl number is Pr = 0.702.

For the top surface of the battery, the heat can be easily dissipated so that the heat convection is strong. The calculations of the convection coefficient can be shown as follows:

Grashof number: $Gr = \dfrac{g\alpha\Delta t l^3}{\nu^2} = 2.26\times10^4$ $\Rightarrow$ Raleigh number: $Ra = Gr\times\Pr = 1.5865\times10^4$

$\Rightarrow$ Nusselt number: $Nu = 0.54Ra^{\frac{1}{4}} = 6.06$ $\Rightarrow$ Convection coefficient: $h = Nu\dfrac{k}{l} = 6.25W/(m^2\cdot K)$

For the bottom surface of the battery, the heat convection is weak.

$$Nu = 0.27Ra^{\frac{1}{4}} = 3.03 \quad \Rightarrow \quad h = Nu\frac{k}{l} = 3.125W/(m^2\cdot K)$$

For the vertical surfaces, they should have the same convection coefficients:

$$Gr = 2.9772296\times10^7 \qquad Nu = 39.89 \qquad h = Nu\frac{k}{l} = 3.75W/(m^2\cdot K)$$

Finite Element Simulations. Figure 2 illustrates the temperature distributions in these two different types of Li-ion batteries. It can be seen that under the same condition (1C electric charge and at the temperature of 293K), the maximum temperature in the cylindrical battery is 326.12K and the largest temperature difference in the battery is 8.57K; while the maximum temperature in the rectangular battery is 320.58K and the largest temperature difference in the battery is 6.33K. It indicates that the rectangular battery is better than the cylindrical one in terms of heat dissipation.

(a) (b)

Fig. 2 Temperature Distribution of (a) cylindrical battery and (b) rectangular battery at 1C293K

The effect of the discharge rate of the battery on the temperature distribution of the battery pack was also investigated. Fig. 3 illustrates the temperature distribution in the battery with different discharge rates. The comparison between Fig. 3(a) and Fig. 3(b) reveals that the temperature of the battery with a faster discharge rate is higher than the temperature of the battery with a slower discharge rate. A slower discharge rate should be chosen to lower the temperature and decrease the temperature difference in the battery.

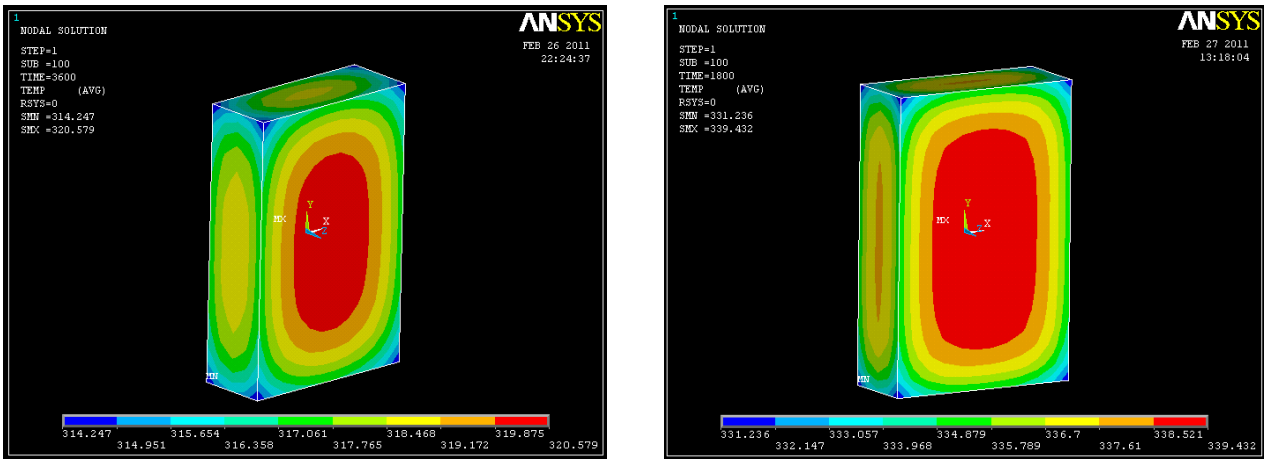

(a) (b)

Fig. 3 Temperature distribution in the battery at (a) 1C discharge and (b) 2C discharge

Due to the demand of high power, EVs usually employ battery packs in which each pack consists of tens of batteries. The cooling strategy of the battery pack is investigated by considering two different strategies. In the first strategy, the cooling gas (air) is blowing along the longitudinal direction of the battery pack, it is called the serial cooling; in the second strategy, the cooling direction is perpendicular to the longitudinal direction of the pack, it is called the parallel cooling.

Figure 4 illustrates the temperature distributions in the battery pack using (a) the serial cooling strategy and (b) the parallel cooling strategy, with the wind speed of 6 m/s which is larger than the critical value 4.2 m/s which is calculated based on the critical Reynolds number of 500000 to differentiate the laminar flow and the turbulent flow. It can be seen in Fig. 4(a) that the air flow will turn to be the turbulent flow at the speed of 6 m/s using the serial cooling strategy. Furthermore, the temperature differences are quite large (about 19 degrees) in the battery pack, which will deteriorate the batteries in the long term. Fig. 4(b) shows that the maximum temperature difference in the battery pack is less than 7 degrees, with the use of the parallel cooling strategy. Comparison of the two figures reveals that the parallel cooling strategy is much better than the serial cooling strategy.

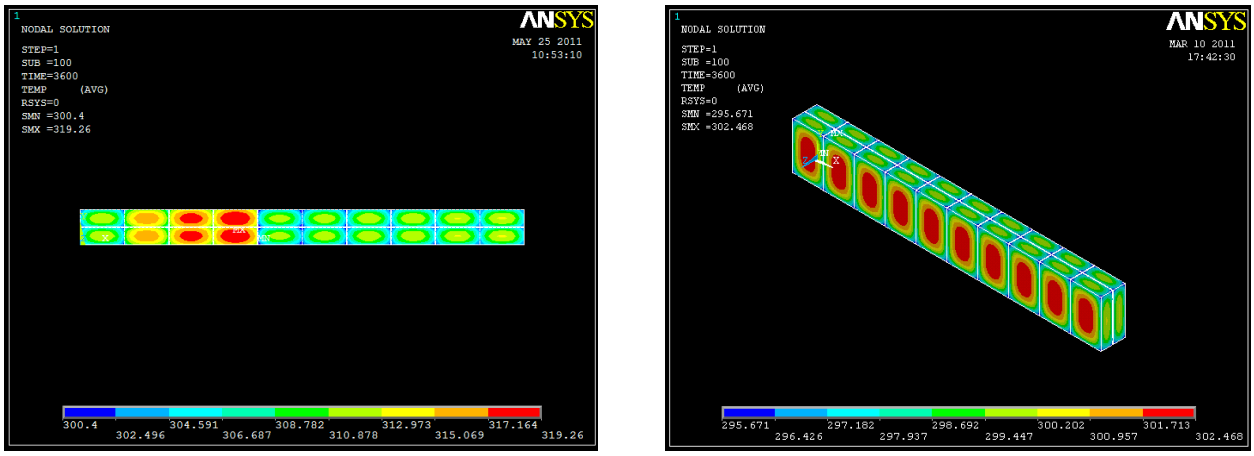

(a) (b)

Fig. 4Temperature distributions in the battery pack with (a) the serial cooling strategy and (b) the parallel cooling strategy. The wind speed is 6 m/s. The convection coefficient is 50 $W/m^2 \cdot K$.

Summary and Conclusions

In this paper, the finite element formulations of the heat conduction equation of the Lithium-ion battery are established for both steady state and transient sate cases. Then the boundary conditions of the battery were discussed and the heat convection coefficients were determined for each surface of the battery. A parametric study was developed to investigate and optimize the temperature distribution in the battery. Finite element results indicate that a rectangular shape battery should be chosen to minimize the temperature difference in the battery. Results also revealed that a slower discharge rate needs to be selected to not only lower the temperature inside the battery, but make the temperature distribution in the battery as uniform as possible. Finally, the Li-ion battery pack was investigated and different cooling strategies were studied. Investigation indicates that the parallel cooling should be chosen to accelerate the heat dissipation and minimize the temperature difference in the battery pack. To acquire more accurate results on the temperature distribution in each battery and the entire battery pack, much more sophisticated finite element models need to be established to simulate the real structure inside the battery.

Acknowledgment

The research presented in this paper was supported by Shenzhen Institutes of Advanced Technology, Chinese Academy of Sciences.

References

[1] M. Einhorn, , W. Roessler; and J. Fleig: Improved performance of serially connected Li-ion batteries with active cell balancing in electric vehicles. *IEEE Transactions on Vehicular Technology*, Vol. 60, No. 6, p 2448-2457, July 2011.

[2] T. M. Bandhauer, S. Garimella, and T. F. Fuller: A critical review of thermal issues in lithium-ion batteries. *Journal of the Electrochemical Society*, Vol. 158, No. 3, p R1-R25, 2011

[3] C. P. Guerrero, J.-S. Li, S. Biller, and G.-X. Xiao: Hybrid/electric vehicle battery manufacturing: The state-of-the-art, *2010 IEEE International Conference on Automation Science and Engineering*, p 281-286, 2010.

[4] J. P. Holman: *Heat Transfer*, p. 4, ninth edition, McGraw-Hill (2002).

[5] R. D. Cook, D. S. Malkus, M. E. Plesha and R. J. Witt: *Concepts and Applications of Finite Element Analysis*, p. 464-466, fourth edition, John Wiley (2001).

Keywords Index

A

Ab Initio Calculation 205
ADAMS 186
Adaptive 190
Adaptive Control 177
Aero-Generator 8
Air Flow 103
Analytic Hierarchy Process (AHP) 298
Anodization 210
Anthropomorphic 293
Anti-Fuse 231
Approximate Root 311
AT89S52 320
Au Embrittleness 267
Au Plating 267
Automated Storage and Retrieval System (AS/RS) 33
Automatic Identification 146

B

Ball System 134
Bending Capacity 157
Block Type 227
Boiler Materials 53
Break Strength 41
BST 231

C

CALPHAD 272
Chaos Control 115
Chaos Synchronization 115
Chaotic Analysis 122
Chattering 190
Coating 255
Codoping 205
Combat Effectiveness 298
Condition Monitoring 161
Control System Structure 165
Correlation Dimension 122
Corrosion Resistance 210
Crack 58
Critical Current 220

D

Damping Force 311
Design 320
Dimer Codopant 205
Dip-Coating 251
Dopant Energy Level 205
Double-Shell Charges 3
Drag Reduction 315
DSP 109
dSPACE Real-Time Emulator 15
Dual Clutch Transmission 95
DV-Xα 205
Dynamic Evolution Control 286
Dynamic Model Downloading 15
Dynamical Walking 165

E

Earthquake Response 196
Elastic Modulus 41
Electric Field Sensor 235
Electric Vehicle (EV) 20, 87
Electronic Structure 205
Electrostriction 235
Evaluation 272
Evaporation Cooling 103

F

Failure Analysis 304
Fault Tree Analysis (FTA) 304
Faults Diagnosis 161
FEA 58
Fiber Bragg Grating 235
Finite Element Analysis (FEA) 138
Finite Element Method (FEM) 130, 324
Finite Element Model (FEM) 196
Finite-Time 115
Flame Sensor 320
Fluid-Structure Interaction (FSI) 130
Fuel Cell Hybrid Vehicle 286
Functionally Graded Materials 68
Fuzzy Synthetic Evaluation 298

G

Gas Pipeline 304
Gear Ratio Optimization 20

H

Herschel-Bulkley Model 311
High Temperature Structural Materials 251
High Velocity Impact 3
High Vertical Vessels 173
Humanoid Robot 165
Hydraulic Excitation Force 130
Hydrodynamic Force 27
Hydrogen Absorption 80
Hydrogen Distribution 80

I

Image Processing 109
Impact Driven Method 63
Impedance Control 177
Impinging Stream 122
Index Loss 220
Intelligent Control 281
Inverter 8
Ion-Bonding Model 272

K

Kinematic Analysis 293
Kolmogorov Entropy 122

L

LabVIEW 161
Large Eddy Simulation (LES) 315
Laser Glass 245
Laser Weapon System 298
Life Prediction 241
Linearization 46
Lithium-Ion Batteries 324
Low Frequency 151
LS-DYNA 74
Lyapunov Exponents 122

M

Magnesium Alloy 210
Magnetorheological Damper 311
Manipulation 293
Matlab 95
Maximum Bending Moment 173
Mercury Attack 267
Mica Paper 215
Miedema Model 272
Mode 196
Mode Shape 58
Modifier 215
Modulated Infrared Sensor 146
Moisture 80
Multi-Arc Ion Plating 255
Multivariable 134

N

N-Value 220
Nanometer Emulsion 227
Nanometer Paint 227
Natural Frequency 58
Non-Newtonian Liquid 63
Nonlinear 134
Nonlinear Fuzzy Comprehensive Assessment 304
Normalized Displacement 53
Numerical Analysis 74
Numerical Simulation 27, 95

O

Oblique Motion 27
Oil Pipeline 304
Operating Status Monitoring 15
Optical 245
Optimization 33
Overload Control 190
Oxidation 251
Oxidation Resistant Coating 251

P

Paper Bonding 41
Paper Break 41
Particle Swarm Optimization Algorithm (PSO) 20, 33
Performance 255
Performance Analysis 138
Photoelectric Sensor 320
PID 146
Plain Wall System 157
Plate System 134
PMSM 87
Point to Point Control 134

Predictive Control 146
Pulse Bias 255
Pure Electric Vehicle 324
PZT 231

R

Rare Earths Element 210
Rehabilitation Training 177
Reinforced Concrete Capacity 157
Response Spectrum Method 196
Riblet 315
Robot 186
Robot Fish 260
Robot Hand 293
Rotating Cylinder 68
Rotating Disk 68

S

S12 MCU 146
Scientific Computation 122
Selective Plating 267
Semiconductor 205
Sensor 241
Sensor Fusion 165
Serial-Port Communication 15
Shadowgraph 63
Shallow Junction 205
Shape Memory Alloyt 260
Shear Punch Test 53
Shear Stress 53
Shock Initiation 3
Silicon 205
Silicon Pressure 241
Simulation 8, 46, 186, 293
Simulation of Aerocraft Attitude 15
SIMULINK 8
Single Chip Microcomputer (SCM) 281
Sliding Mode Control 286
Slotted Shell 151
Small Size 151
Small Specimen Testing 53
Smart Cars 281
SOPC 87
Static/Dynamical Behavior 138
STC89C52 281
Stereo Vision 109
Stiffness 46
Strain Rate Effects 74
Strength 215
Supersonic Jet 63
Support Vector Regression (SVR) 241
Surface Modification 215
Suspension 46

T

Taylor Vortex 103
Temperature Field 95
Termianal Sliding Mode 190
Thermal 245
Thermal Analysis 324
Thermodynamic Properties 272
Thermoelasticity 68
Three-Axis Turn Table 15
Time Delay Control 286
Titanium Weld Joints 80
Tombstone 267
Track Control 134
Transducer 151
Turbo-Generator 103
Turbulence Control 315

U

U-Shaped Rail 33
UHV 196
ULSI 205
Ultimate Tensile Stress 53
Underwater 260
Underwater Explosion Loading 74

V

Variable Structure Systems 190
Vibration 58
Vibration Analysis (VA) 161
Vibration Exciter 130
Virtual Prototype 186
Viscous Flow 27
Visual Instruments 161

W

Walking Robots 177
Weibull Distribution 220
Weight 173
Welding Atmosphere 80
Wet Clutch 95
Wind Load 173

Wind Turbine Gearbox 138

Y

Yield Strength 41
Ytterbium 245

Authors Index

B

Bazrafshan, E. 74, 80
Bi, S. 165
Biswal, B.B. 293

C

Cai, L.S. 320
Cao, Z.M. 272
Chen, S. 151
Chen, W.T. 251
Chen, X.M. 315
Cheng, X.S. 20, 95
Chien, K. 251
Cui, L.G. 281

D

Das, H.C. 58
Di, J.J. 196
Du, G.W. 272
Du, H. 46

F

Fan, H.M. 186
Fan, L.D. 245
Fan, Y.J. 161

G

Gao, H. 251
Gao, J.S. 103
Gu, G.B. 103
Gu, Q. 20, 95
Gu, X.L. 267
Guo, A.G. 138
Guo, L.H. 298
Guo, Y. 161

H

Harada, H. 251
Hayafuji, Y. 205
He, L. 320
He, P.C. 190
He, Y.F. 231
Huang, P.H. 260
Huang, Y.B. 33

I

Illias, S. 210
Ismail, K.A. 210

J

Javadi, M. 68
Jia, L.S. 190
Jing, W. 138

K

Kasamnimitporn, C. 63
Kawanishi, H. 205
Keong, C.K. 157
Khorshidvand, A.R. 68
Kim, Y.B. 286
Koohsar, A.A.S. 74, 80

L

Lan, Y. 151
Li, H. 298
Li, K.E. 115
Li, L. 134
Li, P. 231
Li, R.H. 315
Li, X. 220
Li, Y. 95
Lin, H. 46
Lin, M. 281
Lin, W. 315
Liu, H. 33
Liu, H.W. 235
Liu, P. 267
Liu, S.P. 215
Liu, X. 3, 95
Liu, X.G. 267

M

Ma, C.Z. 227
Matthujak, A. 63
Miao, L.X. 130
Min, H.Q. 165
Mo, H.X. 165

N

Nanda, J. 58
Nasereddini, S.M.S. 74, 80
Nooraizedfiza, Z. 210

P

Parhi, D.R. 58
Parida, P.K. 293
Pianthong, K. 63
Prakash, R.V. 53

Q

Qi, F.J. 227
Qi, H. 87
Qian, J.W. 177
Qian, Y.P. 215
Qiao, Z.Y. 272

R

Raju, N. 53
Ramesh, T. 53
Rohim, R. 157

S

Salleh, M.M. 210
Shen, L.Y. 177
Sittiwong, W. 63
Song, J. 8
Song, Y.F. 122
Sun, Q.G. 196
Sun, S.Q. 134
Sun, W. 138
Sun, X.J. 138
Suresh, S. 53

T

Tang, M.L. 320
Tang, Q.Y. 231
Tang, Y.H. 315
Tao, J.S. 41
Thatoi, D.N. 58, 293
Tian, J. 173

W

Wang, G. 231
Wang, J. 260
Wang, K.P. 272
Wang, W. 320
Wang, Y.L. 190
Wang, Y.S. 95, 220, 235
Wang, Z.W. 15
Wei, J.H. 46
Wen, Z. 177
Wu, B. 324
Wu, C.H. 161
Wu, H.Y. 320
Wu, L.H. 245
Wu, L.T. 251
Wu, N.H. 315
Wu, P.L. 241
Wu, R.T. 251
Wu, X. 304
Wu, X.F. 196

X

Xiao, C.Y. 304
Xie, D.C. 15
Xie, X.D. 231
Xing, H.J. 311
Xing, Y. 33
Xu, G.Q. 324
Xu, X.Y. 304
Xu, Y.H. 115

Y

Yan, C. 227
Yang, P.S. 41
Yang, W.J. 286
Yang, Y.N. 109
Yee, H.M. 157
Yuan, L. 231

Z

Zain, M.Z.M. 210
Zang, X.J. 8
Zeng, Q.H. 15
Zhai, Z.H. 241
Zhan, C.S. 27
Zhang, G.C. 227
Zhang, H.X. 130
Zhang, H.Y. 235
Zhang, J.W. 122
Zhang, Q.M. 3
Zhang, W.G. 190

Zhang, X.W. 215
Zhang, Y.M. 281
Zhang, Y.N. 177
Zhang, Y.R. 220
Zhang, Z.N. 173
Zhao, C.B. 315
Zhao, J. 235
Zhao, X.B. 267
Zhao, Y. 87
Zheng, F. 146
Zheng, L. 324
Zhou, Y.B. 109
Zhou, Y.C. 196
Zhu, Y.B. 215
Zhuang, Z.J. 165
Zou, L.J. 255